Modelling magnetar formation

Paul Barrère

université PARIS-SACLAY

Modelling magnetar formation

Modélisation de la formation des magnétars

Thèse de doctorat de l'université Paris-Saclay

École doctorale n°127, Astronomie & Astrophysique d'Île-de-France (AAIF)
Spécialité de doctorat: Astronomie et Astrophysique
Graduate School : Physique, Référent : Faculté des sciences d'Orsay

Thèse préparée dans l'unité de recherche **Astrophysique, Instrumentation et Modélisation de Paris-Saclay (Université Paris-Saclay, CNRS, CEA)**, sous la direction de **Jérôme GUILET**, Directeur de Recherche et le co-encadrement de **Raphaël RAYNAUD**, Maître de Conférences

Thèse soutenue à Paris-Saclay, le 5 septembre 2024, par

Paul BARRÈRE

Composition du jury

Membres du jury avec voix délibérative

Geoffroy LESUR Directeur de Recherche, Université Grenoble Alpes (IPAG)	Président
Laurène JOUVE Maîtresse de Conférences, HDR, Université Paul Sabatier (IRAP)	Rapporteuse & Examinatrice
Jose PONS Professeur, Universidad de Alicante	Rapporteur & Examinateur
Samuel LANDER Professeur assistant, University of East Anglia	Examinateur
Nanda REA Professeure, Universitat Autònoma de Barcelona (ICE)	Examinatrice

THESE DE DOCTORAT
NNT : 2024UPASP060

université PARIS-SACLAY
ÉCOLE DOCTORALE
Astronomie
et Astrophysique
d'Île-de-France (AAIF)

Titre: Modélisation de la formation des magnétars
Mots clés: Simulations numériques — Magnétohydrodynamique — Dynamo — Sursauts gamma — Étoile à neutrons — Supernovae

Résumé: Les magnétars sont des jeunes étoiles à neutrons isolées qui arborent les champs magnétiques les plus intenses observés dans l'Univers (10^{14}-10^{15} G). Leur dissipation est à l'origine d'un large éventail d'émissions à hautes énergies. Associés à une rotation rapide, les magnétars peuvent être le moteur central d'explosions plus énergétiques que les supernovae à effondrement de cœur classiques, telles que les hypernovae et les supernovae superlumineuses. L'origine du champ magnétique des magnétars est encore une question ouverte, mais qui est cruciale pour comprendre les observations qui leur sont associées. L'amplification du champ magnétique par effet dynamo dans la proto-étoile à neutrons (PNS) est un mécanisme prometteur pour générer des champs magnétiques extrêmes dans les progéniteurs arborant un cœur en rotation rapide. Cependant, il est encore incertain que la fraction de ces progéniteurs soit suffisante pour expliquer l'ensemble de la population des magnétars. En outre, l'observation de rémanents de supernovae associés à des magnétars indique que les magnétars se forment majoritairement dans des supernovae standards, avec des périodes de rotation initiales de la PNS plus lente que 5 ms.

L'objectif principal de cette thèse est alors d'étudier un scénario de formation des magnétars alternatif impliquant un progéniteur en rotation lente. Ici, la rotation de la PNS n'est plus déterminée par celle du progéniteur, mais par l'accrétion du *fallback*, soit la matière initialement éjectée lors de l'explosion et restée liée gravitationnellement à la PNS qui finit par retomber sur la PNS. Le cisaillement déclenche une dynamo dite de Tayler-Spruit, alors que les autres mécanismes dynamos — entretenus par l'instabilité magnétorotationnelle ou la convection — ne peuvent se développer dans cette configuration. En établissant un modèle semi-analytique de ce scénario, nous montrons que des champs magnétiques aussi intenses que celui des magnétars peuvent être générés pour une PNS accélérée jusqu'à des périodes de rotation de $\lesssim 28$ ms. Cette première étude démontre donc la pertinence de notre scénario pour former des magnétars dans des supernovae avec des énergies standards et extrêmes.

Néanmoins, l'existence de la dynamo de Tayler-Spruit est restée longtemps controversée et les modélisations analytiques — établies par Spruit (2002) et Fuller et al. (2019) — reposent sur des hypothèses physiques non-testées. C'est pourquoi nous avons réalisé des simulations numériques 3D d'un modèle simplifié d'intérieur de PNS pour étudier ce mécanisme dynamo. En plus de démontrer pour la première fois l'existence de la dynamo de Tayler-Spruit dans une configuration où la rotation croît avec le rayon, ces simulations mettent en évidence une richesse de comportements dynamiques et de branches dynamos, associées à différentes géométries du champ magnétique, qui n'étaient pas prédites par les modèles analytiques. Nous trouvons aussi que la branche produisant les champs magnétiques les plus forts valident globalement les prédictions de Fuller et al. (2019).

En appliquant l'étude numérique de la dynamo à notre scénario, nous montrons que des dipôles magnétiques de l'ordre de ceux des magnétars classiques sont générés pour des périodes de rotation de $\lesssim 6$ ms. Notre scénario peut donc expliquer la formation des magnétars dans des explosions extrêmes, mais cette nouvelle contrainte est proche de la limite pour former des magnétars dans des supernovae standards, révélant une tension entre notre scénario et les observations. Les simulations montrent aussi que les champs magnétiques formés pour des rotations plus lentes concordent avec les observations de magnétars possédant des dipôles magnétiques plus faibles ($\lesssim 4 \times 10^{13}$ G) tout en arborant une composante non-dipolaire ~ 100 plus intenses. Ce dernier résultat est soutenu par la première étude numérique — menée en collaboration avec A. Igoshev — de l'évolution à long terme d'un champ magnétique généré par la dynamo de Tayler-Spruit dans une croûte d'étoile à neutrons.

université PARIS-SACLAY

ÉCOLE DOCTORALE
Astronomie
et Astrophysique
d'Île-de-France (AAIF)

Title: Modelling magnetar formation
Keywords: Numerical simulations — Magnetohydrodynamics — Dynamo — Gamma ray bursts — Neutron star — Supernovae

Abstract: Magnetars are young isolated neutron stars harbouring the strongest magnetic fields observed in the Universe (10^{14}-10^{15} G). Their dissipation powers a wide range of high-energy emissions. Associated with a fast rotation, magnetars may be the central engine of explosions which are more energetic than classical core-collapse supernovae, such as hypernovae and superluminous supernovae. The origin of magnetar magnetic fields remains an open question, but it is crucial to understand the luminous phenomena they are associated with. Magnetic field amplification through dynamo action in the proto-neutron star (PNS) is a promising mechanism to generate ultra-strong magnetic fields in a progenitor harbouring a fast-rotating core. However, it is still unclear whether the fraction of these progenitors is sufficient to explain the entire magnetar population. Besides, the observation of supernova remnants associated with magnetars indicates that magnetars mostly form in standard supernovae, with initial PNS rotation periods slower than 5 ms.

The main objective of this thesis is then to investigate an alternative magnetar formation scenario involving a slow-rotating progenitor. Here, the PNS rotation is not determined by that of the progenitor but by the accretion of fallback, which is the matter initially ejected by the SN explosion that remains gravitationally bound to the compact remnant and eventually falls back onto its surface. The induced shear triggers the so-called Tayler-Spruit dynamo, while other dynamo processes — driven by the magnetorotational instability and convection — are disfavoured in this configuration. Using a semi-analytical modelling of the scenario, we show that magnetic fields as strong as in magnetars can be generated for a PNS spun up to rotation periods of $\lesssim 28$ ms. This first study demonstrates the relevance of our scenario to form magnetars in supernovae with standard and extreme energies.

Nevertheless, the existence of the Tayler-Spruit dynamo has remained controversial and its analytical models — provided by Spruit (2002) et Fuller et al. (2019) — rely on untested physical assumptions. For these reasons, we performed 3D numerical simulations of a simplified PNS interior to investigate this dynamo mechanism. Beyond demonstrating for the first time the existence of the Tayler-Spruit dynamo in a configuration with a rotation increasing with the radius, these simulations show a richness of dynamical behaviours and dynamo branches associated with different magnetic field geometries, which were not predicted by analytical models. We also find that the branch generating the strongest magnetic fields is in global agreement with the predictions of Fuller et al. (2019).

By applying the numerical study to our scenario, we show that magnetic dipoles of typical magnetars are generated for rotation periods of $\lesssim 6$ ms. Therefore, our scenario can explain magnetar formation in extreme explosions, but this new constraint is close to the limit for magnetar formation in standard supernovae, revealing a tension between our scenario and observations. The simulations also show that magnetic fields formed for slower rotations are consistent with the observations of magnetars displaying weaker magnetic dipoles ($\lesssim 4\times10^{13}$ G) while harbouring a ~ 100 stronger non-dipolar component. This last result is supported by the first numerical investigation — led in collaboration with A. Igoshev — of the long-term evolution of a magnetic field generated by the Tayler-Spruit dynamo in a neutron star crust.

À papi Maurice et à tonton Patou,
qui sont partis rejoindre les étoiles à neutrons.
À toute ma famille, à tous.tes mes ami.es, et à tous les proches,
qui m'ont accompagné de près ou de loin le long de cette aventure,
pour le moins, enrichissante.

Remerciements

Nous sommes une dizaine de jours après la soutenance de cette thèse de doctorat, marquant la fin de cette stimulante aventure scientifique et humaine de trois ans, de huit années d'études, mais aussi le début d'une carrière d'astrophysicien, post-doctorant d'abord et, j'espère, permanent ensuite. Ces lignes, je les écris pour remercier les nombreuses personnes qui m'ont accompagné pendant toute, ou une partie de, ces trois (trop) courtes années.

Premièrement, je te tiens, évidemment, à remercier les (ex-)membres de l'équipe supernovae du LMPA. Tout d'abord, je tiens à exprimer ma profonde gratitude à mes encadrants, Jérôme et Raphaël, dont le soutien indéfectible, la patience, les conseils éclairés ont été essentiels tout au long de ce parcours. Vous êtes devenus des modèles pour moi, que ce soit en termes de savoir et rigueur scientifique, d'humilité, ou d'humanité. C'était un réel plaisir de faire cette thèse avec vous. Je vous suis profondément reconnaissant pour la confiance que vous m'avez accordée pour mener ce projet qui, même s'il était initialement incertain, a donné de beaux résultats astrophysiques et a permis de mettre en avant de la belle physique.

Ensuite, je suis très reconnaissant à Alexis, qui est comme mon grand frère de thèse, qui m'a permis de donner un séminaire (très sportif) au Max Planck à Potsdam, et qui a toujours été très disponible pour discuter de tout et de rien (et de science évidemment !), ce qui m'a bien aidé et rassuré dans les périodes de stress, notamment durant cette intense troisième année. Je suis très content que tu aies été impliqué dans mon travail de thèse, et nous continuerons évidemment, toi, Jérôme, Raphaël, et moi, à collaborer pour continuer à dévoiler les mystères derrière les mécanismes dynamos et les champs magnétiques astrophysiques.

Enfin, je remercie Anne-Cécile, Thierry et Matteo, qui ont été aussi de vrais soutiens pendant cette thèse. Anne-Cécile, ça a été un plaisir de te connaître, je te souhaite le meilleur pour la suite de ta carrière dans l'enseignement. Encore bravo pour l'agrégation (que tu as quand même bien survolé !). Thierry, c'est toujours un plaisir de discuter science avec toi de par tes questions très pertinentes, et de t'écouter parler de SASI. Je serai toujours très admiratif de ton intuition et de ton sens de la physique. D'ailleurs, bravo pour la soumission du premier article de la série *Analytic insight into the physics of SASI* ! Matteo, ça a été un très grand plaisir d'avoir été ton co-bureau. Merci pour ta bonne humeur permanente, tes tiramisus, ton pointeur Logitech Spotlight, d'avoir été le meilleur interprète quand on été en conférence en Italie, de m'avoir donné des conseils pour mon entretien au fellowship au MPA, etc, etc... Je te souhaite le meilleur pour la suite !

Secondly, I wish to thank Laurène Jouve, Jose Pons, Nanda Rea, Sam Lander, and Geoffroy Lesur for constituting my PhD jury despite your busy agendas during the beginning of the academic term. Thank you for reading my manuscript and attending my defense. It was a real pleasure for me to show you my work and I hope it will bring further discussions and collaborations in the future! I am grateful to Antoine Strugarek and Jérôme Novak for following the evolution of my work and for the discussions during the committee meetings. I also thank the different persons I have been collaborating with: Hans-Thomas Janka, Florentin Daniel, Christophe Gissinger, Ludovic Petitdemange, Andrei Igoshev, Toby Wood, Rainer Hollerbach, and Basile Gallet.

Je souhaite particulièrement remercier François Rincon et Thierry Roudier qui m'ont encadré pendant mon premier stage d'astrophysique en L3 à l'IRAP. Cette expérience m'a fait

découvrir une fascination pour la dynamique des fluides astrophysique. François, je te suis aussi très reconnaissant pour m'avoir donné le goût de la physique derrière les problèmes de dynamo et de turbulence. Je te souhaite une bonne reconversion dans le domaine de l'écologie théorique. Thierry, je souhaite une bonne retraite pleine d'observations du Soleil avec ton nouveau coronado !

Troisièmement, je souhaite aussi remercier les autres personnes que j'ai côtoyées aux DAp. Je pense d'abord aux autres membres du LMPA. Merci aux permanents : Patrick, pour les discussions très intéressantes sur la science, la politique, et l'écologie, Matthias, pour tes supers cours de mécanique des fluides en M2 et de m'avoir fait découvrir le stage/thèse proposé par Jérôme, et enfin Ugo pour ton soutien et toutes ces discussions à la cafêtéria et dans le RER B. Merci également à Noé, Tine, Valentin, Gabriel, Tung, Maxime, Adnan, et Jack pour ces petites pauses — d'à peine une heure — à la cafêtéria pour sortir la tête du guidon et se détendre un peu. Merci particulièrement à Adnan qui a été un gros soutien moral durant ces trois ans (notamment vers la fin de la thèse où c'était très intense émotionnellement pour moi) et à Jack pour toutes ces discussions politiques et les manifs que l'on a faites ensemble.

Je remercie aussi les autres doctorant.es du DAp avec j'ai eu la chance de discuter de tout et de rien : Leïla (merci pour ton implication à raviver les interactions entre doctorants après la période COVID), Nicolas, Fabian, Clara, Tristan, Noa (j'espère que tu as enfin une clef de bureau à l'UPC), et Maxime (merci pour les marches au fin fond de la région parisienne). Enfin, un grand merci à l'équipe administrative — Christelle Duval, Laura Ricchi, Virginie Katra, et Chrissy Gigan — qui a été (très) patiente avec moi, notamment pour faire les ordres de mission.

Enfin, merci à Jérémy Neveu et Chi-Tuong Pham pour m'avoir permis d'enseigner les méthodes numériques pour les L1 durant les trois années de thèse.

Finalement, je remercie énormément mes proches qui ont contribué à rendre mes années de thèse plus agréables. Tout d'abord, mes amis, que je connais soit depuis l'année de M2, Thomas, Corentin, Gaël, Romain, Enya, Marion, Marie, Nathan, Alexandre, Lucas, Antoine, soit depuis la L3, Izia, Anna, et Jean-Baptiste, soit depuis la seconde, Justine (que je connais depuis bien plus longtemps), Adrien, Thomas, Julia, Jason, Lisa, Jade, Sarah, soit depuis le collège, Célian, Valentin, et Simon, soit depuis la maternelle, Mathias, Thomas, et Adrien (sans oublier les compagnes Marion, Lucile, et Juliette, qui ont rejoins la bande). Je remercie spécialement qui a fait le meilleur pot de thèse de l'histoire des pots de thèse et que je suis très heureux d'avoir retrouvé à Paris.

Enfin, je remercie chaleureusement ma famille : mes parents, ma sœur (qui commence sa thèse), mes grands-parents, mes oncles et tantes, mes cousins et cousines. Vous avez été un soutien formidable, non seulement tout au long de cette thèse, mais aussi tout au long de ma vie. Je te remercie tout particulièrement, toi, Juliette, qui a toujours été là pour me supporter, même dans les moments éprouvants. Merci à toi d'être dans ma vie et de m'apporter autant de joie au quotidien. Je tiens aussi à dédier cette thèse à ceux qui sont partis — bien trop tôt — durant ces trois dernières années : papi Maurice et tonton Patrick. Même si vous nous manquez terriblement, je sais que vous nous regardez maintenant depuis les étoiles (à neutrons).

Look again at that dot. That's here. That's home. That's us. On it everyone you love, everyone you know, everyone you ever heard of, every human being who ever was, lived out their lives. The aggregate of our joy and suffering, thousands of confident religions, ideologies, and economic doctrines, every hunter and forager, every hero and coward, every creator and destroyer of civilization, every king and peasant, every young couple in love, every mother and father, hopeful child, inventor and explorer, every teacher of morals, every corrupt politician, every "superstar," every "supreme leader," every saint and sinner in the history of our species lived there-on a mote of dust suspended in a sunbeam.

The Earth is a very small stage in a vast cosmic arena. Think of the endless cruelties visited by the inhabitants of one corner of this pixel on the scarcely distinguishable inhabitants of some other corner, how frequent their misunderstandings, how eager they are to kill one another, how fervent their hatreds. Think of the rivers of blood spilled by all those generals and emperors so that, in glory and triumph, they could become the momentary masters of a fraction of a dot.

Our posturings, our imagined self-importance, the delusion that we have some privileged position in the Universe, are challenged by this point of pale light. Our planet is a lonely speck in the great enveloping cosmic dark. In our obscurity, in all this vastness, there is no hint that help will come from elsewhere to save us from ourselves.

The Earth is the only world known so far to harbor life. There is nowhere else, at least in the near future, to which our species could migrate. Visit, yes. Settle, not yet. Like it or not, for the moment the Earth is where we make our stand.

It has been said that astronomy is a humbling and character-building experience. There is perhaps no better demonstration of the folly of human conceits than this distant image of our tiny world. To me, it underscores our responsibility to deal more kindly with one another, and to preserve and cherish the pale blue dot, the only home we've ever known.

Carl Sagan, *Pale Blue Dot: A Vision of the Human Future in Space*

Contents

List of Figures

List of Tables

List of acronyms
Liste des acronymes

NS	Neutron star (*Étoile à neutrons* in French)
PNS	Proto-neutron star (*Proto-étoile à neutrons* in French)
PSR	Pulsar (*Pulsar* in French)
SGR	Soft gamma repeater (*Sursauteur gamma mou* in French)
AXP	Anomalous X-ray pulsar (*Pulsar X anormal* in French)
XINS	X-ray isolated neutron star (*Étoiles à neutrons X isolées* in French)
BNS	Binary neutron star (*Binaires d'étoiles à neutrons* in French)
SN	Supernova (*Supernova* in French)
HN	Hypernova (*Hypernova* in French)
SLSN	Super-luminous supernova (*Supernova super-lumineuse* in French)
GRB	Gamma-ray burst (*Sursaut gamma* in French)
FRB	Fast radio burst (*Sursaut radio rapide* in French)
GW	Gravitational wave (*Onde gravitationnelle* in French)
MHD	Magnetohydrodynamics (*Magnétohydrodynamique* in French)
EMF	Electromotive force (*Force électromotrice* in French)
MRI	Magnetorotational instability (*Instabilité magnétorotationnelle* in French)
RMS	Root mean square (*Moyenne quadratique* in French)

Several physical quantities
Diverses quantités physiques

Gravitational constant	$G = 6.674\,30(15) \times 10^{-11}\,\mathrm{m^3\,kg^{-2}\,s^{-1}}$
Boltzmann constant	$k_B = 1.380\,649 \times 10^{-23}\,\mathrm{J\,K^{-1}}$
Light velocity in vacuum	$c = 299\,792\,458\,\mathrm{m\,s^{-1}}$
Electron-volt	$\mathrm{eV} = 1.602\,176\,634 \times 10^{-19}\,\mathrm{J}$
Erg	$\mathrm{erg} = 10^{-7}\,\mathrm{J}$
Solar mass	$M_\odot = 1.988\,47 \times 10^{30}\,\mathrm{kg}$
Solar radius	$R_\odot = 6.957 \times 10^{8}\,\mathrm{m}$
Light-year	$\mathrm{ly} = 9\,460\,730\,472\,580\,800\,\mathrm{m}$
Parsec	$\mathrm{pc} = 3.09 \times 10^{16}\,\mathrm{m}$
Radius	r
Time	t
Lenght-scale	d
Time-scale	τ
Velocity	v
Magnetic field	B
Density	ρ
Temperature	T, ΔT
Pressure	P
Kinematic viscosity	ν
Thermal diffusivity	κ
Resistivity	η
Angular rotation frequency	Ω, $\Delta\Omega$
Rotation period	$P \equiv 2\pi/\Omega$
Gravitational acceleration	g
Thermal expansion coefficient	α
Brunt-Väisälä frequency	$N \equiv \alpha g \Delta T / d$
Ekman number	$E = \nu/(d^2\Omega)$
Thermal Prandtl number	$Pr = \nu/\kappa$
Magnetic Prandtl number	$Pm = \nu/\eta$
Rayleigh number	$Ra = \alpha g \Delta T d^3/(\nu\kappa)$
Rossby number	$\Delta\Omega/\Omega$
Elsasser number	$\Lambda = B^2/(4\pi\rho\eta\Omega)$

General introduction

Étendez vous sur le sol, la nuit, loin des lumières. Fermez les yeux.
Après quelques minutes, ouvrez les sur la voûte étoilée...Vous aurez le vertige.
Collé à la surface de votre vaisseau spatial, vous vous sentirez dans l'espace.
Goûtez en longuement l'ivresse.
Hubert Reeves, *Patience dans l'azur. L'évolution cosmique*

The Universe, through its elusive richness, has never ceased to spur the curiosity of astrophysicists, amateur astronomers, and anybody who takes the time to wander into the beauty of a clear night sky. The coupled progress in fundamental sciences and technology has allowed for a significant advancement in the observation and comprehension of the immense diversity of astrophysical objects from planets to galaxy clusters. Especially, the theoretical speculations made by Landau (1932) and Baade & Zwicky (1934) and the discovery of the radio signal originally named *Little Green Men-1* — because the extreme regularity of the signal could be a sign of extraterrestrial intelligence — by Jocelyn Bell (Hewish et al., 1968) paved the way for the study of strange objects, called neutron stars (NSs). These stars of about twenty-five kilometres in diameter are more massive than the Sun, which makes them extremely dense objects. Indeed, a teaspoon of matter from a NS would be at least as heavy as 200,000 Eiffel Towers!

There is now a consensus that NSs are formed during the explosion of stars of at least eight solar masses, which are called core-collapse supernovae (CCSNe). These explosions happen when the iron core of the progenitor star reaches a critical mass above which it collapses under the gravitational force. The collapse stops when the central object reaches the nuclear density of $4 \times 10^{14}\,\mathrm{g\,cm^{-3}}$ due to the strong nuclear force repulsion between the neutrons. The newly born proto-neutron star (PNS) is formed. The matter that is still collapsing forms a stalling accretion shock around the compact object. The schock is heated by the absorption of neutrinos. The induced gain of energy makes the shock grow until it reaches the stellar outer layers to make the whole star explode. This formation scenario is confirmed by the observation of NSs found in the centre of the remnant expelled from the progenitor star (example of the Crab nebula in Fig 1). These explosions can be easily observed in other galaxies because it is more luminous than the entire host galaxy, i.e. as luminous as tens of billions of Suns. One to three supernovae per century are expected to occur in the Milky Way, but the last one observed in our Galaxy is SN 1604 by Johannes Kepler in 1604. This can be explained by the fact that the observations are impeded by the Milky Way plane.

The multiplication of observations with terrestrial observatories in the radio domain (e.g. Arecibo, Green Bank Telescope, LOFAR, MeerKAT) and space telescopes in the X-ray (e.g. ROSAT, Chandra X-ray observatory, XMM-Newton, NuSTAR, NICER) and γ- ray domains (e.g. Fermi, Integral) showed a very rich variety of electromagnetic events associated with NSs, which shows a real a NS zoo (a zoo in which they can not be exploited of course). The majority of NSs are named radio pulsars because they emit a periodic radio signal like a lighthouse from their magnetic poles. The exact mechanism behind this emission is still debated, but

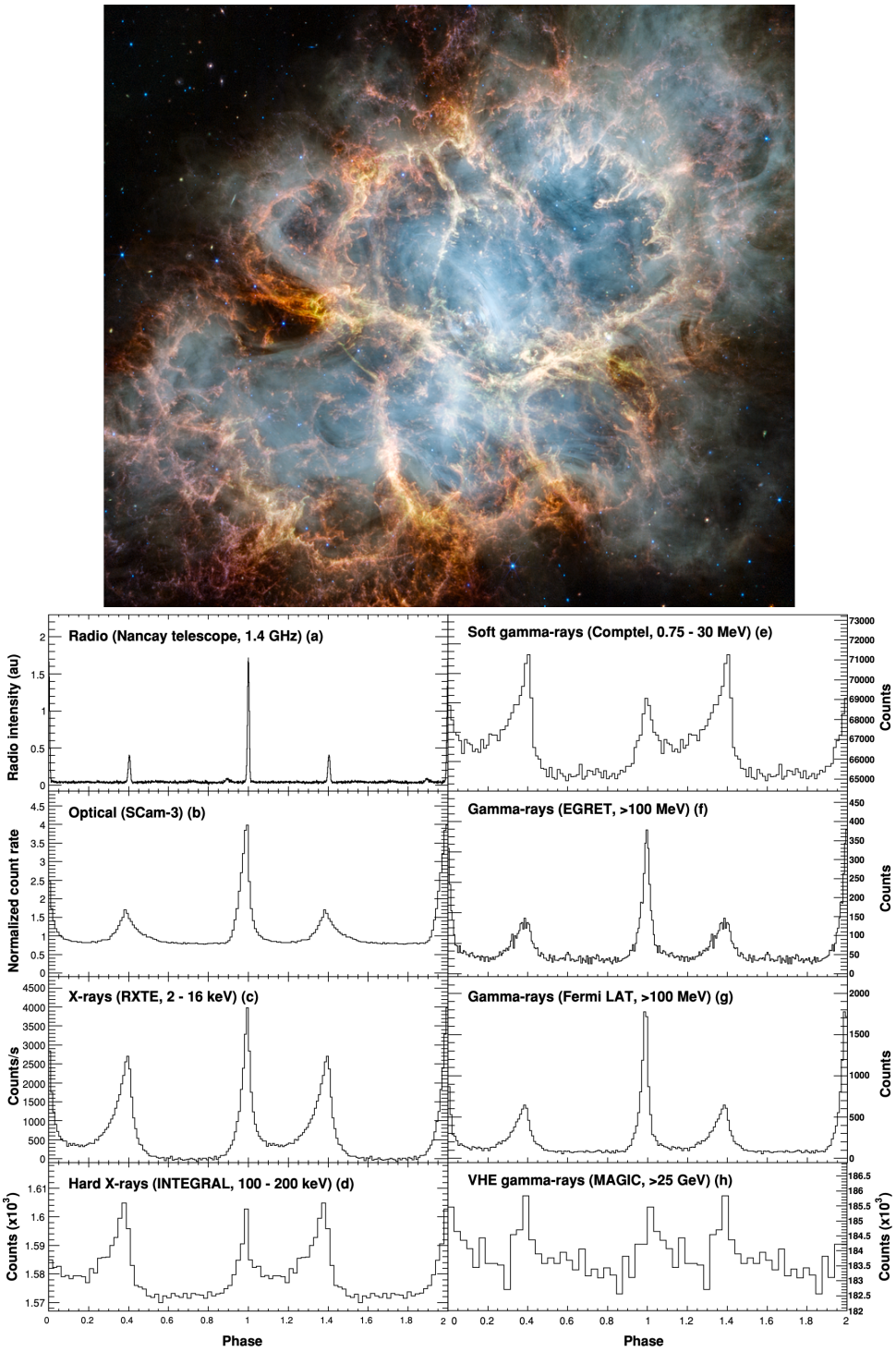

Figure 1 — Top: Crab nebula observed by JWST (Credit: NASA, ESA, CSA, STScI, Tea Temim (Princeton University)). Down: Crab pulsar signal in different wavelengths (Abdo et al., 2010).

we know it is due to the spin-down of the NS by a strong magnetic dipole of $10^{11} - 10^{13}\,\mathrm{G}$ at the surface, which, if misaligned with the rotation axis, produces the observed regular pulsation (as seen in the plot of Fig. 1). Some pulsars evolve in binary systems, in which they can acquire fast rotation periods of a few milliseconds due to the accretion of matter from a companion star. Several X-ray emissions can also be associated with NSs: (i) thermal emission from young and hot NS called central compact objects (CCOs) near the centre of some supernova remnants, (ii) emission due to accretion around NSs called accreting X-ray pulsars, and (iii) purely thermal emission from the surface of radio-quiet NSs called X-ray dim isolated NSs (XDINS), which are located close to the Earth ($\lesssim 500\,\mathrm{pc}$).

During this thesis, we focused on another type of NS called magnetars. These objects emit a wide variety of high-energy signals and gather two classes of NSs: the Soft Gamma Repeaters (SGRs) and the Anomalous X-ray Pulsars (AXPs). Their signals are too energetic to be caused by the mechanisms that were previously mentioned. They are actually produced by the dissipation of strong magnetic fields, which explains the name "magnetar" (Duncan & Thompson, 1992). By measuring the rotation period and its associated period derivative, we can infer that their surface magnetic dipole ranges between $10^{14} - 10^{15}\,\mathrm{G}$, which is about 100 times stronger than in typical pulsars. This makes magnetars the astrophysical objects harbouring the strongest magnetic fields in the Universe! These magnetic fields may be the relic of the progenitor iron core magnetic field, or generated during the PNS stage, i.e. within a few seconds after the collapse of the progenitor core. In combination with a rotation period of a few milliseconds, the proto-magnetar may be the central engine of explosions that are more energetic than typical CCSNe. While the typical CCSNe have a kinetic energy of $\sim 10^{51}\,\mathrm{erg}$ and a luminous energy of $10^{49}\,\mathrm{erg}$, the kinetic energy of extreme explosions such as hypernovae is $\sim 10^{52}\,\mathrm{erg}$ and the luminous energy of superluminous supernovae (SLSNe) is $10^{51}\,\mathrm{erg}$. The mechanism behind these events may be the injection of rotational energy in the ejecta after its extraction by the strong magnetic fields. This constitutes the millisecond magnetar model, which is often used to interpret the light curves of these explosions. Thus, magnetars are a crucial research topic in high-energy astrophysics. Two central astrophysical questions emerge from the observation of magnetars:

(i) Why do some NSs harbour stronger magnetic fields than others?

(ii) Which mechanisms can form such strong magnetic fields?

A first type of formation scenario invokes the conservation of magnetic flux during core collapse to amplify the magnetic field. In these "pre-collapse" scenarios, the population of pulsars and magnetars would therefore be explained by the diversity of iron core magnetic fields in massive stars (Ferrario & Wickramasinghe, 2006). Another type of scenario, however, suggests that the magnetic fields are generated by dynamo action in the early PNS stage (Thompson & Duncan, 1993). The cases of the convective dynamo and the magnetorotational instability (MRI)-driven dynamo have been studied numerically (e.g. Raynaud et al., 2020, 2022, Reboul-Salze et al., 2021, 2022) and have been shown to produce very strong magnetic fields in fast rotating PNSs. In these "post-collapse" scenarios, the dichotomy between pulsars and magnetars originates from the capacity of the PNS interior to trigger an efficient dynamo action. However, these types of scenarios rely on their respective assumptions of strongly magnetised ($\sim 10^{10} - 10^{11}\,\mathrm{G}$) and fast rotating progenitor iron core (rotation period $P_{\mathrm{core}} \sim 10 - 60\,\mathrm{s}$), which are still poorly constrained by observations and stellar evolution models. This leads to the central question of this thesis:

(iii) Can magnetars form from weakly magnetised and slow-rotating progenitors?

To investigate this problem, we propose a new magnetar formation scenario involving the matter falling back onto the PNS after the explosion and another dynamo mechanism called the Tayler-Spruit dynamo. The initial PNS is supposed to be weakly magnetised and slowly rotating. About $\sim 10\,\mathrm{s}$ after the explosion, a part of the SN fallback is asymmetrically accreted onto the PNS surface, which spins its rotation up to periods $P \lesssim 10\,\mathrm{ms}$. This phase creates differential rotation in the PNS interior with the surface rotating faster than the core. While other dynamo mechanisms are disfavored, we argue that the differential rotation triggers the development of the Tayler-Spruit dynamo to amplify and finally maintain magnetar-like magnetic fields. Similarly to the MRI-driven dynamo, the Tayler-Spruit dynamo is driven by large-scale differential rotation in a stable stratified flow and an instability of the toroidal magnetic field, called Tayler instability. This mechanism is often invoked to efficiently transport angular momentum in stellar radiative zones. Finally, the dynamo amplifies and finally maintains magnetar-like magnetic fields. The specific questions stemming from this new scenario structure this manuscript after the introductive Part I (Chaps. 1–4):

- **Can the Tayler-Spruit dynamo form strong enough magnetic fields? If yes, is the amplification fast enough and in which range of fallback accreted mass? Can this scenario be applied to BNS mergers?** In Chap 5, we develop a semi-analytical model of our new magnetar formation scenario and demonstrate that magnetars can be formed for accreted fallback masses higher than one-hundredth of solar mass. However, this model relies on several assumptions on the non-linear processes underlying the dynamo action.

- **Can we find the Tayler-Spruit dynamo in numerical simulations? If yes, how is it impacted by different fluid properties? And what is the magnetic field geometry?** The numerical part of this work consists of several investigations of the Tayler-Spruit dynamo in three-dimensional spherical numerical simulations. The two first chapters provide some of the first numerical investigations on the Tayler-Spruit dynamo. We explore the impact of the large-scale shear (Chap. 6) and of the thermal stratification (Chap. 7). These studies led to the discovery of bistability between two distinct Tayler-Spruit dynamos which differ by the intensity and the geometry of their magnetic field. We called them the *hemispherical* and the *dipolar* Tayler-Spruit dynamo branches. The latter is shown to be promising to form magnetars. Finally, we analyse the growth of the magnetic field from a mean-field point of view and model the rich variety of the Tayler-Spruit dynamo behaviours as a two-mode dynamical system (Chap. 8). While the dynamo is shown to produce magnetar-like magnetic fields, we must investigate whether these fields remain strong enough to produce the observed magnetar X-ray activity after $10^3 - 10^6\,\mathrm{yr}$.

- **How does this newly formed magnetic field evolve in the cooling PNS/NS? Can we reproduce the observational characteristics of magnetars?** In Chap 9, we present a recent work done in collaboration with Andrei Igoshev in which we numerically investigate the relaxation of a Tayler-Spruit dynamo-generated magnetic field in a realistic NS structure. This evolution study is the first to use a dynamo-generated magnetic configuration as an initial condition and demonstrates that the 'dipolar' Tayler-Spruit dynamo can explain the formation of magnetars harbouring a weak magnetic dipole.

This investigation is crucial to understand magnetar formation since we make the link for the first time between the PNS and magnetars.

I

Scientific problem

1

The observation of magnetars

Contents

We are all in the gutter, but some of us are looking at the stars.
Oscar Wilde, *Lady Windermere's Fan*

Magnetars are neutron stars (NS) harbouring the strongest magnetic fields in the Universe, whose dissipation powers some of the most luminous events of the Milky Way. In combination with a millisecond rotation, newly formed magnetars are suspected to be the central engine of the most extreme extragalactic phenomena. The central role of magnetars in the field of high-energy astrophysics makes it a crucial object to investigate. We will start by introducing the historical context behind the observation of magnetar (Sect. 1.1). Then, we will situate magnetars among the whole population of Galactic NSs (Sect. 7.3), and explain how they could power extragalactic luminous events (Sect. 1.3).

1.1 . Historical context

1.1.1 . An unusual γ-ray burst source

The observation of the NSs called magnetars is historically bound to the emergence of spatial high-energy astronomy in the 70's. Indeed, the first reported emission of NS later understood as a magnetar was observed among several γ-ray bursts (GRBs), which are extremely energetic explosive, very luminous, and prompt events detected in the γ-ray spectral domain. These events are usually associated with cataclysmic such as the merger of two NSs or a black hole and a NS, and a very energetic explosion of a massive star, called a supernova (SN). However, some sources produce several short bursts. The first repetitive source was detected in the direction of the Large Magellanic Cloud (LMC) by the Konus detectors aboard the Venera 11 and Venera 12 spacecrafts (Mazets et al., 1979a,c).

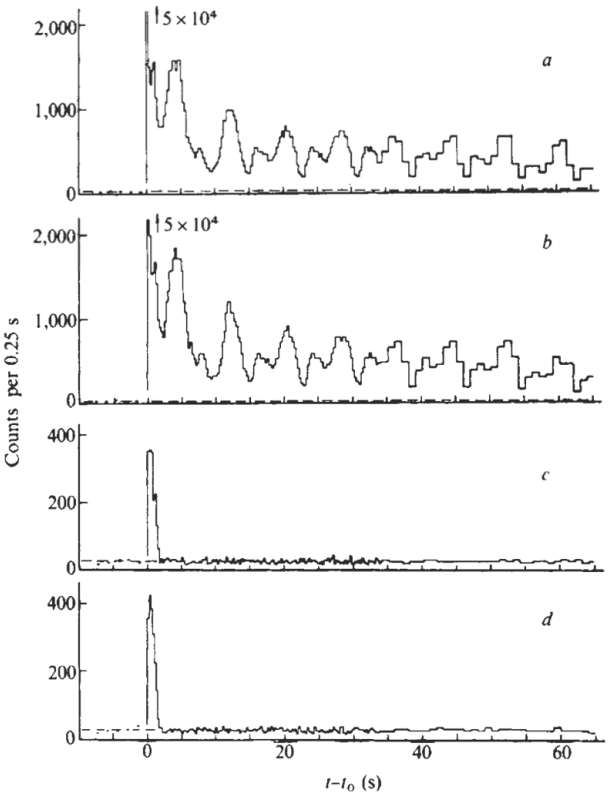

Figure 1.1 — Time structure of the bursts in the energy range $50-150\,\mathrm{keV}$. (a) 5 March 1979, Venera 12; (b) 5 March 1979, Venera 11; (c) 6 March 1979, Venera 12; (d) 6 March 1979, Venera 11. Dashed line indicates background count rate. Points before t_0 show previous history of the bursts. *Figure adapted from Mazets et al. (1979a).*

The observed light curves, i.e. the time evolution of the number of photons detected per time unit, are displayed in Fig. 1.1, and show two bursts detected on the 5 (curves *a* and *b*) and 6 (curves *c* and *d*) March 1979, respectively. In addition to the repetitive character, the observed $8\,\mathrm{s}$ periodic pulsations in the tail of the two first light curves and the association to the SN remnant N49 (confirmed by Cline et al., 1982) strongly suggest the NS nature of the source. The $8\,\mathrm{s}$-pulsations are interpreted as a NS rotation period of $8\,\mathrm{s}$, which is much longer than typical pulsar periods of $0.1-1\,\mathrm{s}$. The spectra associated with the bursts, i.e. the signal intensity as a function of the photon energy, are similar to those associated with some NSs emitting in the X-ray domain and are "softer" than those associated with GRBs, i.e. the detected photons have a lower energy. This source (and others) will then be named *Soft Gamma Repeaters (SGR)*.

Following the observation of this source, now labelled SGR 0526–66[1], another source sharing similar characteristics, now referred as SGR 1900+14, is reported (Mazets et al., 1979b, 1981), whose rotation period of $5.2\,\mathrm{s}$ is not measured before the new observation of bursts by XMM-Newton (Mereghetti et al., 2006). The existence of this new class of NS is accepted after the detection of a third source, SGR 1806–20 (Laros et al., 1986), which

[1]The murky names used to identify NSs consist of an abbreviation, which can be the NS class for instance (or something more mysterious), and the numbers represent the equatorial celestial coordinates in the reference frame J2000.

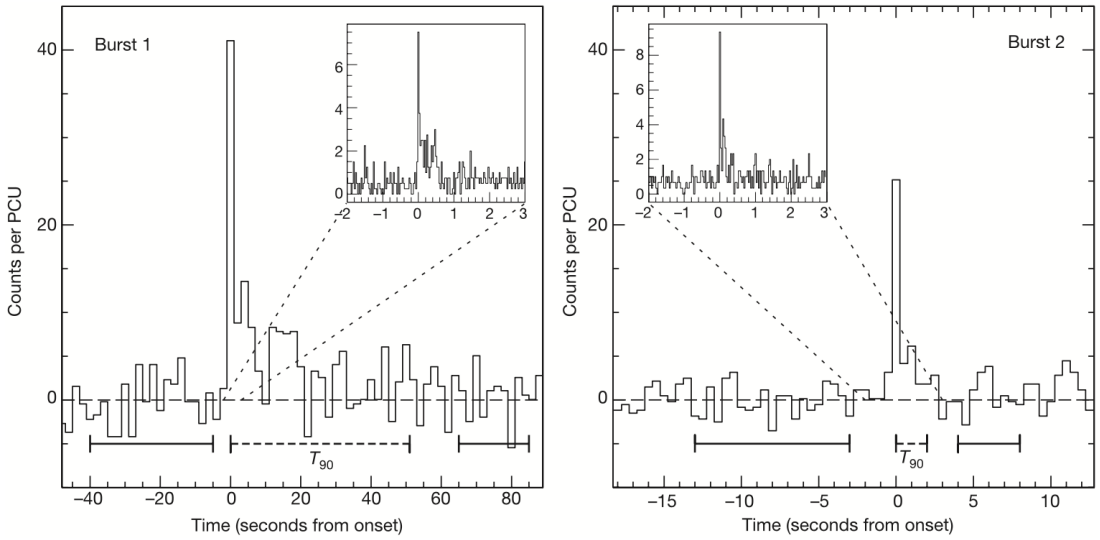

Figure 1.2 — Light curves of the two bursts emitted by the AXP 1E 1048.1–5937. *Figure adapted from Gavriil et al. (2002).*

produced ~ 100 bursts between the 13$^{\text{th}}$ August 1978 and the 27$^{\text{th}}$ June 1986, with a peak activity around 1983-1984 (Laros et al., 1987). Since then, 18 SGRs have been observed.

1.1.2 . The magnetar model

The first interpretation of these bursts implies a NS accreting material from a stellar companion in a binary system (Mazets et al., 1979a,c). However, this interpretation is strongly questionable for two reasons: (i) the source SGR 0526–66 has a proper velocity of $1200 \pm 300\,\mathrm{km\,s^{-1}}$ (Duncan & Thompson, 1992, Rothschild et al., 1994), which is very unlikely for a tight binary system, and (ii) the luminosity needed to power the radio emission of the nebula associated with SGR 1806–20, G10.0–0.3 (Kulkarni et al., 1994, Corbel & Eikenberry, 2004), would cause an outward pressure stopping the accretion. As an alternative scenario, Duncan & Thompson (1992) (and also Paczynski, 1992) proposed the *magnetar* model, in which the bursts are due to the dissipation of very strong magnetic fields in the NS. While Duncan & Thompson (1992) focus on the origin of these extreme magnetic fields (this question is thoroughly discussed in Chap. 2), Thompson & Duncan (1995, 1996) describe in detail this dissipation mechanism: (i) strong internal magnetic fields cause stresses in the NS crust until it cracks, which (ii) causes the injection of an Aflvén wave into the magnetosphere. (iii) If the magnetic field is weak enough at the injection radius, the magnetic field lines open and release the plasma initially trapped in the magnetosphere. This is the released luminous energy from this event which constitutes the burst in the γ-ray domain. This modelling as a strongly magnetised NS is supported by the inference of the rotation period and age of SGR 0526–66, thanks to its associated SN remnant (Shull, 1983), which suggests a strong spun-down due to a strong magnetic dipole. The first precise measures of the SGR spin-down rate made by Kouveliotou et al. (1998, 1999) further confirm the strong magnetic field hypothesis.

1.1.3 . Link with Anomalous X-ray Pulsars

During the same period, some pulsars showing peculiar emissions in the X-ray domain, named *Anomalous X-ray Pulsars (AXPs)* by van Paradijs et al. (1995), were observed. The first

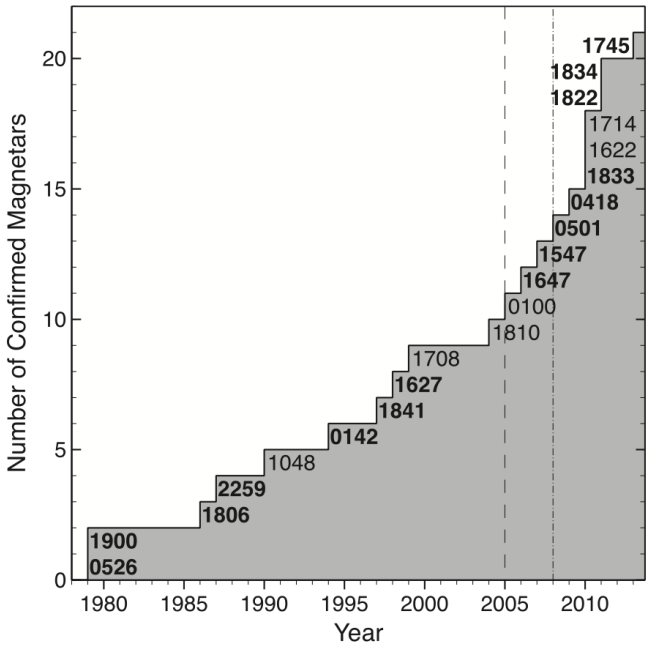

Figure 1.3 — Number of discovered magnetars from 1979 to 2014. *Figure from Olausen & Kaspi (2014).*

source of this kind is 1E 2258+586 (Gregory & Fahlman, 1980), which is associated with the SN remnant CTB 109. This source shows a 7 s rotation period (Dib & Kaspi, 2014) and a soft X-ray spectrum, which reminds the properties of SGR 0526–66 (as noticed by Thompson & Duncan, 1993, Corbet et al., 1995). Three additional AXPs were reported a few years later: 1E 1841–045 (Kriss et al., 1985), 1E 1048.1–5937 (Seward et al., 1986), and 4U 0142+614 (Hellier, 1994, Israel et al., 1994). While AXPs were first interpreted as a new class of binary systems composed of a NS and a low-mass stellar companion, called Low-Mass X-ray Binaries, Thompson & Duncan (1996) explicitly suggest that AXPs and SGRs are strongly related due to their observational properties, which can also be explained by the magnetar model. This link is observationally confirmed a few years later after the observation of a SGR-activity from two AXPs (Gavriil et al., 2002, Kaspi et al., 2003), which explains why both SGRs and AXPs are now commonly referred to as magnetars.

1.2 . Galactic magnetars

Thanks to new spatial high-energy observatories such as the Rossi X-ray Timing Explorer (1995–2012), XMM-Newton (1999–end of 2025), Chandra (1999–), Swift (2004–), and Fermi Gamma-Ray Telescope (2008–), many other magnetar-activities were detected. According to the McGill Online Magnetar Catalog (Olausen & Kaspi, 2014), which gathers the properties of the observed magnetars, 30 magnetars were discovered until 2020. To those we must add the newly discovered SGRs with Swift: SGR J1830–0.645 (Page et al., 2020, Gogus et al., 2020, Younes et al., 2020) and Swift J1555.2–5402 (Coti Zelati et al., 2021, Israel et al., 2021). Besides, the most recent candidate is the unusual GLEAM-X J162759.5-523504.3, which was

detected in the radio domain with the rotation period of $1091\,\mathrm{s}$ (Hurley-Walker et al., 2022)[2]. This number is tiny compared to the total number of observed NS, which is currently ~ 3200. However, magnetars are young NSs (see Sect. 1.2.1) and population studies tend to show that 10 to $40\,\%$ of NS were born as magnetars (Gill & Heyl, 2007, Beniamini et al., 2019). As shown in Fig. 1.3, the number of discovered magnetars increased faster after 2004, which corresponds to the commissioning of the Swift observatory. Let us hope for this trend to continue, so more relevant statistics can be produced on magnetars to better constrain their properties.

1.2.1 . A drop in an ocean of neutron stars

As the historical frame is now set, we must situate magnetars among the rich neutron star zoology. Observed NS can be roughly classified according to their rotation P and spin-down rates $\dot{P}$. Hence, the NS population is usually displayed in a diagram representing $\dot{P}$ as a function of P, called the $P-\dot{P}$ diagram. An (almost) up-to-date $P-\dot{P}$ diagram from Olausen & Kaspi (2014) is illustrated in Fig. 1.4. In this same plot, are presented:

Grey/blue Radio pulsars, which are the most commonly observed neutron stars. Their emissions in the radio domain are driven by the extraction of rotational energy by a magnetic dipole. As this emission originates from the magnetic poles, the misalignment between the dipole and rotation axes causes the observed pulsating signal. Most pulsars show a rotation period of $P \sim 0.1-1\,\mathrm{s}$ and a spin-down rate of $\dot{P} \sim 10^{-16}-10^{-13}\,\mathrm{s\,s^{-1}}$. Note that some of these radio pulsars are found to be transient.

Light grey Radio pulsars in binary systems, whose rotations are extremely fast compared to typical pulsars. They are thought to be spun up to $P \lesssim 10\,\mathrm{ms}$ with a very low spin-down rate of $\dot{P} \sim 10^{-20}\,\mathrm{s\,s^{-1}}$ due to the accretion of material from their companion star.

Yellow X-ray (dim) Isolated Neutron Stars (XINS), which are NS close enough to the Earth so their surface thermal emission can be observed in the X-ray domain. These NSs constitute the so-called 'Magnificent Seven'. Interestingly, no radio emission from XINS has been detected so far and is not associated with any SN remnant. Compared to radio pulsars, they show slower rotation periods of $P \sim 2-10\,\mathrm{s}$.

Red Magnetars, whose rotation periods and their associated derivatives are the largest, both ranging between $P \sim 2-12\,\mathrm{s}$ and $\dot{P} \sim 10^{-13}-10^{-9}\,\mathrm{s\,s^{-1}}$.

Among the diversity of NS classes, we must mention *Central Compact Objects (CCOs)*, which are not plotted in this $P-\dot{P}$ diagram. This class gathers a dozen objects emitting in X-ray that are detected in the centre of several nebulae. This name was first used by Pavlov et al. (2000) and suggests that the nature of CCOs was uncertain due to the lack of detection in other wavelength domains. The measure of P and $\dot{P}$ was measured for three of them because they finally produced a radio pulsar-like emission (Zavlin et al., 2000, Gotthelf et al., 2005, Gotthelf & Halpern, 2009) confirming their NS nature. Those three CCOs show typical radio pulsar $P \sim 0.1-0.4\,,s$ but weaker rotation braking $\dot{P} \sim 10^{-18}-10^{-17}\,\mathrm{s\,s^{-1}}$. Moreover, CCO 1E 161348–5055 was found to show magnetar-like emission 36 years after its discovery (Rea et al., 2016).

[2]Despite no detection of any magnetar-like activity, GLEAM-X J162759.5-523504.3 is more luminous than the maximum dipole spin-down luminosity expected for a radio pulsar. This suggests another emission mechanism, which could be powered by strong magnetic fields as in magnetars.

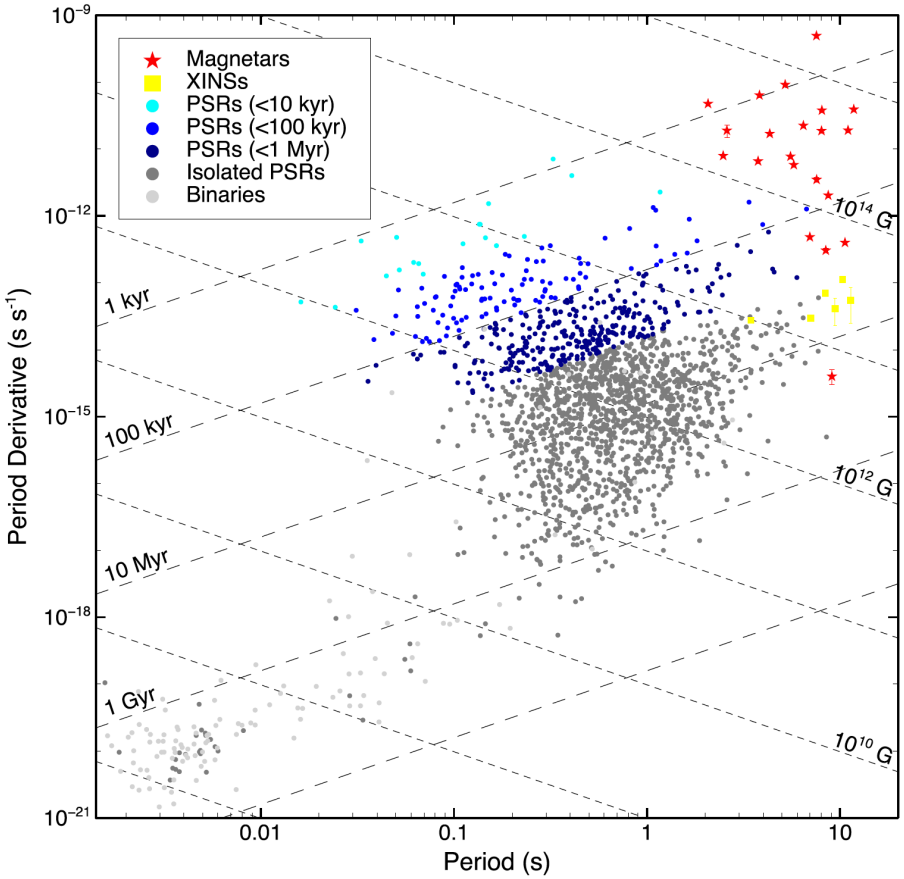

Figure 1.4 — NS $P - \dot{P}$ diagram, which represents the NS spin-down rate as a function of the NS rotation period. The characteristic ages and the magnetic dipole strengths are indicated by the diagonal dotted and dashed lines, respectively. The different classes of NSs are distinguished by different colours. *Figure adapted from Olausen & Kaspi (2014).*

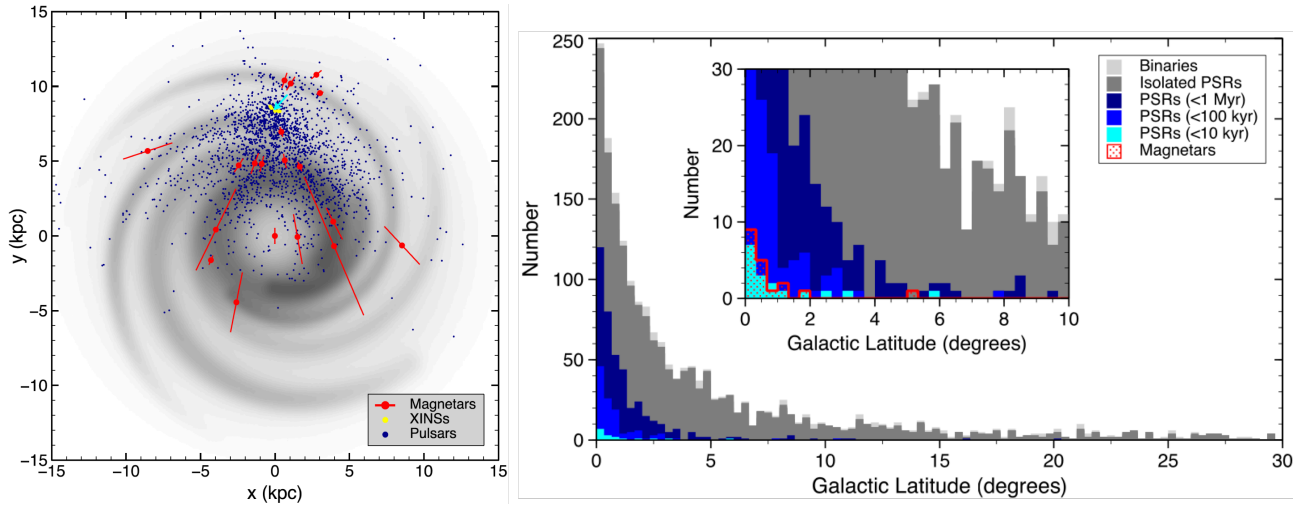

Figure 1.5 — Spatial distribution of the Galactic NS positions in the Galactic plane (left) and as a function of the Galactic latitude (right). The inset in the plot on the right is a zoom-in close to the origin so that the distribution of magnetars can be clearly seen. The colours are the same as those used in the $P-\dot{P}$ diagram (Fig. 1.4). *Figures adapted from Olausen & Kaspi (2014).*

Besides, this magnetar is quite unusual because of its 6.7 hour rotation period (De Luca et al., 2006).

From the measure of P and $\dot{P}$, several quantities can be inferred. First, assuming that the rotation is braked due to the extraction of rotational energy by a surface magnetic dipole in the vacuum, we can infer the strength of the dipole using the relation

$$B_{\rm dip}\sin\alpha = \sqrt{\frac{3Ic^3}{8\pi^2R^6}P\dot{P}} \sim 1.7\times10^{14}\left(\frac{P}{5\,{\rm s}}\right)^{1/2}\left(\frac{\dot{P}}{10^{-11}\,{\rm s\,s^{-1}}}\right)^{1/2}{\rm G}, \tag{1.1}$$

with the NS moment of inertia $I\sim1.6\times10^{45}\,{\rm g\,cm^2}$, the light speed c, and the NS radius $R=12\,{\rm km}$. The inclination angle is often set to $\alpha=\pi/2\,{\rm rad}$, so that $B_{\rm dip}$ is the minimum magnetic dipole. We therefore infer that magnetars harbour extreme magnetic dipoles of $B_{\rm dip}\sim10^{14}-10^{15}\,{\rm G}$ (except for the so-called low-magnetic field magnetars, which we will discuss in Sect. 1.2.3). This is ~100 stronger than in typical radio pulsars. This magnetic field is plotted in the $P-\dot{P}$ diagram in Fig. 1.4 (dotted grey lines).

Second, the luminosity emitted due to the dipole spin-down

$$L_{\rm SD}\equiv4\pi^2I\dot{P}/P^3\sim5\times10^{33}\left(\frac{\dot{P}}{10^{-11}\,{\rm s\,s^{-1}}}\right)\left(\frac{P}{5\,{\rm s}}\right)^{-3}{\rm erg\,s^{-1}}. \tag{1.2}$$

This value is ~100 smaller than the usual AXP quiescent X-ray luminosity of $L_{\rm X}\sim10^{35}\,{\rm erg\,s^{-1}}$ (Kouveliotou, 1999), which confirms that they are not driven by rotation like radio pulsars. Note that this luminosity can also be as low as $L_{\rm X}\sim10^{30}\,{\rm erg\,s^{-1}}$ in some SGRs. This makes the range of possible magnetar $L_{\rm X}$ very broad and constitutes an important question to understand magnetar evolution.

Finally, a characteristic age $\tau_{\rm NS}\equiv P/(2\dot{P})$ can be defined by assuming that . This age tends to overestimate the real age of the NS, which can be measured thanks to the associated SN

remnant. Therefore, the strong spin-down rates and large rotation periods of magnetars show that magnetars must be young NSs with characteristic ages of $\tau_{\rm NS} \sim 10^3 - 10^5\,{\rm yr}$. The youth of magnetars is also supported by two other arguments. First, 11 (and potentially 12) out of the 32 magnetars are associated with SN remnants, which is a much larger fraction than for the whole population of NSs (133 out ~ 3000, Igoshev et al., 2022). This association is an indication of youth because the remnant lifetime (i.e. the time for the remnant gas to reach the density of the interstellar medium) is $\sim 10^6\,{\rm yr}$ (Bamba & Williams, 2022) and the NS did not have the time to move away from the nebula despite the possible strong kick induced by the SN explosion (see Sect. 2.1.2). Note that the kinetic energy of these SN remnants is similar to those associated with other NSs (Vink & Kuiper, 2006, Martin et al., 2014, Zhou et al., 2019). This has consequences on magnetar formation scenarios, which we will discuss in the next chapter (Chap. 2). Second, by looking at NS positions in the Milky Way illustrated in Fig. 1.5, we see that their Galactic latitude (i.e. the angle between the line passing through the Earth and the Galactic centre, and the line passing through the Earth and the observed object) remains below $5°$. Magnetars are therefore confined close to the Galactic plane. Moreover, as the typical magnetar proper motion (regarding those for which a velocity measure could be done) is similar to pulsars ($\sim 100-300\,{\rm km\,s^{-1}}$, Helfand et al., 2007, Deller et al., 2012, Tendulkar et al., 2012, 2013), a magnetar only needs $1-3\times10^5\,{\rm yr}$ to cover their typical height above the Galactic plane of $30\,{\rm pc}$. We must however remain cautious about this argument as the statistics are still poor. Note that the magnetar distribution in the Galactic plane (plot on the left in Fig. 1.5) shows that magnetars are not detected much behind the Galactic centre. The same is true for all NSs indicating a clear observational bias against NS further than $\sim 15\,{\rm kpc}$ from the Earth.

1.2.2 . A rich diversity of emissions

The study of magnetar general characteristics detailed in the previous section has been eased by the wide variety of luminous events emitted by magnetars. They cover a large range of wavelengths, from γ-ray to the radio domain, and luminosities from $\sim 10^{30}\,{\rm erg\,s^{-1}}$ in quiescence phase to $\sim 10^{47}\,{\rm erg\,s^{-1}}$ for the brightest emitted flare. This fosters detailed study of the physics behind magnetar magnetic fields in order to explain this richness of luminous events.

Short chaotic bursts The most common luminous manifestation of magnetars is their X-ray *short bursts*. Their distribution over time is chaotic, with some magnetars producing bursts during a short time before entering a 'dormant' phase for several years. This is the case for the first observed magnetar SGR 0526-66, which produced the two very energetic detected bursts in 1979 before becoming silent, though it showed AXP behaviour two decades later (Kulkarni et al., 2003). Other magnetars such as SGR 1806–20, which we mentioned earlier, are very active and can produce hundreds or even thousands of bursts during months or years. A typical case of very active magnetar is SGR J1550–5418 (or historically 1E 1547.0–5408, Lamb & Markert, 1981), which emitted 286 bursts during a single week between 22 and 29 January 2009 (van der Horst et al., 2012).

Fig. 1.6 displays bursts detected in the hard X-ray domain (energy between $20-200\,{\rm keV}$ or frequency between $4.8\times10^9 - 4.8\times10^{10}\,{\rm GHz}$) by Mereghetti et al. (2020) and produced by the typical magnetar SGR 1935+2154, which has a rotation period of $P = 3.2\,{\rm s}$ and a surface magnetic dipole of $B_{\rm dip} = 2.2\times10^{14}\,{\rm G}$ (Israel et al., 2016). As in Fig. 1.1, the five plots represent the

number of detected photons per time unit, which is equivalent to a luminosity, as a function of the observation time. Burst C is single-peaked, which is the most common form of burst light curves with usually a rise phase shorter than the decay phase. But burst signals can be more complex with two peaks (bursts D) or even three (bursts F, G, and I). These bursts last between $0.11\,\mathrm{s}$ (burst C) and $0.75\,\mathrm{s}$ (burst G), which is close to the typical burst duration of $0.1\,\mathrm{s}$ for magnetars. Their X-ray peak luminosities are measured between 10^{39} and $10^{41}\,\mathrm{erg\,s^{-1}}$, which is the middle of the large luminosity range spanned by magnetars 10^{36}–$10^{43}\,\mathrm{erg\,s^{-1}}$. The exact mechanism of magnetar short bursts is still an open question but must be related to crustal stresses induced by the strong internal magnetic fields (see e.g. the model of Lander, 2023). Interestingly, some short bursts come with tails (decay phases) far longer than the prompt emission (peaked phase), ranging from a few to thousands of seconds. These tails were observed for several magnetars such as the previously mentioned SGR 1900+14 (Lenters et al., 2003), SGR 1806–20 (Göğüş et al., 2011), and SGR J1550–5418 (Muş et al., 2015) and remind the shape of giant flare light curves, which we will present later in this section.

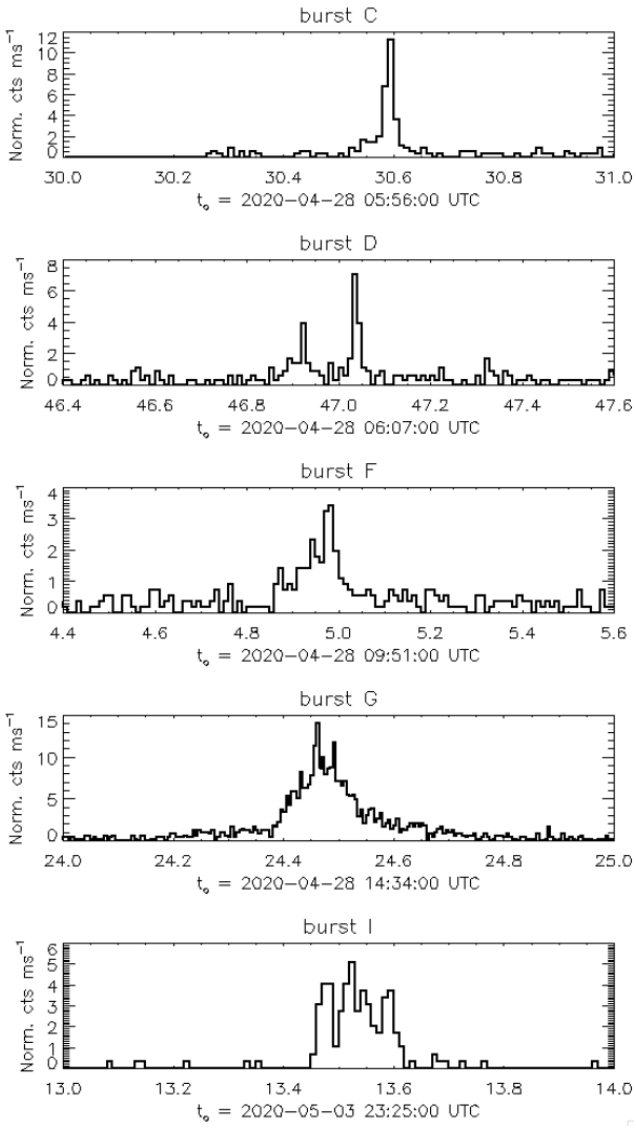

Figure 1.6 — X-ray light curves of some bursts emitted by the magnetar SGR 1935+2154in the $0.5-10\,\mathrm{keV}$ energy domain. The time on the x-axis is in seconds. *Figure adapted from Mereghetti et al. (2020).*

Outbursts During an active period, the magnetar can enter an *outburst* phase, in which the detected X-ray flux, i.e. the luminosity per surface unit, suddenly increases. These phases are particularly prone to the emision of short bursts (e.g. van der Horst et al., 2012, Younes et al., 2017), even though it not always the case (e.g. Gavriil et al., 2002). SGR 1935+2154 entered four outburst phases between 2014 and 2016, whose associated X-ray flux is plotted in Fig. 1.7. Compared to the decay phase which is seen to last $10-100\,\mathrm{days}$, the flux increase is very sudden and can reach $6-7$ times the flux in the quiescent state, which is displayed by the black dashed line in Fig. 1.7. This increase is actually pretty small compared to other magnetar outbursts which can reach ~ 2000 (Coti Zelati et al., 2018). Such an event is therefore ideal to discover magnetars whose quiescent X-ray luminosity is too weak to be detected (usually $\lesssim 10^{33}\,\mathrm{erg\,s^{-1}}$). These magnetars are called *transient* magnetars, in opposition to *permanent* magnetars.

The enhanced luminosity in outburst phases eases the extraction of the pulsed signal from which the magnetar rotation period and its derivative are measured. The method behind the measures is the *phase-coherent timing*, which is used for every pulsating NS. It roughly consists in measuring the arrival time of each pulse at the detector during a certain period which can be several years and fitting a spin-down model from which we infer the rotational properties (see e.g. Hobbs et al., 2006, Edwards et al., 2006). Such a method was applied to the observation of SGR 1935+2154, whose pulse profile during the 2014 outburst is shown in Fig. 1.8 for different energy intervals in the X-ray domain. SGR 1935+2154 pulse is quite sinusoidal without any sign of variation (Israel et al., 2016), which contrasts with the wide variety of profiles from magnetars which can even vary during an outburst (see e.g. Fig. 2 of Mereghetti et al., 2015, for 1E 2259+586). These profile variations combined with a potential short outburst lifetime make however the measurements of P and $\dot{P}$ more difficult.

Still, the rotational properties are usually measured with high precision as values as weak as $10^{-21}\,\mathrm{s\,s^{-1}}$ can be inferred for $\dot{P}$. It is therefore possible to notice the sudden period vari-

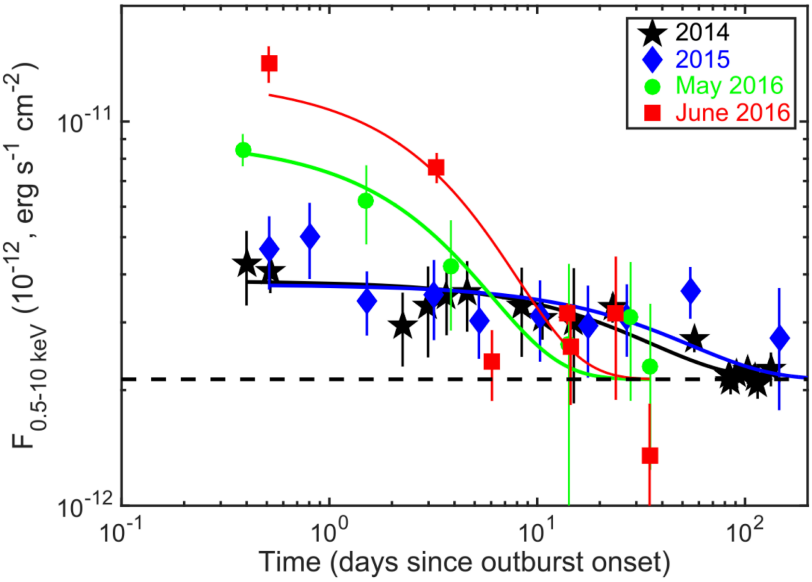

Figure 1.7 — X-ray flux emission during the four outburst phases of SGR 1935+2154 between 2014 and 2016. One must be careful with the units of the flux, which are actually in $\mathrm{erg\,s^{-1}\,cm^{-2}}$ and not in $10^{-12}\,\mathrm{erg\,s^{-1}\,cm^{-2}}$. *Figure adapted from Younes et al. (2017).*

ations ΔP, from magnetar (and also young pulsar) pulsed signal, with $\Delta P/P \sim 10^{-9} - 10^{-5}$. These spin-ups, called *glitches*, were first observed in the pulsar PSR 0833–45, more commonly called Vela pulsar (Reichley & Downs, 1969) and are particularly frequent in magnetars compared to other NS classes. This phenomenon is expected to be related to the superfluid nature of the NS core (e.g. Anderson & Itoh, 1975, Ruderman, 1976, Haskell & Melatos, 2015, Layek & Yadav, 2020, Layek et al., 2023, Bagchi et al., 2024), and often coincides with outburst phases for magnetars. A following recovery phase of at least a fraction of the initial rotation speed is generally reported and is very strong in magnetars, such that it recovers at least its initial rotation period and even spins down (e.g. Kaspi et al., 2003, Livingstone et al., 2010, Gavriil et al., 2011). Surprisingly, the opposite phenoma, called *anti-glitches*, is only observed in magnetars (Woods et al., 1999, Archibald et al., 2013, Şaşmaz Muş et al., 2014), with $\Delta P/P \sim 10^{-7}$. However, their origin is still unclear and may be related to magnetospheric phenomena or an over-recovery from a glitch.

Giant flares Among the thousands of detected bursts produced by Galactic magnetars, three of them especially stand out by their extreme energies. The sources are actually the three first observed magnetars: SGR 0526–66 (Mazets et al., 1979a,c, Evans et al., 1980), SGR 1900+14 (Hurley et al., 1999), and SGR 1806–20 (Hurley et al., 2005, Mereghetti et al., 2005, Gotz et al., 2006), whose γ-ray peaked energies range between 10^{44} and $10^{47}\,\mathrm{erg\,s^{-1}}$. These events are therefore $1 - 1000$ times more luminous than the combined luminosity of the whole Galatic star population. The release of magnetic energy from unstable twisted magnetic field lines in the corona due to large-scale and deep crustal failures could explain these extreme events, which is similar to solar coronal mass ejection (see e.g. Lyutikov, 2006, Lander, 2023). As these failures are themselves caused by strong magnetic field-induced stresses, these events could give information about the evolution of the strong internal magnetic field. The light curves of the two most recent events are plotted in Fig. 1.9. Like some

bursts, the signal consists of a prompt emission and a tail, which lasts $0.2\,\mathrm{s}$ and several minutes, respectively. Like the less energetic burst of SGR 0526–66 in Fig. 1.1, the tail (also called the *afterglow*) shows oscillations whose period corresponds to the magnetar rotation period.

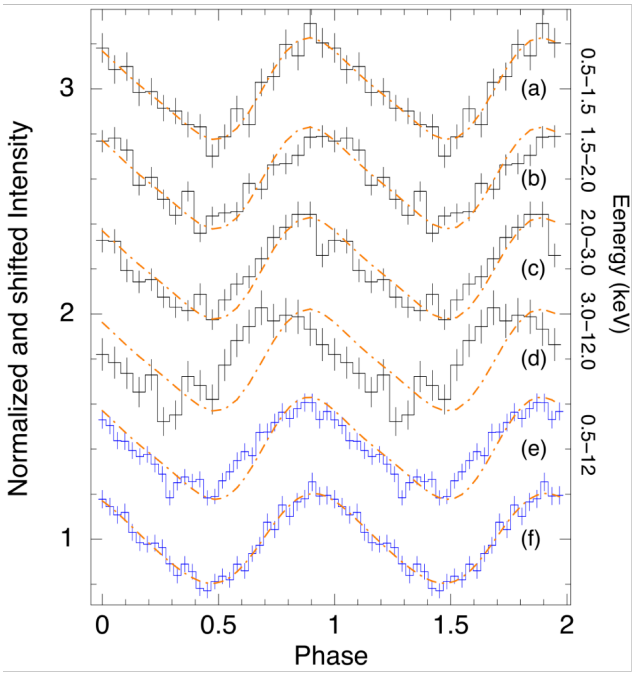

Figure 1.8 — Intensity of the pulsed signal detected during the 2014 outburst of SGR 1935+2154 for different X-ray domain energies. Red lines represent the best fit of the signal by assuming a model with two sinusoids *Figure adapted from Israel et al. (2016)*.

Other oscillations can be found by looking at the spectrogram of the signal, i.e. the intensity or power in the time-frequency plane. They are called *Quasi-Periodic Oscillations (QPOs)* and were found in the two latter giant flares. Israel et al. (2005b) report a robust QPO of $\sim 92.5\,\mathrm{Hz}$ between $170\,\mathrm{s}$ and $220\,\mathrm{s}$ after the flare onset of SGR 1806–20, and potentially two other QPOs at $\sim 18\,\mathrm{Hz}$ and $\sim 30\,\mathrm{Hz}$ in the same interval. In the flare afterglow of SGR 1900+14, Strohmayer & Watts (2005) find a QPO at $\sim 84\,\mathrm{Hz}$ in a $\sim 0.5\,\mathrm{s}$ interval $\sim 63\,\mathrm{s}$ after the flare onset. By focusing on the rotational phase associated with the $84\,\mathrm{Hz}$-QPO, at least other oscillations are detected with frequencies of $53.5\,\mathrm{Hz}$ and $155.1\,\mathrm{Hz}$. These QPOs are transient and so are present in specific rotational phases. QPOs were also found in the burst of the magnetar SGR J1550–5418 (Huppenkothen et al., 2014). This variety of QPO modes could be caused by magneto-elastic oscillations in the NS with strong enough magnetic fields. These oscillations were modelled by Gabler et al. (2016, 2018) (see also Bretz et al., 2021), which can provide the average magnetic strength in a magnetar interior. According to this model, SGR 1806–20 has a very strong magnetic fields of $\sim 2\times10^{15}\,\mathrm{G}$, which is 10 times stronger than its surface magnetic dipole inferred from its spin-down.

Finally, giant flares are most energetic in the soft γ-ray domain and can therefore be similar to short γ-ray bursts (GRBs) but less energetic, as for the 1979 event from SGR 0526–66. As most GRBs are extragalactic sources, some of them are interpreted as extragalactic magnetars (Ofek et al., 2008, Hurley et al., 2010, Svinkin et al., 2021, Mereghetti et al., 2024). Most of the candidates are proposed with lukewarm confidence because it is hard to exclude more energetic events located farther than expected. However, Mereghetti et al. (2024) show strong confidence in the latter detection because of the similarity with the 2004 giant flare from 1806–20.

Lower-energy emission While magnetars are mostly observed in the γ-ray and X-ray domain, counterparts in the optical and infrared domains were detected for six (potentially 11) magnetars (see the McGill Catalog Olausen & Kaspi, 2014). Only three of them have shown optical pulsations, whose profiles are similar to those observed in X-ray: 4U 0142+61 (Kern

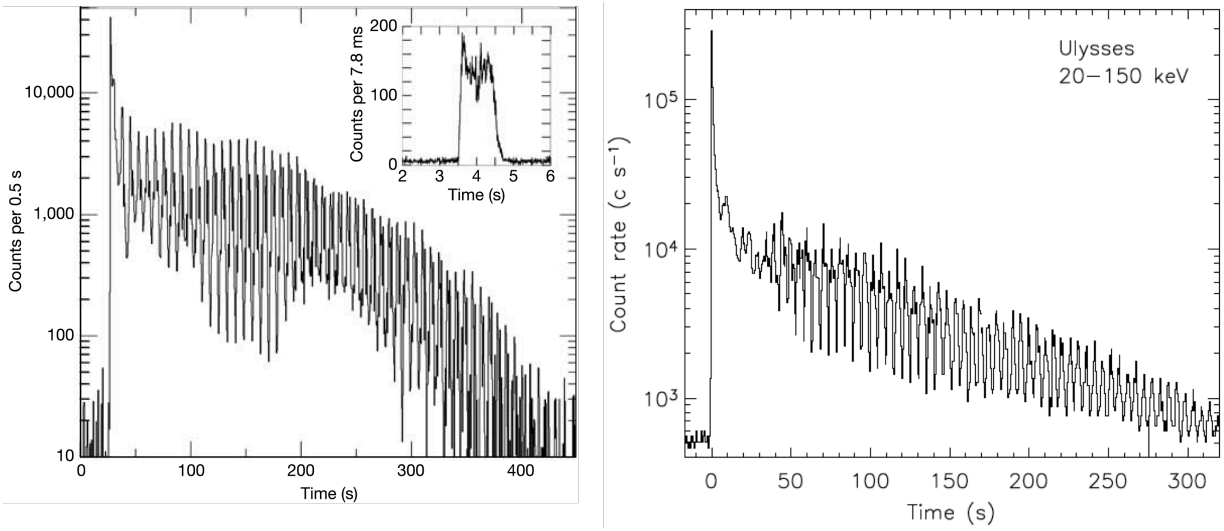

Figure 1.9 — Light curves of the giant flares produced on 27 Decembre 2004 by SGR 1806–20 (left) and on 27 August 1998 by SGR 1900+14 (right). *Figures adapted from Hurley et al. (2005) and Hurley et al. (1999), respectively*.

& Martin, 2002, Dhillon et al., 2005), 1E 1048.1–5937 (Dhillon et al., 2009), SGR 0501+4516 (Dhillon et al., 2011). Infrared counterparts are also seen to be correlated (Tam et al., 2004, Rea et al., 2004, Israel et al., 2005a) or not (Durant & van Kerkwijk, 2006, Testa et al., 2008, Wang et al., 2008, Tam et al., 2008) to X-ray activity phases. While an infrared/X-ray correlation could betray the presence of a dust disk around the magnetar (Tam et al., 2004, Kaplan et al., 2009), the absence of correlation challenges this interpretation and rather supports a magnetospheric origin (Wang et al., 2008).

Seven magnetars (including the recently discovered transient GLEAM-X J16275) produced transient bursts or radio pulsations (Camilo et al., 2006, 2007, Levin et al., 2010, Eatough et al., 2013, Shannon & Johnston, 2013, Lynch et al., 2015, CHIME/FRB Collaboration et al., 2020, Hurley-Walker et al., 2022). We focus first on radio pulsating sources since it concerns six out of the radio magnetars and come back to the only source of radio bursts in Sect. 1.3.1. An example of radio emission from magnetar SGR J1745–2900 is displayed in Fig. 1.10. These pulses remind a lot of radio pulsars but their profile changes on time scales of minutes to days. Other several common properties emerge from the different radio observations (Rea et al., 2012b): (i) the transient radio pulses appear with a time delay after X-ray outburst onset, during its decay, (ii) the radio and X-fluxes decay at the same time. Despite some differences with pulses from radio pulsars, Rea et al. (2012b) proposed that the mechanism is also powered by rotational energy. The fact that radio magnetars share the common property of having a lower X-ray quiescent luminosity than their dipole spin-down luminosity supports this idea. Indeed, this suggests that the internal magnetic fields are not strong enough to produce powerful currents in the twisted magnetosphere that can disrupt the radio emission mechanism. This scenario explains well why the radio emission is only observed during the outburst decay. An implication is that radio magnetars must emit radio pulses in their quiescent state. As none of these radio pulses were detected in this state, they may not be intense enough to be detected.

1.2.3 . Magnetars with low-magnetic dipoles

Magnetars were (and are still) commonly defined as neutron stars harbouring magnetic dipoles $\gtrsim 10^{14}\,\mathrm{G}$ or stronger than the critical electron magnetic field of $4.4\times10^{13}\,\mathrm{G}$. However, the observation of the transient magnetar SGR 0418+5729 (Rea et al., 2010) made this definition obsolete as its measured magnetic dipole is $B_{\rm dip}\sim 6\times10^{12}\,\mathrm{G}$, which is ~ 17 times weaker than expected for a typical magnetar. Since then, two other magnetars were reported as *low-magnetic field magnetars*: Swift J1818.0–1607 (Rea et al., 2012a, Scholz et al., 2012) and 3XMM J185246.6+003317 (Rea et al., 2014), whose dipoles are $B_{\rm dip}\sim 1.4\times10^{13}\,\mathrm{G}$ and $B_{\rm dip}\lesssim 4.1\times10^{13}\,\mathrm{G}$, respectively. If we consider $B_{\rm dip}\sim 10^{14}\,\mathrm{G}$ as the lower limit for classical magnetars, we may also consider CXOU J164710.2–455216 (An et al., 2013) and 1E 2259+586 (Dib & Kaspi, 2014) as low-magnetic field magnetars as their magnetic fields are $B_{\rm dip}\lesssim 6.6\times10^{13}\,\mathrm{G}$ and $B_{\rm dip}\sim 5.9\times10^{13}\,\mathrm{G}$, respectively. The discovery of low-magnetic field magnetars is very important because they provide observational proof that magnetar activity does not rely on the surface magnetic dipole measured via the magnetic spin-down model. This will have consequences on the investigations of the magnetar formation problem (see Chap. 9).

Interestingly, absorption lines (illustrated in Fig. 1.11) were detected in the spectral evolution of two magnetars only: SGR 0418+5729 and Swift J1822.3–1606, which harbour the weakest magnetic dipoles. Similar features were already observed in the emission of some pulsars (e.g. Truemper et al., 1978, Bignami et al., 2003, Kargaltsev et al., 2012). These lines have been interpreted as cyclotron absorption (by either proton or electron) lines. The energy of these lines E_B are therefore related to the magnetic field B intensity

$$E_B\sim 9.3\left(\frac{m_e}{m}\right)\left(\frac{B}{10^{12}\,\mathrm{G}}\right)\mathrm{keV}, \tag{1.3}$$

for a NS with a mass and radius of $1.4\,\mathrm{M}_\odot$ and $12\,\mathrm{km}$, respectively. m_e is the electronic mass and m is the particle mass (electronic or protonic mass in our case). On the one hand, if the absorber is an electron, the magnetic field near the NS surface should be $B\sim10^{12}\,\mathrm{G}$ with $E_B\sim10\,\mathrm{keV}$, which is contradictory because below the measured value of the magnetic dipole of $B<B_{\rm dip}\sim6\times10^{12}\,\mathrm{G}$. On the other hand, if the absorber is a proton, we infer $B\sim2\times10^{14}-10^{15}\,\mathrm{G}$ and $B\sim6\times10^{14}-2.5\times10^{15}\,\mathrm{G}$ for the SGR 0148+5729 and Swift J1822.3–1606, respectively. This demonstrates the existence of small-scale magnetic fields, and thus non-dipolar magnetic components with strengths $30-170$ times stronger $B_{\rm dip}$. The form of the line in the spectra can be explained as the manifestation of small-scale magnetic field arcs at the NS surface. This result is crucial because it confirms that strong (small-scale or not) non-dipolar magnetic fields are sufficient to produce magnetar activity. This result is in line with the observation of modulations in the light curve of some magnetars that can be interpreted as precession motions caused by stronger toroidal internal magnetic fields reaching $\sim10^{16}\,\mathrm{G}$ (Makishima et al., 2014, 2016, 2019, 2021).

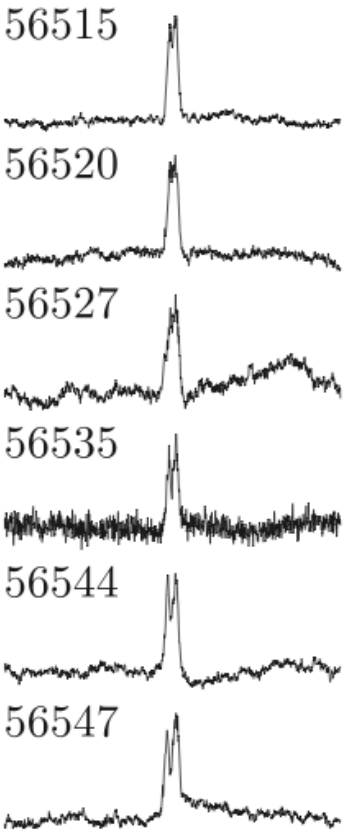

Figure 1.10 — Radio pulse profiles at different rotational phase of SGR J1745–2900. *Figure adapted from Lynch et al. (2015).*

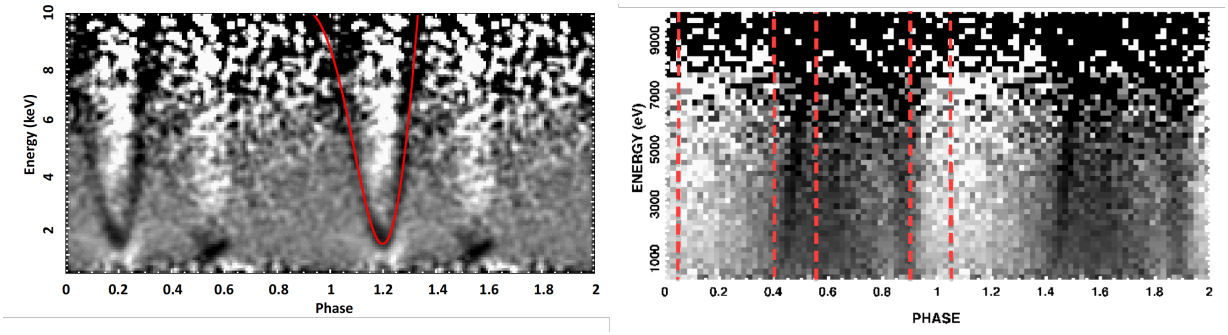

Figure 1.11 — Two X-ray spectra of magnetars SGR 0418+5729 (left) and SWIFT J1822.3–1606 (right). The solid red lines follow the absorption line (left) and the red dashed lines constrain the regions showing an absorption line (right). *Figures adapted from Tiengo et al. (2013) and Rodríguez Castillo et al. (2016), respectively*.

1.2.4 . Stellar progenitors

While most observations focus on the magnetar properties, a few attempt to infer the properties of the progenitor star, especially its mass. These investagations focus on magnetars associated to star clusters or wind bubble produced by the progenitor. They show that magnetars are formed in massive stars with a wide range of initial masses. For instance, the coincidence of the AXP 1E 1048.1–5937 with a wind bubble suggests that its massive progenitor had a mass around $30-40\,\mathrm{M}_\odot$(Gaensler et al., 2005). The study of clusters associated to magnetars show that the magnetars SGR 1806–20 and CXOU J164710.2–455216 stem from a progenitor with an initial mass of $\sim 48-55\,\mathrm{M}_\odot$ (Muno et al., 2006, Bibby et al., 2008, Clark et al., 2008) while the progenitor of SGR 1990+14 had a mass of $\sim 17\,\mathrm{M}_\odot$ (Davies et al., 2009).

1.3 . Magnetars as engine of the most extreme astrophysical events

In the previous section, we have seen that magnetars are the source of a variety of very energetic events from short bursts and outbursts to Galactic and potentially extragalactic giant flares. The magnetic field strength and geometry of magnetars are the key ingredients behind these emissions. In this section, we will show that even more energetic events could involve magnetars and their magnetic fields as their powerful engine.

1.3.1 . Fast Radio Bursts

General picture Fast Radio Bursts (FRBs) are millisecond (or even shorter) very bright bursts in the radio spectral domain, mostly between the frequencies $400-800\,\mathrm{Hz}$ and around $1.4\times 10^3\,\mathrm{Hz}$, i.e. in the energy band $1.7-5.8\times10^{-6}\,\mathrm{eV}$. Before moving further, we must mention that the notion of luminosity (which can be seen, we recall, as an energy, or a number of photons, per unit of time) is usually replaced by the notion of *flux density* in radio astronomy. This quantity measures an energy per unit of time, surface, and frequency, which is equivalent to a luminosity per unit of surface and frequency and a luminosity flux per unit of frequency. Its associated unit is the Jansky, noted $\mathrm{Jy}=1\times10^{-23}\,\mathrm{erg\,s^{-1}\,cm^{-2}\,Hz^{-1}}$ in CGS units. Moreover, distances d are estimated via the combination of the *dispersion measure* $\mathrm{DM}\equiv\int_0^d n_e ds$, which represent the integral of the electronic density n_e along the line of sight, and electro-density models for different media (Cordes & Lazio, 2002, Yao et al., 2017). We use the term disper-

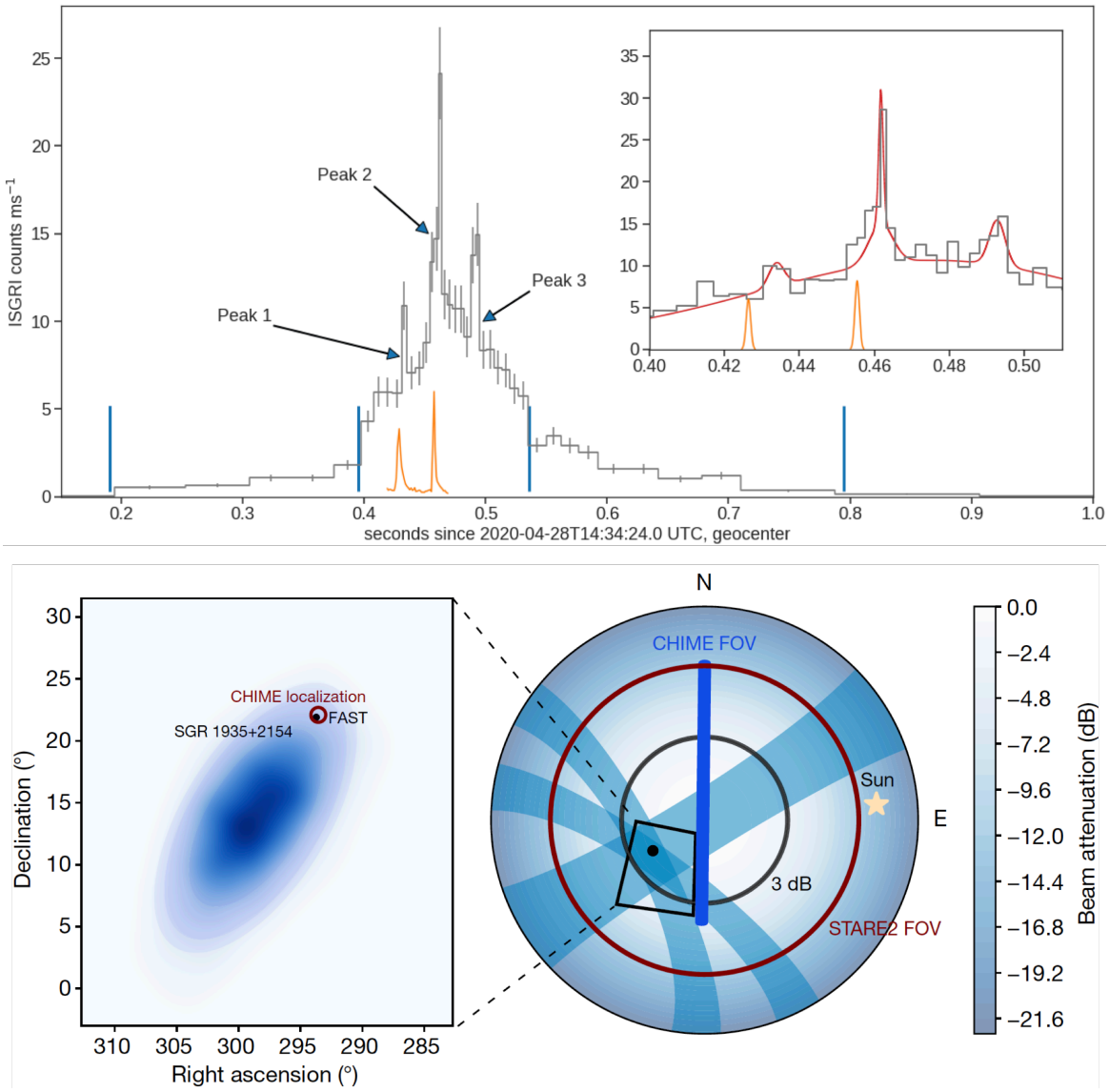

Figure 1.12 — Superposition of FRB 200428 (orange line) and SGR 1935+2154 (grey line) burst light curves (top) and their location in the right ascension-declination plane. *Figures adapted from Mereghetti et al. (2020) and Bochenek et al. (2020), respectively*.

sion because photons with higher frequencies arrive before those with lower frequencies due to the signal propagation in the ionised interstellar medium.

Compared to γ-ray bursts, the study of FRBs is very recent, as the first FRB was found by Lorimer et al. (2007) in archive radio data from 2001. The peak flux density reaches $S_{\rm peak} \gtrsim 30\,{\rm Jy}$ and the dispersion measure is ${\rm DM} = 375\,{\rm pc\,cm^{-3}}$. The former is one order of magnitude greater than the brightness of typical pulsars, and the latter indicates that the source is extragalactic, which stresses the great brightness of these bursts. Four other FRBs were reported six years later, confirming the extragalactic and bright character of the FRB sources (Thornton et al., 2013). By taking into account the large distance of the extragalactic sources, we can infer that FRBs are $\sim 10^{10}$ more luminous than typical pulsars. Around 2019, the number of reported FRBs was ~ 60 (Petroff et al., 2019) but skyrocketed to ~ 600 since the commissioning of the Canadian Hydrogen Intensity Mapping Experiment Fast Radio Burst project (CHIME/FRB) (CHIME/FRB Collaboration et al., 2021). Cordes & Chatterjee (2019) suggest that the detection rate for FRBs with $S_{\rm peak} > 1\,{\rm Jy}$ should be $10^3 - 10^4\,{\rm sky^{-1}\,day^{-1}}$ in the absence of selection and observational bias. This rate is very large compared to other astrophysical transients.

These osbervation of FRBs highlighted a rich variety of FRBs. First, bursts have a wide diversity of profiles and duration from $0.1\,{\rm ms}$ to $\sim 1\,{\rm s}$ (Petroff et al., 2022). Second, the population of FRBs can be separated between repeating and non-repeating FRBs. 50 repeating sources have been reported so far (Chime/Frb Collaboration et al., 2023). Despite periodictiy being found in two sources (CHIME/FRB Collaboration et al., 2020), the appearance of FRB activity for the same source is chaotic. Likewise, the time distribution of bursts in one FRB event seems generally stochastic in spite of the presence of sub-bursts periodicity in one source (Chime/Frb Collaboration et al., 2022). Microsecond and even nanosecond sub-bursts substructures were also observed in some repeating sources (e.g. Nimmo et al., 2022, Snelders et al., 2023). The FRB population is listed on the website https://www.frbcat.org and see the reviews Petroff et al. (2019, 2022) for a complete treatment of this topic.

FRB emission mechanism(s) A wide variety of models (~ 50 listed in the wiki https://frbtheorycat.org) have been proposed to explain the FRB emission mechanism(s), including exotic models invoking alien light sails (Lingam & Loeb, 2017) and the decay of cosmic string cusps (Brandenberger et al., 2017). Apart from these models, they can be roughly sorted into two families: *cataclysmic* and *repeating* models. The former usually invokes compact object mergers (e.g. Totani, 2013, Kashiyama et al., 2013, Mingarelli et al., 2015), or NS collapse (Zhang, 2014, Fuller & Ott, 2015, Most et al., 2018). However, the existence of repeating FRBs rules out cataclysmic origins for at least a fraction of FRBs. The two main repeating models in which a magnetar is involved are magnetar-driven synchrotron maser ('far-away' model, e.g. Metzger et al., 2019, Margalit et al., 2020) and magnetospheric process-driven coherent emission ('close-in' model, e.g. Kumar & Bošnjak, 2020, Lyubarsky, 2020, Lu et al., 2020).

In the former model, the magnetar releases a millisecond ultra-relativistic ejecta shell which collides with a mildly relativistic magnetized ionised shell, which were released following a previous major flare. The shell decelerates due to both reverse and forward shocks, the latter of which produces the observed coherent radio emission (i.e. the FRB) through the synchrotron maser mechanism. The forward shock also heats electrons powering (incoherent) synchrotron γ-ray/X-ray emission, similar to a GRB afterglow. Assuming that these powerful

flares are expected to occur more frequently in young magnetars, this model suggests that too young or too old magnetars can become FRB quiet. Indeed, if the time between the flares is too short, the emission is trapped as the medium is too dense, and old magnetars are too little active to produce energetic flares.

The latter model invokes an initial disturbance produced by a release of energy (e.g. a burst or outburst) that spreads across the NS surface. This causes secondary perturbations in the magnetosphere in the form of Alfvén waves. As Alfvén waves propagate along magnetic field lines, they reach longer distances from NS surface near the magnetic poles where the plasma density drops. In this region, the perturbation-induced currents strongly accelerate charged particles, which emits one or several powerful coherent radio bursts. An important point that we can draw from both models is their prediction of magnetar high-energy emissions, such as bursts or giant flares, along with the FRB.

FRB 200428 from SGR 1935+2154 In 2020, CHIME/FRB Collaboration et al. (2020), Bochenek et al. (2020), and Mereghetti et al. (2020) report for the first time the emission of a FRB from a Galactic magnetar SGR 19835+2154. The concerned FRB 200428 is composed of two components and is very bright with a peak at $S_{\rm peak} \sim 110 - 150\,{\rm kJy}$ (CHIME/FRB Collaboration et al., 2020). The dispersion measure ${\rm DM} \sim 332.7\,{\rm pc\,cm^{-3}}$ and the position in the Galactic plane indicate that the source is not extragalactic. Note that this short distance implies that the FRB intrinsic luminosity is actually one or two order of magnitudes below those of typical extragalactic FRBs. Moreover, Fig. 1.12 shows that the two first peak of the SGR 1935+2154 X-ray burst coincide with both components of FRB 200428 and that the source location of FRB 200428 is only $0.3°$ from the position of SGR 1935+2154. The link between both signals is therefore robust enough to consider SGR 1935+2154 as their source, and thus confirms the connection between FRBs and magnetars. The typical character of SGR 1935+2154 makes the observation of future FRBs from the other magnetars likely.

Both repeating FRB models predict a connection between the radio and X-ray bursts, but the close time coincidence of the signals favors close-in models. Moreover, the maser model predicts a decrease of the frequency with time, as the shock decelerates, which is not observed. However, FRB 200428 is not representative of the diverse population of FRBs and does not exclude the other proposed FRB models.

1.3.2 . Extreme explosions

Hypernovae Some SN explosions harbour ~ 10 times more energetic ejecta than typical SNe, i.e. kinetic energy of $\sim 10^{52}\,{\rm erg}$. These explosions are called *hypernovae*. As magnetars, their observation is strongly related to GRBs. The distribution of GRB duration is bi-modal (i.e. with two peaks), which supports the dichotomy between short and long GRBs, with the mean durations $0.2\,{\rm s}$ and $30\,{\rm s}$, respectively. This bimodality suggests different astrophysical events. While short GRBs are thought to result from binary NS-NS or black hole (BH)-NS mergers (see Sect.. 2.2.3), long GRBs and hypernovae are likely to be the product of the core collapse of a massive star. Long GRBs are extragalactic and the most energetic events of the Universe. As giant flares, their signal consists of a prompt and afterglow emission. A fraction of the latter shows a plateau phase, which suggests a late injection of energy by a central engine (e.g. Zhang et al., 2006, Nousek et al., 2006, O'Brien et al., 2006).

The first link between hypernovae and long GRBs was proposed after the observation of SN 1998bw. Its light curve is displayed in Fig. 1.13, from which we note that SN 1998bw is

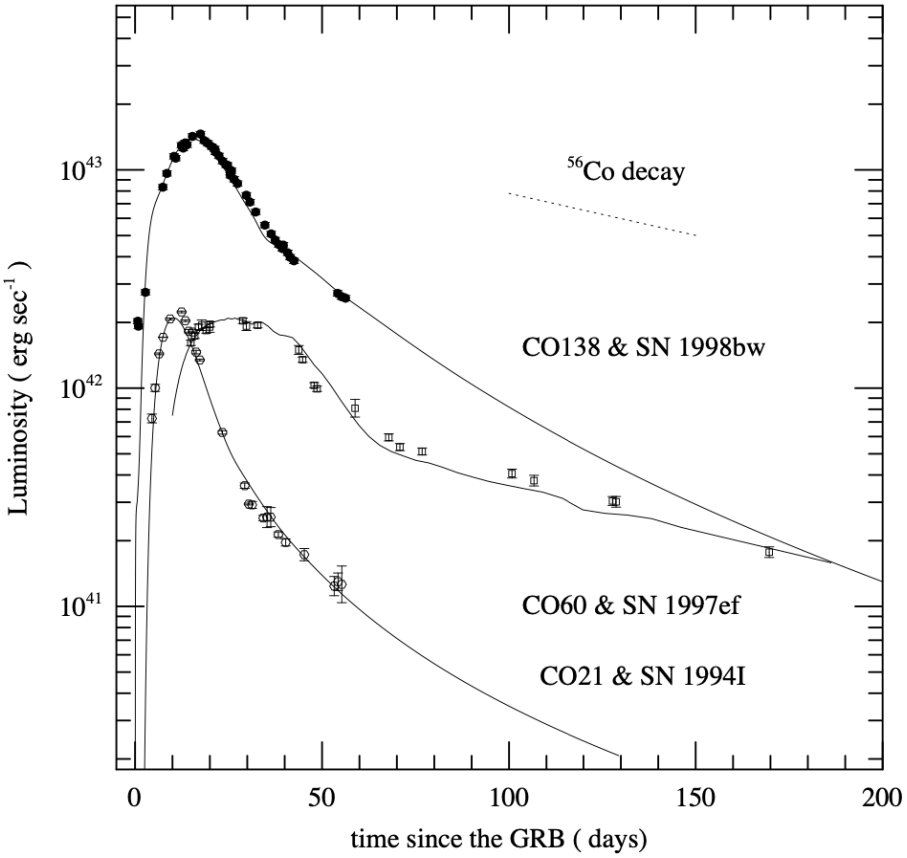

Figure 1.13 — Light curves of the hypernovae SN 1998bw, along with those of SN 1994I and SN 1997ef. *Figures adapted from Iwamoto et al. (1998).*

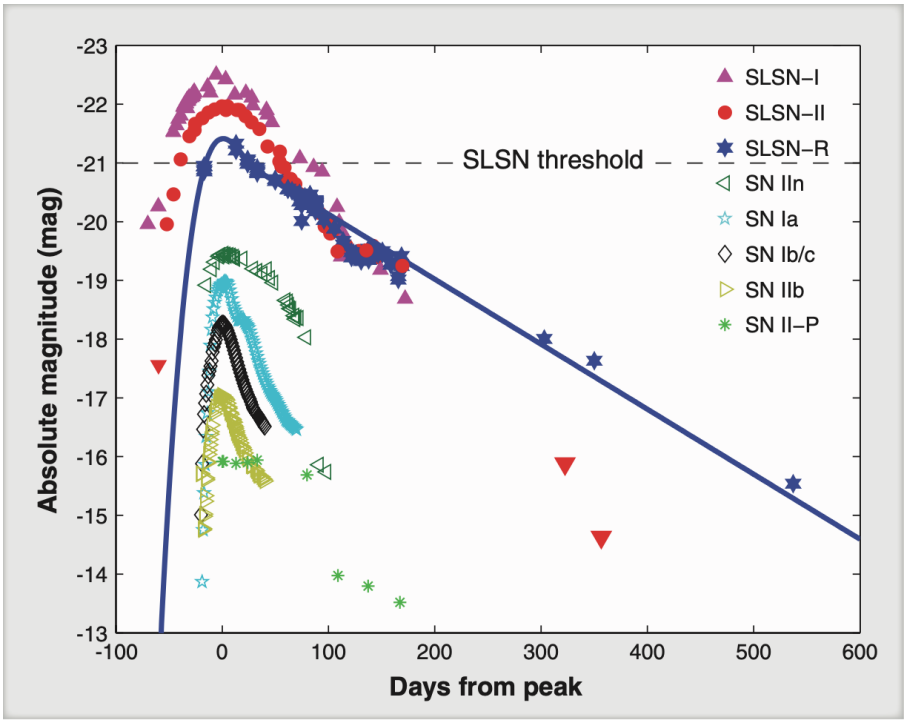

Figure 1.14 — Ligth curves of eight SNe, of which three are SLSNe. The luminosity is measured by the absolute magnitude, which decreases for greater luminosities. *Figures adapted from Gal-Yam (2012).*

~ 10 times more luminous than the two other displayed typical SNe SN 1994I and SN 1997ef, which is explained by the radioactive decay of an unusually high mass of ejected nickel $^{56}\mathrm{Ni}$. The iron FeII emision lines in the spectrum of SN 1998bw are broader than that of typical SNe, which indicates large ejecta velocities and so large explosion kinetic energy. The latter is as large as $\sim 2-5\times10^{52}\,\mathrm{erg}$, which is more than 10 times larger that of typical SNe (Wang & Wheeler, 1998, Iwamoto et al., 1998, Galama et al., 1998). In addition to the absence of hydrogen and helium in the spectrum, the width of the FeII lines explains why hypernovae are also referred to as SN Ic Broad-Lined (BL).

The late appearance of the oxygen OI emission lines also show that the ejecta must be divided into a fast and a slow component, which both correspond to a FeII-rich bipolar and a OI-rich equatorial flow, respectively. The former components suggest the existence of a jet, which could be the source of fast energy injection to explain the high mass of ejected nickel $^{56}\mathrm{Ni}$. This jet may also be related to the GRB. To produce the GRB, a part of the jet must be ultra-relativistic with a Lorentz factor $\gamma \equiv \left(\sqrt{1-v^2/c^2}\right)^{-1} \sim 100$, which corresponds to a flow velocity of $v \sim 0.995c$. Also, the ejecta energy must be larger than the energy radiated in γ-ray, expected to be $\sim 10^{51}\,\mathrm{erg}$ in long GRBs (Bloom et al., 2003). However, many SNe have been identified as hypernovae (e.g. Taddia et al., 2019) but not all of them are associated with a GRB (e.g. Berger et al., 2002, Pignata et al., 2011, Milisavljevic et al., 2015). This confirms that the presence of a relativistic jet is not sufficient to produce a long GRB.

Superluminous supernovae In the family of extreme SNe, hypernovae are accompanied by superluminous supernovae (SLSNe), which are SNe with typical kinetic energy but are

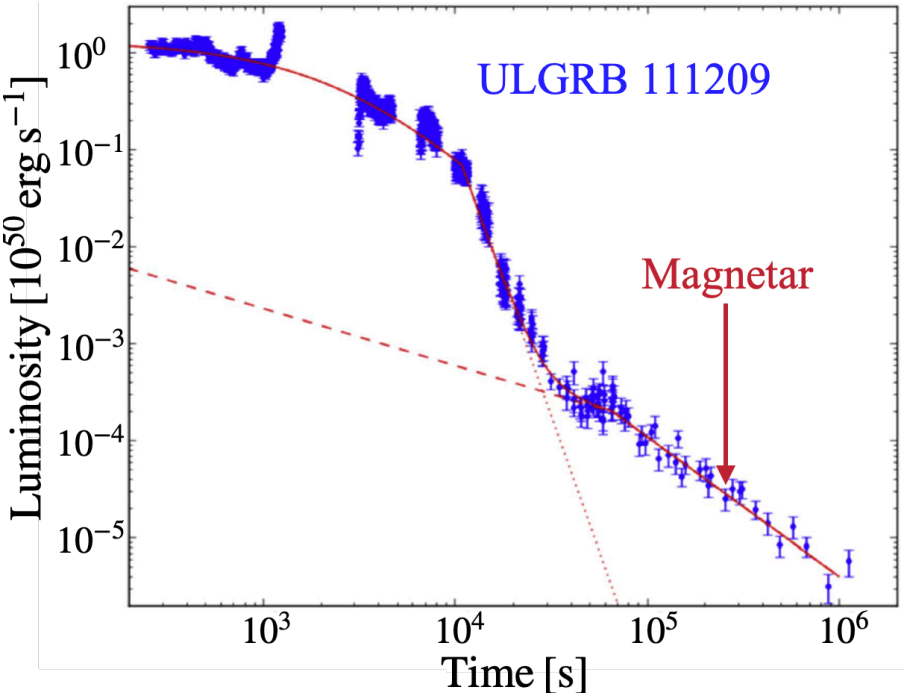

Figure 1.15 — Light curve of the ultra-long GRB 111209 (blue dots) on which a millisecond magnetar model is overplotted (red solid line). *Figures adapted from Gompertz & Fruchter (2017).*

$10-100$ more luminous. These luminous explosions were first noticed by Richardson et al. (2002) and the new class of SLSNe was confirmed after several observations of SNe with a peak luminosity $> 7\times10^{43}\,\mathrm{erg\,s^{-1}}$. Another condition to consider an explosion as a SLSN is that this luminosity must be exceeded during at least $48\,\mathrm{h}$. The light curves of three SLSNe are illustrated in Fig. 1.14 along with five typical SNe. The luminosity of SLSNe evolves more slowly than most SNe, with an increase lasting $\sim 50\,\mathrm{days}$ and a decrease of several hundreds of days. Most SLSN ($\sim 90\,\%$) do not show the presence of hydrogen in their spectrum, which classifies them as SLSN–I (see the classification of SNe in Sect. 2.1.2), but show the same global properties as the others, referred to as SLSN–II.

1.3.3 . Millisecond magnetar model

Hypernovae and SLSNe are too energetic to be explained by the classical neutrino-driven core-collapse SNe model (see Sect. 2.1), in which most of the gravitational energy reservoir ($E_{\mathrm{grav}} \sim 10^{53}\,\mathrm{erg}$) is radiated in neutrinos ($E_\nu \sim E_{\mathrm{grav}}$) while only $\sim 10^{-2}E_{\mathrm{grav}}$ is converted into kinetic energy and $\sim 10^{-4}E_{\mathrm{grav}}$ is radiated in light. Other physical mechanisms must be proposed, in which a large enough fraction of the gravitational energy reservoir is converted into kinetic energy and light.

The fast rotation of the newly formed proto-neutron star (PNS) could provide this energy (e.g. Wheeler et al., 2000, Mazzali et al., 2014, Margalit et al., 2018, Metzger et al., 2018). The rotational energy is roughly approximated by

$$E_{\mathrm{rot}} \equiv \frac{1}{2} I\Omega^2 \sim 3.2\times10^{52}\left(\frac{P}{1\,\mathrm{ms}}\right)^{-2}\mathrm{erg}, \tag{1.4}$$

with a moment of inertia $I = 1.6\times10^{45}\,\mathrm{g\,cm^2}$. This energy reservoir is therefore larger than

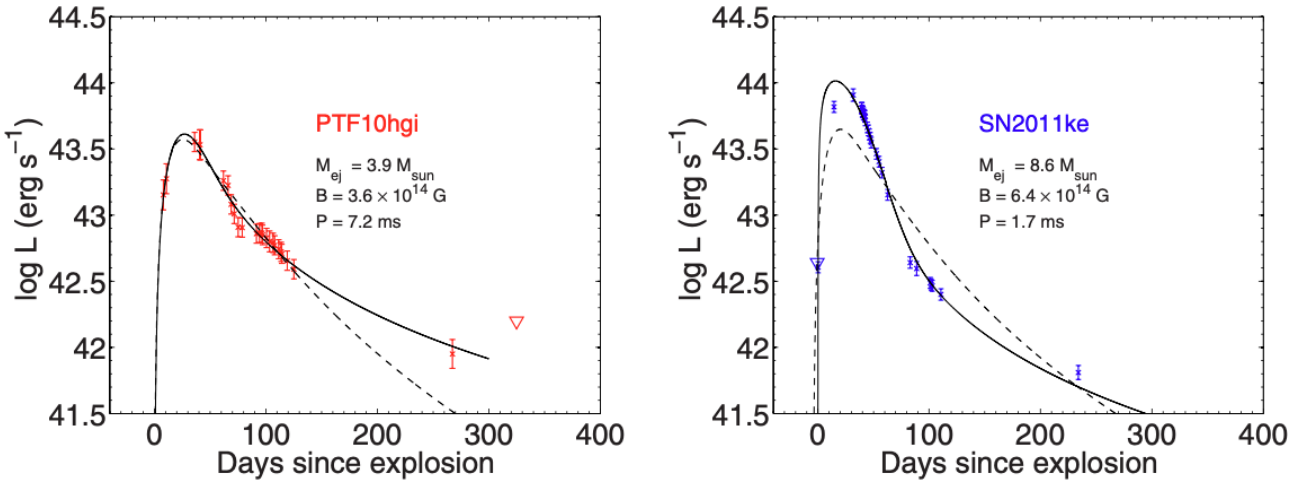

Figure 1.16 — Light curves of the SLSNe PTF10hgi (left, red dots) and SN2011ke (right, blue dots), on which the best fit of the millisecond magnetar model is overplotted (black solid lines). The black dashed is the fit of a ^{56}Ni decay model. *Figures adapted from Inserra et al. (2013).*

the energies of the extreme explosions. The angular momentum can stem from either the rotation of the progenitor star core or a fast spin-up from fast and massive enough fallback accretion (Barrère et al., 2022). To inject this energy into the ejecta, the NS must harbour strong large-scale magnetic fields, often simplified as an axial dipole, which will extract the NS rotational energy. A NS with $B_{\rm dip} \sim 10^{14} - 10^{16}\,{\rm G}$ and $P = 1\,{\rm ms}$, will produce a very large spin-down luminosity of $L_{\rm dip} \sim 6\times10^{45} - 6\times10^{49}\,{\rm erg\,s^{-1}}$. The only neutron stars that harbour such strong magnetic fields are magnetars. Therefore, fast-rotating newly formed magnetars are great candidates to drive these extreme explosions and constitute the *millisecond magnetar* model. Although extreme explosions account for only $1\,\%$ of CCSNe, compared to magnetars, which constitute approximately $10\,\%$ of young NSs, they are nonetheless crucial for understanding the formation of a fraction of the magnetar population.

Application to hypernovae The formation of jets can be explained by strong magnetic fields. Indeed, differential rotation in the magnetar will shear the strong dipole into a toroidal magnetic field, which will concentrate the flow towards the magnetic poles due to strong magnetic pressure. The jet will propagate through the other star layers to produce the *magnetorotational explosion*. This energy must be injected within a timescale $< 1\,{\rm s}$ (Barnes et al., 2018). Magnetars with $B_{\rm dip} \gtrsim 10^{16}\,{\rm G}$ could inject the energy fast through magnetic dipole spin-down only (Suwa & Tominaga, 2015). The presence of a disk penetrating the PNS magnetosphere could enable the efficient transfer of the PNS angular momentum to the disk (propeller regime). This would enhance the magnetar spin-down such that a weaker dipolar magnetic field of $B_{\rm dip} \sim 2\times10^{15}\,{\rm G}$ would be enough (Metzger et al., 2018). The millisecond scenario could also explain why some hypernovae are not associated with a GRB, as some rotation velocities and magnetic field strength may not produce a jet with enough kinetic energy to produce the GRB, but strong enough to drive the energetic explosion. However, some uncertainties remain on the jet stability and the magnetic field amplification process. Still, as shown in Fig. 1.15, millisecond magnetar models reproduce very well the light curves of long

GRBs and easily explain the appearance of a plateau phase in the afterglow (e.g. Nomoto et al., 2011, Metzger et al., 2015, Cano et al., 2016, Gompertz & Fruchter, 2017, Margalit et al., 2018, Lin et al., 2020).

Application to superluminous supernovae The millisecond magnetar model could also explain SLSNe if the energy injection is made at later times. This implies the energy extraction by the magnetic fields to be slower, which can be done for weaker magnetic fields $B_{\rm dip} \sim 10^{14}-10^{15}\,{\rm G}$ (e.g. Woosley, 2010, Kasen & Bildsten, 2010, Nicholl et al., 2013, Margalit et al., 2018, Lin et al., 2021). Millisecond magnetar models for SLSNe usually use three free parameters: the magnetic dipole strength, the magnetar rotation period, and the mass of the ejecta. Best fits of two SLSNe light curves are displayed in Fig. 1.16 and show that millisecond magnetar models reproduce, again, very well the observations, for magnetars with millisecond periods and a $\rm few \times 10^{14}\,G$ magnetic fields.

Alternatives Overall, the boundary between hypernovae and SLSNe is not clear as they could be explained by a magnetorotational explosion driven by a millisecond magnetar. Future observations will hopefully find hybrid extreme SNe which could bridge the gap between SLSNe and hypernovae. Still, other mechanisms have been proposed to explain one or both extreme events. A popular mechanism is the *collapsar* model (Woosley, 1993), in which a rotating massive star quickly collapses into a BH. The angular momentum allows the sustainment of an accretion disc around the BH, whose strong magnetic fields extract the rotational energy to produce the bipolar jet and equatorial winds. The main difference with the millisecond magnetar is therefore the central engine but both models invoke the extraction of rotational energy by a strong magnetic field. However, the collapsar model requires more angular momentum to maintain a Keplerian disc and the millisecond magnetar provides a consistent mechanism to explain the plateau in the afterglow of some long GRBs. An intermediate scenario mentions a supermassive magnetar that is maintained by its rotation in a first instance and then collapses into a BH after its strong spin-down (Dessart et al., 2012, Obergaulinger & Aloy, 2017).

To produce a SLSN, pair-instability SNe of $\gtrsim 60\,{\rm M}_\odot$ massive stars (see Sect. 2.1.2) was also invoked but reproduce the spectra of only few SLSNe (Dessart et al., 2012, Kozyreva et al., 2014, Tolstov et al., 2017). Finally, the SN luminosity could be enhanced thanks to the interaction of the shock with the circumstellar medium, but the proposed models struggle to explain SLSN spectra (Gal-Yam, 2019).

1.4 . Conlusion: magnetars as key objects of high-energy astrophysics

In this chapter, we discussed the observation of magnetars and explained their importance in the context of Galactic and extragalactic high-energy astrophysics. This conclusion section aims at summarising the diversity of observational constraints characterising magnetars.

- The detection of a pulsed signal from a magnetar provide precise measures of the NS rotation period P and spin-dow rate $\dot{P}$. Among the NS population, magnetars show **the longest rotation periods $\mathbf{P \sim 2-12\,s}$** and **the strongest spin-down $\mathbf{\dot{P} \sim 10^{-13}-10^{-9}\,s.s^{-1}}$**.

- This strong rotation braking suggests that **magnetars are young NSs** with a characteristic age of $10^3 - 10^5\,\mathrm{yr}$, which can be considered as an upper limit of their real age. This is also supported by the fact that magnetars are mostly located in the Galactic plane and the observation of SN remnants with which $\sim 1/3$ of magnetars are associated. Population syntheses estimate that magnetars represent $\sim 10-40\,\%$ of the young NS population.

- Assuming that the rotation is braked by a rotating surface magnetic dipole in the vacuum, we infer that most magnetars harbour **magnetic dipoles of $\mathbf{B_{dip} \sim 10^{14} - 10^{15}\,G}$**, which is ~ 100 times stronger than that of typical pulsars. A few magnetars show nonetheless weak magnetic dipoles $B_{\rm dip} \sim 6 \times 10^{12} - 4.1 \times 10^{13}\,\mathrm{G}$, which implies that strong magnetic dipoles are not necessary to produce magnetar-like luminous activity.

- The presence of **stronger non-dipolar magnetic fields** is confirmed by the observation of absorption lines in the X-ray spectrum of two magnetars. If they are interpreted as proton cyclotron absorption lines, they indicate the presence of $\sim 2 \times 10^{14} - 10^{15}\,\mathrm{G}$ small-scale magnetic fields at the magnetar surface, which is ~ 100 times stronger than their spin-down dipole. Since these magnetars are low-magnetic field magnetars, this discovery shows that magnetars must harbour a strong total magnetic field despite a weak magnetic dipole. Moreover, the interpretation of modulations in the pulsed signal of some magnetars as precession movements suggests the presence of $\sim 10^{16}\,\mathrm{G}$ internal toroidal magnetic fields.

- **The strong magnetic fields of magnetars constitute the energy reservoir of their wide variety of high-energy emissions** unlike pulsars whose emission stems from the extraction of rotational energy. These emissions can reach peak luminosities from $10^{39} - 10^{41}\,\mathrm{erg\,s^{-1}}$ for short bursts to $10^{44} - 10^{47}\,\mathrm{erg\,s^{-1}}$ for giant flares. The detection of quasi periodic oscillations in the light curve of two giant flares could inform us about the dynamics in the NS interior.

- The investigations of star clusters and wind bubbles associated with magnetars indicate that the progenitor stars of magnetars cover **a wide range of masses** from $\sim 17\,\mathrm{M_\odot}$ to $\sim 55\,\mathrm{M_\odot}$.

- A fast rotating magnetar may be **the central engine of extreme explosions** such as hypernovae/long GRBs and SLSNe. Using a millisecond magnetar model, the light curve of some long GRBs (SLSNe) can be interpreted as the result of an explosion driven by magnetars with a magnetic dipole of $\sim 10^{15} - 10^{16}\,\mathrm{G}$ ($\mathrm{few} \times 10^{14}\,\mathrm{G}$) and a rotation period of $\sim 1\,\mathrm{ms}$ ($\mathrm{few} \times \mathrm{ms}$).

The magnetic field of magnetars is thus the key ingredient to explain the variety of luminous events we described in this chapter. In the following chapter, we will therefore address the raising question of the origin of these magnetic fields and detail the physics of the explosion mechanisms and magnetic field amplification.

2

The question of magnetar formation

Contents

In order to explain the diverse events related to magnetars, investigating their formation is crucial. To this end, we will begin by briefly introducing how the progenitor stars form and evolve until their explosion, whose mechanism will be detailed (Sect. 2.1). We will focus on the classical neutrino-driven supernovae as it is the event from which Galactic magnetar are expected to originate, although we briefly discuss the magnerotational mechanism afterwards. Then, we will review the different mechanisms that could lead to the formation of a magnetar (Sect. 2.2). Finally, we will question the various scenarios to vindicate the need to investigate the new mechanism that is central in this thesis: the Tayler-Spruit dynamo in a proto-neutron star spun up by supernovae fallback (Sect. 2.3).

2.1 . Core-collapse supernovae

2.1.1 . Star formation and evolution

Interstellar medium Stars are vast balls of hot plasmas, i.e. ionised gas. They are all formed in the *interstellar medium*, which constitutes the space between stars in the Galaxy. This space is predominantly composed of neutral/ionised gas and dust grains, which are particules composed of one or several large molecules. The complexity of the interstellar medium is characterised by its multiphase character, which translates into the co-existence of gases in different equilibrium states:

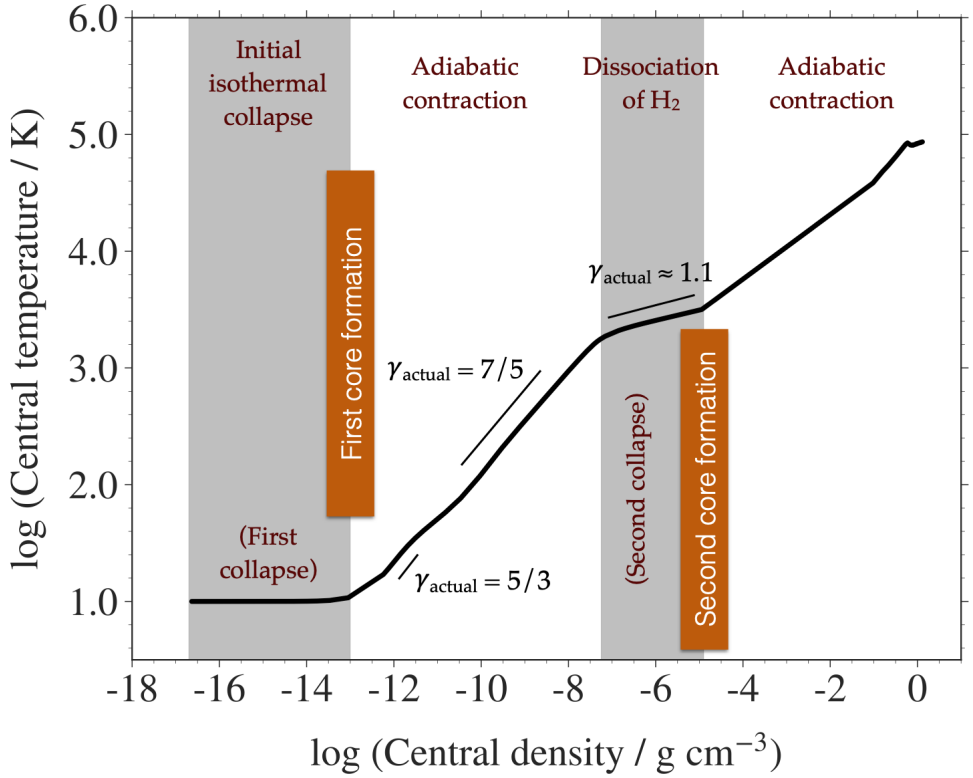

Figure 2.1 — Temperature in the molecular cloud as a function of its density during the formation of the proto-star. *Figures adapted from Bhandare et al. (2020).*

- The *hot ionised medium* consists of hot gas with a temperature of $T \sim 3.2 \times 10^5\,\mathrm{K}$ and a small particule density of $n \sim 4 \times 10^{-3}\,\mathrm{cm}^{-3}$. The large temperature is due to collisions of the medium with the shocks of SN explosions.

- *HII regions* are former molecular clouds in which stellar formation has occurred. The hydrogen is ionised by the ultraviolet emission from massive stars.

- The *warm neutral medium* is composed of hydrogen atoms with a temperature of $T \sim 5 \times 10^3\,\mathrm{K}$ and a particular density of $n \sim 0.6\,\mathrm{cm}^{-3}$.

- The *cold neutral medium* harbours a cold temperature of $T \sim 10^2\,\mathrm{K}$ compared to the other media but is much denser ($n \sim 30\,\mathrm{cm}^{-3}$). This density protects their internal region composed of hydrogen molecules from ultraviolet emissions.

- *Molecular clouds* are the densest regions ($n \sim 10^3 - 10^4\,\mathrm{cm}^{-3}$ corresponding to a mass densities around $\rho \sim 10^{-21} - 10^{-20}\,\mathrm{g\,cm}^{-3}$) and are the place in which stars form.

A star is born The interstellar medium is prone to constant compressions and heating processes caused by a combination of turbulence, gravitation, magnetic fields, stellar emissions, SNe, etc. Beyond changing the equilibrium state of the medium, these processes can destabilise the dense molecular clouds and trigger stellar formation. The cloud is considered

unstable when it reaches the so-called *Jean mass*, which reads

$$M_{\mathrm{J}} = \frac{\pi}{6}\left(c_s^2\frac{\pi}{G}\right)^{3/2}\frac{1}{\sqrt{\rho}}, \tag{2.1}$$

where c_s, G, and ρ, are the sound speed in the cloud, the gravitational constant, and cloud density, respectively. The consecutive stages of the proto-star formation are described by Larson (1969) and are illustrated in Fig. 2.1. The stages are characterised by an *adiabatic index* γ, which is the ratio between the heat capacities at constant volume and pressure.

(i) The cloud enters the first contraction phase. While the compression heats the gas, the thermal emission of dust grains cools it such that the process is isothermal and $\gamma = 0$.

(ii) The first contraction stops when the medium becomes optically thick at $\rho = 10^{-13}\,\mathrm{g\,cm^{-3}}$. The thermal emission of dust grains can no longer leave the newly formed *first Larson core*. Therefore the contraction phase becomes adiabatic ($\gamma = 5/3$). After reaching $100\,\mathrm{K}$, molecule rotational modes are excited, which decrease the adiabatic index to $\gamma = 7/5$.

(iii) As the temperature reaches $2-3\times10^3\,\mathrm{K}$, the hydrogen molecules dissociate, which consume much more energy, so the adiabatic index drops to $\gamma \sim 1.1$ and the gas enters a second collapse phase.

(iv) Finally, at a density of $\rho \sim 10^{-3}\,\mathrm{g\,cm^{-3}}$, all the molecules are dissociated. This stage marks the formation of the *second Larson core*. The contraction is adiabatic again and continues until reaching temperatures $T \gtrsim 10^6\,\mathrm{K}$ when the nuclear reactions start to produce helium in the internal regions.

The core thus forms the new proto-star. The remaining matter surrounds the proto-star by forming a *protoplanetary disk*, which is accreted and altered by the proto-star emission until its disappearance.

Main sequence The newly formed star enters the *main sequence* phase, into which it will stay most of its life. The long-term stability of stars relies on the compensation between the gravitation, which tends to collapse the star, and the pressure produced by the nuclear reactions occurring in the stellar core, which tends to expand the star. The reaction occurring in the main sequence stellar core forms helium atoms from 4 hydrogen atoms

$$4\,{}^1\mathrm{H} \longrightarrow {}^4\mathrm{He}. \tag{2.2}$$

However, this reaction can occur via different reaction chains/cycles: while the helium is formed via the proton-proton (PP) chain in the core of low-mass stars ($M_* \lesssim 1.1\,\mathrm{M}_\odot$), the carbon-nitrogen-oxygen (CNO) cycle is active in the core of more massive stars ($M_* \gtrsim 1.1\,\mathrm{M}_\odot$). The effect of different chains influences the structure of the star as low-mass stars have a radiative core, while more massive stars develop a convective core. The main sequence phase timescale is around the time for the star to consume $10\,\%$ of the hydrogen, which can be formulated by

$$\tau_{\mathrm{nuc}} = 0.1\frac{\chi M_* c^2}{L_*}, \tag{2.3}$$

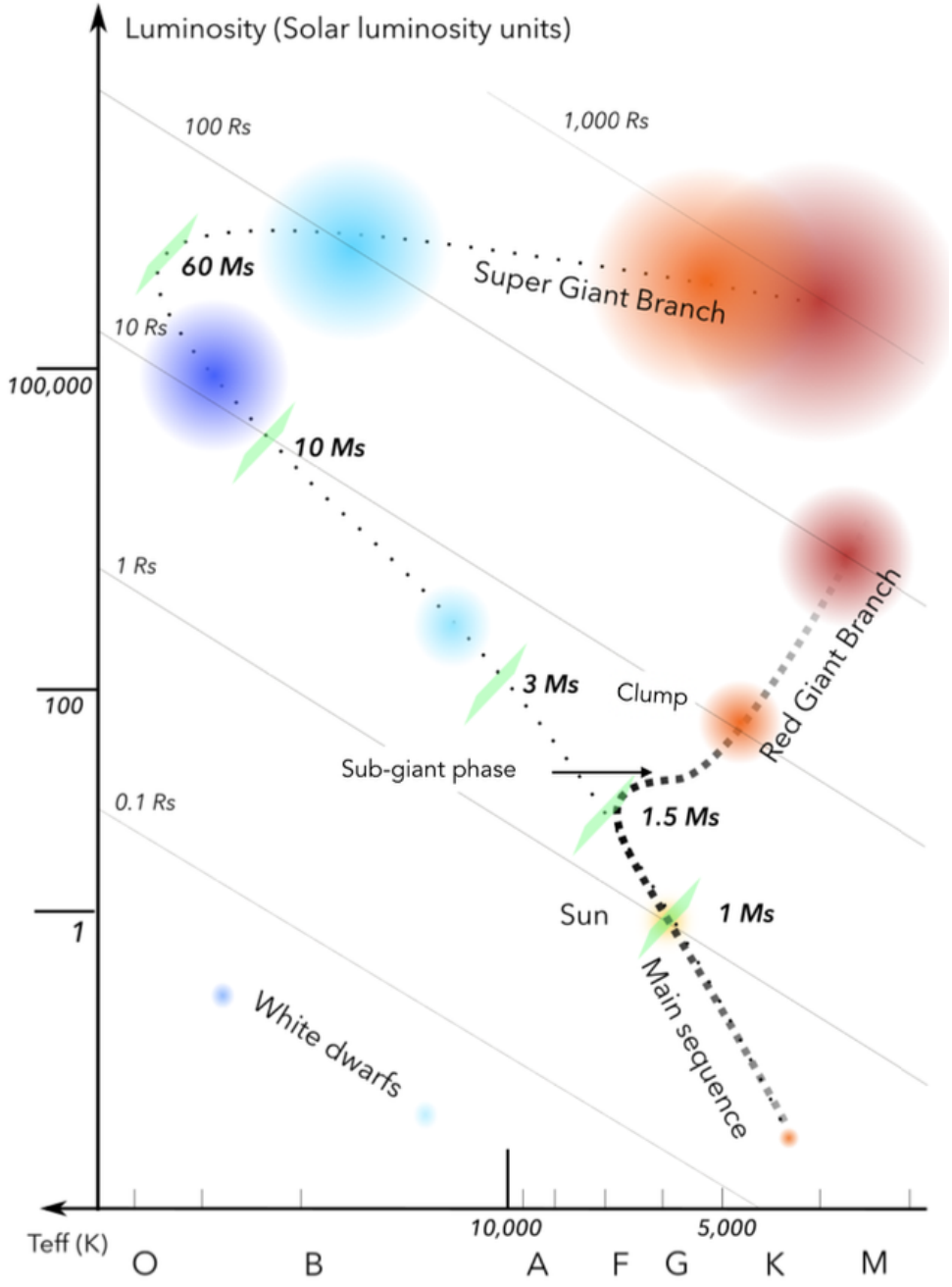

Figure 2.2 — Scheme of the stellar evolution in the Hertzsprung-Russell diagram, which represents the star luminosities as a function of their effective temperature. The dashed and dotted lines illustrate the path of the low-/intermediate-mass stars ($M_* \leqslant 8\,\mathrm{M}_\odot$) and massive stars ($M_* \geqslant 8\,\mathrm{M}_\odot$), respectively. Note that solar units are noted with the index $\bullet_s$ instead of the usual $\bullet_\odot$. *Figures adapted from Bugnet (2020).*

where χ is the yield of the nuclear reaction and L_* is the star luminosity. Therefore, the lifetime of a star depends on its mass and luminosity. If we assume the common mass-luminosity relation

$$\left(\frac{L_*}{L_\odot}\right) \sim \left(\frac{M_*}{M_\odot}\right)^4 , \tag{2.4}$$

low-mass stars live longer than intermediate-mass or massive stars. For instance, the main sequence phase of a Sun-like star ($M_* \sim 1\,\mathrm{M}_\odot$) lasts $\sim 10\,\mathrm{Gyr}$, which is 1000 times longer than for a $10\,\mathrm{M}_\odot$ star. This phase is visible as a diagonal from low to large effective temperatures[1] and surface luminosities in the so-called Hertzsprung-Russell (HR) diagram, which is illustrated in Fig. 2.2.

End of life of low-/intermediate-mass stars Once the whole hydrogen is consumed in the burning region, i.e. where the nuclear reactions take place, stars with masses $0.6\,\mathrm{M}_\odot \leqslant M_* \leqslant 8\,\mathrm{M}_\odot$ brutally contract to reach a new equilibrium state. The hydrogen is burnt in a layer around the core forming a *burning shell*. The star enters a short *sub-giant phase* in which the effective temperature drops due to the expansion of the envelope (external layers), which lets the thermal energy leave the star. The temperature drop is compensated by the increase of the stellar radius such that the luminosity $L_* \propto r_*^2 T_*^4$ remains constant.

The star leaves this state and follows the red giant branch when the helium core reaches the Schönberg-Chandrasekhar limit ($M_{\mathrm{He}} \sim 0.1 M_*$, Schönberg & Chandrasekhar, 1942), above which the helium core contracts. The gas in the core of low-mass stars ($0.6\,\mathrm{M}_\odot \leqslant M_* \leqslant 2\,\mathrm{M}_\odot$) becomes too dense for the thermal pressure to compensate the gravitation. The free electrons occupy all the lowest energy levels and create a degeneracy pressure such that the Pauli exclusion principle (i.e. fermions can not occupy the same quantum state) remains respected. The matter therefore becomes degenerate. In the case of intermediate-mass stars ($2\,\mathrm{M}_\odot \leqslant M_* \leqslant 8\,\mathrm{M}_\odot$), the gas is not dense enough in the core to become degenerate, so it collapses brutally. During this phase, the superficial layers are much less gravitationally bound to the star due to the envelope expansion and so can be expelled by the stellar wind.

When the core reaches the temperature of $T \sim 10^8\,\mathrm{K}$, the helium is burnt to produce carbon atoms $^{12}\mathrm{C}$ and oxygen $^{16}\mathrm{O}$ atoms (and also beryllium atoms $^{8}\mathrm{Be}$ but it is very unstable). The exact three-step reaction chain, called triple-α, reads

$$^2\mathrm{He} + {}^2\mathrm{He} \longrightarrow {}^8\mathrm{Be}, \tag{2.5}$$

$$^8\mathrm{Be} + {}^2\mathrm{He} \longrightarrow {}^{12}\mathrm{C} + 2\,\gamma, \tag{2.6}$$

$$^{12}\mathrm{C} + {}^2\mathrm{He} \longrightarrow {}^{16}\mathrm{O} + \gamma, \tag{2.7}$$

where γ denotes a γ-ray photon. The helium burning causes an increase of the tempereature in the stellar core. While the core of intermediate-mass stars can expand to find a new equilibrium, the core of low-mass stars can not expand due to its degenerate state (the pressure degeneracy depends very little on the temperature). The temperature therefore increases dramatically and the triple-α reactions run away as its power strongly depends on the temperature ($\propto T^{40}$). This causes a large region to burn helium in a the same short time period (a few seconds), which releases a large amount of energy. This sudden event conistutes

[1] The term 'effective' indicates that the temperature is measured in the star black body spectrum. The main sequence star place in this diagonal depends on its mass.

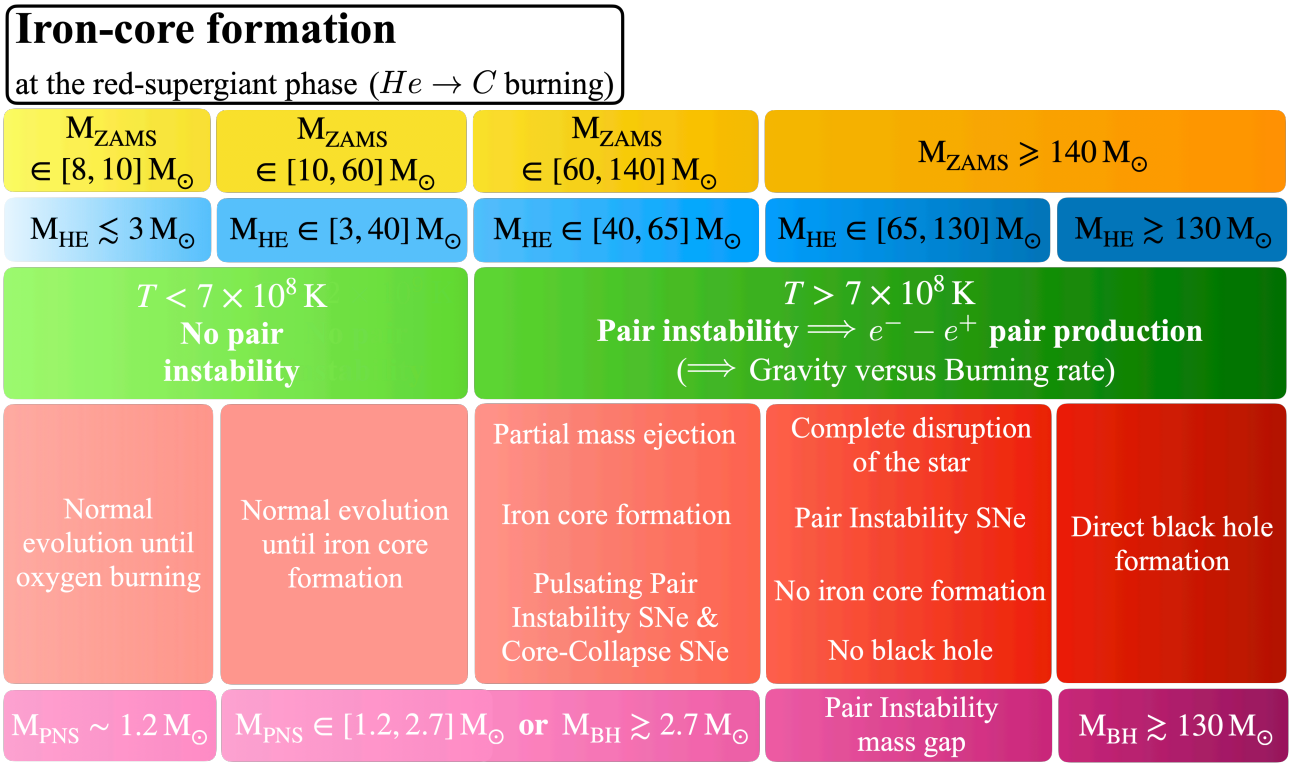

Figure 2.3 — Array describing the fate of massive stars as a function of the mass of their helium core.

the so-called *helium flash* and stops when the temperature becomes high enough for the thermal pressure to exceed the degeneracy pressure, eliminating the degeneracy. Once the helium is entirely consumed, most of the envelope has been blown by stellar winds to form the *planetary nebula* and the remaining external layers contract onto the inert degenerate carbon-oxygen core, forming a *white dwarf*.

2.1.2 . Supernova explosion mechanism

Fate of massive stars For massive stars ($M_* \geqslant 8\,M_\odot$), the evolution slightly differs as suggested by the HR diagram (Fig. 2.2). Their core is already massive enough to ignite helium burning before reaching the degeneracy critical density (as intermediate-mass stars). Unlike lower-mass stars, they are massive enough to produce new contraction episodes and ignite new nuclear reactions. These successive ignitions result in an onion-structured star, within which each burning shells form heavier elements as we go deeper into its interior.

The evolution and explosion mechanism of the massive star depends on its mass. The different end-of-life scenarios can therefore be classified according to the star Zero-Age-Main-Sequence mass (ZAMS) mass $M_{\rm ZAMS}$, i.e. the mass of the star when it enters the main sequence phase. However, the mass of the star changes along its evolution depending on its properties such as the metallicity and the rotation, which makes the estimation of its mass during the late stages uncertain for a specific value of $M_{\rm ZAMS}$. Instead, we will use the helium core mass at the onset of the ^{4}He burning phase, noted $M_{\rm He}$. Its value is more robust to predict how the star will end its life since no helium is expected to be expelled from the star from the helium burning phase to the explosion. The different explosions are summarised with respect to $M_{\rm He}$ in Fig. 2.3. We also display an approximation of the corresponding $M_{\rm ZAMS}$.

$\leqslant 3\,\mathrm{M}_\odot$ In this mass range, the successive ignitions stop after the burning of the oxygen $^{16}\mathrm{O}$ in the core of the lightest of the massive star. As the burning stops, the following contraction does not result in the burning of new elements but in a degenerated core. Neon $^{20}\mathrm{Ne}$ and magnesium $^{24}\mathrm{Mg}$ nuclei capture the free electrons, which lowers the degeneracy pressure. The unstable degenerate core ends up collapsing and the star explodes like in classical neutrino-driven CCSNe (Hillebrandt et al., 1984). This short range of masses translates into very few candidates of this kind of SNe, called *electron-capture supernovae (ECSNe)*(Hosseinzadeh et al., 2018, Hiramatsu et al., 2021, Valerin et al., 2022). The remaining compact object is expected to be a NS due to the low mass of the progenitor core.

$3-40\,\mathrm{M}_\odot$ For this range of masses, the helium core is large enough to burn new elements until the production of iron $^{56}\mathrm{Fe}$. These stars explode through the standard neutrino-driven CCSN mechanism, which will be explained in detail later.

$40-65\,\mathrm{M}_\odot$ For helium cores between ~ 40 and $65\,\mathrm{M}_\odot$, the temperature reaches $\gtrsim 7\times10^8\,\mathrm{K}$ after the burning of $^{16}\mathrm{C}$. With such temperatures, a large quantity of γ-ray photons are energetic enough to be converted into electron-positron pairs. This lowers the radiative pressure and destabilises the star core (Fowler & Hoyle, 1964, Barkat et al., 1967, Rakavy & Shaviv, 1967). The induced collapse causes the brutal ignition of $^{16}\mathrm{O}$ burning and ejects large masses from the envelop of the star. Several similar episodes can happen until the formation of the iron core. As in typical SN explosions, the core collapses and the outer regions of the star are blasted by the expanding shock front. This type of explosion is called *pulsational (or pulsating) pair-instability supernovae (PPISNe)*. The compact remnant of PPISNe is expected to be a BH due to the high progenitor mass but a massive NS could be maintained for fast enough rotations (Rahman et al., 2022).

$65-130\,\mathrm{M}_\odot$ When the helium core reaches a mass $M_\mathrm{He}\gtrsim 65\,\mathrm{M}_\odot$, the nature of the SNe changes. As in the previous case, a pair-instability occurs after $^{14}\mathrm{C}$ burning, but here the onset of $^{16}\mathrm{O}$ burning is so energetic that the whole star blows up, leaving no remaining core or compact object. Thus, these disruptive explosions called *pair-instability supernovae (PISN)* leave a gap in the mass distribution of BHs between $\sim 60\,\mathrm{M}_\odot$ and $\sim 130\,\mathrm{M}_\odot$.

$\gtrsim 130\,\mathrm{M}_\odot$ Finally, the massive stars exceeding roughly $\sim 300\,\mathrm{M}_\odot$ end up collapsing into a BH with a mass of $\gtrsim 130\,\mathrm{M}_\odot$, without any explosion.

Note that some of the values of M_He used to define these intervals remain approximative, especially both lower and upper limits of PISNe. Indeed, the core rotation, which depends on the treatment of angular momentum transport, or uncertainties on the nuclear reaction rate can significantly change these limits by several tens of solar masses (Renzo et al., 2020, Marchant & Moriya, 2020, Woosley & Heger, 2021).

Standard explosion mechanism As mentionned in the previous chapter (Chap. 1), $\sim 1/3$ of magnetars are associated to SN remnants whose kinetic energy is consistent with that of classical CCSNe. Therefore, most magnetars are formed in these explosions. Hence, we focus on the classical CCSN mechanism, which is also the most common sort of SNe observed in the Universe. The different stages of the mechanism illustrated in the scheme of Fig. 2.4 will structure the following description of the mechanism.

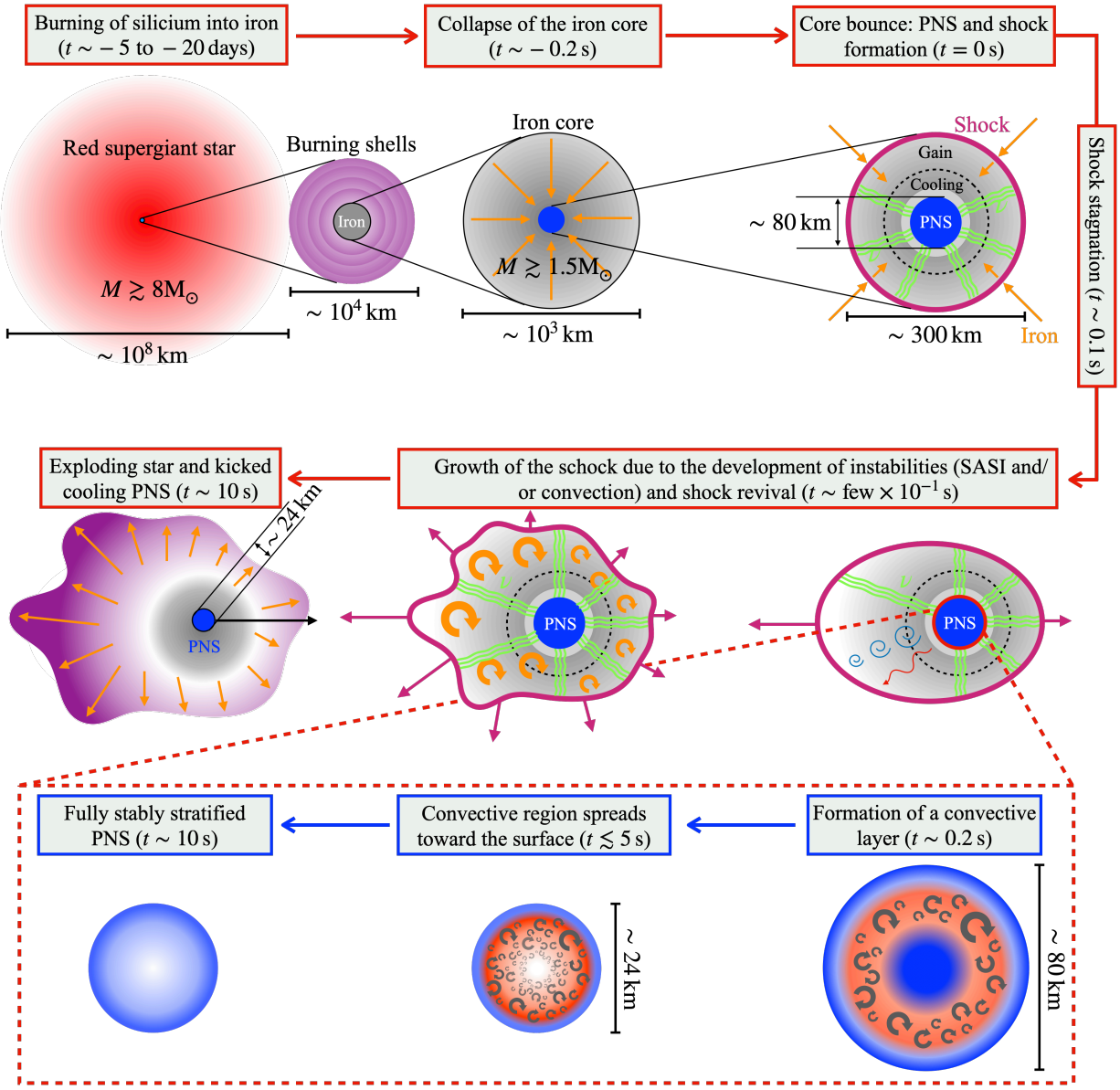

Figure 2.4 — Scheme of the standard core-collapse supernova mechanism with the evolution of the stratification in the PNS interior. The arrows illustrate the fluid motion, among which the circling ones represent the convective motions. The green oscillating curves represent the neutrino emission. In the SASI development phase, the blue swirls and the wavy red arrows represent the acoustic wave and vorticity perturbations, respectively.

t − few days The last burning phase occurring in the massive star core is the burning of silicon ^{28}Si into iron ^{56}Fe. The iron ^{56}Fe is one of the elements with the strongest nuclear binding energy, which is the difference between the mass of the whole atom nucleus and the sum of the mass of each nucleon contained in this same nucleus. This implies that the burning of ^{56}Fe into heavier elements consumes more energy than it releases, which runs counter to the principle of minimum energy. Therefore, the iron accumulates in the core and the ^{28}Si burning reservoir wanes in a timescale of 5 to 20 days. Since the core does not release nuclear energy, it contracts due to gravity. The iron core becomes degenerate, which favours the inverse β decay reaction

$$\mathrm{p} + \mathrm{e}^- \longrightarrow \mathrm{n} + \nu_e \,, \tag{2.8}$$

where p, e^-, n and ν_e are the symbols of the proton, electron, neutron, and electronic neutrino, respectively. The latter is a very light elementary particle that interacts sparsely with matter but is essential in the CCSN process. Due to this reaction, the fraction of neutrons in the core increases with the direct consequence of lowering the mass limit above which the electron degeneracy pressure can no longer compensate for gravity. This mass is the so-called Chandrasekhar mass limit, which reads

$$M_{\mathrm{Ch}} = 1.45 \left(\frac{Y_e}{0.5} \right)^2 \mathrm{M}_\odot \,, \tag{2.9}$$

where Y_e is the electron fraction, i.e. the difference between the number of electrons and positrons per baryon.

t−0.2 s Once this limit is reached, the iron core with a radius of $\sim 1500\,\mathrm{km}$ collapses within $\sim 0.2\,\mathrm{s}$ and reaches at its centre extreme densities and temperature of $\rho \sim 10^{14}\,\mathrm{g\,cm^{-3}}$ and $T \sim 10^{11}\,\mathrm{K}$, respectively. Under such conditions, the atom nuclei disintegrate and the core becomes a dense and hot soup of nucleons which constitutes the proto-neutron star (PNS). The adiabatic index is also strongly stiffed, from the index of a relativistic degenerate object $\gamma = 4/3$ to $\gamma \sim 2 - 4$, depending on the used equation of state (e.g. Haensel & Zdunik, 2007, Koliogiannis & Moustakidis, 2019, Routray et al., 2024). At this stage, the strong interaction force of nucleons stops the collapse when the PNS radius (usually defined by the radius at which the density is $\rho = 10^{11}\,\mathrm{g\,cm^{-3}}$) reaches $\sim 80\,\mathrm{km}$. This causes the formation of the shock at the radius of $\sim 10\,\mathrm{km}$, where the collapse becomes supersonic. This stage is the so-called *core bounce*, which is usually used as the reference time $t = 0\,\mathrm{s}$ in the study of CCSNe.

t= 0 s Although the shock radius keeps growing, a large part of the gravitational energy is consumed by the neutrino emission by inverse β decay (Eq. (2.9)) and by the photodissociation of ^{56}Fe

$$^{56}\mathrm{Fe} + \gamma \longrightarrow 13\,^4\mathrm{He} + 4\,\mathrm{n}, \tag{2.10}$$

$$^4\mathrm{He} + \gamma \longrightarrow 2\,\mathrm{p} + 2\,\mathrm{n}, \tag{2.11}$$

while the infalling matter goes through the shock. The bounce alone is thus insufficient to expand the shock at distances larger than $\sim 70\,\mathrm{km}$ from the PNS. During this *stalled shock* phase, the shock is stationnary and the matter surrounding the stellar core keeps

collapsing reaching supersonic velocities around one tenth of the speed of light in vacuum until it reaches the shock front.

The energy gained by the absorption of electronic and anti-electronic neutrinos emitted by the cooling PNS

$$\nu_e + n \longrightarrow e^- + p, \tag{2.12}$$
$$\overline{\nu}_e + p \longrightarrow e^+ + n \tag{2.13}$$

is the key ingredient of the shock revival (Bethe & Wilson, 1985). $\sim 4-10\,\%$ of the emitted neutrinos is absorbed by the matter in the zone between the shock and the PNS. The region in which the absorption rate is larger (lower) than the emission rate is called the *gain (cooling) region*. While the cooling region is near the PNS surface, the gain region is localised near the shock. The radius that defines the boundary between both regions is called the *gain radius* (black dotted circle in Fig. 2.4).

The neutrino heating in the vicinity of the shock increases the thermal pressure, which makes the shock grow. The infalling matter crossing the shock must therefore be advected slowly enough to be heated before reaching the cooling region. A criterion for the shock revival is thus to have an advective timescale larger than the heating timescale (e.g. Burrows & Goshy, 1993, Janka, 2001). However, the first 1D numerical simulations of CCSN failed to satisfy this criterion and so to produce a purely radial explosion by implementing neutrino heating only. This indicates the necessity of multi-dimensional ingredients such as instabilities to obtain a more efficient neutrino heating and so decrease this heating timescale.

t+0.2s It is now fairly consensual that (magneto)hydrodynamical instabilities play a crucial to enhance the neutrino heating. On the one hand, the *standing accretion shock instability (SASI)* (Blondin et al., 2003) is a very promising candidate as it was proven to help to produce explosions in 3D CCSN numerical simulations (e.g. Takiwaki et al., 2021). The SASI consists of an advective-acoustic cycle, in which the perturbed PNS outer boundary emits acoustic waves towards the shock front that injects vorticity perturbations in returning towards the PNS (Foglizzo et al., 2007). Since this cycle necessitates the presence of an accretion shock and a dense central core, SASI can appear in other astrophysical contexts such as stellar formation (Ahmad et al., 2023). On the other hand, *a convective instability* can occur in regions with a strong enough negative entropy gradient to overcome the stabilising effect of the electron fraction profile. Many investigations aim at understanding the influence several parameters such as the rotation on the dynamics (e.g. Yamasaki & Foglizzo, 2008, Blondin et al., 2017, Kazeroni et al., 2017, 2018, Summa et al., 2018, Andresen et al., 2019, Glas et al., 2019, Walk et al., 2023) and the interaction between the SASI and convection (Buellet et al., 2023).

The motion caused by these instabilities create asymmetries in the front shock shape. This causes some areas to spend enough time in the gain region to be heated, which makes the gain region expand in these areas. The amount of absorbed energy increases and the shock thus grows asymetrically.

$t \gtrsim$ few $\times 10^{-1}$ s The shock finally reaches the regions beyond the iron core and propagates at a typical velocity of $\sim 3 \times 10^3\,\mathrm{km\,s^{-1}}$ (Kjær et al., 2010). In red-supergiant star with a typical radius of $10^8\,\mathrm{km}$, the shock thus needs a bit more than $9\,\mathrm{hours}$ to reach the most external layers of the star, which the observed electromagnetic signal of the SNe. Meanwhile, the nascent PNS contracts until reaching a final radius around $12-13\,\mathrm{km}$. This contraction phase influences the PNS internal structure, in which a convective layer develops and expands, almost reaching the PNS surface a few seconds after its formation. When the contraction is over, the convective region disappears as the entropy profile becomes less steep. After $10\,\mathrm{s}$, the PNS finally reaches its fully stably stratified structure. Note that the PNS can also collapse into a BH if the accretion of matter makes it reach the Tolman–Oppenheimer–Volkoff (TOV) mass limit.

Now that we described the main stages of the classical neutrino-driven SN explosion, it is interesting to look at the energy budget of the explosion. This type of explosion is called gravitational because the energy resevoir of the explosion is the gravitation. A total gravitational energy of $E_{\mathrm{grav}} \sim 3 \times 10^{53}\,\mathrm{erg}$ is liberated during the explosion. The majority of this energy ($\sim 99\,\%$) ends up into neutrino radiation that goes through the star without interacting with the matter. While a small fraction of neutrinos is absorbed, its energy is converted into kinetic energy ($E_{\mathrm{kin}} \sim 10^{51}\,\mathrm{erg}$) and thermal energy. Then, a bit less than $10\,\%$ of the gravitational energy is also converted into rotational energy in the core ($E_{\mathrm{rot}} \sim 10^{52}\,\mathrm{erg}$), a fraction of which is radiated in gravitational waves (GWs) due to the asymmetry of the shock ($E_{\mathrm{GW}} \sim 10^{46} - 10^{50}\,\mathrm{erg}$). Finally, once the shock reaches the star surface, the quasi-adiabatic expansion of the stellar envelope converts its thermal energy into electromagnetic radiation ($E_{\mathrm{rad}} \sim 10^{49}\,\mathrm{erg}$).

Multi-messenger astronomy provide observational constrains to test the neutrino-driven CCSN mechanism. On the one hand, the majority of neutrinos can leave the star without interacting with the stellar matter. Their detection by current (e.g. Super-Kamiokande, IceCube) and future (e.g. DUNE, JUNO, KM3NeT) detectors will allow us to probe the first phases of the explosions. The observed delay between the reception of neutrinos and SN must match the theoretical predictions, which can validate the global scenario or not. To this date, only the observation of the SN 1987A was completed by the detection of neutrinos (Hirata et al., 1987, Bionta et al., 1987). The observed neutrinos arrived to the detectors $3\,\mathrm{hours}$ before the electromagnetic signal, which supports the neutrino-driven mechanism and confirm the presence of a PNS. On the other hand, the different instabilities are expected to be detectable through the emission of GWs. The CCSNe numerical simulations show that the GW signal is dominated by the PNS oscillations at frequencies $\gtrsim 400\,\mathrm{Hz}$ and the SASI at $\sim 100\,\mathrm{Hz}$ (e.g. Radice et al., 2019, Mezzacappa et al., 2020, Andresen et al., 2021). For slow rotations, these signals could be observed by the current detectors if the source is at a Galactic distance $\sim 10\,\mathrm{kpc}$. Future detectors such as the Einstein Telescope and Cosmic Explorer will enlarge this distance and play a crucial role in the study of CCSNe.

Magnetorotational explosion mechanism As discussed in Sect 1.3.2, a strong magnetic field combined with a fast rotation influences significantly the explosion mechanism. A strong magnetic dipole of $\sim 10^{14} - 10^{15}\,\mathrm{G}$ can efficiently extract the energy of the newly formed PNS to inject it into the ejecta in the form of kinetic energy. This mechanism allow to inject more kinetic energy into the ejecta than in the neutrino-driven mechanism. Magnetorotational explosions are therefore good candidates to explain the observation of extreme explosions and

have been investigated using axisymmetric (i.e. no variations in the azimuthal direction) (e.g. Burrows et al., 2007, Dessart et al., 2008, Takiwaki et al., 2009, Bugli et al., 2020) and three-dimensional (3D) general relativistic numerical simulations (e.g. Mösta et al., 2014, Kuroda et al., 2020, Obergaulinger & Aloy, 2020, 2021, 2022, Bugli et al., 2021, 2023).

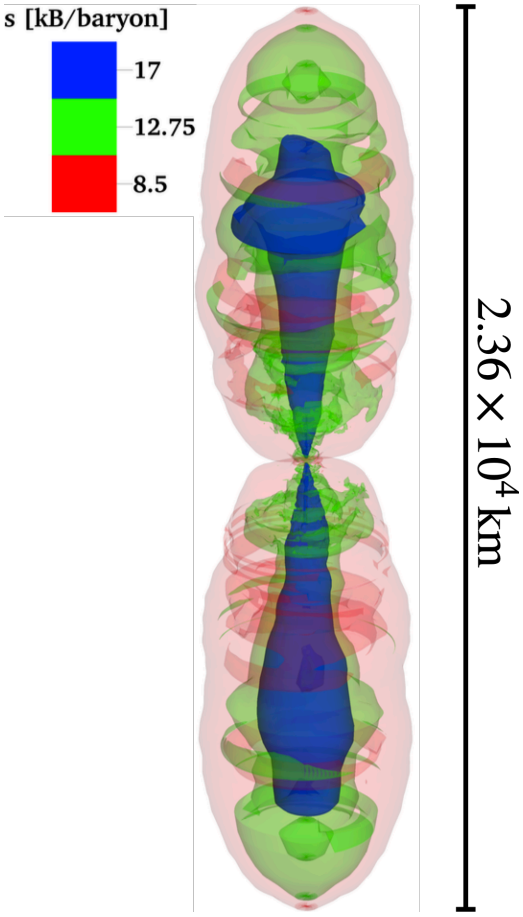

Figure 2.5 — Snapshot of a magnetorotational explosion with an initial strong magnetic dipole $410\,\mathrm{ms}$ after the onset. The isosurfaces show the entropy of the ejecta. *Figures adapted from Bugli et al. (2021).*

Although they do not reproduce the large kinetic energies of hypernovae, they can reproduce the formation of bipolar jets, which allows the study of its stability and its ability to drive the explosion. They strongly influence the explosion dynamics and produce gravitational waves. In particular, Bugli et al. (2020, 2021, 2023) investigated the impact of the initial magnetic field geometry on the ejecta dynamics. They show that the aligned dipole is the best magnetic geometry to form a stable jet and launch powerful explosions. Figure 2.5 illustrates the jet formation in a simulated magnetorotational explosion. This snapshot is taken at $410\,\mathrm{ms}$ after the explosion onset and the ejecta already has a vertical size of $2.36 \times 10^4\,\mathrm{km}$, which shows how fast the jet is launched. The equatorial dipole and quadrupole geometries produce jets quickly prone to non-axisymmetric instabilities but do not prevent the onset of the magnetorotational explosion (see also Mösta et al., 2014).

The presence of strong asymmetry in the explosion produces GWs, whose signature is constrained is some numerical simulations Bugli et al. (2023). Their amplitude is stronger in the absence of any magnetic field due to the presence of a hydrodynamic instability (called low $T/|W|$) but magnetic models only show weak GW emission. Overall, numerical simulations of magnetorotational explosions are essential investigation tools as they provide a better understanding of the explosion physical mechanism and predictions for the future multi-messenger observations.

Classification of supernovae Despite the lack of multi-messenger observations, SNe have been thoroughly investigated since their first historical observations between during the II$^{\mathrm{nd}}$ and IV$^{\mathrm{th}}$ century, which were interpreted as 'guest stars'. Thanks to modern telescopes, the observation of extragalactic SN is now very common, which compensates for the low Galactic SN rate of $2-3$ per century. For instance, 19859 SNe were detected in 2023[2] and the detection rate has been $\sim 2 \times 10^4\,\mathrm{yr}^{-1}$ since 2019. The future Vera Rubin observatory is even expected to multiply the number of detections by 100! The amount of SN observations provides a SN

[2] https://www.rochesterastronomy.org/sn2023/snstats.html

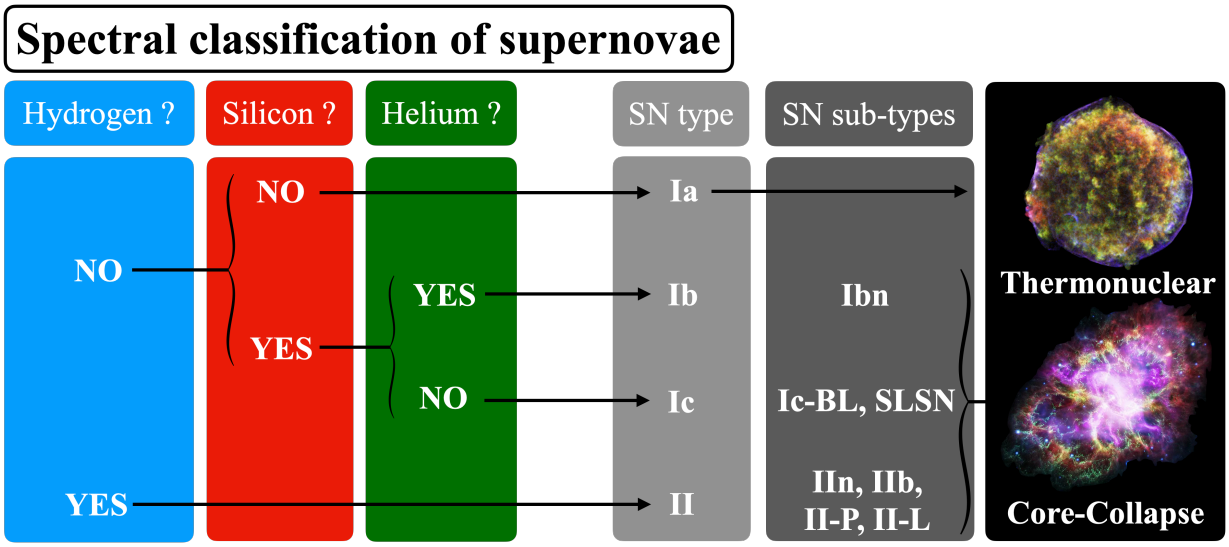

Figure 2.6 — SN classification according to their spectral properties.

classification depending on their observational and especially their spectral properties. The most common SN families are summed up in Fig 2.6. The distinction is made between SNe without and with hydrogen absorption lines, which are referred to as the *type I* and *type II* SNe, respectively. The former is also divided into three classes: *type Ia* with no traces of silicon, *type Ib* with the presence of silicon and helium lines, and *type Ic* which show traces of silicon but no helium lines. As mentioned in Sect. 1.3.2, the exceptional hypernovae and SLSNe are mostly type Ic SNe but a few SLSNe can be type II SNe.

The observations suggest that type Ia SNe have a different nature from the other SNe. First, they are interestingly observed in every type of galaxy, while the other SNe are observed in late-type (i.e. spiral) galaxies only. Their presence in late-type galaxies is not surprising since massive stars do not form in early-type (i.e. elliptical) galaxies and do not have long enough lifetimes to stay stable until the late phases of their host galaxy. Second, the absence of silicon is not expected for a CCSNe as this element is produced around the massive star iron core. These SNe are the product of runaway nuclear reactions in a white dwarf heated by the accretion of matter from a binary companion. These explosions, called *thermonuclear supernovae*, completely disrupt the white dwarf. The mechanism of this type of explosion will not be detailed here as the topic is beyond the scope of this thesis.

2.1.3 . Supernova fallback

The initial rotation period of most NSs is around $10-100\,\mathrm{ms}$ (e.g. Popov & Turolla, 2012, Igoshev et al., 2022) but its origin remains unclear. While it intuitively stems from the angular momentum of the progenitor iron core and so depends on the transport mechanisms in the star (e.g. Heger et al., 2005, Ott et al., 2006, Ma & Fuller, 2019, Fuller & Lu, 2022), the PNS rotation may be influenced by hydrodynamic instabilities following the core bounce (e.g. Blondin & Mezzacappa, 2007, Guilet & Fernández, 2014, Kazeroni et al., 2016, 2017). However, recent 3D CCSN numerical simulations suggest that the initial NS period is determined by the asymmetric accretion of matter that is initially ejected during explosion but remains gravitationally bound to the PNS, and so eventually falls back onto the PNS (Powell & Müller,

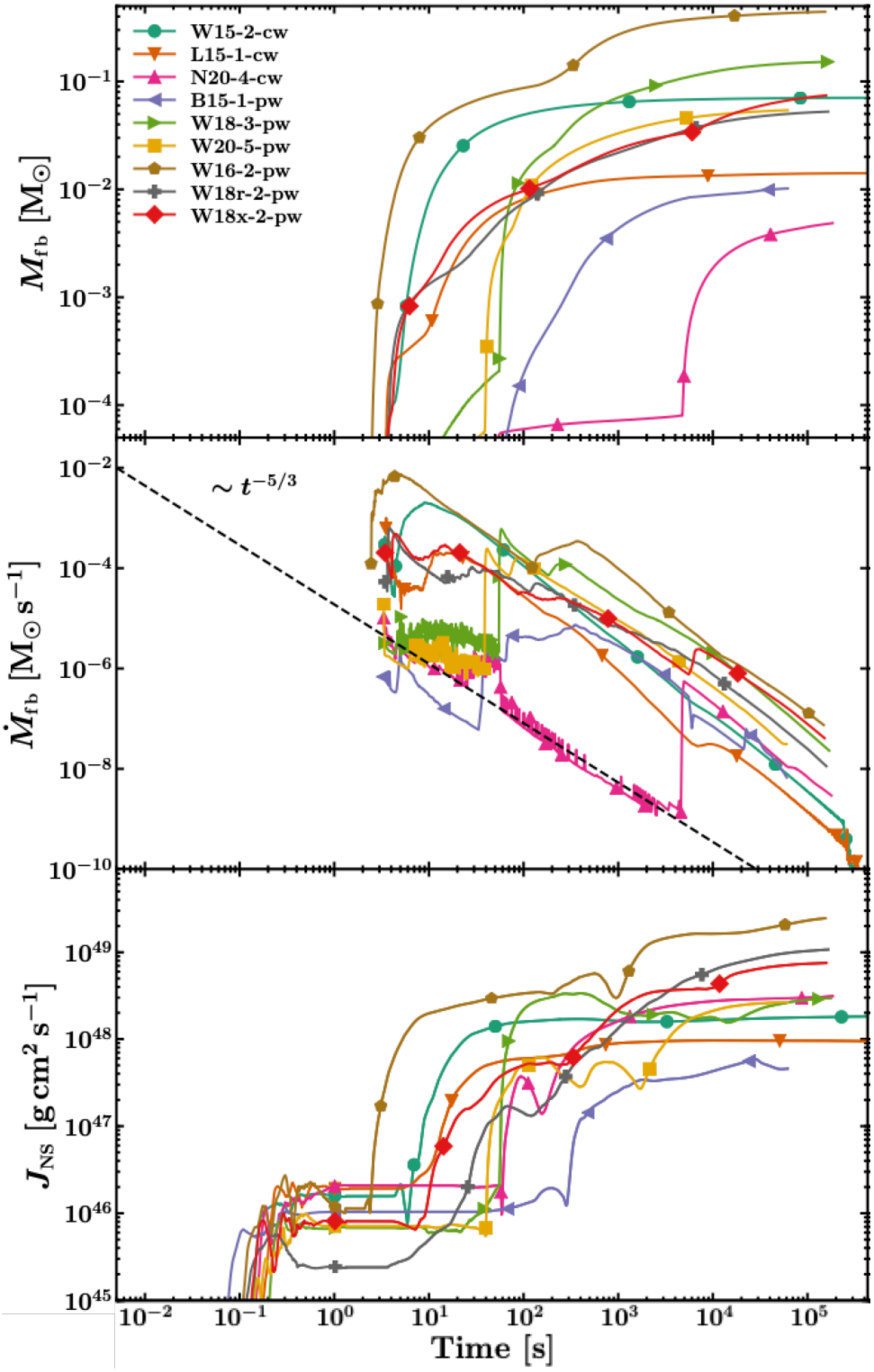

Figure 2.7 — Fallback properties as functions of the time after the core bounce for a set of 3D CCSN models of single-star progenitors. $M_{\rm fb}$ and $\dot{M}_{\rm fb}$ are the time-integrated fallback mass and accretion rate (the dashed line displays the asymptotic scaling $\sim t^{-5/3}$), $J_{\rm NS}$ is the NS angular momentum, assuming that all fallback matter with its angular momentum gets accreted by the compact object. *Figures adapted from Janka et al. (2022).*

2020, Chan et al., 2020, Stockinger et al., 2020, Janka et al., 2022). In addition to the initial NS period, the study of fallback accretion is also motivated by the problem of the spin-kick alignment, i.e. the alignment of the NS rotation axis with that of the kick velocity, which is observed in several pulsars (e.g. Romani & Ng, 2003, Ng et al., 2007, Yao et al., 2021). Janka et al. (2022) argues that this alignment is due to the asymmetric fallback accretion connected to the displacement of the NS (which is challenged by Müller, 2023).

Exemples of fallback and NS angular momentum $J_{\rm NS}$ evolution from 3D CCSN simulations of Janka et al. (2022) are displayed in Fig. 2.7, from which we can draw several observations:

- $5-10\,{\rm s}$ after the core bounce, we observe a steep increase of the NS angular momentum from $J_{\rm NS}\sim 10^{46}\,{\rm g\,cm^2\,s^{-1}}$ to $J_{\rm NS}\sim 10^{47}-10^{49}\,{\rm g\,cm^2\,s^{-1}}$, which corresponds to a spin-up from a rotation period of $P=2\pi I_{\rm NS}/J_{\rm NS}\sim 1\,{\rm s}$ to $P\sim 0.001-0.1\,{\rm s}$. This coincides with a sudden increase of the fallback mass up to $M_{\rm fb}\sim 10^{-3}-10^{-1}\,{\rm M_\odot}$. Note that the values of P may be overestimated because the NS is expected to move from the centre of the explosion due to the kick induced by the explosion while the NS remains in the centre of the integration domain in 3D CCSN simulations.

- After $\sim 10\,{\rm s}$, the mass-fallback rate $\dot{M}_{\rm fb}$ follows the asymptotic scaling-law $t^{-5/3}$, which is predicted for spherical accretion (Chevalier, 1989).

- Roughly $10-10^3\,{\rm s}$ after the bounce, the backward propagation of a reverse shock amplifies the fallback accretion, which translates into a local peak in the evolution of $\dot{M}_{\rm fb}$.

In addition, the specific angular momentum of the fallback matter can reach the Keplerian specific angular momentum

$$j_{\rm kep}\sim 1.5\times 10^{16}\left(\frac{M_{\rm NS}}{1.4\,{\rm M_\odot}}\right)^{1/2}\left(\frac{r_{\rm NS}}{12\,{\rm km}}\right)^{1/2}{\rm cm^2\,s^{-1}}\,, \tag{2.14}$$

which suggests that a fallback disk can form around the PNS. The interaction between the PNS magnetic dipole and the disc may strongly spin down the PNS in a propeller regime, which may explain the observation of ultra-long-period pulsars and magnetars (Chap. 9, Beniamini et al., 2020, Ronchi et al., 2022) and the light curve of luminous and extreme SNe (e.g. Dexter & Kasen, 2013, Metzger et al., 2018, Lin et al., 2020, 2021). Thus, these simulations demonstrate that fallback accretion is a key ingredient in determining the birth NS rotation period and may play an important for magnetar formation.

2.2 . The origin of magnetar magnetic fields

While the global picture of the CCSN explosions is well understood, the formation of the ultra-strong magnetic fields observed in magnetars remains an open question. The different scenarios can be sorted in two families: pre-collapse (Sect. 2.2.1) and post-collapse scenarios (Sect. 2.2.2). While the former relies on magnetic flux conservation of a magnetised iron core during its collapse, the latter argues that the magnetic field is amplified in the PNS by dynamo action.

2.2.1 . Pre-collapse scenarios: magnetic flux conservation

Fossil field hypothesis In this scenario, the iron core magnetic fields are expected to be strong enough to be amplified up to $10^{14}-10^{15}\,\mathrm{G}$ due to magnetic flux conservation during the core collapse. An order of magnitude for the necessary magnetic field B_{Fe} can be calculated by assuming a constant magnetic flux

$$\Phi_B \sim B_{\mathrm{Fe}} r_{\mathrm{Fe}}^2 \sim B_{\mathrm{NS}} r_{\mathrm{NS}}^2 \sim \mathrm{cst}. \tag{2.15}$$

Thus,

$$B_{\mathrm{Fe}} \sim B_{\mathrm{NS}} \left(\frac{r_{\mathrm{NS}}}{r_{\mathrm{Fe}}}\right)^2 \sim 6.4\times10^9 \left(\frac{B_{\mathrm{NS}}}{10^{14}\,\mathrm{G}}\right)\left(\frac{r_{\mathrm{NS}}}{12\,\mathrm{km}}\right)^2\left(\frac{r_{\mathrm{Fe}}}{1500\,\mathrm{km}}\right)^{-2}\mathrm{G}. \tag{2.16}$$

This scenario, also called *fossil field hypothesis*, is supported by the measure of the magnetic field at the surface of some massive stars, which is nonetheless different from B_{Fe}. The strength of these magnetic fields is inferred from the observation of the Zeeman effect, which translates into the split of emission lines (see the reviews Donati & Landstreet, 2009, Reiners, 2012). Recent surveys such as MiMeS and BOB found that $\sim 10\,\%$ of massive stars harbour strong surface magnetic fields of $\sim 10^2-10^3\,\mathrm{G}$ (Grunhut et al., 2017, Schöller et al., 2017, Sikora et al., 2019), which usually have simple geometry as they are well modelled by a tilted dipole (Kochukhov et al., 2019). The fraction of magnetised massive stars is therefore similar to the fraction of NS born as magnetars. Therefore, magnetic massive stars are assumed to be the progenitor of magnetars, while non-magnetic stars may be the progenitor of pulsars. Moreover, the magnetic flux in magnetic stars

$$\Phi_B(r=r_*) \sim 4.9\times10^{26}\left(\frac{B(r=r_*)}{10^3\,\mathrm{G}}\right)\left(\frac{r_*}{10\,\mathrm{R}_\odot}\right)^2 \mathrm{G\,cm^2}, \tag{2.17}$$

which is icomparable to the flux in magnetars

$$\Phi_B(r=r_{\mathrm{NS}}) \sim 1.4\times10^{26}\left(\frac{B_{\mathrm{NS}}}{10^{14}\,\mathrm{G}}\right)\left(\frac{r_{\mathrm{NS}}}{12\,\mathrm{km}}\right)^2 \mathrm{G\,cm^2}. \tag{2.18}$$

Finally, the recent observation of a Wolf-Rayet (WR) star, i.e. a massive star which ejects a great part of its mass by the expulsion of its outer layers, with a $4.3\times10^4\,\mathrm{G}$ surface magnetic field falls into the line (Shenar et al., 2023) as the NS magnetic field resulting from magnetic flux conservation is

$$B_{\mathrm{NS}} \sim B_{\mathrm{WR}} \left(\frac{r_{\mathrm{WR}}}{r_{\mathrm{NS}}}\right)^2 \sim 1.1\times10^{14}\left(\frac{B_{\mathrm{WR}}}{10^{14}\,\mathrm{G}}\right)\left(\frac{r_{\mathrm{WR}}}{0.88\,\mathrm{R}_\odot}\right)^2\left(\frac{r_{\mathrm{NS}}}{12\,\mathrm{km}}\right)^{-2}\mathrm{G}. \tag{2.19}$$

Although these observations support this scenario, the magnetic flux conservation concerns the magnetised iron core only because the rest of the star does not have time to collapse before its ejection by the front shock. The extrapolation used to infer the neutron star magnetic field from the measures at the surface of a massive star is thus strongly questionable. Using B_{Fe} is therefore more relevant for the magnetic flux argument, but B_{Fe} is not constrained by the observations despite the significant progress made by asteroseismology (Prat et al., 2020). Furthermore, population synthesis does not provide a definitive answer regarding whether the fossil field hypothesis can account for the populations of both pulsars and magnetars (Ferrario & Wickramasinghe, 2006, Makarenko et al., 2021). This suggests that a fraction of Galactic magnetars may not be the product of a fossil field. Finally, the

massive star strong dipole (and the induced stellar winds) spins down the star (Meynet et al., 2011, Potter et al., 2012, Keszthelyi et al., 2020, 2021) as shown by observations (Shultz et al., 2018, 2019b,a). Thus, this scenario does not account for fast-rotating magnetars, which are suspected to be the central engine of the most extreme explosions (see Sect. 1.3.2).

Fossil field If magnetars stem from strongly magnetised massive stars, we may wonder what the origin of stellar core magnetic fields is. First, the magnetic field of massive stars may also be a fossil field. Assuming a roughly spherical molecular cloud with a realistic magnetic field of $4 \times 10^{-6}\,\mathrm{G}$ (a value measured by Ching et al., 2022) and a typical density of $n \sim 10^3\,\mathrm{cm}^{-3}$, the magnetic Jean length is about $L_\mathrm{J} \sim 1\,\mathrm{pc}$ (Mestel, 2001), which is the typical size of a molecular cloud. Using magnetic flux conservation, we can estimate an average magnetic field of $\sim 7 \times 10^7\,\mathrm{G}$ for a $10\,\mathrm{R}_\odot$ star formed by the collapse of the cloud. Despite the underlying rough approximations, the magnetic fields of a star are not unlikely to stem from the magnetic field of the progenitor molecular.

Dynamo in the progenitor star Second, the non-linear coupling between a turbulent flow motion and a magnetic field called *dynamo action*, could amplify the magnetic field in different regions of stars during their main sequence or late stages. On the hand, the stellar core and the burning shells are unstable to convection during the main sequence phase and the late evolution stages, respectively. According to 3D numerical simulations, this instability can lead to a convective dynamo producing magnetic fields of $\sim 10^5\,\mathrm{G}$ in the core during main sequence (Augustson et al., 2016) and of $\sim 10^{10}\,\mathrm{G}$ in the burning shells during the late stages (Varma & Müller, 2023, Leidi et al., 2023). On the other hand, the stably stratified zones in large-scale shearing flows are also prone to dynamo action, which are driven by MHD instability such as the magnetorational instability (MRI) (e.g. Jouve et al., 2015, 2020, Meduri et al., 2024) or the Tayler instability (e.g. Spruit, 2002, Fuller et al., 2019). These dynamos could produce the surface magnetic fields of main sequence magnetised massive stars but also contribute to the magnetic field amplification during the late stages of the star. The generated magnetic fields would contribute to the chemical element mixing and angular momentum transport, which significantly influence the stellar evolution up to the explosion mechanism and the remaining compact object properties (e.g. Wheeler et al., 2015, Griffiths et al., 2022, Fuller & Lu, 2022).

Main sequence star merger Third, these magnetised massive stars could be the product of two main-sequence massive star mergers. The observations of massive stars demonstrate that most of them evolve in binary systems (Sana et al., 2012), which suggests that some of them must end up merging. Moreover, the recent observations of the massive star HD 148937 show that it is probably the product of a star merger (Frost et al., 2024). While the two stars merge, numerical simulations have shown that the magnetic field is amplified by MHD instabilities, which could be the MRI, even though magnetised shear instabilities such as the Kelvin-Helmotz instability may also play a role in this amplification (Schneider et al., 2019). Assuming $R_* = 5\,\mathrm{R}_\odot$ and magnetic flux conservation, the resulting magnetic field at the surface is $\sim 9 \times 10^3\,\mathrm{G}$, which is consistent with observations. The magnetic flux is $\Phi_B = 4 \times 10^{28}\,\mathrm{G cm}^2$ in the innermost $1.5\,\mathrm{M}_\odot$ of the merger remnant. This flux would imply a very strong magnetic field around $B_\mathrm{NS} \sim 3 \times 10^{16}\,\mathrm{G}$ in the magnetar. However, the question of the magnetic relaxation to the expected tilted dipole and star spin-down remains unclear as

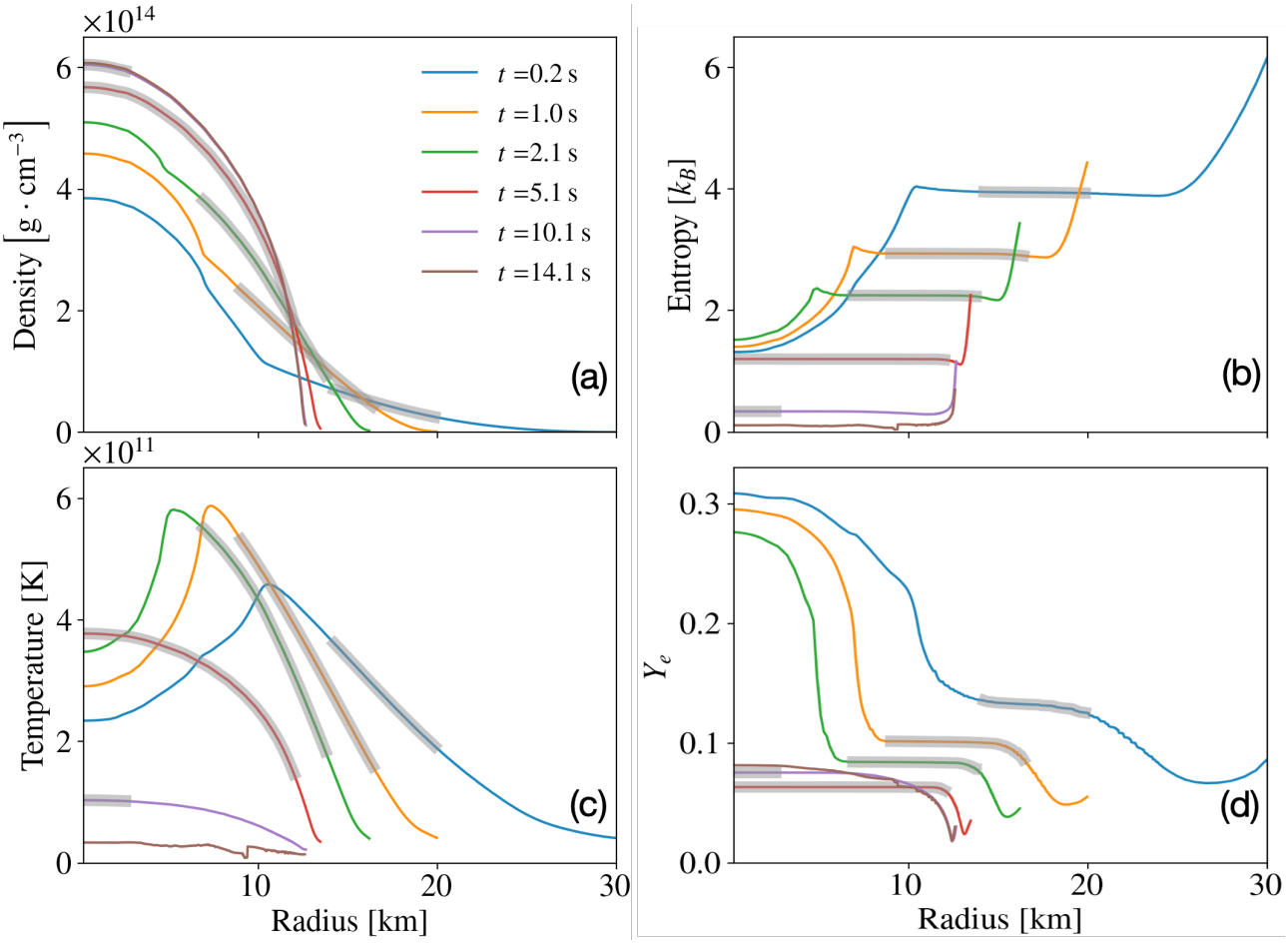

Figure 2.8 — Radial profiles of the PNS density (a), entropy (b), temperature (c), electron fraction (d) at different evolution times. The grey bands indicate the regions unstable to convection according to the Ledoux criterion. The data were provided by 1D CCSN simulations of PNS evolution from the code of Pascal (2021), Pascal et al. (2022). The EoS used is RG(SLY4) (Chabanat et al., 1998, Gulminelli & Raduta, 2015, Raduta & Gulminelli, 2019a).

three-dimensional numerical simulations are required (Schneider et al., 2020). Besides, the magnetic flux vary significantly in the star since $\Phi_B = 3.5 \times 10^{23}\,\mathrm{G\,cm^2}$ at the mass coordinate $16.9\,\mathrm{M}_\odot$, which is lower than at $1.5\,\mathrm{M}_\odot$. This challenges the usual extrapolation used to infer the B_{NS} from the measure of the star surface magnetic field.

Magnetic field stability Once the magnetic field in the star is formed, the field is either maintained by dynamo action or decays due to the resistivity. The latter case raises the question of the magnetic field geometry as it is expected to reach a stable configuration. This problem applies to several astrophysical questions, such as the main sequence star mergers we have just mentioned and the magnetic field evolution of white dwarves and NSs. Analytical studies demonstrated that purely poloidal (Markey & Tayler, 1973, Wright, 1973, Flowers & Ruderman, 1977) and purely toroidal (Tayler, 1973, Goossens & Tayler, 1980, Goossens et al., 1981) magnetic fields are unstable. This indicates that stable configurations must consist

of both components. Duez & Mathis (2010), Duez et al. (2010) analytically derived a family of stable configurations in barotropic equilibrium (i.e. parallel density and pressure gradients), which are also stable in numerical simulations including stable stratification. In the stable configuration of their simulation, the toroidal magnetic energy represents $\sim 95\,\%$ of the total magnetic energy corresponding to a ratio of the toroidal to the poloidal magnetic energies $E_\mathrm{T}/E_\mathrm{P} \sim 18$. Other numerical simulations investigations suggest a minimum ratio $E_\mathrm{T}/E_\mathrm{P} \gtrsim 0.25$ (Braithwaite, 2006, 2008, 2009, Akgün et al., 2013, Becerra et al., 2022b). The maximum of $E_\mathrm{T}/E_\mathrm{P}$ depends on the stratification and the ratio of the gravitational to the total magnetic energy (Becerra et al., 2022a).

Stable stratification is also a key ingredient to reach stability, as confirmed by numerical simulations in which no stable configuration is found for a constant entropy profile (Mitchell et al., 2015, Becerra et al., 2022a,b). However, numerical simulations including the effect of rotation of this stability and implementing initial magnetic geometries stemming from a saturated dynamo state are sorely lacking.

2.2.2 . Post-collapse scenarios: dynamo action in the proto-neutron star

Alternatively, a promising mechanism to produce strong magnetic fields is the dynamo action in the newly born PNS interior, hence the name 'post-collapse-scenarios'. Here, we will only focus on three dynamo process: the convective dynamo, the magnetorotational instbility (MRI)-driven dynamo, and the Tayler instability-driven dynamo (also called Tayler-Spruit dynamo). A general introduction to the rich problem of the dynamo in astrophysics will be given in the next chapter (more precisely in Sect. 3.2). A dynamo was first invoked by Duncan & Thompson (1992) to explain the strong magnetic field of magnetars. Since then, 3D numerical simulations brought crucial results in this direction for different dynamo mechanisms and strongly motivate the investigations undertaken during the preparation of this thesis.

Proto-neutron star structure In order to identify which regions are potentially prone to a specific dynamo process and when, we must look at how the PNS internal structure evolves. 1D CCSN numerical simulations provide the evolution of the PNS thermodynamical properties in the radial direction (see e.g. Hüdepohl, 2014, Pascal, 2021, Pascal et al., 2022), which depend on the implemented PNS equation of state (EoS). Compared to 2D and 3D CCSN simulations, these 1D simulations have the advantage to focus on the evolution of the PNS without having to resolve the evolution of the ejecta. The lower numerical cost allows to run more models and integrate several seconds of the PNS evolution.

To identify which region of the PNS is stable to convection, we use the Ledoux stability criterion, which reads

$$C_\mathrm{L} \equiv \partial_S \rho\big|_{P,Y_e}\, d_r S + \partial_{Y_e} \rho\big|_{P,S}\, d_r Y_e < 0\,, \tag{2.20}$$

where P, S, and ρ, are the pressure, entropy, and density, respectively. d_r is the derivative in the radial direction. Since $\partial_S \rho$ and $\partial_{Y_e}\rho$ are usually negative, this criterion indicates that negative entropy and electron fraction gradients convectively destabilise the fluid. The perturbation of a stably stratified region ($C_\mathrm{L} < 0$) produces gravity waves characterised by the *Brunt-Väisälä frequency*

$$N^2 = \frac{g}{\rho} C_\mathrm{L}\,, \tag{2.21}$$

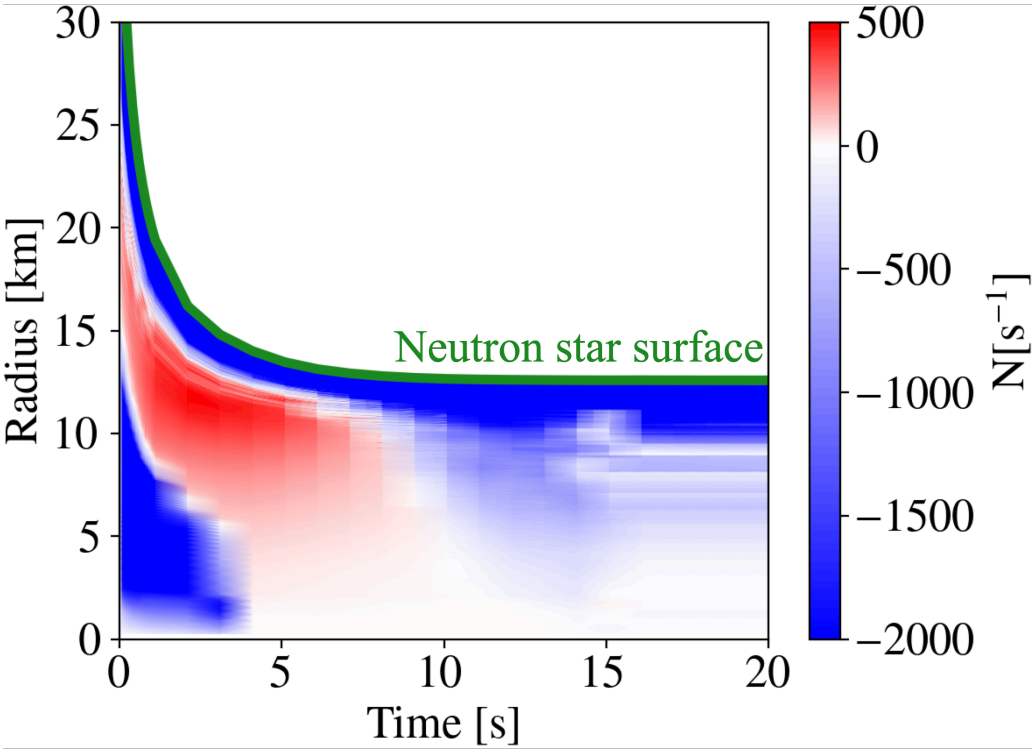

Figure 2.9 — Evolution of the PNS radius (green line) and map of the Brunt-Väsälä frequency. The stably stratified regions are indicated by $N < 0$ (blue). The origin of the time axis corresponds to the core bounce. The data were produced by 1D CCSN simulations of PNS evolution from the code of Pascal (2021), Pascal et al. (2022). The EoS used is RG(SLY4) (Chabanat et al., 1998, Gulminelli & Raduta, 2015, Raduta & Gulminelli, 2019a).

where $g = -\partial_r \Phi$ is the local gravitational acceleration with Φ the PNS gravitational potential. The stability criterion can therefore be rewritten as $N^2 > 0$. In the following, we choose to define the Brunt-Väisälä frequency like in Hüdepohl (2014)

$$N \equiv \mathrm{sign}(C_\mathrm{L}) \sqrt{-\frac{g}{\rho} |C_\mathrm{L}|}, \tag{2.22}$$

so that $N < 0$ ($N > 0$) for stably stratified (convectively unstable) regions.

As an example, Fig. 2.8 shows the evolution of the PNS density, entropy, temperature and electron fraction from a model run with the code of Pascal (2021), Pascal et al. (2022). We find the appearance of the convective zone (green band) and its evolution as described in Sect. 2.1.2. This zone corresponds to the region with $N > 0$ in Fig. 2.9. We observe that the convective zone spreads into the inner part of the PNS after $\sim 4\,\mathrm{s}$ until its disappearance at $\gtrsim 10\,\mathrm{s}$. Note that the values of N in the convective zone are artificially high because 1D simulations can not take into account the flattening of the unstable gradient by the convection. We also notice that the PNS reaches its final radius ($\sim 13\,\mathrm{km}$) $\sim 10\,\mathrm{s}$ after the core bounce.

Convective dynamo The existence of a convective zone during $\sim 5\,\mathrm{s}$ can be enough to produce a dynamo thanks to the convective motions and the rotation. This type of dynamo drives the magnetic fields of several astrophysical objects such as planets and stars, like the

Earth and the Sun. Numerical simulations have shown the existence of convective dynamos with a wide variety of geometries and dynamics. The convective dynamos are usually sorted as a function of their magnetic field topology, which can harbour either a dominant axial dipole (dipolar dynamo) or not (multipolar dynamo) (e.g. Gastine & Wicht, 2012, Schrinner et al., 2014, Raynaud et al., 2015, Zaire et al., 2022, Pinçon et al., 2024). The appearance of one of the geometries depends mostly on the rotation, the density gradient, and the magnetic diffusivity (also called resistivity).

The first numerical simulations of a convective dynamo in a PNS were performed by Raynaud et al. (2020). They modelled the convective zone of a PNS $0.2\,\mathrm{s}$ after the core bounce and obtained different convective dynamos. In the time series shown in Fig. 2.10 of a PNS rotating with a period of $P = 2.1\,\mathrm{ms}$, the magnetic field (red and orange lines) exponentially grows until reaching a first plateau. The magnetic strength is already strong with a root mean square (rms) magnetic dipole of $\sim 10^{14}\,\mathrm{G}$. A secondary growth amplifies the magnetic field until the dipole reaches $\sim 10^{15}\,\mathrm{s}$. Therefore, two saturated states are reached: a *weak* and a *strong* branch. The geometry of both the flow and magnetic field change between these solutions. While in the weak branch, the magnetic field does not show any dominant large-scale component, a large-scale $10^{16}\,\mathrm{G}$–toroidal magnetic emerges in the strong dynamo. The saturated states in both branches are independent of the intial magnetic field, which indicates the presence of a supercritical bifurcation.

The saturated magnetic field in the strong branch is in a super-equipartition state, i.e. the ratio of the magnetic to the kinetic energy densities $E_\mathrm{B}/E_\mathrm{K} > 1$. Figure 2.11 shows that this ratio in this branch scales like

$$E_\mathrm{B}/E_\mathrm{K} \propto Ro^{-1}, \tag{2.23}$$

where $Ro \equiv u/(d\Omega)$ with u the convective velocity, d the width of the convective zone, and Ω the angular velocity. This scaling demonstrates that the super-equipartition state is characterised by the balance between the Lorentz force created by the strong magnetic fields and the Coriolis force due to the fast rotation (Augustson et al., 2016). This balance is called the *magnetostrophic equilibrium*. From Eq. (2.23), a scaling for the magnetic flux can be inferred

$$\Phi_\mathrm{B} \sim r_\mathrm{NS}^2 B \propto (M_\mathrm{NS}^2 r_\mathrm{NS} \Phi_o j^3)^{1/6}, \tag{2.24}$$

where Φ_o and j are the heat flux at the outer sphere and the specific angular momentum of the PNS. Thus, the magnetic field scales as

$$B \propto \left(\frac{M_\mathrm{NS}^2 \Phi_o}{r_\mathrm{NS}^8}\right)^{1/6} \Omega^{1/2}. \tag{2.25}$$

Masada et al. (2022) also investigated numerically the PNS convection but using different PNS evolution models and at different PNS evolution stages. They also find a dynamo solution but whose saturated state is always in a turbulent regime, i.e. $E_\mathrm{B}/E_\mathrm{K} < 1$. Therefore, they only find the weak dynamo branch and not find the strong branch discovered by Raynaud et al. (2020).

A second study by Raynaud et al. (2022) also investigates the dynamo in a $5\,\mathrm{s}$–old PNS and the induced GW signal. While the magnetic field mitigates the GW amplitude in the weak dynamo regime (slow rotation), the GW amplitude steeply increases with rotation in the strong dynamo regime (fast rotation), whatever the PNS age:

$$h_\mathrm{fast} \propto h_\mathrm{slow} Ro^{-4/3} \propto \Omega^{8/5}, \tag{2.26}$$

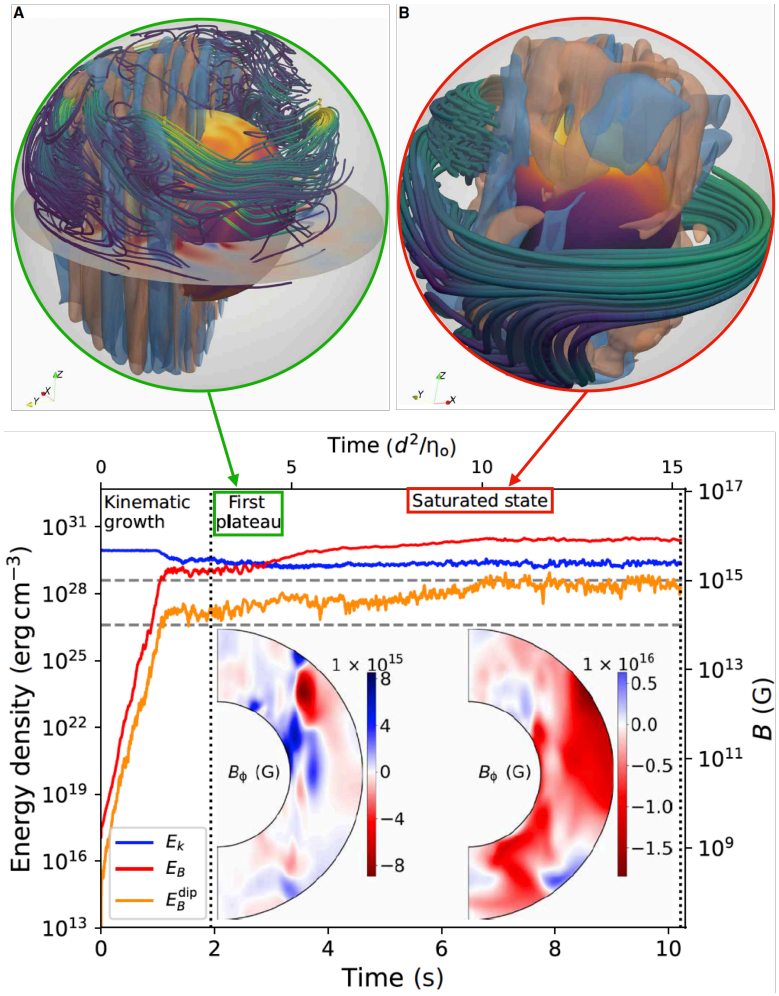

Figure 2.10 — Numerical simulations of the convective dynamo in a fast rotating PNS ($P = 2.1\,\mathrm{ms}$). Top: Figures A and B are three-dimensional snapshots of the 'weak' and 'strong' dynamo branches. Green/violet lines, red/blue isosurfaces, and colours on the inner sphere are the magnetic field lines, radial velocity, and entropy, respectively. Bottom: Time series (in physical and resistive units) of the kinetic (blue), magnetic (red), and magnetic dipole (orange) energy densities. Inset: meridional slices of the azimuthal magnetic field in the weak and strong branches, respectively. *Figures adapted from Raynaud et al. (2020).*

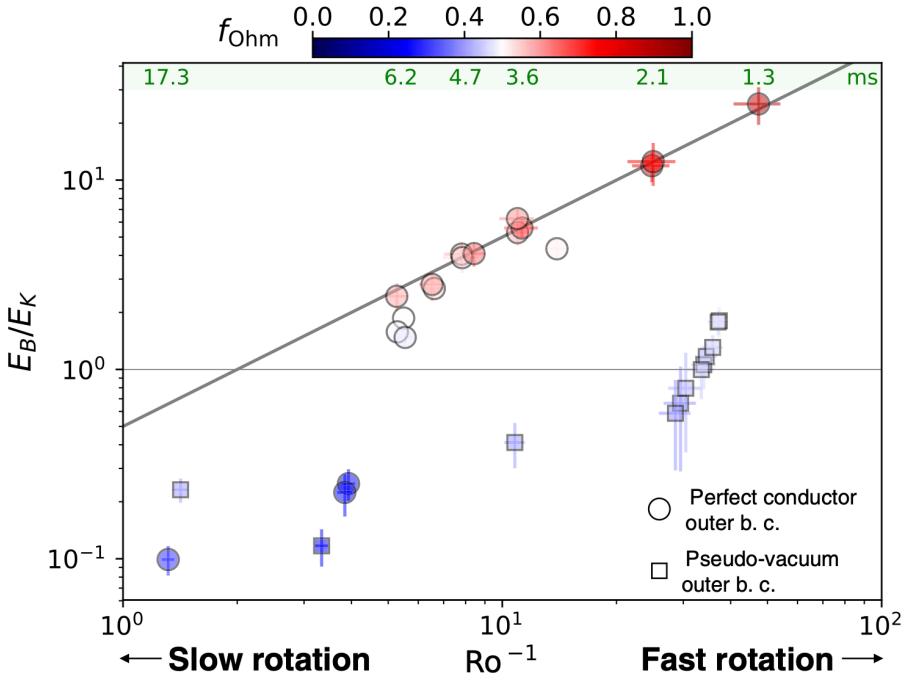

Figure 2.11 — Ratio of the magnetic to the kinetic energy densities as a function of the inverse Rossby number, which is equivalent to the rotation rate of the outer sphere. The solid grey line is the best-fit scaling $E_{\rm B}/E_{\rm K} = 0.5 Ro^{-1}$. The rotation period is also plotted in the green banner on the top of the plot. $f_{\rm Ohm}$ is the ratio of ohmic to total dissipation *Figures adapted from Raynaud et al. (2020)*

where $h_{\rm fast}$ ($h_{\rm slow}$) is the GW amplitude in the fast (slow) rotation regime. The strain spectrogram and the characteristic strain spectrum for the same convective dynamo case with $P = 2.1\,{\rm ms}$ are plotted in Fig. 2.12. During the growth of the magnetic field (blue curve), several peaks emerge in the characteristic strain spectrum, which are interpreted as inertial modes. These waves are linked to the Coriolis force, which acts as a restoring force. When the strong saturated state is reached, these peaks disappear but a mode at low frequencies ($\sim 10\,{\rm Hz}$) appears in the spectrogram. This mode is caused the strong toroidal magnetic field, which makes it a direct GW signature of the dynamo.

Although the convective dynamo is a promising mechanism to generate magnetar-like magnetic fields, the convective layer is always located below a stably stratified layer. The magnetic field lines must be lifted to the surface to explain the different astrophysical events related to magnetars. Thus, the dynamics of the stably stratified zone, including its interaction with the convective layer, must be investigated.

MRI-driven dynamo Dynamo action can also develop in stably stratified zones in the presence of differential rotation. Indeed, these regions are prone to MHD instabilities which can generate large-scale magnetic fields via a non-linear process. The latter will be winded by the differential rotation to feed the MHD instability. This looping process can amplify the magnetic field until saturation due to diffusivities created by the instability-induced turbulence. This type of dynamo was reported in numerical simulations for several MHD instabilities, such as the magnetic buoyancy (Cline et al., 2003), the Tayler instability (Petitdemange et al., 2023, Barrère et al., 2023), and the MRI (Rincon et al., 2007).

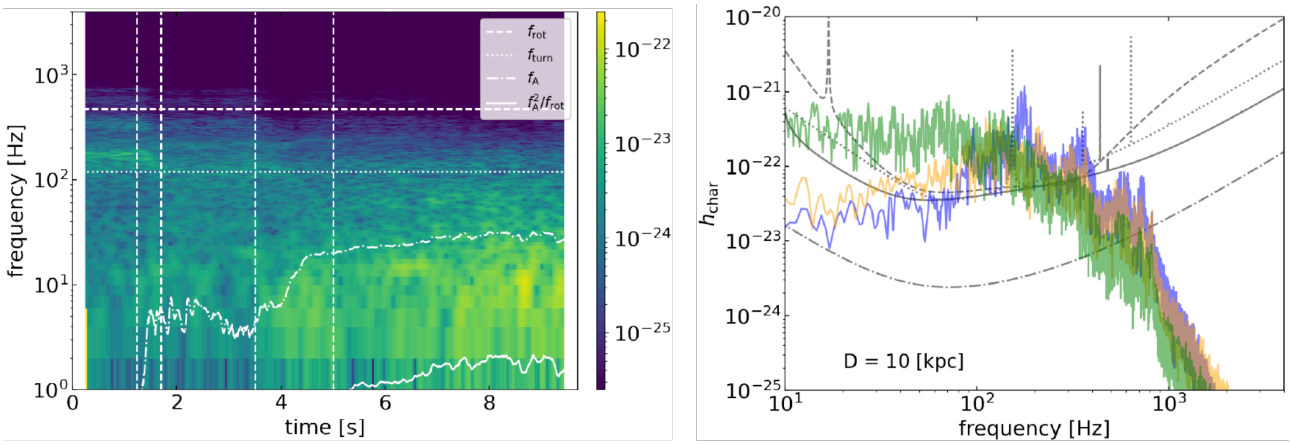

Figure 2.12 — GW signature of the convective dynamo with a rotation period of $P = 2.1\,\mathrm{ms}$. Left: GW spectrogram du signal upon which the following characteristic frequencies are overplotted: the rotation frequency f_{rot}, the convective *turnover* frequency f_{turn}, and the Alfvén frequency f_{A}. Right: GW characteristic strain for different phases of the dynamo: linear growth (blue), weak dynamo saturation (orange), strong dynamo saturation (green). Grey lines denote the sensibility of several GW observatories. *Figures adapted from Raynaud et al. (2022)*

The latter develops in differentially rotating stably stratified regions with an angular frequency that decreases with the radius, i.e. the shear rate $q \equiv r/\Omega\, d_r\Omega < 0$. In the ideal case without any diffusivity and viscosity, the flow satisfying $q < 0$ is unstable to the MRI whatever the magnetic field strength. Therefore, differentially rotating flows which are hydrodynamically stable according to the Rayleigh criterion $q \leqslant 2$ becomes unstable in the presence of a magnetic field. The growth rate of the instability reads $\sigma = q\Omega/2$ and so does not depend on the magnetic field neither. The instability can be seen as an oscillatory deformation of inital large-scale vertical magnetic field lines. Therefore, during the growth, the MRI modes form horizontal layers alternating the sign of the generated horizontal magnetic. These layers are called the *channel modes*, whose wavelength is proportional to the magnetic field.

Differentially rotating flows with $q < 0$ are common in astrophysics, which explains why the MRI was invoked in the context of accretion disks (e.g. Hawley et al., 1996, Fromang et al., 2007, Lesur & Ogilvie, 2008, Riols et al., 2013, Held et al., 2024) and stellar radiative zones (e.g. Wheeler et al., 2015, Jouve et al., 2015, 2020, Griffiths et al., 2022, Meduri et al., 2024). But this configuration naturally appears during the core collapse and the PNS contraction, which makes the MRI-driven dynamo another promising mechanism to produce strong magnetic fields in the PNS stably stratified zone, as first suggested by Akiyama et al. (2003).

The first numerical simulations aimed at modelling local regions of the nascent PNS. The most commonl setup is the *shearing box* in which the modelled region must be small enough to consider a differential rotation $\Delta\Omega \ll \Omega$. However, the box must be big enough to resolve the typical length scale of the turbulent flow and magnetic field, so that periodic boundary conditions can be applied. Local simulations using this set-up (or a shearing-disc set-up, Obergaulinger et al., 2009) show that a strong magnetic field reaching $\sim 10^{14} - 10^{15}\,\mathrm{G}$ can be maintained in the regime of millisecond rotation periods (Masada et al., 2012). The first simulation of MRI in a global setup also show that the dynamo produces a large-toroidal

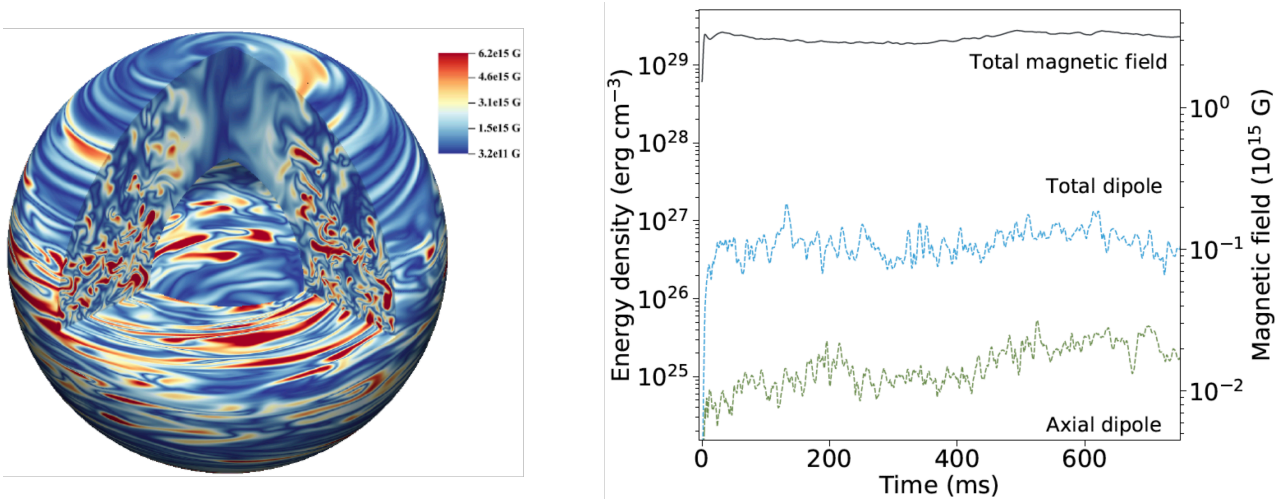

Figure 2.13 — Numerical simulations of MRI-driven dynamo in a fast rotating PNS ($P \sim 1\,\mathrm{ms}$). Left: Three-dimensional snapshot of the magnetic field intensity. Right: Time series of the total magnetic energy (black), the total magnetic dipole energy (blue), and the magnetic axial dipole energy (green). *Figures adapted from Reboul-Salze et al. (2021).*

magnetic-field of $10^{15} - 10^{16}\,\mathrm{G}$ in the same rotation regime, which is consistent with the formation of a magnetar (Mösta et al., 2015).

Reboul-Salze et al. (2021) also produced global models of MRI-driven dynamos in a spherical unstratified PNS rotating with a period of $P \sim 1\,\mathrm{ms}$. Despite a dominant small-scale geometry (see snapshot in Fig. 2.13), this study demonstrates that the dynamo can produce a $120°$-tilted magnetic dipole of $\sim 10^{14}\,\mathrm{G}$, which represent $\sim 5\,\%$ of the total magnetic field (see time series in Fig. 2.13). In a follow-up, Reboul-Salze et al. (2022) investigated the impact of a realistic density profile of the stably stratified outer region of a $0.2\,\mathrm{s}$–old PNS. The magnetic dipole is still mostly equatorial but with a strength of $\sim 6 \times 10^{12}\,\mathrm{G}$, which is ~ 17 times weaker than in the unstratified model. Using magnetic flux conservation, the dipole reach $\sim 7 \times 10^{13}\,\mathrm{G}$ at the end of the PNS contraction, which is in the low range of the classical magnetar dipoles. However, the magnetic field in now dominated by an axisymmetric toroidal magnetic field of $\sim 1.4 \times 10^{14}\,\mathrm{G}$, which should be sufficient to produce magnetar-like acitivty. Besides, the axisymmetric magnetic field harbour an oscillatory behavior that is well described by a $\alpha\Omega$ mechanism (see Sect. 3.2.5 for a detailed introduction to this kind of mechanism).

The impact of other ingredients specific to PNS physics has been investigated in other studies:

- The neutrinos interact with the PNS matter, which is optically thick until a few seconds after its formation. In a very fast rotating and young PNS with a radius of $40\,\mathrm{km}$, the neutrino can prevent the development of the MRI in the inner region if the initial magnetic field is $\lesssim 10^{12}\,\mathrm{G}$ (Guilet et al., 2015). Between 20 and $30\,\mathrm{km}$, the neutrinos act as a drag force or a viscosity that can slow down the growth of the MRI modes and so impact the saturated strength of the large-scale magnetic fields. However, the neutrinos do not influence the MHD in the PNS outer region.

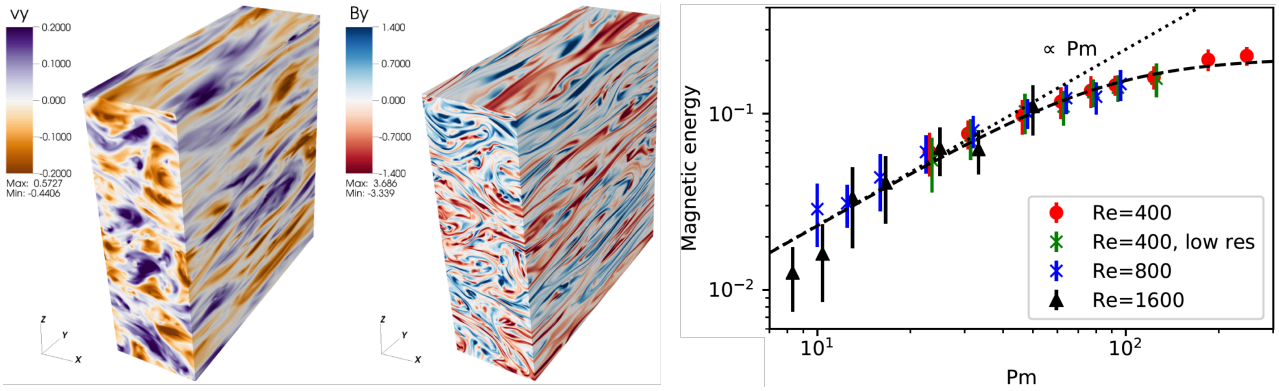

Figure 2.14 — Local simulations of the MRI-driven dynamo in the high-Pm regime. Left: Snapshots of the y-component (equivalent to the azimuthal direction in spherical coordinates) of the velocity and magnetic fields. Right: Time and spatial average of the magnetic energy in the saturated state as a function of the magnetic Prandtl number Pm and for different values of the Reynolds number Re. *Figures adapted from Guilet et al. (2022).*

- Second, the thermal stratification due to entropy gradient significantly influences the MRI. Guilet & Müller (2015) report that stronger stratifications decrease the MRI growth rate, while the magnetic energy increases. This suggests that stratification delay the development of secondary instabilities that saturate the instability. In the global simulations of (Reboul-Salze et al., 2022), the MRI modes are killed at the equator where N/Ω is the larger.

- Finally, the question of the low-resistivity regime is critical for PNS as the resistivity is $\sim 10^{11} - 10^{13}$ times smaller than the neutrino viscosity (Thompson & Duncan, 1993, Barrère et al., 2023). This regime (as any astrophysical regime) is unreachable by current numerical simulations but may significantly impact the dynamo mechanism (see Sect 3.2) and so the MRI-driven dynamo. New numerical studies in a shearing box set-up are optimistic as the magnetic energy increases with Pm at moderate values of Pm and plateaus at large Pm (Guilet et al., 2022, Held & Mamatsashvili, 2022). These two regimes are illustrated by the right plot in Fig. 2.14. At large Pm, the viscous and resistive scales are clearly seperated. This can be seen in the snapshots the velocity and magnetic fields at $Pm = 256$ in the same figure since the typical length scale of the magnetic field is far smaller than that of the velocity field.

2.2.3 . Alternative scenarios

After introducing the main magnetar formation scenarios, we briefly mention two alternative mechanisms:

- Binary NS mergers can result in the formation of very massive millisecond magnetars, whose magnetic field could explain the plateau phase in the X-ray emission of some short gamma-ray bursts (Metzger et al., 2008, Lü & Zhang, 2014, Gompertz et al., 2014). This magnetic field could be the product of the MRI-driven dynamo as it would develop in similar physical conditions as in a PNS (Guilet et al., 2017). Heavy numerical simulations of relativistic MHD demonstrated that the MRI contributes to amplify the

magnetic field of the compact remnant up to $\sim 10^{16} - 10^{17}\,\mathrm{G}$ (see App. C.3.5 and e.g. Kiuchi et al., 2024). As in the millisecond magnetar model for hypernovae/long GRBs and SLSNe, the extreme generated magnetic dipole efficiently spins down the magnetar to power the explosion ejecta. If the magnetar mass excceeds the TOV mass limit, the strong spin-down can cause its collapse into a BH since the rotation may not be fast enough to balance the gravity. This collapse can be observed as a sudden drop in the light curve during the afterglow emission. Nonetheless, the merger rate is very weak ($\sim 3 \times 10^{-14}\,\mathrm{R}_{\mathrm{MW}}^{-3}\,\mathrm{yr}^{-1}$, with R_{RW} the Milky Way disc radius) and so the majority of magnetars are not the result of a binary NS merger.

- Finally, the tricky problem of dynamo action in the low-resistivity regime motivated the study of a new dynamo mechanism which could amplify the magnetic field at later stages of the PNS evolution. This stage must be late enough for the PNS to be optically thin to neutrinos, i.e. the high neutrino viscosity vanishes. Therefore, Pm becomes lower (but still large as calculated in the Supplementary Materials of Chap 6), which could ease the development of large-scale magnetic fields. Lander (2021) suggests that the precession motion of the PNS could produce a dynamo $\sim 100\,\mathrm{s}$ after the PNS formation. However, this scenario is still preliminary and deserves further investigations.

2.3 . The necessity of a new scenario

To recap, the pre-collapse scenario is an intuitive way to explain the formation of magnetars, but the magnetic field of the progenitor core needs to be strong and to survive the full stellar evolution (Spruit, 2008). Moreover, it may be difficult for this scenario to explain the population of both pulsars and magnetars (Makarenko et al., 2021). Also, numerical simulations suggest that the efficiency of both convective and MRI-driven dynamos increases for faster PNS rotation (Raynaud et al., 2020, 2022, Reboul-Salze et al., 2021, 2022), which makes them good candidates to explain the central engine of extreme explosions. However, it may be more challenging for them to explain magnetar formation in standard SNe, which requires slower initial rotation of the PNS. Indeed, the observed SN remnants associated with Galactic magnetars have an ordinary kinetic explosion energy (Vink & Kuiper, 2006, Martin et al., 2014, Zhou et al., 2019). This suggests that most Galactic magnetars are formed in standard SNe, which is consistent with the fact that extreme explosions represent about $1\,\%$ of all SNe, whereas magnetars constitute at least $10\,\%$ of the whole Galactic young neutron-star population (Kouveliotou et al., 1994, Gill & Heyl, 2007, Beniamini et al., 2019). Under the assumption that all the rotational energy of the PNS is injected into the kinetic energy of the explosion, the kinetic energy of the proto-magnetar must not exceed the standard kinetic energy of a SN explosion of $10^{51}\,\mathrm{erg}$, which translates into a constraint on its initial rotation period of $\gtrsim 5\,\mathrm{ms}$ (Vink & Kuiper, 2006).

All things considered, the aforementioned scenarios require that the progenitor core be either strongly magnetised or fast rotating. It remains uncertain whether one of these conditions is met in a sufficient number of progenitors. We therefore present the first investigation of a new scenario wherein magnetars form from a slowly rotating, weakly magnetised progenitor. We consider the situation in which a newly formed PNS is spun up by the matter initially ejected by the SN explosion that remains gravitationally bound to the compact remnant and eventually falls back onto its surface. As the accretion is asymmetric, recent

numerical simulations suggest that the fallback can bring a significant amount of angular momentum to the PNS surface (Chan et al., 2020, Stockinger et al., 2020, Janka et al., 2022). We investigate the possibility that a magnetar may form due to the dynamo action triggered by the spin-up from this fallback accretion. In this scenario, the MRI is expected to be stable because the PNS surface rotates faster than the core. Convection is also stable because the PNS is fully stably stratified at the start of the fallback, i.e. roughly $\sim 5-10\,\mathrm{s}$ after the core bounce (Stockinger et al., 2020, Janka et al., 2022). We suggest that the magnetic field is amplified by another dynamo mechanism: the so-called Tayler-Spruit dynamo, which is driven by the Tayler instability. This dynamo is usually invoked for magnetic field amplification in the context of stellar interior physics, especially because of its suspected implications for angular momentum transport and the magnetic desert in Ap/Bp stars (e.g. Rüdiger & Kitchatinov, 2010, Szklarski & Arlt, 2013, Bonanno & Guarnieri, 2017, Guerrero et al., 2019, Ma & Fuller, 2019, Bonanno et al., 2020, Jouve et al., 2020). However, this dynamo process has never been studied in the framework of magnetar formation.

3

Physical modelling: Astrophysical fluid dynamics

Contents

As briefly mentioned in the previous chapter, the Tayler-Spruit dynamo is a crucial mechanism to understand angular momentum transport in stellar interiors and could produce the magnetic fields of magnetars. This dynamo mechanism is central to this thesis, which is why we devote a chapter to its modelling. We will start by presenting the general framework of the astrophysical fluid dynamics modelling and describe the mathematical formalism of the magnetohydrodynamics (MHD) approach (section 3.1). Then, we will introduce the rich and complex dynamo problem (section 3.2). Finally, we will describe the Tayler instability and its capacity to sustain a dynamo (section 3.3). Note that we will take into account neither the relativistic effects nor the quantum effects in this chapter and that the equations will be written using the cgs units convention.

3.1 . Magnetohydrodynamics (MHD) theory

3.1.1 . Modelling of astrophysical plasmas

Most of the matter in the Universe is in a plasma state, i.e. a gas mostly composed of electrons and ions. The motion of these charged particles allows the plasma to conduct electricity and so harbour a magnetic field. The electromagnetic field also produces feedback by modifying the motion of the particles, which makes the electromagnetic field an integral component of the plasma. This coupling between the charged particles and the electromagnetic field tends to generate two complementary tendencies: on the one hand, a disorganised behaviour due to thermal agitation, on the other hand, an ordered tendency due to electromagnetic feedback. The plasma dynamics is therefore intrinsically strongly non-linear. The propagation of perturbations in the plasma is also complex because it implies both collisions or sound waves and electromagnetic waves. Plasma physics is thus located between statistical mechanics (description of a large number of particles) and electromagnetism. The *mechanical* part of the plasma dynamics is governed by the equation

$$m d_t \mathbf{v} = q(\mathbf{E} + \frac{1}{c}\mathbf{v} \times \mathbf{B}), \tag{3.1}$$

where $\mathbf{E}$, $\mathbf{B}$, and v are the respective electric, magnetic, and velocity fields. m, q and c are the mass and the charge of the particle and the speed of light in vacuum, respectively. The *electromagnetic* part is governed by Maxwell's equations, which reads in their local form (with CGS convention)

$$\boldsymbol{\nabla} \cdot \mathbf{E} = 4\pi\rho \qquad \text{(Poisson's equation)}, \tag{3.2}$$

$$\boldsymbol{\nabla} \cdot \mathbf{B} = 0 \qquad \text{(Solenoidal condition)}, \tag{3.3}$$

$$\boldsymbol{\nabla} \times \mathbf{E} = -\frac{1}{c}\partial_t \mathbf{B} \qquad \text{(Faraday's law)}, \tag{3.4}$$

$$\boldsymbol{\nabla} \times \mathbf{B} = \frac{1}{c}(4\pi\mathbf{J} + \partial_t \mathbf{E}) \qquad \text{(Ampere's equation)}, \tag{3.5}$$

where ρ and $\mathbf{J} \equiv \rho\mathbf{v}$ are the respective charge density and electric current.

Depending on their number density n and temperature T, astrophysical plamas show a wide phenomenological diversity from the solar wind ($n \sim 3 - 10\,\mathrm{cm}^{-3}$, $T \sim 10^4 - 10^6\,\mathrm{K}$ at 1 AU) to neutron stars (NSs, $n \sim 10^{37}\,\mathrm{cm}^{-3}$, $T \sim 10^6 - 10^{11}\,\mathrm{K}$ depending on their age). However, every plasma is considered as *quasi-neutral* from a macroscopic point of view, i.e. on large spatial scales. These scales must be large enough to consider that every charge interacts continuously with a large number of neighbouring particles, which creates a long-range Coulomb force. Also, any deviation from this quasi-neutral state is compensated quickly due to the strong electrostatic forces in the plasma. We can therefore define characteristic length and time scales above which every plasma respects the quasi-neutrality. First, the Debye length

$$\lambda_\mathrm{D} \equiv \sqrt{\frac{k_\mathrm{B} T}{4\pi n q^2}}, \tag{3.6}$$

where k_B is the Boltzmann constant. The Debye length can be seen as the limit below which the electron "motion" is driven by thermal agitation (deviation from neutrality) and above which the electrostatic force damps this agitation. Since particles with opposite charges attract each other, they tend to create an accumulation of opposite charges around them at

a distance $\sim \lambda_{\rm D}$. This fluctuation in charge density screens the electric fields, in the sense that the electric (or Coulomb) potential decreases exponentially and becomes negligible at lengths greater than $\lambda_{\rm D}$ (Debye & Hückel, 1923). Second, the plasma (or Langmuir) frequency

$$\omega_{pe} \equiv \sqrt{\frac{4\pi n_e e^2}{m_e}}, \tag{3.7}$$

where n_e, m_e and e are the electron density, the mass of the electron and the elementary charge, respectively. $2\pi/\omega_{pe}$ can be seen as the timescale for the electrostatic force to restore the neutrality of the plasma.

From these two characteristic scales, we define the criteria which underlie the descriptions of plasmas:

(i) The typical scale of the system L must be larger than the Debye length:
$L/\lambda_{\rm D} \gg 1$.

(ii) The number of particles in a sphere of radius $\lambda_{\rm D}$ (Debye sphere) must be large (plasma approximation):
$n\lambda_{\rm D}^3 \gg 1$.

(iii) The quasi-neutrality imposes similar densities of positive and negative charges:
$n_e = \sum_\alpha n_\alpha$, where α represent the different species of ions.

(iv) The collision frequency between electrons and the neutral particles of the plasma f_c must not be too large:
$2\pi f_c < \omega_{pe}$.

We can add that the distance between particles must be larger than the thermal de Broglie wavelength (for relativistic electrons)

$$\lambda_{\rm B} \equiv \frac{hc}{(8\pi)^{1/3} k_{\rm B} T} < n^{-1/3}, \tag{3.8}$$

(h is the Planck constant) to consider the plasma as *classical*, as opposed to a *quantum* plasma. According to this criterion, the interior of a proto-neutron star (PNS) can either be a classical or a quantum plasma depending on its temperature and so its age. The minimum temperature for a classical PNS interior is

$$T_c = \frac{hc}{(8\pi)^{1/3} k_{\rm B}} n^{1/3} \sim 10^{10} \left(\frac{n}{10^{37}\,{\rm cm}^{-3}}\right)^{1/3} {\rm K} \tag{3.9}$$

Below T_c, quantum effects can appear in PNSs such as neutron superfluidity and proton superconuctivity for temperatures. However, 1D core-collapse supernovae (CCSNe) simulations show that temperatures above $10^{10}\,{\rm K}$ are maintained in the PNS even $\sim 15\,{\rm s}$ after the core bounce, when the fallback accretion starts (e.g. Pons et al., 1999, Roberts, 2012, Hüdepohl, 2014, Roberts & Reddy, 2017). In the context of our new magnetar formation scenario, the PNS interior is therefore a classical plasma.

A criterion can also be defined to consider a plasma as *relativistic*:

$$k_{\rm B} T_e > m_e c^2, \tag{3.10}$$

i.e. $T_e \gtrsim 6 \times 10^9\,\mathrm{K}$. This temperature is easily reached in PNSs where the temperature exceeds $10^{10}\,\mathrm{K}$.

Finally, we define the plasma coupling parameter as the ratio between the electrostatic interaction and the thermal energy

$$\Gamma \equiv \frac{q^2}{k_B T n^{-1/3}}\,. \tag{3.11}$$

From this parameter, we infer the Landau length $r_L \equiv q^2/(k_\mathrm{B} T)$. Therefore, depending on the distance between particles $d \sim n^{-1/3}$, the plasma can either be in a *kinetic* ($\Gamma > 1, d > r_L$) or in a *correlated* ($\Gamma < 1, d < r_L$) regime. The PNS interior interior is strongly correlated with

$$\Gamma \sim 8 \times 10^{-14} \left(\frac{T}{5 \times 10^{10}\,\mathrm{K}}\right)^{-1} \left(\frac{n}{10^{37}\,\mathrm{cm}^{-3}}\right)^{-1/3} \ll 1\,. \tag{3.12}$$

To conclude this short introduction to plasma theory, we will see the different approaches to understanding the strong non-linear dynamics of astrophysical plasmas:

Corpuscular approach The so-called theory of orbits consists in studying the motion of single particles evolving in a fixed electromagnetic background field. Though this approach may appear simple, the main difficulty remains in the non-linear equations of motion, especially with complex electromagnetic field configurations. This theory describes precisely the motion of particles in plasmas with low densities where the effect of neighbouring particles is small compared to the background field. The astrophysical applications are therefore the solar corona, the cosmic rays, or the Van Allen belts.

Statistical approach In this approach, called the kinetic theory, the focus is on large groups of N particles in a $6 \times N$-dimensional space. The evolution of the system is therefore described as one point in the $6 \times N$-dimensional state space, instead of N points in the usual 6-dimensional phase space of positions and velocities. Since describing the coupled evolution of each particle is difficult and costly for large values of N, the system is not usually described by a single point in the state space but as a density of states of the system, which is a probability density function. This density of states contains all the information of the plasma, and its evolution is described by the Liouville equation. However, we usually look at the evolution of reduced probability densities which represent the probability of finding a particle in a subset of the state space. We must therefore solve a set of N equations, called the BBGKY hierarchy. This system allows approximations and truncations, which lead to different well-known equations: the Vlasov equation, the Boltzmann equation, and the Fokker-Planck equation. Though we lose the discernability of particles, this approach provides a macroscopic description of the plasma.

Fluid approach This approach assumes a non relativistic plasma in which each species is in local thermodynamical equilibrium, i.e. the distribution of these species is determined by collisions only (Maxwellian distribution). Therefore, macroscopic quantities can be defined such as the density, the (mean) velocity, temperature, and the pressure by averaging the distribution. The plasma is thus composed of several fluids, which interact with an electromagnetic field. This field is reduced to the magnetic field because the electric field is usually strongly reduced due to the screening phenomena mentioned earlier. In the limit of long

timescales $\lambda \gg \omega_{pe}^{-1}$, the plasma can be seen as a single conducting fluid and the macroscopic quantities are therefore those of ions because the electrons are far lighter. This approach is called the MHD theory.

Which approach for proto-neutron stars? While introducing the description of plasmas, we have seen that the hot PNS interior can be considered as a classical plasma containing relativistic electrons. The strong correlation of the PNS interior allows us to use a fluid approach. The treatment of relativistic electrons would require a bi-fluid approach. However, in such extreme densities and temperature, the collisions are fast enough to describe the different species in the PNS with the same thermodynamical quantities and so as one single plasma. That is why we use the MHD approximation in this thesis work to model the dynamics of the PNs interior (except in Chap. 9) .

3.1.2 . Resistive MHD set of equations

The five equations governing plasma dynamics in the MHD approximation are a mix of hydrodynamic equations and Maxwell equations. The first equation illustrates *the conservation of mass (continuity equation)*:

$$\partial_t \rho + \boldsymbol{\nabla} \cdot (\rho \mathbf{v}) = 0\,, \tag{3.13}$$

where ρ is the fluid density. The second equation is *the solenoidal condition* Eq. (3.3), which reflects the non-existence of magnetic monopoles and the nullity of the magnetic flux through a closed surface. The third equation describes *the conservation of momentum (equation of motion or Navier-Stokes equation)*, which reads in a rotating frame

$$\rho\left(\partial_t \mathbf{v} + \mathbf{v}\cdot\boldsymbol{\nabla}\mathbf{v} + 2\boldsymbol{\Omega}\times\mathbf{v}\right) = -\boldsymbol{\nabla} p + \rho\mathbf{g} + \frac{\mathbf{J}\times\mathbf{B}}{c} + \boldsymbol{\nabla}\cdot\boldsymbol{\sigma}\,, \tag{3.14}$$

where Ω is the angular frequency of the rotating frame, $\mathbf{g}$ the gravitational acceleration, and p a modified pressure which includes the centrifugal force. This formulation clearly shows the respective forces applied to the fluid: the Coriolis force, the pressure of the fluid, the gravitational force, the Lorentz force, and the force due to viscous frictions, respectively. Note that the electric force was neglected in the non-relativistic Lorentz force because of the screening effect mentioned earlier. Thios force can be rewritten using Eq. (3.5)

$$\frac{\mathbf{J}\times\mathbf{B}}{c} = \frac{1}{4\pi}(\boldsymbol{\nabla}\times\mathbf{B})\times\mathbf{B} = \boldsymbol{\nabla}\left(\frac{B^2}{8\pi}\right) + \frac{1}{4\pi}(\mathbf{B}\cdot\boldsymbol{\nabla})\mathbf{B}\,, \tag{3.15}$$

where we also neglected the current displacement term $\partial_t \mathbf{E}/c$ by invoking the long timescale approximation of MHD theory. The first and second terms are the magnetic pressure and the magnetic tension, respectively. In the viscous friction term, the Cauchy stress tensor $\boldsymbol{\sigma}$ is given by:

$$\sigma_{ij} = 2\nu\rho\left[\frac{1}{2}\left(\partial_{x_j} v_i + \partial_{x_i} v_j\right) - \frac{1}{3}\delta_{ij}\boldsymbol{\nabla}\cdot\mathbf{v}\right] \sim \nu\rho\partial_{x_j} v_i\,, \tag{3.16}$$

with ν the kinematic viscosity and δ_{ij} is the Kronecker symbol. The fourth equation is *the induction equation*, which represents the evolution of the magnetic field. Using Eq. (3.4), it reads

$$\partial_t B = -c\boldsymbol{\nabla}\times\mathbf{E}\,. \tag{3.17}$$

In order to derive an expression for the electric field $\mathbf{E}$, we subtract the equation of motion of the electrons from the one of ions. We finally obtain *the generalised Ohm's law*

$$\mathbf{E} = -\frac{\mathbf{v}\times\mathbf{B}}{c} + \frac{\eta}{c}\mathbf{J} + \frac{\mathbf{J}\times\mathbf{B}}{n_e e c} - \frac{(\mathbf{J}\times\mathbf{B})\times\mathbf{B}}{\gamma\rho_i\rho_e} - \frac{\boldsymbol{\nabla}\cdot\mathbf{P}_e}{n_e e c} + \frac{m_e}{n_e e^2}\partial_t\mathbf{J}, \tag{3.18}$$

where e is the (absolute value of the) charge of the electron and γ is the collision coupling constant between ions and electrons. η is the resistivity (or magnetic diffusivity), which reads

$$\eta = 2\times10^{-5}\left(\frac{\rho}{4\times10^{14}\,\mathrm{g\,cm^{-3}}}\right)^{-1/3}\left(\frac{Y_e}{0.2}\right)^{-1/3}\mathrm{cm^2\,s^{-1}}, \tag{3.19}$$

for relativistic and degenerated electrons (Thompson & Duncan, 1993), where Y_e is the electron fraction. The different terms of Eq. (3.18) represent:

(i) the electromotive force, in which the electric field is generated by the motion of electrons,

(ii) the resistivity caused by collisions between electrons and other species,

(iii) the Hall effect, which creates an electric field due to the drift between electrons and ions,

(iv) the ambipolar diffusion, which generates an electric field due to a drift between protons and neutral particles,

(v) the electronic pressure,

(vi) the contribution of the electron inertia to the electric current.

In cold NSs, the Hall effect is important in the crust, while the ambipolar diffusion is the main diffusion process in the NS core. However, the large frequency of collisions between particles in hot PNSs allows to neglect these effects, and also the electronic pressure and the inertial terms. Therefore, (except in Chap. 9) we will only keep the first two terms of Ohm's law and so limit our theoretical framework to the so-called resistive MHD. We can now rewrite the induction equation

$$\partial_t\mathbf{B} = \boldsymbol{\nabla}\times(\mathbf{v}\times\mathbf{B}) + \eta\boldsymbol{\Delta}\mathbf{B}, \tag{3.20}$$

where we assumed an homogeneous resisvity η. Note that if the resistivity is neglected (the equivalent of infinite electric conductivity) and so is the viscosity, we refer to the so-called ideal MHD. The fifth equation is *the energy (or heat) equation*, which formulates the evolution of the entropy, noted s:

$$\rho T(\partial_t s + \mathbf{v}\cdot\boldsymbol{\nabla}s) = \boldsymbol{\nabla}\cdot(k\boldsymbol{\nabla}T) + \Phi_v + \eta\frac{(\boldsymbol{\nabla}\times\mathbf{B})^2}{4\pi} + \epsilon, \tag{3.21}$$

where $k$is the thermal conductivity. In the following, k will be considered homogenous. This allow us to use the thermal diffusivity $\kappa \equiv k/(\rho_0 c_p)$, with ρ_0 and c_p, the mean density and specific heat capacity at constant pressure, respectively. Φ_v is the viscous heating, which reads

$$\Phi_v \equiv 2\rho\left[\frac{1}{4}\sum_i\sum_j(\partial_{x_j}v_i + \partial_{x_i}v_j)^2 - \frac{1}{3}\boldsymbol{\nabla}\cdot\mathbf{v}\right]. \tag{3.22}$$

The two last terms are the Ohmic heating and source terms, respectively. Finally, we must add an *equation of state (EoS)* to close the system of equations. One can use a simple relation describing the variations of density due to temperature and pressure:

$$\frac{1}{\rho} d\rho = -\alpha_T dT + \beta_p dp, \tag{3.23}$$

where

$$\alpha_T \equiv -\frac{1}{\rho} \partial_T \rho|_p \tag{3.24}$$

and

$$\beta_p \equiv \frac{1}{\rho} \partial_p \rho|_T \tag{3.25}$$

are the thermal expansions and the compressibility, respectively. Note that we can add the impact of the electron fraction, which would require the addition of another equation similar to Eq. (3.21) to take into account its evolution. The electron fraction is a very important quantity in the context of NS physics as seen in the previous chapter (Sect. 2.2.2). The question of the EoS is still a very active research topic. Hundreds of EoS have been developped[1] (e.g. Lattimer & Swesty, 1991, Shen et al., 2011, Gulminelli & Raduta, 2015, Raduta & Gulminelli, 2019b) for hot and cold NS matter, which can even include exotic matter such as hyperons or quarks (e.g. Otto et al., 2020). The observations of NSs in the X-ray domain with NICER are crucial to constrain the relation between the NS radius and mass and so to find a realistic EoS and understand the NS structure.

3.1.3 . Conservation laws in ideal MHD

Similarly to hydrodynamics, there exist conserved quantites in the framework of ideal MHD. First, the magnetic flux $\Phi_B \equiv \int_\Sigma \mathbf{B} \cdot \mathbf{dS}$ evolves as

$$d_t \Phi_B = \int_\Sigma \partial_t \mathbf{B} \cdot \mathbf{dS} + \oint_{\partial\Sigma} \mathbf{B} \cdot (\mathbf{v} \times \mathbf{dl}), \tag{3.26}$$

where Σ is a surface with a contour noted $\partial\Sigma$ which follows the fluid motion. $\mathbf{dS}$ and $\mathbf{dl}$ are the respective associated infinitesimal elements of the surface Σ and contour $\partial\Sigma$. Using the ideal induction equation

$$\partial_t \mathbf{B} = \boldsymbol{\nabla} \times (\mathbf{v} \times \mathbf{B}) \tag{3.27}$$

and the right vector calculus identity, we have

$$d_t \Phi_B = \int_\Sigma \boldsymbol{\nabla} \times (\mathbf{v} \times \mathbf{B}) \cdot \mathbf{dS} - \oint_{\partial\Sigma} (\mathbf{v} \times \mathbf{B}) \cdot \mathbf{dl}. \tag{3.28}$$

Finally, we use Stokes' theorem and obtain

$$d_t \Phi_B = \int_\Sigma \boldsymbol{\nabla} \times (\mathbf{v} \times \mathbf{B}) \cdot \mathbf{dS} - \boldsymbol{\nabla} \times (\mathbf{v} \times \mathbf{B}) \cdot \mathbf{dS} = 0. \tag{3.29}$$

Thus, the magnetic flux is conserved.
From this first conservation law, we can infer that the motion of an element of the fluid surface crossing a magnetic field line follows the advection of the field line. Conversely, the

[1] Many of the EoS are listed with their tables in open access on the website https://compose.obspm.fr.

magnetic field line can only follow the evolving element of the fluid surface. The magnetic field line is therefore "frozen" in the fluid. This can also be demonstrated analytically. Indeed, the induction equation can be rewritten

$$\partial_t \mathbf{B} + \mathbf{v}\cdot\boldsymbol{\nabla}\mathbf{B} = \mathbf{B}\cdot\boldsymbol{\nabla}\mathbf{v} - (\boldsymbol{\nabla}\cdot\mathbf{v})\mathbf{B}. \tag{3.30}$$

Using the continuity equation (3.13), the previous equation can be rewritten

$$\partial_t\left(\frac{\mathbf{B}}{\rho}\right) + \mathbf{v}\cdot\boldsymbol{\nabla}\left(\frac{\mathbf{B}}{\rho}\right) = \left(\frac{\mathbf{B}}{\rho}\cdot\boldsymbol{\nabla}\right)\mathbf{v}. \tag{3.31}$$

Let $\boldsymbol{\delta}\mathbf{l}$ be an infinitesimal segment advected by the flow. The velocity variation between both ends of the segment is $\delta\mathbf{v} = \boldsymbol{\delta}\mathbf{l}\cdot\boldsymbol{\nabla}\mathbf{v}$. Therefore, the evolution of $\boldsymbol{\delta}\mathbf{l}$ reads

$$\partial_t\boldsymbol{\delta}\mathbf{l} + \mathbf{v}\cdot\boldsymbol{\nabla}\boldsymbol{\delta}\mathbf{l} = (\boldsymbol{\delta}\mathbf{l}\cdot\boldsymbol{\nabla})\,\mathbf{v}. \tag{3.32}$$

Thus, $\mathbf{B}/\rho$ and $\boldsymbol{\delta}\mathbf{l}$ have the same transport equation and are advected and distorted the same way. The conservation of the magnetic flux and the freezing of the magnetic field lines constitute Alfvén's theorem.

Second, the magnetic helicity in a volume V is defined as

$$H_m \equiv \int_V \mathbf{A}\cdot\mathbf{B}dV, \tag{3.33}$$

with $\mathbf{A}$ the magnetic vector potential $\mathbf{B} = \boldsymbol{\nabla}\times\mathbf{A}$. Qualitatively, magnetic helicity measures the knottedness of the magnetic field within the volume V. Since

$$\partial_t\mathbf{A} = -c(\mathbf{E} + \boldsymbol{\nabla}\Phi_e) = \mathbf{v}\times\mathbf{B} - c\boldsymbol{\nabla}\Phi_e, \tag{3.34}$$

where Φ_e is the electric potential and using the ideal induction equation (Eq. (3.27)), we have

$$\partial_t(\mathbf{A}\cdot\mathbf{B}) = (\mathbf{v}\times\mathbf{B})\cdot\mathbf{B} - c\boldsymbol{\nabla}\Phi_e\cdot\mathbf{B} + \mathbf{A}\cdot\boldsymbol{\nabla}\times(\mathbf{v}\times\mathbf{B}), \tag{3.35}$$

which can be rearranged in the following explicitly conservative local evolution equation for $\mathbf{A}\cdot\mathbf{B}$:

$$\partial_t(\mathbf{A}\cdot\mathbf{B}) + \boldsymbol{\nabla}\cdot[\Phi_e\mathbf{B} + \mathbf{A}\times(\mathbf{v}\times\mathbf{B})] = 0. \tag{3.36}$$

Thus, the magnetic helicity is conserved. This law formulates the conservation of magnetic linkages in the absence of resistivity or magnetic reconnection.

3.1.4 . MHD waves and instabilities

MHD waves The presence of the magnetic field in the hydrodynamic equations adds more complexity to the fluid dynamics. In the case of waves, the magnetic pressure and tension in the Lorentz force can act as restoring forces and so produce new kinds of waves. As a reminder, in a rotating hydrodynamic fluid, the pressure, the Coriolis force, and the gravitational force can produce the sound, inertial, and gravity waves, respectively.

To demonstrate the existence of these MHD waves (and instabilities), we will use the perturbative method, which consists in decomposing the fields and scalar quantities in an averaged and a perturbed component: $\mathbf{F} = \mathbf{F}_0 + \boldsymbol{\delta}\mathbf{F}$ and $Q = Q_0 + \delta Q$ with $|\boldsymbol{\delta}\mathbf{F}| \ll |\mathbf{F}_0|$ and $\delta Q \ll Q$. This method will allow us to linearise the MHD equations, i.e. eliminate the non-linear terms, which greatly simplifies the equations to solve.

In the cartesian frame $(\mathbf{e}_x,\mathbf{e}_y,\mathbf{e}_z)$, let us consider a non-rotating isothermal fluid with a uniform magnetic field $\mathbf{B}_0 = B_0\mathbf{e}_z$. The small perturbations of a field $\mathbf{F}$ and a scalar quantity Q are expressed in the following form $\boldsymbol{\delta}\mathbf{F} \propto \delta Q \propto \exp[i(\omega t - \mathbf{k}\cdot\mathbf{x})]$ where ω and k are the pulsation and the wave number, respectively. Assuming a fluid initially at rest with constant pressure and density ρ_0, the perturbed ideal MHD equations read

$$\partial_t \delta\rho = -\rho_0 \boldsymbol{\nabla}\cdot\boldsymbol{\delta}\mathbf{v}, \tag{3.37}$$

$$\rho_0 \partial_t \boldsymbol{\delta}\mathbf{v} = \frac{(\boldsymbol{\nabla}\times\boldsymbol{\delta}\mathbf{B})\times\mathbf{B}_0}{4\pi} - c_s^2\boldsymbol{\nabla}\delta\rho, \tag{3.38}$$

$$\partial_t \boldsymbol{\delta}\mathbf{B} = \boldsymbol{\nabla}\times(\boldsymbol{\delta}\mathbf{v}\times\mathbf{B}_0), \tag{3.39}$$

where $c_s \equiv \sqrt{\partial_\rho p|_s}$ is the sound speed in the fluid. The perturbed density and magnetic field can be written

$$\delta\rho = \frac{\mathbf{k}\cdot\boldsymbol{\delta}\mathbf{v}}{\omega}, \tag{3.40}$$

$$\boldsymbol{\delta}\mathbf{B} = \frac{(\mathbf{k}\cdot\boldsymbol{\delta}\mathbf{v})\mathbf{B}_0 - (\mathbf{k}\cdot\mathbf{B}_0)\boldsymbol{\delta}\mathbf{v}}{\omega}. \tag{3.41}$$

Assuming that the perturbation propagates in the xz-plane and defining ϕ the angle between $\mathbf{B}_0$ and $\mathbf{k}$, the perturbed equation of motion (3.38) in which we incorporated the expression of $\delta\rho$ and $\boldsymbol{\delta}\mathbf{B}$ (Eqs. 3.40 and 3.41) read

$$\begin{pmatrix} \omega^2 - (v_\mathrm{A}^2 + c_s^2)k^2 & 0 & -c_s^2 k^2\cos\phi \\ 0 & \omega^2 - v_\mathrm{A}^2 k^2 & 0 \\ -c_s^2 k^2\cos\phi & 0 & \omega^2 - c_s^2 k^2 \end{pmatrix} \begin{pmatrix} \delta v_x \\ \delta v_y \\ \delta v_z \end{pmatrix} = 0, \tag{3.42}$$

where $k \equiv |\mathbf{k}|$ is the norm of the wave number and $v_\mathrm{A} \equiv |\mathbf{B}_0|/\sqrt{4\pi\rho_0}$ is the Alfvén velocity. By calculating the determinant of the matrix, we obtain the following dispersion relation

$$(\omega^2 - v_\mathrm{A}^2 k^2)(\omega^4 - \omega^2(v_\mathrm{A}^2 + c_s^2)k^2 + v_\mathrm{A}^2 c_s^2 k^4\cos^2\phi) = 0, \tag{3.43}$$

Therefore, we have a first new kind of wave $\omega^2 = v_\mathrm{A}^2 k^2$, which is called **the Alfvén wave**. This wave is transversal (i.e. field perturbations are perpendicular to k and $\mathbf{B}_0$) and is due to magnetic tension. The other waves are described by the eigenmodes

$$\omega_\pm^2 = \frac{1}{2}\left((v_\mathrm{A}^2 + c_s^2)k^2 \pm \sqrt{(v_\mathrm{A}^2 + c_s^2)^2 k^4 - 4v_\mathrm{A}^2 c_s^2 k^2\cos^2\phi}\right), \tag{3.44}$$

where ω_+ and ω_- are the *fast and slow magnetosonic modes*, respectively. First, for $\phi = 0$ (transversal wave), $\omega_+ = \pm v_\mathrm{A} k$ and $\omega_- = \pm c_s k$ are the Alfvén and sonic modes, respectively. Second, for the $\phi = \pi/2$ (longitudinal waves), $\omega_+ = \pm\sqrt{v_\mathrm{A}^2 + c_s^2}k$ is the fastest magnetosonic mode with a speed of $c_{sm} \equiv \sqrt{v_\mathrm{A}^2 + c_s^2}$ and the slow mode does not propagate/oscillate $\omega_- = 0$. The three eigenmodes can be illustrated in a phase diagram as in Fig. 3.1.

MHD instabilities: case of the MRI Conductive fluids are also prone to new instabilities in the presence of a magnetic field, such as the Tayler instability (Tayler, 1973) and the MRI (Balbus & Hawley, 1991). The latter, which was mentioned in the previous chapter in the context of magnetar formation (Chap. 2), is the most famous example because it shows that a

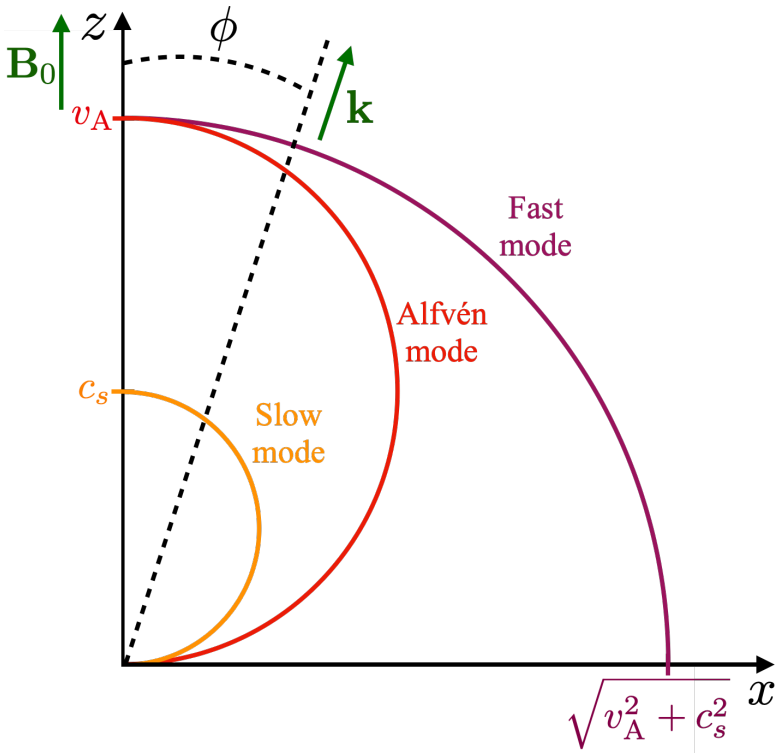

Figure 3.1 — Phase diagram of the three magnetosonic modes.

weak magnetic field can destabilise a hydrodynamically stable fluid in differential rotation. To demonstrate the existence of such instability, let us consider a fluid in the cylindrical frame $(\mathbf{e}_s,\mathbf{e}_z,\mathbf{e}_\phi)$ with a constant density ρ_0 and an initial azimuthal velocity $\mathbf{v}_{\phi,0} = s\Omega(s)\mathbf{e}_\phi$. The rotation profile is assumed to depend only on the cylindrical radius $\Omega(s) = \Omega_0 s^{-q}$, where

$$q \equiv d_{\ln s} \ln \Omega \tag{3.45}$$

is the shear rate. The fluid is considered to be in hydrostatic equilibrium, i.e. $-\boldsymbol{\nabla} p + \rho \mathbf{g} = 0$ and we introduce a uniform magnetic field $\mathbf{B}_0 = B_0 \mathbf{e}_z$. We only consider perturbations along the z-axis $\boldsymbol{\delta}\mathbf{F} \propto \delta Q \propto \exp[i(\omega t - k_z z)]$, which implies that δv_z and δB_z are uniform according to the continuity equation and the solenoidal condition. We therefore impose $\delta v_z = 0$ and integrate δB_z in B_0. The linearised equations of ideal MHD now read

$$\partial_t \mathbf{v} = -\boldsymbol{\delta}\mathbf{v} \cdot \boldsymbol{\nabla}\mathbf{v}_{\phi,0} - 2\Omega(s)\mathbf{e}_z \times \boldsymbol{\delta}\mathbf{v} + \frac{1}{4\pi\rho_0}(\boldsymbol{\nabla} \times \boldsymbol{\delta}\mathbf{B}) \times \mathbf{B}_0\,, \tag{3.46}$$

$$\partial_t \mathbf{B} = \boldsymbol{\nabla} \times (\mathbf{v}_{\phi,0} \times \boldsymbol{\delta}\mathbf{B} - \mathbf{B}_0 \times \boldsymbol{\delta}\mathbf{v})\,. \tag{3.47}$$

After some algebra and incorporating the perturbed magnetic field in the equation of motion, the latter read

$$\begin{pmatrix} \omega^2 - v_A^2 k_z^2 & 2i\omega\Omega_0 \\ -i\Omega_0\left((2-q)\omega + q v_A^2 k_z^2/\omega\right) & \omega^2 - v_A^2 k_z^2 \end{pmatrix} \begin{pmatrix} \delta v_s \\ \delta v_\phi \end{pmatrix} = 0\,. \tag{3.48}$$

The determinant of the matrix gives the following dispersion relation

$$\omega^4 - \omega^2(v_A^2 k_z^2 + \bar{\kappa}^2) + v_A^2 k_z^2 (v_A^2 k_z^2 - 2q\Omega_0^2) = 0\,, \tag{3.49}$$

where $\bar{\kappa}^2 \equiv 2(2-q)\Omega_0^2$ is the epicyclic frequency. We see that for the hydrodynamic case ($v_A = 0$), the relation becomes $\omega^2 = \bar{\kappa}^2$ and we find the Rayleigh criterion because the fluid

is stable for $q \leq 2$. In the magnetic case, the stability criterion becomes $k_z^2 v_\mathrm{A}^2 - 2q\Omega^2 \geq 0$ and the critical wave number below which the fluid is MRI-unstable is $k_c^2 = 2q\Omega_0^2/v_\mathrm{A}^2$. Thus, the MRI develops if the rotation rate decreases with the cylindrical radius s. We also notice that any magnetic field strength destabilises the fluid if any values of k_z are permitted (infinite domain). Diffusivities introduce a minimum magnetic field strength, while a finite domain implies a maximum one. The growth rate of the MRI most unstable mode is

$$\sigma = -\,\mathrm{Im}(\omega) = q\Omega_0/2\,, \tag{3.50}$$

and so does not depend on the magnetic field strength. Note that the influence of the magnetic field strength on the MRI appears when we consider non-ideal MHD, i.e. when $\nu \neq 0$, $\eta \neq 0$, or $\kappa \neq 0$.

3.2 . Dynamo theories

The following section introduces the rich field of dynamo theory and has been inspired by the review of Rincon (2019). Tobias (2021) is also a very nice review of the topic.

3.2.1 . Astrophysical dynamos

The picture provided by the MHD theory of plasma modelling suggests that the flows of (turbulent) fluids may amplify and self-sustain their own magnetic fields. The questions of the growth and the saturation of the magnetic fields, constitute the so-called dynamo problem. This problem is central in astrophysics to explain the extremely rich variety of magnetic fields observed in the Universe. This includes scales as large as galactic clusters (hot intracluster medium, galaxies, interstellar medium) to stellar and planetary scales (stars, compact objects, planets) whose magnetic field span a wide range of strengths from 10^{-6} to $10^{15}\,\mathrm{G}$. On cosmological scales (typically intracluster medium, Megaparsec scale), the magnetic fields are more difficult to measure precisely but are expected to be between $10^{-16}\,\mathrm{G}$ and $10^{-9}\,\mathrm{G}$. The bond between the dynamo theory and astrophysics is also historic since this problem was first invoked by Larmor (1919) to explain the magnetic field measured arount the solar sunspots. Most observed astrophysical dynamos can be sorted in the following categories:

- the origin of cosmic magnetic fields (Kulsrud & Zweibel, 2008);
- the galactic helical dynamo, which may be driven by supernova (SN)-induced turbulence (Brandenburg, 2015, Subramanian, 2019);
- the dynamos driven by rotating convection, which is applied to stellar convective zones (see reviews by Käpylä et al., 2023, Charbonneau & Sokoloff, 2023), Earth outer core (see review by Landeau et al., 2022), white dwarf stars (Isern et al., 2017), and PNSs (Duncan & Thompson, 1992, Raynaud et al., 2020, 2022, Masada et al., 2022);
- the subcritical dynamos driven by magnetohydrodynamical (MHD) instabilities in shear flows, which could operate in stably stratified media, such as accretion disks (e.g. Hawley et al., 1996, Rincon et al., 2008, Lesur & Ogilvie, 2008) and stellar radiative zones (e.g. Spruit, 2002, Cline et al., 2003).

However, the dynamo problem seems pretty complex, especially due to the first strong constraints which constitute the anti-dynamo theorems of Cowling (1933) and Zeldovich &

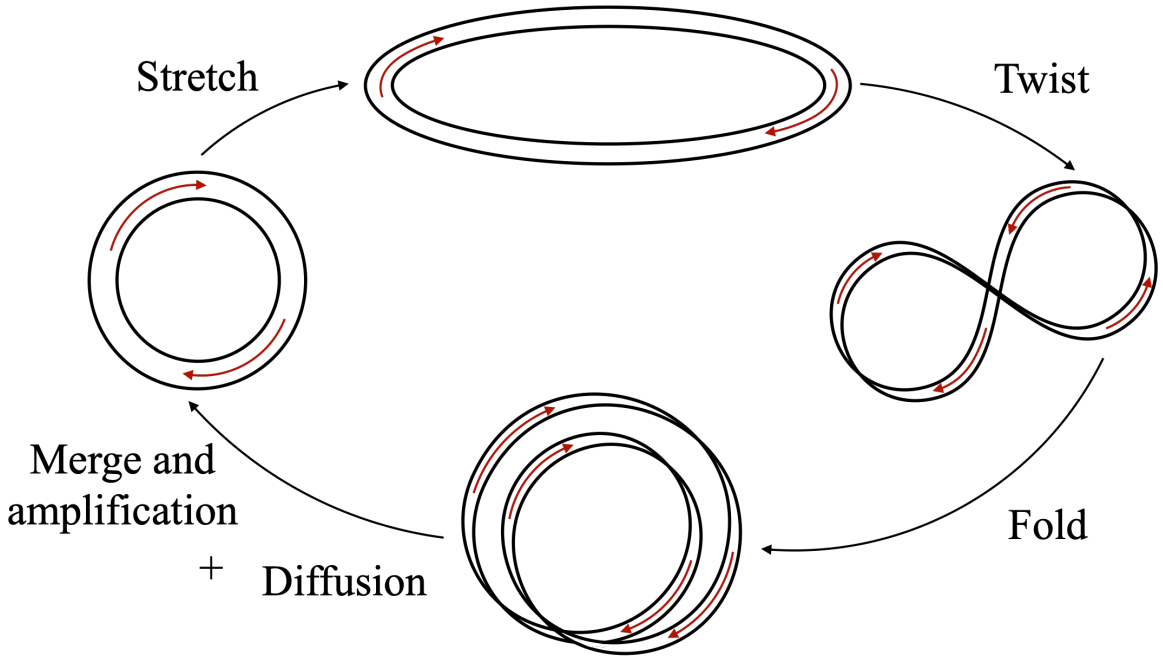

Figure 3.2 — Schematic illustrating the stretch-twist-fold model of Vaĭnshteĭn & Zel'dovich (1972) *(inspired from Vaĭnshteĭn & Zel'dovich (1972) and Rincon (2019))*. The red lines illustrate the magnetic field lines.

Ruzmaikin (1956). They indicate that self-exciting fluids must have three-dimensional and non-axisymmetric geometries (see Sect. 3.2.2 for the demonstrations). It already suggests that 3D turbulence plays a crucial role in dynamo theory, as noticed by the first studies on magnetic field amplification using a statistical approach (Batchelor, 1950, Schlüter & Biermann, 1950).

The second hurdle involves the dimensionless parameters that influence the fluid dynamics and so the dynamo mechanism:

(i) The kinematic and magnetic Reynolds numbers $Re \equiv v_0 l_0/\nu$ and $Rm \equiv v_0 l_0/\eta$, with v_0 and l_0 the typical fluctuation velocity and lengthscale in the fluid, respectively. They measure the ratio of the inertia to the viscous effects and the ratio of the inductive to the resistive effects, respectively. Most astrophysical objects are in a turbulent state with $Re \gg 1$ and $Rm \gg 1$ (e.g. $Rm \sim 10^6$ and $Rm \sim 10^{17}$ in hot PNSs). However, this high-Rm regime is poorly understood. Indeed, in this regime, turbulence is expected to quickly amplify small-scale magnetic fields and may prevent the growth of large-scale magnetic fields.

(ii) The magnetic Prandtl number $Pm \equiv \nu/\eta = Rm/Re$ helps to dinstinguish different MHD regimes. At large $Pm \gg 1$, the magnetic field is dissipated at smaller scales than the turbulent flow. This regime is found in dense and hot astrophysical objects such as hot PNSs ($Pm \sim 10^{13}$), intracluster or warm interstellar medium. At small $Pm \ll 1$, the turbulence is still active at the resistive scales. Many astrophysical objects sustaining a magnetic field are in this regime such as stars ($Pm \sim 10^{-2}$ – $Pm \sim 10^{-6}$) and the Earth's core ($Pm \sim 10^{-5}$). Intuitively, this low-Pm regime may not favor dynamo action because the turbulent flow contributes to the diffusion of the magnetic field at all scales larger

than the resisitive scale. However, some complications can also occur at large values of Pm caused by stochastic magnetic field reconnection (Jafari et al., 2018, Lander, 2021) or a 'reversed dynamo' effect (Brandenburg & Rempel, 2019).

Thus, astrophysical objects can sustain a dynamo in extremely different regimes, which are out of reach for our analytical and numerical models. A hope resides in the possibility of establishing asymptotic models to give a trend of the dynamics in these regimes. For instance, some numerical simulations were pushed to $Pm \sim 256$ in Guilet et al. (2022) for the MRI-driven dynamo, which may catch a glimpse of this asymptotic regime.

The third obstacle is that the growth rate of the dynamo must become independent of Rm in the high-Rm regime to be relevant for astrophysical objects. This kind of dynamo is called *fast* because it is opposed to *slow* dynamos, which evolve on ohmic timescales $\tau_{\rm Ohm} = l_0^2/\eta$ and whose growth rate tends to 0 in the high-Rm regime. The former is clearly relevant in the high-Rm regime and so for astrophysics. Besides introducing this concept, Vaĭnshteĭn & Zel'dovich (1972) also propose a simple fast dynamo mechanism, which is illustrated in Fig. 3.2. It consists in reproducing an initial torus magnetic tube by stretching, twisting, and folding it so that its intern magnetic field increases by a factor of 2 at each cycle. Note that for merging the two connected torus, the resistivity must be non-zero, so the magnetic field is not exactly amplified by 2. However, for $Rm \to +\infty$, the growth rate tends toward $\ln 2$ per turnover time, i.e. per time to complete the cycle. Finn & Ott (1988) show that the presence of a turbulent flow is necessary for these fast dynamo to occur.

The fourth crucial difficulty is that the observed astrophysical magnetic fields are present at every length scale of the astrophysical objects: from the object length scale to the dissipative scales. This multiscale aspect of the dynamo problem is not surprising due to the strong nonlinearity of conducting fluid dynamics. The generation of small-scale magnetic fields, i.e. small compared to the typical fluid length scale, was first analytically investigated in the Kazantsev's model (Kazantsev, 1968), which can be extended to take into account the non-linear regime of the dynamo. A phenomenological approach was also introduced by Moffatt & Saffman (1964) and Zel'dovich et al. (1984). The important question arising from the small-scale dynamo problem is therefore the generation of large-scale magnetic fields from small-scale turbulent flows. This problem is thus central in this thesis to explain magnetar formation. It is well accepted that rotation and large-scale differential rotation play a crucial role in astrophysical large-scale dynamos. The phenomenological model of Parker (1955) is a pioneering work in this field and is sketched in Fig. 3.3. This model is the first to introduce a mechanism to generate a large-scale poloidal magnetic field from a large-scale toroidal component, which is now called *α-effect* (see Sects. 3.2.4–3.2.5 for a more detailed discussion). The classical mathematical approach is the mean-field dynamo theory (Steenbeck et al., 1966, Moffatt, 1970, Vaĭnshteĭn, 1970). Despite some limitations, this approach is still widely used, especially as a numerical analysis tool, as we will see for the specific case of the Tayler-Spruit dynamo in Chap. 8. Though being far from reaching realistic astrophysical parameters, the large-scale dynamo problem is now often investigated in larger and larger numerical simulations to better grasp the non-linear nature of the dynamo processes. Finally, the use of quasi-linear appoaches (e.g. Lesur & Ogilvie, 2008) and dynamic system theory tools (e.g. Berhanu et al., 2007, Pétrélis et al., 2009, Gissinger, 2010, Herault et al., 2011, Riols et al., 2013) helps understand the rich variety of dynamical behaviours of different dynamo processes.

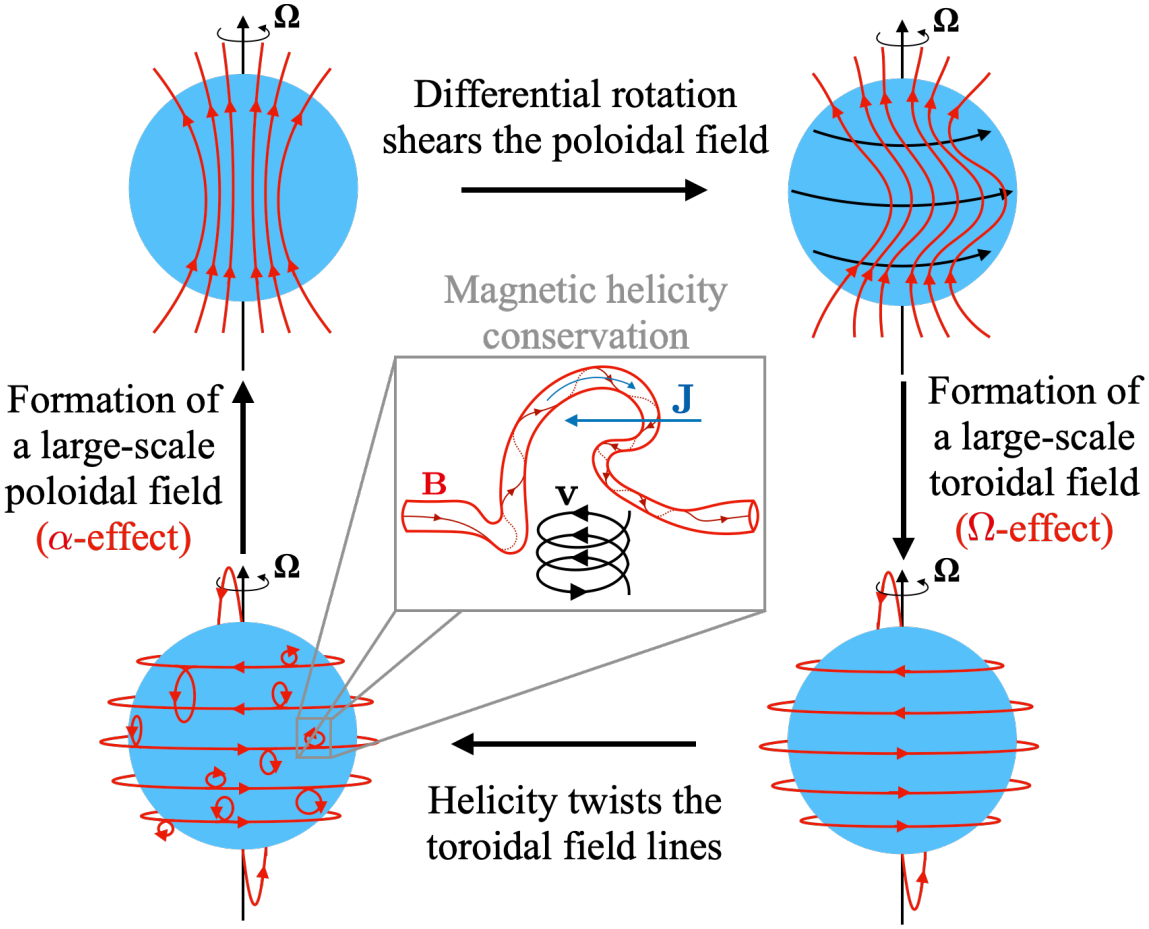

Figure 3.3 — Schematic of Parker's model where poloidal and toroidal magnetic fields are coupled via the differential rotation and the helical turbulence (inspired from Rincon (2019)). The red lines illustrate the magnetic field lines and $\mathbf{\Omega}$ is the rotation axis. The inset figure displays the twist of a magnetic flux tube (red lines) by the helical flow (black line), which creates a large-scale electric current (blue arrow). Due to magnetic helicity conservation, the magnetic field lines in the tube are also twisted (red lines), which generates small-scale currents.

3.2.2 . Anti-dynamo theorems

This section aims at demonstrating that neither axisymmetric fields nor planar motion can sustain a dynamo. (Cowling (1933) and Zeldovich & Ruzmaikin (1956) theorems, respectively) Note that other similar anti-dynamo theorems exist for magnetic fields of the form $\mathbf{B}(x,y,t)$ or purely toroidal magnetic fields. All of these theorems suggest that the flow and the magnetic field must have a complex enough structure for a source term to appear in the induction equation and for a dynamo to occur.

Cowling's theorem Let us decompose an axisymmetric magnetic field into a poloidal and a toroidal component in the spherical frame $(\mathbf{e}_r,\mathbf{e}_\theta,\mathbf{e}_\phi)$:

$$\mathbf{B} = \mathbf{B}_{\rm pol} + \mathbf{B}_{\rm tor} = \boldsymbol{\nabla} \times \chi \mathbf{e}_\phi + \psi \mathbf{e}_\phi \,, \tag{3.51}$$

where $r\sin\theta\chi$ is a poloidal flux-function and $\psi/(r\sin\theta)$ the toroidal magnetic field. We also consider a velocity field with a large-scale differential rotation

$$\mathbf{v} = \mathbf{v}_{\rm pol} + r\sin\theta\Omega_0 \mathbf{e}_\phi \,. \tag{3.52}$$

By injecting them in the resistive induction equation (3.20) and "uncurling" it for the poloidal component (as in Moffatt & Dormy, 2019, Chap. 3), we have

$$\partial_t \chi + \frac{1}{r\sin\theta}(\mathbf{v}_{\rm pol}\cdot\boldsymbol{\nabla})(r\sin\theta\chi) = \eta\left(\Delta - \frac{1}{r^2\sin^2\theta}\right)\chi \,, \tag{3.53}$$

$$\partial_t \psi + r\sin\theta(\mathbf{v}_{\rm pol}\cdot\boldsymbol{\nabla})\left(\frac{\psi}{r\sin\theta}\right) = r\sin\theta(\mathbf{B}_{\rm pol}\cdot\boldsymbol{\nabla})\Omega_0 + \eta\left(\Delta - \frac{1}{r^2\sin^2\theta}\right)\psi \,. \tag{3.54}$$

The induction equation for the poloidal component (3.53) shows an advection term on its left-hand side and a diffusion term on its right-hand side but no source term to produce a poloidal magnetic field. Therefore, $\mathbf{B}_{\rm pol}$ must decay. The induction equation for the toroidal component (3.54) has however a source term $r\sin\theta(\mathbf{B}_{\rm pol}\cdot\boldsymbol{\nabla})\Omega_0$, which is called the Ω-effect and formulates the winding of the poloidal field. Since $\mathbf{B}_{\rm pol}$ decays, this effect tends to disappear. Thus, both components are doomed to decay and no dynamo action can occur.

Zel'dovich's theorem Now, let us suppose a two-dimensional flow, which is equivalent to supposing an arbitrary direction defined by a unit vector $\mathbf{u}$ such that $\mathbf{u}\cdot\mathbf{v} = 0$. This implies that the component of the magnetic field following this direction must decay

$$\partial_t(\mathbf{B}\cdot\mathbf{u}) + \mathbf{v}\cdot\boldsymbol{\nabla}(\mathbf{B}\cdot\mathbf{u}) = \eta\Delta(\mathbf{B}\cdot\mathbf{u}) \,. \tag{3.55}$$

For the sake of simplicity, we will consider a cartesian frame $(\mathbf{e}_x,\mathbf{e}_y,\mathbf{e}_z)$ and assume that $\mathbf{u} = \mathbf{e}_z$. Since $\mathbf{B}_z$ is damped, $\mathbf{B} = (B_x, B_y)$ is two-dimensional and its components can be written

$$B_x = \partial_y\phi + \partial_x\varphi \,, \tag{3.56}$$

$$B_y = -\partial_x\phi + \partial_y\varphi \,, \tag{3.57}$$

where ϕ and φ are the solenoidal and potential functions, respectively. Using the solenoidal condition (Eq. (3.3)), we obtain

$$\partial_x^2\varphi + \partial_y^2\varphi = -\partial_z B_z \,. \tag{3.58}$$

As B_z is damped, φ is expected to be damped too, after a long enough time. Therefore, $\mathbf{B} = (\partial_y\phi, -\partial_x\phi) = \boldsymbol{\nabla}_{\rm 2D}\times\phi\mathbf{e}_z$, with $\boldsymbol{\nabla}_{\rm 2D} \equiv (\partial_x,\partial_y)$. This form is similar to the expression of the poloidal component used in the previous demonstration, therefore ϕ follows the same kind of equation as χ (Eq. (3.53)). Thus, ϕ also decays and the magnetic field can not be sustained.

3.2.3 . Different regimes

An important distinction must be emphasized between two dynamo theories: the *kinematic* and *dynamical* dynamo theories, where the former is a (great) simplifaction of the latter. The kinematic approach is relevant in fluids with negligible magnetic energy compared to the kinetic energy of the flow. In this context, the back-reaction of the magnetic field on the flow via the Lorentz force can be ignored. This translates into the use of an imposed velocity field $\mathbf{v}$ that is independent of the magnetic field $\mathbf{B}$ in the induction equation (3.20), which simplifies greatly the problem. Therefore, investigating the kinematic dynamo problem consists in finding the types of velocity profiles leading to an exponential growth of $\mathbf{B}$, which can be initially infinitesimal. These dynamos are characterised by a critical magnetic Reynolds number Rm_c above which the imposed flow can stretch the magnetic field lines enough to overcome the resistivity. A classical kinematic theory is the mean-field dynamo theory, which will be described in Sect. 3.2.5.

The dynamical description of the dynamo process must solve the full set of nonlinear MHD equations (Eqs. (3.13)–(3.21)) or its approximations (see Sect. 4.2) including the backreaction of the Lorentz force on the flow. In this problem, the non-linear saturation of the dynamo must be described. This problem is therefore relevant for astrophysical objects, which harbour usually magnetic fields in their saturated regime. For instance, the back-reaction of the generated magnetic field can balance the growth of the dynamo and so saturate the magnetic field. A plot of the strength of this saturated magnetic field as a function of one are several parameters constitutes a *bifurcation diagram*. In the simple case of the saturation of a kinematic dynamo due to the Lorentz force, the bifurcation diagram is similar to the plot on the left in Fig. 3.4. For $Rm < Rm_c$, the dynamo action is not excited by the flow, the solution is hydrodynamic. For $Rm > Rm_c$, the magnetic field is amplified exponentially and saturates due to the feedback on the flow. This transition from the non-dynamo solution to the saturated dynamo is called the *supercritical bifurcation*. However, the Lorentz force can trigger a second kinf of destabilisation and so produce more complex dynamics. This kind of dynamics translates into a *subcritical bifurcation*, which is illustrated by the plot on the right in Fig. 3.4. As in the previous example, an initially weak magnetic field is not amplified for $Rm < Rm_c$. But for $Rm > Rm_c$ this initially weak magnetic field is amplified via a non-linear growth due to the Lorentz force until saturation. If the resulting saturated magnetic field is used as an initial condition, the dynamo solution can be maintained until a turning point at $Rm_t < Rm < Rm_c$, which betrays the presence of a hysteresis. Much more complex dynamics can also appear with e.g. bistability between several dynamo solutions, i.e. the presence of a pair of non-linear dynamos that exists for a common range of Rm (or other parameters). This rich variety of dynamics has been observed in numerical studies of several dynamos such as the convective dynamo (e.g. Gissinger et al., 2012, Raynaud & Tobias, 2016, Dormy et al., 2018, Zaire et al., 2022), and MHD instability-driven dynamos in shear flows: the MRI-driven dynamo (e.g. Rincon et al., 2007, Herault et al., 2011, Riols et al., 2013, Riols, 2014), and the Tayler-Spruit dynamo (Petitdemange et al., 2023, Daniel et al., 2023, Barrère et al., 2023, 2024a,b), as we will discuss in this thesis.

3.2.4 . Parker's phenomenological model

Despite the complexity of the dynamo problem, phenomenological models are intuitive ways to identify mechanisms, which may overcome the difficulties we discussed earlier. A historical example is of phenomenological model proposed by Parker (1955). Parker's mech-

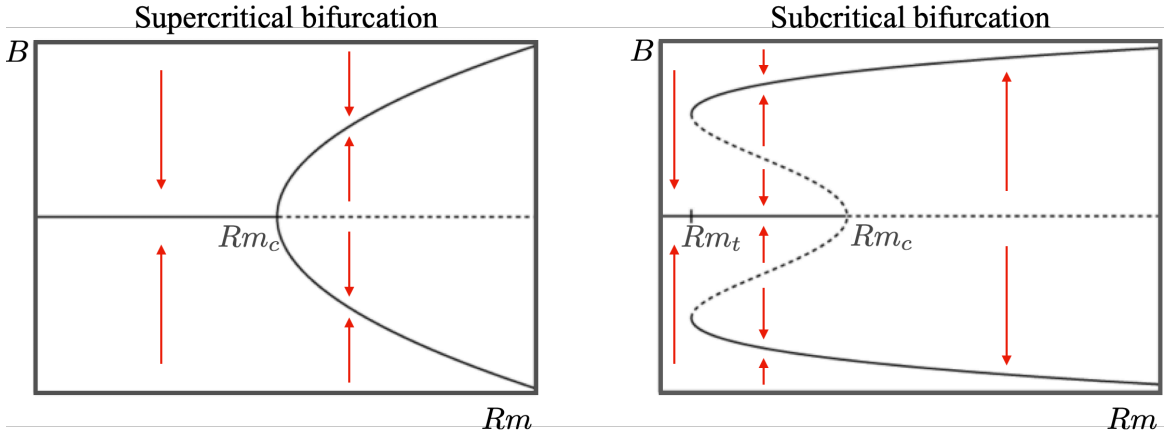

Figure 3.4 — Examples of bifurcation diagrams for a supercritical (left) and a subcritical (right) transition *(inspired by Dormy (2011, Fig. 1))*. Rm_c and Rm_t are the critical Rm and the turning point, respectively. The red lines describe the approximate trajectories of a system from different initial conditions. Dotted and solid lines represent the unstable and stable branches of the birfurcation.

anism involves both *poloidal* and *toroidal* components of the magnetic field. Qualitatively, these components represent the field in the direction following the small ring and the large circular ring of a torus, respectively. Parker's mechanism starts with a large-scale poloidal magnetic field, which is sheared into a large-scale toroidal magnetic field[2]. The main objective of Parker (1955) is to propose a mechanism to generate a poloidal field from a toroidal field using the helicity of the flow. The helical velocity twists the magnetic flux tube to create a loop and therefore a poloidal component. As illustrated in the inset of Fig. 3.3, we emphasize that during the twist, the magnetic helicity is still conserved as the created "large-scale" magnetic helicity by the loop is compensated by the "small-scale" helicity generated by the twist of the magnetic field lines in the tube. Assuming that most of the swirls rotate in the same direction, all the loops tend to form a large-scale poloidal magnetic field, which completes the loop. Note that if the helical velocity swirls in the appropriate direction, it is possible to produce poloidal magnetic field lines anti-parallel to the initial one, which therefore creates an oscillatory dynamo. This simple model can thus be applied to the solar and stellar convective zones and is the first to invoke the helicity of the flow to generate a poloidal magnetic field. This mechanism is now known as the α-effect (Steenbeck et al., 1966). Nevertheless, this model and especially the use of α-effect faces a potentially important issue in the high-Rm regime. Indeed, the small-scale magnetic fields produce a significant feedback on the helical flow and alter strongly the growth of the large-scale magnetic fields, which becomes very slow (Mininni et al., 2005, Brandenburg, 2005, Subramanian & Brandenburg, 2014, Bhat et al., 2016, e.g.). This can be interpreted as a *catastrophic α-quenching* due to the conservation of magnetic helicity (e.g. Gruzinov & Diamond, 1994, Cattaneo & Hughes, 1996, Brandenburg, 2001)[3].

3.2.5 . Mean field approach

[2]The winding of a poloidal field (or Ω-*effect*) was already known before this model (e.g. Cowling, 1933, Bullard & Gellman, 1954).

[3]The catastrophic α-quenching is still strongly debated (e.g. Field & Blackman, 2002, Hughes, 2018)

The mean-field dynamo theory is a statistical theory that aims at describing analytically the growth of the magnetic field in large-scale dynamos (Steenbeck et al., 1966, Moffatt, 1970, Vaĭnshteĭn, 1970). The mathematics behind this approach has been massively studied and is still widely used. In this section, we will introduce the main aspects of the theory, so see the classical textbooks by Moffatt (1978) (and its new edition Moffatt & Dormy (2019)) and Krause & Raedler (1980), and the following recent reviews Hughes (2018), Brandenburg (2018) for detailed and complete presentations.

The main tenet behind the mean-field approach is the scale separation of the velocity and magnetic fields into a "large-scale" and a "small-scale" component, which represent the rms mean-field and the fluctuation varying around it, respectively. This mean-field can be averaged quantity in time, on a number of realisations, or on one or several space dimensions depending on the investigated system. In this thesis, we will average the fields along the longitudinal direction $\mathbf{e}_\phi$, so that the mean field and the fluctuations are the axisymmetric and non-axisymmetric parts of the field, respectively. Nonetheless, whatever the average used, it must commute with the space and time derivatives and the integration operators, and satisfy the Reynolds rules

$$\overline{F+H} = \overline{F} + \overline{H}, \tag{3.59}$$

$$\overline{F\overline{H}} = \overline{F}\,\overline{H}, \tag{3.60}$$

where $\overline{\bullet}$ is the average operator, and F and H are arbitrary functions of space and time. In the following, we will note the velocity and magnetic fields

$$\mathbf{v} = \overline{\mathbf{v}} + \mathbf{v}', \tag{3.61}$$

$$\mathbf{B} = \overline{\mathbf{B}} + \mathbf{B}', \tag{3.62}$$

where $\overline{\mathbf{v}'} = \overline{\mathbf{B}'} = 0$, by definition. Note that the fluctuations are different from the perturbations we used to derive the properties of MHD waves and the MRI in Sect. 3.1.4 because the fluctuations can be arbitrarily large compared to the mean field.

Let us now average the induction equation (3.20),

$$\partial_t \overline{\mathbf{B}} = \boldsymbol{\nabla} \times \left(\overline{\mathbf{v}} \times \overline{\mathbf{B}} + \overline{\mathbf{v}' \times \mathbf{B}'} \right) + \eta \Delta \overline{\mathbf{B}}. \tag{3.63}$$

The first term on the right-hand side of the equation contains both the advection and the stretching (the equivalent of the Ω-effect in differentially rotating flows) of the magnetic field by the large-scale velocity field. The second term called the mean *electromotive force (EMF)* $\boldsymbol{\mathcal{E}} \equiv \overline{\mathbf{v}' \times \mathbf{B}'}$ is crucial for the dynamo mechanism in the mean-field approach. This term drives the dynamo and is a formulation of the statistical cross-correlation between the fluctuations of both velocity and magnetic fields which were anticipated in Parker's model (see Sect. 3.2.4). To find an expression of the EMF, it is sensible to derive the induction equation for the fluctuating magnetic field. For that, we subtract the mean induction equation (3.63) to the full induction equation (3.20),

$$\partial_t \mathbf{B}' = \boldsymbol{\nabla} \times \left[(\mathbf{v}' \times \overline{\mathbf{B}}) + (\overline{\mathbf{v}} \times \mathbf{B}') + (\mathbf{v}' \times \mathbf{B}' - \boldsymbol{\mathcal{E}}) \right] + \eta \boldsymbol{\Delta} \mathbf{B}'. \tag{3.64}$$

First, the term $\mathbf{v}' \times \overline{\mathbf{B}}$ formulates the induction of $\mathbf{B}'$ due to the shearing and tangling of the mean magnetic field by the small-scale velocity field. This term is important to have a mean-field dynamo action. Second, the term $\overline{\mathbf{v}} \times \mathbf{B}'$ describes the advection of $\mathbf{B}'$ by the large-scale

flow. This term is usually considered as subdominant in this approach. Third, $(\mathbf{v}' \times \mathbf{B}' - \boldsymbol{\mathcal{E}})$ is often referred to as the "pain in the neck" term and must be coped with by introducing new assumptions because of its quadratic character in fluctuations.

If $\mathbf{v}$ does not depend on $\overline{\mathbf{B}}$ (kinematic approach), Eq. (3.64) becomes a linear relation between $\mathbf{B}'$ and $\overline{\mathbf{B}}$. Therefore, $\boldsymbol{\mathcal{E}}$ can be expanded as

$$(\overline{\mathbf{v}' \times \mathbf{B}'})_i = a_{ij}\overline{B}_j + b_{ijk}\partial_k \overline{B}_j + o(c_{ijkl}\partial_l \partial_k \overline{B}_j)\,, \tag{3.65}$$

where the expansion is stopped at the second order because the spatial derivative is slow. For astrophysical fluids, the EMF is usually written with vectors and tensors to separate clearly the different symmetries (Krause & Raedler, 1980)

$$(\overline{\mathbf{v}' \times \mathbf{B}'})_i = \alpha_{ij}\overline{B}_j + (\boldsymbol{\gamma} \times \overline{\mathbf{B}})_i - \beta_{ij}(\boldsymbol{\nabla} \times \overline{\mathbf{B}})_j - [\boldsymbol{\delta} \times (\boldsymbol{\nabla} \times \overline{\mathbf{B}})]_i - \frac{\kappa_{ijk}}{2}(\partial_j \overline{B}_k + \partial_k \overline{B}_j)\,. \tag{3.66}$$

The vectors and tensors are defined as a function of the previous tensors $\mathbf{a}$ and $\mathbf{b}$

$$\alpha_{ij} = \frac{1}{2}(a_{ij} + a_{ji})\,, \tag{3.67}$$

$$\gamma_i = -\frac{1}{2}\varepsilon_{ijk}a_{jk}\,, \tag{3.68}$$

$$\beta_{ij} = \frac{1}{4}(\varepsilon_{ikl}b_{jkl} + \varepsilon_{jkl}b_{ikl})\,, \tag{3.69}$$

$$\delta_i = \frac{1}{4}(b_{jji} - b_{jij})\,, \tag{3.70}$$

$$\kappa_{ijk} = -\frac{1}{2}(b_{ijk} + b_{ikj})\,. \tag{3.71}$$

where ε_{ijk} is the Levi-Civita tensor. It can be useful to consider the symmetries in a given flow to determine which of the coefficients are supposed to be zero or not. First, the tensors can only be constructions of the Kronecker symbol δ_{ij} and ε_{ijk} in isotropic flows, so $\boldsymbol{\delta}$ and $\boldsymbol{\kappa}$ vanish. Second, since $\boldsymbol{\alpha}$, $\boldsymbol{\delta}$, and $\boldsymbol{\kappa}$ are pseudo-vectors/tensors, they must vanish in parity-invariant flows. Finally, the homogeneity of the flow cancels the effect of $\boldsymbol{\gamma}$ and the tensors are independent of space.

In the common case of pseudo-isotropic homogeneous flows (e.g. parity broken by a helical flow), only the constant $\alpha_{ij} = \alpha\delta_{ij}$ and $\beta_{ij} = \beta\delta_{ij}$ remain non-zero. The mean induction equation (3.63) becomes

$$\partial_t \overline{\mathbf{B}} = \boldsymbol{\nabla} \times \left(\overline{\mathbf{v}} \times \overline{\mathbf{B}} + \alpha\overline{\mathbf{B}}\right) + (\eta + \beta)\Delta\overline{\mathbf{B}}\,. \tag{3.72}$$

Here, the term $\alpha\boldsymbol{\nabla} \times \overline{\mathbf{B}}$ drives the mean-field dynamo via the so-called α-effect, which is strongly related to the kinetic and magnetic helicities. The β coefficient acts here as a turbulent diffusivity produced by the dynamo, which can compensate the growth of the dynamo. If we add a Ω-effect and ignore the produced anisotropy, there exist three dynamo solutions which produce an exponential growth of the magnetic field. These mean-field dynamos are illustrated in Fig. 3.5. They differ as to the way of generating the mean toroidal magnetic field, which is whether via the α-effect (α^2 dynamo), the Ω-effect ($\alpha\Omega$ dynamo), or both at the same time ($\alpha^2\Omega$ dynamo).

In astrophysical objects, the fluids are more complex with no real symmetries in the flow. In the framework of this thesis, the fluid we consider is always anisotropic because of the rotation and the large-scale shear. Therefore many additional effects occur. First of all, the

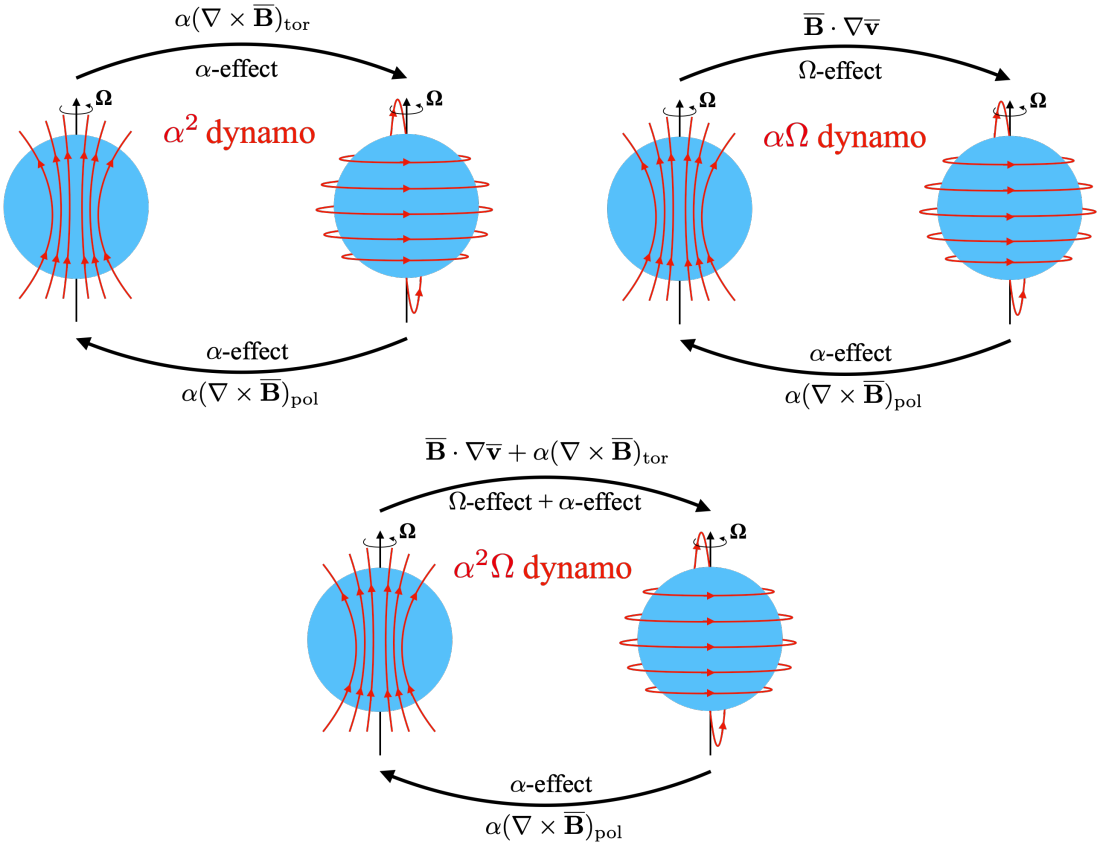

Figure 3.5 — Scheme of the α^2, $\alpha\Omega$, and $\alpha^2\Omega$ dynamo loops.

non-diagonal terms of the α tensor must be non-zero if the flow symmetry is broken. These terms participate in the large-scale transport of the magnetic field. An additional effect related to the vector γ, called *turbulent pumping*, also contributes to the large-scale transport in inhomogeneous flows.

Second, the (not physically intuitive) Rädler (Rädler, 1969a,b) and shear-current effects (Rogachevskii & Kleeorin, 2003) contribute to the induction in the presence of rotation and large-scale shear. They involve the coefficients $\boldsymbol{\delta} \equiv \delta_\Omega \boldsymbol{\Omega}$ and $\boldsymbol{\delta} \equiv \delta_W \boldsymbol{\nabla} \times \overline{\mathbf{v}}$, respectively. The former effect survives as long the system rotates whatever the properties of the conducting fluid (e.g. Moffatt & Proctor, 1982). In rotating flows with broken equatorial symmetry (i.e. non-parity-invariant), both α and Rädler effects must coexist, but the latter seems to be subdominant (Käpylä et al., 2009), which could be due to the slow spatial derivative in $\boldsymbol{\nabla} \times \overline{\mathbf{B}}$.

The mean-field approach is very useful because it can provide simplified equations to describe the growth of large-scale magnetic fields. A first application of the theory is the derivation of low-dimensional non-linear models, which use the same idea of separating the mean field from the fluctuations. They usually involve coupled non-linear time evolution equations of large-scale magnetic field modes with different equatorial symmetries (often called dipole and quadrupole modes) to describe the dynamics at the vicinity of the dynamo threshold (e.g. Ravelet et al., 2008, Gallet & Pétrélis, 2009, Gissinger, 2010, to describe the dynamos in the VKS experiment). Such kind of models are also applied to supercritical dynamos that are far from the threshold (high-Rm regime) for stellar convection (e.g. Jennings & Weiss, 1991, Tobias, 1996, Weiss, 2005).

A second application is the use of the mean-field theory as an analysis tool for numerical simulations. This kind of analysis aims at extracting the dynamo vectors and tensors we described in this section (Eqs. (7.22)–(3.71)) to capture which terms of the electromotive force dominate the growth of the magnetic field. There exist several methods for the extraction: e.g. method using correlations between $\boldsymbol{\mathcal{E}}$ and derivatives of $\overline{\mathbf{B}}$ (as done by Reboul-Salze et al., 2022), the singular value decomposition (Racine et al., 2011, Simard et al., 2016), the test-field method (Schrinner et al., 2005, Brandenburg, 2005, Schrinner et al., 2007), and the most recent IROS method (Bendre et al., 2023). The extracted tensors can also be compared to their analytical expressions, which can be calculated via the first-order smoothing approximation (FOSA) (Moffatt, 1978), the third-order eddy-damped quasi-normal Markovian (EDQNM) (Orszag, 1970, Pouquet et al., 1976), or the third-order τ-approximation (MTA) (Vainshtein & Kichatinov, 1983) closure schemes. Still, this exercise is very complex and can be numerically costly for sophisticated methods such as the test-field.

While the mean-field approach has brought a lot of interesting results, we must keep in mind its limitations (Cattaneo & Hughes, 1996, Hughes & Cattaneo, 2008, Tobias et al., 2011, Tobias, 2021). First, the basic mean-field theory is kinematic, so it can not capture the non-linear saturation and the dynamics of the saturated state. The attempts to saturate the mean-field dynamos suggest that the magnetic helicity participates in the saturation process. This may cause catastrophic α-quenching as observed numerically, though the numerical simulations never reached the asymptotic Rm regime. Second, the kinematic approach assumes an EMF driven by a non-magnetic turbulent flow whereas the Lorenz force drives the turbulent flow in the case of dynamos driven by MHD instabilities. In this case, the relation between the EMF and the large-scale magnetic fields is certainly non-linear, i.e. the mean-field decomposition of Eq. (3.65) is not valid. Third, the small-scale MHD turbulence can not be ignored in the high-Rm regime. This implies that a solution to the large-scale dynamo problem must start from a small-scale turbulent saturated state, which is not taken into account by the mean-field theory. Finally, isolating the different contributions in the electromotive force must not make us forget neither that all these effects are certainly acting at the same time in realistic flows, nor the strong non-linear and 3D nature of the dynamo problem.

3.3 . The Tayler-Spruit dynamo

3.3.1 . The Tayler instability

After stating the generalities about plasma description and introducing the specific problem of dynamo action, we focus our attention on the dynamo mechanism that is central in this thesis: the Tayler-Spruit dynamo. This mechanism is driven by a large-scale shear flow and an MHD instability called the Tayler instability. The discovery of this instability was first made analytically by Tayler (1973) by investigating the stability of a purely toroidal magnetic field $\mathbf{B} = B_\phi \mathbf{e}_\phi$. For that purpose, Tayler (1973) used the energy principle of Bernstein et al. (1958), which predicts that the adiabatic stability of an ideally conducting, non-rotating, and incompressible fluid (i.e. $\eta = 0$) depends on the sign of the variation of a potential energy δW produced by a perturbation. If there exists a perturbation such that $\delta W < 0$, the system is unstable. Therefore the strategy consists in finding the necessary and sufficient criteria for this condition to be satisfied. By supposing a field configuration separable in r and θ in a stably stratified fluid, Goossens (1980) found the following analytical expression of the

(geometrical) criteria for instability in spherical coordinates (r,θ,ϕ)

$$c_{m=0} \equiv \frac{B_\phi^2}{2\pi r^2 \sin^2\theta}\left(\cos^2\theta - \sin\theta\cos\theta\partial_\theta \log B_\phi\right) < 0\,, \tag{3.73}$$

for axisymmetric perturbations, and

$$c_{m\neq 0} \equiv \frac{B_\phi^2}{4\pi r^2 \sin^2\theta}\left(m^2 - 2\cos^2\theta - 2\sin\theta\cos\theta\partial_\theta \log B_\phi\right) < 0\,, \tag{3.74}$$

for non-axisymmetric perturbations. These criteria give the regions in which the geometry of B_ϕ makes the fluid Tayler unstable, which works whatever the strength of B_ϕ. The absence of radial derivatives is due to the seration of the magnetic field in two radial- and latitudinal-dependent functions. In the general case, the radial structure can influence the stability. These criteria show that the instability is most likely to occur near the polar axis. Goossens (1980) also showed that the perturbations with a non-axysimmetric mode $|m| = 1$ is the only perturbation to trigger an instability for all values of l. The Tayler instability is therefore a kink-type instability. Note that no differential rotation is needed to destabilise B_ϕ, unlike the MRI. A current inducing B_ϕ is the only ingredient necessary, which makes the Tayler instability a current-driven instability.

However, many ingredients are expected to stabilise the fluid such as the rotation and the diffusivity. To take these effects into account, we use a perturbative method as in Sect. 3.1.4 for the MRI, which will give explicitely the growth rate and the wavelength of the unstable modes. The following reasoning is similar to what was done in Zahn et al. (2007) and Ma & Fuller (2019). The viscosity is neglected, while the thermal and magnetic diffusivities are included. In the spherical frame $(\mathbf{e}_r,\mathbf{e}_\theta,\mathbf{e}_\phi)$, we assume a pertubation of the form

$$\delta Q \propto \exp\left[i(k_r r + l\theta + m\phi - \omega t)\right], \tag{3.75}$$

with l and m the spherical harmonic degree and order (see Sect. 4.3.3) and k_r the radial wavenumber. We assume a strong buoyancy force such that the $k_r r$ is large compared to l/r and m/r (WKB approximation see Gough, 2007, for an introduction). We also use the Boussinesq approximation (see Chap. 4). Since the thermal diffusion κ is expected to be large at the length scale of the instability, we suppose the fluid to be barotropic, i.e. the density depends on the pressure only. This equivalent to ignoring the baroclinic term $(\boldsymbol{\nabla}\rho \times \boldsymbol{\nabla} p)$. Finally, the Tayler instability develops on an azimuthal background field of the form

$$\mathbf{B}_0 = B_0 f(\theta)\mathbf{e}_\phi\,, \tag{3.76}$$

where f is an arbitrary function of the colatitude θ. We neglect the radial dependency of the background field to simplify the calculation. After (a very long week-end doing) a lot of calculations, we obtain a 6^{th}-order dispersion relation in ω (see App. A for the full expression).

For rotation angular frequencies larger than the Alfvén frequency $\Omega \gg \omega_\text{A} \equiv B_0/\sqrt{4\pi\rho r^2}$, we expect the growth rate of the Tayler instability to be $\gamma_\text{TI} \equiv \omega_\text{A}^2/\Omega$. So we define the quanti-

ties

$$\alpha \equiv \omega \frac{\Omega}{\omega_{\rm A}^2}, \tag{3.77}$$

$$H \equiv \frac{\eta\Omega}{\omega_{\rm A}^2}, \tag{3.78}$$

$$K \equiv \frac{\kappa\Omega}{\omega_{\rm A}^2}, \tag{3.79}$$

$$n^2 \equiv \left(\frac{l}{k_r r}\right)^2 \frac{N_\mu^2}{\omega_{\rm A}^2}, \tag{3.80}$$

where N_v is the chemical composition component of the Brunt-Väisälä frequency N. In the limit of $\kappa \to \infty$, the dispersion relation reduces to a $2^{\rm nd}$-order relation

$$m^2\left[m^2\alpha F(\theta) + n^2(\alpha + iHk_r^2)\right] - \alpha\left[2(\alpha + iHk_r^2)\cos\theta + mG(\theta)\right]^2 = 0. \tag{3.81}$$

with the functions

$$F(\theta) \equiv \left(\frac{f(\theta)}{\sin\theta}\right)^2, \tag{3.82}$$

$$G(\theta) \equiv \left(\frac{(f(\theta)\sin\theta)' f(\theta)}{\sin^2\theta}\right), \tag{3.83}$$

and the derivative along θ noted $\bullet'$. We set α purely real, so we can seperate Eq. (A.79) into the real and imaginary parts, respectively:

$$m^2(m^2F(\theta) + n^2) - (2\alpha\cos\theta + mG(\theta))^2 + 4H^2k_r^4\cos^2\theta = 0, \tag{3.84}$$

$$m^2n^2 - 4(2\alpha\cos\theta + mG(\theta))\cos\theta\alpha. \tag{3.85}$$

By solving the reduced dispersion relation (A.79), we can show that the fluid is Tayler unstable for

$$m^2\frac{F(\theta)}{G(\theta)^2} < 1. \tag{3.86}$$

Thus for a toroidal magnetic field resulting from the shearing of a magnetic dipole, i.e. $f(\theta) = \cos\theta\sin\theta$, we find that $|m| = 1$ is the only unstable mode, which develops near the poles $\theta \in [0, \pi/5] \cup [4\pi/5, \pi]$. Since $\gamma_{\rm TI} \equiv \omega_{\rm A}^2/\Omega$, the rotation stabilises the fluid.

A minimum magnetic strength can be derived by reasoning on the Tayler mode radial length scales (Spruit, 1999). The strong stable stratification (i.e. $N \gg \Omega$) implies almost horizontal displacements; i.e. $l_h/(k_r r) \ll 1$, where l_h is Tayler mode horizontal length scale, i.e. in the directions θ and ϕ. The work against stable stratification of an unstable displacement with an amplitude ξ reads $1/2\, l^2/(k_r r)^2 N^2\xi^2$. For the instability to occur, this work must be smaller than the energy gained by the magnetic field due to the displacement $1/2\,\omega_{\rm A}^2\xi^2$. This leads to a minimum radial length scale

$$l_{\rm TI} \equiv k_r r < l\frac{\omega_{\rm A}}{N} \sim r\frac{\omega_{\rm A}}{N}, \tag{3.87}$$

where r is the typical length of the system (the radius in the case of a fluid in a spherical configuration like in stars or planets). Also, in a resistive fluid, $l_{\rm TI}$ can not be smaller than the resistive scale, at which the magnetic field is dissipated, i.e.

$$l_{\rm TI}^2 > \eta\gamma_{\rm TI}^{-1} \sim \eta\frac{\Omega}{\omega_{\rm A}^2}\,. \tag{3.88}$$

These two constraints on $l_{\rm TI}$, thus impose a minimum strength on the toroidal magnetic field, noted B_ϕ

$$B_\phi > \sqrt{4\pi\rho r^2}\Omega\left(\frac{N}{\Omega}\right)^{1/2}\left(\frac{\eta}{r^2\Omega}\right)^{1/4} \tag{3.89}$$

Note that the viscosity must also participate in the stabilisation, but we will rather describe its impact qualitatively in Chap. 5.

The Tayler instability has also been studied further analytically, numerically, and experimentally, mainly in the context of cylindrical Taylor-Couette flows (e.g. Rüdiger & Kitchatinov, 2010, Rüdiger & Schultz, 2010, Seilmayer et al., 2012, Kirillov et al., 2014, Rüdiger et al., 2018) and stellar radiative zones (e.g. Szklarski & Arlt, 2013, Bonanno & Guarnieri, 2017, Guerrero et al., 2019, Bonanno et al., 2020). The recent numerical simulations in a cylindrical (Ji et al., 2023) and in spherical geometries (our simulations in App. B) confirm the presence of a dominating $m = 1$ unstable mode growing with the expecting rate $\omega_{\rm A}^2/\Omega$. In the regime $\omega_{\rm A} > \Omega$, the growth rate seems to follow another scaling law $\gamma_{\rm TI} \propto \omega_{\rm A}^{4.5}/\Omega^2$ (Ji et al., 2023).

Some of these studies also showed the proximity between the MRI and the Tayler instability, despite their different nature, which can make them difficult to differentiate in numerical simulations. For instance, Jouve et al. (2020) reported a $m = 1$ unstable mode in a numerical simulation of a stably stratified fluid with an initial spherical (i.e. only radial-dependent) rotation profile. In their setup, the rotation decreases with the radius, which makes the fluid prone to both the MRI of a toroidal magnetic field (azimuthal-MRI, noted AMRI for short) and the Tayler instability. While the $m = 1$ mode is usually characteristic of Tayler instability, the dispersion relation of Acheson & Gibbons (1978) for MHD instabilities which includes viscosity and diffusivities indicates that a MRI-type instability with a dominant $m = 1$ mode can also develop for large thermal diffusivities. Moreover, the modes are located where the shear is maximum, whereas the Tayler modes are rather located where the latitudinal gradient of B_ϕ is strong according to the criterion Eq. (3.74). Therefore, Jouve et al. (2020) concluded that the instability in their simulation is the AMRI and not the Tayler instability. Kirillov et al. (2014) investigated this boundary between the AMRI and the Tayler instability. They show that the instability domains of both instabilities in the parameter space can overlap, which confirms that both instabilities are difficult to distinguish. However, regions in which the cylindrical radial gradient of B_ϕ is positive are prone the Tayler instability only, whereas regions with strong negative gradients are prone to AMRI.

3.3.2 . Dynamo driven by the Tayler instability

The major question stemming from the previous section is whether the Tayler instability can sustain dynamo action in a shear flow like the MRI and the magnetic buoyancy. This issue is furthermore crucial in astrophysical stably stratified fluids, especially stellar radiative zones. Indeed, the advent of the helioseismology and the asteroseismology provided new information about the interior of the Sun and stars, and especially the rotation. This research

field consists in measuring oscillations at the star surface, which are the signature of pressure and gravity waves (the so-called p- and g-modes) propagating in the star interior (see e.g. Ballot, 2004, Bugnet, 2020). Recent asteroseismic measurements brought several results on the rotation profile in radiative zones and they all show that cores rotate slower than predicted by stellar evolution models. The Sun's radiative zone is in quasi-rigid rotation (Eggenberger et al., 2005, Howe, 2009, Gough, 2015, Eggenberger et al., 2019a, 2022) and the known angular momentum transport (AMT) mechanism can not explain the spin rate of sub-/red giants (e.g. Cantiello et al., 2014, Belkacem et al., 2015a,b, Fuller et al., 2015, Spada et al., 2016, Ouazzani et al., 2019, Eggenberger et al., 2019c, den Hartogh et al., 2020, Moyano et al., 2024, and many others). This abundant literature demonstrates the importance of the AMT problem since the 2000's.

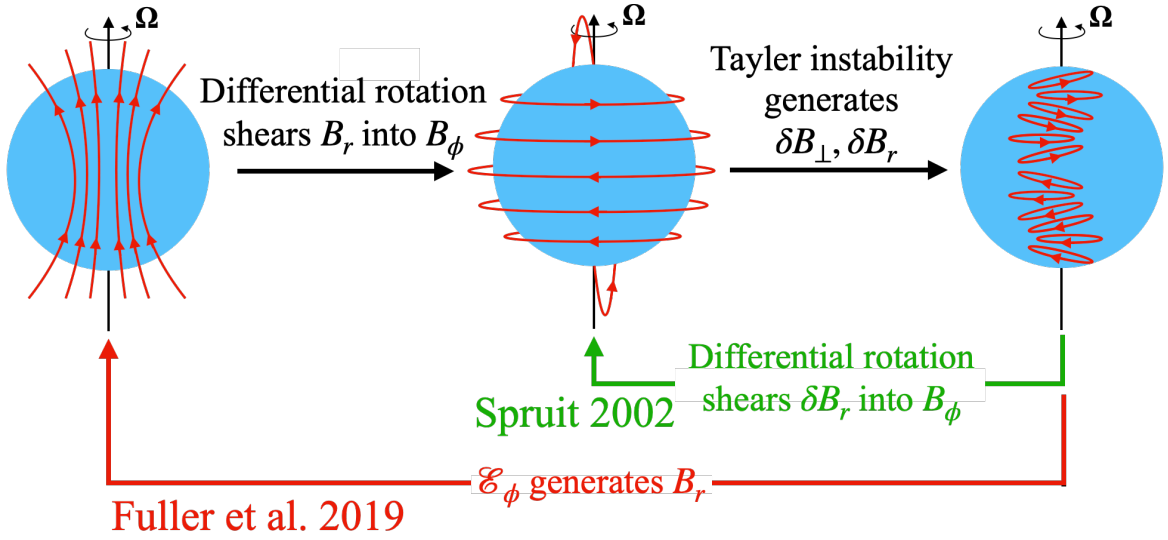

Figure 3.6 — Scheme of Tayler-Spruit dynamo loop as theorised by Spruit (2002) and Fuller et al. (2019). B_r, B_ϕ are the large-scale radial and azimuthal magnetic fields, and δB_r, $\delta B_\perp$ represent the perturbed radial and horizontal components of the magnetic field, respectively. $\mathscr{E}_\phi$ is the azimuthal component of the electromotive force.

Magnetic fields are suspected to play a crucial role in the AMT. Spruit (2002) is the first to propose that a dynamo mechanism driven by the Tayler instability could transport AM efficiently. As illustrated in Fig. 3.6, the mechanism of Spruit (2002) starts with an initial poloidal (or radial) magnetic field B_r which is sheared into a toroidal (or azimuthal) magnetic field B_ϕ by the differential rotation. Once B_ϕ reaches the critical strength in Eq. (3.89), the Tayler instability develops and produces a new B_r. This newly generated B_r can be sheared again to close the dynamo. The magnetic field is therefore amplified until the turbulent dissipation of B_ϕ compensates its growth due to the shearing. Using a reasoning in order of magnitudes (detailed in Chap. 5), Spruit (2002) derives saturated values for B_r and B_ϕ, and also the produced AMT characterised by the Maxwell torque $T \sim B_r B_\phi$. Though appealing, this reasoning faces criticism (Denissenkov & Pinsonneault, 2007, Zahn et al., 2007, Fuller et al., 2019):

(i) The large-scale azimuthal field B_ϕ is quasi-constant on length scales around $l_{\rm TI}$. So, the displacements produced by the Tayler instability may not mix the large-scale field lines by reconnecting them. Therefore, the dissipation of the large-scale B_ϕ may be overestimated. Moreover, the ratio B_r/B_ϕ may not be the same for axisymmetric and

non-axisymmetric magnetic fields as the stable stratification may not act the same way on the radial Tayler modes and axisymmetric B_r.

(ii) The Tayler instability dominant mode is non-axisymmetric ($m = 1$). Therefore, its shearing generates a mostly non-axisymmetric azimuthal field B_ϕ.

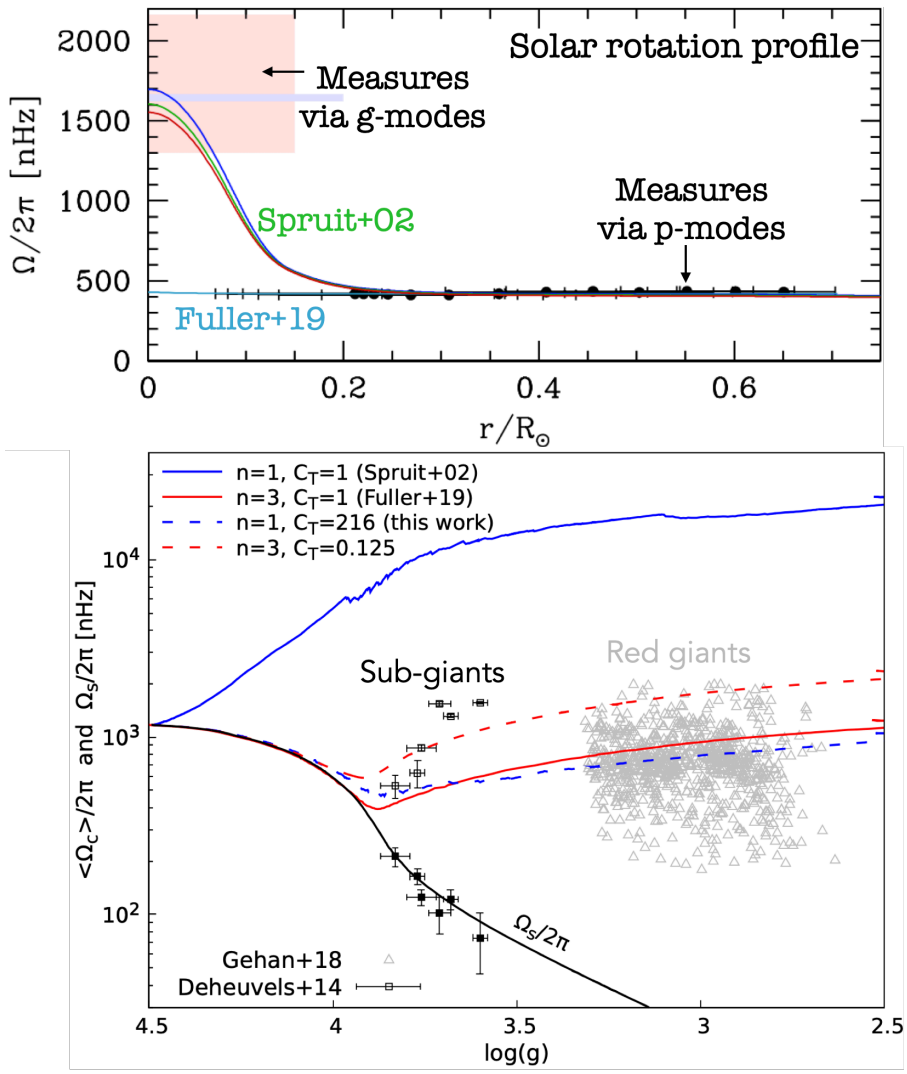

Figure 3.7 — *Top:* Rotation profile in the Sun as measured by helioseismology and simulated via a stellar evolution code including the Tayler-Spruit dynamo (modified plot from Eggenberger et al. (2019a)). *Bottom:* Core and surface rotation in sub- and red giant stars as measured by asteroseismology and simulated by stellar evolution codes including different parametrisation of the Tayler-Spruit dynamo. *(modified plot from Eggenberger et al. (2022))*.

These critics motivated the revised mechanism derived by Fuller et al. (2019). This model overcomes the critics by seperating axisymmetric B_r, B_ϕ and non-axisymmetric δB_r, $\delta B_\perp$ magnetic fields. B_ϕ is now amplified by the shear of a B_r generated by a non-linear induction, i.e. the azimuthal electromotive force $\mathcal{E}_\phi$. Fuller et al. (2019) also derive different turbulent dissipation rates for the Tayler modes δB_r, $\delta B_\perp$ and the axisymmetric magnetic fields B_r, B_ϕ. The saturated B_r and B_ϕ therefore differ from the derivation of Spruit (2002), and are found

to be stronger (see Chap. 5). Thus, the modelling of Fuller et al. (2019) provides more efficient AMT than Spruit (2002).

The prescriptions of both Spruit (2002) and Fuller et al. (2019) have been implemented in one-dimensional (1D) stellar evolution codes, such as MESA (Paxton et al., 2011, 2013, 2015, 2018, 2019, Jermyn et al., 2023) and GENEC (Eggenberger et al., 2008). For the Sun, these models show that the prescription of Spruit (2002) explains well the rotation profile of the solar radiative zone (Eggenberger et al., 2019a, 2022). However, the revised model of Fuller et al. (2019) provided such efficient AMT that the rotation profile is flat, which is not consistent with the measures of g-modes, as seen in the top plot of Fig. 3.7. For sub- and red giants, the original mechanism does not provide enough AMT to explain the rotation of these stars unlike the revised Tayler-Spruit model, which fits well the measurements in red giants (see the bottom plot of Fig. 3.7). However, the latter can not explain the rotation of both sub- and red giants (Fuller et al., 2019, Eggenberger et al., 2019c), which suggests that different AMT mechanisms must be occurring during the sub-giant phase (Eggenberger et al., 2019b). Note that, the Tayler-Spruit dynamo could also be involved in the mixing of chemical elements in stellar interiors but is found to be ineffective, unlike other MHD instabilities like the MRI.

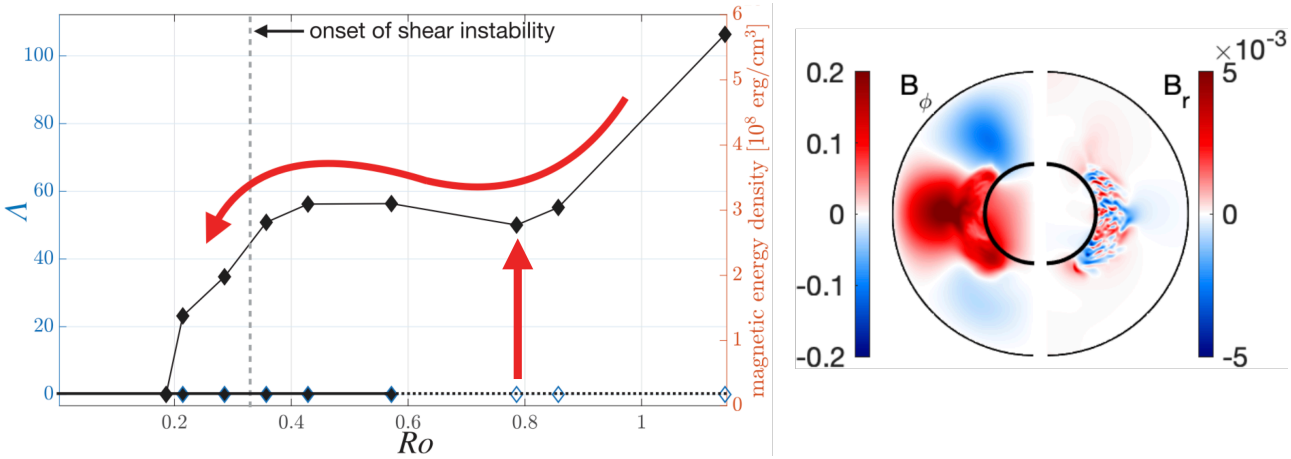

Figure 3.8 — *Left:* Bifurcation diagram representing the magnetic energy (characterised by the Elsasser number Λ) as a function of the input differential rotation noted Ro (adapted from Petitdemange et al. (2023)). *Right:* Meridional slices of the azimuthal B_ϕ and the radial B_r magnetic fields *(adapted from Petitdemange et al. (2024))*.

While the inclusion of the Tayler-Spruit dynamo has made significant progress in the AMT problem, this dynamo mechanism was for a long time elusive in numerical simulations. Braithwaite (2006) claims the presence of this dynamo in numerical simulations in cylindrical geometry, but it is not clear whether the Tayler instability is present in these simulations instead of kinematic small-scale dynamo. Moreover, the numerical simulations of Zahn et al. (2007) in spherical geometry do not show any sign of dynamo action even though they observe the Tayler instability. The different results between these two numerical studies may reside in the setups: the latter uses perfect conducting boundary conditions whereas the former imposes the magnetic field to be normal to the boundary. Furthermore, Braithwaite (2006) uses a volumetric forcing to force differential rotation whereas the differetial rotation can spread out of the integration domain in the simulation of Zahn et al. (2007). This can significantly influence the possibility to produce a dynamo. More recent numerical simulations in spherical geometry and using a volumetric forcing for differential rotation also captured

the development of the Tayler instability but no dynamo action was reported (Meduri et al., 2024).

In the past year, new numerical simulations by Petitdemange et al. (2023) found a dynamo sharing many properties with the Tayler-Spruit dynamo. These simulations were performed in a spherical Taylor-Couette setup, i.e. the fluid evolves between an inner and outer sphere on which we impose a constant rotation rate, noted Ω_i and Ω_o, respectively. This investigation was conducted in the context of stellar radiative zones, and so $\Omega_i < \Omega_o$. The differential rotation is characterised by the dimensionless number $Ro = 1 - \Omega_o/\Omega_i$. This configuration is similar to the setup we will use in Chap. 6. Petitdemange et al. (2023) show that the simulated dynamo is strongly subcritical as displayed in the left plot of Fig. 3.8. Indeed, this bifurcation diagram has many resemblances with the plot of the subcritical bifurcation in Fig. 3.4. For $Ro < 0.78$, an initially weak magnetic is not amplified and tends to a hydrodynamic solution. However, for $Ro > 0.78$, the weak magnetic field is amplified exponentially due to a kinematic dynamo driven by a shear instability. When B_ϕ reaches the critical strength of the Tayler instability, a secondary non-linear growth amplifies the magnetic field, which saturates above the saturation strength of the kinematic dynamo. By starting the simulations from strong magnetic fields in their saturated states, the dynamo can be maintained to Ro smaller than both critical Ro of the kinematic dynamo and of the shear instability as indicated by the red arrows. A second important result is that the saturated magnetic field fits very well the analytical prescriptions of Spruit (2002) as confirmed by the following studies (Daniel et al., 2023, Petitdemange et al., 2024). The meridional slices in Fig. 3.8 show that the Tayler modes are located around the equator close the inner sphere, which is not the expected location by the geometrical criterion of Goossens & Tayler (1980) (Eqs. (3.73)-(3.74)). However, the results of Kirillov et al. (2014) we have discussed in the previous section show that the Tayler instability can also develop in regions with positive radial gradients of the axisymmetric B_ϕ. However, we will see that our simulations, with $\Omega_i < \Omega_o$, show a richer dynamics and quite different results. A detailed comparison between their simulations and ours will be discussed in Chap. 7.

4

Numerical modelling: the MagIC code

Contents

The study of astrophysical objects involves an immense set of complex physical processes in interaction. In order to attempt to (at most partially) take them into account and to overcome the limits of the analytical approach, numerical simulations are key tools in astrophysics. Astrophysical conducting fluid dynamics does not escape the rule since it is necessary to capture fully their non-linear nature. To produce the numerical models presented in this manuscript, we used the pseudo-spectral code MagIC (except in Chap. 9). First, we briefly describe the setup of MagIC in Sect. 4.1. Then, in Sect. 4.2, we derive the different approximations of the MHD equations solved by the code. In Sect. 4.3, we present the formalism to project the equations in the spectral space. Finally, we introduce the numerical

methods used to integrate the equations in Sect. 4.4. This chapter is inspired by the online documentation of MagIC (https://magic-sph.github.io/index.html, https://github.com/magic-sph) and a course given by Thomas Gastine in July 2017. Note that each chapter of the manuscript involving numerical simulations (Chaps. B–8, 9) includes a section that recalls the specific methods used to carry out the associated study. Note that, in the following, we will use the notation $d_x \equiv d/dx$ and $\partial_x \equiv \partial/\partial x$ to express the derivative of a quantity with respect to x.

4.1 . Numerical setup

MagIC simulates the evolution of an electrically conducting fluid enclosed between two rotating spheres. This configuration is adapted to model the MHD phenomena that occurs in different astrophysical objects, such as planets, stars, or proto-neutron stars. Note that the inner sphere can also be removed to simulate other astrophysical systems such as the Earth core before the crystalization of the inner core. The figure 4.1 shows different axis defining the spherical frame ($\mathbf{e}_r$,$\mathbf{e}_\theta$,$\mathbf{e}_\phi$) in which MagIC solves the equations, the rotation axis $\mathbf{\Omega}$ in the polar direction $\mathbf{e}_z$, and different length scales: r_i and r_o the radii of the inner and outer spheres, respectively, and the sphere width $d \equiv r_o - r_i$. We also define the dimensionless parameter called the aspect ratio $\chi \equiv r_i/r_o$. In the following, we also note Ω_i and Ω_o the angular rotation frequencies of the inner and outer spheres, respectively. As MagIC uses a spherical geometry, the equations of this chapter will only be written in the spherical coordinates (radius r, colatitude θ, longitude ϕ). The components of a vector $\mathbf{F}$ will be noted $(F_r, F_\theta, F_\phi) \equiv (\mathbf{F}\cdot\mathbf{e}_r, \mathbf{F}\cdot\mathbf{e}_\theta, \mathbf{F}\cdot\mathbf{e}_\phi)$.

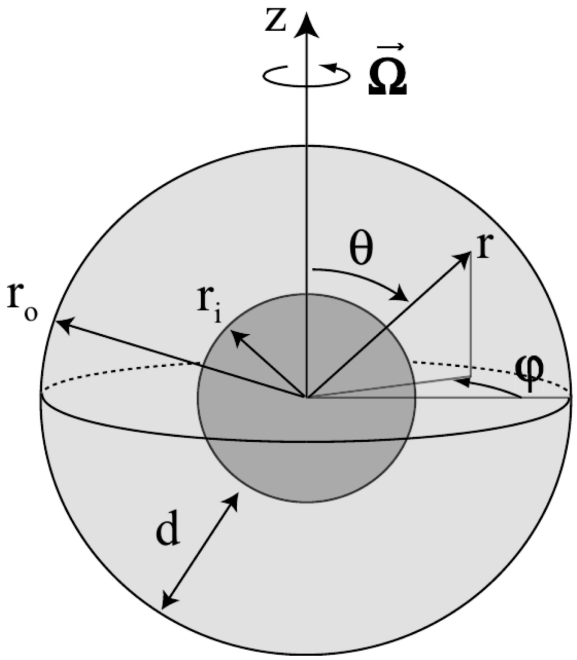

Figure 4.1 — Scheme of the numerical domain in which the fluid evolves.

4.2 . Approximations of the resistive MHD equations

Solving the full resistive MHD equations (3.13)–(3.23) is numerically costly, especially because of the presence of sound waves. Indeed, if the sound waves are much faster than the rest of the fluid, the timestep necessary to resolve the sound wave propagation will be much smaller than the timestep necessary to capture the global dynamics. For this reason, the MagIC code solves MHD equations using two approximations called Boussinesq and anelastic. Both filter out sound waves and so can be applied for fluids with typical velocities v negligible compared to the fluid sound speed c_s, i.e. in the low Mach number regime $Ma \equiv v/c_s \ll 1$. These approximations are especially adapted for flows driven by buoyancy, i.e. stably-stratified and convective flows.

4.2.1 . Boussinesq approximation

According to Rayleigh (1916), the *Boussinesq approximation* was first used by Boussinesq (1903), though a similar approximation was also invoked by Oberbeck (1879). The idea behind the approximation is to neglect all density fluctuations in the fluid equations except in the buoyancy term, where this fluctuation is multiplied by gravity. Historically, the Boussinesq approximation was derived for fluids whose density perturbations depend on the temperature perturbations only. This simplifies the EoS (3.23), which becomes

$$\rho = \rho_0(1-\alpha_T(T-T_0)) = \rho_0(1-\alpha_T\Delta T)\,, \tag{4.1}$$

where ρ_0 and T_0 are the mean density and temperature. The entropy and the temperature are now equivalent quantities, ignoring a multiplication factor. Indeed, the variation of entropy, which reads

$$dS = \partial_T S|_p dT + \partial_p S|_T dp = \frac{c_p}{T_0}dT - \frac{\alpha_T}{\rho_0}dp\,, \tag{4.2}$$

where c_p is the specific heat capacity at constant pressure, becomes

$$T_0 ds = c_p dT\,. \tag{4.3}$$

However, in proto-neutron stars (PNSs) the electron fraction Y_e also play an important role in the buoyancy force (see Sect. 2.2.2). To take into account the effect of Y_e, we define the buoyancy variable

$$\Theta \equiv \frac{-g_0}{N^2}\frac{r}{r_0}\frac{\delta\rho}{\rho_0}\,, \tag{4.4}$$

where the amplitude of the gravitation acceleration g_0 is defined via the expression $\mathbf{g} = -g_0 r/r_o \mathbf{e}_r$ and N is the Brunt-Väisälä frequency (Eq. 2.22) and assume that both T and Y_e have equal diffusivities, which are gathered in the usual thermal diffusivity κ.

The resistive first-order MHD equations for a Boussisnesq PNS interior are now rewritten

$$\boldsymbol{\nabla}\cdot\mathbf{v} = 0\,, \tag{4.5}$$

$$\boldsymbol{\nabla}\cdot\mathbf{B} = 0\,, \tag{4.6}$$

$$\rho_0\left(\partial_t\mathbf{v} + \mathbf{v}\cdot\boldsymbol{\nabla}\mathbf{v} + 2\boldsymbol{\Omega}\times\mathbf{v}\right) = -\boldsymbol{\nabla}\delta p - \rho_0 N^2\Theta\mathbf{e}_r + \frac{1}{4\pi}(\boldsymbol{\nabla}\times\mathbf{B})\times\mathbf{B} + \rho_0\nu\boldsymbol{\Delta}\mathbf{v}\,, \tag{4.7}$$

$$\partial_t\mathbf{B} = \boldsymbol{\nabla}\times(\mathbf{v}\times\mathbf{B}) + \eta\boldsymbol{\Delta}\mathbf{B}\,, \tag{4.8}$$

$$\partial_t\Theta + \mathbf{v}\cdot\boldsymbol{\nabla}\Theta = \kappa\Delta\Theta\,, \tag{4.9}$$

where δp is the temperature and non-hydrostatic pressure. We notice that the energy equation becomes the classical heat equation in which we removed the viscous heating and the Joule effect, and replaced the temperature by the buoyancy variable. The `MagIC` code solves dimensionless equations based on the following choice of units:

- Time is in units of viscous time $t \to (d^2/\nu)\,t$, which can be changed in the current version of `MagIC`.
- Length is in units of shell thickness $r \to rd$.
- The buoyancy variable is in units of the buoyancy variable gap between the shells $\Theta \to (\Theta_o - \Theta_i)\Theta$.
- Magnetic field is substitued by $B \to \sqrt{4\pi\rho_0\eta\Omega_o}B$.

Eqs. (4.7)-(4.9) become,

$$\partial_t \mathbf{v} + \mathbf{v}\cdot\boldsymbol{\nabla}\mathbf{v} + \frac{2}{E}\mathbf{e}_z \times \mathbf{v} = -\boldsymbol{\nabla}\delta p + \frac{Ra}{Pr}\Theta\mathbf{e}_r + \frac{1}{EPm}(\boldsymbol{\nabla}\times\mathbf{B})\times\mathbf{B} + \boldsymbol{\Delta}\mathbf{v}, \tag{4.10}$$

$$\partial_t \mathbf{B} = \boldsymbol{\nabla}\times(\mathbf{v}\times\mathbf{B}) + \frac{1}{Pm}\boldsymbol{\Delta}\mathbf{B}, \tag{4.11}$$

$$\partial_t \Theta + \mathbf{v}\cdot\boldsymbol{\nabla}\Theta = \frac{1}{Pr}\Delta\Theta, \tag{4.12}$$

where we define the following dimensionless numbers:

- the *Ekman number* $E \equiv \nu/(d^2\Omega_o)$,
- the *Rayleigh number* $Ra \equiv N^2 d^4/(\nu\kappa)$,
- the *thermal Prandtl number* $Pr \equiv \nu/\kappa$,
- and the *magnetic Prandtl number* $Pm \equiv \nu/\eta$.

The Ekman number represents the ratio of the viscous force to the Coriolis force and the Rayleigh number formulates the ratio of the thermal transport timescale through diffusive processes to the transport timescale by convection.

4.2.2 . Anelastic approximation

Unlike the Boussinesq approximation, the *anelastic approximation* includes a non-constant density profile and filters out the sound waves at the same time. This approach consists in assuming that the flow and the magnetic field only produce small disturbances of a thermodynamical *reference (or background) state*. A thermodynamical quantity Q is denoted $Q = Q_0 + \delta Q$. The point is to solve the MHD equations at the first order of the small parameter

$$\epsilon \sim \frac{\delta\rho}{\rho_0} \sim \frac{\delta T}{T_0} \sim \frac{\delta p}{p_0} \sim \ldots \ll 1. \tag{4.13}$$

The reference state is assumed to be stationary and in hydrostatic equilibrium, i.e.

$$\boldsymbol{\nabla} p_0 = -\rho_0 g_0 \mathbf{e}_r, \tag{4.14}$$

and only depends on the radius in spherical geometry. For a convective fluid, we expect the background to be isentropic because of mixing due to the convective cells. However, in a stably stratified fluid, the entropy is not homogeneous. We express the density and the temperature gradients as a function of the entropy and the pressure gradients

$$\frac{\boldsymbol{\nabla} T_0}{T_0} = \frac{1}{T_0}\partial_s T|_p \boldsymbol{\nabla} S_0 + \frac{1}{T_0}\partial_p T|_s \boldsymbol{\nabla} p_0 = \frac{1}{c_p}\boldsymbol{\nabla} S_0 - \frac{\alpha_T}{c_p}\mathbf{g}_0\,, \tag{4.15}$$

$$\frac{\boldsymbol{\nabla}\rho_0}{\rho_0} = \frac{1}{\rho_0}\partial_s \rho|_p \boldsymbol{\nabla} S_0 + \frac{1}{\rho_0}\partial_p \rho|_s \boldsymbol{\nabla} p_0 = -\frac{\alpha_T}{c_p} T_0 \boldsymbol{\nabla} S_0 + \beta_p \rho_0 \mathbf{g}_0\,. \tag{4.16}$$

For the sake of simplicity, the effect of the electron fraction Y_e on the buoyancy is taken into account by defining an effective entropy gradient $\boldsymbol{\nabla} S_{\rm eff}$ such that

$$\left.\frac{\partial\rho}{\partial S}\right|_{p,Y_e}\frac{dS}{dr} + \left.\frac{\partial\rho}{\partial Y_e}\right|_{p,S}\frac{dY_e}{dr} = \left.\frac{\partial\rho}{\partial S_{\rm eff}}\right|_{p,Y_e}\frac{dS_{\rm eff}}{dr}\,. \tag{4.17}$$

In the following, we avoid the notation with the index $\bullet_{\rm eff}$ to make the mathematical expressions a bit less cumbersome.

For an adiabatic system (i.e. $\boldsymbol{\nabla} S_0 = 0$), both density and temperature gradients are characterised by the *dissipation* and the *compressibility* numbers, which are defined by

$$Di = \frac{\alpha_T d}{c_p} g_0\,, \tag{4.18}$$

$$Co = \beta_p d \rho_0 g_0\,, \tag{4.19}$$

respectively. These parameters can be determined by the input reference state. Note that we find the Boussisnesq approximation for $Di, Co \to 0$. To derive the anelastic continuity equation, we decompose Eq. (3.13)

$$\partial_t \rho_0 + \partial_t \delta\rho + \boldsymbol{\nabla}\cdot(\rho_0\mathbf{v}) + \boldsymbol{\nabla}\cdot(\delta\rho\mathbf{v}) = 0\,. \tag{4.20}$$

The first is zero because the reference state is stationary and $\boldsymbol{\nabla}\cdot(\delta\rho\mathbf{v}) \ll \boldsymbol{\nabla}\cdot(\rho_0\mathbf{v})$ because $\delta\rho \ll \rho_0$. We then assume that the variation timescale of the density is similar to the timesacled associated to $\mathbf{v}$ and that the typical length of density gradient is not not "too small" such that we can compare the two remaining terms:

$$\frac{[\partial_t\delta\rho]}{[\boldsymbol{\nabla}\cdot(\rho_0\mathbf{v})]} \sim \frac{[\partial_t\delta\rho]}{[\mathbf{v}\cdot\boldsymbol{\nabla}\rho_0]} \sim \frac{\delta\rho}{\rho_0} \sim \epsilon\,. \tag{4.21}$$

Therefore, the anelastic continuity equation reads

$$\boldsymbol{\nabla}\cdot(\rho_0\mathbf{v}) = 0\,. \tag{4.22}$$

Thus, the sound waves are filtered out. Before writing the other equations, we must introduce the reduced pressure $\delta p/\rho_0$. This new term stems from the so-called LBR formalism, in which the buoyancy is written

$$\frac{\delta\rho}{\rho_0}\mathbf{g}_0 = -\frac{\alpha_T T_0}{c_p}\delta S\mathbf{g}_0 - \frac{\delta p}{\rho_0^2}\boldsymbol{\nabla}\rho_0\,. \tag{4.23}$$

Parameter	Earth's core	Giant planets	Sun	PNS (with neutrino viscosity)
E	10^{-15}	10^{-18}	10^{-15}	$10^{-10}-10^{-8}$
Ra	10^{27}	10^{30}	10^{24}	5×10^{11}
Pr	0.1	0.1	10^{-6}	5×10^{-5}
Pm	10^{-6}	10^{-7}	10^{-3}	10^{11}

Table 4.1 — Values of `MagIC` input dimensionless parameters for different astrophysical objects.

This formalism is named after Lantz (1992) and Braginsky & Roberts (1995) and allows the use of the entropy instead of the temperature. It is therefore not necessary to calculate pressure, density and temperature variations. Indeed, by using the same reasoning to derive the anelastic continuity equation (Eq. (4.22)) and injecting Eq. (4.23) in the equation of motion (Eq. (3.14)), we obtain

$$\boldsymbol{\nabla}\cdot(\rho_0\mathbf{v})=0\,, \tag{4.24}$$

$$\boldsymbol{\nabla}\cdot\mathbf{B}=0\,, \tag{4.25}$$

$$\partial_t\mathbf{v}+\mathbf{v}\cdot\boldsymbol{\nabla}\mathbf{v}+2\boldsymbol{\Omega}\times\mathbf{v}=-\boldsymbol{\nabla}\left(\frac{\delta p}{\rho_0}\right)-\frac{\alpha_T T_0}{c_p}\delta S\mathbf{g}+\frac{1}{4\pi\rho_0}(\boldsymbol{\nabla}\times\mathbf{B})\times\mathbf{B}+\frac{1}{\rho_0}\boldsymbol{\nabla}\cdot\boldsymbol{\sigma}\,, \tag{4.26}$$

$$\partial_t\mathbf{B}=\boldsymbol{\nabla}\times\left(\mathbf{v}\times\mathbf{B}-\eta(r)\boldsymbol{\nabla}\times\mathbf{B}\right), \tag{4.27}$$

$$\rho_0 T_0\left(\partial_t\delta S+\mathbf{v}\cdot\boldsymbol{\nabla}\delta S\right)=\boldsymbol{\nabla}\cdot(\kappa(r)\rho_0 T_0\boldsymbol{\nabla}\delta S)+\Phi_v+\eta(r)\frac{(\boldsymbol{\nabla}\times\mathbf{B})^2}{4\pi}\,. \tag{4.28}$$

Moreover, the energy is conserved in this formulation, which is not the case for all formulations (e.g. anelastic Navier-Stokes approaches), especially in stably stratified fluids (Brown et al., 2012). Note that we make an additional assumption to derive the entropy equation (Eq. (4.28)) because the term $\boldsymbol{\nabla}\cdot(\kappa\boldsymbol{\nabla}T_0)$ should appear while expanding the equation of energy (Eq. (3.21)). This term formulates the temperature diffusion and is very small in astrophysical objects because their Ra is very large (see Table 4.1) compared to the critical Ra_c for the onset of convection ($Ra_c\sim10^3$). However, these regimes cannot be reached in current numerical simulations, in which the diffusivities are over-estimated. The temperature diffusion will therefore act as a heat source or sink that could drive or hinder the convection to develop. This motivates the assumption of a dominating entropy diffusion in turbulent flows so that κ is an estimation of the turbulent diffusivity. The entropy is scaled in units of entropy contrast between the spheres $S\rightarrow(S_o-S_i)S$. The dimensionless version of anelastic equations thus reads

$$\boldsymbol{\nabla}\cdot(\rho_0\mathbf{v})=0\,, \tag{4.29}$$

$$\boldsymbol{\nabla}\cdot\mathbf{B}=0\,, \tag{4.30}$$

$$\partial_t\mathbf{v}+\mathbf{v}\cdot\boldsymbol{\nabla}\mathbf{v}+\frac{2}{E}\mathbf{e}_z\times\mathbf{v}=-\boldsymbol{\nabla}\left(\frac{\delta p}{\rho_0}\right)-\frac{Ra}{Pr}\delta S g_0\mathbf{e}_r+\frac{1}{PmE\rho_0}(\boldsymbol{\nabla}\times\mathbf{B})\times\mathbf{B}+\frac{1}{\rho_0}\boldsymbol{\nabla}\cdot\boldsymbol{\sigma}\,, \tag{4.31}$$

$$\partial_t\mathbf{B}=\boldsymbol{\nabla}\times(\mathbf{v}\times\mathbf{B})-\frac{1}{Pm}\boldsymbol{\nabla}\times\left(\eta(r)\boldsymbol{\nabla}\times\mathbf{B}\right), \tag{4.32}$$

$$\rho_0 T_0\left(\partial_t\delta S+\mathbf{v}\cdot\boldsymbol{\nabla}\delta S\right)=\frac{1}{Pr}\boldsymbol{\nabla}\cdot(\kappa(r)\rho_0 T_0\boldsymbol{\nabla}\delta S)+\frac{Pr\,Di}{Ra}\Phi_v+\frac{Pr\,Di}{Pm^2\,E\,Ra}\eta(r)(\boldsymbol{\nabla}\times\mathbf{B})^2\,. \tag{4.33}$$

4.2.3 . Validity of the approximations for the modelling of a proto-neutron star

In PNSs, the use of the MHD approximations is globally relevant. First, the PNS fluid v and Alfvén v_A velocities are

$$v \lesssim r_{NS}\Omega \sim 7.5\times10^{8}\left(\frac{\Omega}{200\pi \mathrm{rad\,s^{-1}}}\right)\mathrm{cm\,s^{-1}}, \tag{4.34}$$

$$v_A = \frac{B}{\sqrt{4\pi\rho_0}} \sim 1.4\times10^{7}\left(\frac{B}{10^{15}\,\mathrm{G}}\right)\left(\frac{\rho_0}{4\times10^{14}\,\mathrm{g\,cm^{-3}}}\right)^{-1/2}\mathrm{cm\,s^{-1}}. \tag{4.35}$$

They are smaller than the sound speed $c_s \sim 10^{10}\,\mathrm{cm\,s^{-1}}$ (Guilet et al., 2015), which suggests that the sound waves should be filtered out in the simulations. Second, the density perturbations associated to the buoyancy force are smaller than the mean density

$$\frac{\delta\rho}{\rho_0} = \frac{\Theta N^2}{g} \lesssim 0.12\left(\frac{N}{10^{3}\,\mathrm{s^{-1}}}\right)^{2}\left(\frac{g}{10^{13}\,\mathrm{cm\,s^{-2}}}\right)^{-1}, \tag{4.36}$$

where we assume $\Theta \lesssim r_{NS}$. The only condition that is not satisfied for the use of these approximations is the static reference state. Indeed, it evolves within the timescale of the second in PNSs, which is shorter than the usual total simulated time (several tens of seconds for the longest simulations).

Since the Tayler-Spruit dynamo is poorly known in numerical simulations, we choose to implement the simplest modelling of the PNS to investigate the dynamo in more and more complex setups progressively. Therefore, the Boussinesq approximation in used in the different numerical studies of this thesis (Chaps. 6-8). The future simulations will use the anelastic approximation to implement a more realistic reference state and investigate the impact of density stratification.

4.3 . Spectral representation

4.3.1 . Why using spectral methods?

Spectral methods consist in expanding the variables in terms of global (mostly nonzero over the whole domain) and usually orthogonal polynomials. These expansions enable the derivation of equations for the coefficients of these polynomials and to have analytical expressions for the derivatives. This makes the method very rapid to converge to the solutions, especially smooth (i.e. highly differentiable) ones. These methods can therefore provide accurate solutions quickly with a reasonable number of points. Moreover, the numerical dissipation is very weak with this approach and allow us to use explicit diffusivities.

However, it is more challenging for these methods to treat less continuous functions compared to other methods such as finite difference/element/volume methods. Moreover, spectral methods are limited to simple geometries from boxes to spheres.

For the problem of the MHD in a PNS, the geometry is simple since the PNS is spherical even for fast rotations (frequencies up to $\sim$500 Hz). The solutions for the velocity and magnetic field components are expected to be smooth because the flow is subsonic. Spectral methods are therefore well suited to solve this problem. In MagIC, the latitudinal and the azimuthal directions are expanded in spherical harmonics and the radial direction in Chebyshev polynomials. The former is well suited for spherical geometries and the latter enable

better treatment of the dynamics close to the boundaries, which are particularly prone to under-resolution.

The MagIC code is pseudo-spectral because the non-linear terms and the Coriolis force (because it involves a cross-product) are first evaluated in the physical space before being expanded in the spectral space. This treatment can be numerically costly due to the back-and-forth transformations between the physical and the spectral space, but computational efficiency is gained thanks to the resulting decoupling of the spherical harmonics modes, whose calculation can be parallelised.

4.3.2 . Poloidal/Toroidal decomposition

In the MagIC code, the vectors which satisfy the solenoidal condition (i.e. divergence-free) are decomposed in a *poloidal* and *toroidal* part, which is called the *Mie representation*. For the anelastic equation, the two solenoidal vectors are

$$\rho_0 \mathbf{v} = \boldsymbol{\nabla} \times (\boldsymbol{\nabla} \times W \mathbf{e}_r) + \boldsymbol{\nabla} \times Z \mathbf{e}_r \,, \tag{4.37}$$

$$\mathbf{B} = \boldsymbol{\nabla} \times (\boldsymbol{\nabla} \times b \mathbf{e}_r) + \boldsymbol{\nabla} \times a_j \mathbf{e}_r \,, \tag{4.38}$$

where W and Z (b and a_j) are the poloidal and toroidal potentials for the mass flux (the magnetic field), respectively. These potentials can be extracted by projecting the field and its curl in the radial direction:

$$\Delta_{\mathrm{H}} b = -\mathbf{B} \cdot \mathbf{e}_r \,, \tag{4.39}$$

$$\Delta_{\mathrm{H}} a_j = -(\boldsymbol{\nabla} \times \mathbf{B}) \cdot \mathbf{e}_r \,, \tag{4.40}$$

where Δ_{H} is the horizontal Laplacian operator:

$$\Delta_{\mathrm{H}} \equiv \frac{1}{r^2 \sin\theta} \partial_\theta \left(\sin\theta \partial_\theta \right) + \frac{1}{r^2 \sin^2\theta} \partial_\phi^2 \,. \tag{4.41}$$

The vector expressed as a function of its potentials therefore reads

$$\mathbf{B} = -\Delta_{\mathrm{H}} b \mathbf{e}_r + \left(\frac{1}{r} \partial_r \partial_\theta b + \frac{1}{r \sin\theta} \partial_\phi a_j \right) \mathbf{e}_\theta + \left(\frac{1}{r \sin\theta} \partial_r \partial_\phi b + \frac{1}{r} \partial_\theta a_j \right) \mathbf{e}_\phi \,, \tag{4.42}$$

which can be rewritten

$$\mathbf{B} = -\Delta_{\mathrm{H}} (b \mathbf{e}_r) + \boldsymbol{\nabla}_{\mathrm{H}} \partial_r b + \boldsymbol{\nabla}_{\mathrm{H}} \times a_j \mathbf{e}_r \,, \tag{4.43}$$

using the horizontal divergence operator

$$\boldsymbol{\nabla}_{\mathrm{H}} \equiv \frac{1}{r \sin\theta} \partial_\theta \sin\theta \mathbf{e}_\theta + \frac{1}{r \sin\theta} \partial_\phi \mathbf{e}_\phi \,. \tag{4.44}$$

The curl of a vector can also be written in a simple form

$$\boldsymbol{\nabla} \times \mathbf{B} = -\Delta_{\mathrm{H}} (a_j \mathbf{e}_r) + \boldsymbol{\nabla}_{\mathrm{H}} \partial_r a_j + \boldsymbol{\nabla}_{\mathrm{H}} \times \Delta_{\mathrm{H}} a_j \mathbf{e}_r \,. \tag{4.45}$$

4.3.3 . Spherical harmonics

As the geometry of the integration domain is spherical, it is sensible to expand the potentials using the *spherical harmonic* functions for the colatitude θ and longitude ϕ

$$Y_l^m(\theta, \phi) \equiv \sqrt{\frac{2l+1}{4\pi} \frac{(l-|m|)!}{(l+|m|)!}} P_l^m(\cos\theta) e^{im\phi} \,, \tag{4.46}$$

$Y_l^m(\theta,\phi)$	$m=0$	$m=\pm1$	$m=\pm2$
$l=0$	$\sqrt{1/(4\pi)}$	Not defined	Not defined
$l=1$	$\sqrt{3/(4\pi)}\cos\theta$	$\mp\sqrt{3/(8\pi)}\sin\theta e^{\pm i\phi}$	Not defined
$l=2$	$\sqrt{5/(16\pi)}(3\cos^2\theta-1)$	$\mp\sqrt{15/(8\pi)}\cos\theta\sin\theta e^{\pm i\phi}$	$\sqrt{15/(32\pi)}\sin^2\theta e^{\pm 2i\phi}$

Table 4.2 — Analytical expressions of the spherical harmonic functions for $l \in [0,2]$.

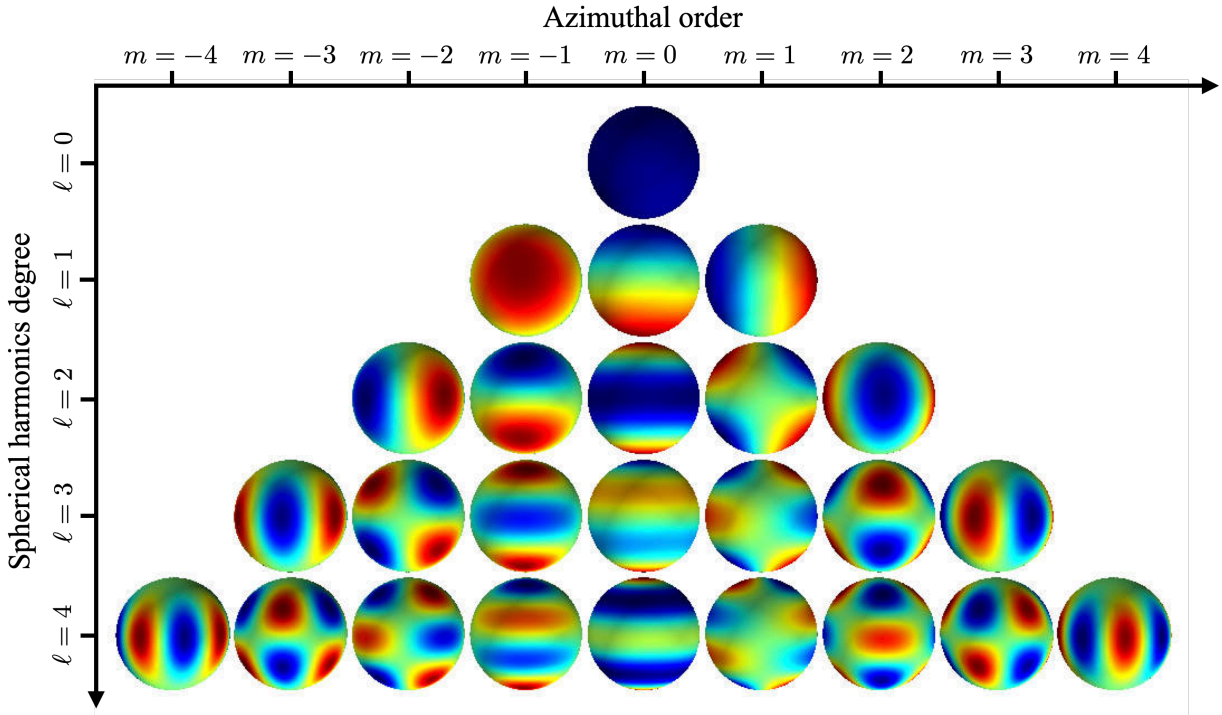

Figure 4.2 — Real part of the spherical harmonic functions Y_ℓ^m for $\ell \in [0,4]$ and $m \in [-\ell,\ell]$.

where $l \geq 0$ and $m \in [-l,l]$ are the spherical harmonic degree and order,

$$c_{lm} \equiv \sqrt{\frac{2l+1}{4\pi}\frac{(l-|m|)!}{(l+|m|)!}} \tag{4.47}$$

is the normalisation factor, and P_l^m is a Legendre polynomial

$$P_l^m(x) = (-1)^m(1-x^2)^{m/2}\left[d_x^m \frac{1}{2^l l!}\left(d_x(x^2-1)^l\right)\right]. \tag{4.48}$$

The expression of c_{lm} can vary depending the normalisation used, which is

$$\int_0^{2\pi}\int_0^{\pi} Y_l^m(\theta,\phi)\,Y_{l'}^{m'}(\theta,\phi)\sin\theta\,d\theta\,d\phi = \delta_{ll'}\delta^{mm'} \tag{4.49}$$

in MagIC, with $\delta_{ij} = \delta^{ij}$ the Kronecker symbol, which equates 1 for $i=j$ and 0 otherwise.

The functions Y_l^m are the eigenfunctions of both operators $L^2 \equiv -r^2\Delta_{\rm H}$ and $L_z \equiv -i\,(\mathbf{r}\times\boldsymbol{\nabla})\cdot\mathbf{e}_z$

$$L^2 Y_l^m = l(l+1)\,Y_l^m, \tag{4.50}$$
$$L_z Y_l^m = m Y_l^m. \tag{4.51}$$

Note that it is simple to switch from Y_l^m to Y_l^{-m} thanks to the relation

$$Y_l^{-m} = (-1)^m Y_l^{m*} \tag{4.52}$$

where the exponent symbol $\bullet^*$ represents the conjugate complex. This property can be noticed from the analytical formulation of the first Y_l^m that is written in Table 4.2. As Y_l^m are a function of θ and ϕ, they can be plotted on spheres as illustrated in Fig. 4.2.

As an example, the spherical harmonic representation of the magnetic poloidal potential, truncated at $l_{\max}$, as done in the code, reads

$$b(r,\theta,\phi) = \sum_{l=0}^{l_{\max}} \sum_{m=-l}^{l} b_{lm}(r) Y_l^m(\theta,\phi), \tag{4.53}$$

where

$$b_{lm}(r) = \frac{1}{\pi} \int_0^{\pi} b_m(r,\theta) P_l^m(\cos\theta) \sin\theta d\theta, \tag{4.54}$$

and

$$b_m(r,\theta) = \frac{1}{2\pi} \int_0^{2\pi} b(r,\theta,\phi) e^{-im\phi} d\phi. \tag{4.55}$$

In practice, Eqs. 4.53 and 4.55 formulate the transformation from the spherical (r,θ,ϕ) to the spectral space (r,l,m) and inverse transformation, respectively. `MagIC` employs a Fast-Fourier Transform (FFT) and uses the Gauss-Legendre quadrature in the longitudinal and latitudinal directions to evaluate Eq. (4.55). Pre-stored values of the Legendre polynomials combined with an inverse FFT provide a solution for Eq. (4.53). This requires the use of at least $n_\phi = 2l_{max}+1$ longitudinal points to evenly cover the whole space in ϕ and the number of latitudinal points is usually $n_\theta = n_\phi/2$ to have a isotropic spherical grid.

4.3.4 . Chebyshev polynomials

Now that the horizontal expansion is 'spectralised', the same process is done for the radial expansion, but using the Chebyshev polynomials (of the first kind)

$$\mathscr{C}_n(\cos\theta) = \cos(n\theta). \tag{4.56}$$

which can be approximated by

$$\mathscr{C}_n(x) \sim \cos(n \arccos x), \tag{4.57}$$

for a variable $x \in [-1,1]$ and a degree $n \in \mathbb{N}$. The analytical expressions of the first $\mathscr{C}_n$ are written in Table 4.3.
These polynomials are solutions of the following ordinary differential equation (ODE)

$$(1-x^2)y'' - xy' + n^2 y = 0, \tag{4.58}$$

where the symbol $\bullet'$ formulates the derivative with respect to x and their literal expression can be written using the Rodrigues formula

$$\mathscr{C}_n(x) = \frac{1}{2^n n!} \left(d^n_{x^n}(x^2-1)^n\right). \tag{4.59}$$

n	$\mathscr{C}_n(x)$
$n=0$	1
$n=1$	x
$n=2$	$2x^2-1$
$n=3$	$4x^3-3x$
$n=4$	$8x^4-8x^2+1$
$n=5$	$16x^5-20x^3+5x$

Table 4.3 — Analytical expressions of six first Chebyshev polynomials $\mathscr{C}_n$.

A nice property of the Chebyshev polynomials is their recurrence relation, which reads

$$\mathscr{C}_0(x) = 1\,, \tag{4.60}$$
$$\mathscr{C}_1(x) = x\,, \tag{4.61}$$
$$\mathscr{C}_{n+1}(x) = 2x\mathscr{C}_n(x) - \mathscr{C}_{n-1}(x)\,. \tag{4.62}$$

In practice, the radial representation of the poloidal magnetic potential, truncated at degree N, reads

$$b_{lm}(r) = \sum_{n=0}^{N} b_{lmn}\mathscr{C}_n(r)\,, \tag{4.63}$$

with

$$b_{lmn} = \frac{2-\delta_{n0}}{\pi}\int_{-1}^{1}\frac{b_{lm}(r(x))}{\sqrt{1-x^2}}\mathscr{C}_n(r(x))dx\,. \tag{4.64}$$

x is then linearly mapped onto the radius range $[r_i, r_o]$ via the relation

$$x(r) = 2\frac{r-r_i}{r_o-r_i} - 1\,. \tag{4.65}$$

In MagIC, the radial grid points are non-linearly mapped

$$x_k = \cos\left(\pi\frac{k-1}{n_r-1}\right), \tag{4.66}$$

for $k \in [1, n_r]$, with n_r the number of grid points in the radial direction, so that the Chebyshev polynomials reads

$$\mathscr{C}_{nk} \equiv \mathscr{C}_n(x_k) = \cos\left(\pi\frac{n(k-1)}{n_r-1}\right). \tag{4.67}$$

With this mapping, the density of grid points is larger next to the boundaries. This allows a better resolution close to the shells, where we expect thermal and viscous boundary layers. Note that the radial direction can be treated with a finite difference method in MagIC. In our simulations, we use the Chebyshev expansion because of the advantages of the spectral expansion discussed in Sect. 4.3.1.

4.3.5 . Exemple of spectral equation

As the mathematical tools to project the potentials in the spectral space, let us derive an example of spectral equation, such as the evolution of the poloidal magnetic potential $\partial_t b$

via the induction equation (Eq. (4.11)) with a constant resisivity η. We focus on the radial component of Eq. (4.11). First, the time derivative reads

$$\partial_t B_r = -\Delta_{\rm H}\partial_t b, \tag{4.68}$$

where we used Eq. (4.39). To expand Eq. (4.68) in spherical harmonics, we use the relation Eq. (4.50) and obtain

$$\partial_t B_r = \sum_{l=0}^{l_{\rm max}} \sum_{m=-l}^{l} \frac{l(l+1)}{r^2} \partial_t b_{lm} Y_l^m. \tag{4.69}$$

Second, the radial resistive term can be rewritten in spherical coordinates

$$\frac{1}{Pm}\mathbf{\Delta B}\cdot\mathbf{e}_r = \frac{1}{Pm}\left(\frac{1}{r^2}\partial_r^2(r^2 B_r) + \Delta_{\rm H} B_r\right). \tag{4.70}$$

So its expansion in spherical harmonics reads

$$\begin{aligned}\frac{1}{Pm}\mathbf{\Delta B}\cdot\mathbf{e}_r &= \frac{1}{Pm}\left(-\frac{1}{r^2}\partial_r^2(r^2\Delta_{\rm H} b) - \Delta_{\rm H}(\Delta_{\rm H} b)\right) \\ &= \frac{1}{Pm}\sum_{l=0}^{l_{\rm max}}\sum_{m=-l}^{l}\frac{l(l+1)}{r^2}\left(\partial_r^2 b_{lm} - \frac{l(l+1)}{r^2} b_{lm}\right) Y_l^m.\end{aligned} \tag{4.71}$$

Let us multiply by Y_l^{m*} and expand in Chebyshev polynomials the new version of the radial induction equation:

$$\frac{l(l+1)}{r^2}\left[\left(\partial_t + \frac{1}{Pm}\frac{l(l+1)}{r^2}\right)\mathscr{C}_n - \frac{1}{Pm}\mathscr{C}_n''\right] b_{lmn} = \int_0^\pi\int_0^{2\pi} \left[(\boldsymbol{\nabla}\times(\mathbf{v}\times\mathbf{B}))\cdot\mathbf{e}_r\right] Y_l^{m*}\sin\theta d\theta d\phi. \tag{4.72}$$

Since the term $[\boldsymbol{\nabla}\times(\mathbf{v}\times\mathbf{B})]\cdot\mathbf{e}_r$ is non-linear, the horizontal component of $\mathbf{v}\times\mathbf{B}$ is calculated in the physical space

$$\mathscr{F}_\theta \equiv (\mathbf{v}\times\mathbf{B})\cdot\mathbf{e}_\theta = v_\phi B_r - v_r B_\phi, \tag{4.73}$$

$$\mathscr{F}_\phi \equiv (\mathbf{v}\times\mathbf{B})\cdot\mathbf{e}_\phi = v_r B_\theta - v_\theta B_r, \tag{4.74}$$

so

$$[\boldsymbol{\nabla}\times(\mathbf{v}\times\mathbf{B})]\cdot\mathbf{e}_r = \frac{1}{r\sin\theta}\left(\partial_\theta(\sin\theta\mathscr{F}_\theta - \partial_\phi\mathscr{F}_\phi)\right). \tag{4.75}$$

Both components are then expanded in spherical harmonics $\mathscr{F}_\theta(\theta,\phi), \mathscr{F}_\phi(\theta,\phi) \longrightarrow \mathscr{F}_{\theta,lm}, \mathscr{F}_{\phi,lm}$. Their θ- and ϕ-derivatives are calculated using recurrence relations:

$$\begin{aligned}\mathscr{N}_{lm} &\equiv \int_0^\pi\int_0^{2\pi}\left[(\boldsymbol{\nabla}\times(\mathbf{v}\times\mathbf{B}))\cdot\mathbf{e}_r\right] Y_l^{m*}\sin\theta d\theta d\phi \\ &= (l+1)c_{lm}\mathscr{F}_{\phi,l-1,m} - l c_{l+1,m}\mathscr{F}_{\phi,l+1,m} - i m\mathscr{F}_{\theta,l,m}.\end{aligned} \tag{4.76}$$

The final expression for the evolution of the magnetic poloidal potential

$$\frac{l(l+1)}{r^2}\left[\left(\partial_t + \frac{1}{Pm}\frac{l(l+1)}{r^2}\right)\mathscr{C}_n - \frac{1}{Pm}\mathscr{C}_n''\right] b_{lmn} = \mathscr{N}_{lm} \tag{4.77}$$

The procedure to transform the equation in the spectral space is the same for the other potentials, the entropy and the pressure[1]. The non-linear terms, such as $\mathbf{v}\times\mathbf{B}$, and the Coriolis force are first treated on the physical grid before being projected in the spectral space.

[1] All the spectral equations are available on https://magic-sph.github.io/numerics.html#spectral-equations.

4.3.6 . Boundary conditions

The approximated MHD equations are solved on a finite grid, so we must impose boundary conditions solve the system. As the equations are formulated in the spectral space, the usual boundary equations can be replaced by expressions in the Chebyshev representation evaluated at the grid points r_i and r_o. In the following, we apply the summation convention for the radial modes n, for the sake of simplicity and clarity.

To mimic the accretion of fallback onto the PNS surface, we impose *rigid (or no-slip)* boundary conditions on the outer sphere, where the horizontal velocities are zero except for the rotation:

$$v_\theta(r_o) = 0\,, \tag{4.78}$$
$$v_\phi(r_o) = r_o\Omega_o\,, \tag{4.79}$$

with r_o and Ω_o the radius and the angular frequency of the outer sphere. The PNS surface is also impenetrable ($v_r(r_o) = 0$). This translates into the Chebyshev representation

$$\mathscr{C}_n W_{lmn} = 0\,, \tag{4.80}$$
$$\mathscr{C}'_n W_{lmn} = 0\,, \tag{4.81}$$
$$\mathscr{C}_n Z_{lmn} = 0\,. \tag{4.82}$$

We apply the same mechanical conditions on the inner sphere. The are no astrophysical reasons for the choice of the condition on the inner sphere because it does not exist in a real PNS. However, imposing an angular frequency on the inner sphere enables a forcing of differential rotation. The configuration in which angular frequencies are imposed on both spherical spheres is called *spherical Couette*.

The magnetic field is formed in the PNS interior but penetrates the surface. Therefore, we impose an external magnetic field that is the extension of the internal field. This external field is described by the potential Φ such that $\mathbf{B} = -\boldsymbol{\nabla}\Phi$ and $\Delta\Phi = 0$ at the surface ($r = r_o$). This condition corresponds to the magnetic field in the vacuum, hence the name *vaccum (or insulating)* boundary condition. We also apply this condition to the inner sphere ($r = r_i$). It can be written in terms of Chebyshev polynomials

$$\mathscr{C}_n a_{j,lmn} = 0\,, \tag{4.83}$$
$$\left[\mathscr{C}'_n(r_i) - \frac{l+1}{r}\mathscr{C}_n(r_i)\right] b_{lmn} = 0\,, \tag{4.84}$$
$$\left[\mathscr{C}'_n(r_o) + \frac{l}{r}\mathscr{C}_n(r_o)\right] b_{lmn} = 0\,. \tag{4.85}$$

For the thermal boundary conditions, we fix constant temperatures/buoyancy variables on both boundaries.

4.4 . Numerical methods

4.4.1 . Time integration

To calculate the evolution of the potentials, we must discretise time $\{t_i\}_{i\in[0,n]}$, and use a numerical scheme to evaluate the potentials at the next time step. A lot of *time-stepping*

schemes have been developed, starting from the most simple scheme, the so-called Euler method. These methods are sorted between *explicit* and *implicit* methods. While the former evaluates the state of the system at a later time $t_{i+1} = t_i + \Delta t$ using the state at the current time t_i, the latter must solve an equation involving both the current and later state. Let Ψ the state of the system, an explicit scheme evaluates

$$\Psi(t_{i+1}) = f(\Psi(t_i)) \tag{4.86}$$

and an implicit scheme solves the equation

$$g(\Psi(t_{i+1}), \Psi(t_i)) = 0 \tag{4.87}$$

to find $\Psi(t_{i+1})$, where f and g are arbitrary functions. Explicit methods are usually easier to implement but are not stable for solving every equation unless the time-step Δt is sufficiently small or the diffusivities are large enough. To solve them, we must use one of the existing implicit schemes, which are theoretically stable. Still, since implicit schemes must solve an equation to find the later state of the system, the equation can be computationally costly to solve. In practice, these methods involve the inversion of a matrix which can be very large. This issue is present in the case of spectral MHD equations because the non-linear terms couple every spherical harmonic mode. Moreover, the Coriolis force couples W_{lmn} with Z_{lmn}, and also couples (l,m,n)–modes with $(l-1,m,n)$– and $(l+1,m,n)$–modes, which makes it costly to solve with an implicit scheme. This fosters the development of *mixed implicit/explicit (IMEX) schemes*.

In the general case, differential equations can be written

$$y_0 = y(t_0)\,, \tag{4.88}$$
$$\partial_t y = \mathscr{I}(y,t) + \mathscr{X}(y,t)\,, \tag{4.89}$$

where $\mathscr{I}$ and $\mathscr{X}$ are the terms treated implicitely and explicitely, respectively. The IMEX methods implemented in `MagIC` are classified into two families: *IMEX multistep* and *IMEX Runge-Kutta multistage* schemes. The former calculates $y_{i+1} \equiv y(t_{i+1})$ using a combination of k previous steps. This translates into

$$y_{i+1} - \sum_{j=1}^{k} a_j y_{(i+1)-j} = \Delta t \left[w_0^{\mathscr{I}} \mathscr{I} \sum_{j=1}^{k} \left(w_j^{\mathscr{I}} \mathscr{I}_{(i+1)-j} + w_j^{\mathscr{X}} \mathscr{X}_{(i+1)-j} \right) \right], \tag{4.90}$$

where we note $\mathscr{I}_i \equiv \mathscr{I}(y_i, t_i)$ and $\mathscr{X}_i \equiv \mathscr{X}(y_i, t_i)$. $\mathbf{a} \in \mathbb{R}^j$, $\mathbf{w}^{\mathscr{I}} \in \mathbb{R}^j$, and $\mathbf{w}^{\mathscr{X}} \in \mathbb{R}^j$ contain weighting factors, which are specific to the chosen IMEX multistep scheme. For the widely used second-order Crank-Nicholson (implicit)/Adam-Bashfort (explicit) (CNAB2) (Ascher et al., 1995), $\mathbf{a} = (1,0)$, $\mathbf{w}^{\mathscr{I}} = (1/2, 1/2)$, and $\mathbf{w}^{\mathscr{X}} = (3/2, -1/2)$. In `MagIC`, 7 IMEX multistep schemes are currently implemented (see Table. 4.4), among which third– and fourth–order schemes.

Before presenting the IMEX multistage schemes, we recall the principle of explicit and implicit Runge–Kutta (RK) methods to introduce the mnemonic tool called the *Butcher tableau*. This family of methods can be generalised by the equation of the form

$$y_{i+1} - y_i = \Delta t \sum_{j=1}^{s} b_j k_j\,, \tag{4.91}$$

Acronym	Order	Reference
CNAB2	2	Ascher et al. (1995)
MODCNAB	2	Ascher et al. (1995)
CNLF	2	Johansson & Kreiss (1963)
SBDF2	2	Ascher et al. (1995)
SBDF3	3	Ascher et al. (1995)
TVB33	3	Cockburn et al. (1989)
SBDF4	4	Ascher et al. (1995)

Table 4.4 — IMEX multistep schemes implemented in MagIC with their associated order.

with

$$k_j = f\left(t_i + c_j \Delta t,\, y_i + \Delta t \sum_{l=1}^{s} a_{jl} k_l\right), \qquad i \in [1, s] \tag{4.92}$$

where s is the number of stages, $\mathbf{A} \equiv [a_{jl}] \in \mathbb{R}^{s\times s}$ is the *Runge-Kutta matrix*, $f = \partial_t y$ is an arbitrary function, $\mathbf{b} \in \mathbb{R}^s$ and $\mathbf{c} \in \mathbb{R}^j$ contain the *weights* and *nodes* of the RK schemes, respectively. These different quantities are displayed in a Butcher tableau

$$\begin{array}{c|cccc} c_1 & a_{11} & a_{12} & \dots & a_{1s} \\ c_2 & a_{21} & a_{22} & \dots & a_{2s} \\ \vdots & \vdots & \vdots & \ddots & \vdots \\ c_s & a_{s1} & a_{s2} & \dots & a_{ss} \\ \hline & b_1 & b_2 & \dots & b_s \end{array}, \tag{4.93}$$

which can be reduced to

$$\begin{array}{c|c} \mathbf{c} & \mathbf{A} \\ \hline & \mathbf{b} \end{array}. \tag{4.94}$$

For instance, the Butcher tableau for the forward and backward Euler methods, the so-called RK4 read, respectively

$$\begin{array}{c|c} 0 & \\ \hline & 1, \end{array}, \qquad \begin{array}{c|c} 1 & 1 \\ \hline & 1 \end{array}, \tag{4.95}$$

and

$$\begin{array}{c|cccc} 0 & & & & \\ 1/3 & 1/3 & & & \\ 2/3 & -1/3 & 1 & & \\ 1 & 0 & 0 & 1 & \\ \hline & 1/6 & 1/3 & 1/3 & 1/6 \end{array}. \tag{4.96}$$

As explicit methods evaluate the next step using only the previous one, the different stages k_i can only involve the previous stages $\{k_j\}_{j<i}$ in the explicit RK schemes. Therefore, the matrix $\mathbf{A}$ must be lower triangular with a zero diagonal. Note also that an explicit RK scheme is consistent if and only if

$$\sum_{i=1}^{s} b_i = 1. \tag{4.97}$$

Another commonly applied condition reads

$$\sum_{l=1}^{j-1} a_{jl} = c_l \,, \tag{4.98}$$

with $j \in [2, s]$, even though it says nothing about the scheme consistency.

Both implicit and explicit RK schemes are used in IMEX multistage schemes, for the $\mathscr{I}$ and $\mathscr{X}$ terms, respectively. 18 of these schemes are implemented in `MagIC` and are listed in Table. 4.5 The scheme we used for our numerical simulations is the third-order BPR353 (Boscarino et al., 2013). Its associated Butcher tableaux for the implicit and explicit RK schemes read

Acronym	s	Order	Reference
ARS222	3	2	Ascher et al. (1997)
ARS232	3	2	Ascher et al. (1997)
ARS233	3	2	Ascher et al. (1997)
ARS343	4	3	Ascher et al. (1997)
ARS433	5	3	Ascher et al. (1997)
LZ232	3	2	Liu & Zou (2006)
LZ453	5	3	Liu & Zou (2006)
KC343	4	3	Kennedy & Carpenter (2003)
KC564	6	4	Kennedy & Carpenter (2003)
KC674	7	4	Kennedy & Carpenter (2003)
KC785	8	5	Kennedy & Carpenter (2003)
PC2	3	3	Jameson et al. (1981)
CB3	4	3	Cavaglieri & Bewley (2015)
CK232	3	3	Carpenter et al. (2005)
MARS343	4	3	Boscarino (2007)
BPR353	**5**	**3**	Boscarino et al. (2013)
DBM453	5	3	Vogl et al. (2019)
BHR553	6	3	Boscarino (2009)

Table 4.5 — IMEX multistage schemes implemented in `MagIC` with their associated number of stages s.

$$\begin{array}{c|ccccc} 0 & 0 & & & & \\ 1 & 1/2 & 1/2 & & & \\ 2/3 & 5/18 & -1/9 & 1/2 & & \\ 1 & 1/2 & 0 & 0 & 1/2 & \\ 1 & 1/4 & 0 & 3/4 & 1/2 & 1/2 \\ \hline & 1/4 & 0 & 3/4 & -1/2 & 1/2 \end{array} \,, \qquad \begin{array}{c|cccc} 0 & & & & \\ 1 & 1/2 & & & \\ 2/3 & 4/9 & 2/9 & & \\ 1 & 1/4 & 0 & 3/4 & \\ 1 & 1/4 & 0 & 3/4 & 0 \\ \hline & 1/4 & 0 & 3/4 & 0 \quad 0 \end{array} \,, \tag{4.99}$$

which we note

$$\begin{array}{c|c} \mathbf{c}^{\mathscr{I}} & \mathbf{A}^{\mathscr{I}} \\ \hline & \mathbf{b}^{\mathscr{I}} \end{array} \,, \qquad \begin{array}{c|c} \mathbf{c}^{\mathscr{X}} & \mathbf{A}^{\mathscr{X}} \\ \hline & \mathbf{b}^{\mathscr{X}} \end{array} \,, \tag{4.100}$$

respectively. Note that the scheme is of *type CK* (which stands for Carpenter and Kennedy (Kennedy & Carpenter, 2003)) because $a_{11} = 0$ and the submatrix $\bar{\boldsymbol{A}} \equiv [a_{jl}]_{j,l\in[2,s]} \in \mathbb{R}^{(s-1)\times(s-1)}$ is invertible for both $\mathbf{A}^{\mathscr{I}}$ and $\mathbf{A}^{\mathscr{X}}$. Type CK schemes permit the construction of higher order IMEX Runge-Kutta schemes. If we come back to the initial problem (Eqs. (4.88)–(4.89)), for each stage $j \in [1, s]$ the scheme must solve the equation

$$(I - \Delta t a^{\mathscr{I}}_{jj} \mathscr{I}) y_j = y_i + \Delta t \sum_{p=1}^{j-1} \left[a^{\mathscr{I}}_{jp} \mathscr{I}(t_i + c_p \Delta t, y_p) + a^{\mathscr{X}}_{jp} \mathscr{X}(t_i + c_p \Delta t, y_p) \right], \tag{4.101}$$

with I the identity matrix. Once y_j is evaluated, the final equation to advance from t_i to t_{i+1} is

$$y_{i+1} = y_i + \Delta t \sum_{j=1}^{s} \left[b^{\mathscr{I}}_j \mathscr{I}(t_i + c_j \Delta t, y_j) + b^{\mathscr{X}}_j \mathscr{X}(t_i + c_j \Delta t, y_j) \right]. \tag{4.102}$$

As an example, we can apply the BPR353 scheme equations to the evolution of the poloidal magnetic potential b_{lmn} (Eq. (4.77)). Since the following expressions are quite complex, we recall the signification of the indexes: l and m are the spherical harmonic degree and order, n is the degree of the Chebyshev polynomial, and k is the index of a grid point in the radial direction. The evolution equation is

$$\begin{aligned} \mathscr{T}_{kn} [b_{lmn}(t + \Delta t) - b_{lmn}(t)] = \Delta t \sum_{j=1}^{5} a^{\mathscr{I}}_{5j} \mathscr{G}_{kn} b_{lmn}(t + c_j \Delta t) \\ + \Delta t \sum_{j=1}^{5} a^{\mathscr{X}}_{5j} \mathscr{N}_{klm}(t + c_j \Delta t), \end{aligned} \tag{4.103}$$

with

$$\begin{aligned} (\mathscr{T}_{kn} - a^{\mathscr{I}}_{jj} \mathscr{G}_{kn}) b_{lmn}(t + c_j \Delta t) = \mathscr{T}_{kn} b_{lmn}(t) + \Delta t \sum_{p=1}^{j-1} a^{\mathscr{I}}_{jp} \mathscr{G}_{pn} b_{lmn}(t + c_p \Delta t) \\ + \Delta t \sum_{p=1}^{j-1} a^{\mathscr{X}}_{jp} \mathscr{N}_{klm}(t + c_p \Delta t), \end{aligned} \tag{4.104}$$

and

$$\mathscr{T}_{kn} \equiv \frac{l(l+1)}{r_k^2} \frac{\mathscr{C}_n(r_k)}{\Delta t}, \tag{4.105}$$

is the matrix that converts b_{lmn} to $B_r(r_k, l, m)$,

$$\mathscr{G}_{kn} \equiv \frac{l(l+1)}{r_k^2} \frac{1}{Pm} \left(\mathscr{C}''_n(r_k) - \frac{l(l+1)}{r_k^2} \mathscr{C}_n(r_k) \right) \tag{4.106}$$

is the matrix formulating the magnetic diffusion term of the induction equation, and $\mathscr{N}_{klm}(t) \equiv \mathscr{N}_{lm}(t, r_k)$ is the non-linear term of the induction equation.

Finally, the choice of the time-step Δt is driven by the *Courant-Friedrichs-Lewy (CFL) condition* (Courant et al., 1928), which indicates that Δt must be smaller than the time for the Alfvén wave or the fluid to cover the distance between two grid points:

$$\Delta t = C \times \min(\Delta t_r, \Delta t_{\mathrm{H}}, \Delta t_{\mathrm{A}}), \tag{4.107}$$

with

$$\Delta t_r \leq \min\left[\frac{\delta r}{|v_r|}\right], \tag{4.108}$$

$$\Delta t_{\rm H} \leq \min\left[\sqrt{\frac{r^2}{l_{\rm max}(l_{\rm max}+1)(v_\theta^2+v_\phi^2)}}\right], \tag{4.109}$$

$$\Delta t_{\rm A} \leq \min\left[\frac{\delta x_{\rm A}}{|v_{\rm A}|}\right], \tag{4.110}$$

where $C \leq 1$ is a constant to adjust the criterion, δr, and $\delta x_{\rm A}$ are the typical radial length scale for advection and the magnetic field typical length scale, respectively. The explicit treatment of the Coriolis force imposes another condition

$$\Delta t \leq \frac{0.1}{\Omega_o}, \tag{4.111}$$

which can be restrictive in the regime of fast rotations. Note that if the sound waves were not filtered out, there would be another criterion associated with the time for a sound wave to cover the distance between two grid points. Since the sound speed is much larger than the fluid and Alfvén velocities, the CFL condition would strongly reduce the timestep.

4.4.2 . Structure of the code and parallelisation

All the ingredients have now been introduced to numerically model the evolution of a Boussinesq or anelastic MHD fluid in a spherical configuration. These ingredients constitute different steps of the `MagIC` code, whose structure is illustrated in Fig. 4.3. Before the computation of the simulation, there is an initialisation phase, which consists in preparing the initial necessary elements of the run. It starts with the reading of the input files, which contains e.g. the parameter values, the initial configuration of the fluid, the output parameters, etc. Then, `MagIC` calculates several constants such as the different volumes and the mass, and initialises the radial and horizontal functions and operators.

The "work" phase, is divided into two parts. During the first part, called *radialLoop* in `MagIC`, the spectral quantities are transformed to the physical grid (θ,ϕ), so the non-linear terms can be calculated. This stage is opportune to create the output in the physical grid, such as movies and graphic files containing the fields at each grid point. Additional quantities are calculated: the courant condition, helicity, horizontal velocities, viscous heating, etc. Finally, the quantities are transformed back to the spectral space (l,m). The second part called *LMLoop* in `MagIC`, consists in updating the potentials and other thermodynamical quantities using the time-stepping scheme. During this stage, spectral outputs are created such as the time-series, the spectra and the checkpoint file. The latter is very useful to start a run using the state of the fluid calculated in another simulation. Finally, the necessary arrays and radial derivatives are calculated for the potential next step.

Such simulations can be very costly in time, especially for simulations of fluids with complex dynamics. This kind of numerical code is therefore heavily parallelised, i.e. the calculations are distributed among several processors. `MagIC` runs on central processing units (CPUs) only because the code adaption for graphics processing units (GPUs) is not complete yet. Our simulations use in general 640 CPUs simultaneously. Although this number is small compared to more massive simulations, our simulations require the use of a (small) fraction

of large supercomputers which are constituted of $100-1000$ nodes containing $10-100$ CPUs each, and so 10^4-10^6 processors in total.

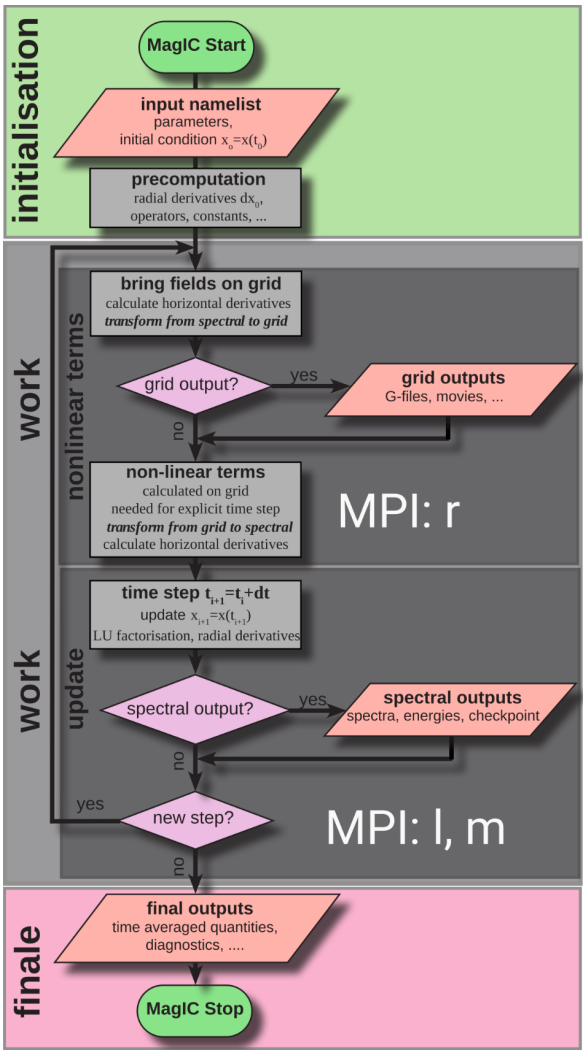

Figure 4.3 — Strucutre of the code MagIC (figure originating from a class of T. Gastine).

In practice, we must use the appropriate interfaces to create communication between the processors and distribute the different tasks. The most common interfaces are *Open Multi-processing (OpenMP)* and *Message Passing Interface (MPI)*. The main difference between them is that the former uses the concept of shared memory, unlike the latter. Sharing memory can be very useful, but this implies additional communications between the processors to avoid conflicts and so more numerical cost. Therefore, combining both OpenMP and MPI is important to build an optimised code. In practice, OpenMP is often used for parallelism within the node and MPI to parallelism between nodes. For an optimal use of MagIC, MPI is also used for the communication within the node. In the structure of MagIC the combination of OpenMP and MPI is implemented as follows:

OpenMP In the radialLoop part, OpenMP can be used for the calculation of non-linear terms and the spherical harmonics transform. It is also used over the (l,m)–modes.

MPI In the radialLoop (LMLoop) part, the radial levels (the spherical (l,m)–modes) can be treated independently, which besides explains the name of each part. r and (l,m) are therefore distributed over MPI ranks in the appropriate parts.

4.4.3 . Resolution check

While a simulation is running, it is always safer to check whether it is resolved. If the simulation has a far too low resolution, the run crashes quickly. However, it may sometimes continue if the time-stepping scheme is stable enough. Therefore, we must look at the outputs to check the resolution. The first diagnostic is to look at the graphic fields directly, in which the obvious signature of under-resolution is the formation of small-scale structures, called *aliases*. These structures can be seen in the left meridional slice in Fig. 4.4. The second outputs to check are the energy spectra. From them, we can infer whether the energy is well

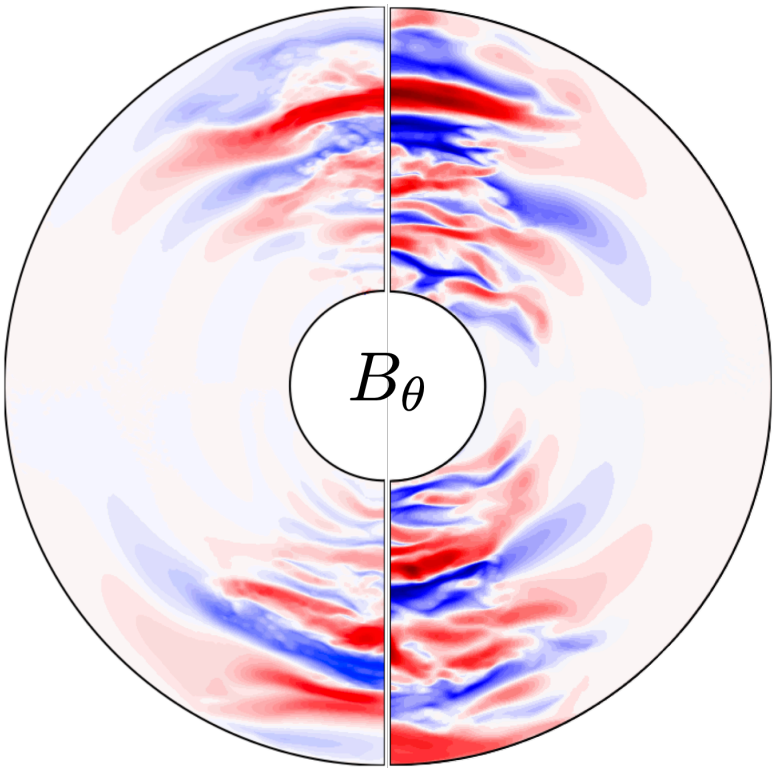

Figure 4.4 — Two meridional slices of the latitudinal magnetic field B_θ for an unresolved (left) and resolved (right) Tayler instability in its saturated state.

dissipated at small scales. The simulation is said to be unresolved when there are less than two orders of magnitude in energy between the injection and the dissipation scale. We see in the top spectra of Fig. 4.5 that the core-mantle boundaries (CMB) is clearly under-resolved. The resolution is less clear for the poloidal and toroidal fields. However, it does not mean we must ignore the simulation because the volume-averaged quantities may actually be right. This suggests that running costly simulations can be avoided, depending on which quantities we wish to look at. Finally, it is also possible to check the conservation of power budget and the heat flux.

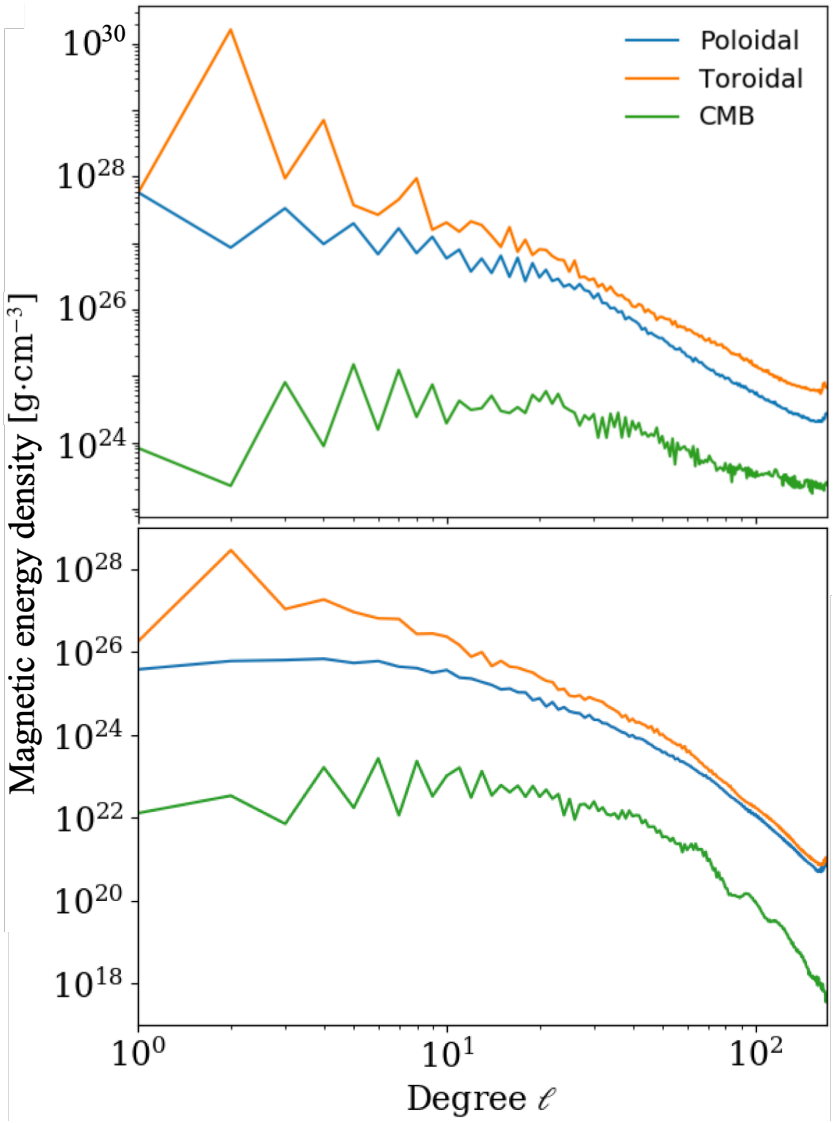

Figure 4.5 — Two spectra of the magnetic energy for an unresolved (top) and resolved (bottom) Tayler instability in its saturated state.

II

Results

5

A new scenario: Tayler-Spruit dynamo in a proto-neutron star spun up by fallback

Contents

This part of the manuscript focuses on the results we obtained during the three years of work on the fallback scenario we briefly introduced in Sect. 2.3. We recall that this scenario is an alternative, which has the advantage of explaining the formation of magnetar magnetic fields from slowly rotating and weakly magnetised progenitor iron cores. As schematized in Fig. 5.1, the rotation of the proto-neutron star (PNS) is determined by the asymmetric accretion of matter gravitationally bound to the PNS that is initially ejected during the explosion but that eventually falls back onto the PNS. The induced differential rotation triggers the development of the Tayler-Spruit dynamo to amplify the magnetic fields until saturation at magnetar-like strengths.

In this chapter, we study our scenario using a semi-analytical approach in the MHD approximation (Chap. 3). We first built a one-zone model consisting of 'average' time evolution equations that capture the main stages sketched in Fig. 5.1. The following text is taken from

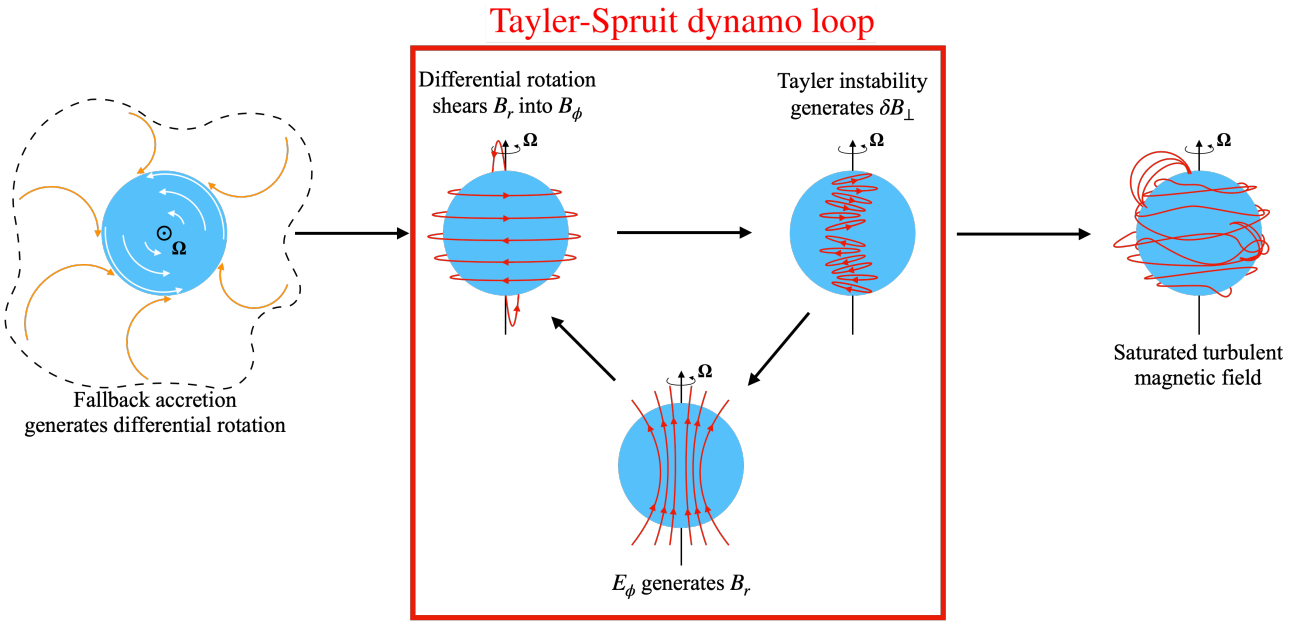

Figure 5.1 — Schematic representation of the different stages of our magnetar formation scenario. The dashed line encloses the region of the fallback (orange arrows). Red and white lines represent the magnetic field lines and fluid motions, respectively. $\mathbf{\Omega}$ and E_ϕ stand for the angular rotation frequency and the azimuthal component of the electromotive force, respectively. B_ϕ and B_r are the axisymmetric azimuthal and radial magnetic field, and $\delta B_\perp$ is the non-axisymmetric perpendicular magnetic field.

the article published in *Astronomy & Astrophysics* (Barrère et al., 2022) and was written in collaboration with Jérôme Guilet, Alexis Reboul-Salze, Raphaël Raynaud, and Hans-Thomas Janka. This study also led to the preparation of an article about the application of this model in binary neutron star mergers. This article was written by Alexis-Reboul-Salze in collaboration with me, Kenta Kiuchi, Raphaël Raynaud, Jérôme Guilet, Sho Fujiyabashi, and Masaru Shibata and will be submitted to *Astronomy & Astrophysics*.

5.1 . Mathematical modelling of the scenario

We start by describing the impact of the SN fallback on the PNS rotation (the differential rotation) and the magnetic field (the shearing of the radial field and the exponential growth of the Tayler instability). Finally, we present the mathematical formalism for the non-linear stages, that is, the saturation mechanism of the dynamo as modelled by Spruit (2002) and Fuller et al. (2019), which we complete by a description of the generation of the radial magnetic field through non-linear induction. For the computation of the time evolution, we only implement the description based on the work of Fuller et al. (2019); but in Sect. 5.2 we compare both models regarding the predictions of the saturated magnetic field.

5.1.1 . Fallback accretion

Our scenario starts a few seconds after the core bounce when a fraction of the fallback matter gets accreted onto the PNS surface. This matter is initially ejected during the explosion but stays gravitationally bound to the PNS, and so begins to be asymmetrically accreted

(Chan et al., 2020). This fallback matter is thought to have a large angular momentum, which can even reach the magnitude of the Keplerian angular momentum (Janka et al., 2022). Therefore, the spin of the PNS is strongly affected and the surface rotation can be accelerated up to millisecond periods. In our scenario, the core of the progenitor is assumed to be slowly rotating. Thus, the PNS surface spins faster than the PNS interior, which creates differential rotation.

To model the accretion onto the PNS surface, we use the asymptotic scaling for the mass accretion rate $\dot{M}_{\rm acc} \propto t^{-5/3}$ from Chevalier (1989). As the accretion mass rate must be finite at the beginning of this accretion regime, we define a start time t_0 such that

$$\dot{M}_{\rm acc} = \frac{A}{(t+t_0)^{5/3}}\,, \tag{5.1}$$

where A is a constant. Then, the accreted mass during this regime is

$$M_{\rm acc} = \int_0^\infty \frac{A}{(t+t_0)^{5/3}}\,dt\,. \tag{5.2}$$

As $M_{\rm acc}$ is constant, we have $A = \frac{2}{3}t_0^{2/3}M_{\rm acc}$ and so the accretion mass rate is

$$\dot{M}_{\rm acc} = \frac{2}{3}M_{\rm acc}\frac{t_0^{2/3}}{(t+t_0)^{5/3}}\,. \tag{5.3}$$

From the fallback matter, only a fraction with angular momentum as large as the Keplerian limit at most will be accreted by the PNS, as discussed by Janka et al. (2022). Therefore, the relation between the average angular rotation frequency of the PNS and the mass accretion rate is

$$\dot{\Omega} = \frac{j_{\rm kep}}{I}\dot{M}_{\rm acc}\,, \tag{5.4}$$

where I stands for the PNS moment of inertia and $j_{\rm kep} \equiv \sqrt{GM_{\rm PNS}r}$ is the specific Keplerian angular momentum at the PNS surface. As the PNS mass changes little and the contraction of the PNS is almost over at the times considered for the fallback accretion, we assume I to be constant. As supposed in Fuller et al. (2019), the angular momentum is transported faster latitudinally than radially due to stratification, meaning that the differential rotation is shellular, that is Ω is constant on spherical shells.

As the accretion process spins up only the outer part of the PNS but not its inner core, the shear rate $q \equiv r\partial_r \ln\Omega$ is also expected to evolve. To describe this effect, we use the approximate expression

$$r\partial_r\Omega \sim \Omega - \Omega(r=0), \tag{5.5}$$

where Ω and $\Omega(r=0)$ are the average and central angular rotation frequencies, respectively. Assuming that the rotation frequency at the centre of the PNS is unchanged by the accretion process (it will change only due to angular momentum transport processes described in Sect. 5.3.1), we infer the time derivative of the shear rate as

$$\dot{q} \sim \frac{\dot{\Omega}}{\Omega}(1-q). \tag{5.6}$$

5.1.2 . Shearing and Tayler instability growth

The differential rotation generated by the fallback will shear the radial component of the large-scale radial magnetic field B_r into the azimuthal field B_ϕ as follows

$$\partial_t B_\phi = q\Omega B_r \,. \tag{5.7}$$

Therefore, we can define a growth rate[1] for B_ϕ:

$$\sigma_{\rm shear} \equiv q\Omega \frac{B_r}{B_\phi} \,. \tag{5.8}$$

As B_ϕ grows, it becomes Tayler unstable. To depict the linear growth of the instability, we make the following assumptions. First, the stratified medium of the PNS interior is characterised by the Brunt-Väisälä frequency (Hüdepohl, 2014):

$$N \equiv \sqrt{-\frac{g}{\rho}\left(\left.\frac{\partial\rho}{\partial S}\right|_{P,Y_e}\frac{dS}{dr} + \left.\frac{\partial\rho}{\partial Y_e}\right|_{P,S}\frac{dY_e}{dr}\right)} \sim 4\times10^3\,{\rm s}^{-1}\,, \tag{5.9}$$

where g, ρ, Y_e, and S are the gravitational acceleration, the PNS mean density, the electron fraction, and the entropy, respectively. In the remainder of this paper, we use the fiducial value $N = 4\times10^3\,{\rm s}^{-1}$ based on the results of the 1D core-collapse supernova (CCSN) simulations from Hüdepohl (2014, Chap. 5). The Brunt-Väisälä frequency is almost uniform in most of the PNS except near the surface where it peaks at $\sim 10^4\,{\rm s}^{-1}$. Hüdepohl (2014) made a comparison between two different equations of state (EOS): Shen (Shen et al., 1998a,b, 2011) and LS220 (Lattimer & Swesty, 1991), and found that the choice of the EOS mainly affects the localisation and duration of the convection but not the value of the Brunt-Väisälä frequency in the stably stratified region. Second, the main background azimuthal field is B_ϕ, which is associated with the Alfvén frequency:

$$\omega_{\rm A} \equiv \frac{B_\phi}{\sqrt{4\pi\rho r^2}} \simeq 11.6\left(\frac{B_\phi}{10^{15}\,{\rm G}}\right){\rm s}^{-1}\,, \tag{5.10}$$

for $r = 12\,{\rm km}$ and $\rho = 4.1\times10^{14}\,{\rm g\,cm}^{-3}$. Finally, the frequencies characterising the PNS are ordered such that

$$N \gg \Omega \gg \omega_{\rm A}\,. \tag{5.11}$$

The development of the Tayler instability is triggered after reaching the critical strength (Spruit, 1999, 2002, Zahn et al., 2007)

$$\begin{aligned} B_\phi > B_{\phi,{\rm c}} &\sim \Omega\left(\frac{N}{\Omega}\right)^{1/2}\left(\frac{\eta}{r^2\Omega}\right)^{1/4}\sqrt{4\pi\rho r^2} \\ &\simeq 2.5\times10^{12}\left(\frac{\Omega}{200\pi\,{\rm rad\,s}^{-1}}\right)^{1/4}{\rm G}\,, \end{aligned} \tag{5.12}$$

where $\eta \sim 10^{-4}\,{\rm cm}^2\,{\rm s}^{-1}$ (Thompson & Duncan, 1993) is the magnetic diffusivity. The fastest-growing perturbations are the $m = 1$ modes with an associated rate of (Ma & Fuller, 2019)

$$\sigma_{\rm TI} \sim \frac{\omega_{\rm A}^2}{\Omega} \simeq 0.21\left(\frac{B_\phi}{10^{15}\,{\rm G}}\right)^2\left(\frac{\Omega}{200\pi\,{\rm rad\,s}^{-1}}\right)^{-1}{\rm s}^{-1}\,. \tag{5.13}$$

[1] We note that this growth rate and the others defined below are rather instantaneous growth rates because they depend on the magnetic field.

As the PNS interior is strongly stratified, we can determine a maximum radial length scale for the instability

$$l_r \sim \frac{\omega_{\rm A}}{N} l_\perp , \tag{5.14}$$

where the horizontal length scale is approximated by $l_\perp \sim r$.

5.1.3 . Spruit's picture of the dynamo

Spruit (2002) proposes that the energy in the azimuthal large-scale field B_ϕ cascades to small scale, that is the form of the non-linear magnetic energy dissipation is

$$\dot{E}_{\rm mag} \sim \gamma_{\rm turb} |B_\phi|^2 , \tag{5.15}$$

where $\gamma_{\rm turb}$ is the turbulent damping rate. To determine this rate, Spruit (2002) argues that the saturation of the instability occurs when the turbulent velocity field generates a sufficiently large effective turbulent diffusivity to balance the growth rate of the instability, that is

$$\gamma_{\rm turb} \sim \frac{\eta_{\rm e}}{l_r^2} \sim \sigma_{\rm TI} , \tag{5.16}$$

where $\eta_{\rm e}$ is an effective turbulent diffusivity.

The solenoidal character of the perturbed magnetic field implies $B_r / l_r \sim B_\phi / l_\perp$, which leads to

$$B_r \sim \frac{\omega_{\rm A}}{N} B_\phi , \tag{5.17}$$

using the relation between length scales of the instability given by Eq. (5.14). As the azimuthal magnetic field B_ϕ is generated via the shear of the radial magnetic field B_r, the dynamo is expected to saturate when the shear (Eq. 5.8) balances the turbulent damping (Eq. 5.16). Thus, the amplitudes of the magnetic field components saturate at

$$B_{\phi,{\rm S}}^{\rm sat} \sim \sqrt{4\pi\rho r^2}\, q \frac{\Omega^2}{N} , \tag{5.18}$$

$$B_{r,{\rm S}}^{\rm sat} \sim \sqrt{4\pi\rho r^2}\, q^2 \frac{\Omega^4}{N^3} . \tag{5.19}$$

This description of the dynamo mechanism has been criticised for two reasons: First of all, if the large-scale component of B_ϕ remains constant on larger length scales than l_r, the displacements produced by the instability are not expected to mix the large-scale field lines to damp B_ϕ through reconnection. Therefore, the damping rate estimated in Eq. (5.16) is overestimated for the large-scale components of the azimuthal field B_ϕ (see Fuller et al., 2019). Secondly, as $m = 1$ modes are dominant, the radial magnetic field B_r produced by the instability is non-axisymmetric, and therefore its shear generates a mostly non-axisymmetric azimuthal field B_ϕ. Hence, the axisymmetric component of the fields B_r and B_ϕ may not be related by Eq. (5.17) (see Zahn et al., 2007).

5.1.4 . A revised model of the dynamo

This section presents a description of the dynamo that completes the model proposed by Fuller et al. (2019) in the sense that we consider the time evolution of the magnetic field. A clear distinction is now made between the 'axisymmetric' components B_ϕ, B_r, and the 'non-axisymmetric' perturbed components $\delta B_\perp$, δB_r, which become the ones connected by the solenoidal condition

$$\delta B_r \sim \frac{\omega_{\rm A}}{N} \delta B_\perp . \tag{5.20}$$

To overcome the previously raised difficulties, Fuller et al. (2019) argue that the energy in the perturbed field $\delta\mathbf{B}$ dissipates to small scales and find that the damping rate is

$$\gamma_{\rm cas} \sim \frac{\delta v_{\rm A}}{r}, \tag{5.21}$$

where $\delta v_{\rm A} \equiv \delta B_\perp / \sqrt{4\pi\rho}$ is the perturbed Alfvén velocity. Thus, equating the instability growth rate (Eq. 5.13) and the damping rate (Eq. 5.21) gives the saturation strength of the perturbed field $\delta B_\perp$ for a given strength of azimuthal field B_ϕ,

$$\delta B_\perp \sim \frac{\omega_{\rm A}}{\Omega} B_\phi \,. \tag{5.22}$$

When the instability is saturated, the non-linear magnetic energy dissipation is then

$$\dot{E}_{\rm mag} \sim \gamma_{\rm cas} |\delta\mathbf{B}|^2 \sim \frac{\delta v_{\rm A}}{r} |\delta B_\perp|^2 \,. \tag{5.23}$$

As the azimuthal field B_ϕ is the dominant magnetic component, $\dot{E}_{\rm mag} \sim B_\phi \partial_t B_\phi$. Hence, a damping rate can be defined for the axisymmetric components B_ϕ and B_r:

$$\gamma_{\rm diss} \equiv \frac{\dot{E}_{\rm mag}}{B_\phi^2} \,. \tag{5.24}$$

As the previous expression of the magnetic energy (Eq. 5.23) is only valid when the instability saturates, we use the expression

$$\dot{E}_{\rm mag} \sim \frac{\omega_{\rm A}^2}{\Omega} |\delta B_\perp|^2 , \tag{5.25}$$

which is valid in both the saturated and non-saturated states. Therefore, the damping rate defined in Eq. (5.24) becomes

$$\gamma_{\rm diss} \sim \frac{\omega_{\rm A}^2}{\Omega} \left(\frac{\delta B_\perp}{B_\phi} \right)^2 . \tag{5.26}$$

To close the dynamo loop, the Tayler instability must generate the axisymmetric radial magnetic field B_r (α-effect), which will be sheared again (Ω-effect). In the framework of the mean field theory, the induction equation reads

$$\partial_t \langle \mathbf{B}_0 \rangle = \boldsymbol{\nabla} \times (\langle \mathbf{v} \rangle \times \langle \mathbf{B}_0 \rangle + \mathbf{E}) - \eta \Delta \langle \mathbf{B}_0 \rangle \,, \tag{5.27}$$

in which we ignore the resistive term. Considering the average symbol $\langle \cdot \rangle$ as an azimuthal average, we note $\langle \mathbf{B}_0 \rangle = \mathbf{B}_0$ in order to remain consistent with our notation of the axisymmetric magnetic field. The electromotive force $\mathbf{E} \equiv \langle \boldsymbol{\delta v} \times \boldsymbol{\delta B}_0 \rangle$ is the important non-linear quantity responsible for the generation of the axisymmetric radial field B_r. In spherical coordinates, the radial component of Eq. (5.27) is

$$\partial_t B_r = \frac{1}{r \sin\theta} \left[\partial_\theta (\sin\theta \, E_\phi) - \partial_\phi E_\theta \right] . \tag{5.28}$$

As B_r is axisymmetric, E_θ can be ignored. By definition, the azimuthal component of electromotive force is

$$E_\phi = \delta v_r \delta B_\theta - \delta v_\theta \delta B_r \,. \tag{5.29}$$

Supposing an incompressible perturbed velocity field and using Eq. (5.20), we write

$$\frac{\delta v_r}{\delta v_\perp} \sim \frac{\delta B_r}{\delta B_\perp} \sim \frac{\omega_\mathrm{A}}{N}, \tag{5.30}$$

and so the azimuthal electromotive force reads

$$E_\phi \sim \delta v_\theta \delta B_r \sim \delta v_r \delta B_\theta \sim \delta v_r \delta B_\perp, \tag{5.31}$$

where we assume that the two terms on the right-hand side of Eq. (5.29) do not cancel. The production of the radial field B_r can be approximated by

$$\partial_t B_r \sim \frac{E_\phi}{r} \sim \frac{\delta v_r \delta B_\perp}{r}. \tag{5.32}$$

We must note that this expression differs from Eq. (29) in Fuller et al. (2019), which appears to contain a typo. As in Fuller et al. (2019) and Ma & Fuller (2019), we expect magnetostrophic balance $\delta v_\perp \sim \delta v_\mathrm{A} \omega_\mathrm{A}/\Omega$, which leads to

$$\delta v_r \sim \frac{\omega_\mathrm{A}^2}{N\Omega} \delta v_\mathrm{A}. \tag{5.33}$$

Thus,

$$\partial_t B_r \sim \frac{E_\phi}{r} \sim \frac{\omega_\mathrm{A}^2}{N\Omega} \frac{\delta B_\perp^2}{\sqrt{4\pi\rho r^2}}, \tag{5.34}$$

and we can define a growth rate for B_r

$$\sigma_\mathrm{NL} \equiv \frac{1}{\sqrt{4\pi\rho r^2}} \frac{\omega_\mathrm{A}^2}{N\Omega} \frac{\delta B_\perp^2}{B_r}. \tag{5.35}$$

The radial field B_r will saturate when its non-linear growth rate (Eq. 5.35) is balanced by the turbulent dissipation (Eq. 5.26). This way, we find the relation between the axisymmetric fields

$$B_r \sim \frac{\omega_\mathrm{A}}{N} B_\phi, \tag{5.36}$$

using Eq. (5.22). We note that this relation is similar to Eq. (5.17) from Spruit (2002), which was derived for the non-axisymmetric components only. Fuller et al. (2019) also established the same relation arguing that the Tayler instability cannot operate when the magnetic tension forces become larger than the magnetic pressure forces leading to the instability.

The azimuthal magnetic field saturates when the shear rate (Eq. 5.8) balances the dissipation rate (Eq. 5.26). Thus, using the relations between the magnetic field components (Eqs. 5.22 and 5.36), we find the magnetic field strengths in the saturated regime derived in Fuller et al. (2019):

$$B_{\phi,\mathrm{F}}^\mathrm{sat} \sim \sqrt{4\pi\rho r^2}\Omega \left(\frac{q\Omega}{N}\right)^{1/3}, \tag{5.37}$$

$$\delta B_{\perp,\mathrm{F}}^\mathrm{sat} \sim \sqrt{4\pi\rho r^2}\Omega \left(\frac{q\Omega}{N}\right)^{2/3}, \tag{5.38}$$

$$B_{r,\mathrm{F}}^\mathrm{sat} \sim \sqrt{4\pi\rho r^2}\Omega \left(\frac{q^2\Omega^5}{N^5}\right)^{1/3}. \tag{5.39}$$

Finally, the angular momentum is redistributed in the PNS through Maxwell stresses associated with an effective angular momentum diffusivity (Spruit, 2002, Fuller et al., 2019):

$$\nu_{\rm AM} = \frac{B_r B_\phi}{4\pi\rho q\Omega}, \tag{5.40}$$

which affects the shear parameter at the rate

$$\gamma_{\rm AM} \equiv \frac{\nu_{\rm AM}}{r^2}. \tag{5.41}$$

5.1.5 . Governing evolution equations

Now that the main equations involved in our scenario have been brought out, we can write the evolution equations for the rotation properties and the magnetic field. The evolution of PNS angular rotation frequency is driven by the fallback accretion rate (Eq. 5.3) as described by Eq. (5.4). Hence,

$$\dot{\Omega} = \frac{2}{3}\Delta\Omega \frac{t_0^{2/3}}{(t+t_0)^{5/3}}, \tag{5.42}$$

where $\Delta\Omega = \Omega_{\rm fin} - \Omega_{\rm init} = M_{\rm acc} j_{\rm kep}/I$. As previously mentioned, the shear rate is also expected to decrease due to angular momentum transport (Eq. 5.41) such that

$$\dot{q} = \frac{\dot{\Omega}}{\Omega}(1-q) - \gamma_{\rm AM} q = \frac{2}{3}\frac{\Delta\Omega}{\Omega}\frac{t_0^{2/3}}{(t+t_0)^{5/3}} - \frac{B_r B_\phi}{4\pi\rho\Omega r^2}. \tag{5.43}$$

Combining the different growth and damping rates given by Eqs. (5.8), (5.13), (5.21), (5.26), and (5.35), we find that the magnetic field evolution is governed by the following equations:

$$\partial_t B_\phi = \left(\sigma_{\rm shear} - \gamma_{\rm diss}\right) B_\phi = q\Omega B_r - \frac{\omega_{\rm A}^2}{\Omega}\frac{\delta B_\perp^2}{B_\phi}, \tag{5.44}$$

$$\partial_t \delta B_\perp = \left(\sigma_{\rm TI} - \gamma_{\rm cas}\right)\delta B_\perp = \frac{\omega_{\rm A}^2}{\Omega}\delta B_\perp - \frac{\delta v_{\rm A}}{r}\delta B_\perp, \tag{5.45}$$

$$\partial_t B_r = \left(\sigma_{\rm NL} - \gamma_{\rm diss}\right) B_r = \frac{\omega_{\rm A}^2}{N\Omega}\frac{\delta B_\perp^2}{\sqrt{4\pi\rho r^2}} - \frac{\omega_{\rm A}^2}{\Omega}\left(\frac{\delta B_\perp}{B_\phi}\right)^2 B_r. \tag{5.46}$$

Equations (5.42)–(5.46) are solved for a typical PNS of 5-10 s in age using the odeint function from the Python package SciPy. The PNS mass and radius are $M_{\rm PNS} = 1.5\,{\rm M}_\odot$ and $r = 12\,{\rm km}$, and so the average density is $\rho = 4.1\times10^{14}\,{\rm g\,cm^{-3}}$. The moment of inertia is estimated using Eq. (12) from Lattimer & Schutz (2005):

$$\begin{aligned} I &= 0.237 M_{\rm PNS} r^2 \left[1 + 4.2\left(\frac{M_{\rm PNS}}{{\rm M}_\odot}\frac{1\,{\rm km}}{r}\right) + 90\left(\frac{M_{\rm PNS}}{{\rm M}_\odot}\frac{1\,{\rm km}}{r}\right)^4\right] \\ &\simeq 1.6\times10^{45}\,{\rm g\,cm^2}. \end{aligned} \tag{5.47}$$

The PNS core is assumed to be initially in solid-body rotation (i.e. $q = 0$) and slowly rotating with an angular rotation frequency $\Omega_{\rm init} = 2\pi\,{\rm rad\,s^{-1}}$ (i.e. an initial rotation period $P_{\rm init} \equiv 2\pi/\Omega_{\rm init} = 1\,{\rm s}$). We note that the results of the time integration weakly depend on these parameters as long as $P_{\rm init} \gtrsim 40\,{\rm ms}$. The parameters of the fallback are chosen to be consistent with the simulations of Janka et al. (2022), with a starting time at $t_0 = 7\,{\rm s}$. The initial magnetic field components B_r, B_ϕ, and $\delta B_\perp$ are initialised at a strength of $10^{12}\,{\rm G}$, which is the typical magnetic field amplitude of regular neutron stars.

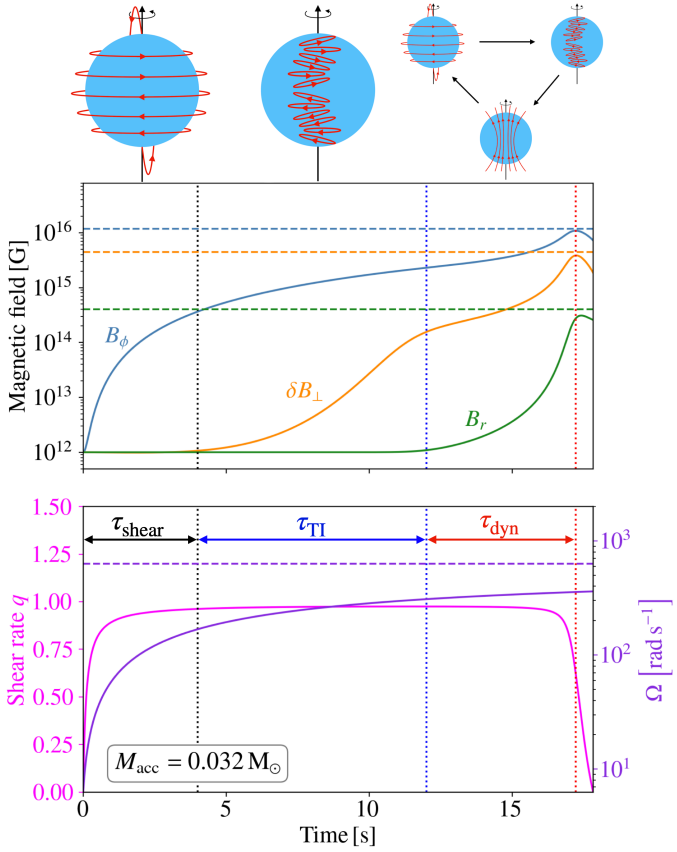

Figure 5.2 — Time evolution of the different components of the magnetic field (top), the dimensionless shear rate, and the angular rotation frequency (bottom) for an accreted mass $M_{\rm acc} = 3.2 \times 10^{-2}\,{\rm M}_\odot$ corresponding to an asymptotic rotation period $P_{\rm fin} = 10\,{\rm ms}$. The different stages of the dynamo process are highlighted by the schematics at the top and their associated timescales by the double arrows. Their ends are illustrated by the dotted vertical lines: winding (black), linear development of the Tayler instability (dark blue), and the whole dynamo loop (red). The horizontal dashed lines (blue, orange, and green) show respectively the saturation intensities $B^{\rm sat}_{\phi,{\rm F}}, \delta B^{\rm sat}_{\perp,{\rm F}}$, and $B^{\rm sat}_{r,{\rm F}}$ (Eqs. 5.37–5.39) evaluated at the time of saturation. The dashed violet horizontal line represents the asymptotic angular rotation frequency $\Omega_{\rm fin}$.

5.2 . Results

We proceed with a twofold presentation of our model outputs: First we present the time evolution, in which we derive analytical predictions for the timescales of the different phases of the scenario and compare them to the integrated evolution. We then present the saturated regime where we focus on the magnetic field intensities reached via the Tayler-Spruit dynamo and provide an 'upper' limit of PNS rotation period (i.e. a 'lower' limit of fallback mass) to form magnetars.

5.2.1 . Time evolution of the magnetic field

The time series for an asymptotic rotation period $P_{\rm fin} \equiv 2\pi/\Omega_{\rm fin} = 10\,{\rm ms}$ displayed in Fig. 5.2 can be split into several phases, which are illustrated by the schematics at the top of the figure:

(i) B_ϕ is strongly amplified for $\sim 4\,{\rm s}$ due to the winding of B_r while the other components stay constant. As the mass-accretion rate is higher in this phase, strong increases in the shear rate and the rotation rate are also noted.

(ii) The Tayler instability develops and amplifies $\delta B_\perp$ for $\sim 8\,{\rm s}$.

(iii) The axisymmetric radial field B_r is generated allowing the dynamo action to occur for $\sim 5\,{\rm s}$. The azimuthal magnetic field saturates at $\sim 17\,{\rm s}$, which corresponds to $\sim 24\,{\rm s}$ after the core bounce.

(iv) The angular momentum transport by the magnetic field, which was negligible during

the first $\sim 16\,\mathrm{s}$, becomes significant as the magnetic field saturates. This stage is discussed in Sect. 5.3.1.

The evolution of the magnetic field is shown until the whole angular momentum is transported, (i.e. when the shear rate reaches $q = 0$) at $t \sim 17.5\,\mathrm{s}$. Further evolution is not considered because our set of equations does not intend to describe either the relaxation phase of the magnetic field to a stable geometric configuration or the dynamics with very low shear where one would expect the Tayler-Spruit dynamo to stop or to act intermittently (Fuller & Lu, 2022).

The different vertical lines in Fig. 5.3 show that the above phases occur at different times for different accreted masses. To better quantify the dependence on this parameter, we derive analytical estimates of the corresponding characteristic timescales τ_{shear}, τ_{TI}, and τ_{dyn} (see Fig. 5.2). First, the shearing phase begins when the fallback matter starts to be accreted on the PNS surface and finishes when the azimuthal magnetic field B_ϕ is strong enough to make the Tayler instability grow as fast as B_ϕ, that is when the growth rate of the instability (Eq. 5.13) is equal to the winding rate (Eq. 5.8). Thus, the Alfvén frequency associated with the intensity of the azimuthal magnetic field at the end of this phase is

$$\omega_{\mathrm{A}} \sim \omega_{\mathrm{A,TI}} \equiv \left(q\Omega^2\omega_{r,0}\right)^{1/3}, \tag{5.48}$$

where $\omega_{r,0} \equiv B_r(t=0)/\sqrt{4\pi\rho r^2}$. Therefore, a characteristic timescale for the shearing stage can be defined as the inverse of the winding growth rate (Eq. 5.13) evaluated at $\omega_{\mathrm{A}} = \omega_{\mathrm{A,TI}}$:

$$\tau_{\mathrm{shear}} \equiv \sigma_{\mathrm{shear}}^{-1} \sim \frac{\omega_{\mathrm{A,TI}}}{q\Omega\omega_{r,0}} = \left(q^2\omega_{r,0}^2\Omega\right)^{-1/3}. \tag{5.49}$$

Second, as the azimuthal field becomes unstable, the Tayler instability grows exponentially until the perturbed field reaches the saturation intensity of Eq. (5.22). The perturbed field at saturation can be approximated by

$$\delta B_\perp(t = t_{\mathrm{sat}}) \sim \delta B_\perp(t = \tau_{\mathrm{shear}}) \exp\left[\sigma_{\mathrm{TI}}(t_{\mathrm{sat}} - \tau_{\mathrm{shear}})\right], \tag{5.50}$$

and so a characteristic timescale for this stage can be defined as

$$\tau_{\mathrm{TI}} \equiv t_{\mathrm{sat}} - \tau_{\mathrm{shear}} \sim \sigma_{\mathrm{TI}}^{-1} \ln\left[\frac{\delta B_\perp(t = t_{\mathrm{sat}})}{\delta B_\perp(t = \tau_{\mathrm{shear}})}\right]. \tag{5.51}$$

Using Eq. (5.22), we have

$$\delta B_\perp(t = t_{\mathrm{sat}}) \sim \frac{\omega_{\mathrm{A}}(t = t_{\mathrm{sat}})}{\Omega} B_\phi(t = t_{\mathrm{sat}}). \tag{5.52}$$

In order to obtain a simple estimate, we make the rough approximations that $\delta B_\perp(t = \tau_{\mathrm{shear}}) \sim \delta B_\perp(t = 0)$ and $B_\phi(t = \tau_{\mathrm{shear}}) \sim B_\phi(t = t_{\mathrm{sat}})$, which leads to

$$\tau_{\mathrm{TI}} \sim \frac{\Omega}{\omega_{\mathrm{A,TI}}^2} \ln\left(\frac{\omega_{\mathrm{A,TI}}^2 r}{\Omega \delta v_{\mathrm{A},0}}\right), \tag{5.53}$$

where $\delta v_{\mathrm{A},0} \equiv \delta v_{\mathrm{A}}(t = 0)$.

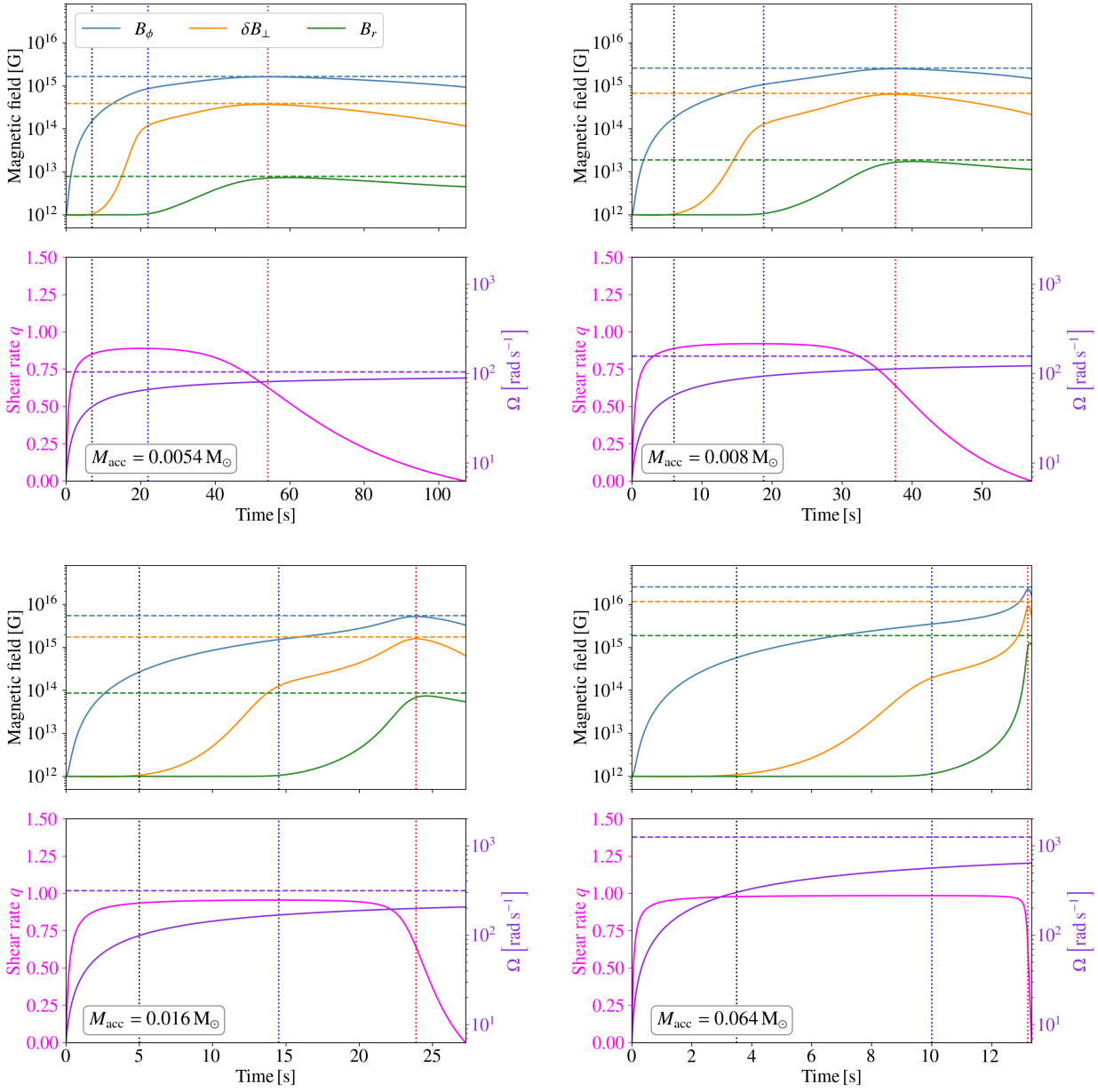

Figure 5.3 — Same as Fig. 5.2 but for total accreted masses of $M_{\rm acc} = \{0.54,\ 0.8,\ 1.6,\ 6.4\} \times 10^{-2}\,{\rm M}_\odot$ (corresponding to $P_{\rm fin} = \{60,\ 40,\ 20,\ 5\}$ms, respectively).

Third, when the perturbed field reaches a sufficient amplitude, the axisymmetric radial field is amplified through non-linear induction, thus closing the dynamo loop. This phase ends when the magnetic field saturates at the intensities given by Eqs. (5.37)–(5.39). Likewise, we estimate the critical strength of the azimuthal field $B_{\phi,\mathrm{dyn}}$ above which the dynamo loop is triggered by equating the growth rate of the radial field B_r (Eq. 5.35) and the winding rate (Eq. 5.8). We obtain the Alfvén frequency associated with $B_{\phi,\mathrm{dyn}}$

$$\omega_{\mathrm{A,dyn}} \equiv \left(qN\Omega^4\omega_{r,0}^2\right)^{1/7}, \tag{5.54}$$

making use of Eq. (5.22). We define the dynamo characteristic timescale as

$$\tau_{\mathrm{dyn}} \equiv \left(\frac{B_\phi}{\partial_t^2 B_\phi}\right)^{1/2}. \tag{5.55}$$

The time derivative of the radial magnetic field is

$$\partial_t B_r \sim \frac{\omega_{\mathrm{A}}^2 \delta v_{\mathrm{A}}}{N\Omega r}\delta B_\perp \sim \frac{\omega_{\mathrm{A}}^3 \delta v_{\mathrm{A}}}{N\Omega^2 r} B_\phi \sim \frac{\omega_{\mathrm{A}}^5}{N\Omega^3} B_\phi, \tag{5.56}$$

using Eq. (5.22). Therefore,

$$\partial_t^2 B_\phi \sim q\Omega\partial_t B_r \sim \frac{q\omega_{\mathrm{A}}^5}{N\Omega^2} B_\phi, \tag{5.57}$$

where q and Ω are assumed to be constant during this phase. Thus, the dynamo characteristic timescale can be approximated as

$$\tau_{\mathrm{dyn}} \equiv \left(\frac{B_\phi}{\partial_t^2 B_\phi}\right)^{1/2} \sim \frac{\Omega}{\omega_{\mathrm{A,dyn}}^2}\left(\frac{N}{q\omega_{\mathrm{A,dyn}}}\right)^{1/2}. \tag{5.58}$$

For the case $P_{\mathrm{fin}} = 10\,\mathrm{ms}$, we have $\tau_{\mathrm{shear}} \simeq 2.3\,\mathrm{s}$, $\tau_{\mathrm{TI}} \simeq 8.5\,\mathrm{s}$, and $\tau_{\mathrm{dyn}} \simeq 5\,\mathrm{s}$, which are similar to the timescales illustrated by the dotted vertical lines in Fig. 5.2. The same observation can be made for $P_{\mathrm{fin}} \leq 30\,\mathrm{ms}$ in Fig. 5.3. However, for $P_{\mathrm{fin}} = 40\,\mathrm{ms}$ ($M_{\mathrm{acc}} = 0.008\,\mathrm{M}_\odot$) and $P_{\mathrm{fin}} = 60\,\mathrm{ms}$ ($M_{\mathrm{acc}} = 0.0054\,\mathrm{M}_\odot$), the dynamo loop phase lasts respectively $\sim 30\,\mathrm{s}$ and $\sim 20\,\mathrm{s}$ (see Fig. 5.3), which is longer than the analytical predictions of $\tau_{\mathrm{dyn}} \simeq 11\,\mathrm{s}$ and $\tau_{\mathrm{dyn}} \simeq 9.2\,\mathrm{s}$. This is due to the presence of a significant stage that is not included in the expression of τ_{dyn} where the growth of B_ϕ slows down before saturation.

The three characteristic timescales defined by Eqs. (5.49), (5.53), and (5.58) are plotted as a function of the fallback mass in Fig. 5.4 in addition to the characteristic timescale for the whole amplification process, which is defined as

$$\tau_{\mathrm{tot}} \equiv \tau_{\mathrm{shear}} + \tau_{\mathrm{TI}} + \tau_{\mathrm{dyn}}. \tag{5.59}$$

The vertical red dashed line represents the lower limit of fallback mass to form typical magnetars, which is estimated in Sect. 5.2.2 (corresponding to an asymptotic rotation period $P_{\mathrm{fin}} \lesssim 30\,\mathrm{ms}$). In the regime relevant to magnetar formation, the analytical and numerical estimates of the duration of the whole amplification process are in reasonable agreement, namely $\tau_{\mathrm{tot}} \lesssim 30\,\mathrm{s}$. In this regime, the phase which takes more time is the development of the Tayler instability. For $P_{\mathrm{fin}} \gtrsim 30\,\mathrm{ms}$, the comparison between the time at which B_ϕ saturates and τ_{tot} shows a significant difference, which is the consequence of the discrepancy noted above between the analytical estimate and numerical solution for τ_{dyn}.

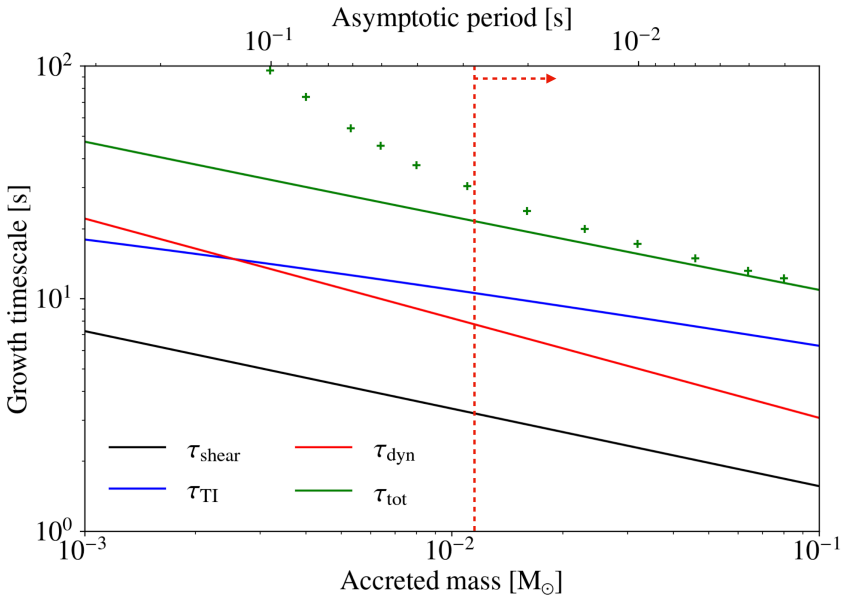

Figure 5.4 — Different characteristic timescales as a function of the accreted mass: winding (black), Tayler instability (dark blue), and dynamo (red). The green line represents the sum of the three timescales. The shear rate is set at $q = 1$. The green crosses represent the entire amplification time obtained by integrating Eqs. (5.37)–(5.39). The red vertical line shows the lower limit of the accreted mass to form a magnetar with a radial field stronger than $B_{\rm Q} \equiv m_e c^2/e\hbar \simeq 4.4 \times 10^{13}\,{\rm G}$ using the predictions of Fuller et al. (2019).

5.2.2 . Magnetic field in the saturated regime

We now focus on the maximum magnetic field obtained at the end of the amplification phase. In the following discussion, this saturated magnetic field will be considered as a proxy for the magnetar's magnetic field and its 'radial' component will be considered a proxy for the 'dipolar' component of the magnetic field. A more precise prediction would require a description of the relaxation towards a stable equilibrium, which is left for future studies.

In the top panel of Figs. 5.2 and 5.3, we see that the saturation intensities are close to their associated horizontal dashed lines, which illustrate the predictions of Eqs. (5.37)–(5.39) for values of the shear rate q and the angular rotation frequency Ω reached at the time of magnetic field saturation. Therefore, these equations can be used to estimate the intensity of the saturated magnetic field. However, the angular frequency at $\tau_{\rm tot}$ is still lower than its asymptotic value represented by the violet dashed line in the bottom panel. We estimate $\Omega(t = \tau_{\rm tot})$ analytically by integrating Eq. (5.42)

$$\Omega(t = \tau_{\rm tot}) = \Omega_{\rm fin} - \left(\frac{t_0}{\tau_{\rm tot} + t_0}\right)^{2/3} (\Omega_{\rm fin} - \Omega_{\rm init})\,. \tag{5.60}$$

Assuming that the timescales for the dynamo are roughly the same for the two models, that is, that of Fuller et al. (2019) and that of Spruit (2002), we also evaluate the expressions of the saturated magnetic field derived by Spruit (2002) (Eqs. 5.18 and 7.20) at $\Omega(t = \tau_{\rm tot})$. We see in Fig. 5.5 that our analytical estimates of the saturated fields (solid lines) are close to the numerical values at the peak of the solutions of Eqs. (5.44)–(5.46) (plus symbols). The small difference that appears for shorter rotation periods is due to the angular momentum transport, as discussed in see Sect. 5.3.1.

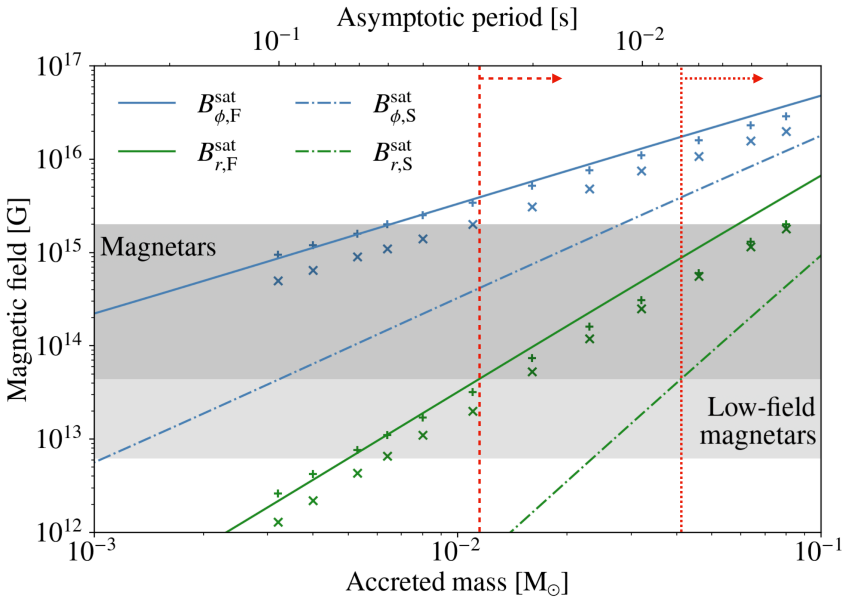

Figure 5.5 — Predicted intensities for the saturated components of the magnetic field as a function of the accreted mass using the formalisms of Fuller et al. (2019) (Eqs. (5.37)–(5.39); solid lines) and Spruit (2002) (Eqs. (5.18)–(7.20); dash-dot lines). The shear rate is set at $q = 1$. These intensities are compared to the magnetic field reached at maximum intensity (blue and green plus signs) and at $q = 0$ (blue and green cross signs) by integrating Eqs. (5.42)–(5.46) for several fallback masses. Grey areas represent the estimated range of the dipolar magnetic field strength from regularly observed magnetars (dark grey) and from the three detected low-field Galactic magnetars (light grey). The vertical lines show the lower limit on the fallback mass (upper limit on the rotation period) needed to form a magnetar with a radial field stronger than $B_{\rm Q} \simeq 4.4 \times 10^{13}\,{\rm G}$ for the prediction of Fuller et al. (2019) (dashed red) and Spruit (2002) (dotted red).

Using the maximum magnetic field as a proxy for the magnetar's magnetic field may lead to an overestimation because a fraction of the magnetic energy can be dissipated during the relaxation to a stable magnetic configuration. Although our model is unable to describe this relaxation process, we can get an idea of the robustness of our proxy by comparing to the magnetic field intensity at the time when $q = 0$. Figure 5.5 shows that this other proxy (cross signs) is smaller by between $\sim 10\,\%$ and $\sim 50\,\%$ but follows the same trends as the maximum magnetic field. Such a moderate difference would not change our main conclusions and suggests that the maximum magnetic field is a meaningful proxy for the final magnetic field.

In Fig. 5.5, the observed range of dipolar magnetic field for magnetars is fixed between the quantum electron critical field $B_{\rm Q} \equiv m_e c^2/e\hbar \simeq 4.4 \times 10^{13}\,{\rm G}$ and $B_{\rm dip} \sim 2 \times 10^{15}\,{\rm G}$, the dipole field of the 'most magnetised' magnetar SGR 1806-20 (Olausen & Kaspi, 2014). We find that the radial magnetic fields $B^{\rm sat}_{r,\rm F}$ and $B^{\rm sat}_{r,\rm S}$ fall in this range for accreted masses $M_{\rm acc} \gtrsim 1.1 \times 10^{-2}\,{\rm M}_\odot$ and $M_{\rm acc} \gtrsim 4 \times 10^{-2}\,{\rm M}_\odot$ (i.e. asymptotic rotation periods $P_{\rm fin} \lesssim 28\,{\rm ms}$ and $P_{\rm fin} \lesssim 8\,{\rm ms}$), respectively. This confirms that magnetar-like magnetic fields can be formed over a wide range of accreted masses. The analytical predictions also show that, in the regime relevant for magnetar formation, the azimuthal component $B_\phi \gtrsim 4 \times 10^{15}\,{\rm G}$ for both saturation mechanisms, which is significantly stronger than the radial component.

For lower accreted masses spinning-up the PNS to periods ranging from 28 to $64\,{\rm ms}$ (between 8 and $14\,{\rm ms}$ for the predictions of Spruit (2002)), our scenario may produce radial mag-

netic fields B_r as strong as the dipolar fields diagnosed in low-field magnetars (Rea et al., 2010, 2012a, 2014). Moreover, the strength of the associated azimuthal field is $B_\phi \sim (1-3)\times 10^{15}\,\mathrm{G}$, which can be related to the non-dipolar magnetic field needed to produce the outbursts and chaotic bursts observed in magnetars (Thompson & Duncan, 1995). This azimuthal magnetic field may also be the source of the proton cyclotron absorption lines observed in two low-field magnetars by Tiengo et al. (2013) and Rodríguez Castillo et al. (2016). Thus, our model provides a possible explanation of low-field magnetar formation. It is an alternative to the initial interpretation proposed by Rea et al. (2010), which invokes $\gtrsim 1\,\mathrm{Myr}$ 'old' (or 'worn-out') magnetars whose initial strong dipolar field of $\sim \mathrm{few}\times 10^{14}\,\mathrm{G}$ has decayed due to Ohmic and Hall processes. This diffusion could be enhanced by the presence of a strong initial toroidal field $\gtrsim 10^{16}\,\mathrm{G}$ (Turolla et al., 2011).

As Eqs. (5.37)–(5.39) give orders of magnitude, Fuller et al. (2019) parameterised them with a prefactor denoted α. We used $\alpha \sim 1$ as obtained by Fuller et al. (2019) for evolved stars in the subgiant and red giant branches by calibrating α on asteroseismic measurements. However, Eggenberger et al. (2019c) find $\alpha \sim 0.5$ for subgiant stars on the one hand, and $\alpha \sim 1.5$ for red giant stars on the other. Also, Fuller & Lu (2022) argue that $\alpha \sim 0.25$ if intermittent dynamo action is considered in radiative zones with insufficient shear to trigger a sustained dynamo. This smaller prefactor would imply a larger limit of accreted mass of $\sim 2\times 10^{-2}\,\mathrm{M}_\odot$ (i.e. a rotation period of $\sim 15\,\mathrm{ms}$).

5.3 . Discussion

5.3.1 . Angular momentum transport

In the previous section, we focused on the magnetic field amplification and did not discuss the angular momentum transport due to the Tayler-Spruit dynamo. Our analytical estimate of the saturated magnetic field is based on the assumption that the differential rotation is not erased before the end of the amplification. Indeed, Figs. 5.2 and 5.3 show that the angular momentum transport due to Maxwell stresses starts to be significant around the time of magnetic field saturation and that most of the angular momentum transport occurs afterwards. This can be explained by comparing the characteristic timescales of the dynamo loop phase τ_{dyn} (Eq. 5.58) with those of angular momentum transport. These can be estimated at saturation using the expression of $B_{\phi,\mathrm{F}}^{\mathrm{sat}}$ (Eq. 5.37) as

$$\tau_{\mathrm{AM}} \equiv \gamma_{\mathrm{AM}}^{-1} = \frac{r^2}{\nu_{\mathrm{AM}}} \sim \left(\frac{N}{\Omega}\right)^2 \Omega^{-1}, \tag{5.61}$$

and

$$\tau_{\mathrm{dyn}} = \left(\frac{N}{q\omega}\right)^{4/3} \Omega^{-1}. \tag{5.62}$$

The ratio of these two timescales is

$$\frac{\tau_{\mathrm{dyn}}}{\tau_{\mathrm{AM}}} \sim \left(\frac{\Omega}{q^2 N}\right)^{2/3} \sim 0.3\left(\frac{P}{10\,\mathrm{ms}}\right)^{-2/3}. \tag{5.63}$$

For all values of the accreted mass and corresponding rotation period considered in this paper, the angular momentum transport is therefore longer than the dynamo timescale. This explains why most of the angular momentum takes place after the dynamo saturation and

justifies a posteriori our analytical estimate of the saturated magnetic field. At fast rotation periods of a few milliseconds, the two timescales are nonetheless close to each other; as a consequence, the angular momentum transport before saturation is not negligible, which explains the moderate discrepancy between our analytical estimate of the saturated magnetic field and the numerical results for short rotation periods (Fig. 5.5).

On the other hand, angular momentum transport due to the neutrino viscosity can be neglected because its typical timescale is much longer than the evolution timescales considered:

$$\tau_n \equiv \frac{r^2}{\nu_n} \gtrsim 3 \times 10^4 \,\mathrm{s}, \tag{5.64}$$

where the neutrino viscosity ν_n is estimated with the approximate analytical expression of Keil et al. (1996) and Guilet & Müller (2015):

$$\nu_n \sim 3 \times 10^8 \left(\frac{\rho}{10^{14}\,\mathrm{g\,cm^{-3}}} \right)^{-2} \left(\frac{T}{5\,\mathrm{MeV}} \right)^2 \mathrm{cm^2\,s^{-1}}. \tag{5.65}$$

5.3.2 . Neutrinos

We demonstrate above that angular momentum transport by either the magnetic field or the neutrino viscosity does not significantly impact our results. However, the neutrino flux coming from the accretion is also expected to extract a fraction of the angular momentum of the PNS (Janka, 2004, Bollig et al., 2021). To investigate whether it does not jeopardise the model, we use the following reasoning. As fallback is assumed to start several seconds after bounce in our model, one may assume that most of the angular momentum extraction by neutrino emission at these late times originate from fallback accretion rather than PNS cooling. Most of the fallback mass is likely to have a specific angular momentum j_0 which exceeds the Keplerian value at the PNS surface. It will therefore assemble into an accretion disk, settling at a radius r_k where $j_\mathrm{kep}(r_\mathrm{k}) = j_0$. Its gravitational binding energy E_bind will be at most all converted into neutrino radiation, that is per baryon with a rest mass m_B:

$$\Delta E_\nu \lesssim E_\mathrm{bind}(r_\mathrm{k}) \sim \frac{G M_\mathrm{PNS} m_\mathrm{B}}{r_\mathrm{k}}, \tag{5.66}$$

where we assume that the disk mass is small compared to the PNS mass. The corresponding specific angular momentum loss is

$$\Delta j_\nu \lesssim \frac{\Delta E_\nu}{m_\mathrm{B} c^2} j_\mathrm{kep}(r_\mathrm{k}) \sim \frac{R_\mathrm{S}}{2 r_\mathrm{k}} j_\mathrm{kep}(r_\mathrm{k}), \tag{5.67}$$

where $R_\mathrm{S} \equiv 2GM_\mathrm{PNS}/c^2$ is the PNS Schwarzchild radius. Δj_ν is maximal at the PNS surface (i.e. when $r_\mathrm{k} = r$), which implies

$$\Delta j_\nu \lesssim 0.185\, j_\mathrm{kep}(r), \tag{5.68}$$

for the same parameters of a typical PNS introduced in Sect. 5.1.5. Therefore, the extraction of angular momentum by neutrino radiation is very inefficient.

5.3.3 . Impact of the viscosity on the Tayler instability

In the reasoning developed above, we do not take into account the effects due to viscous processes, which might be important because they could be much larger than the effects of the resistivity in PNSs. Therefore, here we aim to address the question of their impact on

the development of the Tayler instability. To the best of our knowledge, no analytical study of the Tayler instability has included the impact of viscosity. Hence, we use an approximate reasoning similar to that of Spruit (2002), which is based on a comparison of the instability growth timescale with the viscous damping timescale. This provides the following instability criterion:

$$\sigma_{\rm TI}^{-1} \sim \frac{\Omega}{\omega_{\rm A}^2} \lesssim \frac{l_r^2}{\nu}, \tag{5.69}$$

with ν being the kinematic viscosity. Using the constraint on the radial length scale l_r due to the stratification (Eq. 5.14), we infer an instability criterion on the azimuthal magnetic field B_ϕ as a function of the viscosity:

$$B_\phi > B_{\phi,\rm c} \sim \Omega \left(\frac{N}{\Omega}\right)^{1/2} \left(\frac{\nu}{r^2\Omega}\right)^{1/4}. \tag{5.70}$$

This equation is similar to Eq. (5.12) but with the magnetic diffusivity substituted by the viscosity. To obtain an order of magnitude of this critical value, we must determine a value of the viscosity which is relevant for our scenario. As the fallback accretion occurs seconds to minutes after the PNS formation, the PNS has cooled down to temperatures $\lesssim 1.1\times10^{11}\,\rm K$ in the core and $\lesssim 5\times10^{10}\,\rm K$ in the outer region ($\lesssim 10\,\rm MeV$ and $\lesssim 5\,\rm MeV$, respectively; Hüdepohl, 2014). The neutrino mean free path can be approximated by (Thompson & Duncan, 1993, Eq. 11):

$$l_n \sim 4\times10^4 \left(\frac{\rho}{10^{14}\,\rm g\,cm^{-3}}\right)^{-1/3} \left(\frac{T}{5\,\rm MeV}\right)^{-3} \left(\frac{f(Y_p)}{1}\right) \rm cm, \tag{5.71}$$

where $f(Y_p)$ is function of the proton fraction close to unity. This length is larger than the maximum radial length scale (Eq. 5.14):

$$l_r \sim 4\times10^3 \left(\frac{B_\phi}{10^{15}\,\rm G}\right) \rm cm. \tag{5.72}$$

Therefore, neutrinos do not provide any relevant viscosity at the Tayler instability length scales and we must consider instead a microscopic viscosity such as the shear viscosity due to neutron–neutron scattering (Cutler & Lindblom, 1987, Eq. 14):

$$\nu_s \sim 3\times10^{-2} \left(\frac{\rho}{10^{14}\,\rm g\,cm^{-3}}\right)^{5/4} \left(\frac{T}{5\,\rm MeV}\right)^{-2} \rm cm^2\,s^{-1}. \tag{5.73}$$

The associated critical magnetic field is therefore

$$B_{\phi,\rm c} \simeq 10^{13} \left(\frac{\nu_s}{3\times10^{-2}\,\rm cm^2\,s^{-1}}\right)^{1/4} \left(\frac{\Omega}{200\pi\,\rm rad\,s^{-1}}\right)^{1/4} \rm G, \tag{5.74}$$

which is four times stronger than the critical magnetic field inferred from the criterion of Spruit (2002) (Eq. 5.12). However, this new critical magnetic field is still much weaker than the characteristic azimuthal magnetic field separating the winding phase from the phase in which the Tayler instability develops (when the growth rate of the Tayler instability reaches the winding rate (Eq. 5.48))

$$B_\phi = \omega_{\rm A,TI}\sqrt{4\pi\rho r^2} \sim 1.3\times10^{15} \left(\frac{\Omega}{200\pi\,\rm rad\,s^{-1}}\right)^{2/3} \left(\frac{B_r}{10^{12}\,\rm G}\right)^{1/3}. \tag{5.75}$$

As a consequence, the viscosity is not expected to prevent the Tayler instability from growing and should not have a significant impact on our results. However, we note that our argument is approximate and would need to be upgraded through a linear analysis of the Tayler instability including the viscous processes.

5.3.4 . Superfluidity and superconductivity

A last potential obstacle for our model may emerge from the crust formation and the superfluidity and superconductivity in the core, which occur during the cooling of the PNS. The outer crust is expected to start freezing a few minutes after the PNS formation and the inner crust forms far later, between 1 and $100\,\mathrm{yr}$ after formation (Aguilera et al., 2008). Therefore, no part of the crust is formed during the time interval involved in our scenario.

The potential early appearance of superfluid neutrons or even superconductive protons in the PNS core at temperatures below $10^8 - 10^{10}\,\mathrm{K}$ is worth discussing because the MHD approximation would not be sufficiently realistic and a multi-fluid approach would be more relevant (Glampedakis et al., 2011, Sinha & Sedrakian, 2015). However, the 1D models of PNS cooling show higher temperatures than $10^{10}\,\mathrm{K}$ in the PNS even after $15\,\mathrm{s}$ (e.g. Pons et al., 1999, Roberts, 2012, Hüdepohl, 2014, Roberts & Reddy, 2017). Moreover, Gusakov & Kantor (2013) and Glampedakis & Jones (2014) brought forward a critical perturbed magnetic field strength above which superfluidity of neutrons dies out. Therefore, the MHD approximation is still valid for describing the PNS internal dynamics during the first $40\,\mathrm{s}$ following the core bounce.

5.4 . Conclusions

In this paper, we propose a new scenario for magnetar formation, in which the Tayler-Spruit dynamo amplifies the large-scale magnetic field of a PNS spun up by SN fallback accretion. We develop a one-zone model describing the evolution of the magnetic field averaged over a PNS subject to fallback accretion. The equations describing the time evolution are solved numerically and compared successfully with analytical estimates of the final magnetic field and of the duration of each stage of the amplification process. Predictions for the different components of the magnetic field are therefore obtained as a function of the accreted mass for the two proposed saturation models of the Tayler-Spruit dynamo (Spruit, 2002, Fuller et al., 2019). Our main conclusions can be summarised as follows:

- Radial magnetic fields spanning the full range of the magnetar dipole intensity can be formed for accreted masses compatible with the results of recent SN simulations. Our model predicts the formation of magnetar-like magnetic fields for accreted masses $M_{\rm acc} \gtrsim 1.1\times10^{-2}\,\mathrm{M}_\odot$ for the saturation model of Fuller et al. (2019) and $M_{\rm acc} \gtrsim 4\times10^{-2}\,\mathrm{M}_\odot$ for the saturation model of Spruit (2002). This corresponds to neutron star final rotation periods $P_{\rm fin} \lesssim 28\,\mathrm{ms}$ and $P_{\rm fin} \lesssim 8\,\mathrm{ms}$, respectively.
- The azimuthal component of the magnetic field is predicted to be in the range $10^{15} - 10^{16}\,\mathrm{G}$, which is stronger than the radial component by a factor of 10 to 100.
- In the regime relevant for magnetar formation, the magnetic field amplification lasts between 15 and $30\,\mathrm{s}$. On such a timescale, the MHD equations assumed in the description of the Tayler-Spruit dynamo are expected to be valid. Furthermore, we have not

identified any other process capable of interfering with the Tayler-Spruit dynamo by transporting angular momentum on a comparable or shorter timescale.

Our results therefore predict that magnetars can indeed be formed in our new scenario. Magnetar formation is possible at sufficiently long rotation periods to be compatible with the lower limit of $5\,\mathrm{ms}$ inferred from regular SN remnants associated with magnetars. With the saturation model of Fuller et al. (2019), the full range of magnetar fields can be obtained within this constraint, even those that exhibit a strong dipolar magnetic field $B_{\mathrm{dip}} \sim 10^{15}\,\mathrm{G}$. On the other hand, with the saturation model proposed by Spruit (2002), only the lower end of the magnetar fields can be obtained with $P_{\mathrm{fin}} < 5\,\mathrm{ms}$, while dipolar magnetic fields $\gtrsim 2\times10^{14}\,\mathrm{G}$ need faster rotation periods.

An important prediction of our scenario is the very intense toroidal magnetic field, which lies between 3×10^{15} and $3\times10^{16}\,\mathrm{G}$ for parameters corresponding to radial magnetic fields in the magnetar range. These values are compatible with the interpretation of the X-ray flux modulations observed in three magnetars as free precession driven by an intense toroidal magnetic field (Makishima et al., 2014, 2016, 2019, 2021).

The intense toroidal magnetic field predicted in our scenario also provides interesting perspectives from which to explain the formation of low-field magnetars. For radial magnetic fields in the range of the dipolar magnetic field deduced for these objects (Rea et al., 2010, 2012a, 2013, 2014), our model predicts a toroidal magnetic field intensity of $\sim 1-3\times10^{15}\,\mathrm{G}$. Such non-dipolar magnetic fields are strong enough to be the energy source of the magnetar-like emission from these objects and to explain the variable absorption lines interpreted as proton cyclotron lines (Tiengo et al., 2013, Rodríguez Castillo et al., 2016). We therefore suggest that some of the low-field magnetars may be born with low dipolar magnetic fields, rather than evolve to this state as assumed in the 'worn-out' magnetar scenario.

A question arising from our study is the location of the magnetic field in the PNS, which cannot be captured by our one-zone model. As the shear due to fallback accretion is expected to be strongest in the outer region of the PNS, one may expect the magnetic field to be preferentially located in these outer layers. Such a concentration of the magnetic field near the surface would have interesting consequences for its long-term evolution because the magnetic field may be confined in the crust without significant magnetic flux threading the superconductive core. The long-term evolution of such a crust-confined magnetic field configuration has been thoroughly investigated by numerical simulations (e.g. Viganò et al., 2013, Gourgouliatos et al., 2016, Pons & Viganò, 2019). By contrast, if the magnetic field is also present in deeper regions, its evolution in the superconductive core and the transition layer with the crust must be taken into account. A few papers studied this evolution in numerical simulations (e.g. Henriksson & Wasserman, 2013, Lander, 2013, Ciolfi & Rezzolla, 2013) but these lead to a slower magnetic field evolution that is incompatible with magnetar observations (Elfritz et al., 2016). These results would favour initial crust-confined magnetic fields but need to be confirmed in more realistic 3D simulations of the magneto-thermal evolution in the whole neutron star. We also note that the localisation of the magnetic field in our magnetar formation scenario should be studied in more detail. On the one hand, the stratification increases by a factor of ~ 2.5 close to the PNS surface, which might weaken the magnetic field and confine it closer to the surface. On the other hand, the shear can be expected to become significant in the bulk of the PNS after angular momentum has been partly redistributed by the Tayler-Spruit dynamo. Some of the magnetic field may also be transported to deeper regions via the Tayler instability or during the relaxation to a stable

equilibrium.

Another relevant question is the geometry of the magnetic field amplified by the Tayler-Spruit dynamo. One should keep in mind that our comparison to magnetars relies on the assumption that the generated radial field B_r is mostly dipolar. Although the real geometry of the poloidal magnetic field generated by the Tayler-Spruit dynamo is not known, it is likely to be partly non-dipolar, meaning that the large-scale dipolar magnetic field is a fraction of the radial field B_r. Therefore, corresponding predictions should be refined by studying dedicated multi-dimensional models. In Petitdemange et al. (2023), a dynamo similar to the Tayler-Spruit dynamo has been found through numerical simulations in a configuration where the surface rotates slower than the core, which is therefore different to the case of spun-up PNS. Moreover, the observed magnetars are cooled-down neutron stars with a stable configuration of magnetic field. Hence, the study of the magnetic field relaxation from a turbulent saturated state to a stable configuration is important to estimate a more realistic intensity of the dipolar poloidal field. Thus, numerical simulations will be essential to further study of the evolution of the magnetic field geometry in our framework.

A salient feature of our fallback scenario is that it decouples magnetar formation from rapid progenitor rotation and from strong magnetisation of the pre-collapse stars. Rapid progenitor rotation is necessary for magnetar formation by the convective dynamo, which requires initial NS spin periods of $\lesssim 10\,\mathrm{ms}$ (Raynaud et al., 2022), and by the magnetorotational instability (Reboul-Salze et al., 2021, 2022). Strong magnetisation of the pre-collapse star on the other hand is a crucial aspect in the fossil field scenario or the stellar merger scenario (Schneider et al., 2019). Instead of requiring fast rotation or strong magnetic field in the progenitor core, our scenario predicts magnetar formation when fallback deposits a sufficient amount of angular momentum on the PNS surface. With the angular momentum of the mass accreted by the NS being limited by the Keplerian value, magnetars are formed for accreted masses of more than $\sim 1.1\times10^{-2}\,\mathrm{M}_\odot$ (case of Fuller et al., 2019) and $\sim 4\times10^{-2}\,\mathrm{M}_\odot$ (case of Spruit, 2002) in our scenario. The fallback mass should be several times larger than the accreted mass, because angular momentum loss must be expected to lead to mass loss during the accretion process. Therefore, fallback masses of more than a few $10^{-2}\,\mathrm{M}_\odot$ to $10^{-1}\,\mathrm{M}_\odot$ seem to be needed. Based on 1D models of neutrino-driven core-collapse SN explosions, this indicates a preference for single stars with zero-age-main-sequence (ZAMS) masses above about $\sim 18\,\mathrm{M}_\odot$ (Sukhbold et al., 2016) and helium stars (hydrogen-stripped stars in binaries) with ZAMS masses above $30-40\,\mathrm{M}_\odot$ (depending on details of the mass-loss evolution); although the compactness differences between the single-star models of Sukhbold & Woosley (2014) compared to those of Sukhbold et al. (2018) as well as 3D explosion effects (which increase the fallback mass; Janka et al., 2022) may shift these ZAMS masses to lower values. This would be consistent with the observations constraining magnetar progenitors to masses higher than $30\,\mathrm{M}_\odot$ (Gaensler et al., 2005, Bibby et al., 2008, Clark et al., 2008) and also with the case of the magnetar SGR1900+14, whose progenitor mass was estimated to be $17\pm2\,\mathrm{M}_\odot$ (Davies et al., 2009).

While our model avoids the uncertainty of the progenitor core rotation and magnetic field, it implies coping with the uncertainties on the fallback process. A precise modeling of the fallback depends on such challenging questions as how a long-lasting post-explosion phase where downflows to the PNS coexist with outflows of neutrino-heated matter transitions into the fallback accretion as discussed by Janka et al. (2022); the complex dynamical processes that determine the fraction of fallback matter that gets accreted by the PNS from a fallback

disk; and the efficiency of the accretion to spin-up the PNS. Our scenario should therefore be explored in more depth by more realistic fallback models.

Following its saturation, the PNS magnetic field may interact with the newly formed disk of fallback matter and is strong enough to influence the fallback accretion mechanism. We did not model this interaction because our study was focused on the phase of magnetic field amplification. Nevertheless, this could strongly influence the rotation of the newly born magnetar. The evolution of the PNS-fallback disk system depends on three characteristic radii (Metzger et al., 2018, Beniamini et al., 2020, Lin et al., 2020, Ronchi et al., 2022): (i) the magnetospheric radius $r_{\rm m}$, which is the radius at which the matter is blocked by the magnetic barrier, (ii) the corotation radius $r_{\rm c}$ where the matter has the same rotation frequency as the PNS, and (iii) the light cylinder radius $r_{\rm lc}$, which is the ratio of light speed to the PNS rotation frequency. The strong magnetic field repels the magnetosphere behind the corotation radius (i.e. $r_{\rm c} < r_{\rm m}$) which stops the accretion and so the PNS spin-up. If the fallback accretion rate of the disk is large enough, the inner part of the disk penetrates the light cylinder (i.e. $r_{\rm lc} > r_{\rm m}$) and opens up a part of the magnetic field lines. The PNS-fallback disk system enters the so-called propeller regime and the PNS angular momentum is transported towards the disk via the magnetic dipole torque. This mechanism is thought to extract the PNS angular momentum very efficiently; for instance Beniamini et al. (2020) even predict magnetars spun down to rotation periods of $\sim 10^6\,$s after $\sim 10^3\,$yr. For this reason, this scenario is often invoked to explain the ultra-long-period magnetars such as 1E 1613 (e.g. De Luca et al., 2006, Li, 2007, Rea et al., 2016) or the recently observed GLEAM-X J162759.5-523504.3 (Ronchi et al., 2022), which have rotation periods of $\sim 2.4\times10^4\,$s and $\sim 1.1\times10^3\,$s, respectively. It would be interesting to include such a spin-down model in our magnetar formation scenario in order to obtain a prediction of the rotation period at later times.

Finally, the PNS-fallback disk system has also been invoked to explain the light curve of luminous and extreme SNe of types Ib/c (e.g. Dexter & Kasen, 2013, Metzger et al., 2018, Lin et al., 2021). We may also expect our scenario to produce these types of explosions depending on the amount of accreted mass during the dynamo process. First, PNSs that have accreted $\sim 2-3\times10^{-2}\,{\rm M}_\odot$ of fallback matter before the magnetic field saturation have rotation periods of around $10-20\,$ms, which are too slow to produce extreme explosions. According to our scenario, their typical magnetic field is of $1-5\times10^{14}\,$G, which would lead to regular luminous SNe Ib/c. Their light curve would be dominated by the PNS spin-down luminosity instead of the ^{56}Ni decay luminosity (Ertl et al., 2020, Afsariardchi et al., 2021). Second, for fallback masses spinning up the PNSs to millisecond rotation periods, the magnetic field saturates a few $10\,$s after the core bounce at $B_r \gtrsim 5\times10^{14}\,$G. The rotational energy can be kept for later times and be slowly extracted to irradiate its environment, which might lead to superluminous SNe I (Woosley, 2010, Kasen & Bildsten, 2010, Bersten et al., 2016, Margalit et al., 2018, Lin et al., 2020, 2021). Finally, to produce extreme explosions such as hypernovae, which have approximately ten times larger kinetic energies and much higher ^{56}Ni yields than the vast majority of CCSNe, an energy injection within a timescale of $\lesssim 1\,$s is required (Barnes et al., 2018) to explain the large masses of ^{56}Ni $\gtrsim 0.2\,{\rm M}_\odot$ inferred from their light curves (e.g. Woosley & Bloom, 2006, Drout et al., 2011, Nomoto et al., 2011). For rotation periods of $\lesssim 1\,$ms, which correspond to rotational energies of $\gtrsim 3\times10^{52}\,$erg, our model provides a radial magnetic field of $B_r \gtrsim 2.6\times10^{16}\,$G, which may be enough to inject the energy quickly through magnetic dipole spin-down only (Suwa & Tominaga, 2015). The presence of a propeller regime would enhance the PNS spin-down such that a weaker dipolar mag-

netic field of $\sim 2 \times 10^{15}\,\mathrm{G}$ would also produce a hypernova (Metzger et al., 2018) but through a propeller-powered explosion. Therefore, our magnetic-field-amplification scenario by PNS accretion or fallback accretion may be of relevance to a wide variety of magnetar-powered phenomena in different types of SN events.

6

Tayler-Spruit dynamo: impact of the differential rotation

Contents

The previous chapter showed that our scenario is promising to form magnetars with sufficient spin-up by the fallback accretion. However, this model relies on uncertain analytical predictions based on untested physical assumptions, especially to describe the saturation of the dynamo. Three-dimensional (3D) numerical simulations are necessary for a reliable description of the strongly non-linear dynamics and the resulting magnetic field geometry. A first premliminary study has been carried out during my master internship to investigate the Tayler instability and is presented in App. B. This chapter presents the first direct numerical simulations of the Tayler-Spruit dynamo in the context of magnetar formation and investigates the impact of differential rotation on the dynamo. The following text stems from a letter published in *Monthly Notices of the Royal Astronomical Society: Letters* (Barrère et al., 2023) and was written in collaboration with Jérôme Guilet, Raphaël Raynaud, and Alexis Reboul-Salze.

6.1 . Numerical setup

We 3D direct numerical simulations of a stably stratified and electrically conducting Boussinesq fluid with the pseudo-spectral code `MagIC` (Wicht, 2002, Gastine & Wicht, 2012, Schaeffer, 2013). The fluid has a constant density $\rho = 3.8 \times 10^{14}\,\mathrm{g\,cm^{-3}}$ (which corresponds to a

proto-neutron star mass of $M = 1.4\,\mathrm{M}_\odot$) and evolves between two concentric spheres of radius $r_i = 3\,\mathrm{km}$ and $r_o = 12\,\mathrm{km}$, rotating at the angular frequencies Ω_i and $\Omega_o = 2\pi \times 100\,\mathrm{rad\,s^{-1}}$, respectively. The imposed differential rotation is characterized by the Rossby number $Ro \equiv 1 - \Omega_i/\Omega_o > 0$, which is varied between 0.125 and 1.2. This spherical Taylor-Couette configuration with positive shear prevents the development of the MRI and allows us to study the system in a statistically steady state. We impose no-slip and insulating boundary conditions at the inner and outer spheres. In all the simulations, we keep fixed the other dimensionless control parameters: the shell aspect ratio $\chi \equiv r_i/r_o = 0.25$, the thermal and magnetic Prandtl numbers $Pr \equiv \nu/\kappa = 0.1$ and $Pm \equiv \nu/\eta = 1$, respectively, the Ekman number $E \equiv \nu/(d^2\Omega_o) = 10^{-5}$, and the ratio of the Brunt-Väisälä to the outer angular frequency $N/\Omega_o = 0.1$. The coefficients ν, κ, η, and $d \equiv r_o - r_i$ are respectively the kinematic viscosity, the thermal diffusivity, the resistivity, and the shell width. As discussed in Sect. 1.3. in the Supplemental Materials, the values of the dimensionless parameters are chosen for numerical convenience because realistic parameters of proto-neutron star interiors are out of reach with the current computing power. The magnetic energy is measured by the Elsasser number $\Lambda \equiv B_{\mathrm{rms}}^2/(4\pi\rho\eta\Omega_o)$. The simulations are initialized either from a nearby saturated state, or with a weak ($\Lambda = 10^{-4}$) or a strong ($\Lambda = 10$) toroidal axisymmetric field with a given equatorial symmetry ; it can be either dipolar (i.e. equatorially symmetric[1] with $l = 2, m = 0$) or quadrupolar (i.e. anti-symmetric with $l = 1, m = 0$). We define a turbulent resistive time $\bar{\tau}_\eta = \left(\pi r_o/\bar{\ell}\right)^2/\eta \sim 0.2d^2/\eta$, where $\bar{\ell} = 10$ is the typical value of the average harmonic degree of the time-averaged magnetic energy spectrum. In the following, we will term a solution *metastable* when a steady state is sustained for a time interval $\Delta t > 0.3\bar{\tau}_\eta$,and *stable* for $\Delta t \geqslant \bar{\tau}_\eta$ (up to $5.7\bar{\tau}_\eta$ for the simulation at $Ro = 0.2$).

6.2 . Results

6.2.1 . Bifurcation diagram

We find in our set of simulations several dynamo branches represented by different colours in the bifurcation diagram shown in Fig. 7.1. When the differential rotation is low, the flow can not amplify a weak magnetic field (black crosses), but when $Ro > Ro_{\mathrm{W}}^c \sim 0.62$, the magnetic field grows exponentially to reach a metastable or a stable saturated dynamo state (black dots). This kinematic dynamo is driven by an hydrodynamic instability of the Stewartson layer whose threshold is $Ro_{\mathrm{hyd}}^c \sim 0.175$ (dashed vertical black line), which is in agreement with Hollerbach (2003). When $Ro \gtrsim 0.8$, the kinematic growth is followed by a non-linear growth and the system transitions directly to another branch with a larger magnetic energy (green circles). Restarting from a nearby saturated solution or a strong toroidal field with quadrupolar symmetry (mauve dashed arrows), we find that the stability of this branch extends to Rossby number as low as $Ro_{\mathrm{H}}^c \sim 0.37 < Ro_{\mathrm{W}}^c$, which indicates that this dynamo is subcritical. By starting from a strong toroidal field with dipolar symmetry, we observe that this subcritical branch is in bistability with another one which presents even stronger saturated magnetic fields $B_{\mathrm{rms}} \in \left[4 \times 10^{14}, 1.1 \times 10^{15}\right]$ G (red circles). This branch is also subcritical since it can be maintained for Rossby numbers as low as $Ro > Ro_{\mathrm{D}}^c \sim 0.19$.

Moreover, the two subcritical branches do not only differ by their magnetic field strength but also by their equatorial symmetry, as seen in the 3D snapshots and the surface maps

[1] For the choice of these definitions, see Gubbins & Zhang (1993).

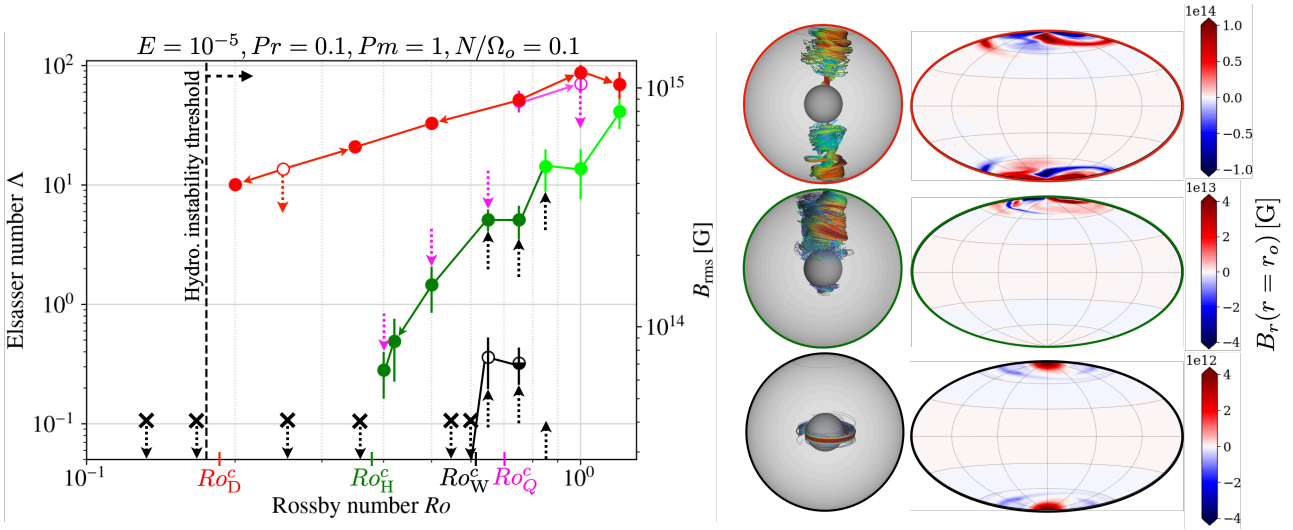

Figure 6.1 — Left: Bifurcation diagram of the time and volume averaged Elsasser number (and root mean square magnetic field) versus the Rossby number. Distinct dynamo branches are represented: dipolar (red), quadrupolar (mauve), hemispherical (green), and kinematic (black) whose respective thresholds are $Ro^c_{\rm D} \sim 0.19$, $Ro^c_{\rm Q} \sim 0.7$, $Ro^c_{\rm H} \sim 0.37$, and $Ro^c_{\rm W} \sim 0.62$. The hydrodynamic instability is triggered for $Ro^c_{\rm hyd} > 0.177$. Dark green circles are stationary hemispherical dynamos and light green ones display parity modulations. Black crosses indicate failed dynamos, empty circles metastable solutions. Arrows attached to circles indicate the initial condition of the associated simulation. The black half empty circle specifies that the solution was found to be metastable in a simulation and stable in another. The error bars indicate the standard deviation. Right: snapshots of the magnetic field lines and surface radial fields associated with the different main dynamo branches at $Ro = 0.75$: dipolar (top), hemispherical (middle), and kinematic (bottom).

of the magnetic field in Fig. 7.1. Indeed, the magnetic field shows a dipolar symmetry on the stronger dynamo branch, whereas it is hemispherical on the weaker one. The latter can be interpreted as the superposition of modes with opposite equatorial symmetry (Gallet & Pétrélis, 2009), which is consistent with the fact that we do find quadrupolar solutions (mauve circles in Fig. 7.1). These are only metastable for $Ro > Ro^c_{\rm Q} \sim 0.7$ and transition to a stable dipolar or hemispherical solution. Finally, we note that the hemispherical dynamos with $Ro \gtrsim 0.8$ (light green circles in Figs 7.1 and 6.2) display parity modulations (i.e. the solution evolves between hemispherical, dipole, and quadrupole symmetric states). This behaviour is reminiscent of the so-called Type 1 modulation identified in other dynamo setups (Knobloch et al., 1998, Raynaud & Tobias, 2016) and likely results from the coupling of modes with opposite parity as the equatorial symmetry breaking of the flow increases at larger Rossby numbers.

6.2.2 . Energy balance

The difference between the three dynamo branches is also clear in Fig. 6.2, where we see that the hemispherical branch saturates below the equipartition, with an energy ratio increasing with Ro from ~ 0.014 up to ~ 0.56. By contrast, the dynamos of the dipolar branch are in a super-equipartition state ($E_b/E_k > 1$) and follow the magnetostrophic scaling $E_b/E_k \propto Ro^{-1}$ characteristic of the Coriolis-Lorenz force balance (Roberts & Soward, 1972, Dormy, 2016, Aubert et al., 2017, Dormy et al., 2018, Augustson et al., 2019, Seshasayanan & Gallet,

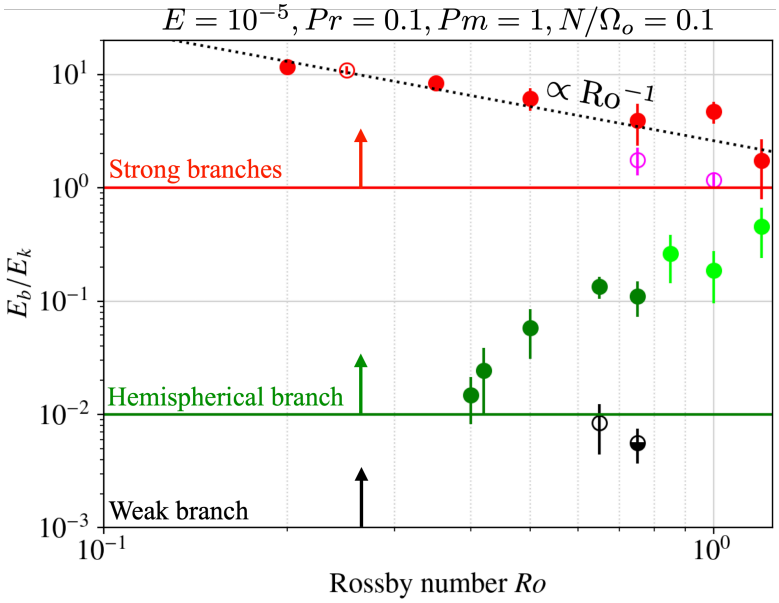

Figure 6.2 — Time-averaged ratio of the magnetic energy to the kinetic energy densities as a function of the Rossby number. The error bars indicate the standard deviation.

2019, Raynaud et al., 2020, Schwaiger et al., 2019). This is also confirmed by force balance spectra shown in Fig. S1 in the Supplemental Materials.

6.2.3 . Two Tayler instability-driven dynamos

Both subcritical dynamos show magnetic fields concentrated along the rotation axis, which differs significantly from the subcritical solutions found with a negative shear by (Petitdemange et al., 2023) ; this is also strikingly different from the magnetic field generated on the equatorial plane by the kinematic dynamo (see 3D snapshots of Fig. 7.1). This suggests that the dipolar and hemispherical dynamos are driven by a different mechanism. We argue that they are driven by the Tayler instability according to the following arguments. First, the axisymmetric toroidal magnetic component is clearly dominant since it contains $53-88\,\%$ of the total magnetic energy. Second, the simulations show a poloidal magnetic field with a dominant $m = 1$ mode (see Supplemental Materials Figs S2 and S3), which is the most unstable mode of the Tayler instability (Zahn et al., 2007, Ma & Fuller, 2019). In the azimuthal cut of the magnetic field component B_s in Fig. 6.3, the Tayler mode also appears clearly close to the poles, where it is expected to develop for a toroidal field generated by the shearing of a poloidal field (see Supplemental Materials Fig. S4). This is also consistent with the 3D snapshots of the dipolar and hemispherical branches in Fig. 7.1 where the toroidal magnetic field seems prone to a kink instability.

Third, as in Petitdemange et al. (2023), the system bifurcates from the kinematic to the hemispherical branch in the vicinity of the threshold of the Tayler instability (Spruit, 1999, 2002)

$$\Lambda_\phi^c \equiv \frac{B_\phi^{c\,2}}{4\pi\rho\eta\Omega_o} \sim \frac{\chi}{1-\chi}\frac{N}{\Omega_o}\sqrt{\frac{Pr}{E}} \sim 3.3\,. \tag{6.1}$$

Indeed, if we focus on the stable and metastable kinematic solutions found at $Ro = 0.75$, we see in Fig. 6.4 that the *local* maximum of the toroidal axisymmetric field is in both cases

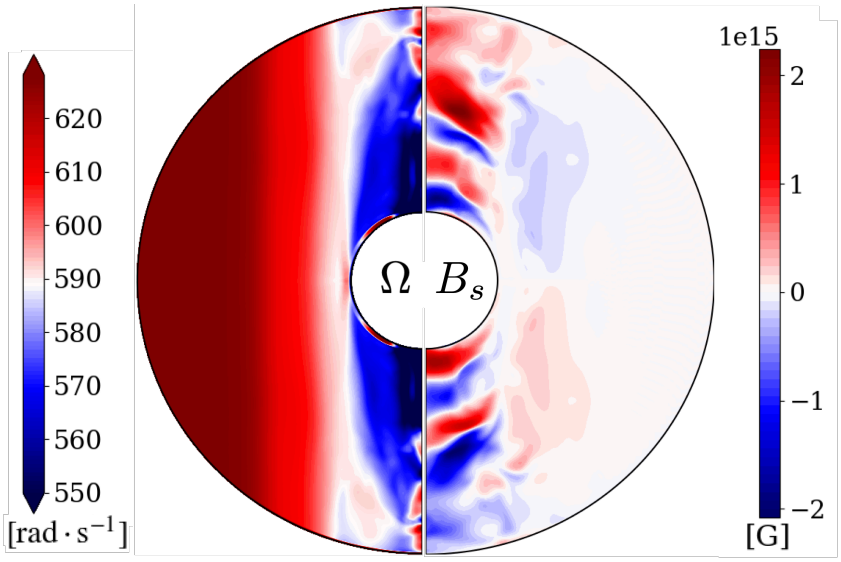

Figure 6.3 — Snapshots of the azimuthal slices of the angular velocity (left) and the magnetic field along the cylindrical radius $s \equiv r\sin\theta$ (right) of the dipolar dynamo at $Ro = 0.75$.

close to the critical value above which it is expected to become unstable. The bifurcation from the kinematic toward the hemispherical branch that is observed for the metastable solution appears hence as the result of turbulent fluctuations departing far enough above the threshold of the Tayler instability.

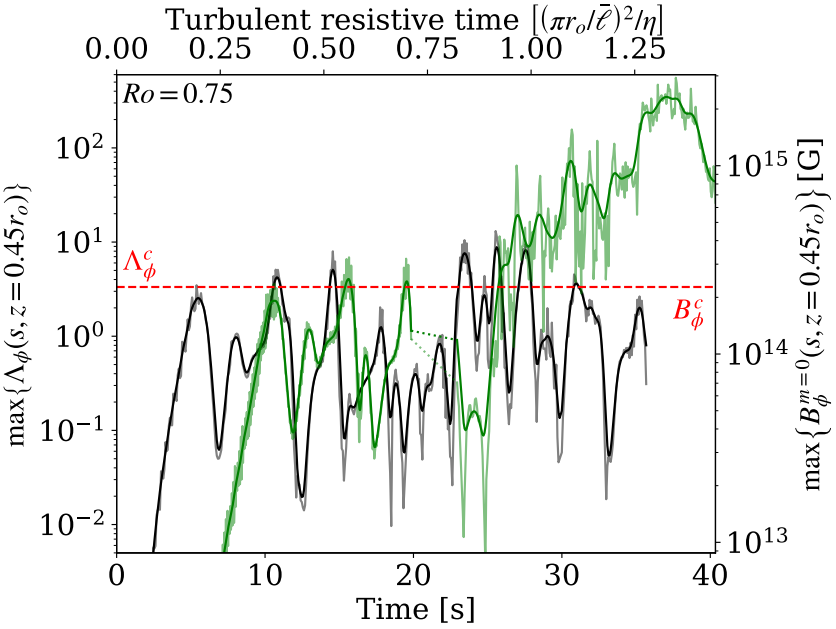

Figure 6.4 — Time series of the maximum along the cylindrical radius s of the axisymmetric toroidal magnetic energy measured locally at $z = 0.45r_o$, for stable (black) and metastable (green) kinematic dynamos at $Ro = 0.75$. The dashed red line indicates the analytical threshold of the Tayler instability (equation 6.1). Dark lines show a running average and dotted green lines around $t \sim 20\,\mathrm{s}$ indicate missing data.

6.2.4 . Magnetic field scaling laws

Finally, we compare our numerical results to the theoretical predictions regarding the saturation of the Tayler-Spruit dynamo. Note that these predictions assume the scale separation $\omega_A \ll \Omega_o \ll N$, where the Alfvén frequency is defined by $\omega_A \equiv B_\phi/\sqrt{4\pi\rho r_o^2} \sim 12.1\left(B_\phi/10^{15}\,\mathrm{G}\right)\mathrm{Hz}$. Our numerical models assume $N/\Omega_o = 0.1$ to limit the computational costs, whereas for a typ-

ical PNS spun up by fallback to a period of $1-10$ ms we expect $N/\Omega_o \sim 1-10$. On the other hand, the achieved magnetic field follows the right scale separation with $\omega_A/\Omega_o \lesssim 0.02$, which is expected to determine the saturation mechanism of the Tayler instability (Ji et al., 2023). Figure 6.5 displays the axisymmetric toroidal and poloidal magnetic fields (top), the dipole field (middle) and the Maxwell torque (bottom) as a function of an effective shear rate q measured locally in the saturated state of the dynamo (see Supplemental Materials Fig. 6.10). For the dipolar branch (red), we find that the power laws $B_{\rm tor}^{m=0} \propto q^{0.36\pm0.05}$ and $B_{\rm pol}^{m=0} \propto q^{0.62\pm0.07}$ fit the saturated magnetic field, while we find $B_s B_\phi \propto q^{1.0\pm0.02}$ or $B_s^{m=0} B_\phi^{m=0} \propto q^{1.1\pm0.04}$, depending on whether we take into account non-axisymmetric contributions to compute the Maxwell torque $T_{\rm M}$. The scaling exponents are thus in good agreement with the theoretical predictions of Fuller et al. (2019) $B_{\rm tor}^{m=0} \propto q^{1/3}$, $B_{\rm pol}^{m=0} \propto q^{2/3}$ and $T_{\rm M} \propto q$ (red dotted lines in Fig. 6.5). Contrary to their prediction, however, our torque is not dominated by the axisymmetric magnetic field, which may be related to their assumption of a stronger stratification. Interestingly, the hemispherical branch (green) does not follow the same scalings: for $q \geq 0.2$, we find $B_{\rm tor}^{m=0} \propto q^{2.1\pm0.31}$ and $B_{\rm pol}^{m=0} \propto q^{2.0\pm0.28}$ for the magnetic field, and $B_s B_\phi \propto q^{2.7\pm0.40}$ or $B_s^{m=0} B_\phi^{m=0} \propto q^{3.8\pm0.70}$ for the Maxwell torque. These results globally support Spruit's predictions (Spruit, 2002) $B_{\rm tor}^{m=0} \propto q$, $B_{\rm pol}^{m=0} \propto q^2$ and $T_{\rm M} \propto q^3$ (green dotted lines)[2]. If we focus on the dipole field, we find the following power laws: $B_{\rm dip} \propto q^{0.66\pm0.03}$ and $B_{\rm dip} \propto q^{1.1\pm0.4}$, for the dipolar and hemispherical branches, respectively. The dipole field on the strong branch therefore follows the same scaling as the axisymmetric poloidal field and is only $\sim 33\%$ weaker.

6.3 . Conclusions

To conclude, we show that the Tayler-Spruit dynamo also exists in the presence of positive shear. We demonstrate for the first time the existence of two subcritical branches of this dynamo with distinct equatorial symmetries, dipolar and hemispherical. Moreover, the former follows Fuller's theoretical predictions, while the latter is in overall agreement with Spruit's model. Compared to the study of Petitdemange et al. (2023) that use a negative shear, our results present a similar dynamical structure, with a bifurcation diagram characterized by a bistability between kinematic and subcritical dynamo solutions. The magnetic field of their Tayler-Spruit dynamo is, however, different since it is characterized by a smaller scale structure localized near the inner boundary in the equatorial plane, and induces a torque scaling according to Spruit's prediction. Our study shows a magnetic field geometry concentrated near the pole in agreement with the expectation of the Tayler-Spruit dynamo and a more complex physics, with the existence of two different branches that can not be captured by a single scaling law. Extended parameter studies will be needed to further assess the impact of the resistivity and the stratification on this dynamo instability and better constrain its astrophysical implications. Our results are of particular importance for stellar evolution models by confirming the existence of the Tayler-Spruit dynamo and by deepening our physical understanding of its complex dynamics. They also give strong support to the new magnetar formation scenario proposed by Barrère et al. (2022), which relies on the development of a Tayler-instability driven dynamo in the presence of a positive shear. We validate the as-

[2] In the case of the toroidal magnetic field, the power law index from the fit is in slight tension with the theoretical prediction. However, this tension is not very significant: it is driven mainly by a single data point and disappears if we change the threshold from $q > 0.2$ to $q > 0.25$ to exclude the model `Ro0.5as` with $q = 0.2$.

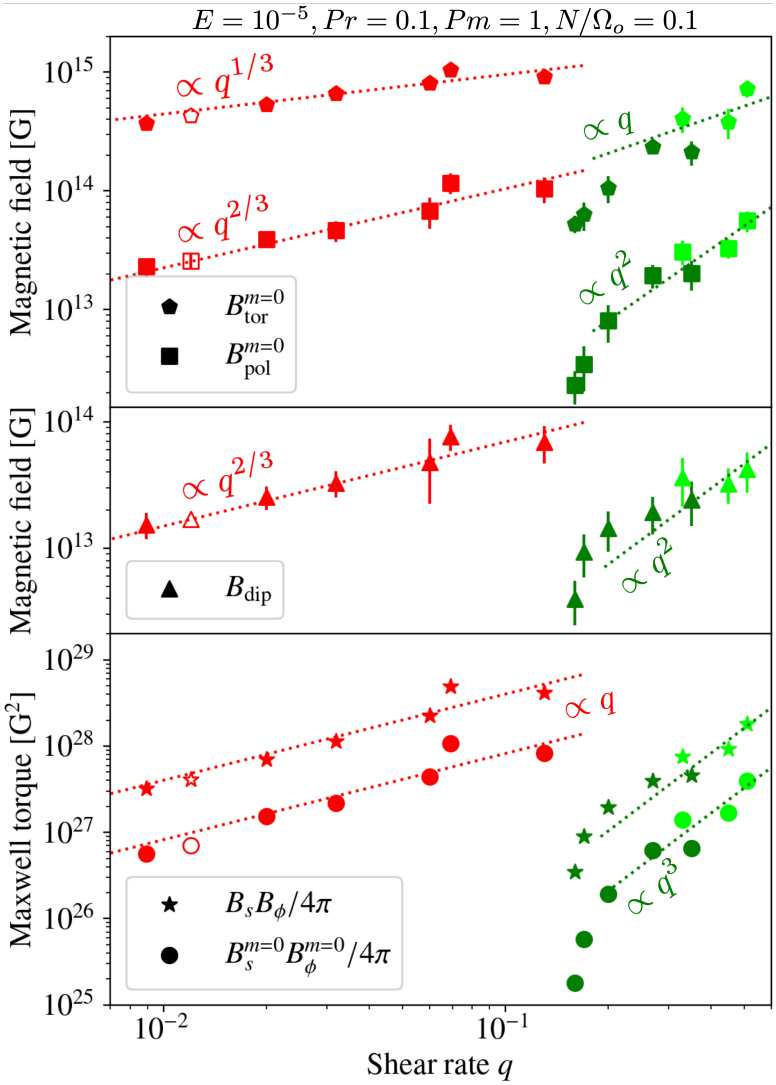

Figure 6.5 — Root mean square (RMS) toroidal and poloidal axisymmetric magnetic fields (top), RMS magnetic dipole (middle), and RMS magnetic torque (bottom) as a function of the time-averaged shear rate measured in the steady state, for the dipolar (red) and hemispherical (green) dynamo branches. Dotted lines shows the best fits obtained with Fuller's (red) and Spruit's (green) theoretical scaling laws, respectively.

sumption that the magnetic dipole is a significant fraction of the poloidal magnetic field and follows the same scaling. Extrapolating our results for the dipolar branch to $q \sim 1$ as expected in Barrère et al. (2022), we obtain a magnetic dipole intensity of $\sim 3.2 \times 10^{14}\,\mathrm{G}$ and an even stronger axisymmetric toroidal field of $\sim 2.1 \times 10^{15}\,\mathrm{G}$. These orders of magnitude are similar to those found in Barrère et al. (2022) for the same rotation period of $P_o \equiv 2\pi/\Omega_o = 10\,\mathrm{ms}$, and fall right in the magnetar range (Olausen & Kaspi, 2014).

6.4 . Additional content

In these section, we present in more details our setup and provide further analyses of the dynamo simulations (force balance, time-averaged spectra, instability criterion, shear rate).

6.4.1 . Set up

Governing equations We model the proto-neutron star differential rotation as a spherical, stably stratified Couette flow. In the reference frame rotating with the surface at the angular

velocity $\mathbf{\Omega}_o = \Omega_o \mathbf{e}_z$, the Boussinesq MHD equations read

$$\boldsymbol{\nabla} \cdot \mathbf{v} = 0\,, \tag{6.2}$$

$$D_t \mathbf{v} = -\frac{1}{\rho}\boldsymbol{\nabla} p' - 2\Omega_o \mathbf{e}_z \times \mathbf{v} + \alpha g T' \mathbf{e}_r + \frac{1}{4\pi\rho}(\boldsymbol{\nabla} \times \mathbf{B}) \times \mathbf{B} + \nu \boldsymbol{\Delta} \mathbf{v}\,, \tag{6.3}$$

$$D_t T' = \kappa \Delta T'\,, \tag{6.4}$$

$$\partial_t \mathbf{B} = \boldsymbol{\nabla} \times (\mathbf{u} \times \mathbf{B}) + \eta \Delta \mathbf{B}\,, \tag{6.5}$$

$$\boldsymbol{\nabla} \cdot \mathbf{B} = 0\,, \tag{6.6}$$

where $\mathbf{v}$ is the velocity field, $\mathbf{B}$ is the magnetic field, p' is the pressure perturbation, T' is the super-adiabatic temperature, ρ is the uniform density, $g = g_o r / r_o$ is the gravitation field, and $\alpha \equiv \rho^{-1}(\partial_T \rho)_p$ is the thermal expansion coefficient. $\mathbf{e}_z$ and $\mathbf{e}_r$ are the unit vectors of the axial and the spherical radial directions, respectively. We apply no-slip, electrically insulating, and fixed temperature boundary conditions on both shells. In the above equations, we assume that the viscosity ν, the thermal diffusivity κ and the magnetic diffusivity η are constant. Apart from the magnetic diffusivity which relates to the electrical conductivity of electrons, the physical interpretation of the other transport coefficients can lead to different estimates, depending on whether neutrinos are considered or not to be the main source of diffusive processes.

Transport coefficients In our magnetar formation scenario, the fallback occurs seconds to minutes after the PNS formation. As discussed in Barrère et al. (2022, Sect. 4.3.), at this stage of the PNS evolution, the diffusive processes are either microscopic or driven by neutrinos depending on whether the length scale l considered is smaller or larger than the neutrino mean free path (Thompson & Duncan, 1993, Eq. 11)

$$l_n \sim 4 \times 10^4 \left(\frac{\rho}{10^{14}\,\mathrm{g\,cm^{-3}}}\right)^{-1/3} \left(\frac{T}{5\,\mathrm{MeV}}\right)^{-3} \mathrm{cm}\,. \tag{6.7}$$

If the length scale satisfies $l > l_n$, then the viscosity and the thermal diffusivity are driven by neutrinos. Using the scalings of Guilet & Müller (2015, Eq. 10) and Thompson & Duncan (1993, Eq. 7), we obtain the following orders of magnitude

$$\nu_n \sim 2 \times 10^6 \left(\frac{\rho}{4 \times 10^{14}\,\mathrm{g\,cm^{-3}}}\right)^{-2} \left(\frac{T}{5\,\mathrm{MeV}}\right)^{2} \mathrm{cm^2\,s^{-1}}\,, \tag{6.8}$$

$$\kappa_n \sim 4 \times 10^{10} \left(\frac{\rho}{4 \times 10^{14}\,\mathrm{g\,cm^{-3}}}\right)^{-2/3} \left(\frac{T}{5\,\mathrm{MeV}}\right)^{-1} \mathrm{cm^2\,s^{-1}}\,. \tag{6.9}$$

If the length scale satisfies $l < l_n$, it is relevant to use a microscopic viscosity such as the shear viscosity due to neutron-neutron scattering (Cutler & Lindblom, 1987, Eq. 14)

$$\nu_s \sim 0.2 \left(\frac{\rho}{4 \times 10^{14}\,\mathrm{g\,cm^{-3}}}\right)^{5/4} \left(\frac{T}{5\,\mathrm{MeV}}\right)^{-2} \mathrm{cm^2\,s^{-1}}\,. \tag{6.10}$$

To determine the thermal diffusivity, we use the calculation of Lee (1950, Eqs. 48–54) for degenerate relativistic electrons

$$\kappa_s = \frac{\lambda}{\rho c_p} = \frac{8\pi^2 c T}{3\rho c_p}\left(\frac{3\pi^2 \rho Y_e}{m_p}\right)^{1/3}\left(\frac{k_B}{e}\right)^2 \frac{1}{4\pi\alpha \ln\Lambda}, \tag{6.11}$$

where λ is the thermal conductivity, c_p is the specific heat at constant pressure, Y_e is the electron fraction, and c is the speed of light in the vacuum. The constants k_B, e, m_p, and $\alpha \equiv e^2/(\hbar c)$ are the Boltzman constant, the electric charge, the proton mass, and the fine structure constant, respectively, and $\ln\Lambda \sim 1$ is the Coulomb logarithm. By using the formula of the specific heat for noninteracting gas of semidegenerate nucleons of Thompson & Duncan (1993)

$$\rho c_p = \left(\frac{\pi}{3}\right)^{2/3}\left(\frac{k_B}{\hbar}\right)^2 \left[f(Y_e)\right]^{-1} \rho^{1/3} m_p^{2/3} T, \tag{6.12}$$

where $f(Y_e) \equiv \left[(1-Y_e)^{1/3} + Y_e^{1/3}\right]^{-1}$, Eq. (6.11) simplifies in

$$\kappa_s = 2\pi \frac{c}{m_p \alpha \ln\Lambda}\left(\frac{\hbar}{e}\right)^2 \left[f(Y_e)\right] Y_e^{1/3} \tag{6.13}$$

$$\sim 30 \left(\frac{Y_e}{0.2}\right)^{1/3} \mathrm{cm^2\,s^{-1}}. \tag{6.14}$$

Assuming that the Wiedemann-Franz law computed by Kelly (1973, Eq. 15) for degenerate, relativistic electrons holds, the thermal diffusivuty κ_s and magnetic diffusivity η are related by

$$\kappa_s = \frac{10\pi^3}{3}\frac{T}{\rho c_p}\left(\frac{k_B}{e}\right)^2 \frac{c^2}{4\pi\eta}. \tag{6.15}$$

Therefore, the magnetic diffusitivity scales like

$$\eta = 2\times 10^{-5}\left(\frac{\rho}{4\times 10^{14}\,\mathrm{g\,cm^{-3}}}\right)^{-1/3}\left(\frac{Y_e}{0.2}\right)^{-1/3} \mathrm{cm^2\,s^{-1}}. \tag{6.16}$$

Parameter regime The above calculations enable us to estimate the different dimensionless numbers characterising the PNS fluid interior at evolution stage we are interested in. For the thermal and magnetic Prandtl numbers, we have

$$Pr \equiv \frac{\nu}{\kappa} \sim \begin{cases} 5\times 10^{-5} & \text{with} \quad \nu = \nu_n, \kappa = \kappa_n \\ 7\times 10^{-3} & \text{with} \quad \nu = \nu_s, \kappa = \kappa_s \end{cases}, \tag{6.17}$$

and

$$Pm \equiv \frac{\nu}{\eta} \sim \begin{cases} 10^{11} & \text{with} \quad \nu = \nu_n \\ 10^{4} & \text{with} \quad \nu = \nu_s \end{cases}. \tag{6.18}$$

The Ekman number can be estimated as:

$$E \equiv \frac{\nu}{r^2\Omega} \sim \begin{cases} 2\times 10^{-9} & \text{with} \quad \nu = \nu_n \\ 2\times 10^{-16} & \text{with} \quad \nu = \nu_s \end{cases}, \tag{6.19}$$

with $r = 12\,\mathrm{km}$ and $\Omega = 200\pi\,\mathrm{rad\,s^{-1}}$. Finally, the stratification of the PNS interior can be characterised by the Brunt-Väisälä frequency

$$N \equiv \sqrt{-\frac{g}{\rho}\left(\left.\frac{\partial\rho}{\partial S}\right|_{P,Y_e}\frac{dS}{dr} + \left.\frac{\partial\rho}{\partial Y_e}\right|_{P,S}\frac{dY_e}{dr}\right)} \sim 4\times 10^3\,\mathrm{s^{-1}}, \tag{6.20}$$

where S is the entropy. The above order of magnitude for N is based on the 1D core-collapse supernova simulations from Hüdepohl (2014, Chap. 5).

In all cases, these parameters are far beyond the reach of any modern supercomputer. To limit the computational time needed to complete our parameter study, we considered the following values $Pr = 0.1$, $Pm = 1$, $E = 10^{-5}$ and $N/\Omega_o = 0.1$. We leave for future work the study of the dependence on the diffusivity coefficients and strength of stratification.

Numerical methods To satisfy the solenoidal conditions (7.1) and (7.5), the velocity and magnetic fields are decomposed in poloidal and toroidal components (Mie representation),

$$\rho\mathbf{u} = \boldsymbol{\nabla}\times(\boldsymbol{\nabla}\times W\mathbf{e}_r) + \boldsymbol{\nabla}\times Z\mathbf{e}_r\,, \tag{6.21}$$

$$\mathbf{B} = \boldsymbol{\nabla}\times(\boldsymbol{\nabla}\times b\mathbf{e}_r) + \boldsymbol{\nabla}\times a_j\mathbf{e}_r\,, \tag{6.22}$$

where W and Z (b and a_j) are the poloidal and toroidal potentials for the velocity (magnetic) field. The whole system of equations is then solved in spherical coordinates by expanding the scalar potentials in Chebyshev polynomials in the radial direction, and in spherical harmonic functions in the angular directions. We refer the reader to the `MagIC` online documentation[3] for an exhaustive presentation of the numerical techniques (see also Wicht, 2002, Gastine & Wicht, 2012, Schaeffer, 2013).

Output parameters We first characterize our models by computing the time average of the kinetic and magnetic energy densities (after filtering out any initial transient). The latter is expressed in terms of the Elsasser number $\Lambda \equiv B_{\rm rms}^2/(4\pi\rho\eta\Omega_o)$ and used to compute different rms estimates of the magnetic field. In addition to the total field, we distinguish the poloidal and toroidal fields based on the Mie representation (Sect. 7.1.2), while the dipole field refers to the $l = 1$ poloidal component.

6.4.2 . Supplemental outputs

Force balance Fig. 6.6 shows a spectrum of the rms forces in the saturated state of the two Tayler-Spruit dynamo branches, following the formalism of Aubert et al. (2017), Schwaiger et al. (2019). The dipolar dynamo saturates due to a balance between the Lorentz force (red line) and the ageostrophic Coriolis force (dashed green line) at all scales (spectrum on the left in Fig. 6.6). This confirms the magnetostrophic balance we deduced from Fig. 2 in the Letter. For the hemispherical dynamo, the same balance is found at small scales ($\ell \gtrsim 20$), but at large scales the inertial force is strong enough to be in balance with the ageostrophic Coriolis force and the Lorentz force.

Time-averaged spectra A wide range of modes ℓ are present in the typical spectra of a dipolar Tayler-Spruit dynamo of Fig. 6.7. The magnetic spectrum shows the presence of a significant large-scale axisymmetric poloidal field. The even (odd) degrees ℓ dominate in the poloidal (toroidal) axisymmetric magnetic spectra, which confirms the dipolar equatorial symmetry at large scales.

The non-axisymmetric modes triggered differ depending on whether the dynamo is Tayler-instability driven, as seen in Figures 6.7 and 6.8. As expected for the Tayler-Spruit dynamo,

[3] https://magic-sph.github.io

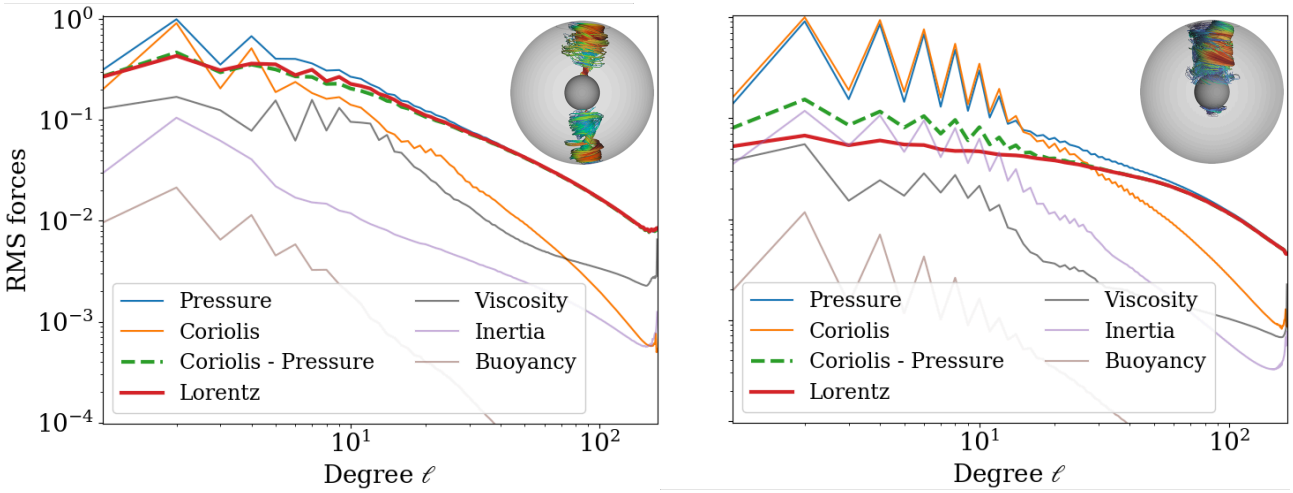

Figure 6.6 — Time-averaged rms force spectra for the dipolar (left) and hemispherical (right) dynamos at $Ro = 0.75$. The rms forces are averaged over the whole computational domain without excluding boundary layers.

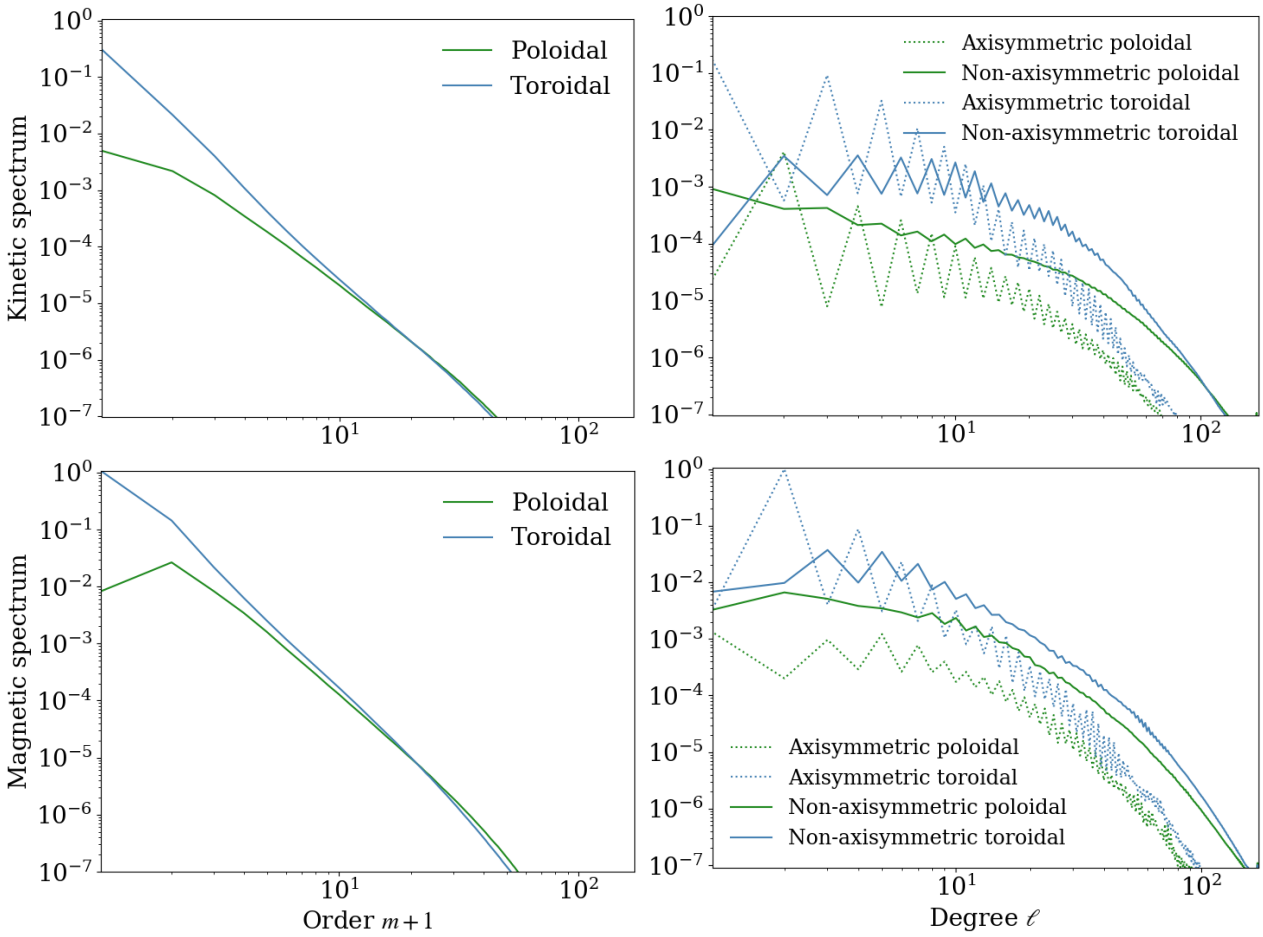

Figure 6.7 — Time averaged kinetic (top) and magnetic (bottom) energy density spectra of the dipolar Tayler-Spruit dynamo at $Ro = 0.75$.

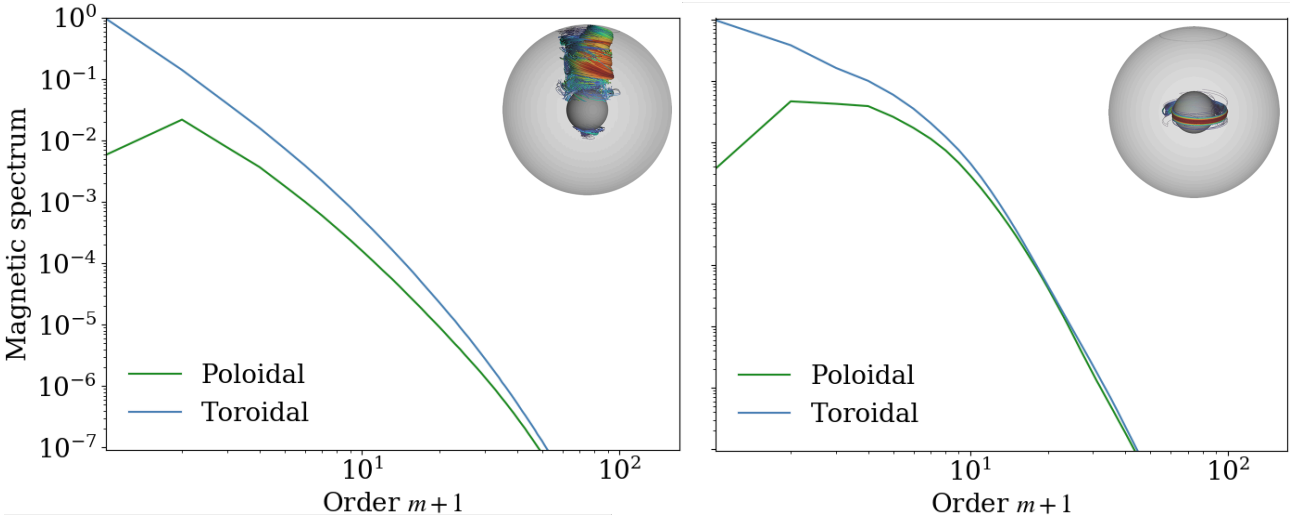

Figure 6.8 — Time averaged m-spectra of the magnetic energy density for the hemispherical Tayler-Spruit dynamo at $Ro = 0.85$ (left) and the kinematic dynamo at $Ro = 0.75$ (right).

the dominating mode is the axisymmetric toroidal magnetic field, but we also observe a dominant $m = 1$ mode in the poloidal magnetic energy, which is a signature of the Tayler instability. By contrast, we see that a wider range of orders $m \in [1,5]$ are present in the poloidal magnetic energy of the kinematic dynamo.

Geometrical criterion for Tayler instability Tayler (1973) showed that any axisymmetric toroidal field is unstable to adiabatic perturbations in ideal MHD (i.e. $\nu = \eta = 0$) in a non-rotating stratified fluid and worked out the necessary and sufficient conditions for magnetic instability (now referred to as *Tayler instability*). In spherical coordinates, they read (Goossens, 1980)

$$c_{m=0} \equiv \frac{B_\phi^2}{2\pi r^2 \sin^2\theta}\left(\cos^2\theta - \sin\theta\cos\theta\partial_\theta \log B_\phi\right) < 0\,, \tag{6.23}$$

for axisymmetric perturbations, and

$$c_{m\neq 0} \equiv \frac{B_\phi^2}{4\pi r^2 \sin^2\theta}\left(m^2 - 2\cos^2\theta - 2\sin\theta\cos\theta\partial_\theta \log B_\phi\right) < 0\,, \tag{6.24}$$

for non-axisymmetric perturbations. Since the $m = 1$ mode is the most unstable (which is consistent with our simulations), we display in Fig. 6.9 the sign of the $c_{m=1}$ coefficient superimposed with the magnetic field for a dipolar and an hemispherical dynamo. We see that in both cases the perturbed magnetic mainly develops inside the tangent cylinder, which globally matches with the areas that are expected to be unstable to the Tayler instability ($c_{m=1} < 0$). This is therefore an additional indication of the presence of the Tayler instability in our simulations.

Measure of the shear rate The differential rotation is characterized by a dimensionless shear rate $q = r\partial_r \ln\Omega$. We define an effective shear rate based on the time average of the rotation profile in the saturated state. Since it is approximately cylindrical (see Fig. 3), we measure Ω locally at a given height $z = 0.45 r_o$ and consider its variation as a function of

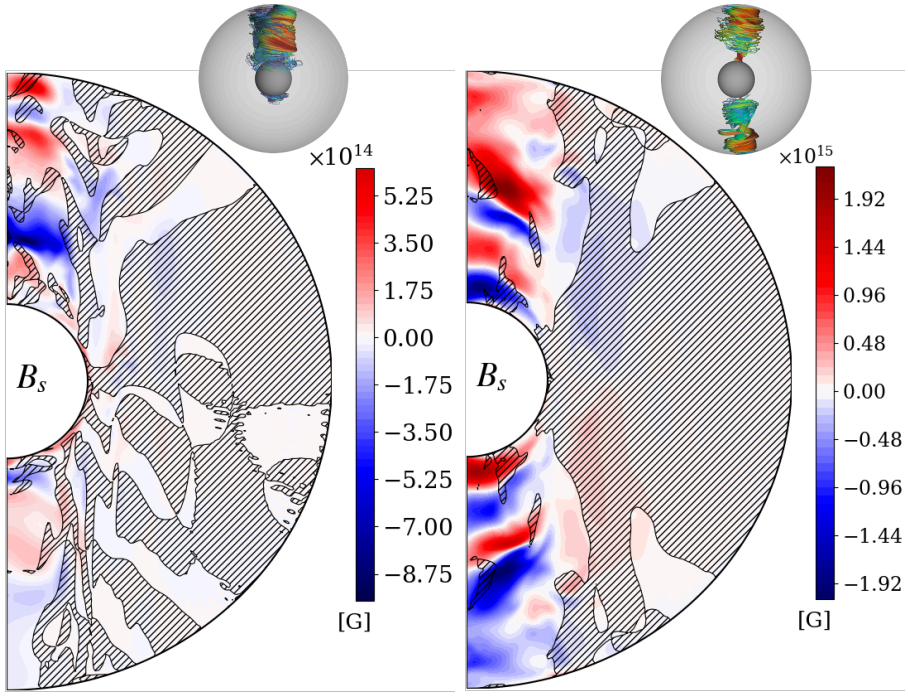

Figure 6.9 — Snapshots of the meridional slices of B_s in the runs Ro0.75w and Ro0.75s. The hatched areas correspond to the regions where the fluid is stable to $m = 1$ perturbations ($c_{m=1} > 0$).

the cylindrical radius s (see Fig. 6.10). This allows us to avoid the Ekman layers, which form around the inner shell. In most of the simulations, the shear is found in a broad region centred on the tangent cylinder, especially in $s \in [0.1, 0.5]\, r_o$. We therefore measure the average slope of the profile in this interval (see Fig. 6.10):

$$q \equiv \frac{\log\Omega(s = 0.5 r_o) - \log\Omega(s = 0.1 r_o)}{\log 0.5 r_o - \log 0.1 r_o} \tag{6.25}$$

6.4.3 . List of models

Tables 6.1 and 6.2 summarize the key parameters of the simulations carried out in this study.

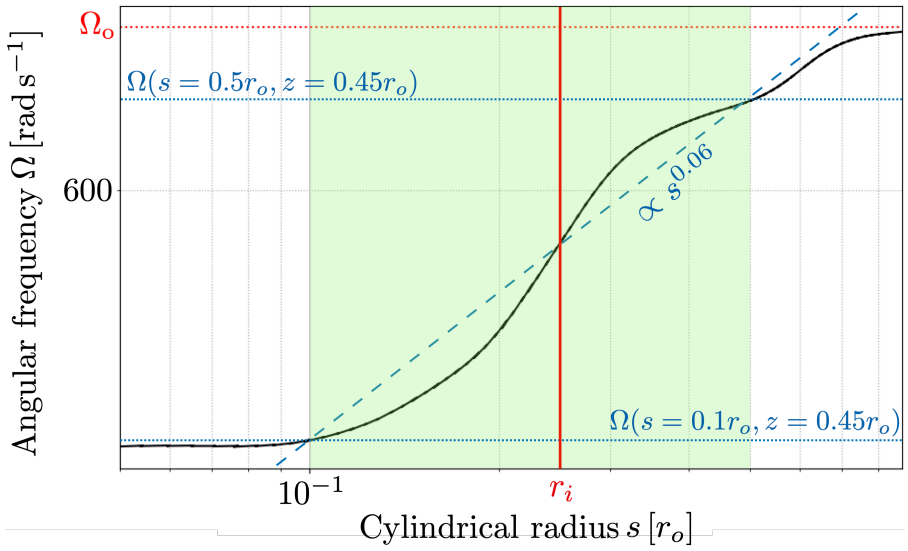

Figure 6.10 — Rotation profile $\Omega(s)$ at $z = 0.45r_o$ in the simulation Ro0.75s. The green region $s \in [0.1, 0.5]\, r_o$ is the zone where we measure the effective shear rate q (slope of the blue dashed line). In this example, $q \sim 0.06$. The vertical red line indicates the position of the tangent cylinder.

Table 6.1 — Overview of the stable (or failed) dynamos solutions. The simulations are named using the value of the Rossby number followed by a letter which characterises the initial condition: 's' for a strong dipole-like magnetic field (either analytic or from a saturated state of the dipolar branch), 'as' for a strong quadrupole-like field (analytic or from a saturated state of the quadrupolar branch), 'h' for the saturated state of the hemispherical branch, 'k' for a saturated state of the kinematic dynamo, and 'w' for a very weak seed field. The second column indicates the input Rossby number. The third column refers to the initial Elsasser number. The last column specifies the type of the dynamo solution: dipolar (DIP), quadrupolar (QUAD), hemispherical (HEM), oscillating (OSC), kinematic (WEAK), non dynamo (NONE). All the simulations have the same aspect ratio $\chi = 0.25$, Ekman number $E = 10^{-5}$, stratification $N/\Omega_o = 0.1$, thermal and magnetic Prandtl numbers $Pr = 0.1$ and $Pm = 1$, and the same resolution $(n_r, n_\theta, n_\phi) = (256, 256, 512)$.

Name	Ro	Λ_i	q	Λ	E_b/E_k	$B_{\rm tor}^{m=0}$ $[10^{14}\,{\rm G}]$	$B_{\rm pol}^{m=0}$ $[10^{14}\,{\rm G}]$	$B_{\rm dip}$ $[10^{14}\,{\rm G}]$	$B_s B_\phi/4\pi$ $[10^{27}\,{\rm G}^2]$	$B_r B_\phi/4\pi$ $[10^{27}\,{\rm G}^2]$	$B_s^{m=0} B_\phi^{m=0}/4\pi$ $[10^{27}\,{\rm G}^2]$	$B_r^{m=0} B_\phi^{m=0}/4\pi$ $[10^{27}\,{\rm G}^2]$	Dynamo
Ro1.2s	1.2	Λ(Ro1s)	0.13	70.11	1.73	9.16	1.04	0.70	41.97	45.70	8.31	25.11	DIP
Ro1s	1	Λ(Ro0.75s)	0.069	87.83	4.74	10.46	1.17	0.77	49.37	53.33	10.80	30.60	DIP
Ro0.75s	0.75	10	0.06	51.85	3.93	8.08	0.68	0.48	22.57	21.10	4.43	10.24	DIP
Ro0.5s	0.5	Λ(Ro0.75s)	0.032	33.06	6.16	6.65	0.46	0.33	11.31	9.84	2.20	4.02	DIP
Ro0.35s	0.35	Λ(Ro0.25s)	0.02	20.87	8.36	5.34	0.39	0.25	7.01	6.39	1.53	2.80	DIP
Ro0.2s	0.2	Λ(Ro0.25s)	0.0089	10.16	11.67	3.70	0.23	0.15	3.22	2.91	0.56	1.27	DIP
Ro0.17s	0.17	Λ(Ro0.25s)	–	–	–	–	–	–	–	–	–	–	NONE
Ro0.125s	0.125	Λ(Ro0.25s)	–	–	–	–	–	–	–	–	–	–	NONE
Ro1as	1	Λ(Ro0.75as)	0.45	13.75	0.19	3.83	0.33	0.32	9.28	7.64	1.68	2.66	HEM
Ro0.75as	0.75	10	0.064	58.22	4.46	8.71	0.67	0.58	21.77	20.47	4.18	10.01	DIP
Ro0.65as	0.65	Λ(Ro0.75as)	0.27	5.15	0.13	2.34	0.19	0.19	3.94	3.13	0.62	0.93	HEM
Ro0.5as	0.5	Λ(Ro0.75as)	0.2	2.32	0.09	1.50	0.11	0.17	2.49	1.73	0.31	0.33	HEM
Ro0.4as	0.4	Λ(Ro0.75as)	0.16	0.28	0.01	0.53	0.02	0.04	0.35	0.27	0.02	0.04	HEM
Ro1.2h	1.2	Λ(Ro1k)	0.51	41.35	0.45	7.28	0.56	0.43	18.27	16.40	3.98	6.90	OSC
Ro0.42h	0.42	Λ(Ro0.5k)	0.17	0.49	0.02	0.63	0.03	0.09	0.89	0.70	0.06	0.07	HEM
Ro1k	1	Λ(Ro0.75w)	0.43	16.68	0.24	4.37	0.34	–	8.71	7.30	1.45	2.62	OSC
Ro0.5k	0.5	Λ(Ro0.75w)	0.2	1.46	0.06	1.06	0.08	0.14	1.96	1.35	0.19	0.22	HEM
Ro0.85w	0.85	10^{-4}	0.33	14.32	0.26	4.07	0.31	0.36	7.58	6.56	1.41	2.57	OSC
Ro0.75w	0.75	10^{-4}	0.35	5.12	0.11	2.13	0.20	0.24	4.59	3.50	0.65	1.00	HEM
Ro0.75w2	0.75	10^{-4}	0.34	0.37	0.01	0.52	0.03	0.08	1.44	1.26	0.06	0.06	KIN
Ro0.65w	0.65	10^{-4}	0.27	4.87	0.13	2.16	0.18	–	3.93	3.11	0.60	0.87	HEM
Ro0.63w	0.63	10^{-4}	–	–	–	–	–	–	–	–	–	–	NONE
Ro0.6w	0.6	10^{-4}	–	–	–	–	–	–	–	–	–	–	NONE
Ro0.55w	0.55	10^{-4}	–	–	–	–	–	–	–	–	–	–	NONE
Ro0.35w	0.35	10^{-4}	–	–	–	–	–	–	–	–	–	–	NONE

Table 6.2 — Same as Table 6.1 but for the metastable solutions.

Name	Ro	Λ_i	q	Λ	E_b/E_k	$B_{\rm tor}^{m=0}$ $[10^{14}\,{\rm G}]$	$B_{\rm pol}^{m=0}$ $[10^{14}\,{\rm G}]$	$B_{\rm dip}$ $[10^{14}\,{\rm G}]$	$B_s B_\phi/4\pi$ $[10^{27}\,{\rm G}^2]$	$B_r B_\phi/4\pi$ $[10^{27}\,{\rm G}^2]$	$B_s^{m=0} B_\phi^{m=0}/4\pi$ $[10^{27}\,{\rm G}^2]$	$B_r^{m=0} B_\phi^{m=0}/4\pi$ $[10^{27}\,{\rm G}^2]$	Dynamo
Ro1as	1	Λ(Ro0.75as)	0.45	70.52	1.18	9.71	0.68	0.47	–	–	–	–	HEM
Ro0.75as	0.75	10	0.064	50.94	1.77	8.13	0.59	0.51	–	–	–	–	DIP
Ro0.75w	0.75	10^{-4}	0.35	0.32	0.01	0.50	0.03	0.08	–	–	–	–	HEM
Ro0.65w	0.65	10^{-4}	0.27	0.36	0.01	0.44	0.03	–	–	–	–	–	HEM
Ro0.25s	0.25	Λ(Ro0.5s)	0.012	13.60	10.90	4.28	0.26	0.17	4.15	3.59	0.70	1.36	DIP

7

Tayler-Spruit dynamo: impact of the stable stratification

Contents

The first numerical simulations of the Tayler-Spruit demonstrated the capacity of the Tayler-Spruit dynamo to produce magnetar-like magnetic fields with a dominant axisymmetric toroidal component. While we varied the forcing for the differential rotation, we kept the ratio of the Brunt-Väisälä frequency to the outer angular rotation frequency constant at $N/\Omega_o = 0.1$. However, the measure of N in one-dimensional core-collapse supernova simulations suggests that this ratio can span a wide range of values $N/\Omega_o \in [0.1, 10]$. In this chapter, we therefore investigate the impact of higher values of N/Ω_o on the dipolar branch of the Tayler-Spruit dynamo, which is the most relevant for magnetars. The following text has been prepared in collaboration with Jérôme Guilet, Raphaël Raynaud, and Alexis Reboul-Salze for submission in *Astronomy & Astrophysics*.

7.1 . Numerical setup

7.1.1 . Governing equations

As in Barrère et al. (2023), we model the PNS interior as a stably stratified and electrically conducting fluid. We also adopt the Boussinesq approximation and consider a fluid with a constant density $\rho = 3.8 \times 10^{14}\,\mathrm{g\,cm^{-3}}$, which corresponds to a PNS with a radius of $r_o = 12\,\mathrm{km}$ and a mass of $M = 1.4\,\mathrm{M_\odot}$. The fluid evolves in a spherical Taylor-Couette configuration, i.e. between two concentric spheres of radius $r_i = 3\,\mathrm{km}$ and r_o which rotates with the respective rates $\Omega_i = 2\pi \times 25\,\mathrm{rad\,s^{-1}}$ and $\Omega_o = 2\pi \times 100\,\mathrm{rad\,s^{-1}}$. In the reference frame rotating with the surface at the angular velocity $\Omega_o = \Omega_o \mathbf{e}_z$, the Boussinesq MHD equations read

$$\nabla \cdot \mathbf{v} = 0, \tag{7.1}$$

$$D_t \mathbf{v} = -\frac{1}{\rho}\nabla p' - 2\Omega_o \mathbf{e}_z \times \mathbf{v} - N^2 \Theta \mathbf{e}_r + \frac{1}{4\pi\rho}(\nabla \times \mathbf{B}) \times \mathbf{B} + \nu \Delta \mathbf{v}, \tag{7.2}$$

$$D_t \Theta = \kappa \Delta \Theta, \tag{7.3}$$

$$\partial_t \mathbf{B} = \nabla \times (\mathbf{u} \times \mathbf{B}) + \eta \Delta \mathbf{B}, \tag{7.4}$$

$$\nabla \cdot \mathbf{B} = 0, \tag{7.5}$$

where $\mathbf{B}$ is the magnetic field, $\mathbf{v}$ is the velocity field, p' is the non-hydrostatic pressure, ρ is the mean density of the PNS, $g = g_o r / r_o$ is the gravitation field, and $\alpha \equiv \rho^{-1}(\partial_T \rho)_p$ is the thermal expansion coefficient. $\mathbf{e}_z$ and $\mathbf{e}_r$ are the unit vectors of the axial and the spherical radial directions, respectively. θ is the buoyancy variable defined by

$$\Theta \equiv -\frac{g}{N^2}\frac{\rho'}{\rho}, \tag{7.6}$$

where ρ' is the density perturbation due to the combined effect of the electron fraction and entropy perturbations and

$$N \equiv \sqrt{-\frac{g}{\rho}\left(\left.\frac{\partial \rho}{\partial S}\right|_{P,Y_e}\frac{dS}{dr} + \left.\frac{\partial \rho}{\partial Y_e}\right|_{P,S}\frac{dY_e}{dr}\right)}, \tag{7.7}$$

is the Brunt-Väisälä frequency with the electron fraction Y_e, and the entropy S, respectively.

In the above equations, we assume that the magnetic diffusivity η, the kinematic viscosity ν, and the "thermal" diffusivity κ are constant. We also assume that the thermal and

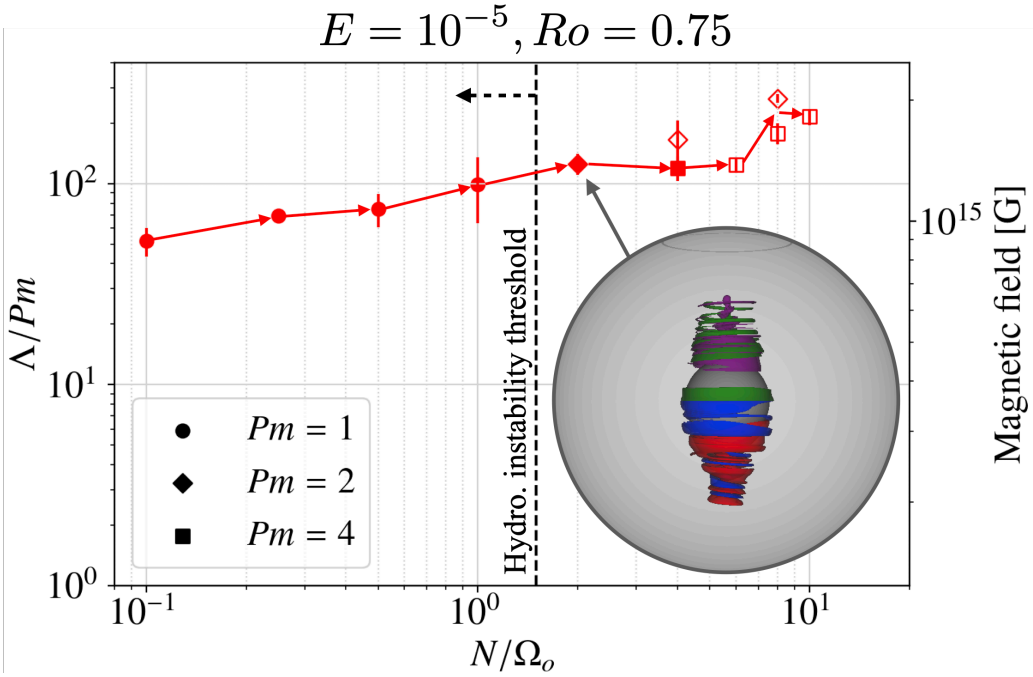

Figure 7.1 — Viscous Elsasser number (and root mean square magnetic field) as a function of the ratio of the Brunt-Väisälä frequency to the rotation rate at the outer sphere. Filled and empty markers represent self-sustained and transient dynamos, respectively. The black dashed vertical line and arrow indicate the zone in which the fluid is hydrodynamically unstable. The inset represents a 3D plot of the radial velocity (violet and green isosurfaces are the positive and negative values, respectively) and the radial magnetic field (red and blue isosurfaces are the positive and negative values, respectively) in a run at $Pm = 2$ and $N/\Omega_o = 2$. The grey arrow points to the run location in the diagram.

lepton number diffusivities are equal, which allows us to describe the buoyancy associated with both entropy and lepton number gradients with the use of a single buoyancy variable θ (Guilet et al., 2015).

Apart from the magnetic diffusivity which relates to the electrical conductivity of electrons, the physical interpretation of the other transport coefficients can lead to different estimates, depending on whether neutrinos are considered or not to be the main source of diffusive processes (see Sect. 1.3 of the supplementary materials in Barrère et al., 2023).

Finally, we apply no-slip, electrically insulating, and fixed buoyancy variable boundary conditions on both shells.

7.1.2 . Numerical methods

We use the open source pseudo-spectral code MagIC[1] (Wicht, 2002, Gastine & Wicht, 2012, Schaeffer, 2013) to integrate Eqs. (7.1)–(7.5) in 3D spherical geometry. To satisfy the solenoidal conditions (7.1) and (7.5), the velocity and magnetic fields are decomposed in poloidal and toroidal components (Mie representation),

$$\rho\mathbf{u} = \nabla \times (\nabla \times W\mathbf{e}_r) + \nabla \times Z\mathbf{e}_r\,, \tag{7.8}$$

$$\mathbf{B} = \nabla \times (\nabla \times b\mathbf{e}_r) + \nabla \times a_j\mathbf{e}_r\,, \tag{7.9}$$

[1] Commit 2266201a5 on https://github.com/magic-sph/magic

where W and Z (b and a_j) are the poloidal and toroidal potentials for the velocity (magnetic) field. The whole system of equations is then solved in spherical coordinates by expanding the scalar potentials in Chebyshev polynomials in the radial direction, and spherical harmonic functions in the angular directions. The time-stepping scheme used is the implicit/explicit Runge-Kutta BPR353 (Boscarino et al., 2013). We refer the reader to the MagIC online documentation[2] for an exhaustive presentation of the numerical techniques.

7.1.3 . Input parameters

The resistivity is controlled by the magnetic Prandtl number $Pm \equiv \nu/\eta$. Though its realistic value in PNSs ($Pm \sim 10^{11}$, Barrère et al., 2023) can not be reached by numerical simulations, we stay in the regime $Pm \geqslant 1$ as we impose $Pm \in [1,4]$. We keep fixed the other dimensionless control parameters: the shell aspect ratio $\chi \equiv r_i/r_o = 0.25$ and width $d \equiv r_o - r_i$, the Ekman number $E \equiv \nu/(d^2\Omega_o) = 10^{-5}$, the thermal Prandtl numbers $Pr \equiv \nu/\kappa = 0.1$, and the Rossby number $Ro \equiv 1 - \Omega_i/\Omega_o = 0.75$, which controls the imposed differential rotation.

The imposed stable stratification is characterized by the Brunt-Väisälä frequency N (Eq. (7.7)). In our parameter study, the ratio N/Ω_o is varied between 0.1 and 10 and so covers the PNS regime. In practice, this ratio is related to the Rayleigh number $Ra \equiv -(N/\Omega)^2 Pr/E^2$, which is negative in the regime of stable stratification.

The resolution is fixed at $(n_r, n_\theta, n_\phi) = (257, 256, 512)$ for all the runs. A few simulations were rerun with a higher resolution of $(n_r, n_\theta, n_\phi) = (481, 512, 1024)$ but showed no significant change compared to runs with the usual resolution (see Appendix).

The simulations are initialized either from a nearby saturated state or a strong ($B_\phi = 3.4 \times 10^{14}\,\mathrm{G}$) toroidal axisymmetric field with a dipolar equatorial symmetry, i.e. equatorially symmetric[3] with $l = 2, m = 0$. We define a turbulent resistive time $\bar{\tau}_\eta = \left(\pi r_o/\bar{\ell}\right)^2/\eta \sim 0.2 d^2/\eta$, where $\bar{\ell} = 10$ is the typical value of the average harmonic degree of the time-averaged magnetic energy spectrum. In the following, we will term a solution 'transient' when a steady state is sustained for a time interval $\Delta t > 0.3\bar{\tau}_\eta$, and 'stable' for $\Delta t \geqslant \bar{\tau}_\eta$.

We start with the run named 'Ro0.75s' from Barrère et al. (2023), where the stratification is $N/\Omega_o = 0.1$. The saturated state of this dynamo is used to initialise the next simulation with a stronger stratification. The whole set of simulations is initiated similarly using the nearby saturated state of a less stratified run. With this procedure, N/Ω_o is increased gradually in order to study the evolution of the dynamo branch.

7.1.4 . Output parameters

We first characterize our models by computing the time average of the kinetic and magnetic energy densities (after filtering out any initial transient). The latter is expressed in terms of the viscous Elsasser number $\Lambda_\nu \equiv \Lambda/Pm = B_{\mathrm{rms}}^2/(4\pi\rho\nu\Omega_o)$ and used to compute different root-mean-square (RMS) estimates of the magnetic field. In addition to the total field, we distinguish the poloidal and toroidal fields based on the Mie representation (Sect. 7.1.2), while the dipole field refers to the $l = 1$ poloidal component.

7.2 . Results

[2] https://magic-sph.github.io

[3] For the choice of these definitions, see Gubbins & Zhang (1993).

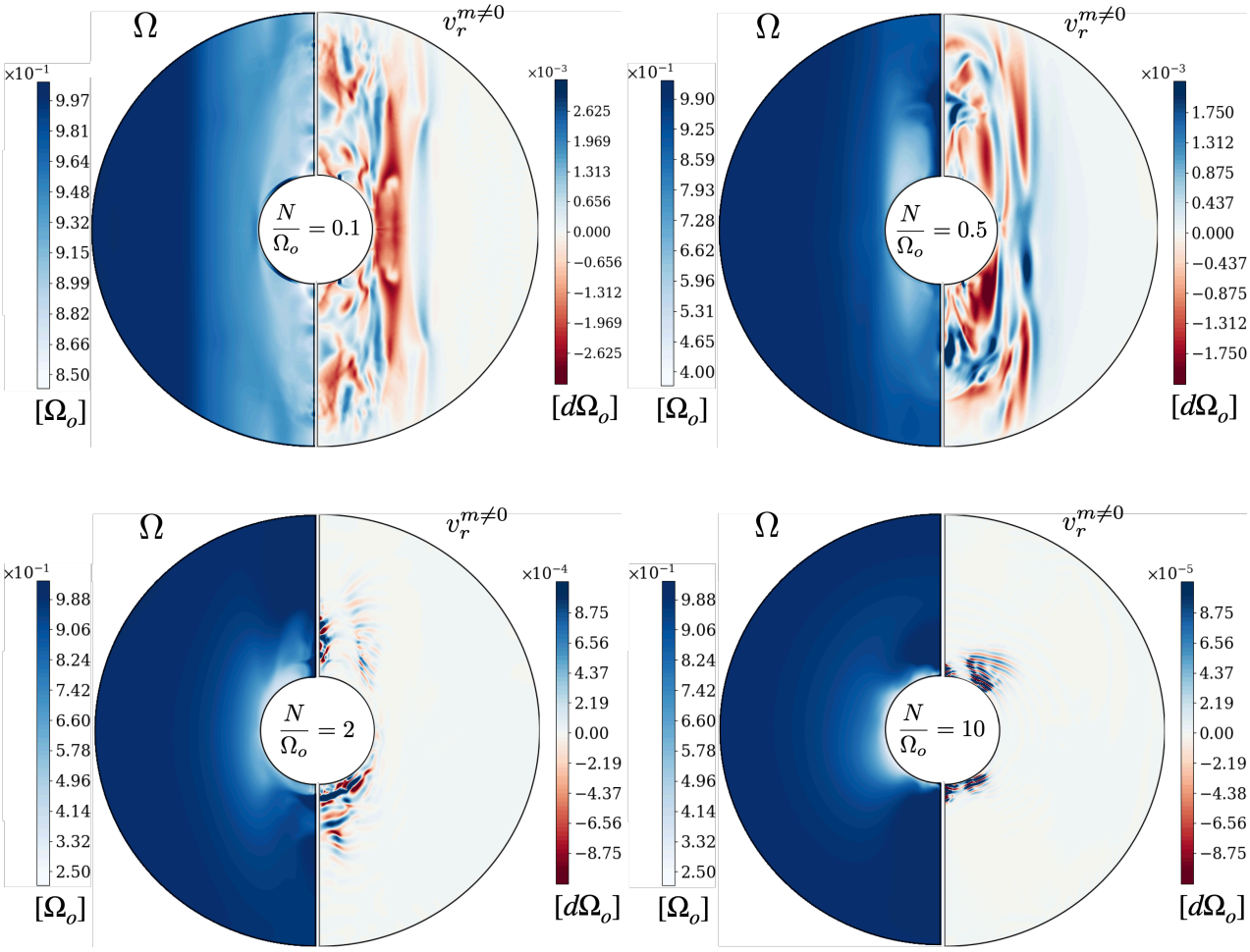

Figure 7.2 — Meridional slices of the angular frequency and the non-axisymmetric radial velocity (left and right slices respectively) for different values of N/Ω_o. Ω and $v_r^{m\neq0}$ are scaled by Ω_o and $d\Omega_o$, respectively.

The following sections gather the different results we obtain from the set of numerical simulations listed in appendix 7.6.2. We first describe the global dynamics of the dipolar Tayler-Spruit dynamo in the parameter space in Sect. 7.2.1. Then, we analyse the influence of stratification on the modes of Tayler instability and on the generated axisymmetric magnetic fields in their saturated state in Sect. 7.2.3 and Sect. 7.2.4, respectively. We also present the angular momentum transport by both Reynolds and Maxwell stresses due to the dynamo and compare the efficiencies of mixing and angular momentum transport in Sect. 7.2.5. Finally, we examine a new intermittent behaviour of the Tayler-Spruit dynamo at $N/\Omega_o \geq 2$, which is observed for the first time (see Sect. 7.2.6).

7.2.1 . Subcritical dynamo sustained at PNS-like stratifications

Fig. 7.1 shows that a self-sustained Tayler-Spruit dynamo can be maintained up to $N/\Omega_o = 1$ for $Pm = 1$. For stronger stratifications, we have to increase Pm (i.e. decrease the resistivity) to maintain the dynamo. For $Pm = 4$, the stationary state is self-sustained up to $N/\Omega_o = 4$ and we obtained transient states up to $N/\Omega_o = 10$. The self-sustained dynamo is therefore present above the threshold for the fluid to be hydrodynamically stable at $N/\Omega_o \sim 1.5$. This confirms the subcritical nature of the Tayler-Spruit dynamo, which was already observed in previous studies (Petitdemange et al., 2023, Barrère et al., 2023). We did not simulate fluids at greater Pm values for reasons of numerical costs. Given the trend with Pm observed in our simulations as well as theoretical expectations on the Tayler instability threshold, we would expect the Tayler-Spruit dynamo to exist at still higher values of N/Ω for the higher values of Pm relevant to a PNS.

7.2.2 . Impact on the differential rotation

The meridional slices of the angular rotation frequency Ω illustrate the impact of stable stratification on the rotation profile: we see that the shear concentrates closer to the inner sphere and increases with N/Ω_o. At the same time, the rotation profile smoothly transits from a quasi-cylindrical to a spherical geometry, which is an effect already observed in stably stratified flows. Analytical and numerical studies of these flows (e.g. Barcilon & Pedlosky, 1967a,b,c, Gaurat et al., 2015, Philidet et al., 2020) indicate that this transition is controlled by the dimensionless parameter $Q \equiv Pr(N/\Omega_o)^2$, which varies between 10^{-3} and 10 in our set of runs. The change in the flow geometry is therefore explained by a transition from a case where neither the rotation nor the buoyancy dominate ($E^{2/3} < Q < 1$) to a buoyancy-dominated flow ($Q \gg 1$).

7.2.3 . Impact on the Tayler modes

As seen in Fig. 7.3, the unstable magnetic modes are located close to the poles where the latitudinal gradient of B_ϕ is positive, which is a first indication of the presence of Tayler modes. To confirm this statement, we use the geometrical criterion of Goossens & Tayler (1980) for the stability of $m = 1$-modes,

$$B_\phi^2\left(1-2\cos^2\theta\right) - \sin\theta\cos\theta\frac{\partial B_\phi^2}{\partial\theta} > 0\,. \tag{7.10}$$

The stability regions displayed by the hatched zones in Fig. 7.3 match very well regions where the unstable modes are absent. This confirms that the Tayler instability is clearly identifiable, no matter the values of N/Ω_o.

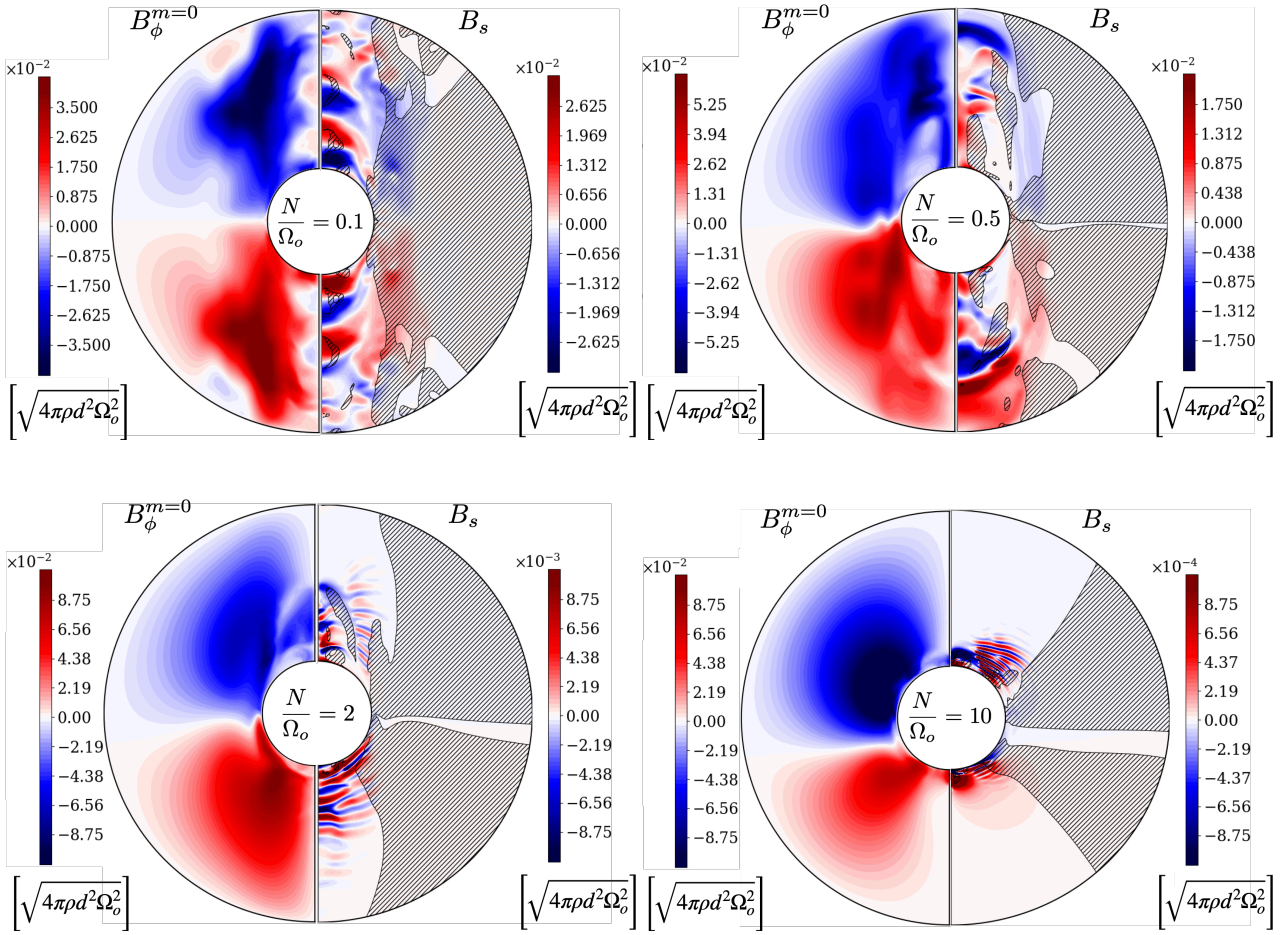

Figure 7.3 — Meridional slices of the axisymmetric azimuthal and the $s = r\sin\theta$-component of the magnetic field (respective left and right slices) for increasing values of N/Ω_o. The magnetic field is scaled by $\sqrt{4\pi\rho d^2\Omega_o^2}$. The hatched regions represent Tayler-stable zones defined by the geometrical criterion of Goossens & Tayler (1980) (see Supplementary Materials in Barrère et al. (2023)).

Moreover, the impact of stratification on the mode structure is striking. The stable stratification tends to stabilise displacements in the radial direction, as we can see looking at the non-axisymmetric radial velocity $v_r^{m\neq0}$ field in Fig. 7.2. As a consequence, the radial length scale of the instability strongly decreases for increasing values of N/Ω_o. This feature is not surprising because Spruit (1999) already constrained the mode maximum radial length scale

$$l_{\rm TI} < l_{{\rm max},N} \equiv r\frac{\omega_{\rm A}}{N}, \tag{7.11}$$

where $\omega_{\rm A} \equiv B_\phi^{m=0}/\sqrt{4\pi\rho r^2}$ is the Alfvén frequency. Note that a lower limit due to resistivity is also predicted

$$l_{\rm TI}^2 > l_{\rm min}^2 \equiv \frac{\eta\Omega_o}{\omega_{\rm A}^2}. \tag{7.12}$$

The length scales measured in our models are compared to these constraints in Fig. 7.4. Since thermal diffusion can mitigate the effect of stratification, we also define an effective Brunt-Väisälä frequency

$$N_{\rm eff} \equiv N\sqrt{\eta/\kappa} = N\sqrt{Pr/Pm} \tag{7.13}$$

and so

$$l_{{\rm max},N_{\rm eff}} \equiv r\frac{\omega_{\rm A}}{N_{\rm eff}} \tag{7.14}$$

to take this effect into account (Spruit, 2002). The Tayler modes in our simulations have length scales ranging from $r_o/4 = 3\,{\rm km}$ at $N/\Omega_o = 0.1$ to $r_o/80 = 0.15\,{\rm km}$ at $N/\Omega_o = 10$. This implies that the Tayler-Spruit dynamo requires higher and higher resolutions at greater stratifications to be resolved. The measured $l_{\rm TI}$ follows very well the upper limit $l_{{\rm max},N_{\rm eff}}$ (red points in Fig. 7.4), but is around one order of magnitude larger than $l_{{\rm max},N}$. This demonstrates the importance of including the mitigation of the stratification by diffusion. The minimum length scale $l_{\rm min}$ (Eq. (7.12)) is almost equal to $l_{\rm TI}$ from $N/\Omega_o = 0.5$ to $N/\Omega = 4$, which indicates that we are close to the instability threshold. For $N/\Omega_o \geqslant 6$, however, $l_{\rm min} \sim 2l_{{\rm max},N_{\rm eff}} \sim 2-3l_{\rm TI}$. The fluid is therefore stable, which is consistent with the transient state we find in our simulations. Thus, the analytical limits for the Tayler modes to develop are validated by our numerical simulations and suggest that the Tayler-Spruit dynamo could be maintained for $N/\Omega_o \in [6,10]$ with $Pm \gtrsim 16-36$.

In addition to the decrease of $l_{\rm TI}$, the Tayler instability modes are strongly affected by high values of N/Ω_o. The time and volume averaged spectrum of the magnetic energy in Fig. 7.5 show that the energy of the large-scale ($l = 1-10$) non-axisymmetric modes (solid lines) drop by two orders of magnitude between $N/\Omega = 0.25$ and at $N/\Omega = 2$ compared to the energy of the dominant axisymmetric toroidal component (blue dotted line). This difference is represented more quantitatively by comparing the total non-axisymmetric magnetic field $B_{\rm tot}^{m\neq0}$ to $B_\phi^{m=0}$ in Fig. 7.6. The ratio drops from ~ 1 to $\sim 2\times10^{-3}$ and follows a power law $B_{\rm tot}^{m\neq0}/B_\phi^{m=0} \propto N_{\rm eff}/\Omega_o^{-1.8\pm0.1}$. Fuller et al. (2019) analytically derived that the ratio between the magnetic field generated by the Tayler instability (noted $\delta B_\perp \sim B_{\rm tot}^{m\neq0}$) and $B_\phi^{m=0}$ follows $\omega_{\rm A}/\Omega_o$. Since $\omega_{\rm A} \propto N_{\rm eff}/\Omega_o^{-1/3}$ (Fuller et al., 2019, and our Sect. 7.2.4), our simulations therefore do not match the analytical prediction. Fuller et al. (2019) derived the ratio by equating the Tayler instability growth rate and a turbulent damping rate $\omega_{\rm A}^2/\Omega_o \sim \delta v_{\rm A}/r$, where $\delta v_{\rm A} \equiv \delta B_\perp/\sqrt{4\pi\rho}$. As the growth rate of the Tayler instability is robust (Zahn et al., 2007, Ma & Fuller, 2019) and well verified in numerical simulations (Ji et al., 2023), our study then questions the prediction of the turbulent damping rate.

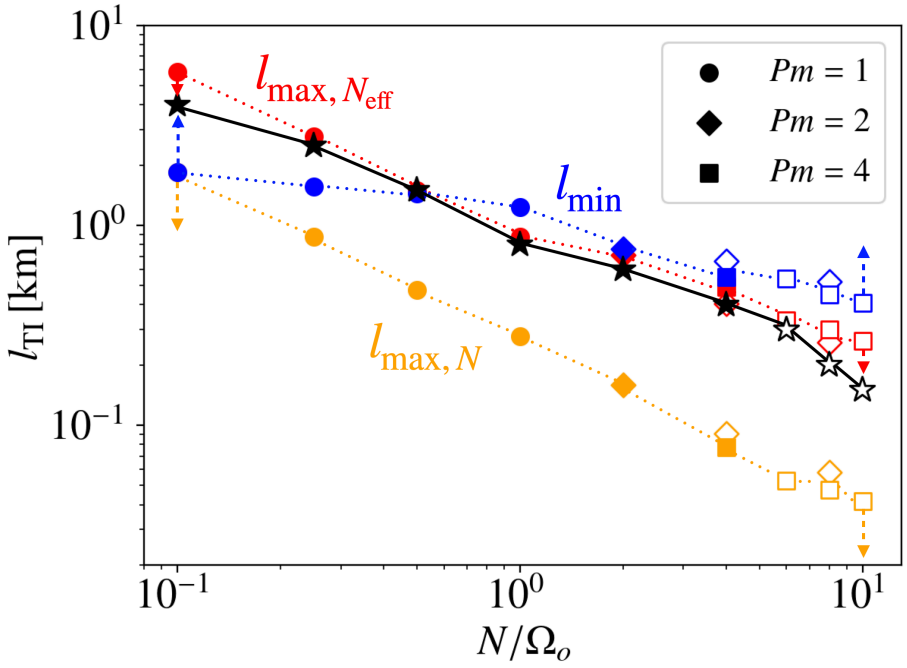

Figure 7.4 — Length scale of the Tayler instability mode measured in the simulations (black stars) as a function of N/Ω_o. The theoretical lower (l_{min} in blue) and upper boundaries of the length scale are also plotted using the classical ($l_{\mathrm{max},N}$ in orange) and the effective ($l_{\mathrm{max},N_{\mathrm{eff}}}$ in red) Brunt-Väisälä frequencies. Filled and empty markers represent self-sustained and transient dynamos, respectively.

7.2.4 . Magnetic field saturation

As in Barrère et al. (2023), we confront the saturated large-scale magnetic fields in our simulations to the analytical predictions. To this end, we first measure the impact of the stratification on the local shear rate q, which influences the magnetic field saturation. Indeed, the rotation profiles of Fig. 7.2 show that the shear concentrates closer to the inner sphere and increases with N/Ω_o. The quantification of this effect is described in Appendix 7.6.1. These larger values of q explain the increase of the magnetic energy with N/Ω_o observed in Fig. 7.1.

In order to study the relation of the magnetic field components with $N_{\mathrm{eff}}/\Omega_o$ while taking into account the variation of q, we use the analytical prescriptions derived by Fuller et al. (2019):

$$B_{\mathrm{tor}}^{m=0} \sim \sqrt{4\pi\rho r_o^2}\Omega_o \left(\frac{q\Omega_o}{N_{\mathrm{eff}}}\right)^{1/3}, \tag{7.15}$$

$$B_{\mathrm{pol}}^{m=0}, B_{\mathrm{dip}} \sim \sqrt{4\pi\rho r_o^2}\Omega_o \left(\frac{q^2\Omega_o^5}{N_{\mathrm{eff}}^5}\right)^{1/3}. \tag{7.16}$$

The exponents of q are all the more robust as they are confirmed by numerical simulations (Barrère et al., 2023). We define dimensionless magnetic field components compen-

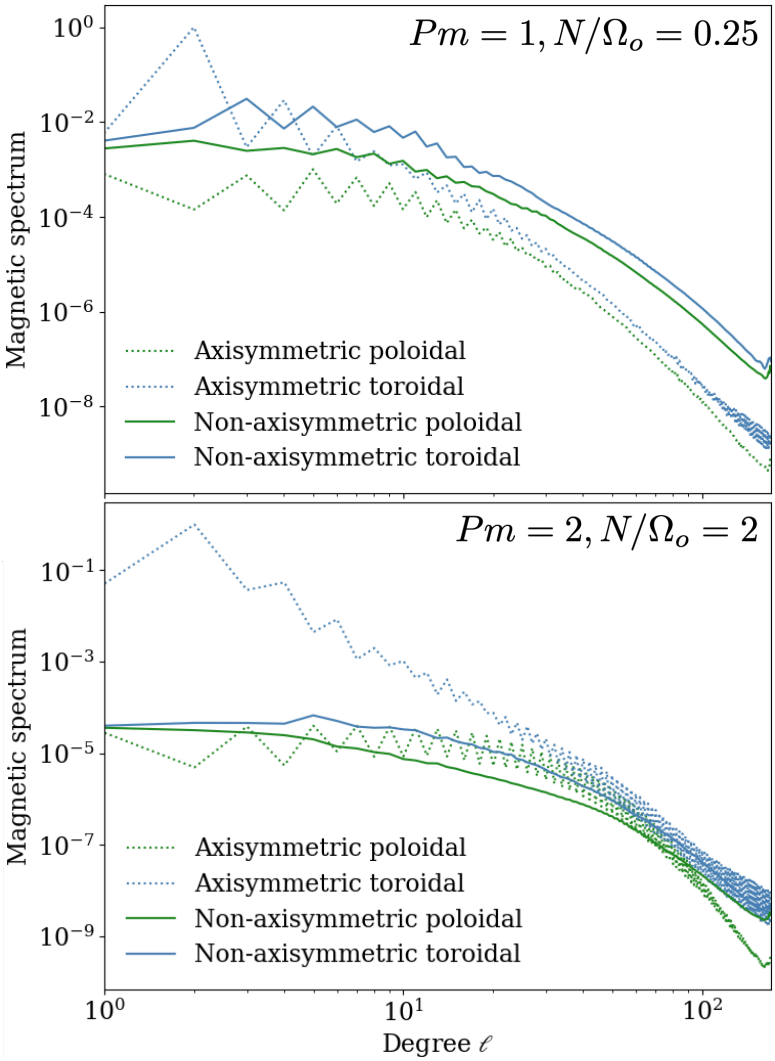

Figure 7.5 — Time and volume averaged spectra of the magnetic energy for the parameters $Pm = 1, N/\Omega_o = 0.25$ (top) and $Pm = 2, N/\Omega_o = 2$ (bottom). The magnetic energy is normalized by the energy of the dominant $(\ell = 2, m = 0)$-mode of the toroidal component.

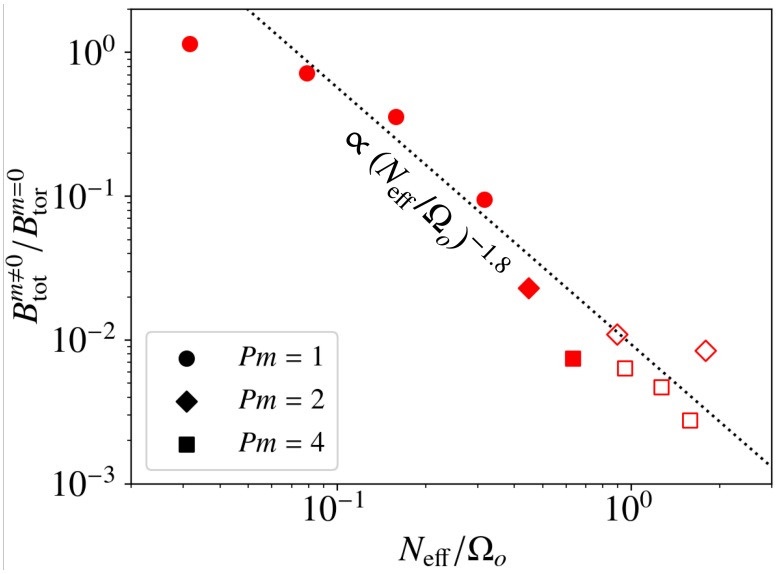

Figure 7.6 — Ratio of the RMS non-axisymmetric magnetic field to the RMS axisymmetric toroidal magnetic field. The dotted line shows the best fit for a power law of $N_{\rm eff}/\Omega_o$. Filled and empty markers represent self-sustained and transient dynamos, respectively.

sated for the effect of the shear in the following way:

$$B_{\rm tor}^{m=0} \longrightarrow \frac{B_{\rm tor}^{m=0}}{\sqrt{4\pi\rho r_o^2\Omega_o^2}q^{1/3}} \tag{7.17}$$

$$B_{\rm pol}^{m=0}, B_{\rm dip} \longrightarrow \frac{B_{\rm pol}^{m=0}}{\sqrt{4\pi\rho r_o^2\Omega_o^2}q^{2/3}}, \frac{B_{\rm dip}}{\sqrt{4\pi\rho r_o^2\Omega_o^2}q^{2/3}}. \tag{7.18}$$

These compensated dimensionless components are plotted in Fig. 7.7as a function of $N_{\rm eff}/\Omega_o$. The theoretical scaling laws (dotted black lines) qualitatively match our data. Since the point at $N_{\rm eff}/\Omega_o = 3\times10^{-2}$ diverges from the scalings due to the weaker effect of stable stratification, we exclude it while calculating the best fits. We obtain the following power-laws $B_{\rm tor}^{m=0} \propto (N_{\rm eff}/\Omega_o)^{-0.11\pm0.05}$, $B_{\rm pol}^{m=0} \propto (N_{\rm eff}/\Omega_o)^{-1.1\pm0.2}$, and $B_{\rm dip} \propto (N_{\rm eff}/\Omega_o)^{-1.5\pm0.1}$. While $B_{\rm tor}^{m=0}$ and $B_{\rm pol}^{m=0}$ follow power-laws slightly less steep than predicted in Eqs. (7.15) and (7.16), $B_{\rm dip}$ is in good agreement with Eq. (7.16).

This agreement with the theory is also found for the ratio $B_r^{m=0}/B_\phi^{m=0} \sim \omega_{\rm A}/N_{\rm eff}$ (Spruit, 2002, Fuller et al., 2019) as seen in Fig. 7.8. Our data is fitted by the power law $B_{\rm pol}^{m=0}/B_{\rm tor}^{m=0} \propto (\omega_{\rm A}/N_{\rm eff})^{0.93\pm0.18}$, which is very close to the prediction. On the other hand, the ratio of the magnetic dipole to the axisymmetric toroidal field follows a somewhat steeper scaling law $B_{\rm dip}/B_{\rm tor}^{m=0} \propto (\omega_{\rm A}/N_{\rm eff})^{1.3\pm0.1}$.

7.2.5 . Angular momentum transport and mixing

The angular momentum transport due to the large-scale magnetic field and turbulence in our simulations is also consistent with the theory of Fuller et al. (2019), as shown in Fig. 7.9. For the Maxwell torque $T_{\rm M}$, we find $B_s B_\phi \propto (N_{\rm eff}/\Omega_o)^{-1.8\pm0.1}$ and $B_s^{m=0}B_\phi^{m=0} \propto (N_{\rm eff}/\Omega_o)^{-1.6\pm0.1}$ depending on whether we take the non-axisymmetric components into account in $T_{\rm M}$. Note

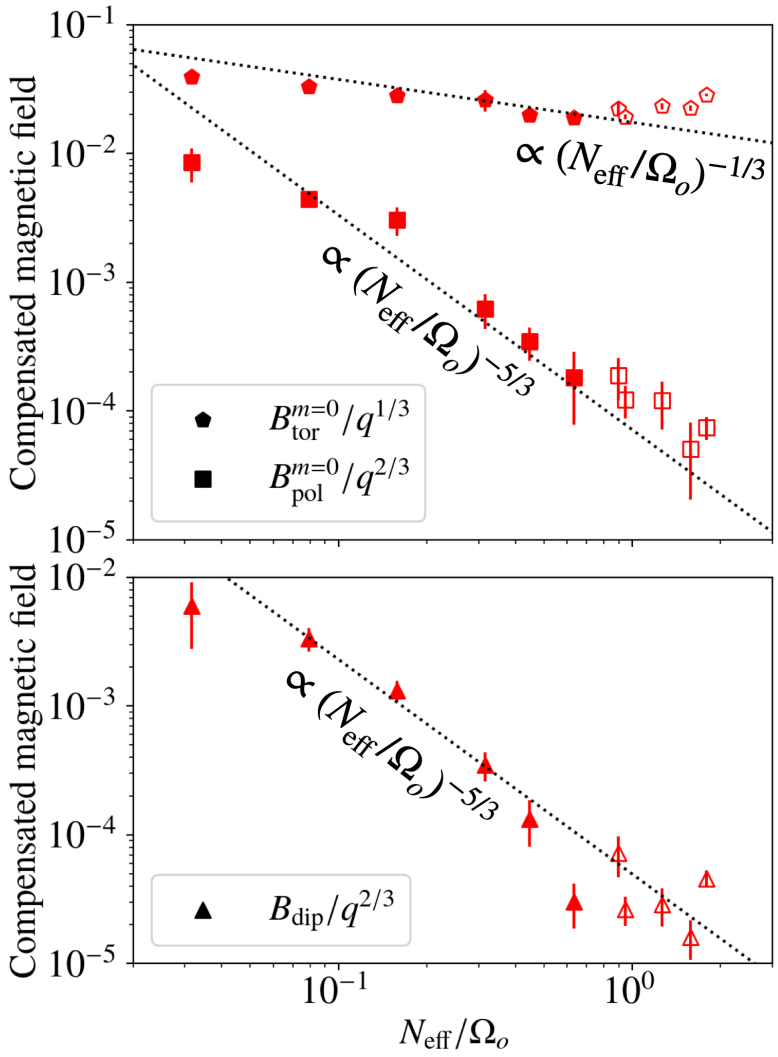

Figure 7.7 — RMS toroidal and poloidal axisymmetric magnetic fields (top), and RMS magnetic dipole (bottom) compensated with the measured shear rate as a function of the ratio between the effective Brunt-Väisälä frequency to the rotation rate at the outer sphere $N_{\rm eff}/\Omega_o$. The magnetic field is rendered dimensionless and compensated for the effect of the shear using Eqs. (7.17) and (7.18). Dotted lines show the best fits of the data with Fuller's theoretical scaling laws (Eqs. (7.15) and (7.16)) within a multiplying factor. Filled and empty markers represent self-sustained and transient dynamos, respectively.

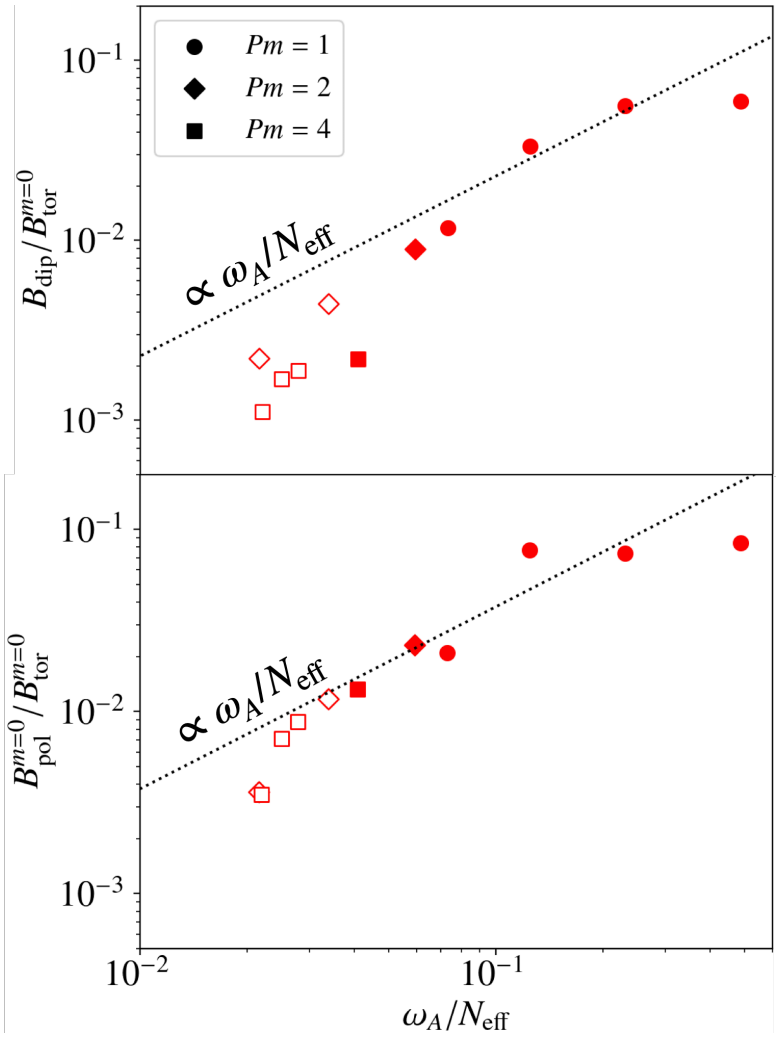

Figure 7.8 — Ratio between the RMS axisymmetric poloidal (top) and the RMS dipolar (bottom) magnetic fields to the axisymmetric toroidal magnetic field. Dotted lines show the best fits of the data with Fuller's theoretical scaling law $B_r/B_\phi \sim \omega_{\rm A}/N_{\rm eff}$ within a multiplying factor. Filled and empty markers represent self-sustained and transient dynamos, respectively.

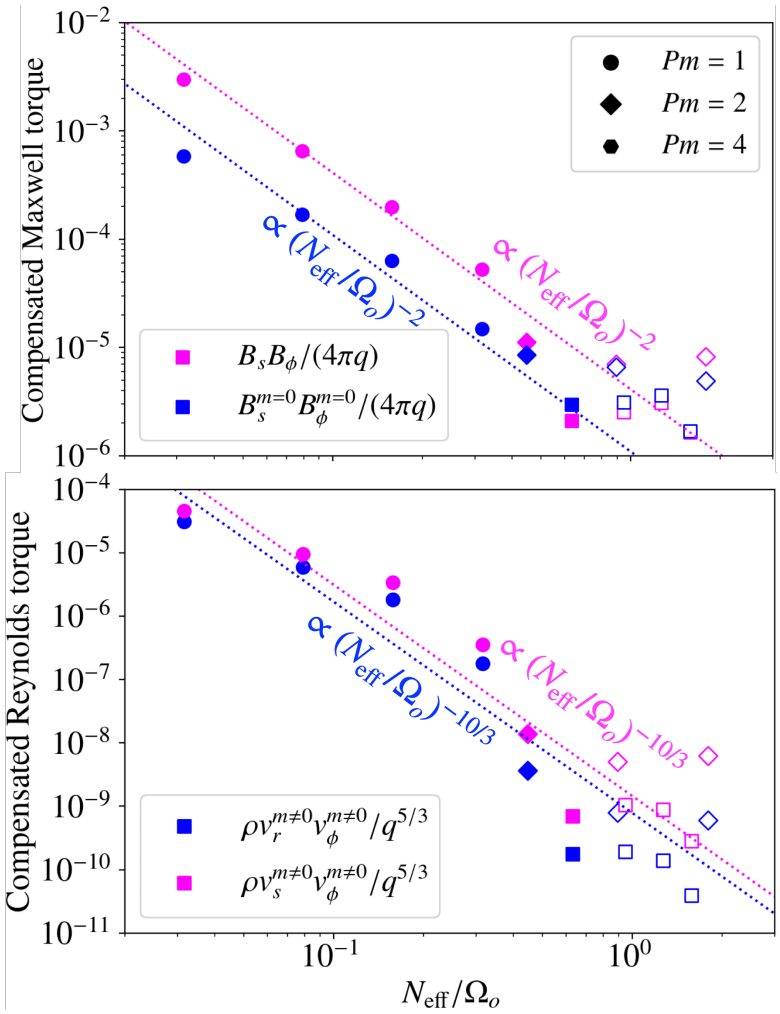

Figure 7.9 — RMS Maxwell (top) and Reynolds (bottom) torques compensated with the measured shear rate as a function of the ratio between the effective Brunt-Väisälä frequency to the rotation rate at the outer sphere. Dotted lines shows the best fits obtained with Fuller's theoretical scaling laws. Filled and empty markers represent self-sustained and transient dynamos, respectively.

that the torque is more and more dominated by the axisymmetric magnetic fields as $N_{\rm eff}/\Omega_o$ increases. This dominance was assumed by Fuller et al. (2019) and can be expected given the results of Sect. 7.2.3. The Reynolds torque values are more dispersed as a function of the stratification, but fit the power laws $v_r^{m\neq0}v_\phi^{m\neq0} \propto (N_{\rm eff}/\Omega_o)^{-3.5\pm0.2}$ and $v_r^{m\neq0}v_\phi^{m\neq0} \propto (N_{\rm eff}/\Omega_o)^{-3.4\pm0.2}$. Despite some scattering at high values of $N_{\rm eff}/\Omega_o$ in the points corresponding to transient dynamos, our data therefore follows well the analytical predictions $T_{\rm M} \propto (N_{\rm eff}/\Omega_o)^{-2}$ and $T_{\rm R} \propto (N_{\rm eff}/\Omega_o)^{-10/3}$ (dotted lines in Figs. 7.9). Moreover, we find $T_{\rm M} \sim 10^2 - 10^3\, T_{\rm R}$, so the magnetic field is much more efficient than turbulence at transporting angular momentum.

The mixing processes are also a crucial question in astrophysics, especially in stars. The Tayler-Spruit dynamo is expected to produce a very limited mixing efficiency compared to the angular momentum transport (Spruit, 2002, Fuller et al., 2019). To measure this effect in our simulations, we define the effective angular momentum transport diffusivity $\nu_{\rm AM} \equiv T_{\rm M}/(\rho q \Omega_o)$ and roughly approximate the effective mixing diffusivity as $\nu_{\rm mix} \equiv q^{-5/3} v^{m\neq0} l_{\rm TI}$, with the rms turbulent velocity $v^{m\neq0} \equiv \sqrt{E_{\rm kin}^{m\neq0}/(2\rho)}$ calculated from the mean non-axisymmetric energy $E_{\rm kin}^{m\neq0}$. We divide by the power law $q^{5/3}$ in the expression of $\nu_{\rm mix}$ to take into account the variation of q like in Figs 7.7 and 7.9.

The ratio $\nu_{\rm mix}/\nu_{\rm AM}$ is plotted in Fig.7.10 and shows that our data is in fair agreement with the scaling $\nu_{\rm mix}/\nu_{\rm AM} \propto {N_{\rm eff}/\Omega_o}^{-5/3}$ of Fuller et al. (2019). The power law $\nu_{\rm mix}/\nu_{\rm AM} \propto {N_{\rm eff}/\Omega_o}^{-1.2\pm0.2}$ best fits our data, which is mildly less steep than predicted. Moreover, our simulations also confirm that $\nu_{\rm mix}/\nu_{\rm AM} \sim 10^{-6} - 10^{-3} \ll 1$ for Tayler-Spruit dynamo. The use of passive scalars evolving in the velocity field in our simulations could help measure more precisely $\nu_{\rm mix}$ even though the approximation we used is satisfactory as a first analysis.

Table 7.1 sums up the comparisons we have done between our data and the different scalings derived by Fuller et al. (2019). Our results thus consolidate the validity of Fuller et al. (2019)'s formalism for the saturation of large-scale magnetic fields and angular momentum transport. Besides, our simulations are not compatible with the analytical prescriptions of Spruit (2002), which read

$$B_{\rm tor}^{m=0} \sim \sqrt{4\pi\rho r_o^2}\Omega_o \left(\frac{q\Omega_o}{N_{\rm eff}}\right) \tag{7.19}$$

$$B_{\rm pol}^{m=0},\, B_{\rm dip} \sim \sqrt{4\pi\rho r_o^2}\Omega_o \left(\frac{q^2\Omega_o^3}{N_{\rm eff}^3}\right) \tag{7.20}$$

$$T_{\rm M} \sim r_o^2\Omega_o^2 q^3 \left(\frac{\Omega_o}{N_{\rm eff}}\right)^4. \tag{7.21}$$

While our simulations support the scaling law of Fuller et al. (2019), we can also constrain the dimensionless normalisation factor, (noted α in Fuller et al. (2019)), that parametrises the saturated strength of the axisymmetric toroidal magnetic field

$$\frac{B_{\rm tor}^{m=0}}{\sqrt{4\pi\rho r_o^2}} = \alpha\Omega_o \left(\frac{q\Omega_o}{N_{\rm eff}}\right)^{1/3}. \tag{7.22}$$

We infer the value of α by fitting our data by the theoretical scaling law. The measures are listed in the last column of Table 7.1 and we find a mean value of $\alpha \sim 10^{-2}$. This value is small

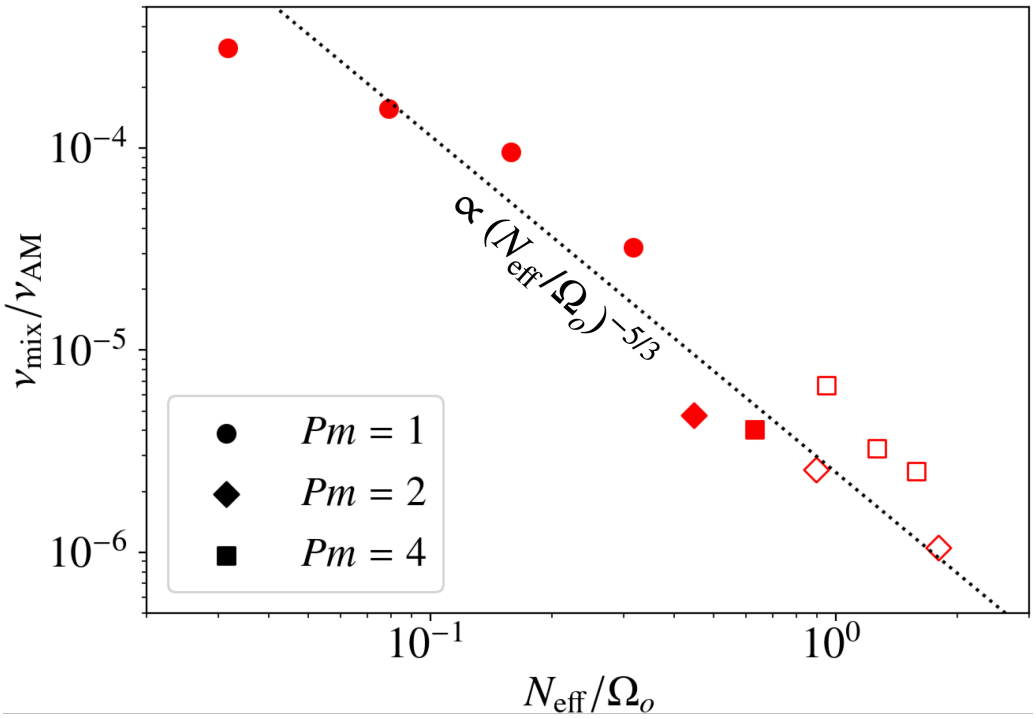

Figure 7.10 — Ratio of the effective mixing diffusivity $\nu_{\rm mix}$ to the effective angular momentum diffusivity $\nu_{\rm AM}$ as a function of $N_{\rm eff}/\Omega_o$. Filled and empty markers represent self-sustained and transient dynamos, respectively.

Table 7.1 — Table that sums up the theoretical and measured scaling laws of the different quantities discussed in Sects. 7.2.4 and 7.2.5, and the dimensionless normalisation factor α defined by Fuller et al. (2019) (see Eq. 7.22)

Quantity (dimensionless)	Fuller et al. (2019)'s scaling law	Best fit exponent	α
$B_{\rm tot}^{m\neq0}/B_{\rm tor}^{m\neq0}$	$\omega_{\rm A}/\Omega_o$	$(N_{\rm eff}/\Omega_o)^{-0.18\pm0.1}$	
$B_{\rm tor}^{m=0}/(\sqrt{4\pi\rho r_o^2\Omega_o^2}q^{1/3})$	$\alpha(N_{\rm eff}/\Omega_o)^{-1/3}$	$(N_{\rm eff}/\Omega_o)^{-0.11\pm0.05}$	0.017 ± 0.001
$B_{\rm pol}^{m=0}/(\sqrt{4\pi\rho r_o^2\Omega_o^2}q^{2/3})$	$\alpha^2(N_{\rm eff}/\Omega_o)^{-5/3}$	$(N_{\rm eff}/\Omega_o)^{-1.1\pm0.2}$	0.009 ± 0.002
$B_{\rm dip}/(\sqrt{4\pi\rho r_o^2\Omega_o^2}q^{2/3})$	$\alpha^2(N_{\rm eff}/\Omega_o)^{-5/3}$	$(N_{\rm eff}/\Omega_o)^{-1.5\pm0.1}$	0.007 ± 0.001
$B_{\rm pol}^{m=0}/B_{\rm tor}^{m=0}$	$\omega_{\rm A}/N_{\rm eff}$	$(\omega_{\rm A}/N_{\rm eff})^{0.93\pm0.2}$	—
$B_{\rm dip}/B_{\rm tor}^{m=0}$	$\omega_{\rm A}/N_{\rm eff}$	$(\omega_{\rm A}/N_{\rm eff})^{1.3\pm0.1}$	—
$B_sB_\phi/(4\pi\rho r_o^2\Omega_o^2q)$	$\alpha^3(N_{\rm eff}/\Omega_o)^{-2}$	$(N_{\rm eff}/\Omega_o)^{-1.8\pm0.1}$	0.016 ± 0.004
$B_s^{m=0}B_\phi^{m=0}/(4\pi\rho r_o^2\Omega_o^2q)$	$\alpha^3(N_{\rm eff}/\Omega_o)^{-2}$	$(N_{\rm eff}/\Omega_o)^{-1.6\pm0.1}$	0.01 ± 0.004
$v_r^{m\neq0}v_\phi^{m\neq0}/(r_o^2\Omega_o^2q^{5/3})$	$(N_{\rm eff}/\Omega_o)^{-10/3}$	$(N_{\rm eff}/\Omega_o)^{-3.5\pm0.2}$	—
$v_s^{m\neq0}v_\phi^{m\neq0}/(r_o^2\Omega_o^2q^{5/3})$	$(N_{\rm eff}/\Omega_o)^{-10/3}$	$(N_{\rm eff}/\Omega_o)^{-3.4\pm0.2}$	—
$\nu_{\rm mix}/\nu_{\rm AM}$	$(N_{\rm eff}/\Omega_o)^{-5/3}$	$(N_{\rm eff}/\Omega_o)^{-1.2\pm0.2}$	—

compared to those inferred by adjusting α in 1D stellar evolution models to the asteroseismic observations of sub-/red giants, which is $\sim 0.25-1$ (Fuller et al., 2019, Fuller & Lu, 2022, Eggenberger et al., 2019c). Either way, our numerical simulations provide a more physically motivated value of α that could be implemented in 1D stellar evolution codes including the Tayler-Spruit dynamo to transport angular momentum.

7.2.6 . Intermittency

When $N/\Omega_o \geq 2$, we find that the Tayler-Spruit dynamo displays an intermittent behaviour, which is clearly visible in the time series of Fig. 7.11 where the non-axisymmetric magnetic energy drops and increases cyclically by two orders of magnitude. This corresponds to the loss and growth of the Tayler instability. The same cycle also occurs for the axisymmetric B_r and B_θ, which illustrates the loss of the dynamo. Those two cycles show a very short lag of $\sim 2.4\,\mathrm{s}$. We then notice that the oscillations of the axisymmetric toroidal and poloidal magnetic energies are in antiphase. This is also observed in the butterfly diagrams in which B_ϕ decreases locally, and so in the volume average when B_r is the strongest. These cycles can be interpreted qualitatively as follows:

(i) $B_\phi^{m=0}$ is close but above the critical strength for the Tayler instability derived by combining Eqs. (7.14) and (7.12)

$$B_{\phi,\mathrm{c}}^{m=0} \equiv \sqrt{4\pi\rho r_o^2}\Omega_o \left(\frac{N_{\mathrm{eff}}}{\Omega_o}\right)^{1/2} \left(\frac{\eta}{r_o^2\Omega_o}\right)^{1/4} \tag{7.23}$$

and the dynamo is acting to generate $B_r^{m=0}$;

(ii) $B_\phi^{m=0}$ decreases slightly below the critical strength due to turbulent dissipation, which kills the Tayler instability and so the dynamo loop ;

(iii) the axisymmetric poloidal magnetic energy drops and the axisymmetric toroidal component increases because of the winding and the lack of turbulent dissipation ;

(iv) $B_\phi^{m=0}$ exceeds the critical strength and the dynamo is active again.

An intermittent Tayler-Spruit dynamo was already proposed by Fuller & Lu (2022) to explain the angular momentum transport in stellar stellar radiative regions with a low shear.

Quantitatively, we find $B_{\phi,\mathrm{c}}^{m=0} \sim 1.4-2.1\times10^{15}\,\mathrm{G}$ for the models with $N/\Omega_o \in [2,10]$, which is very close to the maximum values $B_\phi^{m=0} \sim 2.5-3\times10^{15}\,\mathrm{G}$ measured in the same models. The proximity to the instability threshold supports our interpretation. To characterise the time evolution of the intermittency, we measure its duty cycle α_{cyc}, i.e. the ratio of the time when the dynamo is active to the period of the cycle. We find that it varies between 0.38 and 0.66, with a tendency to decrease with N/Ω_o as seen in Fig. 7.12. The same trend is observed for the period of these cycles P_{cyc}, which ranges between $3\,\mathrm{s}$ and $30\,\mathrm{s}$. This is consistent with the fact that we get closer to the dynamo threshold.

7.3 . Application to magnetar formation

The previous analyses support the formalism of Fuller et al. (2019), which was used to model our magnetar formation scenario in Barrère et al. (2022). To compare our numerical

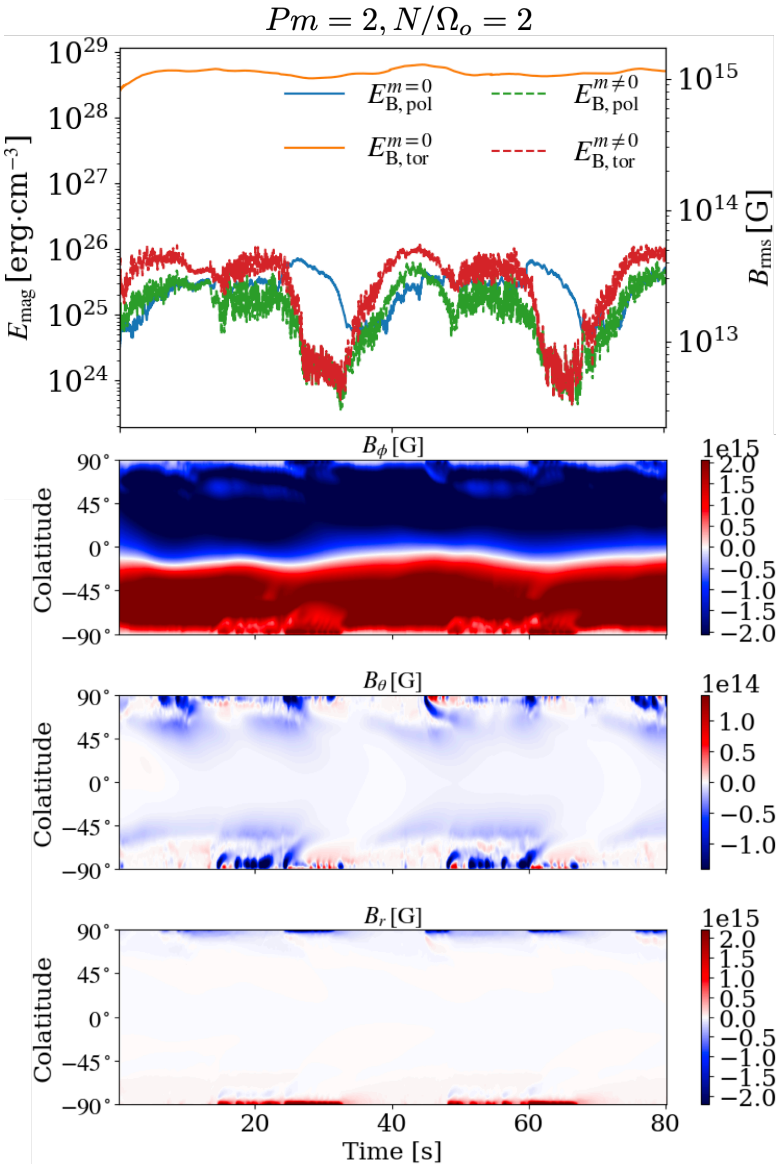

Figure 7.11 — Top: Time series of the magnetic energy. Bottom: Butterfly diagram showing the latitudinal structure time evolution of different axisymmetric magnetic field components averaged between the radii $r = 5$ and $r = 6\,\mathrm{km}$. The magnetic energy was converted to physical units by fixing $N = 10^{-3}\,\mathrm{s}^{-1}$

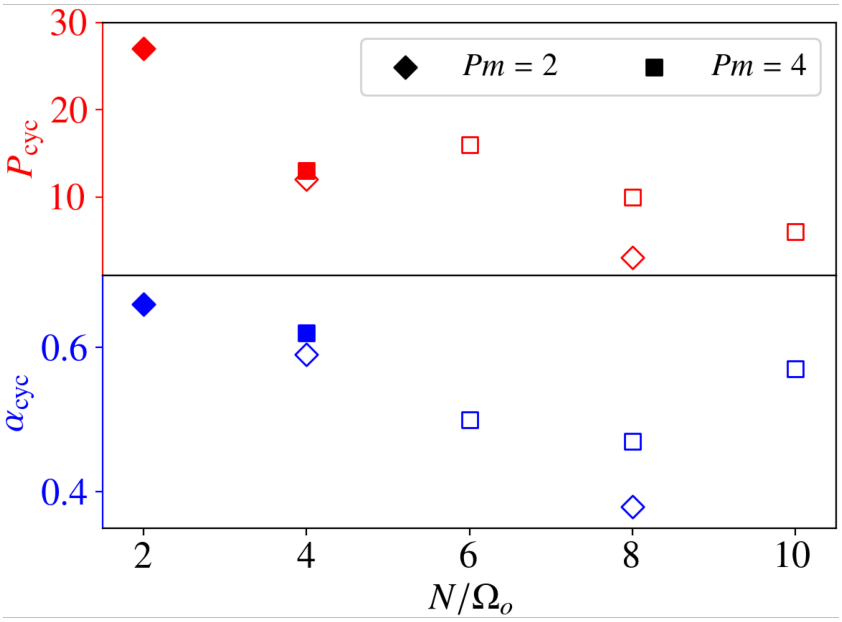

Figure 7.12 — Period of the cycle $P_{\rm cyc}$ (top) and the duty cycle $\alpha_{\rm cyc}$ (bottom) of the intermittent dynamo as a function of the input N/Ω_o. Filled and empty markers represent self-sustained and transient dynamos, respectively.

simulations to this model, the magnetic field is converted into physical units by fixing the following parameters to typical values in PNSs: the PNS radius $r_o = 12\,\mathrm{km}$, mass $M = 1.4\,\mathrm{M}_\odot$ that corresponds to a constant PNS density of $\rho \sim 4.1 \times 10^{14}\,\mathrm{g\,cm^{-3}}$, and Brunt-Väisälä frequency $N = 1\,\mathrm{kHz}$. We therefore obtain the magnetic field strength of $B_{\rm tor}^{m=0}$, $B_{\rm pol}^{m=0}$ and $B_{\rm dip}$ as a function of the angular frequency of the outer sphere, which is displayed in Fig. 7.13.

The red markers correspond to the magnetic field measured in the simulations, while the blue markers correspond to the values extrapolated to $q = 1$. This plot is similar to Fig. 5 in Barrère et al. (2022), except that we define, here, a low-field magnetar as a magnetar with $B_{\rm tor}^{m=0} \geqslant 10^{14}\,\mathrm{G}$ but $B_{\rm dip} < 4.4 \times 10^{13}\,\mathrm{G}$. Since considering the changes of q is equivalent to set $q = 1$, we can compare our numerical results to Barrère et al. (2022). As shown in the previous sections, the magnetic field follows well Fuller et al. (2019)'s scaling law for Ω_o. However, the saturated magnetic field in our simulations is ~ 17 times weaker than in the model in Barrère et al. (2022), which shifts the upper limit of rotation period to form magnetar-like magnetic fields to $P \sim 6\,\mathrm{ms}$. This new limit corresponds to a lower accreted fallback mass limit of $\sim 5 \times 10^{-2}\,\mathrm{M}_\odot$, which is still consistent with recent supernova simulations (see the discussion in Barrère et al., 2022).

For rotation periods longer than $6\,\mathrm{ms}$, the magnetic dipole is too weak for a classical magnetar but the Tayler-Spruit dynamo still produces strong total magnetic fields above $10^{14}\,\mathrm{G}$. The observations of absorption lines in the X-ray spectra of low-field magnetars (Tiengo et al., 2013, Rodríguez Castillo et al., 2016) and 3D numerical simulations of magnetic field long-term evolution in NSs (Igoshev et al., 2021) suggest that this is enough to produce magnetar-like luminous activity.

7.4 . Discussion

Here, we discuss the simplifications we used for the modelling of the PNS interior evolution: the mechanism to force the differential rotation (Sect. 7.4.1) and the Boussinesq approximation (Sect. 7.4.2). In Sect. 7.4.3, we finally compare our results on the Tayler-Spruit dynamo (Barrère et al., 2023, this article) and the Tayler-Spruit dynamo obtained in other numerical simulations (Petitdemange et al., 2023, Daniel et al., 2023, Petitdemange et al., 2024).

7.4.1 . Forcing of the differential rotation

To force the differential rotation, we chose to use a spherical Taylor-Couette configuration, in which a constant rotation rate is imposed on both inner and outer spheres. In this setup, the rotation profile is free to evolve as the angular momentum is transported by turbulence and large-scale magnetic fields. The imposed rotation of the outer sphere roughly mimics the maintenance of the surface rotation due to fallback accretion, once the PNS surface is already spun up significantly. However, the rotation profile evolution does not describe the beginning of the accretion during which the surface is spun up and the differential rotation, first concentrated close to the surface, is transported in the PNS interior.

Maintaining the rotation on both spheres allows us to inject energy into the flow and try to control the shear rate. As noticed in Sect. 7.2.4 and quantified in App. 7.6.1, the stable stratification however significantly changes the shear rate. This complicates the measure of the respective scaling exponents with N/Ω_o and q independently. In addition, we observe in Fig. 7.2 that most of the shear is concentrated closer and closer to the inner sphere. As confirmed by our simulations, this restricts significantly the domain in which the Tayler-Spruit dynamo can operate and participate to make the dynamo more difficult to sustain. Thus, to investigate stronger stratification regimes, it will be necessary to change the forcing method and perhaps opt for a volumetric forcing as used for instance by Meduri et al. (2024).

7.4.2 . Validity of the Boussinesq approximation

To model the PNS interior, we used the Boussinesq approximation, which reduces the numerical cost and allows us to produce a few tens of models to better understand the physics of the Tayler-Spruit dynamo. Despite the importance of the density gradient, this approximation is easonable in the case of PNS interior:

(i) The sound speed is close to the speed of light $c_s \sim 10^{10}\,\mathrm{cm\,s^{-1}}$ (Hüdepohl, 2014, Pascal, 2021, private communication), so $v_\mathrm{A}/c_s \lesssim v_\phi/c_s \lesssim 10^{-2}$, where $v_a \equiv r_o\omega_\mathrm{A}$ and v_ϕ are the typical Alfvén and azimuthal speeds.

(ii) The density perturbation associated to the buoyancy term is small compared to the PNS mean density: $\delta\rho/\rho = \theta N^2/g \lesssim 9\times10^{-2}$, with $N = 10^3\,\mathrm{s^{-1}}$, $g \sim GM/r_o \sim 1.3\times10^{13}\,\mathrm{cm\,s^{-2}}$, and $\theta \lesssim r_o$ is the buoyancy variable (Eq. 7.6).

The impact of density gradient on the Tayler-Spruit dynamo has never been investigated so far in numerical simulations. Therefore, future work should consider more realistic PNS density profiles.

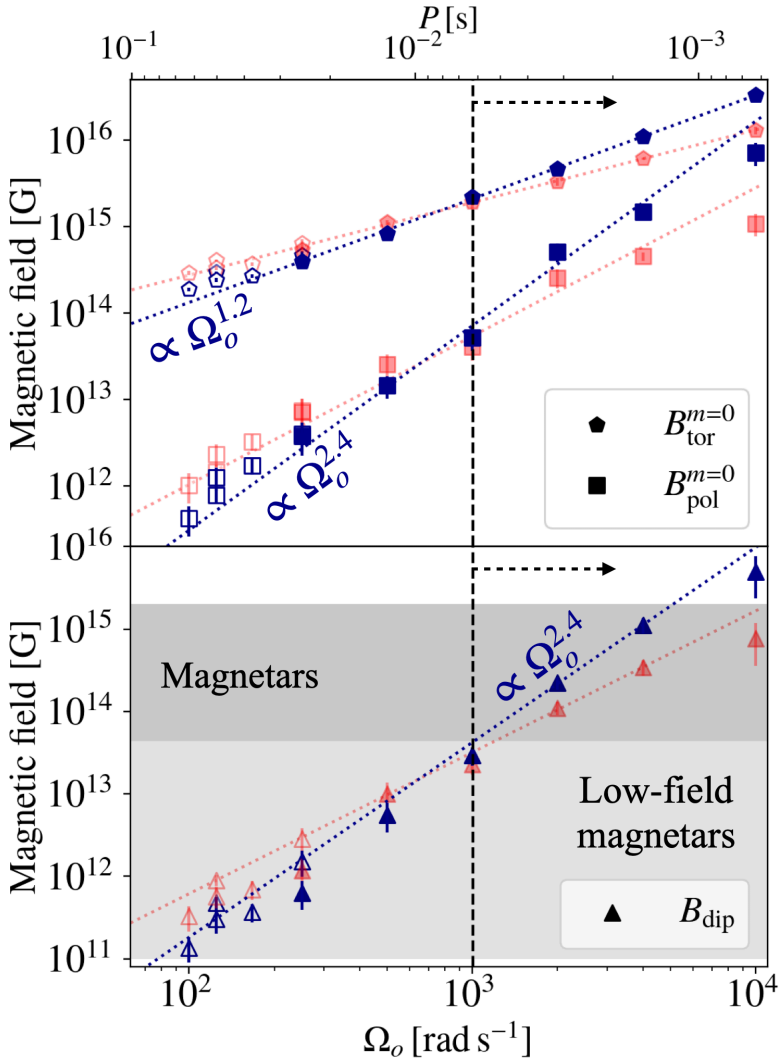

Figure 7.13 — Magnetic strength of the axisymmetric toroidal $B_{\rm tor}^{m=0}$ (pentagons) and poloidal $B_{\rm pol}^{m=0}$ (squares) components (upper panel), as well as that of the magnetic dipole $B_{\rm dip}$ (triangles, lower panel) as a function of the angular frequency of the outer sphere, which represents the PNS surface. The red markers correspond to the magnetic field measured in the simulations, while the blue markers correspond to the values extrapolated to $q = 1$. The dotted lines are the best power-law fit of the data. The dark and light grey regions represent the range of magnetic field for classical magnetars ($B_{\rm dip} \geqslant 4.4 \times 10^{13}$ G) and low-field magnetars ($B_{\rm tor}^{m=0} \geqslant 10^{14}$ G). The black dashed line and arrow illustrate the rotation period below which the dynamo can form classical magnetar-like magnetic fields. Filled and empty markers represent self-sustained and transient dynamos, respectively.

7.4.3 . Comparison with other numerical models

In the literature, only a few other studies investigate numerically the Tayler-Spruit dynamo (Petitdemange et al., 2023, Petitdemange et al., 2024, Daniel et al., 2023). The main difference between our setup and theirs is the opposite shear, i.e. in their setup the inner boundary rotates faster than the outer one. As in our studies, they find a subcritical bifurcation at the Tayler instability threshold to a self-sustained state with a dominant axisymmetric toroidal magnetic field. However, many differences can be noticed:

- The generated magnetic structure in their simulations has a smaller scale and is localized near the inner sphere in the equatorial plane. The impact of stable stratification on the length scale of these modes may deserve a deeper analysis. It is still unclear why this configuration is stable for one sign of the shear and not the other.
- As in Barrère et al. (2023), a hemispherical dynamo solution is also found by Petitdemange et al. (2024) as they move from a laminar dynamo solution to the strong Tayler-Spruit dynamo by increasing N/Ω_o. However, they do not find bistability between the hemispherical and the strong solutions as in Barrère et al. (2023).
- While the dipolar and hemispherical dynamos we found in Barrère et al. (2023) are in good agreement with the predictions of Fuller et al. (2019) and Spruit (2002), respectively, all their models, including those of the hemispherical solution, are in agreement with the analytical model of Spruit (2002).

Therefore, the few numerical studies of the Tayler-Spruit dynamo indicate a much more complex physics than anticipated analytically, with the existence of a wide variety of dynamo solutions. So far, only Daniel et al. (2023) propose a non-linear model of the subcritical transition to the Tayler-Spruit dynamo of Petitdemange et al. (2023). In order to include the other solutions we discovered, we must further investigate the dynamics of the dynamo using tools from dynamic system theory.

7.5 . Conclusions

7.5.1 . Summary

Following our previous study Barrère et al. (2023), we performed numerical simulations of the dipolar Tayler-Spruit dynamo to investigate how it behaves in the stratification regime of PNSs. We first show that a self-sustained dynamo is maintained in this regime for $N/\Omega_o \leqslant 4$. With increasing N/Ω_o, on the one hand, the Tayler modes have reduced radial length scales as expected theoretically, but their energy decreases faster than predicted by Fuller et al. (2019), which may indicate an underestimation of the turbulent dissipation. On the other hand, the large-scale magnetic fields generated by the dynamo are in good agreement with the analytical work of Fuller et al. (2019).

The overall agreement is also observed for both Maxwell and Reynolds torques, the former of which dominates the angular momentum transport. By measuring an approximate mixing diffusivity, we also determined the efficiency of the mixing process due to the Tayler-Spruit dynamo and found that mixing is far less efficient than the angular momentum transport, as predicted theoretically. We also constrained for the first time the dimensionless normalisation factor $\alpha \sim 10^{-2}$, which is much weaker than expected to explain the rotation

rate of sub-/red giant cores. Finally, our simulations demonstrate for the first time that the Tayler-Spruit dynamo can become intermittent as the saturated $B_\phi^{m=0}$ is close to the Tayler instability threshold.

To conclude the investigation, we applied our numerical results to the magnetar formation scenario of Barrère et al. (2022). While our data follow the theoretical scaling law, the lower limit of the angular frequency to form classical magnetar-like dipoles is larger than derived in Barrère et al. (2022) with a period of $\sim 6\,\mathrm{ms}$. This rotation period corresponds to an accreted fallback mass of $\sim 5\times10^{-2}\,\mathrm{M}_\odot$, which is still reasonable according to CCSN simulations (e.g. Sukhbold et al., 2016, 2018, Chan et al., 2020, Janka et al., 2022).

7.5.2 . Long-term evolution of the magnetic field

After $\sim 100\,\mathrm{s}$, the fallback accretion becomes too weak to maintain the differential rotation in the PNS. The newly formed strong large-scale magnetic fields transport the angular momentum efficiently, which damps the differential rotation and the dynamo will eventually stop. The magnetic field is expected to enter a relaxation phase in which its structure changes to reach a stable configuration. The exact shape of this magnetic field is still an open question and, more generally, the magnetic relaxation problem in astrophysics remains debated (e.g. Braithwaite, 2006, Duez & Mathis, 2010, Duez et al., 2010, Akgün et al., 2013, Becerra et al., 2022a,b). It is however well acknowledged that the magnetic configuration is complex, mixing both large-scale poloidal and toroidal components. Thus, 3D numerical simulations including rotation and thermal/density stratifications are required to investigate this stage of the PNS evolution.

On longer timescales of $\sim 1-100\,\mathrm{kyr}$, the remaining strong toroidal magnetic fields located in the NS crust are prone to Hall diffusion and instability (Rheinhardt & Geppert, 2002), which modifies their structures and so can influence the magnetar emission. The strong magnetic field-induced stresses could also cause failures or plastic deformations, which are suspected to explain the origin of magnetar bursts (e.g. Thompson & Duncan, 1995, Perna & Pons, 2011, Lander et al., 2015, Lander & Gourgouliatos, 2019). It is therefore crucial to run 3D numerical simulations of magnetic field evolution in a NS structure using dynamo-generated initial magnetic configuration to better constrain these properties. Further investigations could also include the relaxation of the dynamo-generated magnetic field to a stable configuration before the PNS becomes a cooled stable NS.

7.5.3 . Interaction with a remaining fallback disc

The magnetic dipole generated by the dipolar Tayler-Spruit dynamo may not be strong enough to spin the magnetar down to the observed $8-12\,\mathrm{s}$ via the magnetic spin-down mechanism. A good alternative would be the propeller mechanism (e.g. Gompertz et al., 2014, Beniamini et al., 2019, Lin et al., 2021, Ronchi et al., 2022). This operates when the magnetosphere is large enough to interact with the remaining fallback disc, i.e. when the Alfvén radius is larger than the corotation radius. In the propeller regime, the inner disk matter is accelerated to super-Keplerian velocity, which produces an outflow and so an angular momentum transfer from the magnetar to the disc. If this mechanism operates in some magnetars, the magnetic dipole which is inferred from the values of the NS rotation period and its associated derivative will be overestimated. It thus fosters numerical studies of the fallback matter in 3D simulations of core-collapse SNe and investigations on the evolution of the potential remaining disc. This will help constrain which progenitors are the best candidates to form

magnetars via our fallback scenario.

7.5.4 . Implications for stellar physics

Our findings are also of importance for the study of stellar radiative zones. Indeed, the scaling laws and the dimensionless normalisation factor α derived from our simulations could be implemented in 1D stellar evolution codes. Evolution models using the prescriptions of Fuller et al. (2019) have already been computed for sub-giant/red giant stars but with larger values of $\alpha \sim 0.25-1$. These studies find a strong flattening of the rotation profile and conclude that the prescribed Tayler-Spruit dynamo can not explain both rotation profiles of sub-giant and red giant stars (Eggenberger et al., 2019c), which suggests that different angular momentum transport mechanisms occur during these two phases (Eggenberger et al., 2019b). The future asteroseismic measurements of the magnetic fields in stellar interiors with PLATO will be crucial to clarify the question of the transport mechanisms. Though the first measurements of magnetic fields in some red giant cores suggest a strong fossil field (Li et al., 2022, 2023, Deheuvels et al., 2023), it will be essential to infer the asteroseismic signature of magnetic fields generated by the simulated Tayler-Spruit dynamos for the future observations. Evolution models including MHD instabilities effects were also performed in the case of massive stars to constrain the rotation rate of the remaining PNS or black hole (Griffiths et al., 2022, Fuller & Lu, 2022). They suggest that the angular momentum transport by MHD instabilities is significant in every stage of the massive star evolution. This stresses the importance of performing 3D anelastic simulations with realistic background profiles of radiative zones at different evolution stages to better constrain the angular momentum transport and infer more robust rotation rates of stellar cores.

7.6 . Appendix

7.6.1 . Measure of the shear rate

The differential rotation is characterized by a dimensionless shear rate $q = r\partial_r \ln\Omega$. We define an effective shear rate based on the time average of the radial rotation profile in the saturated state at the colatitude of $\theta = \pi/8\,\mathrm{rad}$. We measure an average slope in the range of radii where half of the Tayler mode energy (approximated by the latitudinal magnetic energy E_{B_θ}) is concentrated around its maximum. We chose this particular method because this range of radii is the region where the dynamo occurs. The measures are displayed in Fig. 7.14 (red plot) along with other measures made with different methods. Whatever the method used, we see that all the measures follow the same trend with an increase of $q \propto N$ until $N/\Omega_o = 4$ after which the values of q stay almost constant.

7.6.2 . List of models

Tables 7.2–7.4 summarize the key parameters and output quantities of the simulations carried out in this study.

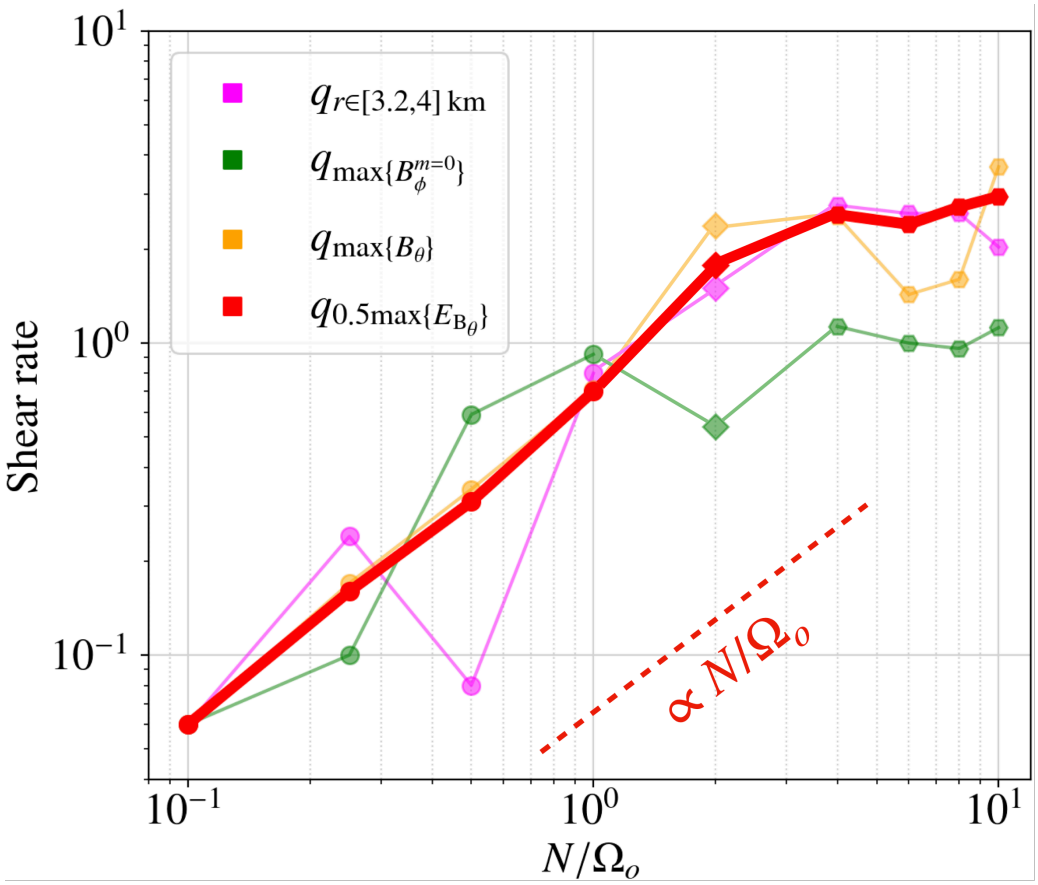

Figure 7.14 — Shear rates q measured locally in the simulations as a function of N/Ω_o. The different colours represent distinct methods to measure q: slope in the rotation profile between 3.2 and $4\,\mathrm{km}$ (pink), q at the maximum of $B_\phi^{m=0}$ and B_θ (green and orange, respectively), and slope in the range of radii where half of the Tayler mode energy (approximated by the latitudinal magnetic energy E_{B_θ}) is concentrated around its maximum (red).

Table 7.2 — Overview of the stable (or failed) dynamo solutions. All the simulations have the same aspect ratio $\chi = 0.25$, Ekman number $E = 10^{-5}$, Rossby number $Ro = 0.75$, thermal and magnetic Prandtl numbers $Pr = 0.1$ and $Pm = 1$, and the same resolution $(n_r, n_\theta, n_\phi) = (256, 256, 512)$. Note that the run named Ro0.75s is the same as in Barrère et al. (2023). This table displays the input parameter of the runs.

Name	Pm	N/Ω_o	$N_{\rm eff}/\Omega_o$	Λ_i
Ro0.75s	1	0.1	0.03	10
Pm1Pr0.1NO0.25	1	0.25	0.08	Λ(Ro0.75s)
Pm1Pr0.1NO0.5	1	0.5	0.16	Λ(Ro0.75s)
Pm1Pr0.1NO1	1	1	0.32	Λ(Pm1Pr0.1NO0.5)
Pm2Pr0.1NO2	2	2	0.45	Λ(Pm1Pr0.1NO1)
Pm2Pr0.1NO4	2	4	0.89	Λ(Pm2Pr0.1NO2)
Pm2Pr0.1NO8	2	8	1.79	Λ(Pm2Pr0.1NO4)
Pm4Pr0.1NO4	4	4	0.63	Λ(Pm2Pr0.1NO4)
Pm4Pr0.1NO6	4	6	0.95	Λ(Pm4Pr0.1NO4)
Pm4Pr0.1NO8	4	8	1.26	Λ(Pm2Pr0.1NO8)
Pm4Pr0.1NO10	4	10	1.58	Λ(Pm2Pr0.1NO10)

Table 7.3 — Same as Table 7.2 but this table displays measured values in the simulations used to produce the plots of the paper.

Name	q	Λ	$B_{\rm tor}^{m=0}$ $\left[10^{-3}\sqrt{4\pi\rho d^2\Omega_o}\right]$	$B_{\rm pol}^{m=0}$ $\left[10^{-3}\sqrt{4\pi\rho d^2\Omega_o}\right]$	$B_{\rm dip}$ $\left[10^{-3}\sqrt{4\pi\rho d^2\Omega_o}\right]$	$B_{\rm tot}^{m\neq0}$ $\left[10^{-3}\sqrt{4\pi\rho d^2\Omega_o}\right]$	$v_{\rm tot}^{m\neq0}$ $[10^{-4}d\Omega_o]$
Ro0.75s	0.06	51.85	21	1.7	1.2	9.3	35
Pm1Pr0.1NO0.25	0.17	69.03	24	1.8	1.4	9.7	34
Pm1Pr0.1NO0.5	0.35	74.71	26	2.0	0.87	6.6	36
Pm1Pr0.1NO1	0.69	99.44	31	0.64	0.36	2.6	19
Pm2Pr0.1NO2	2.37	251.25	36	0.82	0.31	1.1	6.0
Pm2Pr0.1NO4	2.57	332.08	41	0.49	0.18	0.61	3.5
Pm2Pr0.1NO8	2.54	531.21	52	0.18	0.10	0.59	3.4
Pm4Pr0.1NO4	2.57	478.89	35	0.46	0.077	0.36	1.6
Pm4Pr0.1NO6	2.59	495.22	35	0.31	0.077	0.31	1.8
Pm4Pr0.1NO8	2.54	714.16	42	0.31	0.077	0.28	1.6
Pm4Pr0.1NO10	3.74	862.86	47	0.15	0.051	0.2	1.1

Table 7.4 — Following of Table 7.3.

Name	$B_sB_\phi/4\pi$ $[10^{-6}\times4\pi\rho d^2\Omega_o^2]$	$B_s^{m=0}B_\phi^{m=0}/4\pi$ $[10^{-6}\times4\pi\rho d^2\Omega_o^2]$	$v_r^{m\neq0}v_\phi^{m\neq0}/4\pi$ $[10^{-8}\times\rho d^2\Omega_o^2]$	$v_s^{m\neq0}v_\phi^{m\neq0}/4\pi$ $[10^{-8}\times\rho d^2\Omega_o^2]$	$l_{\rm TI}$ [km]	$P_{\rm cyc}$ [s^{-1}]	$\alpha_{\rm cyc}$
Ro0.75s	15	2.9	52	76	2.8	–	–
Pm1Pr0.1NO0.25	9.1	2.4	56	89	2.5	–	–
Pm1Pr0.1NO0.5	5.7	1.8	58	110	1.5	–	–
Pm1Pr0.1NO1	3.0	0.84	18	35	0.8	–	–
Pm2Pr0.1NO2	2.2	1.7	2.8	10	0.6	27	0.66
Pm2Pr0.1NO4	1.5	1.4	7	4.4	0.4	12	0.59
Pm2Pr0.1NO8	1.7	1.0	0.52	5.3	0.2	13	0.38
Pm4Pr0.1NO4	0.45	0.63	0.16	0.61	0.4	3	0.62
Pm4Pr0.1NO6	0.53	0.67	0.17	0.94	0.3	16	0.5
Pm4Pr0.1NO8	0.65	0.75	0.12	0.77	0.2	10	0.47
Pm4Pr0.1NO10	0.50	0.52	0.066	0.46	0.15	6	0.57

8

From stationnary to reversing Tayler-Spruit dynamo

Contents

In the previous chapter, we looked at the impact of stable stratification on the dipolar Tayler-Spruit dynamo. Here, we study the same effect on the hemispherical Tayler-Spruit dynamo. This chapter focuses on the dynamics of the dynamo and not on the magnetic field strength like in the previous chapters, which are applied more specifically to the context of magnetar formation. The following text is being prepared for submission in *Physical Review Fluids* in collaboration with Alexis Reboul-Salze, Jérôme Guilet, Raphaël Raynaud, and Basile Gallet.

8.1 . Introduction

Magnetic fields are ubiquitous in most astrophysical objects from neutron stars to cosmic scales, including stars, accretion disks and planets. They span a wide range of strengths, from 10^{-6} in hot intracluster medium (Carilli & Taylor, 2002, Bonafede et al., 2010) to $10^{15}\,\mathrm{G}$ (Kaspi & Beloborodov, 2017) in magnetars. The question of their amplification and sustainment is very tough due to its strong non-linear nature and is still actively investigated (see e.g. the reviews (Brandenburg & Subramanian, 2005, Kulsrud & Zweibel, 2008, Federrath, 2016, Rincon, 2019, Tobias, 2021)). Most observed astrophysical dynamos can be sorted in the following categories: (i) the galactic helical dynamo, which may be driven by supernova (SN)-induced turbulence (Brandenburg, 2015, Subramanian, 2019), (ii) the dynamos driven by rotating convection, which is applied to stellar convective zones (Käpylä et al., 2023, Charbonneau & Sokoloff, 2023), Earth outer core (Landeau et al., 2022), and white dwarf stars (Isern et al., 2017), and (iii) the subcritical dynamos driven by magnetohydrodynamical (MHD) instabilities in shear flows, which could operate in stably stratified media, such as accretion disks (Hawley

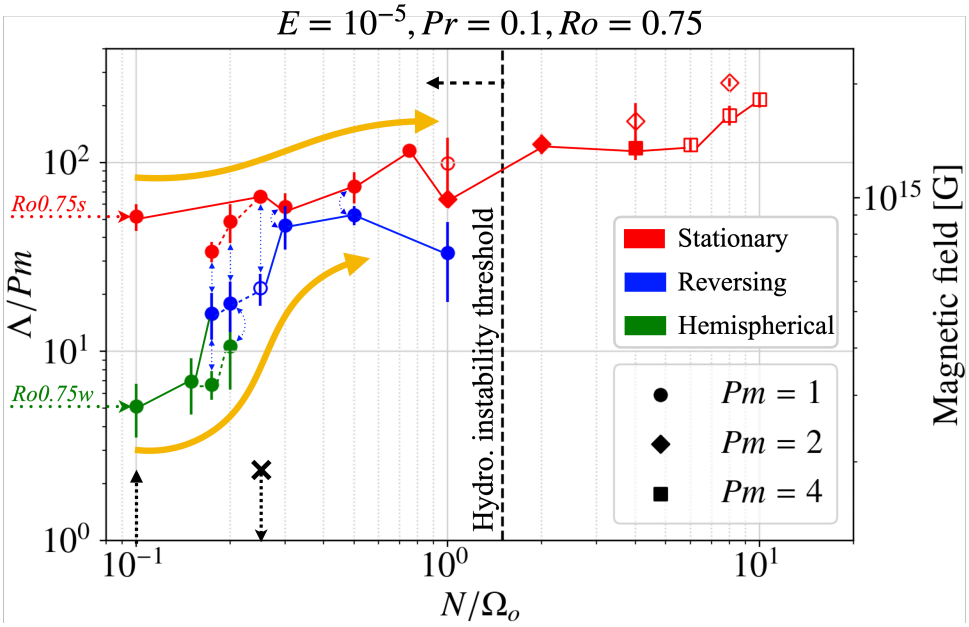

Figure 8.1 — Viscous Elsasser number (and root mean square magnetic field) as a function of the ratio of the Brunt-Väisälä frequency to the rotation rate at the outer sphere. Filled and empty markers represent self-sustained and transient dynamos, respectively. The black dashed vertical line and arrow indicate the zone in which the fluid is hydrodynamically unstable. The orange arrows illustrate in which direction we extended both dipolar/stationary and hemispherical branches reported by Barrère et al. (2023) at $N/\Omega_o = 0.1$ and $Ro = 0.75$. The different colours represent different saturated states of the Tayler-Spruit dynamo: the stationary (red), hemispherical (green), and reversing (blue) states.

et al., 1996, Rincon et al., 2007, Lesur & Ogilvie, 2008) and solar/stellar radiative zones (Spruit, 2002, Cline et al., 2003, Vasil et al., 2024).

The dynamo problem is all the more difficult as astrophysical magnetic fields show a rich variety of geometries such as the ancient Martian hemispherical magnetic field (Acuna et al., 1999, Langlais et al., 2004). The magnetic fields can also harbour complex temporal dynamics like the chaotic reversals and excursions of terrestrial magnetic field (Korte & Mandea, 2019) or the solar periodic reversals (Hathaway, 2010). Similar dynamics were also observed in the Von Karman Sodium (VKS) experiment, which consists in generating a self-sustained magnetic field in a turbulent von Karman swirling flow of liquid sodium forced by two counter-rotating bladed disks (Monchaux et al., 2007, Berhanu et al., 2007, Ravelet et al., 2008, Monchaux et al., 2009). Numerical simulations constitute an important tool to study these magnetic states and the transition between them. Several numerical models of rotating, convection-driven dynamo manage to reproduce hemispherical (Stanley et al., 2008, Amit et al., 2011, Dietrich & Wicht, 2013, Landeau et al., 2017) and oscillatory magnetic fields (Raynaud & Tobias, 2016, Strugarek et al., 2017, 2018). Rich dynamics are also observed in numerical simulations of the magnetorotational instability (MRI)-driven dynamos in stably stratified shear flows (Herault et al., 2011, Riols et al., 2013, 2017, Reboul-Salze et al., 2022).

Here, we focus on the *Tayler-Spruit* dynamo, which is — similarly to the MRI-driven dynamo — a subcritical dynamo driven by an MHD instability called the Tayler instability. This instability feeds off a toroidal field in a stably stratified medium due to the presence of an electric current along the axis of symmetry (Tayler, 1973, Goossens et al., 1981). The produced

electromotive force can generate a large-scale poloidal magnetic field that will be sheared to strengthen the toroidal component and thus close a dynamo loop (Spruit, 2002, Denissenkov & Pinsonneault, 2007, Zahn et al., 2007, Fuller et al., 2019). Despite a lack of numerical evidence, their analytical prescriptions were widely implemented in 1D stellar evolution codes and show promising results to explain helio/asteroseismic observations (Cantiello et al., 2014, Eggenberger et al., 2019c,a, den Hartogh et al., 2020, Griffiths et al., 2022, Eggenberger et al., 2022, Fuller & Lu, 2022). This mechanism is also promising to form magnetar-like magnetic fields ($10^{14}-10^{15}\,\mathrm{G}$) in proto-neutron stars spun up by supernova fallback accretion (Barrère et al., 2022). While the Tayler-Spruit dynamo was identified for the first time in numerical simulations very recently (Petitdemange et al., 2023), we demonstrated the existence of two Tayler-Spruit dynamos in bistability that harbour distinct magnetic field geometry: equatorially symmetric and hemispherical (Barrère et al., 2023, 2024b).

In this article, we report the existence of a reversing Tayler-Spruit dynamo. This echoes the behaviour we shortly mentioned in our first numerical study (Barrère et al., 2023) for strong differential rotation forcing. We argue that this rich diversity of dynamo states results from the equatorial symmetry breaking of the flow. This drives the interaction between two axisymmetric unstable dynamo modes with a dipolar and a quadrupolar geometry. While this type of model explains well the dynamics observed in the VKS experiment (Gallet & Pétrélis, 2009, Gissinger, 2010) and the dynamics of the Earth and Sun magnetic field (Knobloch & Landsberg, 1996, Pétrélis et al., 2009, Gissinger et al., 2012), we show for the first time that it also accounts for the dynamics of the Tayler-Spruit dynamo.

Note that the numerical methods are the same in the previous chapter (Chap. 7). The only differences are that the stable stratification is varied in the range $N/\Omega_o \in [0.1, 1]$.

8.2 . Results

8.2.1 . A diversity of dynamical regimes

The different saturated states found in our numerical simulations and their associated average magnetic energy density in terms of Λ_ν are gathered in the bifurcation diagram in Fig. 8.1. We report the existence of three distinct Tayler-Spruit dynamo states, which are represented by different colours. Starting from the saturated state of the run 'Ro0.75s' from Barrère et al. (2023) at $N/\Omega_o = 0.1$, we obtain the red branch, which shows the strongest magnetic fields. This is the extension for larger N/Ω_o of the 'dipolar' branch found in Barrère et al. (2023) and has been thoroughly studied in a previous study (Barrère et al., 2024b). This state is characterised by a predominant axisymmetric toroidal component $(l = 2, m = 0)$ that remains stationary. This dynamo has been maintained in a self-sustained state to $N/\Omega_o = 4$ and in a transient state to $N/\Omega_o = 10$. Note that self-sustained states for $N/\Omega_o > 4$ are expected to be reached by decreasing the resistivity (Barrère et al., 2024b). To avoid confusing the dipolar branch with the dipolar mode that we will define in Sect. 8.2.2, we will refer to this dynamo state as the *stationary* state.

Restarting from the saturated hemispherical dynamo of the run 'Ro0.75w', we find that the *hemispherical* state can be maintained up to $N/\Omega_o = 0.15$. For $N/\Omega_o \geqslant 0.175$ the magnetic field can successively enter several saturated states in the same time series. A typical example is the time series at $N/\Omega_o = 0.2$. The associated time series of the latitudinal profile of the axisymmetric toroidal magnetic field $B_\phi^{m=0}$ (called butterfly diagram) and of the symmetric

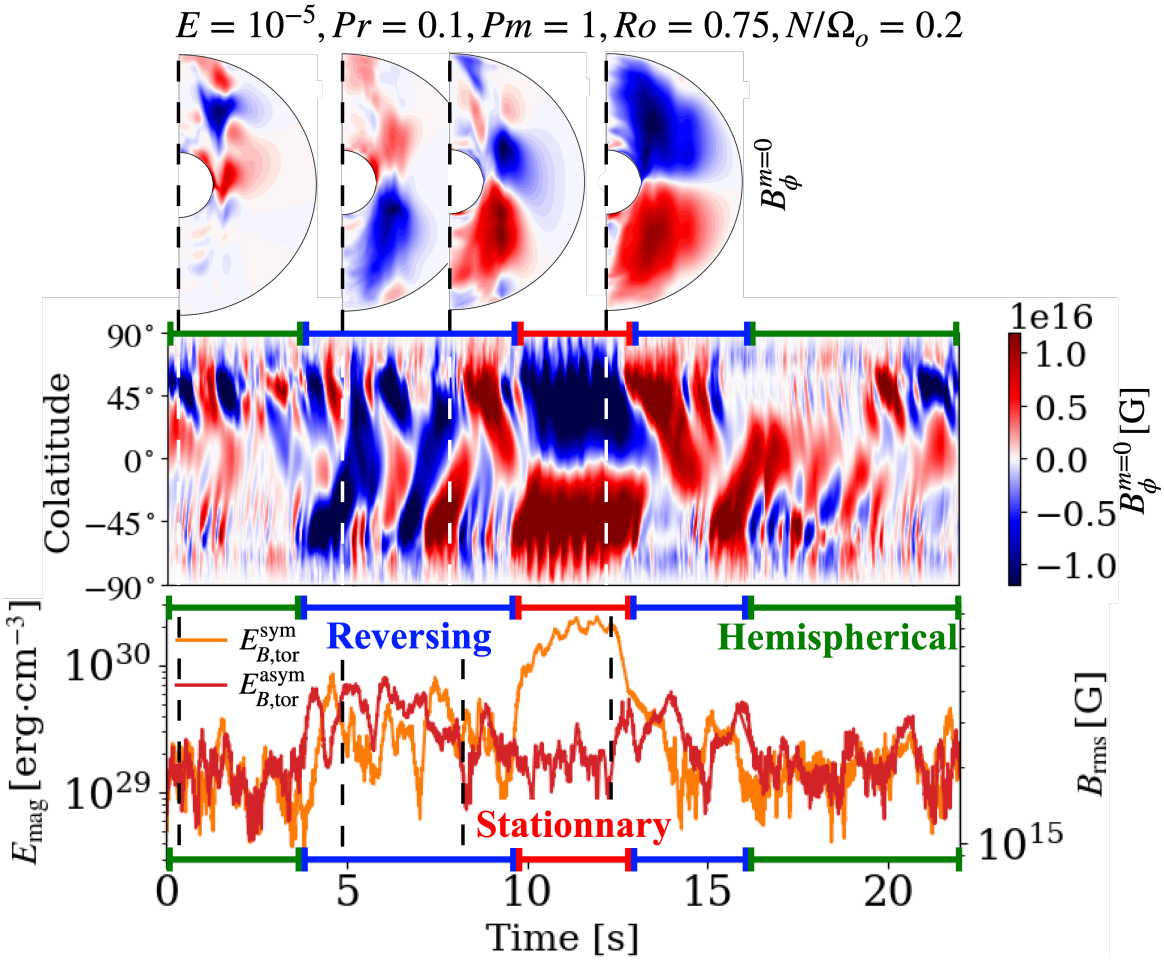

Figure 8.2 — Top and middle: Meridional slices and butterfly diagram of the axisymmetric toroidal field $B_\phi^{m=0}$ averaged between the radii $r = 5\,\mathrm{km}$ and $r = 6\,\mathrm{km}$. Bottom: Time series of the symmetric ($E^{\rm sym}_{B,\rm tor}$, orange) and anti-symmetric ($E^{\rm asym}_{B,\rm tor}$, red) components of the toroidal magnetic energy for the run at $N/\Omega_o = 0.2$. The different lines on top/bottom of the plots have colours corresponding to the different saturated states as in Fig. 8.1.

(anti-symmetric) magnetic energy $E^{\rm sym}_{B,\rm tor}$ ($E^{\rm asym}_{B,\rm tor}$) are displayed in Fig. 8.2. The initial magnetic field in this run is the hemispherical state of the run at $N/\Omega = 0.15$, which is maintained until $t = 4\,$s. This state is characterised by the concentration of magnetic field in one hemisphere. This is consistent with the butterfly diagram and the first meridional slice (top and middle panels of Figure 8.2), in which the northern hemisphere contains $50-75\,\%$ of the magnetic energy. The time series shows that $E^{\rm sym}_{B,\rm tor} \sim E^{\rm asym}_{B,\rm tor}$, which is consistent with the interpretation of the hemispherical geometry as the result of the superposition of modes with opposite equatorial symmetry (Gallet & Pétrélis, 2009).

Between $t = 4\,$s and $t = 10\,$s, the dynamo enters a first *reversing* state. In the second meridional slice and the butterfly diagram, we see that a large-scale $B_\phi^{m=0}$ form in the southern hemisphere, which then migrates towards the opposite hemisphere. During this migration, $B_\phi^{m=0}$ reverses, i.e. a large-scale $B_\phi^{m=0}$ with the opposite sign forms in the southern atmosphere (third meridional slice). The reversals translate into oscillations of $E^{\rm sym}_{B,\rm tor}$ and $E^{\rm asym}_{B,\rm tor}$. The change of symmetry is due to the migration of a patch of $B_\phi^{m=0}$ through the equator ($E^{\rm sym}_{B,\rm tor} < E^{\rm asym}_{B,\rm tor}$) and the formation a patch with the opposite sign in one hemisphere ($E^{\rm sym}_{B,\rm tor} > E^{\rm asym}_{B,\rm tor}$). These modulations were already observed by Barrère et al. (2023) in the regime of strong forcing of differential rotation ($Ro \gtrsim 0.8$). The reversals are mostly periodic and the period tends to increase with N/Ω_o.

Finally, the magnetic field enters the stationary state we mentioned. The predominance of the $(l = 2, m = 0)$-magnetic field is clear in the fourth meridional slice and the butterfly diagram between $t = 10\,$s and $t = 13\,$s. This translates into a large $E^{\rm sym}_{B,\rm tor} \sim 10 E^{\rm asym}_{B,\rm tor}$. While the stationary state is maintained in most simulations (Barrère et al., 2023, 2024b), the dynamo reverts back to the reversing state, and then the hemispherical state at $t \geqslant 13\,$s. Note that the hemispherical state can switch from one hemisphere to another as seen at the end of this simulation.

For $N/\Omega_o \geqslant 0.25$, no hemispherical state can be maintained, even transiently. The dynamo either oscillates between the reversing and the stationary states, or remains in the stationary state. Although our simulations are not long enough to capture more than 4 transitions between two states, these transitions do not seem to occur periodically. Moreover, the dynamics significantly depend on the initial conditions for the magnetic field, which suggests a chaotic transition between these states (Riols et al., 2013). After $N/\Omega_o > 1$, the dynamo is lost at $Pm = 1$ since the resistivity becomes too large for the fluid to remain Tayler unstable (Barrère et al., 2024b). However, this complex dynamics does not reappear for $Pm > 1$, and only the stationary branch can be maintained.

8.2.2 . Two-modes modelling

Our numerical simulations of the Tayler-Spruit dynamo cover the features of dynamos found in the VKS experiment. Low-dimensional models show that the different states are well explained by the interaction between two large-scale dynamo modes with opposite equatorial symmetries, called *dipolar* (equatorially symmetric field) and *quadrupolar* (equatorially anti-symmetric field) modes (Pétrélis et al., 2009, Gallet & Pétrélis, 2009, Gissinger, 2010). Gallet & Pétrélis (2009) provide a model in which the equatorial symmetry breaking of the flow drives this interaction. This results in the generation of both hemispherical and reversing dynamos, depending on the imposed symmetry breaking.

In order to verify whether this interpretation fits our numerical simulations, we extract the dipolar/quadrupolar modes and the symmetry breaking of the flow. To this end, we expand

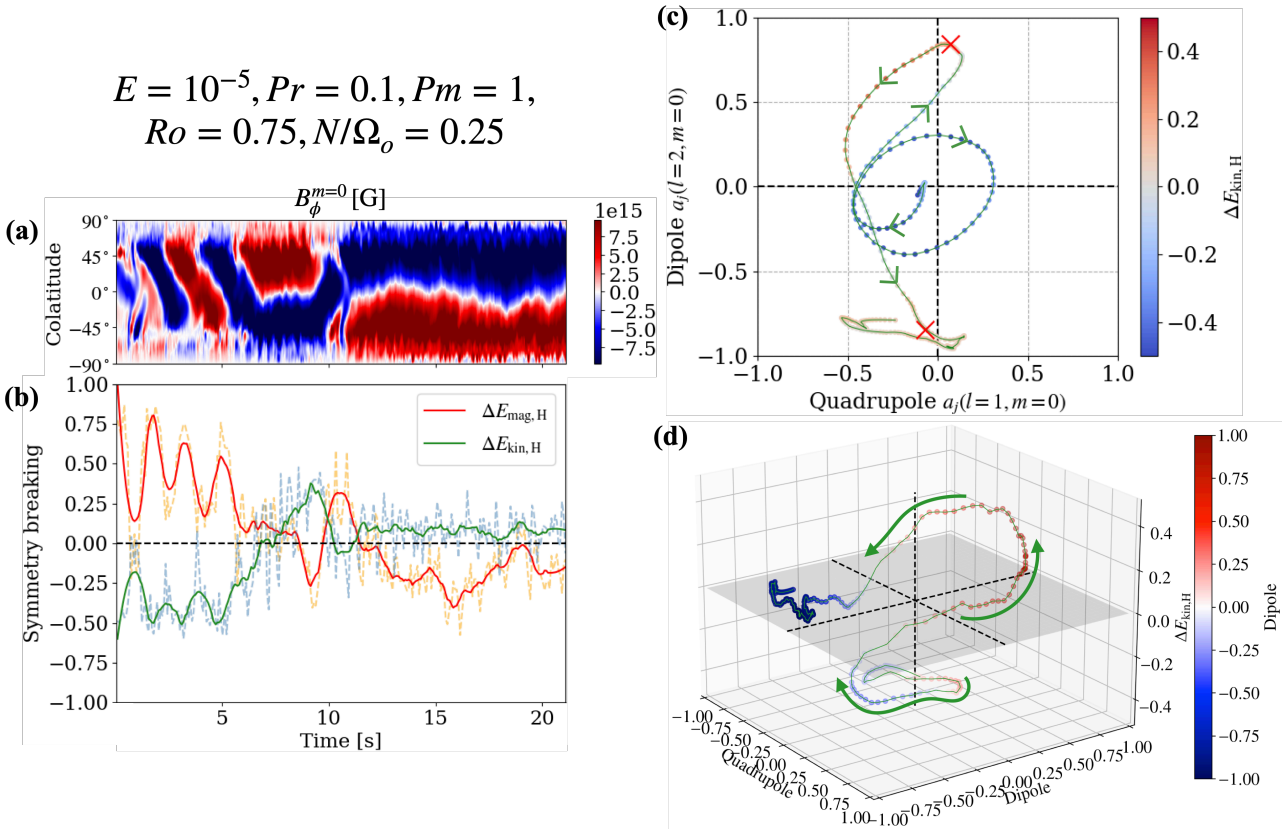

Figure 8.3 — Time evolution of several quantities of the run at $N/\Omega_o = 0.25$. (a): Butterfly diagram of $B_\phi^{m=0}$. (b): Time evolution of the symmetry breaking the flow $\Delta E_{\mathrm{kin,H}}$ (dashed blue and solid green for the raw and smoothed measures) and the magnetic field $\Delta E_{\mathrm{mag,H}}$ (dashed orange and solid red for the raw and smoothed measures). (c) Trajectory the dynamo in the phase space dipole–quadrupole. The values of the modes are normalised by the maximum value of the dipolar or the quadrupolar modes. The curve is coloured by the symmetric breaking of the flow $\Delta E_{\mathrm{kin,H}}$. The red crosses indicate the fixed point location. They are estimated by looking at the local minimum of the velocity in the phase space. (d): 3D plot the phase space along the vertical axis representing $\Delta E_{\mathrm{kin,H}}$. The colour represents the value of the normalised dipole mode. The grey plane illustrates the plane at $\Delta E_{\mathrm{kin,H}} = 0$ and the green arrows indicate the direction of the trajectory.

$B_\phi^{m=0}$ into spherical harmonics. The dominant equatorially symmetric and anti-symmetric components are the respective $l = 2$ and $l = 1$ modes in most of simulations. Therefore, we define the dipolar and the quadrupolar modes as the $l = 2$ and $l = 1$ modes of $B_\phi^{m=0}$, noted $a_j(l = 2, m = 0)$ and $a_j(l = 1, m = 0)$, respectively. To quantify the symmetry breaking, we define the parameter

$$\Delta E_{\mathrm{kin,H}} \equiv \frac{E_{\mathrm{kin,N}} - E_{\mathrm{kin,S}}}{E_{\mathrm{kin,N}} + E_{\mathrm{kin,S}}}, \tag{8.1}$$

which measures the difference between the total kinetic energy in the northern $E_{\mathrm{kin,N}}$ and the southern $E_{\mathrm{kin,S}}$ hemispheres. Therefore, the flow symmetry is broken when $E_{\mathrm{kin,H}} \neq 0$.

Fig. 8.3 shows the evolution of the dipolar/quadrupolar modes and the equatorial symmetry breaking of the flow $\Delta E_{\mathrm{kin,H}}$ for a run at $N/\Omega_o = 0.25$. The butterfly diagram (panel (a)) of $B_\phi^{m=0}$ and the time series of $\Delta E_{\mathrm{kin,H}}$ (green curve in the panel (b)) show that the dynamo switches between several states that match with different values of the symmetry breaking:

(i) Until $t = 6\,\mathrm{s}$, $\Delta E_{\mathrm{kin,H}} \sim -0.5$ while the dynamo is in a reversing state;

(ii) The symmetry breaking then increases and tends toward $\Delta E_{\mathrm{kin,H}} = 0$, which corresponds to the transition to the first stationary state between $t = 6\,\mathrm{s}$ and $t = 10\,\mathrm{s}$;

(iii) $\Delta E_{\mathrm{kin,H}}$ becomes positive and peaks at $\Delta E_{\mathrm{kin,H}} \sim 0.35$ when $t = 10\,\mathrm{s}$, which matches the beginning of the magnetic field reversal;

(iv) Finally, $\Delta E_{\mathrm{kin,H}}$ decreases and the magnetic field completes its reversal. The dynamo is maintained in a stationary state and $\Delta E_{\mathrm{kin,H}} \sim 0.1$ stalls.

Therefore, $\Delta E_{\mathrm{kin,H}}$ is strongly related to the dynamics of the dynamo.

While the flow symmetry breaking may drive the dynamics of the dynamo, the generated magnetic field acts back onto the flow. To observe this effect, we define a parameter similar to $\Delta E_{\mathrm{kin,H}}$ to measure the symmetry breaking of the magnetic field

$$\Delta E_{\mathrm{mag,H}} \equiv \frac{E_{\mathrm{mag,N}} - E_{\mathrm{mag,S}}}{E_{\mathrm{mag,N}} + E_{\mathrm{mag,S}}}. \tag{8.2}$$

The evolution of this parameter is plotted as the red curve in Fig. 8.3, panel (b). We observe that $\Delta E_{\mathrm{kin,H}}$ and $\Delta E_{\mathrm{mag,H}}$ are in anti-phase. This shows that the magnetic field in one hemisphere lowers the energy kinetic energy in the same hemisphere, i.e. the dynamo action in one hemisphere transfers the kinetic energy into magnetic energy. Therefore, the magnetic field also influences the equatorial symmetry of the flow, which explains the non-constant value of $\Delta E_{\mathrm{kin,H}}$. This differs from the VKS experiment, in which the symmetry breaking is controlled by the imposed frequencies on the rotating impellers.

A correlation with $\Delta E_{\mathrm{kin,H}}$ is also found in the phase space dipole–quadrupole. The trajectory of the magnetic field in this 2D phase space is shown in panel (c) of Fig. 8.3 with a colour map illustrating the value of $\Delta E_{\mathrm{kin,H}}$. During the reversing phase, the magnetic field moves along a limit cycle with $\Delta E_{\mathrm{kin,H}} \sim 0.5$. When $\Delta E_{\mathrm{kin,H}}$ tends toward 0, the magnetic field then diverges toward a first fixed point (red cross at $(-0.07, 0.84)$) where the magnetic field dynamics slows. As $\Delta E_{\mathrm{kin,H}}$ increases the magnetic field reverses and so moves toward the cycle. As soon as it reaches the cycle, $\Delta E_{\mathrm{kin,H}}$ decreases and the magnetic field diverges toward the same fixed point but with an opposite sign (red cross at $(0.07, -0.84)$. After that, the magnetic field moves around the fixed point and $\Delta E_{\mathrm{kin,H}}$ remains quasi-constant. The same trajectory is also visible in a 3D plot of the phase space with $\Delta E_{\mathrm{kin,H}}$ as a vertical axis (panel (d)). The trajectory is consistent with the presence of a saddle-node bifurcation as modelled by Pétrélis et al. (2009): when $\Delta E_{\mathrm{kin,H}} = 0$, the dipole–quadrupole space contains two unstable and stable fixed points with opposite signs. In our case, the stable mode is the dipolar mode because the stable fixed points are located near the axis $a_j(l = 1, m = 0) = 0$. As the equatorial symmetry of the flow is broken ($\Delta E_{\mathrm{kin,H}} \neq 0$), the (dipolar) stable and (quadrupolar) unstable fixed points with the same sign are closer and closer. Once they collide, the fixed points disappear and the magnetic field follows a limit cycle. Cyclic structures emerging of saddle-node bifurcation were also observed in shearing-box simulations of the non-linear magnetorotational (MRI)-driven dynamo (Herault et al., 2011, Riols et al., 2013, 2017). These cycles are unstable, which explains the difficulty of capturing them in our numerical simulations and the necessity of Newton's method to converge them.

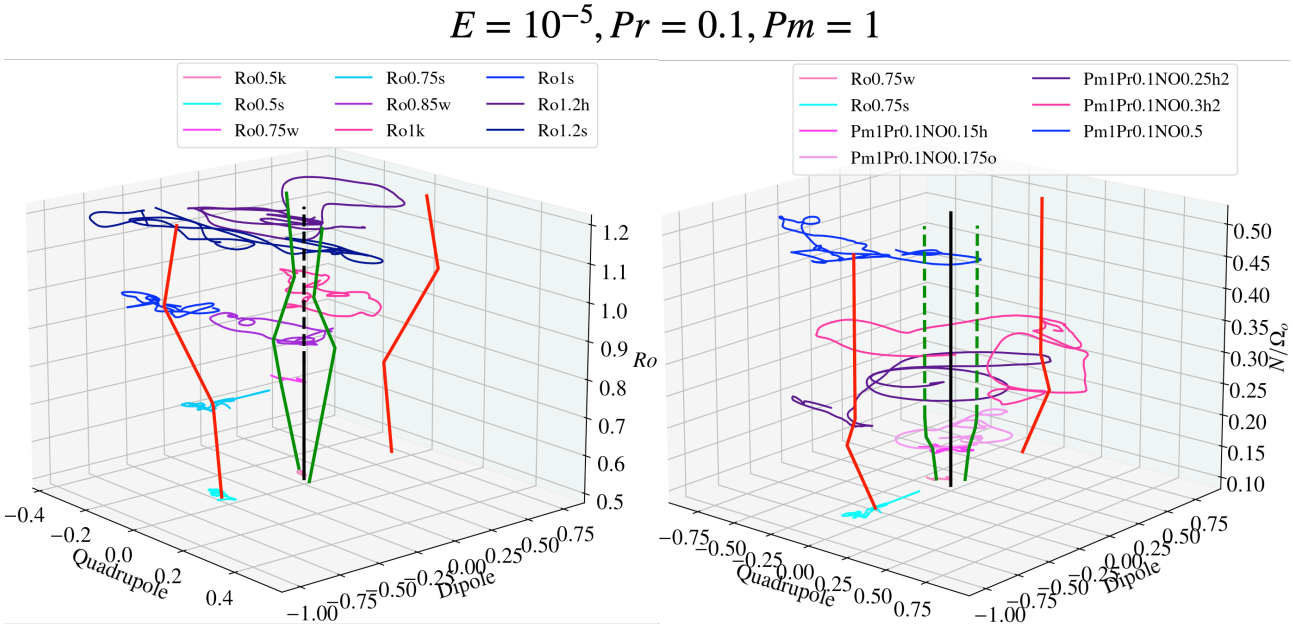

Figure 8.4 — 3D bifurcation diagrams of the dipole–quadrupole phase spaces of several simulations as a function of the Rossby number Ro (left) and ratio N/Ω_o (right). The simulations on the left plot were studied in Barrère et al. (2023). The red and green curves represent the stationary and the hemispherical branches, respectively. The black vertical axis is the origin of the phase space $a_j(l = 1, m = 0) = a_j(l = 2, m = 0) = 0$. The dashed (solid) lines indicate that the branch is stable (unstable).

This interpretation also provides a good explanation for the other structures found in the phase space for other simulations in which the magnetic field oscillates between the stationary and the reversing states, i.e. when $N/\Omega_o \in [0.25, 1]$. For simulations in which the magnetic field can also explore to the hemispherical state ($N/\Omega_o \in [0.175, 0.2]$), the model of Gallet & Pétrélis (2009) also predicts that the flow symmetry breaking can also result in the localisation of the magnetic field in one hemisphere. This is consistent with our simulations since the hemispherical phases correspond to $|\Delta E_{\mathrm{kin,H}}| \sim 0.25 - 0.5$. It remains however unclear how to determine in our simulations why the symmetry breaking results in the localisation of the magnetic field instead of reversals. The absence of a hemispherical state for $N/\Omega_o \geqslant 0.25$ indicates that stable stratification plays a role in preventing the magnetic field from reaching this state.

The trajectory of several simulations is gathered in Fig. 8.4, which displays the 3D bifurcation diagram of the dipole–quadrupole space as a function of the different parameters we varied: N/Ω_o (in this study) and Ro (in Barrère et al. (2023)). In the latter, we observe that the dynamics are also more and more complex as Ro increases. In these simulations, our interpretation still works and is besides intuitive, as large values of Ro are prone to produce turbulence contributing to breaking the flow equatorial symmetry.

8.3 . Conclusions

To conclude, we have reported for the first time the existence of complex dynamics of the Tayler-Spruit dynamo involving three dynamo states:

(i) the stationary state that is characterised by an axisymmetric toroidal magnetic field

with an equatorial symmetry,

(ii) the hemispherical state, in which the magnetic field is concentrated in one hemisphere,

(iii) the reversing state.

We have demonstrated that the dynamics of the Tayler-Spruit dynamo can result from the non-linear coupling of two unstable modes with opposite equatorial symmetries. This interaction is driven by the equatorial symmetry of the flow $\Delta E_{\rm kin,H}$, which causes the transition from a stationary state ($|\Delta E_{\rm kin,H}| = 0 - 0.1$) to a hemispherical or a reversing dynamo ($|\Delta E_{\rm kin,H}| = 0.25 - 0.5$). The transition is consistent with the disappearance of the stationary state through a saddle-node bifurcation. Future simulations with longer integration times will help characterise the transition quantitatively. Thus, the results of this study confirm the importance of the breaking of the flow's equatorial symmetry in the magnetic field dynamics.

One may wonder whether the dynamo can be described as a mean-field dynamo (α^2, $\alpha\Omega$, $\alpha^2\Omega$, or shear current-driven dynamo). An α effect can not be ruled out since the kinetic helicity is not negligible in our simulations. The extraction of the mean-field dynamo tensors α and β using several methods (correlations between the electromotive force and derivatives of the axisymmetric magnetic field (as done by Reboul-Salze et al., 2022), the singular value decomposition (Racine et al., 2011, Simard et al., 2016), and the most recent IROS method (Bendre et al., 2023)) suggests that both the diagonal α and non-diagonal β coefficient may contribute equally to the electromotive force, but this is not clear for every numerical model. Further analysis will help clarify which mean-field mechanism generates the large-scale magnetic fields. However, the relation between the electromotive force and the axisymmetric magnetic field is rather non-linear, unlike what is assumed in the mean-field theory. Moreover, subcritical non-linear dynamos in the vicinity of the dynamo threshold do not usually reduce to standard mean-field dynamos (Cline et al., 2003, Davies & Hughes, 2011, Riols et al., 2013).

This rich dynamics observed for $Pm = 1$ does not appear for larger Pm in our simulations. In the context of the magnetar formation, our results, therefore, suggest that this rich dynamics does not appear in proto-neutron stars where $Pm \sim 10^4 - 10^{11}$ depending on the dominant viscous process (Supplementart Materials of Barrère et al., 2023). Unlike in our simulations, the inner layers usually rotate faster than the outer layers in stellar radiative zones. Since no such dynamics were reported in numerical simulations with the stellar differential rotation, it is still unclear whether these dynamics can appear in these regions.

9

From proto-neutron star dynamo to magnetars

Contents

While the previous studies of the fallback scenario focused on the formation of the magnetic field during the proto-neutron star stage, understanding the evolution of this magnetic field on timescales of $1-1000\,\mathrm{kyr}$ is essential to predict the NS emission and compare it to magnetar light curves. In this chapter, we summarise a study carried out with Andrei Igoshev in which we investigate the long-term evolution of a magnetic field generated by the Tayler-Spruit dynamo in the crust of a cold neutron star (NS). We also study the implication for the induced X-ray emission. The following text is inspired by an article submitted to *Nature Astronomy* that was written by Andrei Igoshev in collaboration with me, Raphaël Raynaud, Jérôme Guilet, Toby Wood, and Rainer Hollerbach (App. C.3.4).

9.1 . Introduction

Two main categories of studies investigate the magnetic field evolution in magnetars. On the one hand, different dynamo mechanisms have been numerically investigated to explain the formation of the strongest magnetic fields, including proto-neutron star (PNS) convection (Thompson & Duncan, 1993, Raynaud et al., 2020, 2022, Masada et al., 2022, White et al., 2022), magnetorotational instability (Reboul-Salze et al., 2021, 2022), and more recently the Tayler–Spruit dynamo (Barrère et al., 2022, 2023, 2024b). These studies focus on the magnetic field dynamics in the PNS between $\sim 0.2-30\,\mathrm{s}$ after the core bounce. On the other hand, the numerical simulations of the coupled evolution of the magnetic fields and the temperature in a cold NS structure aim at better interpreting the observed light curve of magnetars (e.g. Igoshev et al., 2021, De Grandis et al., 2021, Dehman et al., 2023). These two families of simulations show many differences. First, the simulated NS structure between the PNS stage and the cold NS is very different. While the PNS interior is usually modelled as a magnetohydrodynamical fluid, the cold NS is composed of two main layers: the crust and the

core. The former consists of a lattice of ions in which relativistic electrons move and the latter is composed of superfluid neutrons and superconductive protons. The magneto-thermal evolution is usually simulated in the crust only (e.g. Viganò et al., 2013, Gourgouliatos et al., 2016, Pons & Viganò, 2019) because the core composition is not well understood and difficult to model (Ciolfi & Rezzolla, 2013, Henriksson & Wasserman, 2013, Lander, 2013, Elfritz et al., 2016, Castillo et al., 2020, Viganò et al., 2021). Therefore, PNS and cold NS simulations solve very different equations. Second, the dynamo simulations capture a few seconds of the PNS evolution, while the magneto-thermal evolution models cover timescales between $1\,\mathrm{kyr}$ and $1\,\mathrm{Myr}$. This is related to the magnetic field dynamics which is in a turbulent state during the first seconds but eventually stabilises and decays on longer-time scales once the NS structure is cooled and stable.

Magneto-thermal models have usually considered idealised, large-scale magnetic fields for the initial condition of their simulations. Although some previous studies have considered more complex field structures, as expected from PNS evolution (De Grandis et al., 2022, Dehman et al., 2023), no direct implementation of an initial magnetic field stemming from a saturated dynamo state have been done to this day. Yet, this link between PNS dynamos and the magneto-thermal evolution is essential to understand the formation and the evolution of magnetars. While this would provide more physically justified initial conditions in magneto-thermal simulations, this link will enable the first connection between PNS dynamo models and the observations. To this end, we ivestigate the magneto-thermal evolution of a magnetic field configuration in the saturated state of the dipolar Tayler-Spruit dynamo (run *Ro0.75s* in Chap. 6) using a modified version of the pseudo-spectral code `PARODY` (Dormy, 1997, Aubert et al., 2008).

9.2 . Methods

The specific numerical methods used in `PARODY` for the magneto-thermal evolution are detailed in the submitted version of the article (App. C.3.4). Here, we focus on how we adapted the magnetic field configuration from our simulation to the integration domain representing the NS crust in `PARODY`, where the ratios between the radius of the inner to that of the outer sphere are $\chi_{\mathrm{PNS}} = 0.25$ and $\chi_{\mathrm{NS}} = 0.9$, respectively. The method consists of extracting the poloidal b and the a_j magnetic potentials in the top $10\,\%$ of the dynamo simulation. Then, we represent the new magnetic potentials as a polynomial expansion of the radius r with the form

$$b^{\mathrm{P}}(r),\, a_j^P(r) = \frac{c_0 + c_1 r + c_2 r^2 + c_3 r^3 + c_4 r^4}{r}, \tag{9.1}$$

and we fit it to the extracted b and a_j, while respecting several conditions. First, we require the numerical fits to exactly coincide with the extracted potentials at the following points: $r_1 = 0.93 r_o$ and $r_2 = 0.96 r_o$. Second, we impose the vacuum boundary condition (Eqs. (4.83)-(4.85)) at the surface and the 'no-currents' boundary condition at the core-crust interface ($r = 0.9 r_o$), i.e.

$$b(0.9 r_o) = 0, \tag{9.2}$$

$$\partial_r a_j(0.9 r_o) = 0. \tag{9.3}$$

Note that the equations for the boundary conditions presented in Sect. 4.3.6 are not exactly the same as those in the submitted article (Supplementary Materials in App. C.3.4), because

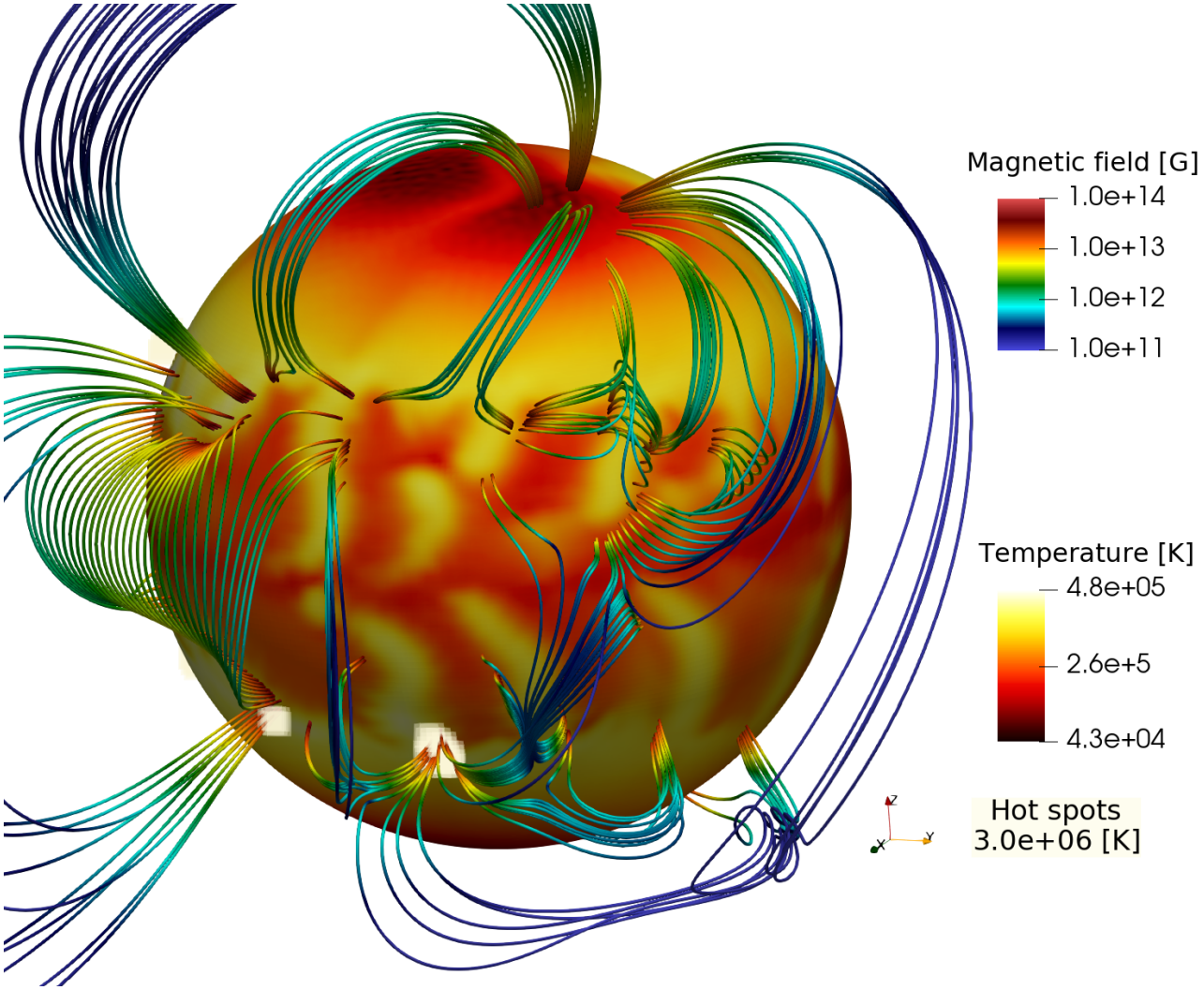

Figure 9.1 — Surface temperature distribution and external magnetic field structure at age 200 kyr.

the MagIC and PARODY codes use different conventions to define the potentials. The equations remain equivalent. Third, we also require our fit for the poloidal potential $b^{\rm P}(r_o)$ to coincide with $b(r_o)$ at the surface. These conditions form a system of equations that we solve to determine the values of the coefficients c_1, c_2, c_3, and c_4. The potentials $b^{\rm P}(r)$ and $a_j^P(r)$ are then implemented as initial conditions in the PARODY code.

9.3 . Results

The magneto-thermal evolution of the NS crust is integrated over a timescale of $1\,\mathrm{Myr}$ and is formulated as electron-MHD. Focusing on the magnetic field, the surface magnetic dipole increases by a factor of only three during the simulation, reaching a maximum value of $1.5\times10^{12}\,\mathrm{G}$. This value is weak compared to classical magnetars ($\gtrsim10^{14}\,\mathrm{G}$) and is more consistent with the magnetars harbouring low magnetic dipoles. Similarly, the quadrupole component of the poloidal magnetic field remains relatively small (maximum of around $6\times10^{12}\,\mathrm{G}$) compared to internal magnetic fields, which are 2 to 3 orders of magnitude larger. Figure 9.1 shows the three-dimensional magnetic field lines and the temperature map at the NS surface, after $200\,\mathrm{kyr}$ of evolution. We observe that the magnetic field harbours a complex topology featuring individual arches elongated in the north-south direction. The local field strength at the footpoints of these arches reaches $10^{14}\,\mathrm{G}$, which is ~100 times stronger than the surface magnetic dipole. Small-scale magnetic fields remain dominant at all times from the beginning of the evolution until $1\,\mathrm{Myr}$ (see Supplementary Materials in App. C.3.4, Sect. 4). These magnetic arcs are consistent with the observation of absorption lines in the X-ray spectra of two magnetars with weak magnetic dipoles: SGR 0418+5729 (Tiengo et al., 2013) and Swift J1822.3–1606 (Rodríguez Castillo et al., 2016).

These small-scale surface magnetic field could also explain the observed light curve of low-magnetic field magnetars via magnetospheric heating. Indeed, the penetration of twisted magnetic field lines could locally form $\sim1\,\mathrm{km}$-hot spots at the surface. The presence of these hot spots ~6 times hotter than maximum the bulk temperature around magnetic footpoints (white spots in Fig. 9.1) explains relatively well the light curves of SGR 0418+5729 and Swift J1822.3–1606 (see Supplementary Materials in App. C.3.4, Sect. 5).

Apart from the pulsed X-ray light curve, magnetars are also characterised by the emission of magnetic field-powered energetic bursts. They are thought to be produced through crust failures or crust plastic deformation (e.g. Thompson & Duncan, 1995, Lander et al., 2015, Lander & Gourgouliatos, 2019). Figure 9.2 displays the surface and inner crustal magnetic fields, which can reach $10^{14}-10^{15}\,\mathrm{G}$. Using the model for crust-yielding of (Lander & Gourgouliatos, 2019) (see Supplementary Materials in App. C.3.4, Sect. 6), we infer the average depth of crust failure regions, which coincide with the regions of the strongest internal magnetic fields (blue map in Fig. 9.2). The potentially released energy from these regions is (Thompson & Duncan, 1995)

$$E_{\rm out}=4\times10^{40}\,\mathrm{erg}\left(\frac{l}{1\,\mathrm{km}}\right)^2\left(\frac{|B|}{10^{15}\,\mathrm{G}}\right)^2\sim2\times10^{39}\,\mathrm{erg}\quad, \tag{9.4}$$

where $l\sim1\,\mathrm{km}$ is the typical size of the failing region. $E_{\rm out}$ can be considered as an upper limit of the possible released energy because we mapped all the regions that could fail by a certain age and so may overestimate the failure depth. $E_{\rm out}$ is therefore consistent with the burst energies of the low-magnetic field magnetars SGR J0418+5729 (van der Horst et al., 2010) and

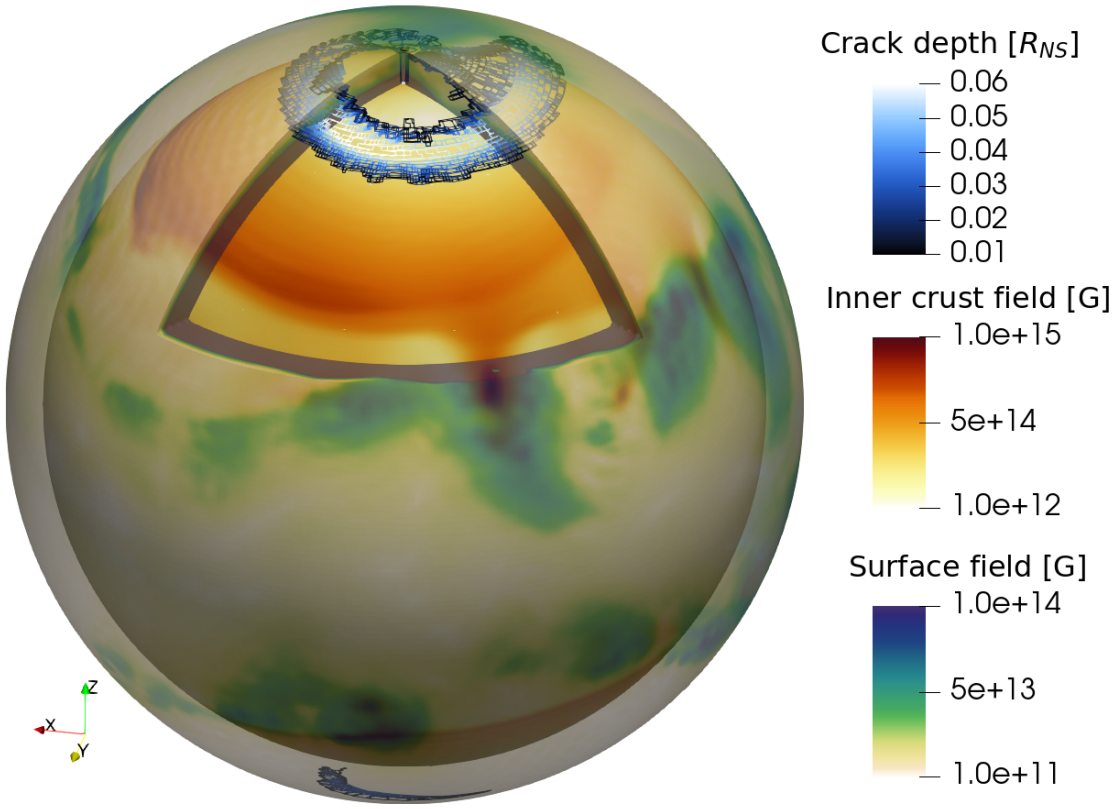

Figure 9.2 — Surface and inner crust magnetic field developed by $200\,\mathrm{kyr}$. Crust-yielding regions are shown in white and blue colours.

CXOU J164710.2–455216 (Muno et al., 2007), which are ~ 100 smaller. This demonstrates the capacity of the dynamo-generated magnetic field to cause magnetar burst activity.

While we covered the impact of the magnetic field on the magnetar luminous activity, we must address the question of magnetar slow rotations. It is all the more necessary because a magnetar with a surface magnetic dipole around $10^{12}\,\mathrm{G}$ and a rotation period of $P = 10\,\mathrm{ms}$ can not spin down the magnetar to their typical rotation periods of $P \sim 2-12\,\mathrm{s}$ in a timescale of $1\,\mathrm{Myr}$. The interaction between the magnetar and the remaining fallback disk, however, can lead to a strong spin-down when the system enters the so-called propeller regime. This phase occurs when a part of the disk penetrates the magnetosphere, which enables the extraction of the angular momentum from the magnetar toward the disk. Using the formalism of (Ronchi et al., 2022), we modelled the evolution of magnetar with a magnetic dipole $B_{\mathrm{NS}} = 10^{12}\,\mathrm{G}$ and a fallback disk with an initial mass of $M_{\mathrm{d},0} = 0.01\,\mathrm{M}_{\odot}$, which corresponds to an inital accretion rate of $\dot{M}_0 = 6.6 \times 10^{29}\,\mathrm{g\,s^{-1}}$. After $200\,\mathrm{kyr}$, we obtain the rotation period of $SI8.5s$. Therefore, the fallback disk can spin down to typical rotation periods for classical and low-magnetic dipole magnetars ($P \sim 8-11\,\mathrm{s}$) in a reasonable timescale. Moreover, the spin-down rate $\dot{P} = 8.5 \times 10^{-13}\,\mathrm{s\,s^{-1}}$ at this same time, which implies a spin-down magnetic dipole of $B_{\mathrm{dip}} = 3.8 \times 10^{13}\,\mathrm{G}$ according to the magnetic spin-down formula (Eq. (1.1)). This indicates that the magnetic dipole inferred from the formula may be overestimated if the magnetar has been spun down through the propeller regime.

9.4 . Conclusions

To conclude, the present numerical study is the first to investigate the magneto-thermal evolution of a magnetic field configuration stemming from a dynamo saturated state. This simulation show that a magnetic field generated by the Tayler-Spruit dynamo can reproduce many characterics of magnetars with a low magnetic dipole: their low magnetic dipole, X-ray light curve, bursts, and rotation periods. This suggests that our fallback scenario is promising to explain a fraction of the magnetar population.

Our scenario is also a good alternative to the 'worn-out' magnetar model, which suggests that magnetars with low magnetic dipoles are old magnetars born with a strong dipole of $\sim 10^{14}\,\mathrm{G}$ (Rea et al., 2012a). However, this model is challenged by our numerical simulation because we do not observe any significant decay of the dipole within a times scale of $1\,\mathrm{Myr}$.

Thus, this work consolidate the idea of a PNS dynamo origin for magnetars and opens new perspectives for testing these dynamos. We suggest that different dynamos leave their unique imprint on magnetic field configurations, thus allowing to identify different magnetic amplification processes using the magneto-thermal properties of young isolated neutron stars. While we suggest that the formation of low-magnetic dipole magnetars is linked to the Tayler-Spruit dynamo, the formation of classical magnetars as well as the internal structure of their magnetic fields remains an open question.

9.5 . Data and materials availability

For the PNS simulation, we used the `MagIC` code (commit 2266201a5), which is open source at https://github.com/magic-sph/magic. The magnetar spin-down was calculated with the GRB code (commit 84788793), also publicly available at https://github.com/rraynaud/GRBs. The results of magneto-thermal simulations can be shared under reasonable request.

General conclusion

Summary of the thesis work

This thesis aims at providing a better understanding of the formation of magnetars. These young neutron stars (NSs) power a wide variety of high-energy emissions due to the dissipation of their ultra-strong magnetic fields ($10^{14} - 10^{15}\,\mathrm{G}$). Understanding the formation of their magnetic is critical to explain these observations. This problem is still actively debated and constitutes the central question of this thesis. To address this question, we have focused on the magnetic field amplification by dynamo action in a newly born proto-neutron star (PNS). Numerical simulations demonstrated that dynamos driven by convection and magnetorotational instability can form magnetar-like magnetic fields in the presence of fast rotations stemming from fast-rotating progenitor cores. While these dynamo mechanisms are good candidates for magnetars formed in extreme explosions, it is more challenging for them to explain the entire magnetar population due to the uncertainty on the fraction of fast-rotating progenitor cores. Moreover, the observation of supernova remnants associated with magnetars demonstrates that most magnetars are formed in classical core-collapse supernovae like most NSs, which require slower PNS rotations compared to extreme explosions. Indeed, assuming that all the rotational energy of the PNS is injected into the kinetic energy of the ejecta, which can not exceed that of typical supernovae ($\sim 10^{51}\,\mathrm{erg}$), the PNS initial rotation period can not exceed $\sim 5\,\mathrm{ms}$ (Vink & Kuiper, 2006).

Our line of attack to tackle these uncertainties has been to investigate a new scenario for magnetar formation in which the magnetic field is amplified by the Tayler-Spruit dynamo in a PNS spun up by fallback accretion. With this scenario, we overcome the two main limitations of the previous candidate processes, since the PNS can harbour an initial low magnetic field and has a rotation that is not determined by that of the progenitor.

In the first instance (Chap. 5), we have built a semi-analytical model that consists of non-linear equations that extend the mathematical formalism of Fuller et al. (2019) that does not capture the time evolution of the magnetic field. The equations describe the coupled time evolution of the PNS rotational properties and magnetic field components. We observe that the magnetic field evolution consists of three phases: (i) the amplification of the azimuthal magnetic field via the winding of the radial magnetic field, (ii) the former component becomes Tayler unstable which produces a non-axisymmetric perturbed magnetic field, and (iii) the electromotive force due to the instability generates a poloidal field, which closes the dynamo loop. In this work, we derived for the first time a growth rate for the Tayler-Spruit dynamo (not to be confused with the growth of the Tayler instability). After deriving the different characteristic timescales of the magnetic field growth, we finally show that the amplification lasts $15 - 30\,\mathrm{s}$. Solutions of the equations show that the radial magnetic field can reach magnetar-like strengths ($B_r \geqslant 4.4 \times 10^{13}\,\mathrm{G}$) for accreted fallback masses $\geqslant 1.1 \times 10^{-2}\,\mathrm{M}_\odot$, which corresponds to a PNS rotation period of $28\,\mathrm{ms}$. We have also found that the azimuthal magnetic field is always $10 - 100$ stronger than the radial component, which is consistent with

the observational trends (Tiengo et al., 2013, Rodríguez Castillo et al., 2016, Makishima et al., 2019). Thus, this first investigation suggests that magnetars can originate from slow-rotating progenitors for accreted masses compatible with recent supernova simulations and resulting in plausible initial rotation periods of the PNS. This first work was published in *Astronomy & Astrophysics* (article in App. C.3.1) and led to an application of this model to the formation of magnetars in binary NS mergers which will be submitted to the same journal soon (draft in App. C.3.5, in collaboration with Alexis Reboul-Salze).

The main drawbacks of the semi-analytical approach are that it relies on strong assumptions to simplify the non-linear aspects of the dynamics and that it does not inform us about the three-dimensional geometry of the magnetic field. Moreover, the Tayler-Spruit dynamo remained elusive in numerical simulations. To address these points, we performed a set of ~ 50 numerical simulations using `MagIC` to investigate the impact of the differential rotation (Chap. 6) and stable stratification (Chaps. 7 and 8) on the Tayler-Spruit dynamo. The PNS interior is modelled as a stably stratified fluid in the Boussinesq approximation. To mimic the forcing of differential rotation due to fallback, we imposed rotation rates on the boundaries such that the outer sphere rotates faster than the inner one (positive shear). These simulations have provided the following fruitful results:

- We reported for the time the existence of the Tayler-Spruit dynamo in the presence of positive shear (Petitdemange et al., 2023, claimed the presence of the Tayler-Spruit dynamo in a setup with a negative shear). The dynamo produces a magnetic field dominated by its axisymmetric toroidal component.

- We identified for the first time the existence of three different behaviours of the Tayler-Spruit dynamo: (i) a steady $l = 2$-axisymmetric toroidal magnetic field (that we call dipolar state), (ii) a hemispherical magnetic field and (iii) a reversing magnetic field. We interpret this rich dynamics as the result of the non-linear coupling between two axisymmetric unstable modes with opposite equatorial symmetry. Their interaction is driven by the equatorial symmetry breaking of the flow (Chap. 8).

- The hemispherical Tayler-Spruit dynamo is in global agreement with the analytical prescriptions derived by Spruit (2002) regarding the variation of the shear rate. Increasing the stable stratification makes this dynamo solution branch off toward the reversing and/or steady state.

- The steady/dipolar Tayler-Spruit dynamo follows the theoretical scaling laws of Fuller et al. (2019) within a dimensionless renormalisation factor $\alpha \sim 0.01$, i.e. we find a toroidal magnetic field around 100 weaker than expected by Fuller et al.'s model. This dynamo can be maintained in a self-sustained (transient) state to stable stratification up to $N/\Omega_o = 4$ ($N/\Omega_o = 10$) with $Pm = 4$.

- When the scaling laws are applied to a typical PNS, we determine that classical magnetar-like magnetic fields (i.e. $B_{\rm dip} \geqslant 4.4 \times 10^{13}\,\mathrm{G}$) can be generated for rotation periods $\lesssim 6\,\mathrm{ms}$, which corresponds to a minimum accreted fallback mass of $\sim 5 \times 10^{-2}\,\mathrm{M}_\odot$. Rotation periods $\lesssim 60\,\mathrm{ms}$ are sufficient to produce $10^{14}\,\mathrm{G}$-total magnetic fields, which may be sufficient to produce magnetar-like luminous activity despite the low magnetic dipole.

This numerical investigation led to three articles: the study about the impact of the shear rate was published in *Monthly Notices of the Royal Astronomical Society: Letters* (published ver-

sion in App. C.3.2)) and two articles about the impact of the stable stratification and the dynamical behaviour of the Tayler-Spruit dynamo will be submitted to *Astronomy & Astrophysics* (submitted version in App. C.3.3)) and *Physical Review Fluids*, respectively.

Though our work supports our magnetar formation scenario, the question of the evolution of the generated magnetic fields from several seconds to their observed age between $1-100\,\mathrm{kyr}$ remains open. In collaboration with Andrei Igoshev, we thereupon implemented a snapshot of the magnetic field configuration in the dynamo-saturated state as an initial condition of a modified version of code PARODY that models the magneto-thermal evolution of a NS crust. While the surface magnetic dipole is weak for a classical magnetar, the non-dipolar magnetic fields are strong enough to produce magnetar bursts via crust failure and can reproduce the light curve of some magnetars with low magnetic dipoles. We have also argued that the disk formed by the fallback matter can interact with the magnetic dipole to strongly spin down the NS via a propeller regime. After modelling the NS-disk interaction, we find that the NS reaches rotation periods of $\sim 10\,\mathrm{s}$ after $\sim 1.7\times10^{5}\,\mathrm{yr}$. This collaborative work (Chap. 9) is the first to link the PNS dynamo to the observation of magnetars and led to the submission of an article to *Nature Astronomy* (submitted version in App. C.3.4)).

Limitations

In this work, we have shown that the Tayler-Spruit dynamo can produce magnetic dipoles as strong as observed in magnetars but also strong large-scale toroidal magnetic fields that can reach $10^{16}\,\mathrm{G}$ (Chaps. 6 and 7). However, our numerical simulations also indicate that the regime of magnetar-like magnetic fields is reached for rotation periods $P \lesssim 6\,\mathrm{ms}$ (Chap. 7), whereas our semi-analytical model has been more optimistic with a lower limit at $P \sim 28\,\mathrm{ms}$ (Chap. 5). The former value is close to the constrain $P \lesssim 5\,\mathrm{ms}$ that is derived from the observation of supernovae remnants associated to magnetars. While this questions the relevance of our scenario to form magnetars born in typical supernovae, we argue that the magnetic field in our simulations may underestimate the strength of the magnetic field that would form in a realistic PNS.

- The Prandtl number in our simulations ($Pm = 1$) is small compared to that of PNSs, which is $Pm \sim 10^{11}$ ($Pm \sim 10^{4}$) for a viscosity dominated by neutrinos (if the shear viscosity dominates) $\sim 10\,\mathrm{s}$ after the core bounce. While the reduction of the magnetic reconnection speed may hinder the development of large-scale dynamos in the high-Pm regime (Jafari et al., 2018, Lander, 2021), numerical simulations of the magnetorotational instability (MRI)-driven dynamo at $Pm \in [8, 256]$ show that the magnetic energy contained in the largest scales increases with Pm. This indicates the presence of a large-scale dynamo at high-Pm (Guilet et al., 2022). Although these simulations are still far from the PNS regime, Guilet et al. (2022) also report the presence of a regime $Pm \gtrsim 100$ consistent with a plateau. This suggests the existence of an asymptotic regime in which the magnetic energy becomes independent of Pm.

- The effect of stable stratification may also be reduced in the PNS due to a strong thermal diffusivity, which is assumed to be equal to the diffusivity associated to the electron fraction. To measure this effect, we can define an effective Brunt-Väisälä frequency like in Chap. 7: $N_{\mathrm{eff}} \equiv N\sqrt{\eta/\kappa} = N\sqrt{Pr/Pm}$. For a $10\,\mathrm{s}$-old PNS, $N_{\mathrm{eff}} = 2.2\times10^{-8}\,\mathrm{N}$ with a neutrino viscosity ($N_{\mathrm{eff}} = 8\times10^{-4}\,\mathrm{N}$ with a shear viscosity), which indicates that the effect of

stable stratification is strongly diminished. Although the regime of very low N_{eff}/Ω_o was not explored numerically, our work suggests that the magnetic field should increase.

Another limitation of our model is related to the forcing of the differential rotation. We have seen that imposing the angular rotation frequency on both boundaries usually leads to a concentration of the shear near the inner sphere. An alternative forcing would be to implement a volumetric body force in the momentum equation, which imposes a background rotation profile. This volumetric forcing was already used to study MHD instabilities and dynamos in stellar radiative zones (e.g. Meduri et al., 2024) and may address the downsides of our forcing. This could especially enable better control of the shear in the integration domain and the exploration of regimes with stronger differential rotation.

Numerical simulations of the Tayler-Spruit dynamo were only performed in simplified models of PNS with a constant density profile, unlike the convective (Raynaud et al., 2020, 2022) and MRI-driven (Reboul-Salze et al., 2022) dynamos. As a direct extension of this thesis work, the Tayler-Spruit dynamo must be investigated with a more realistic density profile. To this end, two different approaches are possible: using thermodynamical profiles of a $\sim 10\,\text{s}$-old PNS resulting from 1D CCSN simulations as background reference states, or implementing polytropic profiles with a polytropic index $n = 1$, i.e. an adiabatic index of $\gamma = 1 + 1/n \sim 2$. The former approach has the advantage of involving a realistic density profile and was used by the previous dynamo studies in PNSs (Raynaud et al., 2020, 2022, Reboul-Salze et al., 2022). The latter approach enables to increase progressively the polytropic index and so the density stratification to study the behaviour of the dynamo. These methods are complementary as using polytropic profiles can be a first step before implementing realistic profiles.

To date, the `MagIC` code solves the approximated MHD equations using static reference states. Although the anelastic approximation provides robust results for the study of convection and MRI-driven dynamos, the PNS thermodynamical profiles vary on timescales shorter than the total integrated time in our dynamo simulations. Therefore, a first improvement would be to implement dynamical reference states in `MagIC`. While this would certainly influence the amplification of the magnetic field, dynamical reference states are crucial to model the relaxation of the magnetic field from a turbulent saturated state toward a stable configuration. The implementation of several other physical ingredients would enable the modelling of more realistic PNSs including for instance relativistic corrections or a (simplified) treatment of neutrinos. Exploring more extreme parameter regimes and implementing finer PNS models imply heavier numerical simulations. Porting `MagIC` on Graphic Processing Units (GPUs) could improve significantly the code efficiency. However, the porting requires a lot of development and the adapted version of `MagIC` for GPUs is not ready yet.

Comparison to other scenarios

Let us unfocus from the dynamo mechanisms to the magnetar formation scenarios. The scenarios involving a fossil field or a convective/MRI-driven dynamo in a fast-rotating PNS during the supernova explosion were quickly invoked to explain the population of magnetars (Duncan & Thompson, 1992, Akiyama et al., 2003, Ferrario & Wickramasinghe, 2006). Among the formation scenarios, our fallback scenario is therefore very new. With respect to the observational constraint of the initial rotation period of the PNS, it remains more challenging for the dynamo scenarios, including our fallback scenario, to explain the formation

of magnetars in typical supernovae compared to the fossil field scenario. However, this scenario remains poorly constrained and further investigations on the magnetic field of massive star cores are sorely needed.

The different scenarios may also be complementary in the sense that each of them could form a more or less large fraction of the magnetar population. This position is supported by our collaborative work linking Tayler-Spruit dynamo in a PNS to magnetars. Indeed, this study shows that the Tayler-Spruit dynamo is a good candidate to explain the formation of magnetars with low-magnetic dipoles. By extension, this result suggests that each scenario could leave distinct signatures on magnetic field configurations, enabling the identification of different magnetic field amplification processes through the analysis of magneto-thermal properties in young isolated NSs.

The future investigations aiming at identifying these signatures should proceed in two steps: (i) identifying the stable configuration of the magnetic field once relaxed from a dynamo-saturated state in realistic PNS thermodynamical profiles, (ii) implementing this configuration as an initial condition of the numerical simulations modelling the magnetic field evolution in a cold NS structure. These investigations would extend our first work in which the relaxation phase is missing and could be applied to the other dynamo mechanisms. A direct application to the fossil field scenario would be difficult since the magnetic field configuration in the progenitor iron core remains unknown. Future asteroseismic observations and numerical modelling of the late stages of massive stars should significantly contribute to the study of the fossil field scenario.

Observational perspectives

The identification of dynamo/fossil-field signatures in the observation of magnetars brings us to reflect upon the future of magnetar observations and the implications for my thesis work. The recent and future observatories that will inform us about the geometry of magnetar magnetic fields are X-ray spatial telescopes with a polarimeter aboard. The most recent of these telescopes is the Imaging X-ray Polarimetry Explorer (IXPE), which was launched at the end of 2021. IXPE measures the polarisation of X-ray photons emitted by an astrophysical object, i.e. the oscillation of the electric field in electromagnetic waves. Due to the strong surface magnetic fields, the X-ray light from magnetars is expected to be strongly polarised, i.e. most of the detected photons have the same polarisation. IXPE observed four magnetars (see the review Taverna & Turolla, 2024) and confirmed that fractions up to $\sim 80\%$ of the light is polarised (Zane et al., 2023). The observation of a variation in this fraction for the magnetar 1E 2259+586 was interpreted as the result of a magnetic field loop at the NS surface (Heyl et al., 2024), which is consistent with the interpretation of X-ray absorption lines in the emission of two magnetars (Tiengo et al., 2013, Rodríguez Castillo et al., 2016) and our work with Andrei Igoshev (Chap. 9). A similar telescope, the X-ray Polarimeter Satellite (XPoSat) was launched at the beginning of 2024, but no study of magnetar emissions with XPoSat has been published yet. Other X-ray observatories are expected to be launched during the next decade such as HEX-P, eXPE, and ATHENA (which does not have a polarimeter).

Future missions more focused on γ-ray bursts (GRBs) will also provide crucial information about magnetars but as a central engine of these events. The Space-based multi-band astronomical Variable Objects Monitor (SVOM) mission will be (or was) launched in June 2024 and will help characterise the events related to millisecond magnetars forming in either binary

NS mergers or hypernovae very soon. This fosters the study of the Tayler-Spruit dynamo in this context. The work done with Alexis Reboul-Salze (App. C.3.5) is the first step to evaluating the relevance of studying the Tayler-Spruit dynamo in the context of binary NS mergers. Future numerical simulation of either the dynamo or the whole merger process should clarify the importance of the Tayler-Spruit dynamo in this event. Likewise, the Tayler-Spruit dynamo could provide the necessary energy injection in the case of hypernovae leading to a long GRB. The study of the impact of stable stratification (Chap. 7) showed that the magnetic dipole and the axisymmetric toroidal magnetic fields can reach $\sim 3 \times 10^{15}\,\mathrm{G}$ and $\sim 10^{16}\,\mathrm{G}$ for a rotation period of $\sim 1\,\mathrm{ms}$. This could be enough to produce a GRB if the magnetar-fallback disk system is in a propeller regime (Metzger et al., 2018).

The Tayler-Spruit dynamo may also influence the gravitational wave (GW) signal from the classical/extreme explosion. Raynaud et al. (2022) find that the strong axisymmetric toroidal magnetic field is accompanied by the growth of the GW amplitude in the low-frequencies ($\sim 10\,\mathrm{Hz}$). Therefore, the dominant axisymmetric toroidal mode generated by the Tayler-Spruit dynamo could also influence the frequency of the GW signal. If the turbulent magnetic field is strong enough to deform the PNS surface and trigger the emission of GW, this low-frequency GW could be detected by future GW detectors such as the Einstein Telescope and Cosmic Explorer for explosions close to the Earth ($\sim 10\,\mathrm{kpc}$). The signal from the convective and the Tayler-Spruit dynamo could produce similar signatures. However, the time arrival of the GW signal compared to that of the first detected neutrinos would differentiate them since the fallback accretion and so the Tayler-Spruit dynamo occurs after the PNS convection ($\sim 10\,\mathrm{s}$ after the core bounce).

Since the fallback accretion emits neutrinos (Janka, 2004, Fryer, 2009, Bollig et al., 2021), the accretion phase could be constrained by the detection of a signature in the neutrino signal. Recent numerical simulations show that higher mass accretion rates produce higher neutrino luminosities and higher neutrino mean energies (Akaho et al., 2024). The associated event rates for the detectors Super-K and DUNE are around $10-100\,\mathrm{s}^{-1}$, which is significantly larger than for a cooling PNS without accretion. Therefore, an increase of neutrino luminosity could be observed when the fallback starts $\sim 10\,\mathrm{s}$ after the core bounce. Akaho et al. (2024) also suggest that the detection of high-energy neutrinos ($\gtrsim 30\,\mathrm{MeV}$) may be the evidence for fallback accretion. Current and future modelling of the neutrino emission by the fallback should help constrain the fallback accretion rate in future detections of supernova neutrinos. Thus, neutrinos may also provide observational constraints for our scenario.

Extension of the scenario

While this thesis is focused on the PNS stage and also addresses the long-term evolution of the NS, our work could be extended to the study of the magnetic fields in the progenitor stars. As mentioned in Sect. 3.3, asteroseismic measurements of the rotation profile in red giants revealed that the core rotates much more slowly than predicted by stellar evolution models (e.g. Mosser et al., 2012, Deheuvels et al., 2015, Gehan et al., 2018). By extrapolation, the core of massive stars ($M > 8\,\mathrm{M}_\odot$) is also expected to spin down, leading to slow-rotating compact remnants. The knowledge of the rotation rate of the core is crucial to predicting the properties of the resulting compact remnant and understanding the diversity of supernova explosions. Recent studies (e.g. Griffiths et al., 2022, Fuller & Lu, 2022) provide predictions of the compact object spin by using 1D stellar evolution codes which take into account the AM

transport due to magnetic fields generated by the Tayler-Spruit or MRI-driven dynamo. Besides, these studies show that magnetic field-driven AM transport is important in most of the evolution phases of massive stars. The main limitation of these studies is that they rely on the derived analytical prescriptions for the Tayler-Spruit dynamo (and MRI). The scaling laws measured in our simulations (Chap. 7) could be implemented in the evolution codes to run future evolution models. Another approach would consist in performing 3D numerical simulations of the Tayler-Spruit dynamo with realistic thermodynamical profiles of radiative zones extracted from the evolution models at different evolution stages. This approach would provide more robust measures of the angular momentum transport during the massive star evolution. Moreover, a better inclusion of the effect of the magnetic fields would provide more realistic progenitors for 3D core-collapse supernova simulations.

Following the evolution of the progenitor until its explosion, a remaining disregarded aspect in the work of the thesis is the fallback accretion. We have relied on the results of 3D core-collapse supernova simulations (Chan et al., 2020, Stockinger et al., 2020, Janka et al., 2022, Coleman & Burrows, 2022). A systematic study of the fallback in these simulations for a wide range of progenitor masses would constrain the properties of the progenitors that will form a magnetar through our fallback scenario. These results would be compared to the observations of a few magnetars associated with a stellar cluster or a bubble nebula from which a progenitor mass has been inferred (Gaensler et al., 2005, Muno et al., 2006, Bibby et al., 2008, Clark et al., 2008, Davies et al., 2009).

III

Appendices

A

Derivation of the Tayler instability properties

Contents

This appendix gathers my notes of the calculations I have done to derive the properties of the Tayler instability. The calculations turned out to be very complex and took some time to be checked several times.

A.1 . Summary of Ma & Fuller 2019 calculation

A.1.1 . Hypotheses

The calculation of linear Tayler modes from Ma & Fuller (2019) is similar to Zahn et al. (2007) but in spherical geometry, so valid for all values of colatitudes θ. All perturbations δQ read

$$\delta Q \propto \exp\{i(k_r r + l\theta + m\phi - \omega t)\}, \tag{A.1}$$

with short radial length scales ($k_r r \gg l, m$) due to strong stratification. They also make an incompressible approximation and ignore the baroclinic terms because large κ at l_{TI}. Finally, the Tayler instability develops on an azimuthal background field of the form

$$\mathbf{B}_0 = B_0 \sin\theta \mathbf{e}_\phi . \tag{A.2}$$

A.1.2 . Fluid equations

Energy equation

Due to large κ, the energy equation reduces to

$$-g\frac{\delta\rho}{\rho} = -\left(N_t^2\left(1+\frac{i\kappa k_r^2}{\omega}\right)+N_\mu^2\right)\xi_r\,, \tag{A.3}$$

where g, ρ, N_t, N_v are the gravitational constant, the density, the thermal and chemical composition components of the Brunt-Väisälä frequency, respectively. ξ_r is the radial component of the displacement vector $\boldsymbol{\xi}$.

Perturbed induction equation

The perturbed induction equation in the MHD limit reads

$$-\omega\boldsymbol{\Delta B} = \boldsymbol{\nabla}\times(-i\omega\boldsymbol{\xi}\times\mathbf{B}_0)-\eta k_r^2\boldsymbol{\Delta B}\,. \tag{A.4}$$

Assuming the incompressible character $\boldsymbol{\nabla}\cdot\xi = 0$ and a strong stratification, i.e. negligible ξ_r terms, the perturbed magnetic field reads

$$\boldsymbol{\delta B} \sim \left(1+\frac{i\eta k_r^2}{\omega}\right)^{-1}\frac{imB_0}{r}\boldsymbol{\xi}\,. \tag{A.5}$$

Continuity equation

In the incompressible case, the continuity equation reads

$$k_r\xi_r+\frac{l}{r}\xi_\theta+\frac{m}{r\sin\theta}\xi_\phi = 0\,. \tag{A.6}$$

Lorentz force

Now, one can express the Lorentz force defined by

$$\mathbf{L} = \frac{1}{4\pi\rho}\left[(\boldsymbol{\nabla}\times\boldsymbol{\delta B})\times\mathbf{B}_0+(\boldsymbol{\nabla}\times\mathbf{B}_0)\times\boldsymbol{\delta B}\right]. \tag{A.7}$$

After a few pages of calculations, it reads

$$L_r = \left(1+\frac{i\eta k_r^2}{\omega}\right)^{-1} m\omega_{\mathrm{A}}^2\left(k_r r\sin\theta\xi_\phi - i\sin\theta\xi_\phi - m\xi_r\right), \tag{A.8}$$

$$L_\theta = \left(1+\frac{i\eta k_r^2}{\omega}\right)^{-1} m\omega_{\mathrm{A}}^2\left(l\sin\theta\xi_\phi - m\xi_\theta - 2i\cos\theta\xi_\phi\right), \tag{A.9}$$

$$L_\phi = \left(1+\frac{i\eta k_r^2}{\omega}\right)^{-1} m\omega_{\mathrm{A}}^2\left(2i\cos\theta\xi_\theta + i\sin\theta\xi_\phi\right). \tag{A.10}$$

Perturbed motion equation

The perturbed equation of motion defined by

$$\frac{\boldsymbol{\nabla}\delta P}{\rho} - \omega^2\boldsymbol{\xi} + g\frac{\delta\rho}{\rho} - 2i\omega\Omega\mathbf{e}_z\times\boldsymbol{\xi} - \mathbf{L} = 0 \tag{A.11}$$

now reads

$$\begin{aligned} ik_r\frac{\delta P}{\rho} &+ \left(-\omega^2 + m\omega_{\mathrm{A}}^2\left(1+\frac{i\eta k_r^2}{\omega}\right)^{-1} + N_t^2\left(1+\frac{i\kappa k_r^2}{\omega}\right)^{-1} + N_\mu^2\right)\xi_r \\ &+ \left(-k_r\sin\theta\, m\omega_{\mathrm{A}}^2\left(1+\frac{i\eta k_r^2}{\omega}\right)^{-1} + im\omega_{\mathrm{A}}^2\left(1+\frac{i\eta k_r^2}{\omega}\right)^{-1} + 2i\omega\Omega\sin\theta\right)\xi_\phi \\ &= 0, \end{aligned} \tag{A.12}$$

$$\begin{aligned} i\frac{l}{r}\frac{\delta P}{\rho} &+ \left(-\omega^2 + m\omega_{\mathrm{A}}^2\left(1+\frac{i\eta k_r^2}{\omega}\right)^{-1}\right)\xi_\theta \\ &+ \left(-l\sin\theta\, m\omega_{\mathrm{A}}^2\left(1+\frac{i\eta k_r^2}{\omega}\right)^{-1} + 2i\cos\theta\, m\omega_{\mathrm{A}}^2\left(1+\frac{i\eta k_r^2}{\omega}\right)^{-1} + 2i\omega\Omega\cos\theta\right)\xi_\phi \\ &= 0, \end{aligned} \tag{A.13}$$

$$\begin{aligned} i\frac{m}{r\sin\theta}\frac{\delta P}{\rho} &- \left(2i\sin\theta\, m\omega_{\mathrm{A}}^2\left(1+\frac{i\eta k_r^2}{\omega}\right)^{-1} + 2i\omega\Omega\sin\theta\right)\xi_r \\ &- \left(i\cos\theta\, m\omega_{\mathrm{A}}^2\left(1+\frac{i\eta k_r^2}{\omega}\right)^{-1} + 2i\omega\Omega\cos\theta\right)\xi_\phi \\ &- \omega^2\xi_\phi \\ &= 0. \end{aligned} \tag{A.14}$$

A.1.3 . Dispersion relation

Here are some definitions:

$$\xi_0 \equiv \frac{\delta P}{\rho} + ir\sin\theta\, m\omega_{\mathrm{A}}^2\left(1+\frac{i\eta k_r^2}{\omega}\right)^{-1}, \tag{A.15}$$

$$A \equiv -\omega^2 + m^2\omega_{\mathrm{A}}^2\left(1+\frac{i\eta k_r^2}{\omega}\right)^{-1}, \tag{A.16}$$

$$B \equiv 2i\cos\theta\, m\omega_{\mathrm{A}}^2\left(1+\frac{i\eta k_r^2}{\omega}\right)^{-1} + 2i\cos\theta\omega\Omega, \tag{A.17}$$

$$C \equiv i\sin\theta\, m\omega_{\mathrm{A}}^2\left(1+\frac{i\eta k_r^2}{\omega}\right)^{-1} + 2i\sin\theta\omega\Omega, \tag{A.18}$$

$$D \equiv N_t^2\left(1+\frac{i\kappa k_r^2}{\omega}\right)^{-1} + N_\mu^2. \tag{A.19}$$

The dispersion relation therefore reads

$$\left[\left(\frac{l}{r}\right)^2 + \left(\frac{m}{r\sin\theta}\right)^2\right]A(A+D) + k_r^2(A^2+B^2) - k_r\frac{l}{r}BC = 0. \tag{A.20}$$

With $D \gg A$ and $k_r r \gg l$, it now reads

$$A^2 + B^2 + \left(\frac{l}{k_r r}\right)^2 D = A^2 + B^2 + A\bar{D} = 0\,. \tag{A.21}$$

Let us use the following dimensionless quantities:

$$\bar{\omega} = \omega/\omega_{\rm A}\,, \tag{A.22}$$
$$\bar{\Omega} = \Omega/\omega_{\rm A}\,, \tag{A.23}$$
$$k = \kappa k_r/\omega_{\rm A}\,, \tag{A.24}$$
$$h = \eta k_r/\omega_{\rm A}\,, \tag{A.25}$$
$$A_t = l^2 N_t^2/(k_r r\omega_{\rm A})^2\,, \tag{A.26}$$
$$A_\mu = l^2 N_\mu^2/(k_r r\omega_{\rm A})^2\,. \tag{A.27}$$

The final form of the dispersion relation is this hideous thing:

$$\begin{aligned}
&\{\,\bar{\omega}^6 - [4\bar{\Omega}^2\cos^2\theta + A_t + A_\mu + 2m^2 + 2hk + h^2]\bar{\omega}^4 \\
&\quad - [8m\bar{\Omega}]\bar{\omega}^3 \\
&\quad + [m^2(A_t + A_\mu) + m^2 - 4m^2\cos^2\theta + 2hk(4\bar{\Omega}^2\cos^2\theta + A_\mu + m^2) + h^2(4\bar{\Omega}^2\cos^2\theta + A_t + A_\mu)]\bar{\omega}^2 \\
&\quad + [8mhk\bar{\Omega}\cos^2\theta]\bar{\omega} \\
&\quad - hkm2A_\mu\,\} \\
&+ i\,\{[2h + k]\bar{\omega}^5 \\
&\quad - [k(4\bar{\Omega}^2\cos^2\theta + A_\mu + 2m^2) + 2h(4\bar{\Omega}^2\cos^2\theta + A_t + A_\mu + m^2) + h^2k]\bar{\omega}^4 \\
&\quad - [8m(k + h)\bar{\Omega}\cos^2\theta]\bar{\omega}^2 \\
&\quad + [k(m^2A_\mu + m^2 - 4m^2\cos^2\theta) + hm^2(A_t + A_\mu) = h^2k(4\bar{\Omega}^2\cos^2\theta + A_\mu)]\bar{\omega}\,\} \\
&= 0\,.
\end{aligned} \tag{A.28}$$

A.2 . Generalisation for a general $\mathbf{B_0}(\theta)$

A.2.1 . Hypotheses

We use the same hypotheses as Ma & Fuller (2019) but now we assume a more general background magnetic field $\mathbf{B}_0 = B_0 f(\theta)\mathbf{e}_\phi$.

A.2.2 . Fluid equations

Induction equation

The energy equation does not change but the induction equation does:

$$\begin{aligned}
\left(1 + \frac{i\eta k_r^2}{\omega}\right)\boldsymbol{\delta B} &= \boldsymbol{\nabla}\times\left(\boldsymbol{\xi}\times B_0 f(\theta)\mathbf{e}_\phi\right) \\
&= \boldsymbol{\nabla}\times\left(B_0 f(\theta)\xi_\theta\mathbf{e}_r - B_0 f(\theta)\xi_r\mathbf{e}_\theta\right) \\
&= \frac{im}{r\sin\theta}B_0 f(\theta)\boldsymbol{\xi} - \left(\frac{B_0 f(\theta)\xi_r}{r} + \frac{B_0 f'(\theta)\xi_\theta}{r}\right)\mathbf{e}_\phi\,.
\end{aligned} \tag{A.29}$$

This expression is more complicated than in Ma & Fuller (2019), where the two last terms are ignored.

Lorentz force

We recall the expression of the Lorentz force

$$\mathbf{L} = \frac{1}{4\pi\rho}\left[(\boldsymbol{\nabla}\times\boldsymbol{\delta B})\times\mathbf{B}_0 + (\boldsymbol{\nabla}\times\mathbf{B}_0)\times\boldsymbol{\delta B}\right]. \tag{A.30}$$

Since the calculation is complex, let us go step by step:

$$\begin{aligned}\boldsymbol{\nabla}\times\boldsymbol{\delta B} = &\left(1+\frac{i\eta k_r^2}{\omega}\right)^{-1}\\ &\times\left\{im\boldsymbol{\nabla}\times\left(\frac{B_0 f(\theta)}{r\sin\theta}\boldsymbol{\xi}\right)-\boldsymbol{\nabla}\times\left(\frac{B_0 f(\theta)\xi_r}{r}\mathbf{e}_\phi\right)-\boldsymbol{\nabla}\times\left(\frac{B_0 f'(\theta)\xi_\theta}{r}\mathbf{e}_\phi\right)\right\}\end{aligned} \tag{A.31}$$

(i)

$$\begin{aligned}&im\boldsymbol{\nabla}\times\left(\frac{B_0 f(\theta)}{r\sin\theta}\boldsymbol{\xi}\right)\\ &= B_0\left[\left(\frac{im}{r^2\sin\theta}f'(\theta)-\frac{ml}{r^2\sin\theta}f(\theta)\right)\xi_\phi+\frac{m^2}{r^2\sin^2\theta}f(\theta)\xi_\theta\right]\mathbf{e}_r\\ &+B_0\left[-\frac{m^2}{r^2\sin^2\theta}f(\theta)\xi_r+\frac{mk_r}{r\sin\theta}f(\theta)\xi_\phi\right]\mathbf{e}_\theta\\ &+B_0\left[\left(-\frac{im}{r^2\sin\theta}f'(\theta)+\frac{ml}{r^2\sin\theta}f(\theta)+\frac{im\cot\theta}{r^2}f(\theta)\right)\xi_r-\frac{mk_r}{r\sin\theta}f(\theta)\xi_\theta\right]\mathbf{e}_\phi,\end{aligned} \tag{A.32}$$

(ii)

$$\begin{aligned}-\boldsymbol{\nabla}\times\left(\frac{B_0 f(\theta)\xi_r}{r}\mathbf{e}_\phi\right) = &-B_0\left[\frac{il}{r^2}f'(\theta)+\frac{1}{r^2}f''(\theta)+\frac{\cot\theta}{r^2}f'(\theta)\right]\xi_\theta\mathbf{e}_r\\ &+B_0\frac{ik_r}{r}f'(\theta)\xi_\theta\mathbf{e}_\theta,\end{aligned} \tag{A.33}$$

(iii)

$$-\boldsymbol{\nabla}\times\left(\frac{B_0 f'(\theta)\xi_\theta}{r}\mathbf{e}_\phi\right) = -B_0\left[\frac{il}{r^2}f(\theta)+\frac{\cot\theta}{r^2}f(\theta)+\frac{1}{r^2}f'(\theta)\right]\xi_r\mathbf{e}_r+B_0\frac{ik_r}{r}f(\theta)\xi_r\mathbf{e}_\theta. \tag{A.34}$$

Therefore,

$$\begin{aligned}\boldsymbol{\nabla}\times\boldsymbol{\delta B} = &\left(1+\frac{i\eta k_r^2}{\omega}\right)^{-1}B_0\\ &\times\left\{\left[-\left(\frac{il}{r^2}f(\theta)+\frac{\cot\theta}{r^2}f(\theta)+\frac{1}{r^2}f'(\theta)\right)\xi_r\right.\right.\\ &-\left(\frac{il}{r^2}f'(\theta)+\frac{1}{r^2}f''(\theta)+\frac{\cot\theta}{r^2}f'(\theta)-\frac{m^2}{r^2\sin^2\theta}f(\theta)\right)\xi_\theta\\ &\left.+\left(\frac{im}{r^2\sin\theta}f'(\theta)-\frac{ml}{r^2\sin\theta}f(\theta)\right)\xi_\phi\right]\mathbf{e}_r\\ &+\left[\left(\frac{ik_r}{r}f(\theta)-\frac{m^2}{r^2\sin^2\theta}f(\theta)\right)\xi_r+\frac{ik_r}{r}f'(\theta)\xi_\theta+\frac{mk_r}{r\sin\theta}f(\theta)\xi_\phi\right]\mathbf{e}_\theta\\ &\left.+\left[\left(-\frac{im}{r^2\sin\theta}f'(\theta)+\frac{ml}{r^2\sin\theta}f(\theta)+\frac{im\cot\theta}{r^2}f(\theta)\right)\xi_r-\frac{mk_r}{r\sin\theta}f(\theta)\xi_\theta\right]\mathbf{e}_\phi\right\}.\end{aligned} \tag{A.35}$$

The first term of the Lorentz force is then

$$
\begin{aligned}
(\boldsymbol{\nabla}\times\boldsymbol{\delta B})\times\mathbf{B}_0 = &\left(1+\frac{i\eta k_r^2}{\omega}\right)^{-1} B_0^2 \\
&\times\left\{\left[\left(\frac{ik_r}{r}f(\theta)^2-\frac{m^2}{r^2\sin^2\theta}f(\theta)^2\right)\xi_r+\frac{ik_r}{r}f'(\theta)f(\theta)\xi_\theta+\frac{mk_r}{r\sin\theta}f(\theta)^2\xi_\phi\right]\mathbf{e}_r\right. \\
&+\left[\left(\frac{il}{r^2}f(\theta)^2+\frac{\cot\theta}{r^2}f(\theta)^2+\frac{1}{r^2}f'(\theta)f(\theta)\right)\xi_r\right. \\
&+\left(\frac{il}{r^2}f'(\theta)f(\theta)+\frac{1}{r^2}f''(\theta)f(\theta)+\frac{\cot\theta}{r^2}f'(\theta)f(\theta)-\frac{m^2}{r^2\sin^2\theta}f(\theta)^2\right)\xi_\theta \\
&\left.\left.-\left(\frac{im}{r^2\sin\theta}f'(\theta)f(\theta)-\frac{ml}{r^2\sin\theta}f(\theta)^2\right)\xi_\phi\right]\mathbf{e}_\theta\right\}.
\end{aligned}
\tag{A.36}
$$

Let us calculate the second term (step by step):

$$
\boldsymbol{\nabla}\times\mathbf{B}_0 = B_0\left\{\frac{1}{r\sin\theta}(f(\theta)\sin\theta)'\mathbf{e}_r-\frac{1}{r}f(\theta)\mathbf{e}_\theta\right\},
\tag{A.37}
$$

and so

$$
\begin{aligned}
(\boldsymbol{\nabla}\times\mathbf{B}_0)\times\boldsymbol{\delta B} = &\left(1+\frac{i\eta k_r^2}{\omega}\right)^{-1} B_0^2 \\
&\times\left\{\left[\frac{1}{r^2}f(\theta)^2\xi_r+\frac{1}{r^2}f'(\theta)f(\theta)\xi_\theta-\frac{im}{r^2\sin\theta}f(\theta)^2\xi_\phi\right]\mathbf{e}_r\right. \\
&+\left[\frac{1}{r^2\sin\theta}(f(\theta)\sin\theta)'f(\theta)\xi_r+\frac{1}{r^2\sin\theta}(f(\theta)\sin\theta)'f'(\theta)\xi_\theta-\frac{im}{r^2\sin^2\theta}(f(\theta)\sin\theta)'f(\theta)\xi_\phi\right]\mathbf{e}_\theta \\
&\left.+\left[\frac{im}{r^2\sin\theta}f(\theta)^2\xi_r+\frac{im}{r^2\sin^2\theta}(f(\theta)\sin\theta)'f(\theta)\xi_\theta\right]\mathbf{e}_\phi\right\}.
\end{aligned}
\tag{A.38}
$$

The Lorentz force now reads[1]

$$
\begin{aligned}
L_r = &\left(1+\frac{i\eta k_r^2}{\omega}\right)^{-1}\omega_A^2\left\{\left(-\frac{m^2}{\sin^2\theta}f(\theta)^2+(1+ik_r r)f(\theta)^2\right)\xi_r\right. \\
&+(1+ik_r r)f'(\theta)f(\theta)\xi_\theta \\
&\left.+\left(\frac{mk_r r}{\sin\theta}f(\theta)^2-\frac{im}{\sin\theta}f(\theta)^2\right)\xi_\phi\right\},
\end{aligned}
\tag{A.39}
$$

$$
\begin{aligned}
L_\theta = &\left(1+\frac{i\eta k_r^2}{\omega}\right)^{-1}\omega_A^2\left\{\left(ilf(\theta)^2+\cot\theta f(\theta)^2+f'(\theta)f(\theta)+\frac{1}{\sin\theta}(f(\theta)\sin\theta)'f(\theta)\right)\xi_r\right. \\
&+\left(ilf'(\theta)f(\theta)+f''(\theta)f(\theta)+\cot\theta f'(\theta)f(\theta)+\frac{1}{\sin\theta}(f(\theta)\sin\theta)'f'(\theta)-\frac{m^2}{\sin^2\theta}f(\theta)^2\right)\xi_\theta \\
&\left.+\left(-\frac{im}{\sin\theta}f'(\theta)f(\theta)+\frac{ml}{\sin\theta}f(\theta)^2-\frac{im}{\sin^2\theta}(f(\theta)\sin\theta)'f(\theta)\right)\xi_\phi\right\},
\end{aligned}
\tag{A.40}
$$

[1] Colors represent terms which are not in the derivation of Ma & Fuller (2019): red, blue, and green for the additional terms multiplied by ξ_r, ξ_θ, and ξ_ϕ, respectively.

$$L_\phi = \frac{im}{\sin\theta} f(\theta)^2 \xi_r + \frac{im}{\sin^2\theta} (f(\theta)\sin\theta)' f(\theta)\xi_\theta \,. \tag{A.41}$$

We can now derive the equation of motion

$$\frac{\boldsymbol{\nabla}\delta P}{\rho} - \omega^2\xi + g\frac{\delta\rho}{\rho} - 2i\omega\Omega\mathbf{e}_z \times \xi - \mathbf{L} = 0\,, \tag{A.42}$$

$$\begin{aligned} ik_r\frac{\delta P}{\rho} &+ \left[-\omega^2 + N_t^2\left(1+\frac{i\kappa k_r^2}{\omega}\right)^{-1} + N_\mu^2 + \left(1+\frac{i\eta k_r^2}{\omega}\right)^{-1}\omega_\mathrm{A}^2\left(\frac{m^2}{\sin^2\theta}f(\theta)^2 - (1+ik_r r)f(\theta)^2\right)\right]\xi_r \\ &- \left(1+\frac{i\eta k_r^2}{\omega}\right)^{-1}\omega_\mathrm{A}^2(1+ik_r r)\,f'(\theta)f(\theta)\xi_\theta \\ &+ \left[\left(1+\frac{i\eta k_r^2}{\omega}\right)^{-1}\omega_\mathrm{A}^2\left(\frac{im}{\sin\theta}f(\theta)^2 - \frac{mk_r r}{\sin\theta}f(\theta)^2\right) + 2i\omega\Omega\sin\theta\right]\xi_\phi \\ &= 0\,, \end{aligned} \tag{A.43}$$

$$\begin{aligned} \frac{il}{r}\frac{\delta P}{\rho} &- \left(1+\frac{i\eta k_r^2}{\omega}\right)^{-1}\omega_\mathrm{A}^2\left[il f(\theta)^2 + \cot\theta f(\theta)^2 + f'(\theta)f(\theta) + \frac{(f(\theta)\sin\theta)' f(\theta)}{\sin\theta}\right]\xi_r \\ &- \left[\omega^2 + \left(1+\frac{i\eta k_r^2}{\omega}\right)^{-1}\omega_\mathrm{A}^2\left(il f(\theta)(f'(\theta)+f''(\theta)+\cot\theta f'(\theta)) + \frac{(f(\theta)\sin\theta)' f'(\theta)}{\sin\theta} - \frac{m^2}{\sin^2\theta}f(\theta)^2\right)\right]\xi_\theta \\ &+ \left[\left(1+\frac{i\eta k_r^2}{\omega}\right)^{-1}\omega_\mathrm{A}^2\left(\frac{im}{\sin\theta}f'(\theta)f(\theta) - \frac{ml}{\sin\theta}f(\theta)^2 + \frac{im}{\sin^2\theta}(f(\theta)\sin\theta)' f(\theta)\right) + 2i\omega\Omega\cos\theta\right]\xi_\phi \\ &= 0\,, \end{aligned} \tag{A.44}$$

$$\begin{aligned} \frac{im}{r\sin\theta}\frac{\delta P}{\rho} &- \left[\left(1+\frac{i\eta k_r^2}{\omega}\right)^{-1}\omega_\mathrm{A}^2\frac{im}{\sin\theta}f(\theta)^2 + 2i\omega\Omega\sin\theta\right]\xi_r \\ &- \left[\left(1+\frac{i\eta k_r^2}{\omega}\right)^{-1}\omega_\mathrm{A}^2\frac{im}{\sin^2\theta}(f(\theta)\sin\theta)' f(\theta) + 2i\omega\Omega\sin\theta\right]\xi_\theta \\ &- \omega^2\xi_\phi \\ &= 0\,. \end{aligned} \tag{A.45}$$

As in Ma & Fuller (2019), we can define the similar terms

$$\xi_0 \equiv \frac{\delta P}{\rho} + imr\omega_\mathrm{A}^2\left(1+\frac{i\eta k_r^2}{\omega}\right)^{-1}\frac{f(\theta)^2}{\sin\theta}\,, \tag{A.46}$$

$$A \equiv -\omega^2 + m^2\omega_\mathrm{A}^2\left(1+\frac{i\eta k_r^2}{\omega}\right)^{-1}\frac{f(\theta)^2}{\sin^2\theta}\,, \tag{A.47}$$

$$B \equiv im\omega_A^2\left(1+\frac{i\eta k_r^2}{\omega}\right)^{-1}\frac{(f(\theta)\sin\theta)' f(\theta)}{\sin^2\theta}+2i\omega\Omega\cos\theta\,, \tag{A.48}$$

$$C \equiv im\omega_A^2\left(1+\frac{i\eta k_r^2}{\omega}\right)^{-1}\frac{f(\theta)^2}{\sin\theta}+2i\omega\Omega\sin\theta\,, \tag{A.49}$$

$$D \equiv N_t^2\left(1+\frac{i\kappa k_r^2}{\omega}\right)^{-1}+N_\mu^2\,. \tag{A.50}$$

But we need to define more terms because of the more complex induction equation:

$$E \equiv (1+k_r r)\omega_A^2\left(1+\frac{i\eta k_r^2}{\omega}\right)^{-1} f(\theta)^2\,, \tag{A.51}$$

$$F \equiv \omega_A^2\left(1+\frac{i\eta k_r^2}{\omega}\right)^{-1}\left(il f(\theta)^2+\cot\theta f(\theta)^2+f'(\theta)f(\theta)+\frac{(f(\theta)\sin\theta)' f(\theta)}{\sin\theta}\right), \tag{A.52}$$

$$G \equiv (1+k_r r)\omega_A^2\left(1+\frac{i\eta k_r^2}{\omega}\right)^{-1} f'(\theta)f(\theta)\,, \tag{A.53}$$

$$H \equiv \omega_A^2\left(1+\frac{i\eta k_r^2}{\omega}\right)^{-1}\left(il f'(\theta)f(\theta)+\cot\theta f'(\theta)f(\theta)+f''(\theta)f(\theta)+\frac{(f(\theta)\sin\theta)' f'(\theta)}{\sin\theta}\right), \tag{A.54}$$

$$I \equiv im\omega_A^2\left(1+\frac{i\eta k_r^2}{\omega}\right)^{-1}\frac{f'(\theta)f(\theta)}{\sin\theta}\,. \tag{A.55}$$

We can use these terms to express the continuity and motion equations

$$k_r\xi_r+\frac{l}{r}\xi_\theta+\frac{m}{r\sin\theta}\xi_\phi=0\,, \tag{A.56}$$

$$\frac{il}{r}\xi_0-F\xi_r+(A-H)\xi_\theta+(B+I)\xi_\phi=0\,, \tag{A.57}$$

$$\frac{im}{r\sin\theta}\xi_0-C\xi_r-B\xi_\theta+A\xi_\phi=0\,, \tag{A.58}$$

$$ik_r\xi_0+(A+D-E)\xi_r-G\xi_\theta+C\xi_\phi=0\,. \tag{A.59}$$

A.2.3 . Dispersion relation

The dispersion relation is given by the determinant of the linear equations, i.e.

$$\begin{vmatrix} 0 & k_r & \frac{l}{r} & \frac{m}{r\sin\theta} \\ \frac{il}{r} & -F & A-H & B+I \\ \frac{im}{r\sin\theta} & -C & -B & A \\ ik_r & A+D-E & -G & C \end{vmatrix}$$

$$= k_r\left[\frac{il}{r}(BC-AG)+(A-H)\left(\frac{im}{r\sin\theta}C-ik_rA\right)+(B+I)\left(\frac{im}{r\sin\theta}G-ik_rB\right)\right]$$

$$+\frac{l}{r}\left[-\frac{il}{r}\left(C^2+A(A+D-E)\right)+F\left(\frac{im}{r\sin\theta}C-ik_rA\right)+(B+I)\left(\frac{im}{r\sin\theta}(A+D-E)+ik_rC\right)\right]$$

$$-\frac{m}{r\sin\theta}\left[\frac{il}{r}(CG+B(A+D-E))+F\left(-\frac{im}{r\sin\theta}G+ik_rB\right)+(A-H)\left(\frac{im}{r\sin\theta}(A+D-E)+ik_rC\right)\right]$$

$$= 0 \tag{A.60}$$

Since this dispersion relation makes me cry, we will use the same approximation as in Ma & Fuller (2019):

$$\boldsymbol{\delta B} \sim \frac{im}{r\sin\theta} B_0 f(\theta)\xi\,, \tag{A.61}$$

which is equivalent to assume $E = F = G = H = I = 0$. We therefore have to deal with the same simplified dispersion relation

$$A^2 + B^2 + A\bar{D} = 0\,, \tag{A.62}$$

and we can use the same dimensionless variables (which are also those used in Zahn et al. (2007)). Once again, let us go step by step. We first divide by $\omega_{\rm A}^4$:

$$A^2 \propto \bar{\omega}^4 + m^4\left(1+\frac{ih}{\bar{\omega}}\right)^{-2}\left(\frac{f(\theta)}{\sin\theta}\right)^4 - 2\bar{\omega}^2 m^2\left(1+\frac{ih}{\bar{\omega}}\right)^{-1}\left(\frac{f(\theta)}{\sin\theta}\right)^2\,, \tag{A.63}$$

$$B^2 \propto -m^2\left(1+\frac{ih}{\bar{\omega}}\right)^{-2}\left[\frac{(f(\theta)\sin\theta)' f(\theta)}{\sin^2\theta}\right]^2 - 4\bar{\omega}^2\bar{\Omega}^2\cos^2\theta - 4m\bar{\omega}\bar{\Omega}\cos\theta\left(1+\frac{ih}{\bar{\omega}}\right)^{-1}\frac{(f(\theta)\sin\theta)' f(\theta)}{\sin^2\theta}\,, \tag{A.64}$$

$$A\bar{D} \propto -\bar{\omega}^2 A_t\left(1+\frac{ik}{\bar{\omega}}\right)^{-1} - \bar{\omega}^2 A_\mu + m^2 A_t\left(1+\frac{ih}{\bar{\omega}}\right)^{-1}\left(1+\frac{ik}{\bar{\omega}}\right)^{-1}\left(\frac{f(\theta)}{\sin\theta}\right)^2 + m^2 A_\mu\left(1+\frac{ih}{\bar{\omega}}\right)^{-1}\left(\frac{f(\theta)}{\sin\theta}\right)^2\,. \tag{A.65}$$

Now, we multiply by $\left(1+\frac{ih}{\bar{\omega}}\right)^2\left(1+\frac{ik}{\bar{\omega}}\right)$:

$$A^2 \propto \bar{\omega}^4\left(1+\frac{ih}{\bar{\omega}}\right)^2\left(1+\frac{ik}{\bar{\omega}}\right) + m^4\left(1+\frac{ik}{\bar{\omega}}\right)\left(\frac{f(\theta)}{\sin\theta}\right)^4 - 2\bar{\omega}^2 m^2\left(1+\frac{ih}{\bar{\omega}}\right)\left(1+\frac{ik}{\bar{\omega}}\right)\left(\frac{f(\theta)}{\sin\theta}\right)^2\,, \tag{A.66}$$

$$B^2 \propto -m^2\left(1+\frac{ik}{\bar{\omega}}\right)\left[\frac{(f(\theta)\sin\theta)' f(\theta)}{\sin^2\theta}\right]^2 - 4\bar{\omega}^2\bar{\Omega}^2\cos^2\theta\left(1+\frac{ih}{\bar{\omega}}\right)^2\left(1+\frac{ik}{\bar{\omega}}\right) \tag{A.67}$$

$$- 4m\bar{\omega}\bar{\Omega}\cos\theta\left(1+\frac{ih}{\bar{\omega}}\right)\left(1+\frac{ik}{\bar{\omega}}\right)\frac{(f(\theta)\sin\theta)' f(\theta)}{\sin^2\theta}\,, \tag{A.68}$$

$$A\bar{D} \propto -\bar{\omega}^2 A_t\left(1+\frac{ih}{\bar{\omega}}\right)^2 - \bar{\omega}^2 A_\mu + m^2 A_t\left(1+\frac{ih}{\bar{\omega}}\right)\left(\frac{f(\theta)}{\sin\theta}\right)^2 \tag{A.69}$$

$$+ m^2 A_\mu\left(1+\frac{ih}{\bar{\omega}}\right)\left(1+\frac{ik}{\bar{\omega}}\right)\left(\frac{f(\theta)}{\sin\theta}\right)^2\,. \tag{A.70}$$

Then, we multiply by $\bar{\omega}^2$:

$$
\begin{aligned}
A^2 \propto\ & (\bar{\omega}^2 + ih\bar{\omega})^2(\bar{\omega}^2 + ik\bar{\omega}) + m^4(\bar{\omega}^2 + ik\bar{\omega})\left(\frac{f(\theta)}{\sin\theta}\right)^4 - 2m^2(\bar{\omega}^2 + ih\bar{\omega})(\bar{\omega}^2 + ik\bar{\omega})\left(\frac{f(\theta)}{\sin\theta}\right)^2 \\
\propto\ & \bar{\omega}^6 + (ik+2ih)\bar{\omega}^5 - \left(h^2 + 2hk + 2m^2\left(\frac{f(\theta)}{\sin\theta}\right)^2\right)\bar{\omega}^4 - \left(ikh^2 + 2im^2(h+k)\left(\frac{f(\theta)}{\sin\theta}\right)^2\right)\bar{\omega}^3 \\
& + \left(m^4\left(\frac{f(\theta)}{\sin\theta}\right)^4 + 2m^2hk\left(\frac{f(\theta)}{\sin\theta}\right)^2\right)\bar{\omega}^2 + im^4k\left(\frac{f(\theta)}{\sin\theta}\right)^2\bar{\omega}, \\
B^2 \propto\ & -m^2(\bar{\omega}^2 + ik\bar{\omega})\left[\frac{(f(\theta)\sin\theta)'f(\theta)}{\sin^2\theta}\right]^2 - 4\bar{\Omega}^2\cos^2\theta(\bar{\omega} + ih)^2(\bar{\omega}^2 + ik\bar{\omega}) \\
& - 4m\bar{\Omega}\cos\theta(\bar{\omega} + ih)(\bar{\omega}^2 + ik\bar{\omega})\frac{(f(\theta)\sin\theta)'f(\theta)}{\sin^2\theta}, \\
\propto\ & 4\bar{\Omega}\cos\theta\bar{\omega}^4 + \left(8ih\bar{\Omega}^2\cos^2\theta + 4ik\bar{\Omega}^2\cos^2\theta - 4m\bar{\Omega}\cos\theta\frac{(f(\theta)\sin\theta)'f(\theta)}{\sin^2\theta}\right)\bar{\omega}^3 \\
& - \left(m^2\left(\frac{(f(\theta)\sin\theta)'f(\theta)}{\sin^2\theta}\right)^2 + 8hk\bar{\Omega}^2\cos^2\theta + 4h^2\bar{\Omega}^2\cos^2\theta + 4im\bar{\Omega}\cos\theta(h+k)\frac{(f(\theta)\sin\theta)'f(\theta)}{\sin^2\theta}\right)\bar{\omega}^2 \\
& - \left(-m^2ik\left(\frac{(f(\theta)\sin\theta)'f(\theta)}{\sin^2\theta}\right)^2 + 4ih^2k\bar{\Omega}^2\cos^2\theta + 4mhk\bar{\Omega}\cos\theta\frac{(f(\theta)\sin\theta)'f(\theta)}{\sin^2\theta}\right)\bar{\omega}, \\
A\bar{D} \propto\ & -A_t(\bar{\omega}^2 + ih\bar{\omega})^2 - A_\mu(\bar{\omega} + ih)^2(\bar{\omega}^2 + ih\bar{\omega}) + m^2A_t(\bar{\omega}^2 + ih\bar{\omega})\left(\frac{f(\theta)}{\sin\theta}\right)^2 \\
& + m^2A_\mu(\bar{\omega} + ih)(\bar{\omega} + ik)\left(\frac{f(\theta)}{\sin\theta}\right)^2 \\
\propto\ & -(A_t + A_\mu)\bar{\omega}^4 - \left(2ihA_t + iA_\mu(2h+k)\right)\bar{\omega}^3 + \left(h^2A_t + 2hkA_\mu + h^2A_\mu + m^2(A_t + A_\mu)\left(\frac{f(\theta)}{\sin\theta}\right)^2\right)\bar{\omega}^2 \\
& + \left(ih^2kA_\mu + im^2hA_t\left(\frac{f(\theta)}{\sin\theta}\right)^2 + im^2(h+k)A_\mu\left(\frac{f(\theta)}{\sin\theta}\right)^2\right)\bar{\omega} - m^2hkA_\mu\left(\frac{f(\theta)}{\sin\theta}\right)^2.
\end{aligned}
$$

Finally, we have the final expression of this foul and demonic dispersion relation:

$$
\begin{aligned}
& \{\bar{\omega}^6 - \left[2m^2F(\theta) + h^2 + 2hk + A_t + A_\mu + 4\bar{\Omega}^2\cos^2\theta\right]\bar{\omega}^4 \\
& - [4m\bar{\Omega}\cos\theta G(\theta)\bar{\omega}]^3 \\
& + \left[m^4F(\theta)^2 + m^2(A_t + A_\mu)F(\theta) - m^2G(\theta)^2\right. \\
& \left. + 2hk\left(m^2F(\theta) + A_\mu + 4\bar{\Omega}^2\cos^2\theta\right) + h^2\left(A_t + A_\mu + 4\bar{\Omega}^2\cos^2\theta\right)\right]\bar{\omega}^2 \\
& + 4mhk\bar{\Omega}\cos\theta G(\theta)\bar{\omega} \\
& - m^2hkA_\mu F(\theta)^2\} \\
& + i\{[2h+k]\bar{\omega}^5 - \left[k\left(2m^2F(\theta) + 4\bar{\Omega}^2\cos^2\theta + A_\mu\right) + 2h\left(m^2F(\theta) + 4\bar{\Omega}^2\cos^2\theta + A_t + A_\mu\right) + h^2k\right]\bar{\omega}^3 \\
& - 4m(h+k)\bar{\Omega}\cos\theta G(\theta)\bar{\omega}^2 \\
& + \left[k\left(m^4F(\theta)^2 - m^2G(\theta)^2 + m^2A_\mu F(\theta)\right)\right. \\
& \left. + m^2h(A_t + A_\mu)F(\theta) + h^2k(4\bar{\Omega}^2\cos^2\theta + A_\mu)\right]\bar{\omega}\} \\
& = 0,
\end{aligned}
\tag{A.71}
$$

with the functions

$$F(\theta) \equiv \left(\frac{f(\theta)}{\sin\theta}\right)^2, \tag{A.72}$$

$$G(\theta) \equiv \left(\frac{(f(\theta)\sin\theta)' f(\theta)}{\sin^2\theta}\right), \tag{A.73}$$

which are defined for the sake of clarity. The equation is very similar to what Ma & Fuller (2019) obtained when $f(\theta) = \sin\theta$ but I highlighted the three terms which differ: $8m\bar{\Omega} \longrightarrow 8m\bar{\Omega}\cos^2\theta$ and $m^2 \longrightarrow m^4$ (two terms). After checking their calculation, it seems these differences may be typos in their article. Since this dispersion relation is already very complex, I will calculate the relation with the other terms of the induction equation in a more or less distant future, if necessary.

A.2.4 . Unstable modes

This complex expression can be rewritten after some algebra

$$\begin{aligned}&\left[\omega(\omega + i\eta k_r^2) - m^2\omega_\mathrm{A}^2 F(\theta)\right] \times \left[\omega - \frac{m^2\omega_\mathrm{A}}{\omega + i\eta k_r^2}F(\theta) - \left(\frac{l}{k_r r}\right)^2 \frac{N_t}{\omega + i\kappa k_r^2} - \left(\frac{l}{k_r r}\right)^2 \frac{N_\mu}{\omega}\right] \\ &- \left[m\omega_\mathrm{A}^2 G(\theta) + 2\Omega\cos\theta(\omega + i\eta k_r^2)\right] \times \left[\frac{m\omega_\mathrm{A}^2}{\omega + i\eta k_r^2} G(\theta) + 2\Omega\cos\theta\right] \\ &= 0\,.\end{aligned} \tag{A.74}$$

Since we expect the the growth rate of the Tayler instability for $\Omega \gg \omega_\mathrm{A}$ to be $\omega_\mathrm{A}^2/\Omega$, we define the quantities

$$\omega \equiv \alpha \frac{\omega_\mathrm{A}^2}{\Omega}, \tag{A.75}$$

$$H \equiv \frac{\eta\Omega}{\omega_\mathrm{A}^2}, \tag{A.76}$$

$$K \equiv \frac{\kappa\Omega}{\omega_\mathrm{A}^2}, \tag{A.77}$$

$$n^2 \equiv \left(\frac{l}{k_r r}\right)^2 \frac{N_\mu^2}{\omega_\mathrm{A}^2}. \tag{A.78}$$

In the limit of $\kappa \to \infty$, the dispersion relation simplifies into

$$m^2\left[m^2\alpha F(\theta) + n^2(\alpha + iHk_r^2)\right] - \alpha\left[2(\alpha + iHk_r^2)\cos\theta + mG(\theta)\right]^2 = 0\,. \tag{A.79}$$

We set α purely real, so we can seperate Eq. (A.79) into the real and imaginary parts, respectively:

$$m^2(m^2F(\theta) + n^2) - (2\alpha\cos\theta + mG(\theta))^2 + 4H^2k_r^4\cos^2\theta = 0\,, \tag{A.80}$$

$$m^2n^2 - 4(2\alpha\cos\theta + mG(\theta))\cos\theta\alpha\,. \tag{A.81}$$

We solve the imaginary part (Eq. (A.81))

$$\alpha = \frac{mF(\theta)}{4\cos\theta}\left(-1 \pm \sqrt{1 + \frac{2n^2}{G(\theta)^2}}\right), \tag{A.82}$$

and substitute the expression in the real part (Eq. (A.80))

$$2m^4F(\theta) - m^2G(\theta)^2\left(1 \pm \sqrt{1+\frac{2n^2}{G(\theta)^2}}\right) + m^2n^2 + 8\cos^2\theta H^2 k_r^4 = 0\,. \tag{A.83}$$

To have a real solution, the following relation must be satisfied

$$2m^4F(\theta) + m^2n^2 < m^2G(\theta)^2\left(1 \pm \sqrt{1+\frac{2n^2}{G(\theta)^2}}\right) \tag{A.84}$$

which can be rewritten

$$\frac{2m^2}{G(\theta)}F(\theta) < -\frac{t^4}{2} + 1 \pm \sqrt{1+\frac{t^2}{2}}\,. \tag{A.85}$$

The right-hand side is maximum when $t \to 0$, thus

$$m^2\frac{F(\theta)}{G(\theta)^2} < 1\,. \tag{A.86}$$

We can easily see that for a toroidal magnetic field generated by the shear of a magnetic dipole, i.e. $f(\theta) = \cos\theta\sin\theta$, we find that $|m| = 1$ is the only unstable mode, which develops near the poles $\theta \in [0, \pi/5] \cup [4\pi/5, \pi]$.

B

Numerical simulations of the Tayler instability

Contents

This appendix presents numerical simulations of the Tayler instability in solid body rotation. We compared the numerical results with the analytical model's predictions (Sects. B.2.1 and B.2.2). This comparison is particularly motivated by the fact that the predictions of Ma & Fuller (2019) regarding nonlinear saturation are based solely on physical arguments requiring validation through numerical simulations. Finally, in subsequent numerical simulations, we look at the clarge-scale radial magnetic field generated by the instability (Sect. B.2.3). We report the existence of an electromotive force which generates a strong large-scale ($l = 3, m = 0$)–poloidal magnetic field in most of the runs. Despite the need for a finer analysis, this first numerical investigation is worth describing in this manuscript as it provides interesting new preliminary results and connects our analytical model (Chap 5) to the numerical simulations of the Tayler-Spruit dynamo (Chaps 6–8).

B.1 . Initial conditions

For the detailed description of the numerical methods, see the introductive chapter 4. In all runs the fluid is in solid body rotation, i.e. we impose $\Omega_o = \Omega_i$. While the realistic magnetic Prandtl number in PNSs ranges between $Pm \sim 10^4 - 10^{11}$ depending on whether the PNS is still optically thick to neutrinos (Barrère et al., 2023), we choose $Pm = 1$ in the following simulations as the astrophysical asymptotic regime is not reachable with the current computing power. We also choose $Pr = 10^{-3}$, which is close to the astrophysical regime.

The explored parameter space is $(B_0, B_{\rm crit}, \eta)$, with B_0 the intial average magnetic field

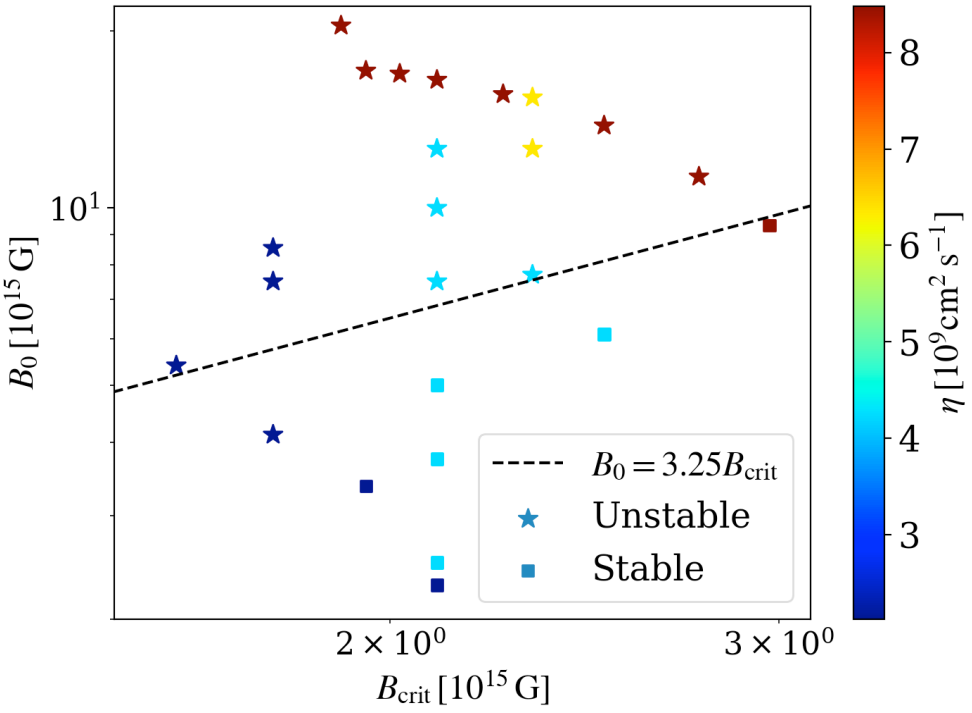

Figure B.1 — Location of the runs showing a Tayler stable (squares) and Tayler unstable (stars) fluid in the parameter space $(B_0, B_{\mathrm{crit}}, \eta)$.

strengh,

$$B_{\mathrm{crit}} = \sqrt{4\pi\rho_0 r_o^2}\Omega_o \left(\frac{N_{\mathrm{eff}}}{\Omega_o}\right)^{1/2} \left(\frac{\eta}{r_o\Omega_o}\right)^{1/4}, \tag{B.1}$$

is the theoretical critical toroidal magnetic strength above which the fluid becomes Tayler unstable, with the effective Brunt-Väisälä frequency $N_{\mathrm{eff}} \equiv N\sqrt{\eta/\kappa} = 316\,\mathrm{s}^{-1}$. As N_{eff} is kept constant, varying B_{crit} is equivalent to changing the PNS angular velocity Ω_o. In practice, this is equivalent to varying the dimensionless parameters λ is the dimensionless initial amplitude of the magneyic field, the Rayleigh number, and the Ekman number.

We choose an initial magnetic field that is purely toroidal and axisymmetric with a configuration $(l = 2, m = 0)$ because this geometry is a product of the winding of an axial magnetic dipole. The profile of the magnetic field reads

$$\mathbf{B}_0(r,\theta) \propto \lambda \sin\left(\pi\frac{r - r_i}{r_i}\right)\sin\theta\cos\theta\mathbf{e}_\phi\,, \tag{B.2}$$

i.e.

$$b_0 = 0\,, \tag{B.3}$$

$$a_{j,0} \propto \lambda r \sin\left(\pi\frac{r - r_i}{r_i}\right)\left(3\cos^2\theta - 1\right). \tag{B.4}$$

To destabilise the fluid, we also impose an initial weak random perturbation $|\delta\mathbf{v}| \ll r_o\Omega_o$.

In our simulations, we infer the values of B_ϕ, B_r, and $\delta B_\perp$ via the respective axisymmetric toroidal, axisymmetric poloidal and non-axisymmetric components of the magnetic energy

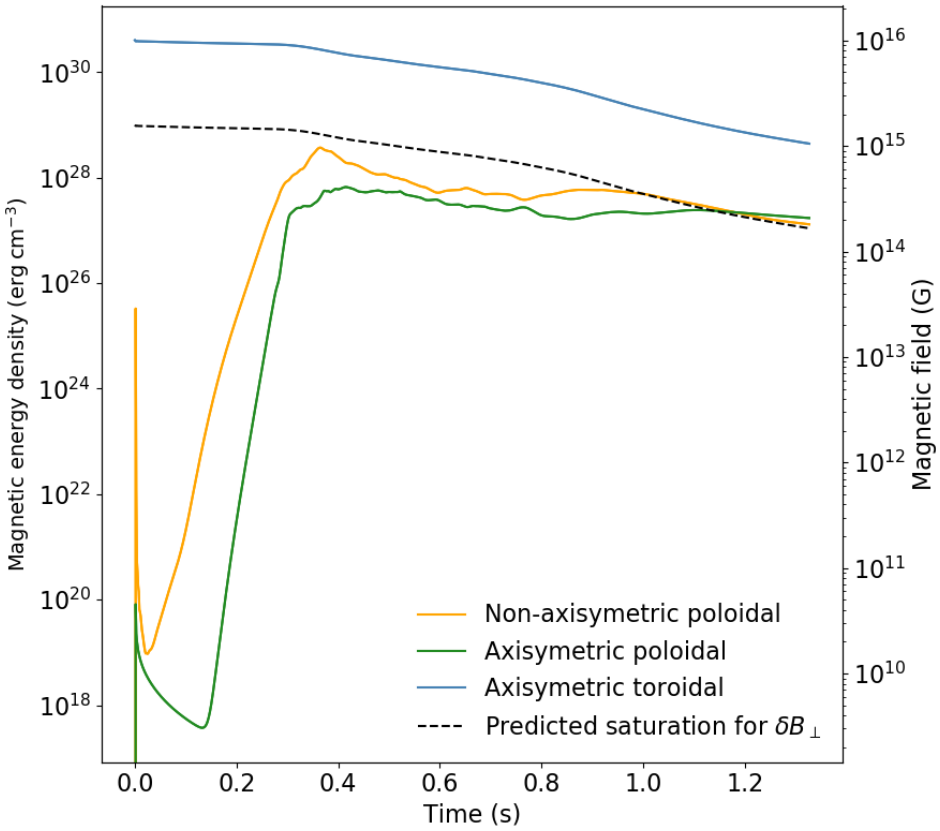

Figure B.2 — Time series of the non-axisymmetric poloidal (orange), axisymmetric poloidal (green), and axisymmetric toroidal (blue) components of the magnetic energy density. The black dashed line illustrates the expected saturation level of the Tayler modes total magnetic energy (Eq. 5.22 acccording to Fuller et al. (2019)).

density. Therefore, they are root mean square magnetic field strengths. Using the total or toroidal non-axisymmetric component for $\delta B_\perp$ does not significantly change the following scaling laws we find. These strengths are measured at the saturation time of the instability, which is when the non-axisymmetric poloidal magnetic field peaks. The growth and dissipation rates were measured by fitting a power law on the non-axisymmetric poloidal component in the linear phase and on the axisymmetric toroidal component during the saturation phase, i.e. after the non-axisymmetric poloidal magnetic field peaked.

B.2 . Results

B.2.1 . Linear phase

In the evolution of magnetic energy (displayed in Fig. B.2), we distinguish several phases. First, we observe a peak in the first milliseconds of the simulations. This peak is a transient phenomenon due to the initial disturbance of the velocity field. This short phase quickly makes room for the expected exponential growth phase for the Tayler instability. Then, we observe the exponential growth and saturation of the perturbed non-axisymmetric component. This component saturates at an intensity on the order of that predicted by Fuller et al.

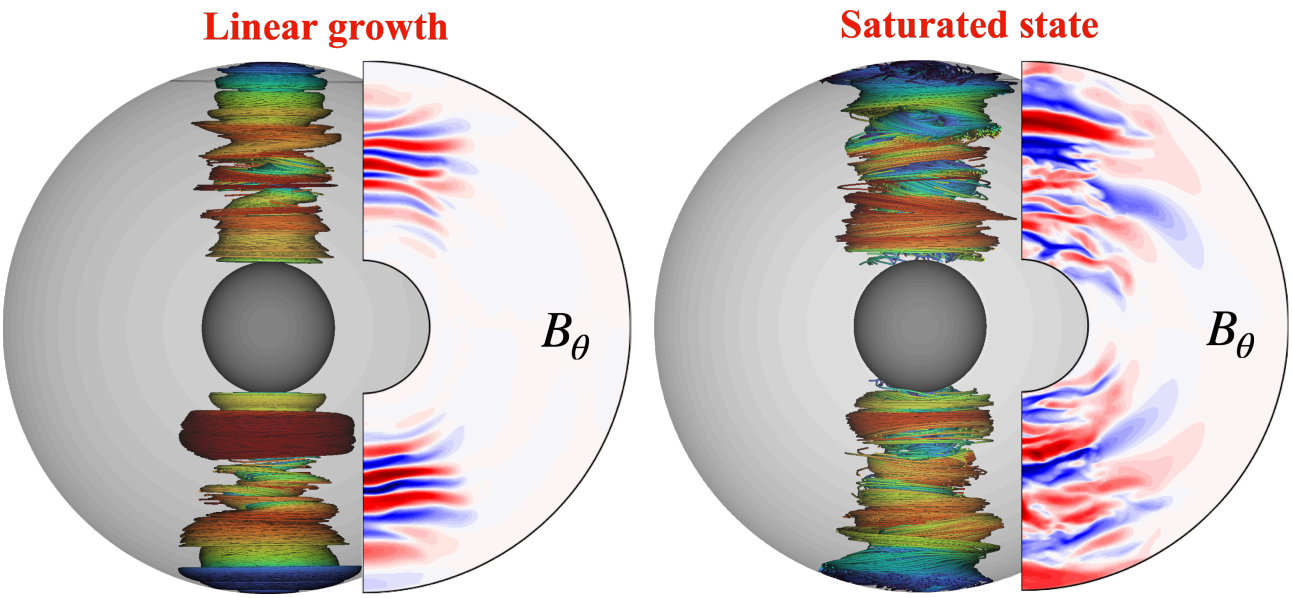

Figure B.3 — Snapshots of the 3D magnetic field lines and meridional slices of the latitudinal magnetic field during the growth (left) and saturated (right) stages of the Tayler instability. These plots clearly show the kink shape of the Tayler instability along the polar axis.

(2019) (Eq. (5.22)), although slightly lower by a factor ~ 2. Finally, we can observe the generation of an axisymmetric poloidal component and the dissipation of the axisymmetric toroidal field due to non-linear effects.

We focus on the development of the observed non-axisymmetric instability. As shown in the left snapshot of Fig. B.3, the instability develops at the poles and is absent at the equator. The mode seems to be mostly $m = 1$, which is characteristic of the Tayler Instability. This is consistent with the spectra which indicate the presence of a dominant $m = 1$ mode in the poloidal energy. As expected, the dominant mode of the magnetic field is the axisymmetric toroidal component (see Fig. B.2).

It is interesting to verify whether the predicted growth rate (Eq. (5.13)) is in agreement with the simulations. These comparisons are grouped in Fig. B.4, and we notice that there is a subset of simulations with large $B_0/B_{\rm crit}$ in which the growth rate is larger than predicted. Since the analytical growth rate is an order of magnitude, one possible explanation is that the actual growth rate passes through these points and not those closer to the stability threshold. Indeed, the closer we get to this threshold, the more the validity of the predictions can be questioned. This point remains to be further explored because there is still a factor of 10 between these points and the prediction.

To conclude the analysis of linear growth, we also compared the stability criterion for the toroidal magnetic field (Eq. (5.12)) with the stability threshold found in our simulations. For this, the values of B_0 and η were fixed, and only the value of $B_{\rm crit}$ varied by changing the rotation frequency. An interval where this threshold is located can thus be deduced. However, we noticed later that the calculation of the parameter λ in the code showed some issues, resulting in different values of the initial magnetic fields for the same value of λ and explaining the varying B_0 in the parameter space. Still, this does not prevent measuring a

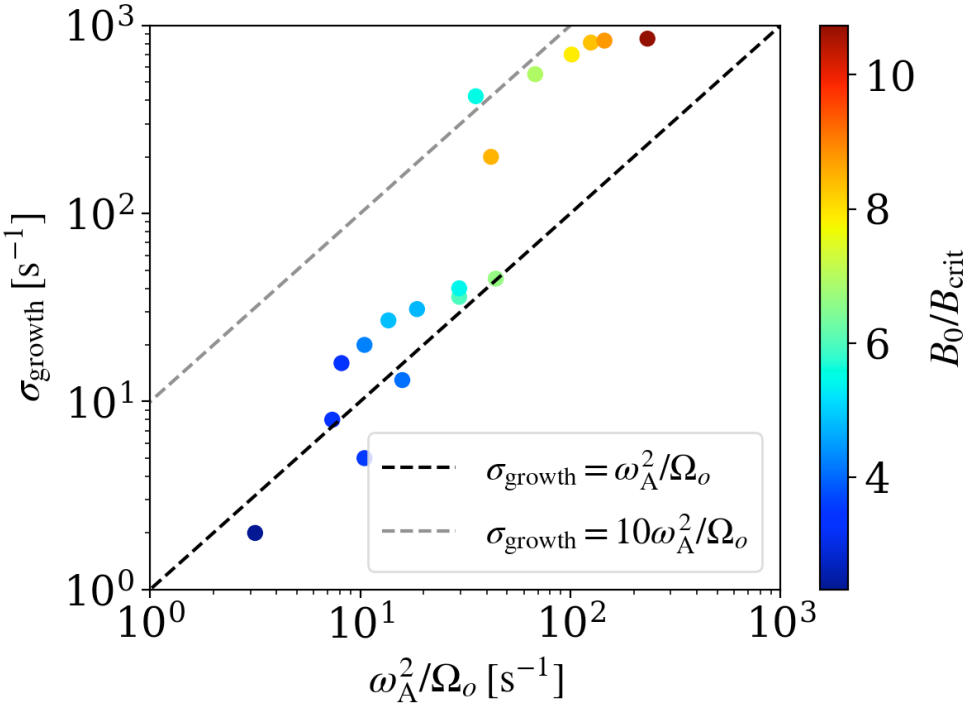

Figure B.4 — Measured growth rate of the Tayler instability as a function of the theoretical prediction. The colour map indicates the distance to the theoretical instability threshold.

mean threshold of $\sim 3.25 B_{\rm crit}$, which is of the same order of magnitude as the theoretical value.

B.2.2 . Non-linear saturated phase

Once turbulent dissipation becomes significant, the Tayler instability saturates (right in Fig B.3), and the axisymmetric toroidal component is diffused more efficiently. As the analytical predictions of Fuller et al. (2019) rely on strong assumptions to simplify the non-linear problem of turbulent diffusion, our simulations are useful to test whether these hypotheses are justified. In the left plot of Fig. B.5, we first compare our simulations to the ratio between the perturbed field generated by the Tayler instability $\delta B_\perp$ and the axisymmetric toroidal field B_ϕ (Eq. (5.22)). The simulations show the same relation within a factor ~ 0.4, thus globally agreeing with this prediction.

For the relation between the two axisymmetric components B_r and B_ϕ (Eq. (5.36)), our measurements (right of Fig. B.5) show a global agreement with the theory for $B_0/B_{\rm crit}$. The values of B_r/B_ϕ are below $\omega_{\rm A}/N_{\rm eff}$ by a factor $4-10$, which remains reasonable.

Finally, the last comparison is with the turbulent dissipation rate of B_ϕ predicted by Eq. (5.26) (left of Fig. B.6). We find a very significant discrepancy (about a factor of 100) from the prediction for simulations closest to the stability threshold. Notably, even the slope does not seem to follow that of the prediction. This discrepancy is not as pronounced in the plot on the right, where the comparison is made with the dissipation rate where Eq. (5.22) is satisfied. However, it is the simulations farthest from the stability threshold that no longer follow Fuller et al.'s prediction. An interesting point to note is that, despite these differences, our measurements are closer to Spruit's prediction than to Fuller et al.'s (grey dashed lines in

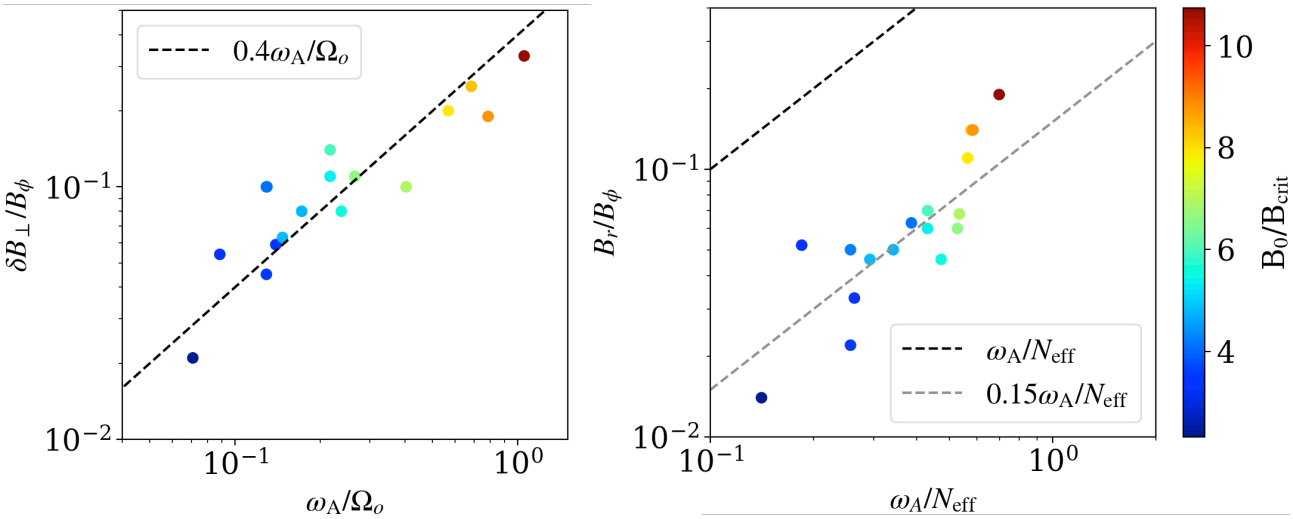

Figure B.5 — Left: Ratio of the perturbed magnetic field produced by the Tayler instability $\delta B_\perp$ to the azimuthal component B_ϕ as a function of the theoretical prediction derived by Fuller et al. (2019). Right: Same as on the left but for the rotation between both axisymmetric radial B_r and azimuthal B_ϕ magnetic fields. The colour map indicates the distance to the theoretical instability threshold.

Fig. B.6).

The results on the non-linear phase confirm Fuller et al.'s prediction on the saturation of $\delta B_\perp$, but do not align well with their other predictions. Since these predictions were made less rigorously than those on the linear development of the instability, this discrepancy with the simulations is less surprising. Nevertheless, a study with simulations further from the stability threshold is necessary to conclude on the validity of Fuller et al.'s predictions. The study of the impact of stable stratification on the whole dynamo loop in Chap. 7 will provide more robust new results on the saturation of the dynamo.

B.2.3 . Generated radial magnetic field

Studying the structure of the axisymmetric radial magnetic field B_r generated is of particular interest because we don't have any analytical predictions for it and this could inform on the geometry of the toroidal field resulting from the winding. To analyse its multipolar structure, a decomposition into latitudinal mode l has been done using the formula

$$B_r(r,\theta) = \sum_{l=0}^{l_{\max}} g_{l,0}(r) P_l^0(\cos\theta)\,, \tag{B.5}$$

where P_l^0 is the Legendre polynomial at the order l and

$$g_{l,0}(r) = \frac{1}{\pi}\int_{-1}^{1} B_r(r,\theta) P_l^0(\cos\theta)\, d\cos\theta\,. \tag{B.6}$$

This diagnostic could be performed on magnetic fields that have evolved over a long enough time to begin observing a dominant mode. Table B.1 gathers the simulations in which this diagnostic has been carried out. The simulations form two sets: one with multipolar B_r fields $l = 3$ (right in Fig. B.7) and the other with mainly dipolar fields (left in Fig. B.7).

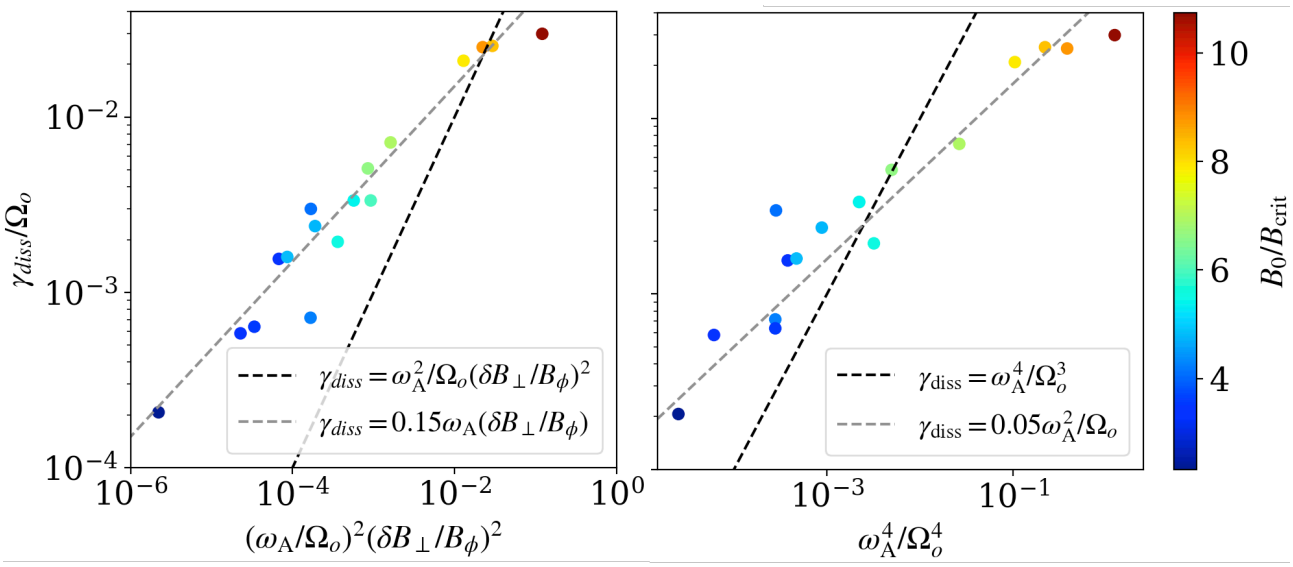

Figure B.6 — Measured turbulent dissipation of B_ϕ as a function of the theoretical prediction derived by Fuller et al. (2019) (black dashed line) and Spruit (2002) (grey dashed line). The colour map indicates the distance to the theoretical instability threshold.

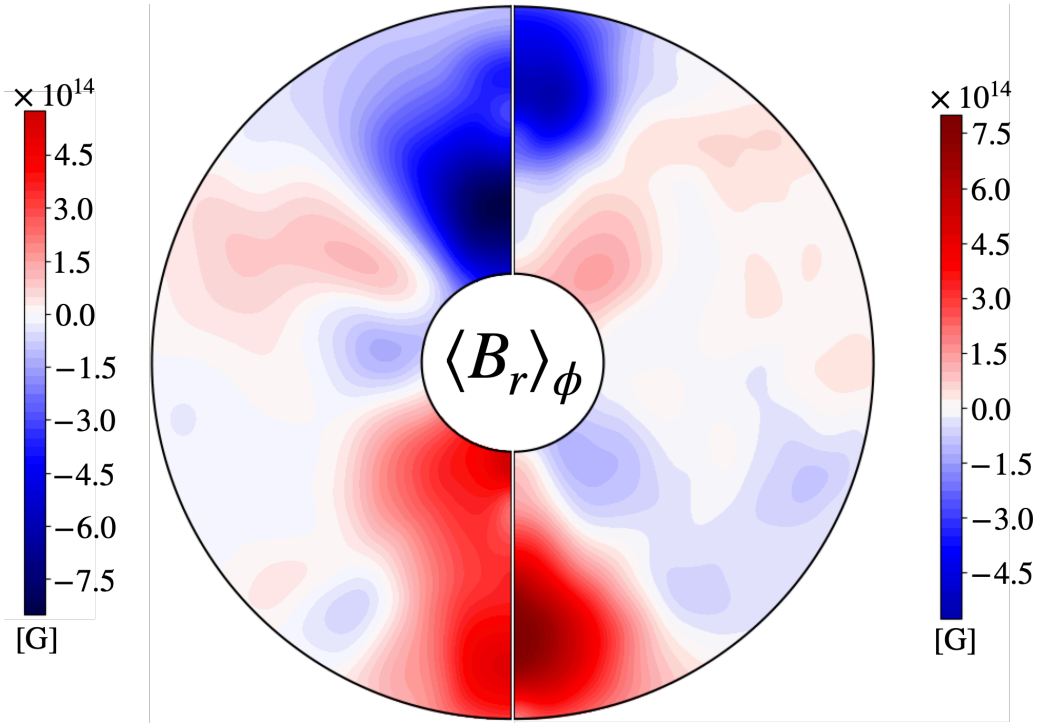

Figure B.7 — Meridional slices of the axisymmetric radial magnetic field after the turbulent dissipation for two runs. The left and right slices of B_r display a magnetic dipole ($l = 1$) and a magnetic quadrupole ($l = 3$), respectively.

We notice that the transition from multipolar to dipolar fields occurs when $B_0/B_{\rm crit} \sim 6$. Since dissipation of small scales is faster, it is likely that the $l = 3$ mode has not dissipated enough by the end of the simulations where $B_0/B_{\rm crit} \leqslant 6$ for the $l = 1$ mode to dominate. To support this explanation, it would be necessary to determine the dominant mode just after the end of turbulent dissipation.

B_0 $[10^{16}\,\mathrm{G}]$	$B_{\rm crit}$ $[10^{16}\,\mathrm{G}]$	$\eta\,[\mathrm{cm^2\,s^{-1}}]$	l
1.26	2.1	4.24×10^9	3
1.00	2.1	4.24×10^9	3
1.54	2.32	6.36×10^9	3
1.26	2.32	6.36×10^9	3
2.04	1.9	8.48×10^9	1
1.71	1.95	8.48×10^9	1
1.69	2.1	8.48×10^9	1
1.65	2.1	8.48×10^9	3
1.56	2.25	8.48×10^9	3
1.38	2.5	8.48×10^9	3
1.13	2.76	8.48×10^9	3

Table B.1 — Predominant l-modes measured for several sets of input parameters.

B.3 . Conclusions

Although this piece of work is preliminary, we can draw some conclusions. The numerical simulations are in global agreement with the analytical predictions about the linear growth phase of the Tayler instability. Additionally, the simulations allowed testing of the analytical predictions on the non-linear phase, which remained more uncertain. The prediction of the saturation of the non-axisymmetric magnetic field is confirmed, while significant differences emerge with those concerning the saturation of the axisymmetric radial magnetic field and the turbulent dissipation of the toroidal field. Furthermore, the analysis of the radial magnetic field structure showed that it can tend towards either a quadrupolar/multipolar or dipolar field. Nonetheless, we remain limited by the resolution, which keeps us far from the extreme conditions of magnetars, particularly regarding resistivity. This implies that the magnetic field in proto-magnetars must be far from the threshold of the Tayler instability, i.e. $B_\phi/B_{\rm crit} \gg 1$. This fosters further analysis and new simulations tending towards this regime.

Since the end of my internship, a similar study was carried out by Ji et al. (2023) but in a cylindrical configuration. They also find a good agreement with the analytical scalings for the linear phase. However, when the usual scale separation $\omega_{\rm A} \ll \Omega_o \ll N$ is not satisfied anymore, i.e. $\omega_{\rm A} \sim \Omega_o$, the growth rate scales with $\omega_{\rm A}^{4.5}/\Omega_o^2$. As the value $\omega_{\rm A}$ in our simulations with the larger $B_0/B_{\rm crit}$ also tends toward Ω_o, this may explain the sudden increase of $\sigma_{\rm growth}$ we observed at $B_0/B_{\rm crit} \gtrsim 6$ (Fig. B.4). Then, they suggest that the subsequent saturation of the Tayler instability is caused by secondary shear instabilities, which are not expected to occur for stronger stratifications. While these secondary instabilities must impact the dissipation

rate of the magnetic field, they find a dissipation much slower than predicted by Spruit (2002), and so than in our simulations. Finally, an amplification of the axisymmetric poloidal field is also observed, indicating the existence of an electromotive force that may drive a dynamo.

As we showed that the Tayler instability can generate an axisymmetric poloidal field, adding differential rotation is crucial to close the theoretical dynamo loop. To this end, a possibility is to impose different rotation rates onto both spherical boundaries, i.e. $\Omega_o \neq \Omega_i$. This configuration is called the spherical Couette configuration and will be used in the following chapters of this thesis (Chaps. 6–8), in which we find the numerical evidence of the Tayler-Spruit dynamo(s) for $\Omega_o > \Omega_i$. The forcing on the outer sphere would be the result of the fallback accretion.

B.4 . List of models

Table B.2 sums up the input parameters of the numerical simulations carried out in the investigation of the Tayler instability.

Name	$\eta\,[\mathrm{cm^2\,s^{-1}}]$	P [ms]	$B_{\mathrm{crit}}\,[10^{15}\,\mathrm{G}]$	$B_0\,[10^{15}\,\mathrm{G}]$	Tayler unstable ?
TS0nu2.12B2.1O4	2.12×10^9	5	2.3	2.1	NO
TS0nu2.12B3.37O3	2.12×10^9	6.67	1.95	3.37	NO
TS0nu2.12B4.12O2	2.12×10^9	10	1.8	4.12	YES
TS0nu2.12B7.5O2	2.12×10^9	10	1.8	7.5	YES
TS0nu2.12B8.55O2	2.12×10^9	10	1.8	8.55	YES
TS0nu2.12B5.4O1.3	2.12×10^9	15	1.6	5.4	YES
TS0nu4.24B6.1O4	4.24×10^9	5	2.5	6.1	NO
TS0nu4.24B7.7O3	4.24×10^9	6.67	2.32	7.7	YES
TS0nu4.24B2.5O2	4.24×10^9	10	2.1	2.5	NO
TS0nu4.24B3.75O2	4.24×10^9	10	2.1	3.75	NO
TS0nu4.24B5.0O2	4.24×10^9	10	2.1	5.0	NO
TS0nu4.24B7.5O2	4.24×10^9	10	2.1	7.5	YES
TS0nu4.24B10.0O2	4.24×10^9	10	2.1	10.0	YES
TS0nu4.24B12.6O2	4.24×10^9	10	2.1	12.6	YES
TS0nu6.36B12.6O2	6.36×10^9	10	2.32	12.6	YES
TS0nu6.36B15.4O2	6.36×10^9	10	2.32	15.4	YES
TS0nu8.48B9.1O4	8.48×10^9	5	2.1	9.1	NO
TS0nu8.48B11.3O3	8.48×10^9	6.67	2.76	11.3	YES
TS0nu8.48B13.8O2	8.48×10^9	10	2.5	13.8	YES
TS0nu8.48B15.6O1.3	8.48×10^9	15	2.25	15.6	YES
TS0nu8.48B16.5O1	8.48×10^9	20	2.1	16.5	YES
TS0nu8.48B16.9O0.85	8.48×10^9	23.5	2.02	16.9	YES
TS0nu8.48B17.1O0.75	8.48×10^9	26.7	1.95	17.1	YES
TS0nu8.48B20.4O0.66	8.48×10^9	30	1.9	20.4	YES

Table B.2 — List of models and their input parameters: the resistivity η, the rotation period of both shells P, the corresponding critical intensity for the Tayler instability B_{crit}, and the initial intensity of the magnetic field B_0. We also mention whether the fluid is Tayler unstable in the last column.

C

Publications et communications

Contents

Dans cette appendice sont listées les publications publiées ou en préparation et les conférences dans lesquelles j'ai eu l'occasion de présenter mes résultatsndans une présentation orale ou un poster.

C.1 . Publications référées et soumises

5. **P. Barrère**, J. Guilet, R. Raynaud, A. Reboul-Salze *Tayler-Spruit dynamo in stably stratified rotating fluids: Application to proto-magnetars* **submitted to A&A,** juillet 2024.

4. A. Igoshev, **P. Barrère**, R. Raynaud, J. Guilet, T. Wood, R. Hollerbach. *From proto-neutron star dynamo to low-field magnetars.* **submitted to Nature Astronomy,** mai 2024.

3. F. Rincon, **P. Barrère**, T. Roudier. *Observational characterisation of large-scale transport and horizontal turbulent diffusivity in the quiet Sun.* **submitted to A&A,** mars 2024.

2. **P. Barrère**, J. Guilet, R. Raynaud, A. Reboul-Salze. *Numerical simulations of the Tayler-Spruit dynamo in protomagnetars.* **MNRAS Letters 526**, L88–L93, septembre 2023. DOI : 10.1093/mnrasl/slad120

1. **P. Barrère**, J. Guilet, A. Reboul-Salze, R. Raynaud, H.-T. Janka. *A new scenario for magnetar formation: Tayler-Spruit dynamo in a proto-neutron star spun up by fallback.* **A&A 668**, A79, décembre 2022. DOI : 10.1051/0004-6361/202244172

C.2 . Présentations et posters

11. Entretien pour les MPA Postdoc Fellowships (oral, invité), *Max Planck Institute for Astrophysics,* Garching, Allemagne. 11 décembre 2023.

10. Séminaire groupe de Physique Stellaire de l'Observatoire de Genève (oral, invité),*Observatoire de Genève,* Genève, Suisse. 7 décembre 2023.

9. Séminaire de l'Albert Einstein Institute (oral, invité), *Albert Einstein Institute,* Berlin, Allemagne. 21 novembre 2023.

8. MIAPbP program: stellar magnetic fields from protostars to supernovae (oral), Garching, Allemagne. 16 au 27 octobre 2023.

7. Séminaire zoom pour le Département d'Astrophysique de l'Université de Valence (oral, invité), *Universidad de Valencia,* Valence, Espagne. 25 août 2023.

6. Journées de la SF2A 2023 (oral), *Université de Strasbourg,* Strasbourg, France. 20 au 23 juin 2023.

5. Thematic school GWsNS-2023: Gravitational waves from neutron stars (poster), *Centre Paul Langevin,* Aussois, France. 4 au 9 juin 2023.

4. Frontiers in dynamo theory: from the Earth to the stars (poster), *Isaac Newton Institute,* University of Cambridge, Cambridge, UK. 14 novembre au 2 décembre 2022.

3. Atelier Codes et Physique Stellaire du PNPS (oral), *Centre de Conférence Jules Janssen,* Observatoire de Paris, Meudon, France. 27 juin au 1er juillet 2022.

2. PHAROS Conference 2022 (oral), *Sapienza Università di Roma,* Rome, Italie. 16 au 19 mai 2022.

1. Workshop ANR BEAMING (oral), *Institut de Recherche en Astrophysique et Planétologie (IRAP),* Observatoire Midi-Pyrénées, Toulouse, France. 28 au 29 mars 2022.

C.3 . Articles

C.3.1 . Article *A new scenario for magnetar formation: Tayler-Spruit dynamo in a proto-neutron star spun up by fallback (published)*

A&A 668, A79 (2022)
https://doi.org/10.1051/0004-6361/202244172

Astronomy & Astrophysics

A new scenario for magnetar formation: Tayler-Spruit dynamo in a proto-neutron star spun up by fallback

P. Barrère[1], J. Guilet[1], A. Reboul-Salze[2], R. Raynaud[1], and H.-T. Janka[3]

[1] Université Paris-Saclay, Université Paris-Cité, CEA, CNRS, AIM, 91191 Gif-sur-Yvette, France
e-mail: paul.barrere@cea.fr
[2] Max Planck Institute for Gravitational Physics (Albert Einstein Institute), 14476 Potsdam, Germany
[3] Max Planck Institute for Astrophysics, Karl-Schwarzschild-Str. 1, 85748 Garching, Germany

Received 2 June 2022 / Accepted 11 October 2022

ABSTRACT

Magnetars are isolated young neutron stars characterised by the most intense magnetic fields known in the Universe, which power a wide variety of high-energy emissions from giant flares to fast radio bursts. The origin of their magnetic field is still a challenging question. In situ magnetic field amplification by dynamo action could potentially generate ultra-strong magnetic fields in fast-rotating progenitors. However, it is unclear whether the fraction of progenitors harbouring fast core rotation is sufficient to explain the entire magnetar population. To address this point, we propose a new scenario for magnetar formation involving a slowly rotating progenitor, in which a slow-rotating proto-neutron star is spun up by the supernova fallback. We argue that this can trigger the development of the Tayler-Spruit dynamo while other dynamo processes are disfavoured. Using the findings of previous studies of this dynamo and simulation results characterising the supernova fallback, we derive equations modelling the coupled evolution of the proto-neutron star rotation and magnetic field. Their time integration for different accreted masses is successfully compared with analytical estimates of the amplification timescales and saturation value of the magnetic field. We find that the magnetic field is amplified within 20−40 s after the core bounce, and that the radial magnetic field saturates at intensities between $\sim 10^{13}$ and 10^{15} G, therefore spanning the full range of a magnetar's dipolar magnetic fields. The toroidal magnetic field is predicted to be a factor of 10–100 times stronger, lying between $\sim 10^{15}$ and 3×10^{16} G. We also compare the saturation mechanisms proposed respectively by H.C. Spruit and J. Fuller, showing that magnetar-like magnetic fields can be generated for a neutron star spun up to rotation periods of $\lesssim$8 ms and $\lesssim$28 ms, corresponding to accreted masses of $\gtrsim 4 \times 10^{-2}\, M_\odot$ and $\gtrsim 1.1 \times 10^{-2} M_\odot$, respectively. Therefore, our results suggest that magnetars can be formed from slow-rotating progenitors for accreted masses compatible with recent supernova simulations and leading to plausible initial rotation periods of the proto-neutron star.

Key words. stars: magnetars – supernovae: general – magnetohydrodynamics (MHD) – dynamo

1. Introduction

Magnetars represent two classes of isolated young neutron stars whose emission is powered by their ultrastrong magnetic field: anomalous X-ray pulsars and soft gamma repeaters. They feature a large spectrum of activity from short bursts (Gotz et al. 2006; Coti Zelati et al. 2018, 2021) to giant flares (Evans et al. 1980; Hurley et al. 1999, 2005; Svinkin et al. 2021), whose signal contains quasi-periodic oscillations (Israel et al. 2005; Strohmayer & Watts 2005; Gabler et al. 2018; Roberts et al. 2021). Moreover, a Galactic magnetar has recently been associated with a fast radio burst (FRB; Bochenek et al. 2020; CHIME/FRB Collaboration et al. 2020), which validates the capability of magnetar scenarios to explain at least a fraction of FRBs.

The pulsed X-ray activity of magnetars shows that they are characterised by a slow rotation period of 2−12 s and a fast spin-down. Under the assumption of a magnetic dipole spin-down, magnetars are therefore constrained to exhibit strong dipolar surface magnetic fields ranging from 10^{14} to 10^{15} G (Kouveliotou 1999; Kaspi & Beloborodov 2017), which are two orders of magnitude larger than in regular neutron stars. Furthermore, several lines of evidence suggest the presence of a non-dipolar magnetic field stronger than the dipolar component. Indeed, absorption lines have been detected in the X-ray spectra of two magnetars: SGR 0418+5729 (Tiengo et al. 2013) and SWIFT J1882.3-1606 (Rodríguez Castillo et al. 2016). If these lines are interpreted as proton cyclotron lines, they are respectively the signature of non-dipolar magnetic fields of $\sim 2 \times 10^{14}$−10^{15} G and $\sim 6 \times 10^{14}$−2.5×10^{15} G, which are stronger than their respective dipolar components by a factor of ∼30−170 (Rea et al. 2010, 2012). Another sign of strong non-dipolar magnetic fields is the detection of a phase modulation in the hard-X-ray emission of a few magnetars. This may be explained by precession movements due to an internal toroidal magnetic field reaching a strength of $\sim 10^{16}$ G (Makishima et al. 2014, 2016, 2019, 2021).

Proto-magnetars may be the central engine of extreme events if they are born rotating with a period of a few milliseconds. Indeed, their large-scale magnetic field can extract a large amount of rotational energy, which may create jets and lead to magnetorotational explosions (Burrows et al. 2007; Dessart et al. 2008; Takiwaki et al. 2009; Kuroda et al. 2020; Bugli et al. 2020, 2021; Obergaulinger & Aloy 2020, 2021, 2022). This process may explain hypernovae that are associated with long gamma-ray bursts (Duncan & Thompson 1992; Zhang & Mészáros 2001; Woosley & Bloom 2006; Drout et al. 2011; Nomoto et al. 2011; Gompertz & Fruchter 2017; Metzger et al. 2011, 2018). Moreover, their spin-down

luminosity is invoked as a source of delayed energy injection to explain superluminous supernovae (SNe; Woosley 2010; Kasen & Bildsten 2010; Dessart et al. 2012; Inserra et al. 2013; Nicholl et al. 2013). Finally, millisecond magnetars, which may be formed in binary neutron star mergers, could also provide an explanation for the plateau phase in the X-ray emission of some short gamma-ray bursts (Metzger et al. 2008; Lü & Zhang 2014; Gompertz et al. 2014).

The central question to understand magnetar formation is the origin of their ultra-strong magnetic field. One type of scenario invokes magnetic flux conservation during the collapse of magnetised progenitors (Ferrario & Wickramasinghe 2006; Hu & Lou 2009). The magnetic field of these progenitors can originate from either a fossil field (Braithwaite & Spruit 2004, 2017) or dynamo action during main sequence star mergers (Schneider et al. 2019, 2020). While the surface magnetic field is constrained by observations (Petit et al. 2019), the magnetic field intensity in the iron core remains unknown, which makes this scenario uncertain. Another class of formation scenarios is the in situ amplification of the magnetic field by a dynamo process after the core collapse, especially at early stages of the proto-magnetar evolution. Two mechanisms have been studied so far: the convective dynamo (Thompson & Duncan 1993; Raynaud et al. 2020, 2022; Masada et al. 2022; White et al. 2022) and the magnetorotational instability (MRI)-driven dynamo (e.g. Obergaulinger et al. 2009; Mösta et al. 2014; Guilet & Müller 2015; Reboul-Salze et al. 2021a,b). The efficiency of these two dynamo mechanisms in the physical conditions relevant to a proto-neutron star (PNS) is still uncertain, in particular because the regime of very high magnetic Prandtl numbers (i.e. the ratio of viscosity to magnetic diffusivity) has not yet been thoroughly explored (Guilet et al. 2022; Lander 2021). Numerical simulations suggest that the efficiency of both dynamos increases for faster PNS rotation (Raynaud et al. 2020, 2022; Reboul-Salze et al. 2021a,b), which makes them good candidates to explain the central engine of extreme explosions. However, it may be more challenging for them to explain magnetar formation in standard SNe, which requires slower initial rotation of the PNS. Indeed, the observed SN remnants associated with Galactic magnetars have an ordinary kinetic explosion energy (Vink & Kuiper 2006; Martin et al. 2014; Zhou et al. 2019). This suggests that most Galactic magnetars are formed in standard SNe, which is consistent with the fact that extreme explosions represent about 1% of all SNe whereas magnetars constitute at least 10% of the whole Galactic young neutron-star population (Kouveliotou et al. 1994; Gill & Heyl 2007; Beniamini et al. 2019). Under the assumption that all the rotational energy of the PNS is injected into the kinetic energy of the explosion, the kinetic energy of the proto-magnetar must not exceed the standard kinetic energy of a SN explosion of 10^{51} erg, which translates into a constraint on its initial rotation period of $\gtrsim$5 ms (Vink & Kuiper 2006).

All things considered, the aforementioned scenarios require that the progenitor core be either strongly magnetised or fast rotating. It remains uncertain as to whether one of these conditions is met in a sufficient number of progenitors. This article presents our investigation of a new scenario wherein magnetars form from a slowly rotating, weakly magnetised progenitor. We consider the situation in which a newly formed PNS is spun up by the matter initially ejected by the SN explosion that remains gravitationally bound to the compact remnant and eventually falls back onto its surface. As the accretion is asymmetric, recent numerical simulations suggest that the fallback can bring a significant amount of angular momentum to the PNS surface (Chan et al. 2020; Stockinger et al. 2020; Janka et al. 2022). We investigate the possibility that a magnetar may form due to the dynamo action triggered by the spin up from this fallback accretion. In this scenario, the MRI is expected to be stable because the PNS surface rotates faster than the core. The fallback starts roughly ~5−10 s after the core bounce (Stockinger et al. 2020; Janka et al. 2022), which may be too late for the development of a convective dynamo. Instead, we suggest that the magnetic field is amplified by another dynamo mechanism: the so-called Tayler-Spruit dynamo, which is driven by the Tayler instability. This instability feeds off a toroidal field in a stably stratified medium due to the presence of an electric current along the axis of symmetry (Tayler 1973; Pitts & Tayler 1985). Spruit (2002) proposed a first model of a dynamo driven by the Tayler instability in a differentially rotating stably stratified region. This model has received criticism from several authors (see Denissenkov & Pinsonneault 2007; Zahn et al. 2007), which has been addressed in the alternative description proposed by Fuller et al. (2019). The Tayler-Spruit dynamo has long been elusive in numerical simulations, but recent numerical simulations provide the first numerical evidence for its existence (Petitdemange et al. 2022). This dynamo is usually invoked for magnetic field amplification in the context of stellar interior physics, especially because of its suspected implications for angular momentum transport and the magnetic desert in Ap/Bp stars (e.g. Rüdiger & Kitchatinov 2010; Szklarski & Arlt 2013; Bonanno & Guarnieri 2017; Guerrero et al. 2019; Ma & Fuller 2019; Bonanno et al. 2020; Jouve et al. 2020). However, this dynamo process has never been studied in the framework of magnetar formation.

In the following, Sect. 2 presents the scenario in more detail and the formalism used by our model. We describe our results in Sect. 3 and discuss them in Sect. 4. Finally, we draw conclusions in Sect. 5.

2. Mathematical modelling of the scenario

To study our scenario, we built a one-zone model consisting in 'average' time evolution equations that capture the main stages sketched in Fig. 1. We start by describing the impact of the SN fallback on the PNS rotation (the differential rotation) and the magnetic field (the shearing of the radial field and the exponential growth of the Tayler instability). Finally, we present the mathematical formalism for the non-linear stages, that is, the saturation mechanism of the dynamo as modelled by Spruit (2002) and Fuller et al. (2019), which we complete by a description of the generation of the radial magnetic field through non-linear induction. For the computation of the time evolution, we only implement the description based on the work of Fuller et al. (2019); but in Sect. 3 we compare both models regarding the predictions of the saturated magnetic field.

2.1. Fallback accretion

Our scenario starts a few seconds after the core bounce when a fraction of the fallback matter gets accreted onto the PNS surface. This matter is initially ejected during the explosion but stays gravitationally bound to the PNS, and so begins to be asymmetrically accreted (Chan et al. 2020). This fallback matter is thought to have a large angular momentum, which can even reach the magnitude of the Keplerian angular momentum (Janka et al. 2022). Therefore, the spin of the PNS is strongly affected and the surface rotation can be accelerated up to millisecond periods. In our scenario, the core of the progenitor is

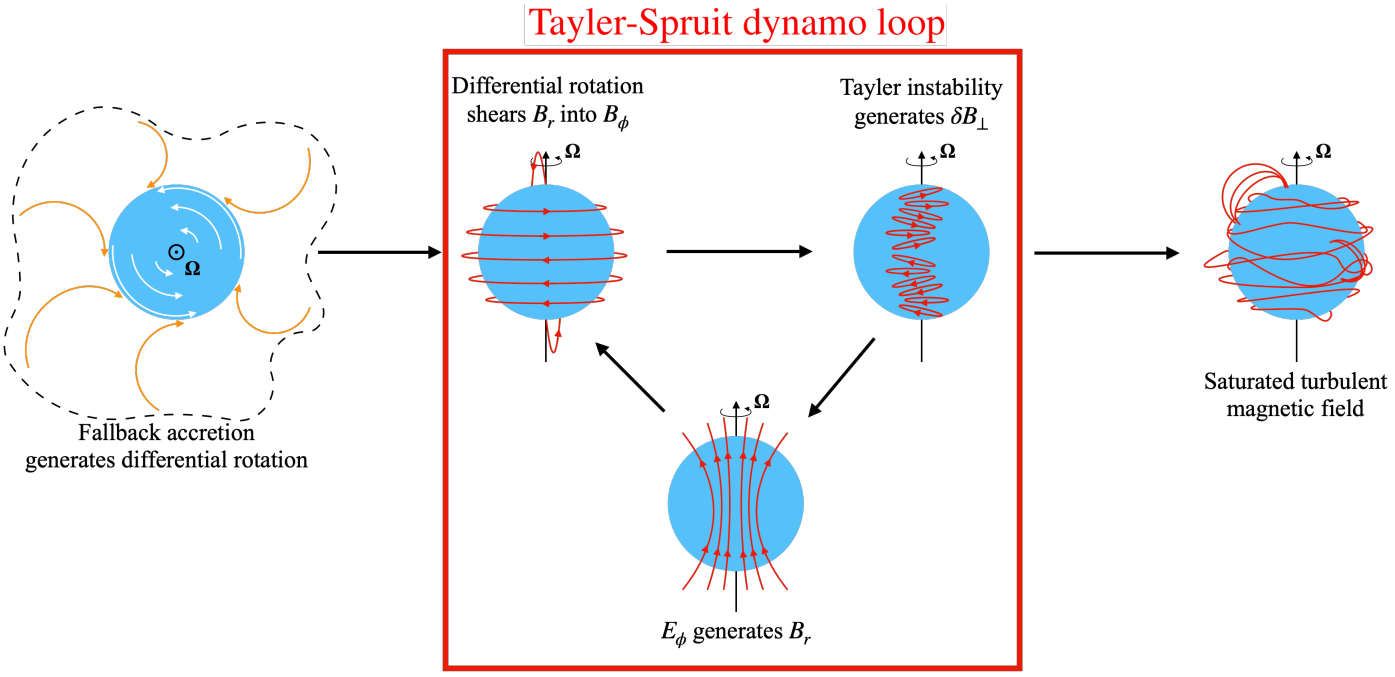

Fig. 1. Schematic representation of the different stages of our magnetar formation scenario. The dashed line encloses the region of the fallback (orange arrows). Red and white lines represent the magnetic field lines and fluid motions, respectively. $\mathbf{\Omega}$ and E_ϕ stand for the angular rotation frequency and the azimuthal component of the electromotive force, respectively. B_ϕ and B_r are the axisymmetric azimuthal and radial magnetic fields, and $\delta B_\perp$ is the non-axisymmetric perpendicular magnetic field.

assumed to be slowly rotating. Thus, the PNS surface spins faster than the PNS interior, which creates differential rotation.

To model the accretion onto the PNS surface, we use the asymptotic scaling for the mass accretion rate $\dot{M}_{\rm acc} \propto t^{-5/3}$ from Chevalier (1989). As the accretion mass rate must be finite at the beginning of this accretion regime, we define a start time t_0 such that

$$\dot{M}_{\rm acc} = \frac{A}{(t+t_0)^{5/3}}, \tag{1}$$

where A is a constant. Then, the accreted mass during this regime is

$$M_{\rm acc} = \int_0^\infty \frac{A}{(t+t_0)^{5/3}} {\rm d}t. \tag{2}$$

As $M_{\rm acc}$ is constant, we have $A = \frac{2}{3} t_0^{2/3} M_{\rm acc}$ and so the accretion mass rate is

$$\dot{M}_{\rm acc} = \frac{2}{3} M_{\rm acc} \frac{t_0^{2/3}}{(t+t_0)^{5/3}}. \tag{3}$$

From the fallback matter, only a fraction with angular momentum as large as the Keplerian limit at most will be accreted by the PNS, as discussed by Janka et al. (2022). Therefore, the relation between the average angular rotation frequency of the PNS and the mass accretion rate is

$$\dot{\Omega} = \frac{j_{\rm kep}}{I} \dot{M}_{\rm acc}, \tag{4}$$

where I stands for the PNS moment of inertia and $j_{\rm kep} \equiv \sqrt{G M_{\rm PNS} r}$ is the specific Keplerian angular momentum at the PNS surface. As the PNS mass changes little and the contraction of the PNS is almost over at the times considered for the fallback accretion, we assume I to be constant. As supposed in Fuller et al. (2019), the angular momentum is transported faster latitudinally than radially due to stratification, meaning that the differential rotation is shellular, that is Ω is constant on spherical shells.

As the accretion process spins up only the outer part of the PNS but not its inner core, the shear rate $q \equiv r\partial_r \ln \Omega$ is also expected to evolve. To describe this effect, we use the approximate expression

$$r\partial_r \Omega \sim \Omega - \Omega(r=0), \tag{5}$$

where Ω and $\Omega(r=0)$ are the average and central angular rotation frequency, respectively. Assuming that the rotation frequency at the centre of the PNS is unchanged by the accretion process (it will change only due to angular momentum transport processes described in Sect. 4.1), we infer the time derivative of the shear rate as

$$\dot{q} \sim \frac{\dot{\Omega}}{\Omega}(1-q). \tag{6}$$

2.2. Shearing and Tayler instability growth

The differential rotation generated by the fallback will shear the radial component of the large-scale radial magnetic field B_r into the azimuthal field B_ϕ as follows

$$\partial_t B_\phi = q\Omega B_r. \tag{7}$$

Therefore, we can define a growth rate[1] for B_ϕ:

$$\sigma_{\rm shear} \equiv q\Omega \frac{B_r}{B_\phi}. \tag{8}$$

[1] We note that this growth rate and the others defined below are rather instantaneous growth rates because they depend on the magnetic field.

As B_ϕ grows, it becomes Tayler unstable. To depict the linear growth of the instability, we make the following assumptions. First, the stratified medium of the PNS interior is characterised by the Brunt-Väisälä frequency (Hüdepohl 2014):

$$N \equiv \sqrt{-\frac{g}{\rho}\left(\left.\frac{\partial\rho}{\partial S}\right|_{P,Y_\mathrm{e}}\frac{\mathrm{d}S}{\mathrm{d}r}+\left.\frac{\partial\rho}{\partial Y_\mathrm{e}}\right|_{P,S}\frac{\mathrm{d}Y_\mathrm{e}}{\mathrm{d}r}\right)}\sim 4\times10^3\,\mathrm{s}^{-1}, \tag{9}$$

where g, ρ, Y_e, and S are the gravitational acceleration, the PNS mean density, the electron fraction, and the entropy, respectively. In the remainder of this paper, we use the fiducial value $N = 4\times10^3\,\mathrm{s}^{-1}$ based on the results of the 1D core-collapse supernova (CCSN) simulations from Hüdepohl (2014, Chap. 5). The Brunt-Väisälä frequency is almost uniform in most of the PNS except near the surface where it peaks at $\sim10^4\,\mathrm{s}^{-1}$. Hüdepohl (2014) made a comparison between two different equations of state (EOS): Shen (Shen et al. 1998a,b, 2011) and LS220 (Lattimer & Swesty 1991), and found that the choice of the EOS mainly affects the localisation and duration of the convection but not the value of the Brunt-Väisälä frequency in the stably stratified region. Second, the main background azimuthal field is B_ϕ, which is associated with the Alfvén frequency:

$$\omega_\mathrm{A} \equiv \frac{B_\phi}{\sqrt{4\pi\rho r^2}} \simeq 11.6\left(\frac{B_\phi}{10^{15}\,\mathrm{G}}\right)\mathrm{s}^{-1}, \tag{10}$$

for $r = 12\,\mathrm{km}$ and $\rho = 4.1\times10^{14}\,\mathrm{g\,cm}^{-3}$. Finally, the frequencies characterising the PNS are ordered such that

$$N \gg \Omega \gg \omega_\mathrm{A}. \tag{11}$$

The development of the Tayler instability is triggered after reaching the critical strength (Spruit 1999, 2002; Zahn et al. 2007)

$$\begin{aligned} B_\phi > B_{\phi,\mathrm{c}} &\sim \Omega\left(\frac{N}{\Omega}\right)^{1/2}\left(\frac{\eta}{r^2\Omega}\right)^{1/4}\sqrt{4\pi\rho r^2} \\ &\simeq 2.5\times10^{12}\left(\frac{\Omega}{200\pi\,\mathrm{rad\,s}^{-1}}\right)^{1/4}\mathrm{G}, \end{aligned} \tag{12}$$

where $\eta \sim 10^{-4}\,\mathrm{cm}^2\,\mathrm{s}^{-1}$ (Thompson & Duncan 1993) is the magnetic diffusivity. The fastest-growing perturbations are the $m = 1$ modes with an associated rate of (Ma & Fuller 2019)

$$\sigma_\mathrm{TI} \sim \frac{\omega_\mathrm{A}^2}{\Omega} \simeq 0.21\left(\frac{B_\phi}{10^{15}\,\mathrm{G}}\right)^2\left(\frac{\Omega}{200\pi\,\mathrm{rad\,s}^{-1}}\right)^{-1}\mathrm{s}^{-1}. \tag{13}$$

As the PNS interior is strongly stratified, we can determine a maximum radial length scale for the instability

$$l_r \sim \frac{\omega_\mathrm{A}}{N}l_\perp, \tag{14}$$

where the horizontal length scale is approximated by $l_\perp \sim r$.

2.3. Spruit's picture of the dynamo

Spruit (2002) proposes that the energy in the azimuthal large-scale field B_ϕ cascades to small scale, that is the form of the non-linear magnetic energy dissipation is

$$\dot{E}_\mathrm{mag} \sim \gamma_\mathrm{turb}|B_\phi|^2, \tag{15}$$

where γ_turb is the turbulent damping rate. To determine this rate, Spruit (2002) argues that the saturation of the instability occurs when the turbulent velocity field generates a sufficiently large effective turbulent diffusivity to balance the growth rate of the instability, that is

$$\gamma_\mathrm{turb} \sim \frac{\eta_\mathrm{e}}{l_r^2} \sim \sigma_\mathrm{TI}, \tag{16}$$

where η_e is an effective turbulent diffusivity.

The solenoidal character of the perturbed magnetic field implies $B_r/l_r \sim B_\phi/l_\perp$, which leads to

$$B_r \sim \frac{\omega_\mathrm{A}}{N}B_\phi, \tag{17}$$

using the relation between length scales of the instability given by Eq. (14). As the azimuthal magnetic field B_ϕ is generated via the shear of the radial magnetic field B_r, the dynamo is expected to saturate when the shear (Eq. (8)) balances the turbulent damping (Eq. (16)). Thus, the amplitudes of the magnetic field components saturate at

$$B_{\phi,\mathrm{S}}^\mathrm{sat} \sim \sqrt{4\pi\rho r^2}q\frac{\Omega^2}{N}, \tag{18}$$

$$B_{r,\mathrm{S}}^\mathrm{sat} \sim \sqrt{4\pi\rho r^2}q^2\frac{\Omega^4}{N^3}. \tag{19}$$

This description of the dynamo mechanism has been criticised for two reasons: First of all, if the large-scale component of B_ϕ remains constant on larger length scales than l_r, the displacements produced by the instability are not expected to mix the large-scale field lines to damp B_ϕ through reconnection. Therefore, the damping rate estimated in Eq. (16) is overestimated for the large-scale components of the azimuthal field B_ϕ (see Fuller et al. 2019). Secondly, as $m = 1$ modes are dominant, the radial magnetic field B_r produced by the instability is non-axisymmetric, and therefore its shear generates a mostly non-axisymmetric azimuthal field B_ϕ. Hence, the axisymmetric component of the fields B_r and B_ϕ may not be related by Eq. (17) (see Zahn et al. 2007).

2.4. A revised model of the dynamo

This section presents a description of the dynamo that completes the model proposed by Fuller et al. (2019) in the sense that we consider the time evolution of the magnetic field. A clear distinction is now made between the 'axisymmetric' components B_ϕ, B_r, and the 'non-axisymmetric' perturbed components $\delta B_\perp$, δB_r, which become the ones connected by the solenoidal condition

$$\delta B_r \sim \frac{\omega_\mathrm{A}}{N}\delta B_\perp. \tag{20}$$

To overcome the previously raised difficulties, Fuller et al. (2019) argue that the energy in the perturbed field $\boldsymbol{\delta B}$ dissipates to small scales and find that the damping rate is

$$\gamma_\mathrm{cas} \sim \frac{\delta v_\mathrm{A}}{r}, \tag{21}$$

where $\delta v_\mathrm{A} \equiv \delta B_\perp/\sqrt{4\pi\rho}$ is the perturbed Alfvén velocity. Thus, equating the instability growth rate (Eq. (13)) and the damping rate (Eq. (21)) gives the saturation strength of the perturbed field $\delta B_\perp$ for a given strength of azimuthal field B_ϕ,

$$\delta B_\perp \sim \frac{\omega_\mathrm{A}}{\Omega}B_\phi. \tag{22}$$

When the instability is saturated, the non-linear magnetic energy dissipation is then

$$\dot{E}_{\rm mag} \sim \gamma_{\rm cas} |\boldsymbol{\delta B}|^2 \sim \frac{\delta v_{\rm A}}{r} |\delta B_\perp|^2 \,. \tag{23}$$

As the azimuthal field B_ϕ is the dominant magnetic component, $\dot{E}_{\rm mag} \sim B_\phi \partial_t B_\phi$. Hence, a damping rate can be defined for the axisymmetric components B_ϕ and B_r:

$$\gamma_{\rm diss} \equiv \frac{\dot{E}_{\rm mag}}{B_\phi^2}. \tag{24}$$

As the previous expression of the magnetic energy (Eq. (23)) is only valid when the instability saturates, we use the expression

$$\dot{E}_{\rm mag} \sim \frac{\omega_{\rm A}^2}{\Omega} |\delta B_\perp|^2, \tag{25}$$

which is valid in both the saturated and non-saturated states. Therefore, the damping rate defined in Eq. (24) becomes

$$\gamma_{\rm diss} \sim \frac{\omega_{\rm A}^2}{\Omega} \left(\frac{\delta B_\perp}{B_\phi} \right)^2 . \tag{26}$$

To close the dynamo loop, the Tayler instability must generate the axisymmetric radial magnetic field B_r (α-effect), which will be sheared again (Ω-effect). In the framework of the mean field theory, the induction equation reads

$$\partial_t \langle \boldsymbol{B} \rangle = \nabla \times (\langle \boldsymbol{v} \rangle \times \langle \boldsymbol{B} \rangle + \boldsymbol{E}) - \eta \Delta \langle \boldsymbol{B} \rangle, \tag{27}$$

in which we ignore the resistive term. Considering the average symbol $\langle \cdot \rangle$ as an azimuthal average, we note $\langle \boldsymbol{B} \rangle = \boldsymbol{B}$ in order to remain consistent with our notation of the axisymmetric magnetic field. The electromotive force $\boldsymbol{E} \equiv \langle \delta \boldsymbol{v} \wedge \delta \boldsymbol{B} \rangle$ is the important non-linear quantity responsible for the generation of the axisymmetric radial field B_r. In spherical coordinates, the radial component of Eq. (27) is

$$\partial_t B_r = \frac{1}{r \sin\theta} \left[\partial_\theta (\sin\theta \, E_\phi) - \partial_\phi E_\theta \right]. \tag{28}$$

As B_r is axisymmetric, E_θ can be ignored. By definition, the azimuthal component of electromotive force is

$$E_\phi = \delta v_r \delta B_\theta - \delta v_\theta \delta B_r. \tag{29}$$

Supposing an incompressible perturbed velocity field and using Eq. (20), we write

$$\frac{\delta v_r}{\delta v_\perp} \sim \frac{\delta B_r}{\delta B_\perp} \sim \frac{\omega_{\rm A}}{N}, \tag{30}$$

and so the azimuthal electromotive force reads

$$E_\phi \sim \delta v_\theta \delta B_r \sim \delta v_r \delta B_\theta \sim \delta v_r \delta B_\perp, \tag{31}$$

where we assume that the two terms on the right-hand side of Eq. (29) do not cancel. The production of the radial field B_r can be approximated by

$$\partial_t B_r \sim \frac{E_\phi}{r} \sim \frac{\delta v_r \delta B_\perp}{r}. \tag{32}$$

We must note that this expression differs from Eq. (29) in Fuller et al. (2019), which appears to contain a typo. As in Fuller et al. (2019) and Ma & Fuller (2019), we expect magnetostrophic balance $\delta v_\perp \sim \delta v_{\rm A} \omega_{\rm A} / \Omega$, which leads to

$$\delta v_r \sim \frac{\omega_{\rm A}^2}{N\Omega} \delta v_{\rm A}. \tag{33}$$

Thus,

$$\partial_t B_r \sim \frac{E_\phi}{r} \sim \frac{\omega_{\rm A}^2}{N\Omega} \frac{\delta B_\perp^2}{\sqrt{4\pi\rho r^2}}, \tag{34}$$

and we can define a growth rate for B_r

$$\sigma_{\rm NL} \equiv \frac{1}{\sqrt{4\pi\rho r^2}} \frac{\omega_{\rm A}^2}{N\Omega} \frac{\delta B_\perp^2}{B_r}. \tag{35}$$

The radial field B_r will saturate when its non-linear growth rate (Eq. (35)) is balanced by the turbulent dissipation (Eq. (26)). This way, we find the relation between the axisymmetric fields

$$B_r \sim \frac{\omega_{\rm A}}{N} B_\phi, \tag{36}$$

using Eq. (22). We note that this relation is similar to Eq. (17) from Spruit (2002), which was derived for the non-axisymmetric components only. Fuller et al. (2019) also established the same relation arguing that the Tayler instability cannot operate when the magnetic tension forces become larger than the magnetic pressure forces leading to the instability.

The azimuthal magnetic field saturates when the shear rate (Eq. (8)) balances the dissipation rate (Eq. (26)). Thus, using the relations between the magnetic field components (Eqs. (22) and (36)), we find the magnetic field strengths in the saturated regime derived in Fuller et al. (2019):

$$B_{\phi,\rm F}^{\rm sat} \sim \sqrt{4\pi\rho r^2}\Omega \left(\frac{q\Omega}{N} \right)^{1/3}, \tag{37}$$

$$\delta B_{\perp,\rm F}^{\rm sat} \sim \sqrt{4\pi\rho r^2}\Omega \left(\frac{q\Omega}{N} \right)^{2/3}, \tag{38}$$

$$B_{r,\rm F}^{\rm sat} \sim \sqrt{4\pi\rho r^2}\Omega \left(\frac{q^2\Omega^5}{N^5} \right)^{1/3}. \tag{39}$$

Finally, the angular momentum is redistributed in the PNS through Maxwell stresses associated with an effective angular momentum diffusivity (Spruit 2002; Fuller et al. 2019):

$$\nu_{\rm AM} = \frac{B_r B_\phi}{4\pi\rho q\Omega}, \tag{40}$$

which affects the shear parameter at the rate

$$\gamma_{\rm AM} \equiv \frac{\nu_{\rm AM}}{r^2}. \tag{41}$$

2.5. Governing evolution equations

Now that the main equations involved in our scenario have been brought out, we can write the evolution equations for the rotation properties and the magnetic field. The evolution of PNS angular rotation frequency is driven by the fallback accretion rate (Eq. (3)) as described by Eq. (4). Hence,

$$\dot{\Omega} = \frac{2}{3} \Delta\Omega \frac{t_0^{2/3}}{(t+t_0)^{5/3}}, \tag{42}$$

where $\Delta\Omega = \Omega_{\rm fin} - \Omega_{\rm init} = M_{\rm acc} j_{\rm kep}/I$. As previously mentioned, the shear rate is also expected to decrease due to angular momentum transport (Eq. (41)) such that

$$\dot{q} = \frac{\dot{\Omega}}{\Omega}(1-q) - \gamma_{\rm AM} q = \frac{2}{3}\frac{\Delta\Omega}{\Omega}\frac{t_0^{2/3}}{(t+t_0)^{5/3}} - \frac{B_r B_\phi}{4\pi\rho\Omega r^2}. \quad (43)$$

Combining the different growth and damping rates given by Eqs. (8), (13), (21), (26), and (35), we find that the magnetic field evolution is governed by the following equations:

$$\partial_t B_\phi = (\sigma_{\rm shear} - \gamma_{\rm diss})\, B_\phi = q\Omega B_r - \frac{\omega_{\rm A}^2}{\Omega}\frac{\delta B_\perp^2}{B_\phi}, \quad (44)$$

$$\partial_t \delta B_\perp = (\sigma_{\rm TI} - \gamma_{\rm cas})\, \delta B_\perp = \frac{\omega_{\rm A}^2}{\Omega}\delta B_\perp - \frac{\delta v_{\rm A}}{r}\delta B_\perp, \quad (45)$$

$$\partial_t B_r = (\sigma_{\rm NL} - \gamma_{\rm diss})\, B_r = \frac{\omega_{\rm A}^2}{N\Omega}\frac{\delta B_\perp^2}{\sqrt{4\pi\rho r^2}} - \frac{\omega_{\rm A}^2}{\Omega}\left(\frac{\delta B_\perp}{B_\phi}\right)^2 B_r. \quad (46)$$

Equations (42)–(46) are solved for a typical PNS of 5–10 s in age using the odeint function from the Python package SciPy. The PNS mass and radius are $M_{\rm PNS} = 1.5\, M_\odot$ and $r = 12$ km, and so the average density is $\rho = 4.1 \times 10^{14}$ g cm^{-3}. The moment of inertia is estimated using Eq. (12) from Lattimer & Schutz (2005):

$$I = 0.237 M_{\rm PNS} r^2 \left[1 + 4.2\left(\frac{M_{\rm PNS}}{M_\odot}\frac{1\,{\rm km}}{r}\right) + 90\left(\frac{M_{\rm PNS}}{M_\odot}\frac{1\,{\rm km}}{r}\right)^4\right]$$
$$\simeq 1.6 \times 10^{45}\ {\rm g\,cm^2}. \quad (47)$$

The PNS core is assumed to be initially in solid-body rotation (i.e. $q = 0$) and slowly rotating with an angular rotation frequency $\Omega_{\rm init} = 2\pi\,{\rm rad\,s^{-1}}$ (i.e. an initial rotation period $P_{\rm init} \equiv 2\pi/\Omega_{\rm init} = 1$ s). We note that the results of the time integration weakly depend on these parameters as long as $P_{\rm init} \gtrsim 40$ ms. The parameters of the fallback are chosen to be consistent with the simulations of Janka et al. (2022), with a starting time at $t_0 = 7$ s. The initial magnetic field components B_r, B_ϕ, and $\delta B_\perp$ are initialised at a strength of 10^{12} G, which is the typical magnetic field amplitude of regular neutron stars.

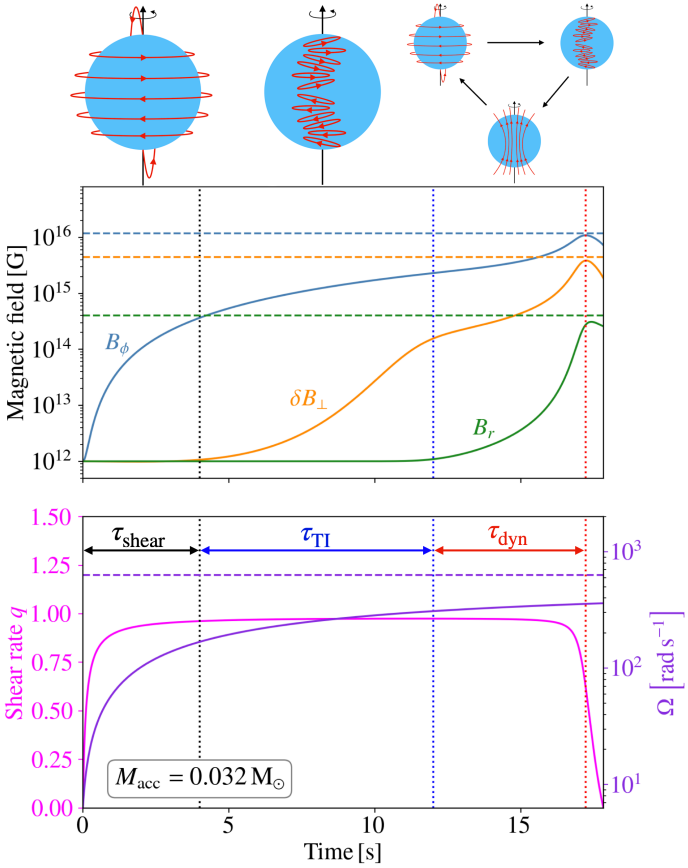

Fig. 2. Time evolution of the different components of the magnetic field (*top*), the dimensionless shear rate, and the angular rotation frequency (*bottom*) for an accreted mass $M_{\rm acc} = 3.2 \times 10^{-2}\, M_\odot$ corresponding to an asymptotic rotation period $P_{\rm fin} = 10$ ms. The different stages of the dynamo process are highlighted by the schematics at the top and their associated timescales by the double arrows. Their ends are illustrated by the dotted vertical lines: winding (black), linear development of the Tayler instability (dark blue), and the whole dynamo loop (red). The horizontal dashed lines (blue, orange, and green) show respectively the saturation intensities $B_{\phi,\rm F}^{\rm sat}$, $\delta B_{\perp,\rm F}^{\rm sat}$, and $B_{r,\rm F}^{\rm sat}$ (Eqs. 37–39) evaluated at the time of saturation. The dashed violet horizontal line represents the asymptotic angular rotation frequency $\Omega_{\rm fin}$.

3. Results

We proceed with a twofold presentation of our model outputs: First we present the time evolution, in which we derive analytical predictions for the timescales of the different phases of the scenario and compare them to the integrated evolution. We then present the saturated regime where we focus on the magnetic field intensities reached via the Tayler-Spruit dynamo and provide an 'upper' limit of PNS rotation period (i.e. a 'lower' limit of fallback mass) to form magnetars.

3.1. Time evolution of the magnetic field

The time series for an asymptotic rotation period $P_{\rm fin} \equiv 2\pi/\Omega_{\rm fin} = 10$ ms displayed in Fig. 2 can be split into several phases, which are illustrated by the schematics at the top of the figure:

(i) B_ϕ is strongly amplified for ∼4 s due to the winding of B_r while the other components stay constant. As the mass-accretion rate is higher in this phase, strong increases in the shear rate and the rotation rate are also noted.

(ii) The Tayler instability develops and amplifies $\delta B_\perp$ for ∼8 s.

(iii) The axisymmetric radial field B_r is generated allowing the dynamo action to occur for ∼5 s. The azimuthal magnetic field saturates at ∼17 s, which corresponds to ∼24 s after the core bounce.

(iv) The angular momentum transport by the magnetic field, which was negligible during the first ∼16 s, becomes significant as the magnetic field saturates. This stage is discussed in Sect. 4.1.

The evolution of the magnetic field is shown until the whole angular momentum is transported, (i.e. when the shear rate reaches $q = 0$) at $t \sim 17.5$ s. Further evolution is not considered because our set of equations does not intend to describe either the relaxation phase of the magnetic field to a stable geometric configuration or the dynamics with very low shear where one would expect the Tayler-Spruit dynamo to stop or to act intermittently (Fuller & Lu 2022).

The different vertical lines in Fig. 3 show that the above phases occur at different times for different accreted masses. To better quantify the dependence on this parameter, we derive analytical estimates of the corresponding characteristic timescales $\tau_{\rm shear}$, $\tau_{\rm TI}$, and $\tau_{\rm dyn}$ (see Fig. 2). First, the shearing phase begins

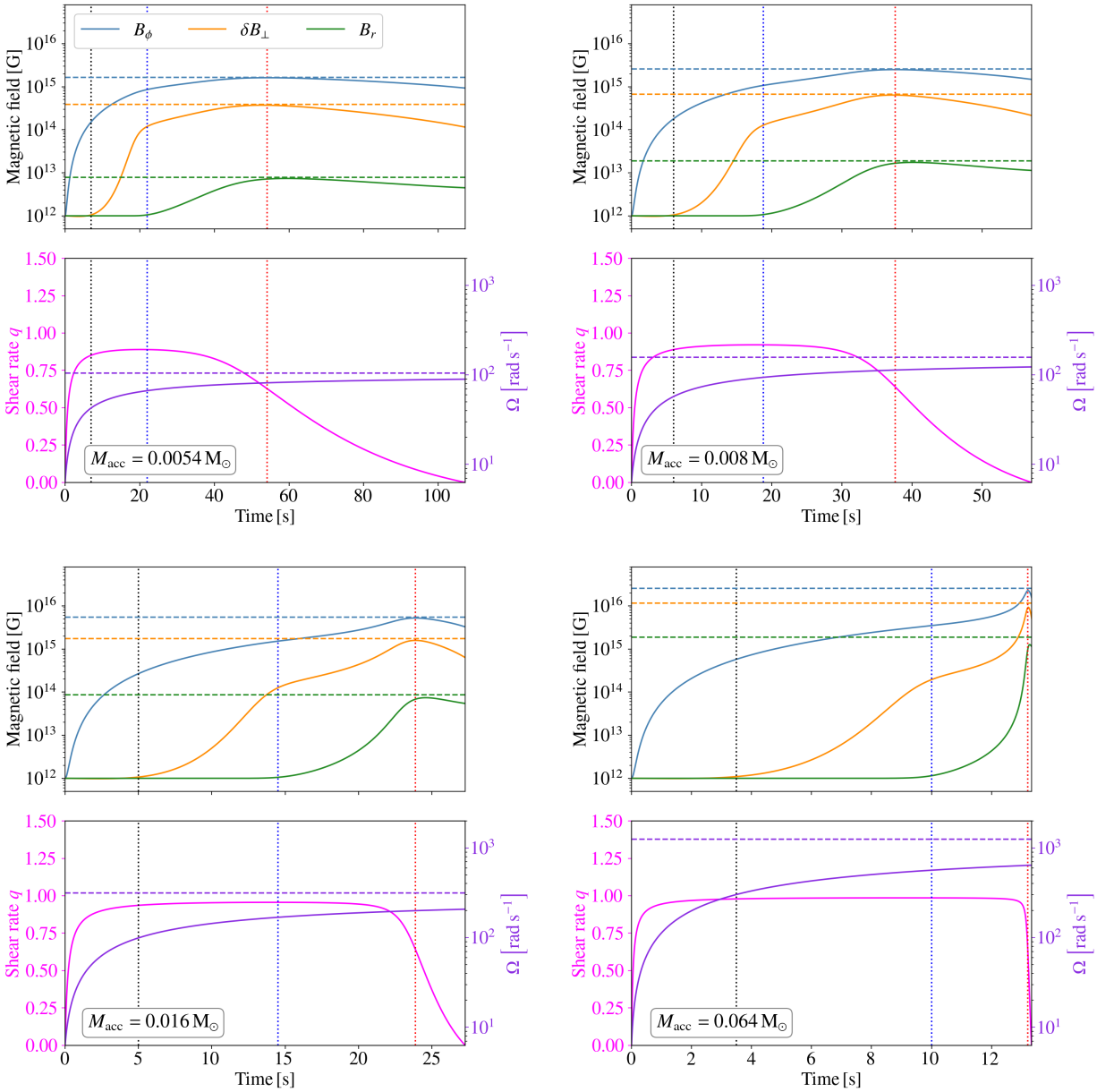

Fig. 3. Same as Fig. 2 but for total accreted masses of $M_{\rm acc} = \{0.54, 0.8, 1.6, 6.4\}\times10^{-2}\,M_\odot$ (corresponding to $P_{\rm fin} = \{60, 40, 20, 5\}$ ms, respectively).

when the fallback matter starts to be accreted on the PNS surface and finishes when the azimuthal magnetic field B_ϕ is strong enough to make the Tayler instability grow as fast as B_ϕ, that is when the growth rate of the instability (Eq. (13)) is equal to the winding rate (Eq. (8)). Thus, the Alfvén frequency associated with the intensity of the azimuthal magnetic field at the end of this phase is

$$\omega_{\rm A} \sim \omega_{\rm A,TI} \equiv \left(q\Omega^2\omega_{r,0}\right)^{1/3}, \tag{48}$$

where $\omega_{r,0} \equiv B_r(t=0)/\sqrt{4\pi\rho r^2}$. Therefore, a characteristic timescale for the shearing stage can be defined as the inverse of the winding growth rate (Eq. (13)) evaluated at $\omega_{\rm A} = \omega_{\rm A,TI}$:

$$\tau_{\rm shear} \equiv \sigma_{\rm shear}^{-1} \sim \frac{\omega_{\rm A,TI}}{q\Omega\omega_{r,0}} = \left(q^2\omega_{r,0}^2\Omega\right)^{-1/3}. \tag{49}$$

Second, as the azimuthal field becomes unstable, the Tayler instability grows exponentially until the perturbed field reaches the saturation intensity of Eq. (22). The perturbed field at saturation can be approximated by

$$\delta B_\perp(t=t_{\rm sat}) \sim \delta B_\perp(t=\tau_{\rm shear})\exp\left[\sigma_{\rm TI}(t_{\rm sat}-\tau_{\rm shear})\right], \tag{50}$$

and so a characteristic timescale for this stage can be defined as

$$\tau_{\rm TI} \equiv t_{\rm sat} - \tau_{\rm shear} \sim \sigma_{\rm TI}^{-1}\ln\left[\frac{\delta B_\perp(t=t_{\rm sat})}{\delta B_\perp(t=\tau_{\rm shear})}\right]. \tag{51}$$

Using Eq. (22), we have

$$\delta B_\perp(t=t_{\rm sat}) \sim \frac{\omega_{\rm A}(t=t_{\rm sat})}{\Omega} B_\phi(t=t_{\rm sat}). \tag{52}$$

In order to obtain a simple estimate, we make the rough approximations that $\delta B_\perp(t=\tau_{\rm shear}) \sim \delta B_\perp(t=0)$ and $B_\phi(t=\tau_{\rm shear}) \sim B_\phi(t=t_{\rm sat})$, which leads to

$$\tau_{\rm TI} \sim \frac{\Omega}{\omega_{\rm A,TI}^2}\ln\left(\frac{\omega_{\rm A,TI}^2 r}{\Omega\delta v_{\rm A,0}}\right), \tag{53}$$

where $\delta v_{\rm A,0} \equiv \delta v_{\rm A}(t = 0)$.

Third, when the perturbed field reaches a sufficient amplitude, the axisymmetric radial field is amplified through nonlinear induction, thus closing the dynamo loop. This phase ends when the magnetic field saturates at the intensities given by Eqs. (37)–(39). Likewise, we estimate the critical strength of the azimuthal field $B_{\phi,\rm dyn}$ above which the dynamo loop is triggered by equating the growth rate of the radial field B_r (Eq. (35)) and the winding rate (Eq. (8)). We obtain the Alfvén frequency associated with $B_{\phi,\rm dyn}$

$$\omega_{\rm A,dyn} \equiv \left(qN\Omega^4\omega_{r,0}^2\right)^{1/7}, \tag{54}$$

making use of Eq. (22). We define the dynamo characteristic timescale as

$$\tau_{\rm dyn} \equiv \left(\frac{B_\phi}{\partial_t^2 B_\phi}\right)^{1/2}. \tag{55}$$

The time derivative of the radial magnetic field is

$$\partial_t B_r \sim \frac{\omega_{\rm A}^2 \delta v_{\rm A}}{N\Omega r}\delta B_\perp \sim \frac{\omega_{\rm A}^3 \delta v_{\rm A}}{N\Omega^2 r} B_\phi \sim \frac{\omega_{\rm A}^5}{N\Omega^3} B_\phi, \tag{56}$$

using Eq. (22). Therefore,

$$\partial_t^2 B_\phi \sim q\Omega\partial_t B_r \sim \frac{q\omega_{\rm A}^5}{N\Omega^2} B_\phi, \tag{57}$$

where q and Ω are assumed to be constant during this phase. Thus, the dynamo characteristic timescale can be approximated as

$$\tau_{\rm dyn} \equiv \left(\frac{B_\phi}{\partial_t^2 B_\phi}\right)^{1/2} \sim \frac{\Omega}{\omega_{\rm A,dyn}^2}\left(\frac{N}{q\omega_{\rm A,dyn}}\right)^{1/2}. \tag{58}$$

For the case $P_{\rm fin} = 10$ ms, we have $\tau_{\rm shear} \simeq 2.3$ s, $\tau_{\rm TI} \simeq 8.5$ s, and $\tau_{\rm dyn} \simeq 5$ s, which are similar to the timescales illustrated by the dotted vertical lines in Fig. 2. The same observation can be made for $P_{\rm fin} \leq 30$ ms in Fig. 3. However, for $P_{\rm fin} = 40$ ms ($M_{\rm acc} = 0.008\,M_\odot$) and $P_{\rm fin} = 60$ ms ($M_{\rm acc} = 0.0054\,M_\odot$), the dynamo loop phase lasts respectively ~30 s and ~20 s (see Fig. 3), which is longer than the analytical predictions of $\tau_{\rm dyn} \simeq 11$ s and $\tau_{\rm dyn} \simeq 9.2$ s. This is due to the presence of a significant stage that is not included in the expression of $\tau_{\rm dyn}$ where the growth of B_ϕ slows down before saturation.

The three characteristic timescales defined by Eqs. (49), (53), and (58) are plotted as a function of the fallback mass in Fig. 4 in addition to the characteristic timescale for the whole amplification process, which is defined as

$$\tau_{\rm tot} \equiv \tau_{\rm shear} + \tau_{\rm TI} + \tau_{\rm dyn}. \tag{59}$$

The vertical red dashed line represents the lower limit of fallback mass to form typical magnetars, which is estimated in Sect. 3.2 (corresponding to an asymptotic rotation period $P_{\rm fin} \lesssim 30$ ms). In the regime relevant to magnetar formation, the analytical and numerical estimates of the duration of the whole amplification process are in reasonable agreement, namely $\tau_{\rm tot} \lesssim 30$ s. In this regime, the phase which takes more time is the development of the Tayler instability. For $P_{\rm fin} \gtrsim 30$ ms, the comparison between the time at which B_ϕ saturates and $\tau_{\rm tot}$ shows a significant difference, which is the consequence of the discrepancy noted above between the analytical estimate and numerical solution for $\tau_{\rm dyn}$.

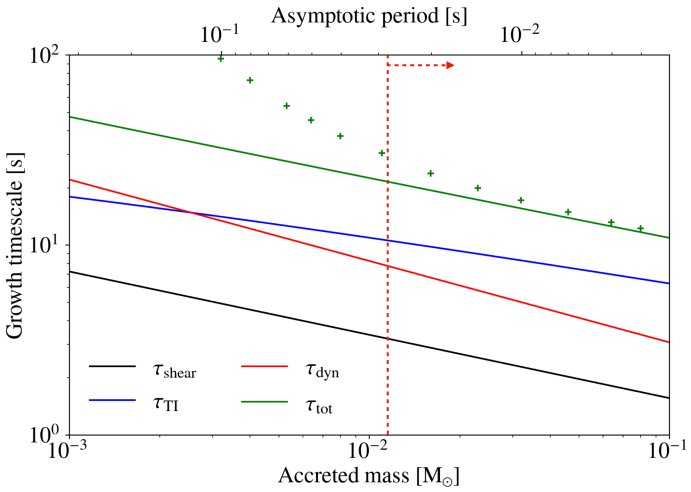

Fig. 4. Different characteristic timescales as a function of the accreted mass: winding (black), Tayler instability (dark blue), and dynamo (red). The green line represents the sum of the three timescales. The shear rate is set at $q = 1$. The green crosses represent the entire amplification time obtained by integrating Eqs. (37)–(39). The red vertical line shows the lower limit of the accreted mass to form a magnetar with a radial field stronger than $B_{\rm Q} \equiv m_{\rm e}c^2/e\hbar \simeq 4.4 \times 10^{13}$ G using the predictions of Fuller et al. (2019).

3.2. Magnetic field in the saturated regime

We now focus on the maximum magnetic field obtained at the end of the amplification phase. In the following discussion, this saturated magnetic field will be considered as a proxy for the magnetar's magnetic field and its 'radial' component will be considered a proxy for the 'dipolar' component of the magnetic field. A more precise prediction would require a description of the relaxation towards a stable equilibrium, which is left for future studies.

In the top panel of Figs. 2 and 3, we see that the saturation intensities are close to their associated horizontal dashed lines, which illustrate the predictions of Eqs. (37)–(39) for values of the shear rate q and the angular rotation frequency Ω reached at the time of magnetic field saturation. Therefore, these equations can be used to estimate the intensity of the saturated magnetic field. However, the angular frequency at $\tau_{\rm tot}$ is still lower than its asymptotic value represented by the violet dashed line in the bottom panel. We estimate $\Omega(t = \tau_{\rm tot})$ analytically by integrating Eq. (42)

$$\Omega(t = \tau_{\rm tot}) = \Omega_{\rm fin} - \left(\frac{t_0}{\tau_{\rm tot} + t_0}\right)^{2/3}(\Omega_{\rm fin} - \Omega_{\rm init}). \tag{60}$$

Assuming that the timescales for the dynamo are roughly the same for the two models, that is, that of Fuller et al. (2019) and that of Spruit (2002), we also evaluate the expressions of the saturated magnetic field derived by Spruit (2002; Eqs. (18) and (19)) at $\Omega(t = \tau_{\rm tot})$.

We see in Fig. 5 that our analytical estimates of the saturated fields (solid lines) are close to the numerical values at the peak of the solutions of Eqs. (44)–(46) (plus symbols). The small difference that appears for shorter rotation periods is due to the angular momentum transport, as discussed in see Sect. 4.1.

Using the maximum magnetic field as a proxy for the magnetar's magnetic field may lead to an overestimation because a fraction of the magnetic energy can be dissipated during the relaxation to a stable magnetic configuration. Although our

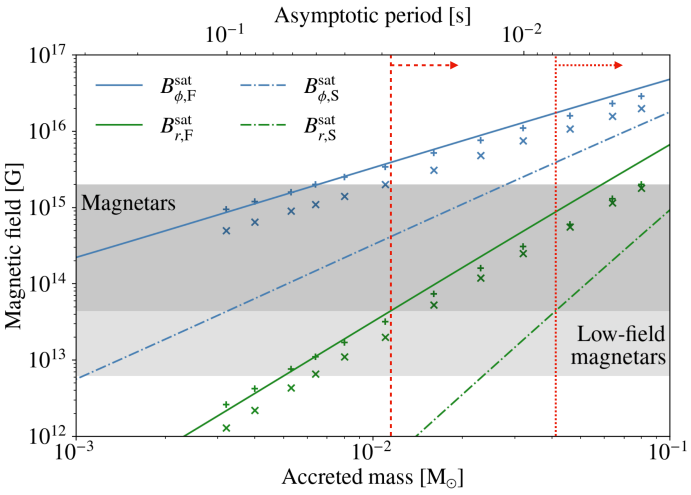

Fig. 5. Predicted intensities for the saturated components of the magnetic field as a function of the accreted mass using the formalisms of Fuller et al. (2019; Eqs. (37)–(39); solid lines) and Spruit (2002; Eqs. (18)–(19); dash-dot lines). The shear rate is set at $q = 1$. These intensities are compared to the magnetic field reached at maximum intensity (blue and green plus signs) and at $q = 0$ (blue and green cross signs) by integrating Eqs. (42)–(46) for several fallback masses. Grey areas represent the estimated range of the dipolar magnetic field strength from regularly observed magnetars (dark grey) and from the three detected low-field Galactic magnetars (light grey). The vertical lines show the lower limit on the fallback mass (upper limit on the rotation period) needed to form a magnetar with a radial field stronger than $B_{\rm Q} \simeq 4.4 \times 10^{13}$ G for the prediction of Fuller et al. (2019; dashed red) and Spruit (2002; dotted red).

model is unable to describe this relaxation process, we can get an idea of the robustness of our proxy by comparing to the magnetic field intensity at the time when $q = 0$. Figure 5 shows that this other proxy (cross signs) is smaller by between ∼10% and ∼50% but follows the same trends as the maximum magnetic field. Such a moderate difference would not change our main conclusions and suggests that the maximum magnetic field is a meaningful proxy for the final magnetic field.

In Fig. 5, the observed range of dipolar magnetic field for magnetars is fixed between the quantum electron critical field $B_{\rm Q} \equiv m_{\rm e}c^2/e\hbar \simeq 4.4 \times 10^{13}$ G and $B_{\rm dip} \sim 2 \times 10^{15}$ G, the dipole field of the 'most magnetised' magnetar SGR 1806-20 (Olausen & Kaspi 2014). We find that the radial magnetic fields $B^{\rm sat}_{r,\rm F}$ and $B^{\rm sat}_{r,\rm S}$ fall in this range for accreted masses $M_{\rm acc} \gtrsim 1.1 \times 10^{-2}\, M_\odot$ and $M_{\rm acc} \gtrsim 4 \times 10^{-2}\, M_\odot$ (i.e. asymptotic rotation periods $P_{\rm fin} \lesssim 28$ ms and $P_{\rm fin} \lesssim 8$ ms), respectively. This confirms that magnetar-like magnetic fields can be formed over a wide range of accreted masses. The analytical predictions also show that, in the regime relevant for magnetar formation, the azimuthal component $B_\phi \gtrsim 4 \times 10^{15}$ G for both saturation mechanisms, which is significantly stronger than the radial component.

For lower accreted masses spinning-up the PNS to periods ranging from 28 to 64 ms (between 8 and 14 ms for the predictions of Spruit 2002), our scenario may produce radial magnetic fields B_r as strong as the dipolar fields diagnosed in low-field magnetars (Rea et al. 2010, 2012, 2014). Moreover, the strength of the associated azimuthal field is $B_\phi \sim (1-3) \times 10^{15}$ G, which can be related to the non-dipolar magnetic field needed to produce the outbursts and chaotic bursts observed in magnetars (Thompson & Duncan 1995). This azimuthal magnetic field may also be the source of the proton cyclotron absorption lines observed in two low-field magnetars by Tiengo et al. (2013) and Rodríguez Castillo et al. (2016). Thus, our model provides a possible explanation of low-field magnetar formation. It is an alternative to the initial interpretation proposed by Rea et al. (2010), which invokes $\gtrsim$1 Myr 'old' (or 'worn-out') magnetars whose initial strong dipolar field of ∼few $\times 10^{14}$ G has decayed due to Ohmic and Hall processes. This diffusion could be enhanced by the presence of a strong initial toroidal field $\gtrsim 10^{16}$ G (Turolla et al. 2011).

As Eqs. (37)–(39) give orders of magnitude, Fuller et al. (2019) parameterised them with a prefactor denoted α. We used $\alpha \sim 1$ as obtained by Fuller et al. (2019) for evolved stars in the subgiant and red giant branches by calibrating α on asteroseismic measurements. However, Eggenberger et al. (2019) find $\alpha \sim 0.5$ for subgiant stars on the one hand, and $\alpha \sim 1.5$ for red giant stars on the other. Also, Fuller & Lu (2022) argue that $\alpha \sim 0.25$ if intermittent dynamo action is considered in radiative zones with insufficient shear to trigger a sustained dynamo. This smaller prefactor would imply a larger limit of accreted mass of $\sim 2 \times 10^{-2}\, M_\odot$ (i.e. a rotation period of ∼15 ms).

4. Discussion

4.1. Angular momentum transport

In the previous section, we focused on the magnetic field amplification and did not discuss the angular momentum transport due to the Tayler-Spruit dynamo. Our analytical estimate of the saturated magnetic field is based on the assumption that the differential rotation is not erased before the end of the amplification. Indeed, Figs. 2 and 3 show that the angular momentum transport due to Maxwell stresses starts to be significant around the time of magnetic field saturation and that most of the angular momentum transport occurs afterwards. This can be explained by comparing the characteristic timescales of the dynamo loop phase $\tau_{\rm dyn}$ (Eq. (58)) with those of angular momentum transport. These can be estimated at saturation using the expression of $B^{\rm sat}_{\phi,\rm F}$ (Eq. (37)) as

$$\tau_{\rm AM} \equiv \gamma_{\rm AM}^{-1} = \frac{r^2}{\nu_{\rm AM}} \sim \left(\frac{N}{\Omega}\right)^2 \Omega^{-1}, \tag{61}$$

and

$$\tau_{\rm dyn} = \left(\frac{N}{q\omega}\right)^{4/3} \Omega^{-1}. \tag{62}$$

The ratio of these two timescales is

$$\frac{\tau_{\rm dyn}}{\tau_{\rm AM}} \sim \left(\frac{\Omega}{q^2 N}\right)^{2/3} \sim 0.3 \left(\frac{P}{10\,\rm ms}\right)^{-2/3}. \tag{63}$$

For all values of the accreted mass and corresponding rotation period considered in this paper, the angular momentum transport is therefore longer than the dynamo timescale. This explains why most of the angular momentum takes place after the dynamo saturation and justifies a posteriori our analytical estimate of the saturated magnetic field. At fast rotation periods of a few milliseconds, the two timescales are nonetheless close to each other; as a consequence, the angular momentum transport before saturation is not negligible, which explains the moderate discrepancy between our analytical estimate of the saturated magnetic field and the numerical results for short rotation periods (Fig. 5).

On the other hand, angular momentum transport due to the neutrino viscosity can be neglected because its typical timescale is much longer than the evolution timescales considered:

$$\tau_{\rm n} \equiv \frac{r^2}{\nu_{\rm n}} \gtrsim 3\times10^4\,{\rm s}, \tag{64}$$

where the neutrino viscosity $\nu_{\rm n}$ is estimated with the approximate analytical expression of Keil et al. (1996) and Guilet & Müller (2015):

$$\nu_n \sim 3\times10^8\left(\frac{\rho}{10^{14}\,{\rm g\,cm^{-3}}}\right)^{-2}\left(\frac{T}{5\,{\rm MeV}}\right)^2 {\rm cm^2\,s^{-1}}. \tag{65}$$

4.2. Neutrinos

We demonstrate above that angular momentum transport by either the magnetic field or the neutrino viscosity does not significantly impact our results. However, the neutrino flux coming from the accretion is also expected to extract a fraction of the angular momentum of the PNS (Janka et al. 2004; Bollig et al. 2021). To investigate whether it does not jeopardise the model, we use the following reasoning. As fallback is assumed to start several seconds after bounce in our model, one may assume that most of the angular momentum extraction by neutrino emission at these late times originate from fallback accretion rather than PNS cooling. Most of the fallback mass is likely to have a specific angular momentum j_0 which exceeds the Keplerian value at the PNS surface. It will therefore assemble into an accretion disk, settling at a radius $r_{\rm k}$ where $j_{\rm kep}(r_{\rm k}) = j_0$. Its gravitational binding energy $E_{\rm bind}$ will be at most all converted into neutrino radiation, that is per baryon with a rest mass $m_{\rm B}$:

$$\Delta E_\nu \lesssim E_{\rm bind}(r_{\rm k}) \sim \frac{GM_{\rm PNS}m_{\rm B}}{r_{\rm k}}, \tag{66}$$

where we assume that the disk mass is small compared to the PNS mass. The corresponding specific angular momentum loss is

$$\Delta j_\nu \lesssim \frac{\Delta E_\nu}{m_{\rm B}c^2} j_{\rm kep}(r_{\rm k}) \sim \frac{R_{\rm S}}{2r_{\rm k}} j_{\rm kep}(r_{\rm k}), \tag{67}$$

where $R_{\rm S} \equiv 2GM_{\rm PNS}/c^2$ is the PNS Schwarzchild radius. Δj_ν is maximal at the PNS surface (i.e. when $r_{\rm k} = r$), which implies

$$\Delta j_\nu \lesssim 0.185\, j_{\rm kep}(r), \tag{68}$$

for the same parameters of a typical PNS introduced in Sect. 2.5. Therefore, the extraction of angular momentum by neutrino radiation is very inefficient.

4.3. Impact of the viscosity on the Tayler instability

In the reasoning developed above, we do not take into account the effects due to viscous processes, which might be important because they could be much larger than the effects of the resistivity in PNSs. Therefore, here we aim to address the question of their impact on the development of the Tayler instability. To the best of our knowledge, no analytical study of the Tayler instability has included the impact of viscosity. Hence, we use an approximate reasoning similar to that of Spruit (2002), which is based on a comparison of the instability growth timescale with the viscous damping timescale. This provides the following instability criterion:

$$\sigma_{\rm TI}^{-1} \sim \frac{\Omega}{\omega_{\rm A}^2} \lesssim \frac{l_r^2}{\nu}, \tag{69}$$

with ν being the kinematic viscosity. Using the constraint on the radial length scale l_r due to the stratification (Eq. (14)), we infer an instability criterion on the azimuthal magnetic field B_ϕ as a function of the viscosity:

$$B_\phi > B_{\phi,{\rm c}} \sim \Omega\left(\frac{N}{\Omega}\right)^{1/2}\left(\frac{\nu}{r^2\Omega}\right)^{1/4}. \tag{70}$$

This equation is similar to Eq. (12) but with the magnetic diffusivity substituted by the viscosity. To obtain an order of magnitude of this critical value, we must determine a value of the viscosity which is relevant for our scenario. As the fallback accretion occurs seconds to minutes after the PNS formation, the PNS has cooled down to temperatures $\lesssim 1.1\times10^{11}$ K in the core and $\lesssim 5\times10^{10}$ K in the outer region ($\lesssim$10 MeV and $\lesssim$5 MeV, respectively; Hüdepohl 2014). The neutrino mean free path can be approximated by (Thompson & Duncan 1993; Eq. (11)):

$$l_{\rm n} \sim 4\times10^4\left(\frac{\rho}{10^{14}\,{\rm g\,cm^{-3}}}\right)^{-1/3}\left(\frac{T}{5\,{\rm MeV}}\right)^{-3}\left(\frac{f(Y_p)}{1}\right){\rm cm}, \tag{71}$$

where $f(Y_{\rm p})$ is function of the proton fraction close to unity. This length is larger than the maximum radial length scale (Eq. (14)):

$$l_r \sim 4\times10^3\left(\frac{B_\phi}{10^{15}\,{\rm G}}\right){\rm cm}. \tag{72}$$

Therefore, neutrinos do not provide any relevant viscosity at the Tayler instability length scales and we must consider instead a microscopic viscosity such as the shear viscosity due to neutron–neutron scattering (Cutler & Lindblom 1987, Eq. (14)):

$$\nu_s \sim 3\times10^{-2}\left(\frac{\rho}{10^{14}\,{\rm g\,cm^{-3}}}\right)^{5/4}\left(\frac{T}{5\,{\rm MeV}}\right)^{-2}{\rm cm^2\,s^{-1}}. \tag{73}$$

The associated critical magnetic field is therefore

$$B_{\phi,{\rm c}} \simeq 10^{13}\left(\frac{\nu_s}{3\times10^{-2}\,{\rm cm^2\,s^{-1}}}\right)^{1/4}\left(\frac{\Omega}{200\pi\,{\rm rad\,s^{-1}}}\right)^{1/4}{\rm G}, \tag{74}$$

which is four times stronger than the critical magnetic field inferred from the criterion of Spruit (2002) (Eq. (12)). However, this new critical magnetic field is still much weaker than the characteristic azimuthal magnetic field separating the winding phase from the phase in which the Tayler instability develops (when the growth rate of the Tayler instability reaches the winding rate; Eq. (48))

$$B_\phi = \omega_{\rm A,TI}\sqrt{4\pi\rho r^2} \sim 1.3\times10^{15}\left(\frac{\Omega}{200\pi\,{\rm rad\,s^{-1}}}\right)^{2/3}\left(\frac{B_r}{10^{12}\,{\rm G}}\right)^{1/3}. \tag{75}$$

As a consequence, the viscosity is not expected to prevent the Tayler instability from growing and should not have a significant impact on our results. However, we note that our argument is approximate and would need to be upgraded through a linear analysis of the Tayler instability including the viscous processes.

4.4. Superfluidity and superconductivity

A last potential obstacle for our model may emerge from the crust formation and the superfluidity and superconductivity in the core, which occur during the cooling of the PNS. The outer crust is expected to start freezing a few minutes after the PNS

formation and the inner crust forms far later, between 1 and 100 yr after formation (Aguilera et al. 2008). Therefore, no part of the crust is formed during the time interval involved in our scenario.

The potential early appearance of superfluid neutrons or even superconductive protons in the PNS core at temperatures below 10^8–10^{10} K is worth discussing because the MHD approximation would not be sufficiently realistic and a multi-fluid approach would be more relevant (Glampedakis et al. 2011; Sinha & Sedrakian 2015). However, the 1D models of PNS cooling show higher temperatures than 10^{10} K in the PNS even after 15 s (e.g. Pons et al. 1999; Roberts 2012; Hüdepohl 2014; Roberts et al. 2017). Moreover, Gusakov & Kantor (2013) and Glampedakis & Jones (2014) brought forward a critical perturbed magnetic field strength above which superfluidity of neutrons dies out. Therefore, the MHD approximation is still valid for describing the PNS internal dynamics during the first 40 s following the core bounce.

5. Conclusions

In this paper, we propose a new scenario for magnetar formation, in which the Tayler-Spruit dynamo amplifies the large-scale magnetic field of a PNS spun up by SN fallback accretion. We develop a one-zone model describing the evolution of the magnetic field averaged over a PNS subject to fallback accretion. The equations describing the time evolution are solved numerically and compared successfully with analytical estimates of the final magnetic field and of the duration of each stage of the amplification process. Predictions for the different components of the magnetic field are therefore obtained as a function of the accreted mass for the two proposed saturation models of the Tayler-Spruit dynamo (Spruit 2002; Fuller et al. 2019). Our main conclusions can be summarised as follows:

- Radial magnetic fields spanning the full range of the magnetar dipole intensity can be formed for accreted masses compatible with the results of recent SN simulations. Our model predicts the formation of magnetar-like magnetic fields for accreted masses $M_{\rm acc} \gtrsim 1.1 \times 10^{-2}\,M_\odot$ for the saturation model of Fuller et al. (2019) and $M_{\rm acc} \gtrsim 4 \times 10^{-2}\,M_\odot$ for the saturation model of Spruit (2002). This corresponds to neutron star final rotation periods $P_{\rm fin} \lesssim 28$ ms and $P_{\rm fin} \lesssim 8$ ms, respectively.
- The azimuthal component of the magnetic field is predicted to be in the range 10^{15}–10^{16} G, which is stronger than the radial component by a factor of 10–100.
- In the regime relevant for magnetar formation, the magnetic field amplification lasts between 15 and 30 s. On such a timescale, the MHD equations assumed in the description of the Tayler-Spruit dynamo are expected to be valid. Furthermore, we have not identified any other process capable of interfering with the Tayler-Spruit dynamo by transporting angular momentum on a comparable or shorter timescale.

Our results therefore predict that magnetars can indeed be formed in our new scenario. Magnetar formation is possible at sufficiently long rotation periods to be compatible with the lower limit of 5 ms inferred from regular SN remnants associated with magnetars. With the saturation model of Fuller et al. (2019), the full range of magnetar fields can be obtained within this constraint, even those that exhibit a strong dipolar magnetic field $B_{\rm dip} \sim 10^{15}$ G. On the other hand, with the saturation model proposed by Spruit (2002), only the lower end of the magnetar fields can be obtained with $P_{\rm fin} < 5$ ms, while dipolar magnetic fields $\gtrsim 2 \times 10^{14}$ G need faster rotation periods.

An important prediction of our scenario is the very intense toroidal magnetic field, which lies between 3×10^{15} and 3×10^{16} G for parameters corresponding to radial magnetic fields in the magnetar range. These values are compatible with the interpretation of the X-ray flux modulations observed in three magnetars as free precession driven by an intense toroidal magnetic field (Makishima et al. 2014, 2016, 2019, 2021).

The intense toroidal magnetic field predicted in our scenario also provides interesting perspectives from which to explain the formation of low-field magnetars. For radial magnetic fields in the range of the dipolar magnetic field deduced for these objects (Rea et al. 2010, 2012, 2013, 2014), our model predicts a toroidal magnetic field intensity of ~ 1–3×10^{15} G. Such non-dipolar magnetic fields are strong enough to be the energy source of the magnetar-like emission from these objects and to explain the variable absorption lines interpreted as proton cyclotron lines (Tiengo et al. 2013; Rodríguez Castillo et al. 2016). We therefore suggest that some of the low-field magnetars may be born with low dipolar magnetic fields, rather than evolve to this state as assumed in the 'worn-out' magnetar scenario.

A question arising from our study is the location of the magnetic field in the PNS, which cannot be captured by our one-zone model. As the shear due to fallback accretion is expected to be strongest in the outer region of the PNS, one may expect the magnetic field to be preferentially located in these outer layers. Such a concentration of the magnetic field near the surface would have interesting consequences for its long-term evolution because the magnetic field may be confined in the crust without significant magnetic flux threading the superconductive core. The long-term evolution of such a crust-confined magnetic field configuration has been thoroughly investigated by numerical simulations (e.g. Viganò 2013; Gourgouliatos et al. 2016; Pons & Viganò 2019). By contrast, if the magnetic field is also present in deeper regions, its evolution in the superconductive core and the transition layer with the crust must be taken into account. A few papers studied this evolution in numerical simulations (e.g. Henriksson & Wasserman 2013; Lander 2013; Ciolfi & Rezzolla 2013) but these lead to a slower magnetic field evolution that is incompatible with magnetar observations (Elfritz et al. 2016). These results would favour initial crust-confined magnetic fields but need to be confirmed in more realistic 3D simulations of the magneto-thermal evolution in the whole neutron star. We also note that the localisation of the magnetic field in our magnetar formation scenario should be studied in more detail. On the one hand, the stratification increases by a factor of ~2.5 close to the PNS surface, which might weaken the magnetic field and confine it closer to the surface. On the other hand, the shear can be expected to become significant in the bulk of the PNS after angular momentum has been partly redistributed by the Tayler-Spruit dynamo. Some of the magnetic field may also be transported to deeper regions via the Tayler instability or during the relaxation to a stable equilibrium.

Another relevant question is the geometry of the magnetic field amplified by the Tayler-Spruit dynamo. One should keep in mind that our comparison to magnetars relies on the assumption that the generated radial field B_r is mostly dipolar. Although the real geometry of the poloidal magnetic field generated by the Tayler-Spruit dynamo is not known, it is likely to be partly non-dipolar, meaning that the large-scale dipolar magnetic field is a fraction of the radial field B_r. Therefore, corresponding predictions should be refined by studying dedicated multi-dimensional models. In Petitdemange et al. (2022), a dynamo similar to the Tayler-Spruit dynamo has been found through numerical simulations in a configuration where the

surface rotates slower than the core, which is therefore different to the case of spun-up PNS. Moreover, the observed magnetars are cooled-down neutron stars with a stable configuration of magnetic field. Hence, the study of the magnetic field relaxation from a turbulent saturated state to a stable configuration is important to estimate a more realistic intensity of the dipolar poloidal field. Thus, numerical simulations will be essential to further study of the evolution of the magnetic field geometry in our framework.

A salient feature of our fallback scenario is that it decouples magnetar formation from rapid progenitor rotation and from strong magnetisation of the pre-collapse stars. Rapid progenitor rotation is necessary for magnetar formation by the convective dynamo, which requires initial NS spin periods of $\lesssim$10 ms (Raynaud et al. 2022), and by the magnetorotational instability (Reboul-Salze et al. 2021a,b). Strong magnetisation of the pre-collapse star on the other hand is a crucial aspect in the fossil field scenario or the stellar merger scenario (Schneider et al. 2019). Instead of requiring fast rotation or strong magnetic field in the progenitor core, our scenario predicts magnetar formation when fallback deposits a sufficient amount of angular momentum on the PNS surface. With the angular momentum of the mass accreted by the NS being limited by the Keplerian value, magnetars are formed for accreted masses of more than $\sim 1.1 \times 10^{-2}\,M_\odot$ (case of Fuller et al. 2019) and $\sim 4 \times 10^{-2}\,M_\odot$ (case of Spruit 2002) in our scenario. The fallback mass should be several times larger than the accreted mass, because angular momentum loss must be expected to lead to mass loss during the accretion process. Therefore, fallback masses of more than a few $10^{-2}\,M_\odot$ to $10^{-1}\,M_\odot$ seem to be needed. Based on 1D models of neutrino-driven core-collapse SN explosions, this indicates a preference for single stars with zero-age-main-sequence (ZAMS) masses above about $\sim 18\,M_\odot$ (Sukhbold et al. 2016) and helium stars (hydrogen-stripped stars in binaries) with ZAMS masses above 30–40 $M_\odot$ (depending on details of the mass-loss evolution); although the compactness differences between the single-star models of Sukhbold & Woosley (2014) compared to those of Sukhbold et al. (2018) as well as 3D explosion effects (which increase the fallback mass; Janka et al. 2022) may shift these ZAMS masses to lower values. This would be consistent with the observations constraining magnetar progenitors to masses higher than 30 $M_\odot$ (Gaensler et al. 2005; Bibby et al. 2008; Clark et al. 2008) and also with the case of the magnetar SGR1900+14, whose progenitor mass was estimated to be $17 \pm 2\,M_\odot$ (Davies et al. 2009).

While our model avoids the uncertainty of the progenitor core rotation and magnetic field, it implies coping with the uncertainties on the fallback process. A precise modelling of the fallback depends on such challenging questions as how a long-lasting post-explosion phase where downflows to the PNS coexist with outflows of neutrino-heated matter transitions into the fallback accretion as discussed by Janka et al. (2022); the complex dynamical processes that determine the fraction of fallback matter that gets accreted by the PNS from a fallback disk; and the efficiency of the accretion to spin-up the PNS. Our scenario should therefore be explored in more depth by more realistic fallback models.

Following its saturation, the PNS magnetic field may interact with the newly formed disk of fallback matter and is strong enough to influence the fallback accretion mechanism. We did not model this interaction because our study was focused on the phase of magnetic field amplification. Nevertheless, this could strongly influence the rotation of the newly born magnetar. The evolution of the PNS-fallback disk system depends on three characteristic radii (Metzger et al. 2018; Beniamini et al. 2020; Lin et al. 2020; Ronchi et al. 2022): (i) the magnetospheric radius r_m, which is the radius at which the matter is blocked by the magnetic barrier, (ii) the corotation radius r_c where the matter has the same rotation frequency as the PNS, and (iii) the light cylinder radius r_lc, which is the ratio of light speed to the PNS rotation frequency. The strong magnetic field repels the magnetosphere behind the corotation radius (i.e. $r_\mathrm{c} < r_\mathrm{m}$) which stops the accretion and so the PNS spin-up. If the fallback accretion rate of the disk is large enough, the inner part of the disk penetrates the light cylinder (i.e. $r_\mathrm{lc} > r_\mathrm{m}$) and opens up a part of the magnetic field lines. The PNS-fallback disk system enters the so-called propeller regime and the PNS angular momentum is transported towards the disk via the magnetic dipole torque. This mechanism is thought to extract the PNS angular momentum very efficiently; for instance Beniamini et al. (2020) even predict magnetars spun down to rotation periods of $\sim 10^6$ s after $\sim 10^3$ yr. For this reason, this scenario is often invoked to explain the ultra-long-period magnetars such as 1E 1613 (e.g. De Luca et al. 2006; Li 2007; Rea et al. 2016) or the recently observed GLEAM-X J162759.5-523504.3 (Ronchi et al. 2022), which have respective rotation periods of $\sim 2.4 \times 10^4$ s and $\sim 1.1 \times 10^3$ s. It would be interesting to include such a spin-down model in our magnetar formation scenario in order to obtain a prediction of the rotation period at later times.

Finally, the PNS-fallback disk system has also been invoked to explain the light curve of luminous and extreme SNe of types Ib/c (e.g. Dexter & Kasen 2013; Metzger et al. 2018; Lin et al. 2021). We may also expect our scenario to produce these types of explosions depending on the amount of accreted mass during the dynamo process. First, PNSs that have accreted ~ 2–$3 \times 10^{-2}\,M_\odot$ of fallback matter before the magnetic field saturation have rotation periods of around 10–20 ms, which are too slow to produce extreme explosions. According to our scenario, their typical magnetic field is of 1–5×10^{14} G, which would lead to regular luminous SNe Ib/c. Their light curve would be dominated by the PNS spin-down luminosity instead of the ^{56}Ni decay luminosity (Ertl et al. 2020; Afsariardchi et al. 2021). Second, for fallback masses spinning up the PNSs to millisecond rotation periods, the magnetic field saturates a few 10 s after the core bounce at $B_r \gtrsim 5 \times 10^{14}$ G. The rotational energy can be kept for later times and be slowly extracted to irradiate its environment, which might lead to superluminous SNe I (Woosley 2010; Kasen & Bildsten 2010; Bersten et al. 2016; Margalit et al. 2018; Lin et al. 2020, 2021). Finally, to produce extreme explosions such as hypernovae, which have approximately ten times larger kinetic energies and much higher ^{56}Ni yields than the vast majority of CCSNe, an energy injection within a timescale of $\lesssim$1 s is required (Barnes et al. 2018) to explain the large masses of ^{56}Ni $\gtrsim 0.2\,M_\odot$ inferred from their light curves (e.g. Woosley & Bloom 2006; Drout et al. 2011; Nomoto et al. 2011). For rotation periods of $\lesssim$1 ms, which correspond to rotational energies of $\gtrsim 3 \times 10^{52}$ erg, our model provides a radial magnetic field of $B_r \gtrsim 2.6 \times 10^{16}$ G, which may be enough to inject the energy quickly through magnetic dipole spin-down only (Suwa & Tominaga 2015). The presence of a propeller regime would enhance the PNS spin-down such that a weaker dipolar magnetic field of $\sim 2 \times 10^{15}$ G would also produce a hypernova (Metzger et al. 2018) but through a propeller-powered explosion. Therefore, our magnetic-field-amplification scenario by PNS accretion or fallback accretion may be of relevance to a wide variety of magnetar-powered phenomena in different types of SN events.

Acknowledgements. We thank the referee Jim Fuller for his thorough reading and relevant comments, which helped improve this paper. This research was supported by the European Research Council through the ERC starting grant MagBURST No. 715368. Hans-Thomas Janka acknowledges support by the Deutsche Forschungsgemeinschaft (DFG, German Research Foundation) through Sonderforschungsbereich (Collaborative Research Centre) SFB-1258 'Neutrinos and Dark Matter in Astro- and Particle Physics (NDM)' and under Germany's Excellence Strategy through Cluster of Excellence ORIGINS (EXC-2094)–390783311. We are grateful to Thierry Foglizzo and Ludovic Petitdemange for useful discussions.

References

Afsariardchi, N., Drout, M. R., Khatami, D. K., et al. 2021, ApJ, 918, 89
Aguilera, D. N., Pons, J. A., & Miralles, J. A. 2008, A&A, 486, 255
Barnes, J., Duffell, P. C., Liu, Y., et al. 2018, ApJ, 860, 38
Beniamini, P., Hotokezaka, K., van der Horst, A., & Kouveliotou, C. 2019, MNRAS, 487, 1426
Beniamini, P., Wadiasingh, Z., & Metzger, B. D. 2020, MNRAS, 496, 3390
Bersten, M. C., Benvenuto, O. G., Orellana, M., & Nomoto, K. 2016, ApJ, 817, L8
Bibby, J. L., Crowther, P. A., Furness, J. P., & Clark, J. S. 2008, MNRAS, 386, L23
Bochenek, C. D., Ravi, V., Belov, K. V., et al. 2020, Nature, 587, 59
Bollig, R., Yadav, N., Kresse, D., et al. 2021, ApJ, 915, 28
Bonanno, A., & Guarnieri, F. 2017, Astron. Nachr., 338, 516
Bonanno, A., Guerrero, G., & Del Sordo, F. 2020, Mem. Soc. Astron. Ital., 91, 249
Braithwaite, J., & Spruit, H. C. 2004, Nature, 431, 819
Braithwaite, J., & Spruit, H. C. 2017, R. Soc. Open Sci., 4, 160271
Bugli, M., Guilet, J., Obergaulinger, M., Cerdá-Durán, P., & Aloy, M. A. 2020, MNRAS, 492, 58
Bugli, M., Guilet, J., & Obergaulinger, M. 2021, MNRAS, 507, 443
Burrows, A., Dessart, L., Livne, E., Ott, C. D., & Murphy, J. 2007, ApJ, 664, 416
Chan, C., Müller, B., & Heger, A. 2020, MNRAS, 495, 3751
Chevalier, R. A. 1989, ApJ, 346, 847
CHIME/FRB Collaboration, Andersen, B. C., Bandura, K. M., et al. 2020, Nature, 587, 54
Ciolfi, R., & Rezzolla, L. 2013, MNRAS, 435, L43
Clark, J. S., Muno, M. P., Negueruela, I., et al. 2008, A&A, 477, 147
Coti Zelati, F., Rea, N., Pons, J. A., Campana, S., & Esposito, P. 2018, MNRAS, 474, 961
Coti Zelati, F., Borghese, A., Israel, G. L., et al. 2021, ApJ, 907, L34
Cutler, C., & Lindblom, L. 1987, ApJ, 314, 234
Davies, B., Figer, D. F., Kudritzki, R.-P., et al. 2009, ApJ, 707, 844
De Luca, A., Caraveo, P. A., Mereghetti, S., Tiengo, A., & Bignami, G. F. 2006, Science, 313, 814
Denissenkov, P. A., & Pinsonneault, M. 2007, ApJ, 655, 1157
Dessart, L., Burrows, A., Livne, E., & Ott, C. D. 2008, ApJ, 673, L43
Dessart, L., Hillier, D. J., Waldman, R., Livne, E., & Blondin, S. 2012, MNRAS, 426, L76
Dexter, J., & Kasen, D. 2013, ApJ, 772, 30
Drout, M. R., Soderberg, A. M., Gal-Yam, A., et al. 2011, ApJ, 741, 97
Duncan, R. C., & Thompson, C. 1992, ApJ, 392, L9
Eggenberger, P., den Hartogh, J. W., Buldgen, G., et al. 2019, A&A, 631, L6
Elfritz, J. G., Pons, J. A., Rea, N., Glampedakis, K., & Viganò, D. 2016, MNRAS, 456, 4461
Ertl, T., Woosley, S. E., Sukhbold, T., & Janka, H. T. 2020, ApJ, 890, 51
Evans, W. D., Klebesadel, R. W., Laros, J. G., et al. 1980, ApJ, 237, L7
Ferrario, L., & Wickramasinghe, D. 2006, MNRAS, 367, 1323
Fuller, J., & Lu, W. 2022, MNRAS, 511, 3951
Fuller, J., Piro, A. L., & Jermyn, A. S. 2019, MNRAS, 485, 3661
Gabler, M., Cerdá-Durán, P., Stergioulas, N., Font, J. A., & Müller, E. 2018, MNRAS, 476, 4199
Gaensler, B. M., McClure-Griffiths, N. M., Oey, M. S., et al. 2005, ApJ, 620, L95
Gill, R., & Heyl, J. 2007, MNRAS, 381, 52
Glampedakis, K., & Jones, D. I. 2014, MNRAS, 439, 1522
Glampedakis, K., Andersson, N., & Samuelsson, L. 2011, MNRAS, 410, 805
Gompertz, B., & Fruchter, A. 2017, ApJ, 839, 49
Gompertz, B. P., O'Brien, P. T., & Wynn, G. A. 2014, MNRAS, 438, 240
Gotz, D., Israel, G. L., Mereghetti, S., et al. 2006, ATel, 953, 1
Gourgouliatos, K. N., Wood, T. S., & Hollerbach, R. 2016, Proc. Natl. Acad. Sci., 113, 3944
Guerrero, G., Del Sordo, F., Bonanno, A., & Smolarkiewicz, P. K. 2019, MNRAS, 490, 4281
Guilet, J., & Müller, E. 2015, MNRAS, 450, 2153
Guilet, J., Reboul-Salze, A., Raynaud, R., Bugli, M., & Gallet, B. 2022, MNRAS, 516, 4346
Gusakov, M. E., & Kantor, E. M. 2013, MNRAS, 428, L26
Henriksson, K. T., & Wasserman, I. 2013, MNRAS, 431, 2986
Hu, R.-Y., & Lou, Y.-Q. 2009, MNRAS, 396, 878
Hüdepohl, L. 2014, Ph.D. Thesis, Technical University of Munich, Germany
Hurley, K., Cline, T., Mazets, E., et al. 1999, Nature, 397, 41
Hurley, K., Boggs, S. E., Smith, D. M., et al. 2005, Nature, 434, 1098
Inserra, C., Smartt, S. J., Jerkstrand, A., et al. 2013, ApJ, 770, 128
Israel, G. L., Belloni, T., Stella, L., et al. 2005, ApJ, 628, L53
Janka, H. T. 2004, in IAU Symp., 218, 3
Janka, H.-T., Wongwathanarat, A., & Kramer, M. 2022, ApJ, 926, 9
Jouve, L., Lignières, F., & Gaurat, M. 2020, A&A, 641, A13
Kasen, D., & Bildsten, L. 2010, ApJ, 717, 245
Kaspi, V. M., & Beloborodov, A. M. 2017, ARA&A, 55, 261
Keil, W., Janka, H. T., & Mueller, E. 1996, ApJ, 473, L111
Kouveliotou, C. 1999, Proc. Natl. Acad. Sci., 96, 5351
Kouveliotou, C., Fishman, G. J., Meegan, C. A., et al. 1994, Nature, 368, 125
Kuroda, T., Arcones, A., Takiwaki, T., & Kotake, K. 2020, ApJ, 896, 102
Lander, S. K. 2013, Phys. Rev. Lett., 110, 071101
Lander, S. K. 2021, MNRAS, 507, L36
Lattimer, J. M., & Schutz, B. F. 2005, ApJ, 629, 979
Lattimer, J. M., & Swesty, D. F. 1991, Nucl. Phys. A, 535, 331
Li, X.-D. 2007, ApJ, 666, L81
Lin, W. L., Wang, X. F., Wang, L. J., & Dai, Z. G. 2020, ApJ, 903, L24
Lin, W., Wang, X., Wang, L., & Dai, Z. 2021, ApJ, 914, L2
Lü, H.-J., & Zhang, B. 2014, ApJ, 785, 74
Ma, L., & Fuller, J. 2019, MNRAS, 488, 4338
Makishima, K., Enoto, T., Hiraga, J. S., et al. 2014, Phys. Rev. Lett., 112, 171102
Makishima, K., Enoto, T., Murakami, H., et al. 2016, PASJ, 68, S12
Makishima, K., Murakami, H., Enoto, T., & Nakazawa, K. 2019, PASJ, 71, 15
Makishima, K., Enoto, T., Yoneda, H., & Odaka, H. 2021, MNRAS, 502, 2266
Margalit, B., Metzger, B. D., Thompson, T. A., Nicholl, M., & Sukhbold, T. 2018, MNRAS, 475, 2659
Martin, J., Rea, N., Torres, D. F., & Papitto, A. 2014, MNRAS, 444, 2910
Masada, Y., Takiwaki, T., & Kotake, K. 2022, ApJ, 924, 75
Metzger, B. D., Quataert, E., & Thompson, T. A. 2008, MNRAS, 385, 1455
Metzger, B. D., Giannios, D., Thompson, T. A., Bucciantini, N., & Quataert, E. 2011, MNRAS, 413, 2031
Metzger, B. D., Beniamini, P., & Giannios, D. 2018, ApJ, 857, 95
Mösta, P., Richers, S., Ott, C. D., et al. 2014, ApJ, 785, L29
Nicholl, M., Smartt, S. J., Jerkstrand, A., et al. 2013, Nature, 502, 346
Nomoto, K., Maeda, K., Tanaka, M., & Suzuki, T. 2011, Ap&SS, 336, 129
Obergaulinger, M., & Aloy, M. Á. 2020, MNRAS, 492, 4613
Obergaulinger, M., & Aloy, M. Á. 2021, MNRAS, 503, 4942
Obergaulinger, M., & Aloy, M. Á. 2022, MNRAS, 512, 2489
Obergaulinger, M., Cerdá-Durán, P., Müller, E., & Aloy, M. A. 2009, A&A, 498, 241
Olausen, S. A., & Kaspi, V. M. 2014, ApJS, 212, 6
Petit, V., Wade, G. A., Schneider, F. R. N., et al. 2019, MNRAS, 489, 5669
Petitdemange, L., Marcotte, F., & Gissinger, C. 2022, arXiv e-prints [arXiv:2206.13819]
Pitts, E., & Tayler, R. J. 1985, MNRAS, 216, 139
Pons, J. A., & Viganò, D. 2019, Liv. Rev. Comput. Astrophys., 5, 3
Pons, J. A., Reddy, S., Prakash, M., Lattimer, J. M., & Miralles, J. A. 1999, ApJ, 513, 780
Raynaud, R., Guilet, J., Janka, H.-T., & Gastine, T. 2020, Sci. Adv., 6, eaay2732
Raynaud, R., Cerdá-Durán, P., & Guilet, J. 2022, MNRAS, 509, 3410
Rea, N., Esposito, P., Turolla, R., et al. 2010, Science, 330, 944
Rea, N., Israel, G. L., Esposito, P., et al. 2012, ApJ, 754, 27
Rea, N., Israel, G. L., Pons, J. A., et al. 2013, ApJ, 770, 65
Rea, N., Viganò, D., Israel, G. L., Pons, J. A., & Torres, D. F. 2014, ApJ, 781, L17
Rea, N., Borghese, A., Esposito, P., et al. 2016, ApJ, 828, L13
Reboul-Salze, A., Guilet, J., Raynaud, R., & Bugli, M. 2021a, A&A, 645, A109
Reboul-Salze, A., Guilet, J., Raynaud, R., & Bugli, M. 2021b, A&A, 667, A94
Roberts, L. F. 2012, Ph.D. Thesis, University of California, Santa Cruz, USA
Roberts, L. F., & Reddy, S. 2017, in Handbook of Supernovae, eds. A. W. Alsabti, & P. Murdin (Springer International Publishing), 1605
Roberts, O. J., Veres, P., Baring, M. G., et al. 2021, Nature, 589, 207
Rodríguez Castillo, G. A., Israel, G. L., Tiengo, A., et al. 2016, MNRAS, 456, 4145
Ronchi, M., Rea, N., Graber, V., & Hurley-Walker, N. 2022, ApJ, 934, 184
Rüdiger, G., & Kitchatinov, L. L. 2010, Geophys. Astrophys. Fluid Dyn., 104, 273
Schneider, F. R. N., Ohlmann, S. T., Podsiadlowski, P., et al. 2019, Nature, 574, 211

Schneider, F. R. N., Ohlmann, S. T., Podsiadlowski, P., et al. 2020, MNRAS, 495, 2796
Shen, H., Toki, H., Oyamatsu, K., & Sumiyoshi, K. 1998a, Nucl. Phys. A, 637, 435
Shen, H., Toki, H., Oyamatsu, K., & Sumiyoshi, K. 1998b, Prog. Theor. Phys., 100, 1013
Shen, H., Toki, H., Oyamatsu, K., & Sumiyoshi, K. 2011, ApJS, 197, 20
Sinha, M., & Sedrakian, A. 2015, Phys. Rev. C, 91, 035805
Spruit, H. C. 1999, A&A, 349, 189
Spruit, H. C. 2002, A&A, 381, 923
Stockinger, G., Janka, H. T., Kresse, D., et al. 2020, MNRAS, 496, 2039
Strohmayer, T. E., & Watts, A. L. 2005, ApJ, 632, L111
Sukhbold, T., & Woosley, S. E. 2014, ApJ, 783, 10
Sukhbold, T., Ertl, T., Woosley, S. E., Brown, J. M., & Janka, H. T. 2016, ApJ, 821, 38
Sukhbold, T., Woosley, S. E., & Heger, A. 2018, ApJ, 860, 93
Suwa, Y., & Tominaga, N. 2015, MNRAS, 451, 282
Svinkin, D., Frederiks, D., Hurley, K., et al. 2021, Nature, 589, 211
Szklarski, J., & Arlt, R. 2013, A&A, 550, A94
Takiwaki, T., Kotake, K., & Sato, K. 2009, ApJ, 691, 1360
Tayler, R. J. 1973, MNRAS, 161, 365
Thompson, C., & Duncan, R. C. 1993, ApJ, 408, 194
Thompson, C., & Duncan, R. C. 1995, MNRAS, 275, 255
Tiengo, A., Esposito, P., Mereghetti, S., et al. 2013, Nature, 500, 312
Turolla, R., Zane, S., Pons, J. A., Esposito, P., & Rea, N. 2011, ApJ, 740, 105
Viganò, D. 2013, Ph.D. Thesis, University of Alacant, Spain
Vink, J., & Kuiper, L. 2006, MNRAS, 370, L14
White, C. J., Burrows, A., Coleman, M. S. B., & Vartanyan, D. 2022, ApJ, 926, 111
Woosley, S. E. 2010, ApJ, 719, L204
Woosley, S. E., & Bloom, J. S. 2006, ARA&A, 44, 507
Zahn, J. P., Brun, A. S., & Mathis, S. 2007, A&A, 474, 145
Zhang, B., & Mészáros, P. 2001, ApJ, 552, L35
Zhou, P., Vink, J., Safi-Harb, S., & Miceli, M. 2019, A&A, 629, A51

C.3.2 . Article *Numerical simulations of the Tayler-Spruit dynamo in proto-magnetars (published)*

Monthly Notices of the ROYAL ASTRONOMICAL SOCIETY

MNRAS **526,** L88–L93 (2023) https://doi.org/10.1093/mnrasl/slad120
Advance Access publication 2023 August 31

Numerical simulations of the Tayler–Spruit dynamo in proto-magnetars

Paul Barrère [1]★ Jérôme Guilet,[1]★ Raphaël Raynaud [2]★ and Alexis Reboul-Salze[3]★

[1]*Université Paris-Saclay, Université Paris Cité, CEA, CNRS, AIM, F-9119 Gif-sur-Yvette, France*
[2]*Université Paris Cité, Université Paris-Saclay, CNRS, CEA, AIM, F-91191 Gif-sur-Yvette, France*
[3]*Max Planck Institute for Gravitational Physics (Albert Einstein Institute), D-14476 Potsdam, Germany*

Accepted 2023 August 24. Received 2023 August 3; in original form 2023 June 20

ABSTRACT

The Tayler–Spruit dynamo is one of the most promising mechanisms proposed to explain angular momentum transport during stellar evolution. Its development in proto-neutron stars spun-up by supernova fallback has also been put forward as a scenario to explain the formation of very magnetized neutron stars called magnetars. Using three-dimensional direct numerical simulations, we model the proto-neutron star interior as a stably stratified spherical Couette flow with the outer sphere that rotates faster than the inner one. We report the existence of two subcritical dynamo branches driven by the Tayler instability. They differ by their equatorial symmetry (dipolar or hemispherical) and the magnetic field scaling, which is in agreement with different theoretical predictions (by Fuller and Spruit, respectively). The magnetic dipole of the dipolar branch is found to reach intensities compatible with observational constraints on magnetars.

Key words: instabilities – magnetic fields – MHD – stars: magnetars – supernovae: general.

1 INTRODUCTION

Magnetars are a class of neutron stars that exhibit magnetic fields whose dipolar component reaches 10^{14}–10^{15} G, which makes them the strongest fields observed in the Universe. Their dissipation are thought to power a wide variety of emissions like giant flares (Evans et al. 1980; Hurley et al. 1999, 2005; Svinkin et al. 2021), fast radio bursts (Bochenek et al. 2020; CHIME/FRB Collaboration 2020), and short chaotic X-ray bursts (Gotz et al. 2006; Coti Zelati et al. 2018, 2021). Combined with a millisecond rotation, they may produce magnetorotational explosions, which are more energetic than standard supernovae explosions (Burrows et al. 2007; Dessart et al. 2008; Takiwaki, Kotake & Sato 2009; Bugli et al. 2020, 2023; Kuroda et al. 2020; Obergaulinger & Aloy 2020, 2021, 2022; Bugli, Guilet & Obergaulinger 2021). The origin of these magnetic fields is therefore a crucial question to understand magnetars and their association to extreme events such as gamma-ray bursts or fast radio bursts. Two classes of scenarios can be distinguished for magnetar formation: (i) the merger of a neutron star binary, which may explain the plateau phase and the extended emission in X-ray sources associated with short gamma-ray bursts (Metzger, Quataert & Thompson 2008; Gompertz, O'Brien & Wynn 2014; Lü & Zhang 2014). These events are interesting for their multimessenger signature but are expected to be too rare to be the main formation channel of Galactic magnetars, (ii) the core-collapse of a massive star, which is confirmed by the observation of Galactic magnetars associated with supernova remnants (Vink & Kuiper 2006; Martin et al. 2014; Zhou et al. 2019). In the latter case, the amplification of the magnetic field may be due either to the magnetic flux conservation during the collapse of the iron core of the progenitor star (Ferrario & Wickramasinghe 2006; Hu & Lou 2009; Schneider et al. 2020) or to a dynamo action in the newly born proto-magnetar. Indeed, two dynamo mechanisms have already been studied by numerical simulations: the convective dynamo (Thompson & Duncan 1993; Raynaud et al. 2020; Masada, Takiwaki & Kotake 2022; Raynaud, Cerdá-Durán & Guilet 2022; White et al. 2022) and the magnetorotational instability (MRI)-driven dynamo (Obergaulinger et al. 2009; Mösta et al. 2014; Reboul-Salze et al. 2021; Guilet et al. 2022; Reboul-Salze et al. 2022). They have been shown to produce magnetar-like magnetic fields for millisecond rotation periods of the proto-magnetar, especially for periods $P \lesssim 10$ ms for the convective dynamo (Raynaud et al. 2020; Raynaud et al. 2022). These scenarios rely on the hypothesis that the rotation of the proto-magnetar is determined by the rotation of the progenitor core. However, it is still uncertain whether there are enough fast-rotating progenitor cores to form all the observed magnetars in the Milky Way, which represent ∼10–40 per cent of the Galactic neutron star population (Kouveliotou et al. 1994; Woods & Thompson 2006; Gill & Heyl 2007; Beniamini et al. 2019).

In Barrère et al. (2022), we developed a new magnetar formation scenario in which the rapid rotation rate of the proto-magnetar is not determined by the progenitor core but by the ejected matter that remains gravitationally bound to the proto-magnetar and eventually falls back on the proto-magnetar surface ∼5–10 s after the core-collapse. Since the accretion is asymmetric, the fallback matter transfers a significant amount of angular momentum to the surface (Chan, Müller & Heger 2020; Janka, Wongwathanarat & Kramer 2022), which makes the surface rotate faster than the core. In Barrère et al. (2022), we argue that this spin-up triggers the amplification of the magnetic field through the Tayler–Spruit dynamo mechanism. This dynamo mechanism can be described as a loop: (i) a poloidal magnetic field is sheared into a toroidal one (Ω-effect), (ii) the toroidal field becomes Tayler unstable after reaching a critical value

★ E-mail: paul.barrere@cea.fr (PB); jerome.guilet@cea.fr (JG); raphael.raynaud@cea.fr (RR); alexis.reboul-salze@aei.mpg.de (AR-S)

(Tayler 1973; Pitts & Tayler 1985), and (iii) the Tayler instability regenerates a poloidal field (Fuller, Piro & Jermyn 2019; Skoutnev, Squire & Bhattacharjee 2022; Ji, Fuller & Lecoanet 2023).

The Tayler–Spruit dynamo was first modelled by Spruit (2002) to explain the angular momentum transport in stellar radiative zones. Fuller et al. (2019) provided a revised description, which tackles the previous critics of Spruit's model (see Denissenkov & Pinsonneault 2007; Zahn, Brun & Mathis 2007). A main difference between both descriptions resides in the saturation mechanism of the dynamo. Spruit (2002) supposes that magnetic energy in the large-scale magnetic field is damped via a turbulent cascade at a rate equal to the growth rate of the Tayler instability, whereas Fuller et al. (2019) rather expect the magnetic energy to cascade from the scale of the instability (and not the large-scale magnetic field) to small scales. This yields distinct magnetic energy damping rates and so different scalings for the saturated magnetic field. Their analytical results are now often included in stellar evolution codes (see e.g. Eggenberger, Maeder & Meynet 2005; Cantiello et al. 2014; Eggenberger, Buldgen & Salmon 2019a; Eggenberger et al. 2019b; Bonanno, Guerrero & Del Sordo 2020; den Hartogh, Eggenberger & Deheuvels 2020; Griffiths et al. 2022). Though this dynamo has long been debated in direct numerical simulations (Braithwaite 2006; Zahn et al. 2007), Petitdemange, Marcotte & Gissinger (2023) recently reported a dynamo solution sharing many characteristics with the Tayler–Spruit model. Their numerical simulations modelled a stellar radiative zone, where the shear is negative, that is, the rotation rate decreases in the radial direction. In this Letter, we demonstrate that the Tayler instability can sustain different dynamo branches in the presence of positive shear, which gives strong support to the magnetar formation scenario of Barrère et al. (2022).

2 NUMERICAL SETUP

We perform three-dimensional (3D) direct numerical simulations of a stably stratified and electrically conducting Boussinesq fluid with the pseudo-spectral code MAGIC (Wicht 2002; Gastine & Wicht 2012; Schaeffer 2013). The fluid has a constant density $\rho = 3.8 \times 10^{14}\,\mathrm{g\,cm^{-3}}$ (which corresponds to a proto-neutron star mass of $M = 1.4\,\mathrm{M_\odot}$) and evolves between two concentric spheres of radius $r_\mathrm{i} = 3\,\mathrm{km}$ and $r_\mathrm{o} = 12\,\mathrm{km}$, rotating at the angular frequencies Ω_i and $\Omega_\mathrm{o} = 2\pi \times 100\,\mathrm{rad\,s^{-1}}$, respectively. The imposed differential rotation is characterized by the Rossby number $Ro \equiv 1 - \Omega_\mathrm{i}/\Omega_\mathrm{o} > 0$, which is varied between 0.125 and 1.2. This spherical Taylor–Couette configuration with positive shear prevents the development of the MRI and allows us to study the system in a statistically steady state. We impose no-slip and insulating boundary conditions at the inner and outer spheres. In all the simulations, we keep fixed the other dimensionless control parameters: the shell aspect ratio $\chi \equiv r_\mathrm{i}/r_\mathrm{o} = 0.25$, the thermal and magnetic Prandtl numbers $Pr \equiv \nu/\kappa = 0.1$ and $Pm \equiv \nu/\eta = 1$, respectively, the Ekman number $E \equiv \nu/(d^2\Omega_\mathrm{o}) = 10^{-5}$, and the ratio of the Brunt–Väisälä to the outer angular frequency $N/\Omega_\mathrm{o} = 0.1$. The coefficients ν, κ, η, and $d \equiv r_\mathrm{o} - r_\mathrm{i}$ are respectively the kinematic viscosity, the thermal diffusivity, the resistivity, and the shell width. As discussed in section 1.3 in the Supplemental Materials, the values of the dimensionless parameters are chosen for numerical convenience because realistic parameters of proto-neutron star interiors are out of reach with the current computing power. The magnetic energy is measured by the Elsasser number $\Lambda \equiv B_\mathrm{rms}^2/(4\pi\rho\eta\Omega_\mathrm{o})$. The simulations are initialized either from a nearby saturated state, or with a weak ($\Lambda = 10^{-4}$) or a strong ($\Lambda = 10$) toroidal axisymmetric field with a given equatorial symmetry; it can be either dipolar (i.e. equatorially symmetric[1] with $l = 2$, $m = 0$) or quadrupolar (i.e. antisymmetric with $l = 1$, $m = 0$). We define a turbulent resistive time $\bar{\tau}_\eta = \left(\pi r_\mathrm{o}/\bar{\ell}\right)^2/\eta \sim 0.2d^2/\eta$, where $\bar{\ell} = 10$ is the typical value of the average harmonic degree of the time-averaged magnetic energy spectrum. In the following, we will term a solution *metastable* when a steady state is sustained for a time interval $\Delta t > 0.3\bar{\tau}_\eta$,and *stable* for $\Delta t \geqslant \bar{\tau}_\eta$ (up to $5.7\bar{\tau}_\eta$ for the simulation at $Ro = 0.2$).

3 RESULTS

We find in our set of simulations several dynamo branches represented by different colours in the bifurcation diagram shown in Fig. 1. When the differential rotation is low, the flow can not amplify a weak magnetic field (black crosses), but when $Ro > Ro_\mathrm{W}^\mathrm{c} \sim 0.62$, the magnetic field grows exponentially to reach a metastable or a stable saturated dynamo state (black dots). This kinematic dynamo is driven by an hydrodynamic instability of the Stewartson layer whose threshold is $Ro_\mathrm{hyd}^\mathrm{c} \sim 0.175$ (dashed vertical black line), which is in agreement with Hollerbach (2003). When $Ro \gtrsim 0.8$, the kinematic growth is followed by a non-linear growth and the system transitions directly to another branch with a larger magnetic energy (green circles). Restarting from a nearby saturated solution or a strong toroidal field with quadrupolar symmetry (mauve dashed arrows), we find that the stability of this branch extends to Rossby number as low as $Ro_\mathrm{H}^\mathrm{c} \sim 0.37 < Ro_\mathrm{W}^\mathrm{c}$, which indicates that this dynamo is subcritical. By starting from a strong toroidal field with dipolar symmetry, we observe that this subcritical branch is in bistability with another one which presents even stronger saturated magnetic fields $B_\mathrm{rms} \in \left[4 \times 10^{14}, 1.1 \times 10^{15}\right]$ G (red circles). This branch is also subcritical since it can be maintained for Rossby numbers as low as $Ro > Ro_\mathrm{D}^\mathrm{c} \sim 0.19$. Moreover, the two subcritical branches do not only differ by their magnetic field strength but also by their equatorial symmetry, as seen in the 3D snapshots and the surface maps of the magnetic field in Fig. 1. Indeed, the magnetic field shows a dipolar symmetry on the stronger dynamo branch, whereas it is hemispherical on the weaker one. The latter can be interpreted as the superposition of modes with opposite equatorial symmetry (Gallet & Pétrélis 2009), which is consistent with the fact that we do find quadrupolar solutions (mauve circles in Fig. 1). These are only metastable for $Ro > Ro_\mathrm{Q}^\mathrm{c} \sim 0.7$ and transition to a stable dipolar or hemispherical solution. Finally, we note that the hemispherical dynamos with $Ro \gtrsim 0.8$ (light green circles in Figs 1 and 2) display parity modulations (i.e. the solution evolves between hemispherical, dipole, and quadrupole symmetric states). This behaviour is reminiscent of the so-called Type 1 modulation identified in other dynamo set-ups (Knobloch, Tobias & Weiss 1998; Raynaud & Tobias 2016) and likely results from the coupling of modes with opposite parity as the equatorial symmetry breaking of the flow increases at larger Rossby numbers.

The difference between the three dynamo branches is also clear in Fig. 2, where we see that the hemispherical branch saturates below the equipartition, with an energy ratio increasing with Ro from ∼0.014 up to ∼0.56. By contrast, the dynamos of the dipolar branch are in a superequipartition state ($E_\mathrm{b}/E_\mathrm{k} > 1$) and follow the magnetostrophic scaling $E_\mathrm{b}/E_\mathrm{k} \propto Ro^{-1}$ characteristic of the Coriolis–Lorenz force balance (Roberts & Soward 1972; Dormy 2016; Aubert, Gastine & Fournier 2017; Dormy, Oruba & Petitdemange 2018; Augustson, Brun & Toomre 2019; Schwaiger, Gastine & Aubert

[1]For the choice of these definitions, see Gubbins & Zhang (1993).

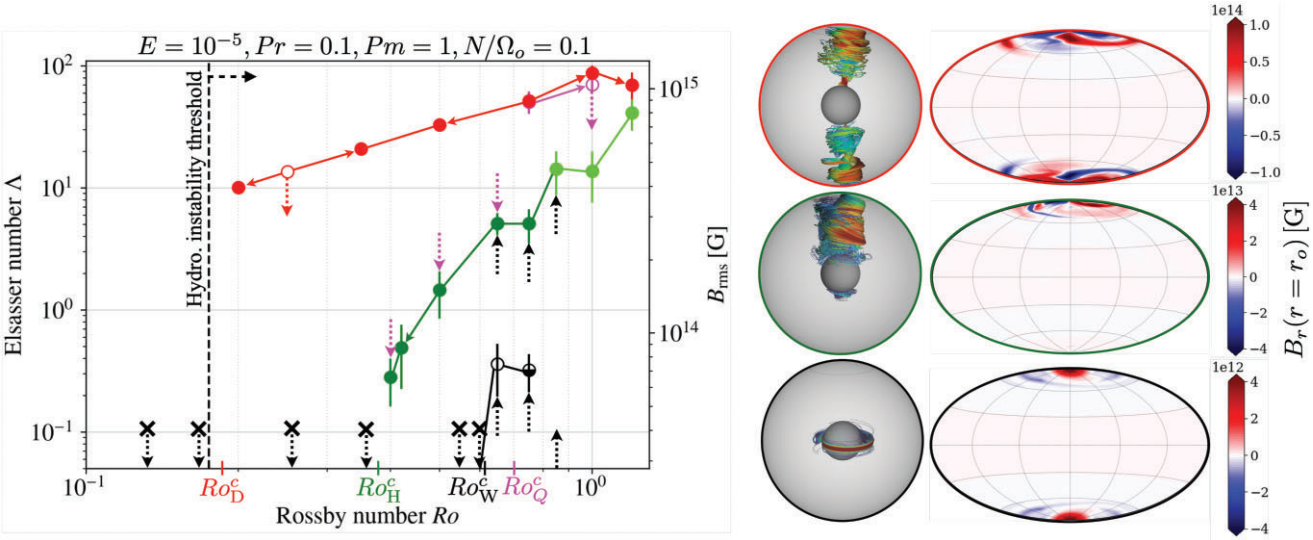

Figure 1. Left: Bifurcation diagram of the time and volume averaged Elsasser number (and root mean square magnetic field) versus the Rossby number. Distinct dynamo branches are represented: dipolar (red), quadrupolar (mauve), hemispherical (green), and kinematic (black) whose respective thresholds are $Ro^c_{\rm D} \sim 0.19$, $Ro^c_{\rm Q} \sim 0.7$, $Ro^c_{\rm H} \sim 0.37$, and $Ro^c_{\rm W} \sim 0.62$. The hydrodynamic instability is triggered for $Ro^c_{\rm hyd} > 0.177$. Dark green circles are stationary hemispherical dynamos and light green ones display parity modulations. Black crosses indicate failed dynamos, empty circles metastable solutions. Arrows attached to circles indicate the initial condition of the associated simulation. The black half empty circle specifies that the solution was found to be metastable in a simulation and stable in another. The error bars indicate the standard deviation. Right: snapshots of the magnetic field lines and surface radial fields associated to the different main dynamo branches at $Ro = 0.75$: dipolar (top), hemispherical (middle), and kinematic (bottom).

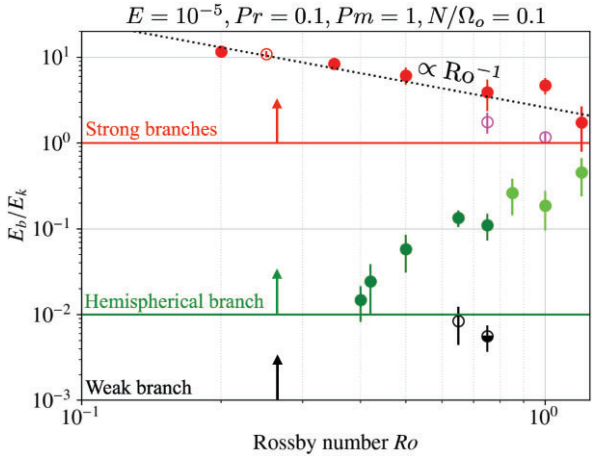

Figure 2. Time-averaged ratio of the magnetic energy to the kinetic energy densities as a function of the Rossby number. The error bars indicate the standard deviation.

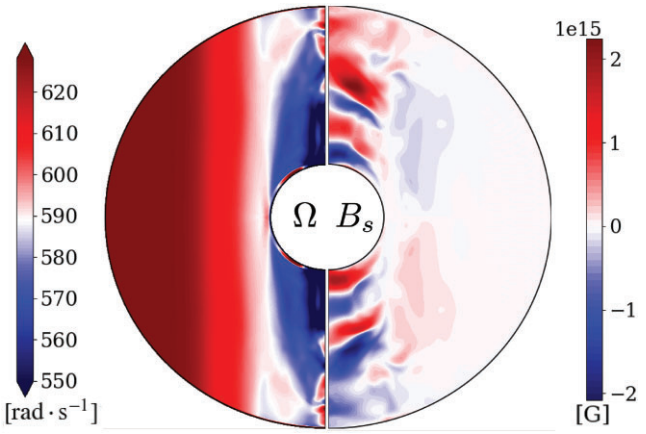

Figure 3. Snapshots of the azimuthal slices of the angular velocity (left) and the magnetic field along the cylindrical radius $s \equiv r\sin\theta$ (right) of the dipolar dynamo at $Ro = 0.75$.

2019; Seshasayanan & Gallet 2019; Raynaud et al. 2020). This is also confirmed by force balance spectra shown in fig. S1 in the Supplemental Materials.

Both subcritical dynamos show magnetic fields concentrated along the rotation axis, which differs significantly from the subcritical solutions found with a negative shear by (Petitdemange et al. 2023); this is also strikingly different from the magnetic field generated on the equatorial plane by the kinematic dynamo (see 3D snapshots of Fig. 1). This suggests that the dipolar and hemispherical dynamos are driven by a different mechanism. We argue that they are driven by the Tayler instability according to the following arguments. First, the axisymmetric toroidal magnetic component is clearly dominant since it contains 53–88 per cent of the total magnetic energy. Second, the simulations show a poloidal magnetic field with a dominant $m = 1$ mode (see Supplemental Materials figs S2 and S3), which is the most unstable mode of the Tayler instability (Zahn et al. 2007; Ma & Fuller 2019). In the azimuthal cut of the magnetic field component B_s in Fig. 3, the Tayler mode also appears clearly close to the poles, where it is expected to develop for a toroidal field generated by the shearing of a poloidal field (see Supplemental Materials fig. S4). This is also consistent with the 3D snapshots of the dipolar and hemispherical branches in Fig. 1 where the toroidal magnetic field seems prone to a kink instability. Third, as in Petitdemange et al. (2023), the system bifurcates from the kinematic to the hemispherical branch in the vicinity of the threshold of the Tayler instability (Spruit 1999, 2002)

$$\Lambda^c_\phi \equiv \frac{B^{c\,2}_\phi}{4\pi\rho\eta\Omega_o} \sim \frac{\chi}{1-\chi}\frac{N}{\Omega_o}\sqrt{\frac{Pr}{E}} \sim 3.3\,. \quad (1)$$

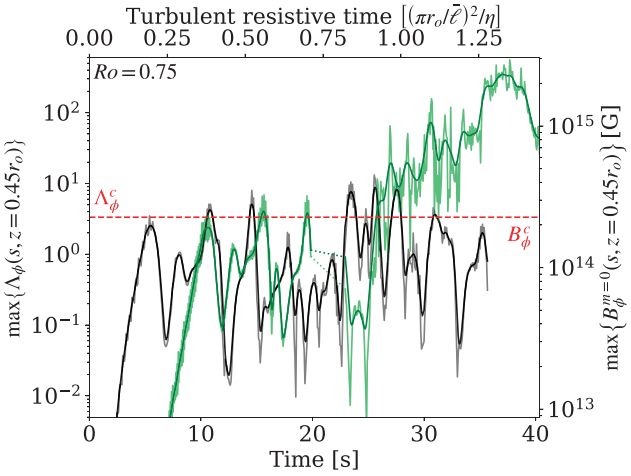

Figure 4. Time series of the maximum along the cylindrical radius s of the axisymmetric toroidal magnetic energy measured locally at $z = 0.45r_o$, for stable (black) and metastable (green) kinematic dynamos at $Ro = 0.75$. The dashed red line indicates the analytical threshold of the Tayler instability (equation 1). Dark lines show a running average and dotted green lines around $t \sim 20$ s indicate missing data.

Indeed, if we focus on the stable and metastable kinematic solutions found at $Ro = 0.75$, we see in Fig. 4 that the *local* maximum of the toroidal axisymmetric field is in both cases close to the critical value above which it is expected to become unstable. The bifurcation from the kinematic toward the hemispherical branch that is observed for the metastable solution appears hence as the result of turbulent fluctuations departing far enough above the threshold of the Tayler instability.

Finally, we compare our numerical results to the theoretical predictions regarding the saturation of the Tayler–Spruit dynamo. Note that these predictions assume the scale separation $\omega_A \ll \Omega_o \ll N$, where the Alfvén frequency is defined by $\omega_A \equiv B_\phi/\sqrt{4\pi\rho r_o^2} \sim 12.1\,(B_\phi/10^{15}\,\mathrm{G})$ Hz. Our numerical models assume $N/\Omega_o = 0.1$ to limit the computational costs, whereas for a typical PNS spun-up by fallback to a period of 1–10 ms we expect $N/\Omega_o \sim 1$–10. On the other hand, the achieved magnetic field follows the right scale separation with $\omega_A/\Omega_o \lesssim 0.02$, which is expected to determine the saturation mechanism of the Tayler instability (Ji et al. 2023). Fig. 5 displays the axisymmetric toroidal and poloidal magnetic fields (top), the dipole field (middle) and the Maxwell torque (bottom) as a function of an effective shear rate q measured locally in the saturated state of the dynamo (see Supplemental Materials fig. S5). For the dipolar branch (red), we find that the power laws $B^{m=0}_{tor} \propto q^{0.36\pm0.05}$ and $B^{m=0}_{pol} \propto q^{0.62\pm0.07}$ fit the saturated magnetic field, while we find $B_s B_\phi \propto q^{1.0\pm0.02}$ or $B^{m=0}_s B^{m=0}_\phi \propto q^{1.1\pm0.04}$, depending on whether we take into account non-axisymmetric contributions to compute the Maxwell torque T_M. The scaling exponents are thus in good agreement with the theoretical predictions of Fuller et al. (2019) $B^{m=0}_{tor} \propto q^{1/3}$, $B^{m=0}_{pol} \propto q^{2/3}$, and $T_M \propto q$ (red dotted lines in Fig. 5). Contrary to their prediction, however, our torque is not dominated by the axisymmetric magnetic field, which may be related to their assumption of a stronger stratification. Interestingly, the hemispherical branch (green) does not follow the same scalings: for $q \geq 0.2$, we find $B^{m=0}_{tor} \propto q^{2.1\pm0.31}$ and $B^{m=0}_{pol} \propto q^{2.0\pm0.28}$ for the magnetic field, and $B_s B_\phi \propto q^{2.7\pm0.40}$ or $B^{m=0}_s B^{m=0}_\phi \propto q^{3.8\pm0.70}$ for the Maxwell torque. These results globally support Spruit's predictions (Spruit 2002) $B^{m=0}_{tor} \propto q$, $B^{m=0}_{pol} \propto q^2$, and $T_M \propto q^3$ (green

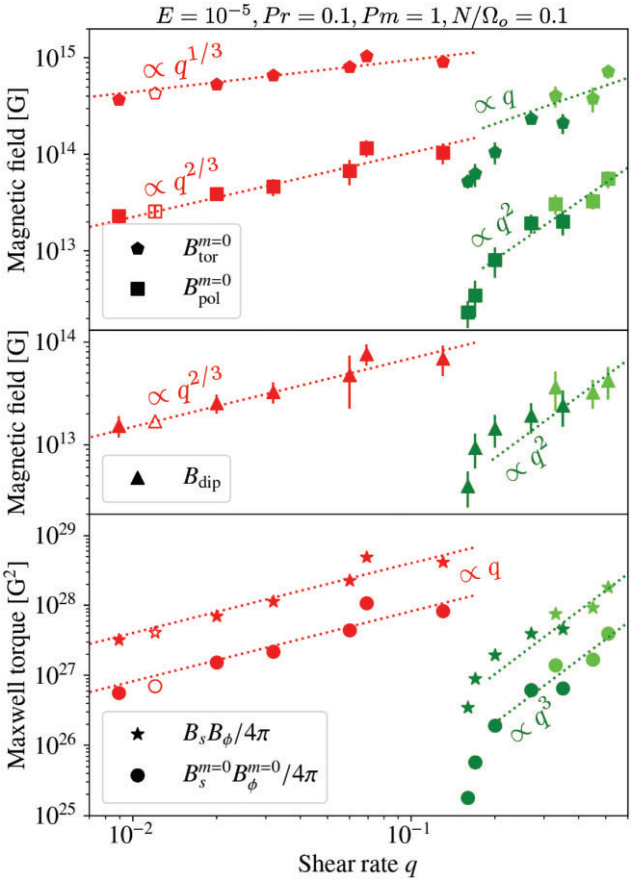

Figure 5. Root mean square (RMS) toroidal and poloidal axisymmetric magnetic fields (top), RMS magnetic dipole (middle), and RMS magnetic torque (bottom) as a function of the time-averaged shear rate measured in the steady state, for the dipolar (red) and hemispherical (green) dynamo branches. Dotted lines shows the best fits obtained with Fuller's (red) and Spruit's (green) theoretical scaling laws, respectively.

dotted lines)[2]. If we focus on the dipole field, we find the following power laws: $B_{dip} \propto q^{0.66\pm0.03}$ and $B_{dip} \propto q^{1.1\pm0.4}$, for the dipolar and hemispherical branches, respectively. The dipole field on the strong branch therefore follows the same scaling as the axisymmetric poloidal field and is only ∼33 per cent weaker.

4 CONCLUSIONS

To conclude, we show that the Tayler–Spruit dynamo also exists in the presence of positive shear. We demonstrate for the first time the existence of two subcritical branches of this dynamo with distinct equatorial symmetries, dipolar, and hemispherical. Moreover, the former follows Fuller's theoretical predictions, while the latter is in overall agreement with Spruit's model. Compared to the study of Petitdemange et al. (2023) that use a negative shear, our results present a similar dynamical structure, with a bifurcation diagram characterized by a bistability between kinematic and subcritical dynamo solutions. The magnetic field of their Tayler–Spruit dynamo

[2]In the case of the toroidal magnetic field, the power-law index from the fit is in slight tension with the theoretical prediction. However, this tension is not very significant: it is driven mainly by a single data point and disappears if we change the threshold from $q > 0.2$ to $q > 0.25$ to exclude the model `Ro0.5as` with $q = 0.2$.

is, however, different since it is characterized by a smaller scale structure localized near the inner boundary in the equatorial plane, and induces a torque scaling according to Spruit's prediction. Our study shows a magnetic field geometry concentrated near the pole in agreement with the expectation of the Tayler–Spruit dynamo and a more complex physics, with the existence of two different branches that can not be captured by a single scaling law. Extended parameter studies will be needed to further assess the impact of the resistivity and the stratification on this dynamo instability and better constrain its astrophysical implications.

Our results are of particular importance for stellar evolution models by confirming the existence of the Tayler–Spruit dynamo and by deepening our physical understanding of its complex dynamics. They also give strong support to the new magnetar formation scenario proposed by Barrère et al. (2022), which relies on the development of a Tayler-instability driven dynamo in the presence of a positive shear. We validate the assumption that the magnetic dipole is a significant fraction of the poloidal magnetic field and follows the same scaling. Extrapolating our results for the dipolar branch to $q \sim 1$ as expected in Barrère et al. (2022), we obtain a magnetic dipole intensity of $\sim 3.2 \times 10^{14}$ G and an even stronger axisymmetric toroidal field of $\sim 2.1 \times 10^{15}$ G. These orders of magnitude are similar to those found in Barrère et al. (2022) for the same rotation period of $P_\mathrm{o} \equiv 2\pi/\Omega_\mathrm{o} = 10$ ms, and fall right in the magnetar range (Olausen & Kaspi 2014).

ACKNOWLEDGEMENTS

We thank F. Daniel, C. Gissinger, and L. Petitdemange and F. Marcotte for fruitful discussions and for sharing the manuscript Petitdemange et al. (2023) before its publication. We also thank A. Igoshev for valuable comments. This work was supported by the European Research Council (MagBURST grant 715368), and the Programme National Physique Stellaire (PNPS) and the Programme National Hautes Énergies (PNHE) programmes of CNRS/INSU, co-funded by CEA and CNES. Numerical simulations have been carried out at the Centre Informatique National de l'Enseignement Supérieur (CINES) on the Jean-Zay supercomputer (DARI project A0130410317).

DATA AVAILABILITY

The data underlying this article will be shared on reasonable request to the corresponding author.

REFERENCES

Aubert J., Gastine T., Fournier A., 2017, J. Fluid Mech., 813, 558
Augustson K. C., Brun A. S., Toomre J., 2019, ApJ, 876, 83
Barrère P., Guilet J., Reboul-Salze A., Raynaud R., Janka H. T., 2022, A&A, 668, A79
Beniamini P., Hotokezaka K., van der Horst A., Kouveliotou C., 2019, MNRAS, 487, 1426
Bochenek C. D., Ravi V., Belov K. V., Hallinan G., Kocz J., Kulkarni S. R., McKenna D. L., 2020, Nature, 587, 59
Bonanno A., Guerrero G., Del Sordo F., 2020, Mem. Soc. Astron. Ital., 91, 249
Braithwaite J., 2006, A&A, 449, 451
Bugli M., Guilet J., Obergaulinger M., Cerdá-Durán P., Aloy M. A., 2020, MNRAS, 492, 58
Bugli M., Guilet J., Obergaulinger M., 2021, MNRAS, 507, 443
Bugli M., Guilet J., Foglizzo T., Obergaulinger M., 2023, MNRAS, 520, 5622
Burrows A., Dessart L., Livne E., Ott C. D., Murphy J., 2007, ApJ, 664, 416
CHIME/FRB Collaboration, 2020, Nature, 587, 54
Cantiello M., Mankovich C., Bildsten L., Christensen-Dalsgaard J., Paxton B., 2014, ApJ, 788, 93
Chan C., Müller B., Heger A., 2020, MNRAS, 495, 3751
Coti Zelati F., Rea N., Pons J. A., Campana S., Esposito P., 2018, MNRAS, 474, 961
Coti Zelati F. et al., 2021, ApJ, 907, L34
den Hartogh J. W., Eggenberger P., Deheuvels S., 2020, A&A, 634, L16
Denissenkov P. A., Pinsonneault M., 2007, ApJ, 655, 1157
Dessart L., Burrows A., Livne E., Ott C. D., 2008, ApJ, 673, L43
Dormy E., 2016, J. Fluid Mech., 789, 500
Dormy E., Oruba L., Petitdemange L., 2018, Fluid Dyn. Res., 50, 011415
Eggenberger P., Maeder A., Meynet G., 2005, A&A, 440, L9
Eggenberger P., Buldgen G., Salmon S. J. A. J., 2019a, A&A, 626, L1
Eggenberger P., den Hartogh J. W., Buldgen G., Meynet G., Salmon S. J. A. J., Deheuvels S., 2019b, A&A, 631, L6
Evans W. D. et al., 1980, ApJ, 237, L7
Ferrario L., Wickramasinghe D., 2006, MNRAS, 367, 1323
Fuller J., Piro A. L., Jermyn A. S., 2019, MNRAS, 485, 3661
Gallet B., Pétrélis F., 2009, Phys. Rev. E, 80, 035302
Gastine T., Wicht J., 2012, Icarus, 219, 428
Gill R., Heyl J., 2007, MNRAS, 381, 52
Gompertz B. P., O'Brien P. T., Wynn G. A., 2014, MNRAS, 438, 240
Gotz D. et al., 2006, Astron. Telegram, 953, 1
Griffiths A., Eggenberger P., Meynet G., Moyano F., Aloy M.-Á., 2022, A&A, 665, A147
Gubbins D., Zhang K., 1993, Phys. Earth Planet. Inter., 75, 225
Guilet J., Reboul-Salze A., Raynaud R., Bugli M., Gallet B., 2022, MNRAS, 516, 4346
Hollerbach R., 2003, J. Fluid Mech., 492, 289
Hu R.-Y., Lou Y.-Q., 2009, MNRAS, 396, 878
Hurley K. et al., 1999, Nature, 397, 41
Hurley K. et al., 2005, Nature, 434, 1098
Janka H.-T., Wongwathanarat A., Kramer M., 2022, ApJ, 926, 9
Ji S., Fuller J., Lecoanet D., 2023, MNRAS, 521, 5372
Knobloch E., Tobias S. M., Weiss N. O., 1998, MNRAS, 297, 1123
Kouveliotou C. et al., 1994, Nature, 368, 125
Kuroda T., Arcones A., Takiwaki T., Kotake K., 2020, ApJ, 896, 102
Lü H.-J., Zhang B., 2014, ApJ, 785, 74
Ma L., Fuller J., 2019, MNRAS, 488, 4338
Martin J., Rea N., Torres D. F., Papitto A., 2014, MNRAS, 444, 2910
Masada Y., Takiwaki T., Kotake K., 2022, ApJ, 924, 75
Metzger B. D., Quataert E., Thompson T. A., 2008, MNRAS, 385, 1455
Mösta P. et al., 2014, ApJ, 785, L29
Obergaulinger M., Aloy M. Á., 2020, MNRAS, 492, 4613
Obergaulinger M., Aloy M. Á., 2021, MNRAS, 503, 4942
Obergaulinger M., Aloy M. Á., 2022, MNRAS, 512, 2489
Obergaulinger M., Cerdá-Durán P., Müller E., Aloy M. A., 2009, A&A, 498, 241
Olausen S. A., Kaspi V. M., 2014, ApJS, 212, 6
Petitdemange L., Marcotte F., Gissinger C., 2023, Science, 379, 300
Pitts E., Tayler R. J., 1985, MNRAS, 216, 139
Raynaud R., Tobias S. M., 2016, J. Fluid Mech., 799, R6
Raynaud R., Guilet J., Janka H.-T., Gastine T., 2020, Sci. Adv., 6, eaay2732
Raynaud R., Cerdá-Durán P., Guilet J., 2022, MNRAS, 509, 3410
Reboul-Salze A., Guilet J., Raynaud R., Bugli M., 2021, A&A, 645, A109
Reboul-Salze A., Guilet J., Raynaud R., Bugli M., 2022, A&A, 667, A94
Roberts P. H., Soward A. M., 1972, Annu. Rev. Fluid Mech, 4, 117
Schaeffer N., 2013, Geochem. Geophys. Geosyst., 14, 751
Schneider F. R. N., Ohlmann S. T., Podsiadlowski P., Röpke F. K., Balbus S. A., Pakmor R., 2020, MNRAS, 495, 2796
Schwaiger T., Gastine T., Aubert J., 2019, Geophys. J. Int., 219, S101
Seshasayanan K., Gallet B., 2019, J. Fluid Mech., 864, 971
Skoutnev V., Squire J., Bhattacharjee A., 2022, MNRAS, 517, 526
Spruit H. C., 1999, A&A, 349, 189
Spruit H. C., 2002, A&A, 381, 923
Svinkin D. et al., 2021, Nature, 589, 211
Takiwaki T., Kotake K., Sato K., 2009, ApJ, 691, 1360
Tayler R. J., 1973, MNRAS, 161, 365

Thompson C., Duncan R. C., 1993, ApJ, 408, 194
Vink J., Kuiper L., 2006, MNRAS, 370, L14
White C. J., Burrows A., Coleman M. S. B., Vartanyan D., 2022, ApJ, 926, 111
Wicht J., 2002, Phys. Earth Planet. Inter., 132, 281
Woods P. M., Thompson C., 2006, in Lewin W., van der Klis M., eds, Compact stellar X-ray sources Vol. 39. Cambridge Univ. Press, Cambridge, p. 547
Zahn J. P., Brun A. S., Mathis S., 2007, A&A, 474, 145
Zhou P., Vink J., Safi-Harb S., Miceli M., 2019, A&A, 629, A51

SUPPORTING INFORMATION

Supplementary data are available at *MNRASL* online.

suppl_data

Please note: Oxford University Press is not responsible for the content or functionality of any supporting materials supplied by the authors. Any queries (other than missing material) should be directed to the corresponding author for the article.

This paper has been typeset from a TEX/LATEX file prepared by the author.

C.3.3 . Article *Tayler-Spruit dynamo in stably stratified rotating fluids: Application to proto-magnetars (submitted)*

Astronomy & Astrophysics manuscript no. output
June 12, 2024

Tayler-Spruit dynamo in stably stratified rotating fluids

Application to proto-magnetars

P. Barrère*[1], J. Guilet[1], R. Raynaud[2], and A. Reboul-Salze[3]

[1]Université Paris-Saclay, Université Paris Cité, CEA, CNRS, AIM, 91191, Gif-sur-Yvette, France
[2]Université Paris Cité, Université Paris-Saclay, CNRS, CEA, AIM, F-91191 Gif-sur-Yvette, France
[3]Max Planck Institute for Gravitational Physics (Albert Einstein Institute), D-14476 Potsdam, Germany

Received ?????; accepted ?????

ABSTRACT

The formation of highly magnetized young neutron stars, called magnetars, is still a strongly debated question. A promising scenario invokes the amplification of the magnetic field by the Tayler-Spruit dynamo in a proto-neutron star (PNS) spun up by fallback. Barrère et al. (2023) supports this scenario by demonstrating that this dynamo can generate magnetar-like magnetic fields in stably stratified Boussinesq models of a PNS interior. To further investigate the Tayler-Spruit dynamo, we perform 3D-MHD numerical simulations with the MagIC code varying the ratio between the Brunt-Väisälä frequency and the rotation rate. We first demonstrate that a self-sustained dynamo process can be maintained for a Brunt-Väisälä frequency about 4 times higher than the angular rotation frequency. The generated magnetic fields and angular momentum transport follow the analytical scaling laws of Fuller et al. (2019), which confirms our previous results. We also report for the first time the existence of an intermittent Tayler-Spruit dynamo. For a typical PNS Brunt-Väisälä frequency of 10^3 s^{-1}, the axisymmetric toroidal and dipolar magnetic fields range between $1.2\times10^{15} - 2\times10^{16}$ G and $1.4\times10^{13} - 3\times10^{15}$ G, for rotation periods between of $1 - 10$ ms. Thus, our results provide numerical evidence that our scenario can explain the formation of magnetars. As the Tayler-Spruit dynamo is often invoked for the angular momentum transport in stellar radiative zones, our results are also of particular importance in this field and we provide a calibration of the Fuller et al.'s prescription based on our simulations, with a dimensionless normalisation factor of the order of 10^{-2}.

Key words. stars: magnetic fields – stars: magnetars – supernovae: general – magnetohydrodynamics (MHD) – dynamo – methods: numerical

1. Introduction

Soft gamma repeaters and anomalous X-ray pulsars are two classes of neutron stars (NSs) that exhibit a wide variety of high-energy emissions from short chaotic bursts during outbursts phases (e.g. Gotz et al. 2006; Younes et al. 2017; Coti Zelati et al. 2018, 2021) to giant flares (Evans et al. 1980; Hurley et al. 1999, 2005; Svinkin et al. 2021), which are the brightest events observed in the Milky Way. These neutron stars are called magnetars because their emissions have been shown to be powered by the dissipation of their ultra-strong magnetic fields (Kouveliotou et al. 1994). Indeed, these emissions show that they rotate with periods of $2-12$ s and have stronger rotation braking than typical NSs (e.g. Rea et al. 2012; Olausen & Kaspi 2014). If the spin-down is due to the extraction of rotational energy by a magnetic dipole, we can infer that most magnetars exhibit a surface magnetic dipole of $10^{14} - 10^{15}$ G, which are the strongest known in the Universe. Three magnetars, however, display weaker magnetic dipoles of $6\times10^{12} - 4\times10^{13}$ G (Rea et al. 2010, 2012, 2013, 2014) but absorption lines detected in the X-ray spectra of two of these magnetars suggest the presence of stronger non-dipolar magnetic fields of $2\times10^{14} - 2\times10^{15}$ G (Tiengo et al. 2013; Rodríguez Castillo et al. 2016). These 'low-field' magnetars therefore demonstrate that an ultra-strong surface magnetic dipole is not necessary for a neutron star to produce magnetar-like emission.

Magnetars are also suspected to be the central engine of extreme events. In combination with a millisecond rotation period, magnetars in their proto-neutron star (PNS) stage may power magnetorotational supernova (SN) explosions which are more energetic than typical neutrino-driven SNe (e.g. Burrows et al. 2007; Dessart et al. 2008; Takiwaki et al. 2009; Kuroda et al. 2020; Bugli et al. 2020, 2021, 2023; Obergaulinger & Aloy 2020, 2021, 2022). The formation of a millisecond magnetar is a popular scenario to explain super-luminous SNe (Woosley 2010; Kasen & Bildsten 2010; Dessart et al. 2012; Inserra et al. 2013; Nicholl et al. 2013) and hypernovae, of which the latter are associated to long gamma-ray bursts (GRBs ; Duncan & Thompson 1992; Zhang & Mészáros 2001; Woosley & Bloom 2006; Drout et al. 2011; Nomoto et al. 2011; Gompertz & Fruchter 2017; Metzger et al. 2011, 2018). In the case of binary NS mergers, the NS remnant may be a magnetar whose magnetic fields power the plateau phase observed in short GRBs afterglows (e.g. Lü & Zhang 2014; Gompertz et al. 2014; Kiuchi et al. 2024).

Recently, the observation of the fast radio burst FRB 200428 was associated to X-ray bursts of the magnetar SGR 1935+2154 (Bochenek et al. 2020; CHIME/FRB Collaboration et al. 2020; Mereghetti et al. 2020; Zhu et al. 2023; Tsuzuki et al. 2024), which supports magnetar-powered emission scenarios to explain at least a fraction of FRBs.

* e-mail: paul.barrere@cea.fr

In order to better understand these phenomena, it is thus essential to investigate the question of magnetar formation and especially the origin of their ultra-strong magnetic fields. The association of a few magnetars with SN remnants suggests that they are born during core-collapse SNe (Vink & Kuiper 2006; Martin et al. 2014; Zhou et al. 2019). The magnetic fields could be amplified during the core-collapse due to the magnetic flux conservation (Ferrario & Wickramasinghe 2006; Hu & Lou 2009; Schneider et al. 2019; Shenar et al. 2023). However, the magnetic field of the iron core of the progenitor star is not constrained by observations and it is uncertain whether this scenario can explain the whole magnetar population (Makarenko et al. 2021). A second type of scenario invokes a dynamo action in the newly formed PNS to generate strong large-scale magnetic fields. Three mechanisms have been studied: the convective dynamo (Thompson & Duncan 1993; Raynaud et al. 2020, 2022; Masada et al. 2022; White et al. 2022), the magnetorotational instability (MRI)-driven dynamo (Obergaulinger et al. 2009; Mösta et al. 2014; Rembiasz et al. 2017; Reboul-Salze et al. 2021, 2022; Guilet et al. 2022), and the Tayler-Spruit dynamo (Barrère et al. 2022, 2023).

The two former dynamos have been shown to form magnetar-like magnetic fields in the case of fast rotation. In the framework of the millisecond magnetar model, these mechanisms are therefore promising to explain the formation of the central engine extreme explosions. Nevertheless, two uncertainties remain. First, SN remnants associated with magnetars show typical explosion energy of $\sim 10^{51}$ erg. This implies that most magnetars were born in standard core-collapse supernovae (CCSNe), which require slower rotation periods of at least 5 ms (Vink & Kuiper 2006). Second, the rotation is assumed to stem from a fast-rotating progenitor core. It is unclear whether there is a large enough fraction of these progenitors to explain the entire magnetar population.

To address these points, we developed in Barrère et al. (2022) a new formation scenario in which the PNS rotation is determined by the fallback, which is the matter that is initially ejected by the SN explosion before eventually falling back onto the PNS. 3D CCSNe numerical simulations show that the fallback accretion can significantly spin up the PNS surface (Chan et al. 2020; Stockinger et al. 2020; Janka et al. 2022). We argued that the differential rotation caused by this spin-up triggers the development of the Tayler-Spruit dynamo. This dynamo mechanism is driven by the combination of the differential rotation and the Tayler instability, which is an instability triggered by perturbations of a purely toroidal magnetic field (Tayler 1973; Goossens & Tayler 1980; Goossens et al. 1981). Studies in stellar evolution (such as Eggenberger et al. 2005; Cantiello et al. 2014; Eggenberger et al. 2019a,b; den Hartogh et al. 2020; Griffiths et al. 2022) often rely on this mechanism to explain the strong angular momentum transport (AMT) inferred via asteroseismology in sub-giant/red giant stars (e.g. Mosser et al. 2012; Deheuvels et al. 2014, 2015; Gehan et al. 2018). As our model in Barrère et al. (2022), these works use analytical prescriptions to model the AMT produced by the large-scale magnetic fields in stellar radiative zones. Two distinct analytical models of the Tayler-Spruit dynamo are used: the original model of Spruit (2002) and the revised one of Fuller et al. (2019), which tackles previous criticism of the original model. The prescriptions, however, can not take into account the strong non-linearity behind the dynamo mechanism, which impels numerical investigations of its 3D complex dynamics to better characterize its effects in both astrophysical contexts.

Petitdemange et al. (2023); Petitdemange et al. (2024); Daniel et al. (2023) performed 3D direct numerical simulations of dynamo action in a stably-stratified Couette flow in the context of stellar radiative layers and so with a differential rotation in which the inner core rotates faster than the outer layer. They argued that the dynamo was driven by the Tayler instability and found scaling laws in agreement with the prescriptions of Spruit (2002). In our numerical study Barrère et al. (2023), the setup is different with an outer sphere rotating faster than the core, which is relevant to our magnetar formation scenario. We demonstrated the existence of more complex dynamics with two Tayler-Spruit dynamo branches, which have distinct magnetic field strengths and geometries: the weaker branch shows a hemispherical field while the strongest one displays a dipolar symmetry, i.e. the magnetic field is equatorially symmetric. Furthermore, the former follows the analytical scaling of Spruit (2002), while the latter is in agreement with the predictions of Fuller et al. (2019). Lastly, the dipolar dynamo could reach axisymmetric toroidal and dipole magnetic fields up to $\sim 2\times10^{15}$ G and $\sim 3\times10^{14}$ G, respectively. Although such intensities seem relevant to form magnetars, these models considered only a fixed ratio of the Brunt-Väisälä to the surface angular frequency $N/\Omega_o = 0.1$, whereas it is expected to cover the range $N/\Omega_o \in [0.1, 10]$ in real PNSs.

Therefore, this article aims at investigating the impact of N/Ω_o on the dipolar Tayler-Spruit dynamo discovered in Barrère et al. (2023). The study of the hemispherical dynamo will lead to another paper more focused on the complex physics behind the Tayler-Spruit dynamos. In the following, Sect. 2 describes the governing equations and the numerical setup of our simulations. We present the results in Sect. 3, which will be applied to the question of magnetar formation in Sect. 4. Finally, we discuss the results and conclude in Sect. 5 and Sect. 6, respectively.

2. Numerical setup

2.1. Governing equations

As in Barrère et al. (2023), we model the PNS interior as a stably stratified and electrically conducting fluid. We also adopt the Boussinesq approximation and consider a fluid with a constant density $\rho = 3.8 \times 10^{14}\,\mathrm{g\,cm^{-3}}$, which corresponds to a PNS with a radius of $r_o = 12\,\mathrm{km}$ and a mass of $M = 1.4\,\mathrm{M_\odot}$. The fluid evolves in a spherical Taylor-Couette configuration, i.e. between two concentric spheres of radius $r_i = 3\,\mathrm{km}$ and r_o which rotates with the respective rates $\Omega_i = 2\pi \times 25\,\mathrm{rad\,s^{-1}}$ and $\Omega_o = 2\pi \times 100\,\mathrm{rad\,s^{-1}}$. In the reference frame rotating with the surface at the angular velocity $\mathbf{\Omega}_o = \Omega_o \mathbf{e}_z$, the Boussinesq MHD equations read

$$\nabla \cdot \mathbf{v} = 0\,, \tag{1}$$

$$D_t \mathbf{v} = -\frac{1}{\rho}\nabla p' - 2\Omega_o \mathbf{e}_z \times \mathbf{v} - N^2 \Theta \mathbf{e}_r + \frac{1}{4\pi\rho}(\nabla \times \mathbf{B}) \times \mathbf{B} + \nu \Delta \mathbf{v}\,, \tag{2}$$

$$D_t \Theta = \kappa \Delta \Theta\,, \tag{3}$$

$$\partial_t \mathbf{B} = \nabla \times (\mathbf{u} \times \mathbf{B}) + \eta \Delta \mathbf{B}\,, \tag{4}$$

$$\nabla \cdot \mathbf{B} = 0\,, \tag{5}$$

where $\mathbf{B}$ is the magnetic field, $\mathbf{v}$ is the velocity field, p' is the non-hydrostatic pressure, ρ is the mean density of the PNS, $g = g_o r/r_o$ is the gravitation field, and $\alpha \equiv \rho^{-1}(\partial_T \rho)_p$ is the thermal expansion coefficient. $\mathbf{e}_z$ and $\mathbf{e}_r$ are the unit vectors of the axial and the spherical radial directions, respectively. θ is the buoyancy variable defined by

$$\Theta \equiv -\frac{g}{N^2}\frac{\rho'}{\rho}\,, \tag{6}$$

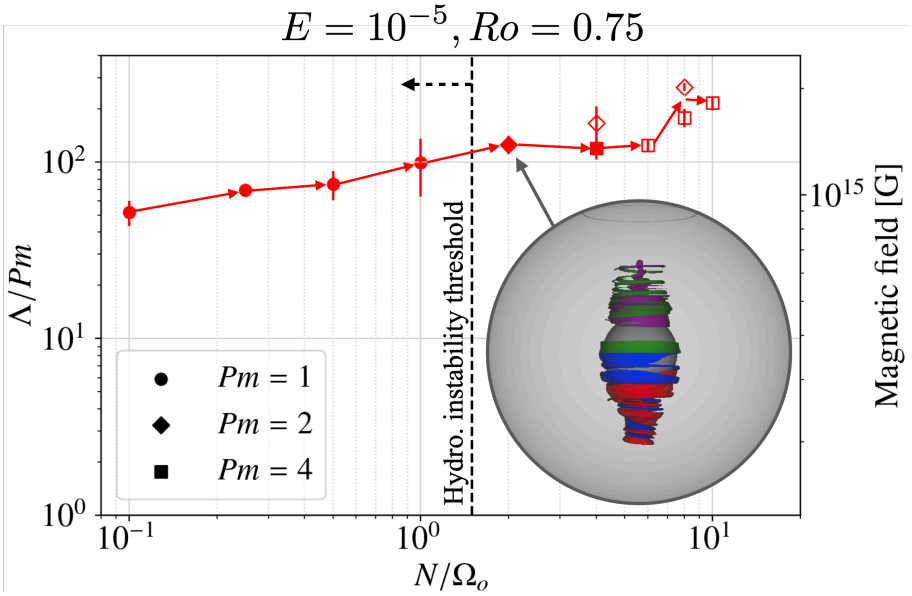

Fig. 1. Viscous Elsasser number (and root mean square magnetic field) as a function of the ratio of the Brunt-Väisälä frequency to the rotation rate at the outer sphere. Filled and empty markers represent self-sustained and transient dynamos, respectively. The black dashed vertical line and arrow indicate the zone in which the fluid is hydrodynamically unstable. The inset represents a 3D plot of the radial velocity (violet and green isosurfaces are the positive and negative values, respectively) and the radial magnetic field (red and blue isosurfaces are the positive and negative values, respectively) in a run at $Pm = 2$ and $N/\Omega_o = 2$. The grey arrow points to the run location in the diagram.

where ρ' is the density perturbation due to the combined effect of the electron fraction and entropy perturbations and

$$N \equiv \sqrt{-\frac{g}{\rho}\left(\left.\frac{\partial\rho}{\partial S}\right|_{P,Y_e}\frac{dS}{dr} + \left.\frac{\partial\rho}{\partial Y_e}\right|_{P,S}\frac{dY_e}{dr}\right)}, \tag{7}$$

is the Brunt-Väisälä frequency with the electron fraction Y_e, and the entropy S, respectively.

In the above equations, we assume that the magnetic diffusivity η, the kinematic viscosity ν, and the "thermal" diffusivity κ are constant. We also assume that the thermal and lepton number diffusivities are equal, which allows us to describe the buoyancy associated with both entropy and lepton number gradients with the use of a single buoyancy variable θ (Guilet et al. 2015).

Apart from the magnetic diffusivity which relates to the electrical conductivity of electrons, the physical interpretation of the other transport coefficients can lead to different estimates, depending on whether neutrinos are considered or not to be the main source of diffusive processes (see Sect. 1.3 of the supplementary materials in Barrère et al. 2023).

Finally, we apply no-slip, electrically insulating, and fixed buoyancy variable boundary conditions on both shells.

2.2. Numerical methods

We use the open source pseudo-spectral code MagIC[1] (Wicht 2002; Gastine & Wicht 2012; Schaeffer 2013) to integrate Eqs. (1)–(5) in 3D spherical geometry. To satisfy the solenoidal conditions (1) and (5), the velocity and magnetic fields are decomposed in poloidal and toroidal components (Mie representation),

$$\rho\mathbf{u} = \nabla\times(\nabla\times W\mathbf{e}_r) + \nabla\times Z\mathbf{e}_r\,, \tag{8}$$
$$\mathbf{B} = \nabla\times(\nabla\times b\mathbf{e}_r) + \nabla\times a_j\mathbf{e}_r\,, \tag{9}$$

where W and Z (b and a_j) are the poloidal and toroidal potentials for the velocity (magnetic) field. The whole system of equations is then solved in spherical coordinates by expanding the scalar potentials in Chebyshev polynomials in the radial direction, and spherical harmonic functions in the angular directions. The time-stepping scheme used is the implicit/explicit Runge-Kutta BPR353 (Boscarino et al. 2013). We refer the reader to the MagIC online documentation[2] for an exhaustive presentation of the numerical techniques.

2.3. Input parameters

The resistivity is controlled by the magnetic Prandtl number $Pm \equiv \nu/\eta$. Though its realistic value in PNSs ($Pm \sim 10^{11}$, Barrère et al. 2023) can not be reached by numerical simulations, we stay in the regime $Pm \geqslant 1$ as we impose $Pm \in [1,4]$. We keep fixed the other dimensionless control parameters: the shell aspect ratio $\chi \equiv r_i/r_o = 0.25$ and width $d \equiv r_o - r_i$, the Ekman number $E \equiv \nu/(d^2\Omega_o) = 10^{-5}$, the thermal Prandtl numbers $Pr \equiv \nu/\kappa = 0.1$, and the Rossby number $Ro \equiv 1 - \Omega_i/\Omega_o = 0.75$, which controls the imposed differential rotation.

The imposed stable stratification is characterized by the Brunt-Väisälä frequency N (Eq. (7)). In our parameter study, the ratio N/Ω_o is varied between 0.1 and 10 and so covers the PNS regime. In practice, this ratio is related to the Rayleigh number $Ra \equiv -(N/\Omega)^2 Pr/E^2$, which is negative in the regime of stable stratification.

The resolution is fixed at $(n_r, n_\theta, n_\phi) = (257, 256, 512)$ for all the runs. A few simulations were rerun with a higher resolution of $(n_r, n_\theta, n_\phi) = (481, 512, 1024)$ but showed no significant change compared to runs with the usual resolution (see Appendix).

The simulations are initialized either from a nearby saturated state or a strong ($B_\phi = 3.4 \times 10^{14}$ G) toroidal axisymmetric field

[1] Commit 2266201a5 on https://github.com/magic-sph/magic

[2] https://magic-sph.github.io

with a dipolar equatorial symmetry, i.e. equatorially symmetric[3] with $l = 2, m = 0$. We define a turbulent resistive time $\bar{\tau}_\eta = \left(\pi r_o/\bar{\ell}\right)^2/\eta \sim 0.2d^2/\eta$, where $\bar{\ell} = 10$ is the typical value of the average harmonic degree of the time-averaged magnetic energy spectrum. In the following, we will term a solution 'transient' when a steady state is sustained for a time interval $\Delta t > 0.3\bar{\tau}_\eta$, and 'stable' for $\Delta t \geqslant \bar{\tau}_\eta$.

We start with the run named 'Ro0.75s' from Barrère et al. (2023), where the stratification is $N/\Omega_o = 0.1$. The saturated state of this dynamo is used to initialise the next simulation with a stronger stratification. The whole set of simulations is initiated similarly using the nearby saturated state of a less stratified run. With this procedure, N/Ω_o is increased gradually in order to study the evolution of the dynamo branch.

2.4. Output parameters

We first characterize our models by computing the time average of the kinetic and magnetic energy densities (after filtering out any initial transient). The latter is expressed in terms of the viscous Elsasser number $\Lambda_\nu \equiv \Lambda/Pm = B^2_{\rm rms}/(4\pi\rho\nu\Omega_o)$ and used to compute different root-mean-square (RMS) estimates of the magnetic field. In addition to the total field, we distinguish the poloidal and toroidal fields based on the Mie representation (Sect. 2.2), while the dipole field refers to the $l = 1$ poloidal component.

3. Results

The following sections gather the different results we obtain from the set of numerical simulations listed in appendix B. We first describe the global dynamics of the dipolar Tayler-Spruit dynamo in the parameter space in Sect. 3.1. Then, we analyse the influence of stratification on the modes of Tayler instability and on the generated axisymmetric magnetic fields in their saturated state in Sect. 3.3 and Sect. 3.4, respectively. We also present the angular momentum transport by both Reynolds and Maxwell stresses due to the dynamo and compare the efficiencies of mixing and angular momentum transport in Sect. 3.5. Finally, we examine a new intermittent behaviour of the Tayler-Spruit dynamo at $N/\Omega_o \geq 2$, which is observed for the first time (see Sect. 3.6).

3.1. Subcritical dynamo sustained at PNS-like stratifications

Fig. 1 shows that a self-sustained Tayler-Spruit dynamo can be maintained up to $N/\Omega_o = 1$ for $Pm = 1$. For stronger stratifications, we have to increase Pm (i.e. decrease the resistivity) to maintain the dynamo. For $Pm = 4$, the stationary state is self-sustained up to $N/\Omega_o = 4$ and we obtained transient states up to $N/\Omega_o = 10$. The self-sustained dynamo is therefore present above the threshold for the fluid to be hydrodynamically stable at $N/\Omega_o \sim 1.5$. This confirms the subcritical nature of the Tayler-Spruit dynamo, which was already observed in previous studies (Petitdemange et al. 2023; Barrère et al. 2023). We did not simulate fluids at greater Pm values for reasons of numerical costs. Given the trend with Pm observed in our simulations as well as theoretical expectations on the Tayler instability threshold, we would expect the Tayler-Spruit dynamo to exist at still higher values of N/Ω for the higher values of Pm relevant to a PNS.

[3] For the choice of these definitions, see Gubbins & Zhang (1993).

3.2. Impact on the differential rotation

The meridional slices of the angular rotation frequency Ω illustrate the impact of stable stratification on the rotation profile: we see that the shear concentrates closer to the inner sphere and increases with N/Ω_o. At the same time, the rotation profile smoothly transits from a quasi-cylindrical to a spherical geometry, which is an effect already observed in stably stratified flows. Analytical and numerical studies of these flows (e.g. Barcilon & Pedlosky 1967a,b,c; Gaurat et al. 2015; Philidet et al. 2020) indicate that this transition is controlled by the dimensionless parameter $Q \equiv Pr(N/\Omega_o)^2$, which varies between 10^{-3} and 10 in our set of runs. The change in the flow geometry is therefore explained by a transition from a case where neither the rotation nor the buoyancy dominate ($E^{2/3} < Q < 1$) to a buoyancy-dominated flow ($Q \gg 1$).

3.3. Impact on the Tayler modes

As seen in Fig. 3, the unstable magnetic modes are located close to the poles where the latitudinal gradient of B_ϕ is positive, which is a first indication of the presence of Tayler modes. To confirm this statement, we use the geometrical criterion of Goossens & Tayler (1980) for the stability of $m = 1$-modes,

$$B_\phi^2\left(1 - 2\cos^2\theta\right) - \sin\theta\cos\theta\frac{\partial B_\phi^2}{\partial\theta} > 0\,. \tag{10}$$

The stability regions displayed by the hatched zones in Fig. 3 match very well regions where the unstable modes are absent. This confirms that the Tayler instability is clearly identifiable, no matter the values of N/Ω_o.

Moreover, the impact of stratification on the mode structure is striking. The stable stratification tends to stabilise displacements in the radial direction, as we can see looking at the non-axisymmetric radial velocity $v_r^{m\neq0}$ field in Fig. 2. As a consequence, the radial length scale of the instability strongly decreases for increasing values of N/Ω_o. This feature is not surprising because Spruit (1999) already constrained the mode maximum radial length scale

$$l_{\rm TI} < l_{{\rm max},N} \equiv r\frac{\omega_{\rm A}}{N}\,, \tag{11}$$

where $\omega_{\rm A} \equiv B_\phi^{m=0}/\sqrt{4\pi\rho r^2}$ is the Alfvén frequency. Note that a lower limit due to resistivity is also predicted

$$l_{\rm TI}^2 > l_{\rm min}^2 \equiv \frac{\eta\Omega_o}{\omega_{\rm A}^2}\,. \tag{12}$$

The length scales measured in our models are compared to these constraints in Fig. 4. Since thermal diffusion can mitigate the effect of stratification, we also define an effective Brunt-Väisälä frequency

$$N_{\rm eff} \equiv N\sqrt{\eta/\kappa} = N\sqrt{Pr/Pm} \tag{13}$$

and so

$$l_{{\rm max},N_{\rm eff}} \equiv r\frac{\omega_{\rm A}}{N_{\rm eff}} \tag{14}$$

to take this effect into account (Spruit 2002). The Tayler modes in our simulations have length scales ranging from $r_o/4 = 3$ km at $N/\Omega_o = 0.1$ to $r_o/80 = 0.15$ km at $N/\Omega_o = 10$. This implies that the Tayler-Spruit dynamo requires higher and higher

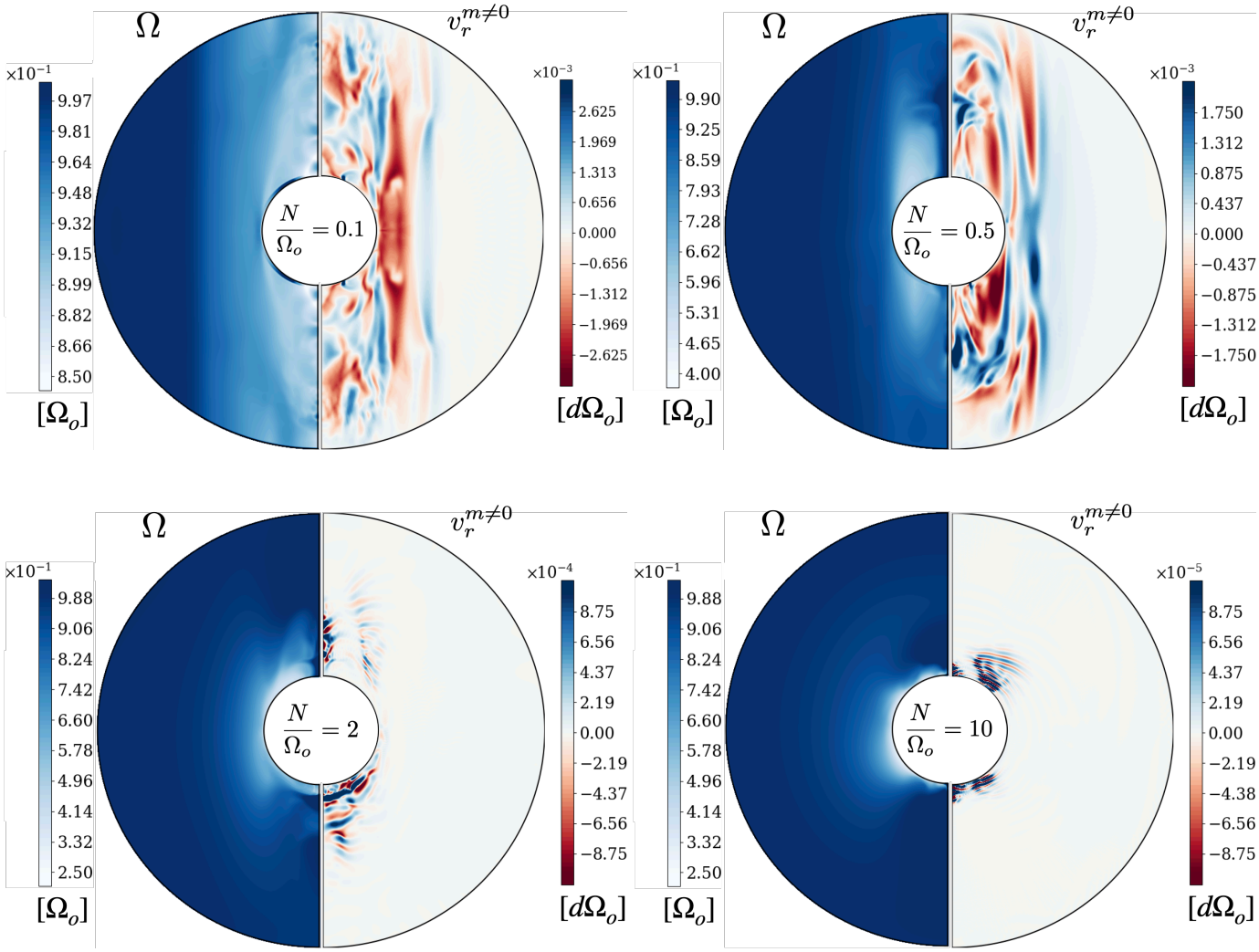

Fig. 2. Meridional slices of the angular frequency and the non-axisymmetric radial velocity (left and right slices respectively) for different values of N/Ω_o. Ω and $v_r^{m\neq0}$ are scaled by Ω_o and $d\Omega_o$, respectively.

resolutions at greater stratifications to be resolved. The measured $l_{\rm TI}$ follows very well the upper limit $l_{{\rm max},N_{\rm eff}}$ (red points in Fig. 4), but is around one order of magnitude larger than $l_{{\rm max},N}$. This demonstrates the importance of including the mitigation of the stratification by diffusion. The minimum length scale $l_{\rm min}$ (Eq. (12)) is almost equal to $l_{\rm TI}$ from $N/\Omega_o = 0.5$ to $N/\Omega = 4$, which indicates that we are close to the instability threshold. For $N/\Omega_o \geqslant 6$, however, $l_{\rm min} \sim 2l_{{\rm max},N_{\rm eff}} \sim 2 - 3l_{\rm TI}$. The fluid is therefore stable, which is consistent with the transient state we find in our simulations. Thus, the analytical limits for the Tayler modes to develop are validated by our numerical simulations and suggest that the Tayler-Spruit dynamo could be maintained for $N/\Omega_o \in [6, 10]$ with $Pm \gtrsim 16 - 36$.

In addition to the decrease of $l_{\rm TI}$, the Tayler instability modes are strongly affected by high values of N/Ω_o. The time and volume averaged spectrum of the magnetic energy in Fig. 5 show that the energy of the large-scale ($l = 1 - 10$) non-axisymmetric modes (solid lines) drop by two orders of magnitude between $N/\Omega = 0.25$ and at $N/\Omega = 2$ compared to the energy of the dominant axisymmetric toroidal component (blue dotted line). This difference is represented more quantitatively by comparing the total non-axisymmetric magnetic field $B_{\rm tot}^{m\neq0}$ to $B_\phi^{m=0}$ in Fig. 6. The ratio drops from ~ 1 to $\sim 2\times10^{-3}$ and follows a power law $B_{\rm tot}^{m\neq0}/B_\phi^{m=0} \propto N_{\rm eff}/\Omega_o^{-1.8\pm0.1}$. Fuller et al. (2019) analytically derived that the ratio between the magnetic field generated by the Tayler instability (noted $\delta B_\perp \sim B_{\rm tot}^{m\neq0}$) and $B_\phi^{m=0}$ follows $\omega_{\rm A}/\Omega_o$. Since $\omega_{\rm A} \propto N_{\rm eff}/\Omega_o^{-1/3}$ (Fuller et al. 2019, and our Sect. 3.4), our simulations therefore do not match the analytical prediction. Fuller et al. (2019) derived the ratio by equating the Tayler instability growth rate and a turbulent damping rate $\omega_{\rm A}^2/\Omega_o \sim \delta v_{\rm A}/r$, where $\delta v_{\rm A} \equiv \delta B_\perp/\sqrt{4\pi\rho}$. As the growth rate of the Tayler instability is robust (Zahn et al. 2007; Ma & Fuller 2019) and well verified in numerical simulations (Ji et al. 2023), our study then questions the prediction of the turbulent damping rate.

3.4. Magnetic field saturation

As in Barrère et al. (2023), we confront the saturated large-scale magnetic fields in our simulations to the analytical predictions. To this end, we first measure the impact of the stratification on the local shear rate q, which influences the magnetic field saturation. Indeed, the rotation profiles of Fig. 2 show that the shear concentrates closer to the inner sphere and increases with N/Ω_o. The quantification of this effect is described in Appendix A. These larger values of q explain the increase of the magnetic energy with N/Ω_o observed in Fig. 1.

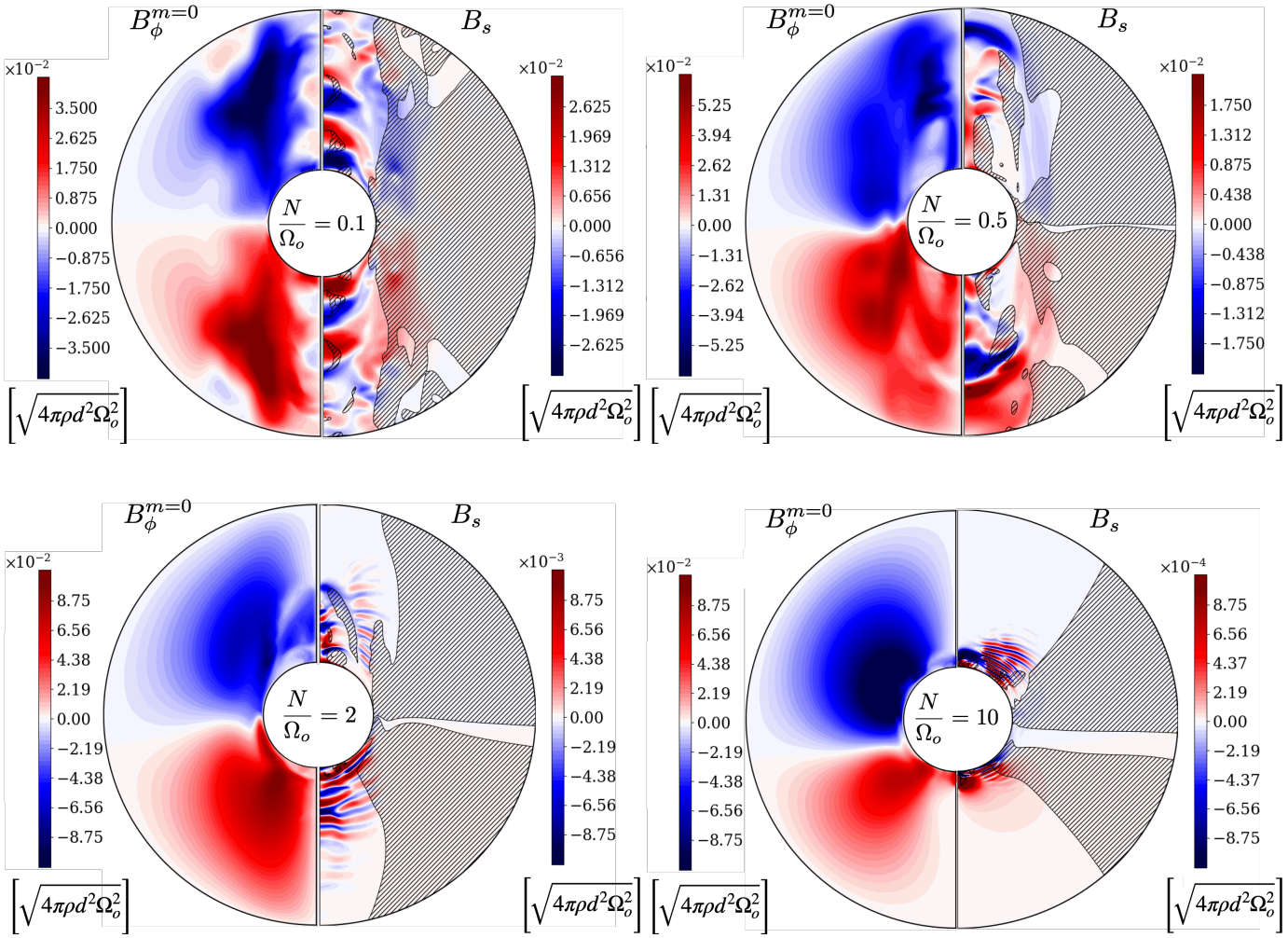

Fig. 3. Meridional slices of the axisymmetric azimuthal and the $s = r\sin\theta$-component of the magnetic field (respective left and right slices) for increasing values of N/Ω_o. The magnetic field is scaled by $\sqrt{4\pi\rho d^2\Omega_o^2}$. The hatched regions represent Tayler-stable zones defined by the geometrical criterion of Goossens & Tayler (1980) (see Supplementary Materials in Barrère et al. (2023)).

In order to study the relation of the magnetic field components with $N_{\rm eff}/\Omega_o$ while taking into account the variation of q, we use the analytical prescriptions derived by Fuller et al. (2019):

$$B_{\rm tor}^{m=0} \sim \sqrt{4\pi\rho r_o^2}\Omega_o \left(\frac{q\Omega_o}{N_{\rm eff}}\right)^{1/3}, \tag{15}$$

$$B_{\rm pol}^{m=0},\, B_{\rm dip} \sim \sqrt{4\pi\rho r_o^2}\Omega_o \left(\frac{q^2\Omega_o^5}{N_{\rm eff}^5}\right)^{1/3}. \tag{16}$$

The exponents of q are all the more robust as they are confirmed by numerical simulations (Barrère et al. 2023). We define dimensionless magnetic field components compensated for the effect of the shear in the following way:

$$B_{\rm tor}^{m=0} \longrightarrow \frac{B_{\rm tor}^{m=0}}{\sqrt{4\pi\rho r_o^2\Omega_o^2}q^{1/3}} \tag{17}$$

$$B_{\rm pol}^{m=0},\, B_{\rm dip} \longrightarrow \frac{B_{\rm pol}^{m=0}}{\sqrt{4\pi\rho r_o^2\Omega_o^2}q^{2/3}}, \frac{B_{\rm dip}}{\sqrt{4\pi\rho r_o^2\Omega_o^2}q^{2/3}}. \tag{18}$$

These compensated dimensionless components are plotted in Fig. 7as a function of $N_{\rm eff}/\Omega_o$. The theoretical scaling laws (dotted black lines) qualitatively match our data. Since the point at $N_{\rm eff}/\Omega_o = 3\times10^{-2}$ diverges from the scalings due to the weaker effect of stable stratification, we exclude it while calculating the best fits. We obtain the following power-laws $B_{\rm tor}^{m=0} \propto (N_{\rm eff}/\Omega_o)^{-0.11\pm0.05}$, $B_{\rm pol}^{m=0} \propto (N_{\rm eff}/\Omega_o)^{-1.1\pm0.2}$, and $B_{\rm dip} \propto (N_{\rm eff}/\Omega_o)^{-1.5\pm0.1}$. While $B_{\rm tor}^{m=0}$ and $B_{\rm pol}^{m=0}$ follow power-laws slightly less steep than predicted in Eqs. (15) and (16), $B_{\rm dip}$ is in good agreement with Eq. (16).

This agreement with the theory is also found for the ratio $B_r^{m=0}/B_\phi^{m=0} \sim \omega_{\rm A}/N_{\rm eff}$ (Spruit 2002; Fuller et al. 2019) as seen in Fig. 8. Our data is fitted by the power law $B_{\rm pol}^{m=0}/B_{\rm tor}^{m=0} \propto (\omega_{\rm A}/N_{\rm eff})^{0.93\pm0.18}$, which is very close to the prediction. On the other hand, the ratio of the magnetic dipole to the axisymmetric toroidal field follows a somewhat steeper scaling law $B_{\rm dip}/B_{\rm tor}^{m=0} \propto (\omega_{\rm A}/N_{\rm eff})^{1.3\pm0.1}$.

3.5. Angular momentum transport and mixing

The angular momentum transport due to the large-scale magnetic field and turbulence in our simulations is also consistent with the theory of Fuller et al. (2019), as shown in Fig. 9. For the Maxwell torque $T_{\rm M}$, we find $B_sB_\phi \propto (N_{\rm eff}/\Omega_o)^{-1.8\pm0.1}$ and $B_s^{m=0}B_\phi^{m=0} \propto (N_{\rm eff}/\Omega_o)^{-1.6\pm0.1}$ depending on whether we take the non-axisymmetric components into account in $T_{\rm M}$. Note that the

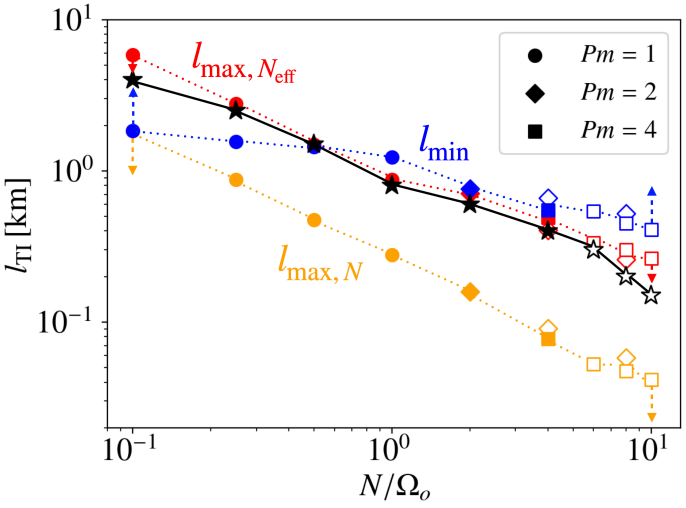

Fig. 4. Length scale of the Tayler instability mode measured in the simulations (black stars) as a function of N/Ω_o. The theoretical lower ($l_{\min}$ in blue) and upper boundaries of the length scale are also plotted using the classical ($l_{\max,N}$ in orange) and the effective ($l_{\max,N_{\rm eff}}$ in red) Brunt-Väisälä frequencies. Filled and empty markers represent self-sustained and transient dynamos, respectively.

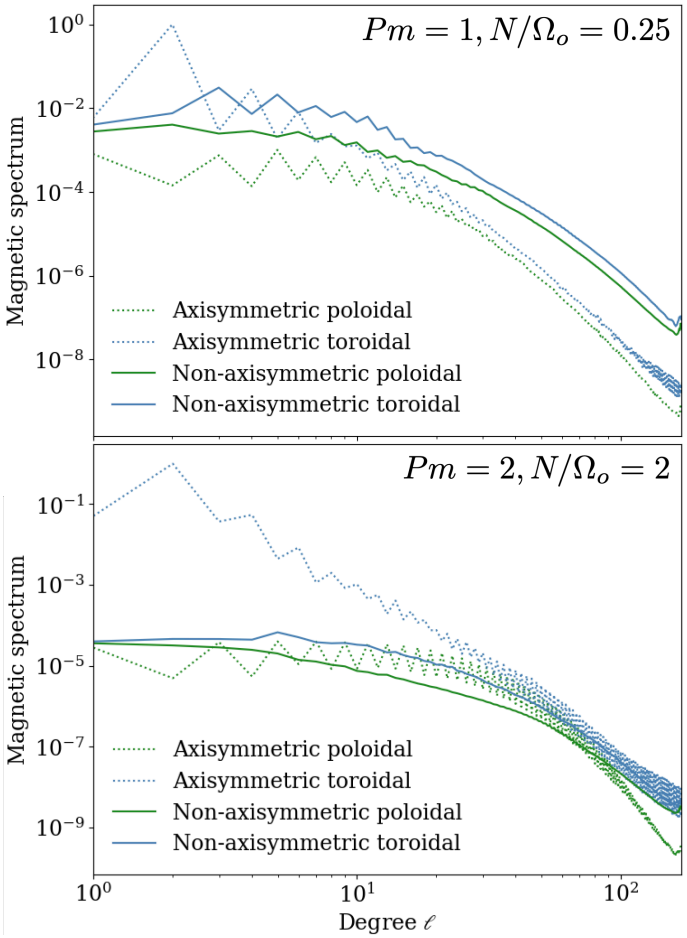

Fig. 5. Time and volume averaged spectra of the magnetic energy for the parameters $Pm = 1, N/\Omega_o = 0.25$ (top) and $Pm = 2, N/\Omega_o = 2$ (bottom). The magnetic energy is normalized by the energy of the dominant $(\ell = 2, m = 0)$-mode of the toroidal component.

torque is more and more dominated by the axisymmetric magnetic fields as $N_{\rm eff}/\Omega_o$ increases. This dominance was assumed by Fuller et al. (2019) and can be expected given the results of Sect. 3.3. The Reynolds torque values are more dispersed as a function of the stratification, but fit the power laws $v_r^{m\neq0}v_\phi^{m\neq0} \propto (N_{\rm eff}/\Omega_o)^{-3.5\pm0.2}$ and $v_r^{m\neq0}v_\phi^{m\neq0} \propto (N_{\rm eff}/\Omega_o)^{-3.4\pm0.2}$. Despite some scattering at high values of $N_{\rm eff}/\Omega_o$ in the points corresponding to transient dynamos, our data therefore follows well the analytical predictions $T_{\rm M} \propto (N_{\rm eff}/\Omega_o)^{-2}$ and $T_{\rm R} \propto (N_{\rm eff}/\Omega_o)^{-10/3}$ (dotted lines in Figs. 9). Moreover, we find $T_{\rm M} \sim 10^2 - 10^3 T_{\rm R}$, so the magnetic field is much more efficient than turbulence at transporting angular momentum.

The mixing processes are also a crucial question in astrophysics, especially in stars. The Tayler-Spruit dynamo is expected to produce a very limited mixing efficiency compared to the angular momentum transport (Spruit 2002; Fuller et al. 2019). To measure this effect in our simulations, we define the effective angular momentum transport diffusivity $\nu_{\rm AM} \equiv T_{\rm M}/(\rho q \Omega_o)$ and roughly approximate the effective mixing diffusivity as $\nu_{\rm mix} \equiv q^{-5/3} v^{m\neq0} l_{\rm TI}$, with the rms turbulent velocity $v^{m\neq0} \equiv \sqrt{E_{\rm kin}^{m\neq0}/(2\rho)}$ calculated from the mean non-axisymmetric energy $E_{\rm kin}^{m\neq0}$. We divide by the power law $q^{5/3}$ in the expression of $\nu_{\rm mix}$ to take into account the variation of q like in Figs 7 and 9.

The ratio $\nu_{\rm mix}/\nu_{\rm AM}$ is plotted in Fig.10 and shows that our data is in fair agreement with the scaling $\nu_{\rm mix}/\nu_{\rm AM} \propto N_{\rm eff}/\Omega_o{}^{-5/3}$ of Fuller et al. (2019). The power law $\nu_{\rm mix}/\nu_{\rm AM} \propto N_{\rm eff}/\Omega_o{}^{-1.2\pm0.2}$ best fits our data, which is mildly less steep than predicted. Moreover, our simulations also confirm that $\nu_{\rm mix}/\nu_{\rm AM} \sim 10^{-6} - 10^{-3} \ll 1$ for Tayler-Spruit dynamo. The use of passive scalars evolving in the velocity field in our simulations could help measure more precisely $\nu_{\rm mix}$ even though the approximation we used is satisfactory as a first analysis.

Table 1 sums up the comparisons we have done between our data and the different scalings derived by Fuller et al. (2019). Our results thus consolidate the validity of Fuller et al. (2019)'s formalism for the saturation of large-scale magnetic fields and angular momentum transport. Besides, our simulations are not compatible with the analytical prescriptions of Spruit (2002), which read

$$B_{\rm tor}^{m=0} \sim \sqrt{4\pi\rho r_o^2}\Omega_o \left(\frac{q\Omega_o}{N_{\rm eff}}\right) \tag{19}$$

$$B_{\rm pol}^{m=0},\ B_{\rm dip} \sim \sqrt{4\pi\rho r_o^2}\Omega_o \left(\frac{q^2\Omega_o^3}{N_{\rm eff}^3}\right) \tag{20}$$

$$T_{\rm M} \sim r_o^2 \Omega_o^2 q^3 \left(\frac{\Omega_o}{N_{\rm eff}}\right)^4 . \tag{21}$$

While our simulations support the scaling law of Fuller et al. (2019), we can also constrain the dimensionless normalisation factor, (noted α in Fuller et al. (2019)), that parametrises the saturated strength of the axisymmetric toroidal magnetic field

$$\frac{B_{\rm tor}^{m=0}}{\sqrt{4\pi\rho r_o^2}} = \alpha\Omega_o \left(\frac{q\Omega_o}{N_{\rm eff}}\right)^{1/3} . \tag{22}$$

We infer the value of α by fitting our data by the theoretical scaling law. The measures are listed in the last column of Table 1 and we find a mean value of $\alpha \sim 10^{-2}$. This value is small compared to those inferred by adjusting α in 1D stellar evolution models to the asteroseismic observations of sub-/red giants, which is $\sim 0.25 - 1$ (Fuller et al. 2019; Fuller & Lu 2022; Eggenberger et al. 2019b). Either way, our numerical simulations provide a

Table 1. Table that sums up the theoretical and measured scaling laws of the different quantities discussed in Sects. 3.4 and 3.5, and the dimensionless normalisation factor α defined by Fuller et al. (2019) (see Eq. 22)

Quantity (dimensionless)	Fuller et al. (2019)'s scaling law	Best fit exponent	α
$B_{\rm tot}^{m\neq0}/B_{\rm tor}^{m\neq0}$	$\omega_{\rm A}/\Omega_o$	$(N_{\rm eff}/\Omega_o)^{-0.18\pm0.1}$	
$B_{\rm tor}^{m=0}/(\sqrt{4\pi\rho r_o^2\Omega_o^2}q^{1/3})$	$\alpha(N_{\rm eff}/\Omega_o)^{-1/3}$	$(N_{\rm eff}/\Omega_o)^{-0.11\pm0.05}$	0.017 ± 0.001
$B_{\rm pol}^{m=0}/(\sqrt{4\pi\rho r_o^2\Omega_o^2}q^{2/3})$	$\alpha^2(N_{\rm eff}/\Omega_o)^{-5/3}$	$(N_{\rm eff}/\Omega_o)^{-1.1\pm0.2}$	0.009 ± 0.002
$B_{\rm dip}/(\sqrt{4\pi\rho r_o^2\Omega_o^2}q^{2/3})$	$\alpha^2(N_{\rm eff}/\Omega_o)^{-5/3}$	$(N_{\rm eff}/\Omega_o)^{-1.5\pm0.1}$	0.007 ± 0.001
$B_{\rm pol}^{m=0}/B_{\rm tor}^{m=0}$	$\omega_{\rm A}/N_{\rm eff}$	$(\omega_{\rm A}/N_{\rm eff})^{0.93\pm0.2}$	—
$B_{\rm dip}/B_{\rm tor}^{m=0}$	$\omega_{\rm A}/N_{\rm eff}$	$(\omega_{\rm A}/N_{\rm eff})^{1.3\pm0.1}$	—
$B_sB_\phi/(4\pi\rho r_o^2\Omega_o^2q)$	$\alpha^3(N_{\rm eff}/\Omega_o)^{-2}$	$(N_{\rm eff}/\Omega_o)^{-1.8\pm0.1}$	0.016 ± 0.004
$B_s^{m=0}B_\phi^{m=0}/(4\pi\rho r_o^2\Omega_o^2q)$	$\alpha^3(N_{\rm eff}/\Omega_o)^{-2}$	$(N_{\rm eff}/\Omega_o)^{-1.6\pm0.1}$	0.01 ± 0.004
$v_r^{m\neq0}v_\phi^{m\neq0}/(r_o^2\Omega_o^2q^{5/3})$	$(N_{\rm eff}/\Omega_o)^{-10/3}$	$(N_{\rm eff}/\Omega_o)^{-3.5\pm0.2}$	—
$v_s^{m\neq0}v_\phi^{m\neq0}/(r_o^2\Omega_o^2q^{5/3})$	$(N_{\rm eff}/\Omega_o)^{-10/3}$	$(N_{\rm eff}/\Omega_o)^{-3.4\pm0.2}$	—
$\nu_{\rm mix}/\nu_{\rm AM}$	$(N_{\rm eff}/\Omega_o)^{-5/3}$	$(N_{\rm eff}/\Omega_o)^{-1.2\pm0.2}$	—

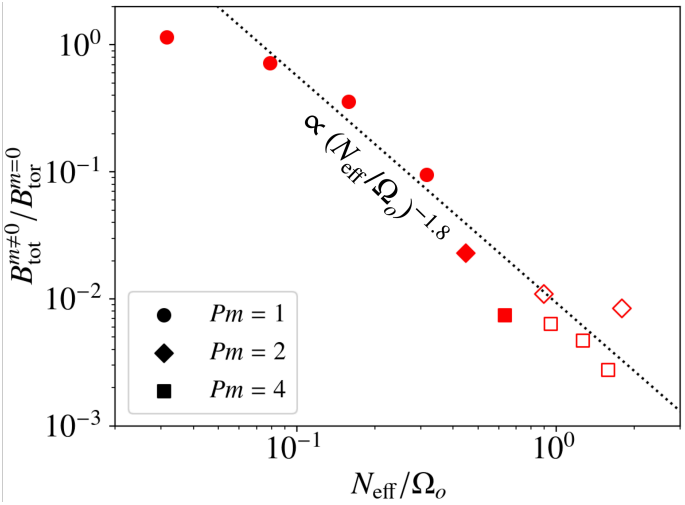

Fig. 6. Ratio of the RMS non-axisymmetric magnetic field to the RMS axisymmetric toroidal magnetic field. The dotted line shows the best fit for a power law of $N_{\rm eff}/\Omega_o$. Filled and empty markers represent self-sustained and transient dynamos, respectively.

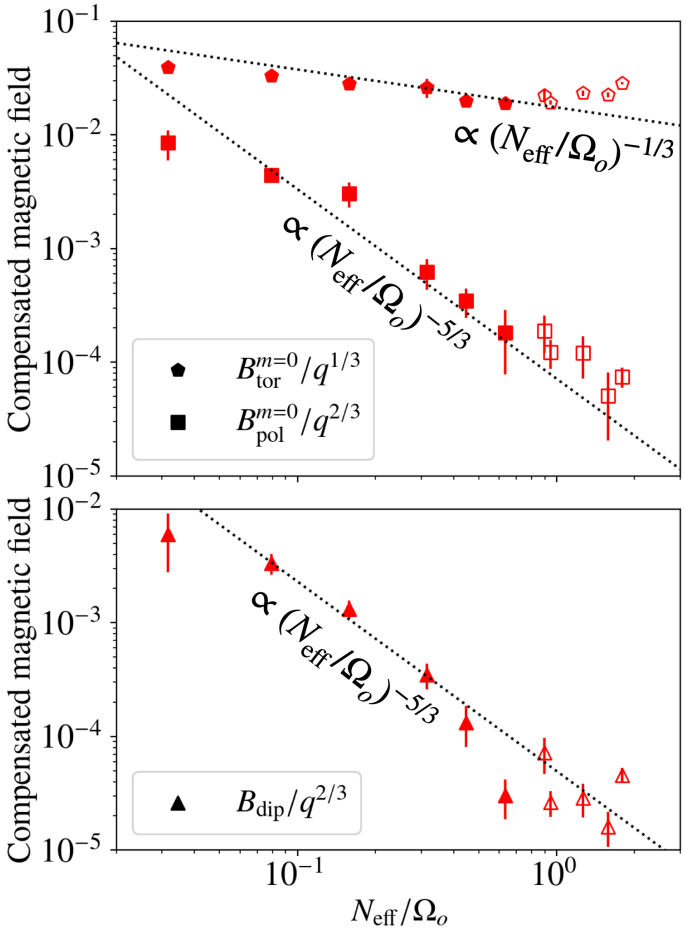

Fig. 7. RMS toroidal and poloidal axisymmetric magnetic fields (top), and RMS magnetic dipole (bottom) compensated with the measured shear rate as a function of the ratio between the effective Brunt-Väisälä frequency to the rotation rate at the outer sphere $N_{\rm eff}/\Omega_o$. The magnetic field is rendered dimensionless and compensated for the effect of the shear using Eqs. (17) and (18). Dotted lines show the best fits of the data with Fuller's theoretical scaling laws (Eqs. (15) and (16)) within a multiplying factor. Filled and empty markers represent self-sustained and transient dynamos, respectively.

more physically motivated value of α that could be implemented in 1D stellar evolution codes including the Tayler-Spruit dynamo to transport angular momentum.

3.6. Intermittency

When $N/\Omega_o \geq 2$, we find that the Tayler-Spruit dynamo displays an intermittent behaviour, which is clearly visible in the time series of Fig. 11 where the non-axisymmetric magnetic energy drops and increases cyclically by two orders of magnitude. This corresponds to the loss and growth of the Tayler instability. The same cycle also occurs for the axisymmetric B_r and B_θ, which illustrates the loss of the dynamo. Those two cycles show a very short lag of ~ 2.4 s. We then notice that the oscillations of the axisymmetric toroidal and poloidal magnetic energies are in antiphase. This is also observed in the butterfly diagrams in which B_ϕ decreases locally, and so in the volume average when

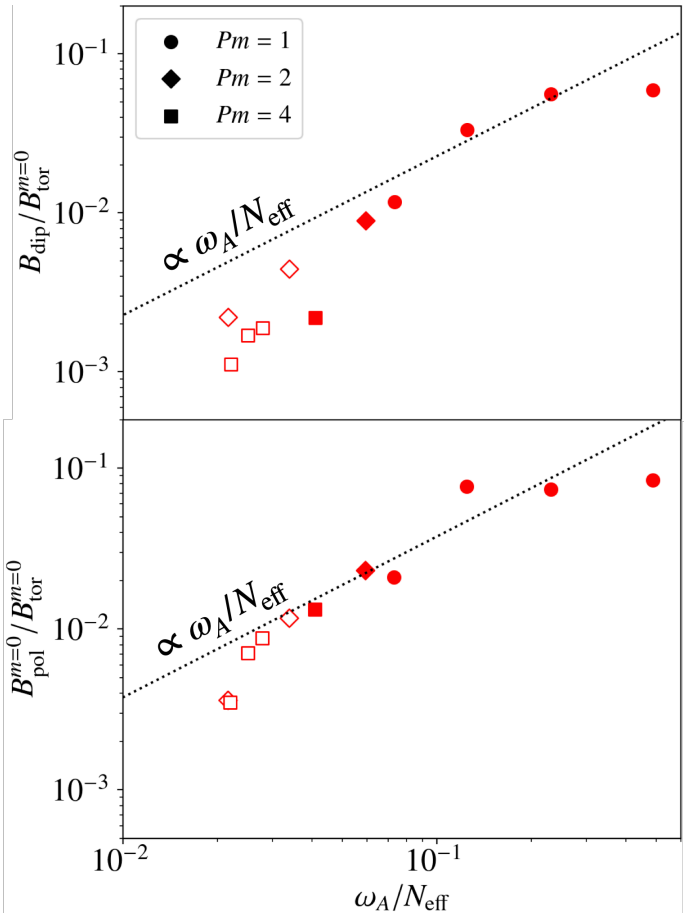

Fig. 8. Ratio between the RMS axisymmetric poloidal (top) and the RMS dipolar (bottom) magnetic fields to the axisymmetric toroidal magnetic field. Dotted lines show the best fits of the data with Fuller's theoretical scaling law $B_r/B_\phi \sim \omega_{\rm A}/N_{\rm eff}$ within a multiplying factor. Filled and empty markers represent self-sustained and transient dynamos, respectively.

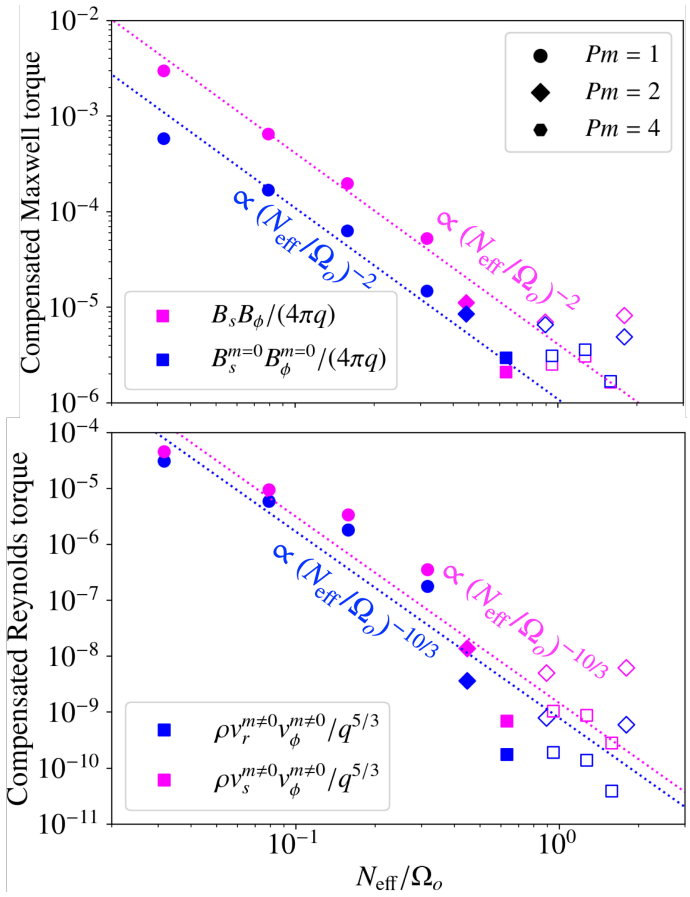

Fig. 9. RMS Maxwell (top) and Reynolds (bottom) torques compensated with the measured shear rate as a function of the ratio between the effective Brunt-Väisälä frequency to the rotation rate at the outer sphere. Dotted lines shows the best fits obtained with Fuller's theoretical scaling laws. Filled and empty markers represent self-sustained and transient dynamos, respectively.

B_r is the strongest. These cycles can be interpreted qualitatively as follows:

(i) $B_\phi^{m=0}$ is close but above the critical strength for the Tayler instability derived by combining Eqs. (14) and (12)

$$B_{\phi,\rm c}^{m=0} \equiv \sqrt{4\pi\rho r_o^2}\Omega_o \left(\frac{N_{\rm eff}}{\Omega_o}\right)^{1/2} \left(\frac{\eta}{r_o^2\Omega_o}\right)^{1/4} \tag{23}$$

and the dynamo is acting to generate $B_r^{m=0}$;

(ii) $B_\phi^{m=0}$ decreases slightly below the critical strength due to turbulent dissipation, which kills the Tayler instability and so the dynamo loop ;

(iii) the axisymmetric poloidal magnetic energy drops and the axisymmetric toroidal component increases because of the winding and the lack of turbulent dissipation ;

(iv) $B_\phi^{m=0}$ exceeds the critical strength and the dynamo is active again.

An intermittent Tayler-Spruit dynamo was already proposed by Fuller & Lu (2022) to explain the angular momentum transport in stellar stellar radiative regions with a low shear.

Quantitatively, we find $B_{\phi,\rm c}^{m=0} \sim 1.4 - 2.1 \times 10^{15}$ G for the models with $N/\Omega_o \in [2, 10]$, which is very close to the maximum values $B_\phi^{m=0} \sim 2.5 - 3 \times 10^{15}$ G measured in the same models. The proximity to the instability threshold supports our interpretation. To characterise the time evolution of the intermittency, we measure its duty cycle $\alpha_{\rm cyc}$, i.e. the ratio of the time when the dynamo is active to the period of the cycle. We find that it varies between 0.38 and 0.66, with a tendency to decrease with N/Ω_o as seen in Fig. 12. The same trend is observed for the period of these cycles $P_{\rm cyc}$, which ranges between 3 s and 30 s. This is consistent with the fact that we get closer to the dynamo threshold.

4. Application to magnetar formation

The previous analyses support the formalism of Fuller et al. (2019), which was used to model our magnetar formation scenario in Barrère et al. (2022). To compare our numerical simulations to this model, the magnetic field is converted into physical units by fixing the following parameters to typical values in PNSs: the PNS radius $r_o = 12$ km, mass $M = 1.4\,{\rm M}_\odot$ that corresponds to a constant PNS density of $\rho \sim 4.1 \times 10^{14}\,{\rm g\,cm^{-3}}$, and Brunt-Väisälä frequency $N = 1$ kHz. We therefore obtain the magnetic field strength of $B_{\rm tor}^{m=0}$, $B_{\rm pol}^{m=0}$ and $B_{\rm dip}$ as a function of the angular frequency of the outer sphere, which is displayed in Fig. 13.

The red markers correspond to the magnetic field measured in the simulations, while the blue markers correspond to the values extrapolated to $q = 1$. This plot is similar to Fig. 5 in Barrère

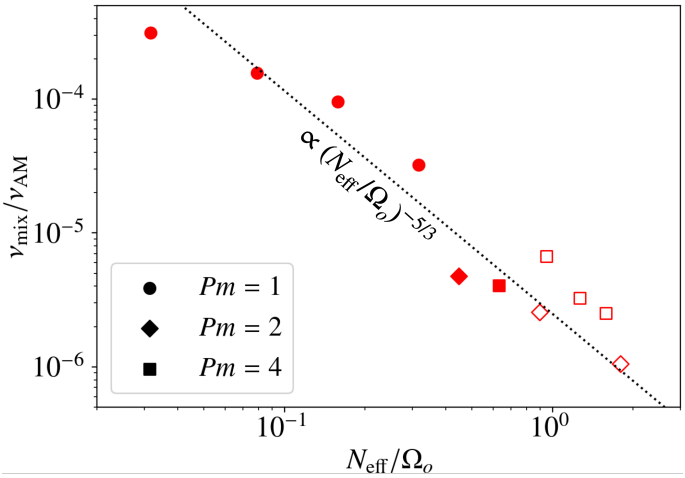

Fig. 10. Ratio of the effective mixing diffusivity $\nu_{\rm mix}$ to the effective angular momentum diffusivity $\nu_{\rm AM}$ as a function of $N_{\rm eff}/\Omega_o$. Filled and empty markers represent self-sustained and transient dynamos, respectively.

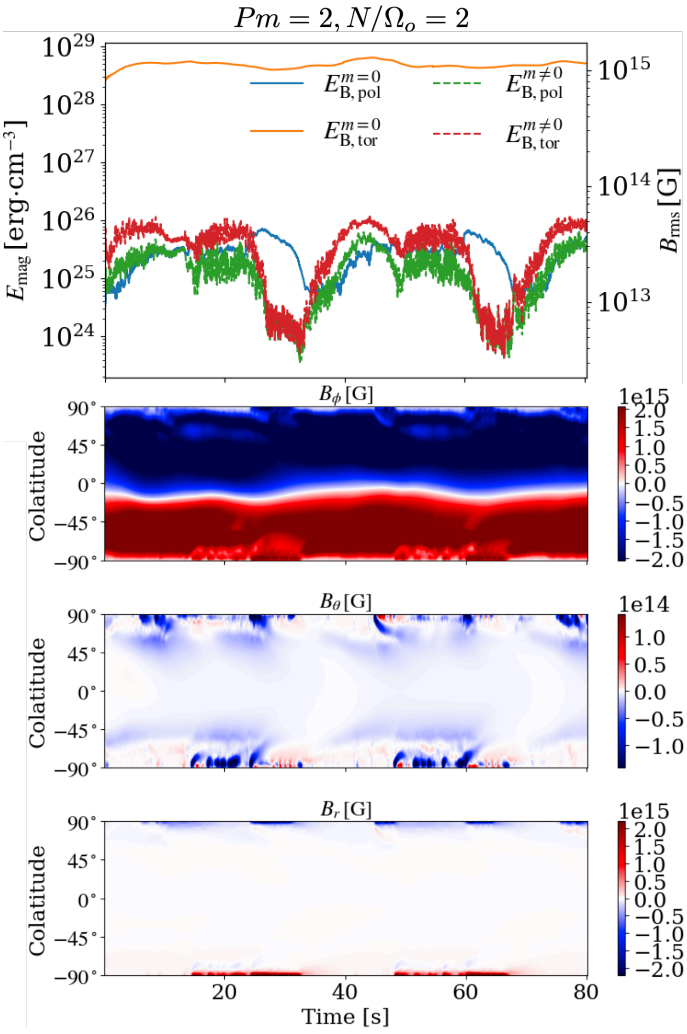

Fig. 11. Top: Time series of the magnetic energy. Bottom: Butterfly diagram showing the latitudinal structure time evolution of different axisymmetric magnetic field components averaged between the radii $r = 5$ and $r = 6$ km. The magnetic energy was converted to physical units by fixing $N = 10^{-3}$ s^{-1}

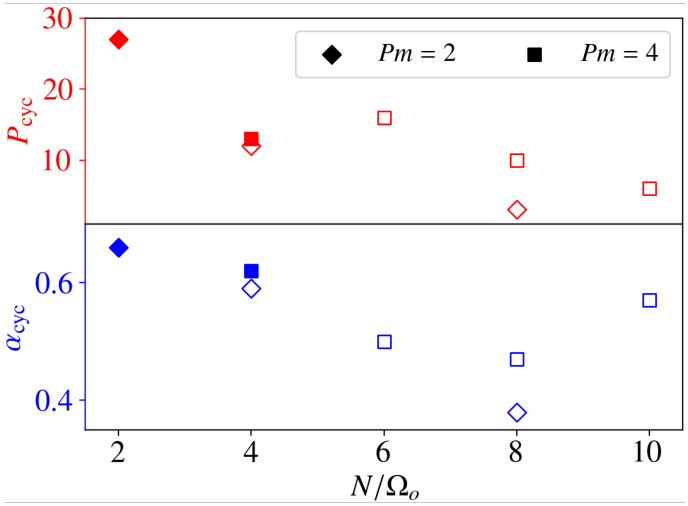

Fig. 12. Period of the cycle $P_{\rm cyc}$ (top) and the duty cycle $\alpha_{\rm cyc}$ (bottom) of the intermittent dynamo as a function of the input N/Ω_o. Filled and empty markers represent self-sustained and transient dynamos, respectively.

et al. (2022), except that we define, here, a low-field magnetar as a magnetar with $B^{m=0}_{\rm tor} \geqslant 10^{14}$ G but $B_{\rm dip} < 4.4 \times 10^{13}$ G. Since considering the changes of q is equivalent to set $q = 1$, we can compare our numerical results to Barrère et al. (2022). As shown in the previous sections, the magnetic field follows well Fuller et al. (2019)'s scaling law for Ω_o. However, the saturated magnetic field in our simulations is $\sim$ 17 times weaker than in the model in Barrère et al. (2022), which shifts the upper limit of rotation period to form magnetar-like magnetic fields to $P \sim 6$ ms. This new limit corresponds to a lower accreted fallback mass limit of $\sim 5 \times 10^{-2}$ M$_\odot$, which is still consistent with recent supernova simulations (see the discussion in Barrère et al. 2022).

For rotation periods longer than 6 ms, the magnetic dipole is too weak for a classical magnetar but the Tayler-Spruit dynamo still produces strong total magnetic fields above 10^{14} G. The observations of absorption lines in the X-ray spectra of low-field magnetars (Tiengo et al. 2013; Rodríguez Castillo et al. 2016) and 3D numerical simulations of magnetic field long-term evolution in NSs (Igoshev et al. 2021) suggest that this is enough to produce magnetar-like luminous activity.

5. Discussion

Here, we discuss the simplifications we used for the modelling of the PNS interior evolution: the mechanism to force the differential rotation (Sect. 5.1) and the Boussinesq approximation (Sect. 5.2). In Sect. 5.3, we finally compare our results on the Tayler-Spruit dynamo (Barrère et al. 2023, this article) and the Tayler-Spruit dynamo obtained in other numerical simulations (Petitdemange et al. 2023; Daniel et al. 2023; Petitdemange et al. 2024).

5.1. Forcing of the differential rotation

To force the differential rotation, we chose to use a spherical Taylor-Couette configuration, in which a constant rotation rate is imposed on both inner and outer spheres. In this setup, the rotation profile is free to evolve as the angular momentum is transported by turbulence and large-scale magnetic fields. The

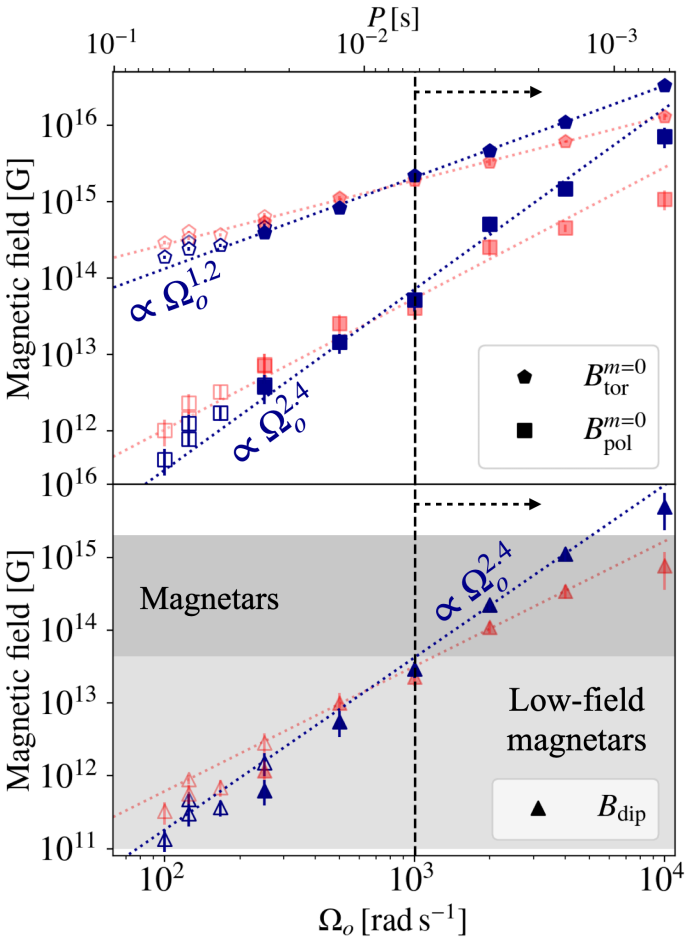

Fig. 13. Magnetic strength of the axisymmetric toroidal $B_{\rm tor}^{m=0}$ (pentagons) and poloidal $B_{\rm pol}^{m=0}$ (squares) components (upper panel), as well as that of the magnetic dipole $B_{\rm dip}$ (triangles, lower panel) as a function of the angular frequency of the outer sphere, which represents the PNS surface. The red markers correspond to the magnetic field measured in the simulations, while the blue markers correspond to the values extrapolated to $q = 1$. The dotted lines are the best power-law fit of the data. The dark and light grey regions represent the range of magnetic field for classical magnetars ($B_{\rm dip} \geqslant 4.4 \times 10^{13}$ G) and low-field magnetars ($B_{\rm tor}^{m=0} \geqslant 10^{14}$ G). The black dashed line and arrow illustrate the rotation period below which the dynamo can form classical magnetar-like magnetic fields. Filled and empty markers represent self-sustained and transient dynamos, respectively.

imposed rotation of the outer sphere roughly mimics the maintenance of the surface rotation due to fallback accretion, once the PNS surface is already spun up significantly. However, the rotation profile evolution does not describe the beginning of the accretion during which the surface is spun up and the differential rotation, first concentrated close to the surface, is transported in the PNS interior.

Maintaining the rotation on both spheres allows us to inject energy into the flow and try to control the shear rate. As noticed in Sect. 3.4 and quantified in App. A, the stable stratification however significantly changes the shear rate. This complicates the measure of the respective scaling exponents with N/Ω_o and q independently. In addition, we observe in Fig. 2 that most of the shear is concentrated closer and closer to the inner sphere. As confirmed by our simulations, this restricts significantly the domain in which the Tayler-Spruit dynamo can operate and participate to make the dynamo more difficult to sustain. Thus, to investigate stronger stratification regimes, it will be necessary to change the forcing method and perhaps opt for a volumetric forcing as used for instance by Meduri et al. (2024).

5.2. Validity of the Boussinesq approximation

To model the PNS interior, we used the Boussinesq approximation, which reduces the numerical cost and allows us to produce a few tens of models to better understand the physics of the Tayler-Spruit dynamo. Despite the importance of the density gradient, this approximation is reasonable in the case of PNS interior:

(i) The sound speed is close to the speed of light $c_s \sim 10^{10}\,{\rm cm\,s^{-1}}$ (Hüdepohl 2014; Pascal 2021, private communication), so $v_{\rm A}/c_s \lesssim v_\phi/c_s \lesssim 10^{-2}$, where $v_a \equiv r_o\omega_{\rm A}$ and v_ϕ are the typical Alfvén and azimuthal speeds.
(ii) The density perturbation associated to the buoyancy term is small compared to the PNS mean density: $\delta\rho/\rho = \theta N^2/g \lesssim 9 \times 10^{-2}$, with $N = 10^3\,{\rm s^{-1}}$, $g \sim GM/r_o \sim 1.3 \times 10^{13}\,{\rm cm\,s^{-2}}$, and $\theta \lesssim r_o$ is the buoyancy variable (Eq. 6).

The impact of density gradient on the Tayler-Spruit dynamo has never been investigated so far in numerical simulations. Therefore, future work should consider more realistic PNS density profiles.

5.3. Comparison with other numerical models

In the literature, only a few other studies investigate numerically the Tayler-Spruit dynamo (Petitdemange et al. 2023; Petitdemange et al. 2024; Daniel et al. 2023). The main difference between our setup and theirs is the opposite shear, i.e. in their setup the inner boundary rotates faster than the outer one. As in our studies, they find a subcritical bifurcation at the Tayler instability threshold to a self-sustained state with a dominant axisymmetric toroidal magnetic field. However, many differences can be noticed:

- The generated magnetic structure in their simulations has a smaller scale and is localized near the inner sphere in the equatorial plane. The impact of stable stratification on the length scale of these modes may deserve a deeper analysis. It is still unclear why this configuration is stable for one sign of the shear and not the other.
- As in Barrère et al. (2023), a hemispherical dynamo solution is also found by Petitdemange et al. (2024) as they move from a laminar dynamo solution to the strong Tayler-Spruit dynamo by increasing N/Ω_o. However, they do not find bistability between the hemispherical and the strong solutions as in Barrère et al. (2023).
- While the dipolar and hemispherical dynamos we found in Barrère et al. (2023) are in good agreement with the predictions of Fuller et al. (2019) and Spruit (2002), respectively, all their models, including those of the hemispherical solution, are in agreement with the analytical model of Spruit (2002).

Therefore, the few numerical studies of the Tayler-Spruit dynamo indicate a much more complex physics than anticipated analytically, with the existence of a wide variety of dynamo solutions. So far, only Daniel et al. (2023) propose a non-linear model of the subcritical transition to the Tayler-Spruit dynamo of Petitdemange et al. (2023). In order to include the other solutions we discovered, we must further investigate the dynamics of the dynamo using tools from dynamic system theory.

6. Conclusions

6.1. Summary

Following our previous study Barrère et al. (2023), we performed numerical simulations of the dipolar Tayler-Spruit dynamo to investigate how it behaves in the stratification regime of PNSs. We first show that a self-sustained dynamo is maintained in this regime for $N/\Omega_o \leqslant 4$. With increasing N/Ω_o, on the one hand, the Tayler modes have reduced radial length scales as expected theoretically, but their energy decreases faster than predicted by Fuller et al. (2019), which may indicate an underestimation of the turbulent dissipation. On the other hand, the large-scale magnetic fields generated by the dynamo are in good agreement with the analytical work of Fuller et al. (2019).

The overall agreement is also observed for both Maxwell and Reynolds torques, the former of which dominates the angular momentum transport. By measuring an approximate mixing diffusivity, we also determined the efficiency of the mixing process due to the Tayler-Spruit dynamo and found that mixing is far less efficient than the angular momentum transport, as predicted theoretically. We also constrained for the first time the dimensionless normalisation factor $\alpha \sim 10^{-2}$, which is much weaker than expected to explain the rotation rate of sub-/red giant cores. Finally, our simulations demonstrate for the first time that the Tayler-Spruit dynamo can become intermittent as the saturated $B_\phi^{m=0}$ is close to the Tayler instability threshold.

To conclude the investigation, we applied our numerical results to the magnetar formation scenario of Barrère et al. (2022). While our data follow the theoretical scaling law, the lower limit of the angular frequency to form classical magnetar-like dipoles is larger than derived in Barrère et al. (2022) with a period of ~ 6 ms. This rotation period corresponds to an accreted fallback mass of $\sim 5 \times 10^{-2}\,M_\odot$, which is still reasonable according to CCSN simulations (e.g. Sukhbold et al. 2016, 2018; Chan et al. 2020; Janka et al. 2022).

6.2. Long-term evolution of the magnetic field

After ~ 100 s, the fallback accretion becomes too weak to maintain the differential rotation in the PNS. The newly formed strong large-scale magnetic fields transport the angular momentum efficiently, which damps the differential rotation and the dynamo will eventually stop. The magnetic field is expected to enter a relaxation phase in which its structure changes to reach a stable configuration. The exact shape of this magnetic field is still an open question and, more generally, the magnetic relaxation problem in astrophysics remains debated (e.g. Braithwaite 2006; Duez & Mathis 2010; Duez et al. 2010; Akgün et al. 2013; Becerra et al. 2022a,b). It is however well acknowledged that the magnetic configuration is complex, mixing both large-scale poloidal and toroidal components. Thus, 3D numerical simulations including rotation and thermal/density stratifications are required to investigate this stage of the PNS evolution.

On longer timescales of $\sim 1 - 100$ kyr, the remaining strong toroidal magnetic fields located in the NS crust are prone to Hall diffusion and instability (Rheinhardt & Geppert 2002), which modifies their structures and so can influence the magnetar emission. The strong magnetic field-induced stresses could also cause failures or plastic deformations, which are suspected to explain the origin of magnetar bursts (e.g. Thompson & Duncan 1995; Perna & Pons 2011; Lander et al. 2015; Lander & Gourgouliatos 2019). It is therefore crucial to run 3D numerical simulations of magnetic field evolution in a NS structure using dynamo-generated initial magnetic configuration to better constrain these properties. Further investigations could also include the relaxation of the dynamo-generated magnetic field to a stable configuration before the PNS becomes a cooled stable NS.

6.3. Interaction with a remaining fallback disc

The magnetic dipole generated by the dipolar Tayler-Spruit dynamo may not be strong enough to spin the magnetar down to the observed $8 - 12$ s via the magnetic spin-down mechanism. A good alternative would be the propeller mechanism (e.g. Gompertz et al. 2014; Beniamini et al. 2019; Lin et al. 2021; Ronchi et al. 2022). This operates when the magnetosphere is large enough to interact with the remaining fallback disc, i.e. when the Alfvén radius is larger than the corotation radius. In the propeller regime, the inner disk matter is accelerated to super-Keplerian velocity, which produces an outflow and so an angular momentum transfer from the magnetar to the disc. If this mechanism operates in some magnetars, the magnetic dipole which is inferred from the values of the NS rotation period and its associated derivative will be overestimated. It thus fosters numerical studies of the fallback matter in 3D simulations of core-collapse SNe and investigations on the evolution of the potential remaining disc. This will help constrain which progenitors are the best candidates to form magnetars via our fallback scenario.

6.4. Implications for stellar physics

Our findings are also of importance for the study of stellar radiative zones. Indeed, the scaling laws and the dimensionless normalisation factor α derived from our simulations could be implemented in 1D stellar evolution codes. Evolution models using the prescriptions of Fuller et al. (2019) have already been computed for sub-giant/red giant stars but with larger values of $\alpha \sim 0.25 - 1$. These studies find a strong flattening of the rotation profile and conclude that the prescribed Tayler-Spruit dynamo can not explain both rotation profiles of sub-giant and red giant stars (Eggenberger et al. 2019b), which suggests that different angular momentum transport mechanisms occur during these two phases (Eggenberger et al. 2019a). The future asteroseismic measurements of the magnetic fields in stellar interiors with PLATO will be crucial to clarify the question of the transport mechanisms. Though the first measurements of magnetic fields in some red giant cores suggest a strong fossil field (Li et al. 2022, 2023; Deheuvels et al. 2023), it will be essential to infer the asteroseismic signature of magnetic fields generated by the simulated Tayler-Spruit dynamos for the future observations. Evolution models including MHD instabilities effects were also performed in the case of massive stars to constrain the rotation rate of the remaining PNS or black hole (Griffiths et al. 2022; Fuller & Lu 2022). They suggest that the angular momentum transport by MHD instabilities is significant in every stage of the massive star evolution. This stresses the importance of performing 3D anelastic simulations with realistic background profiles of radiative zones at different evolution stages to better constrain the angular momentum transport and infer more robust rotation rates of stellar cores.

Acknowledgements. This work was supported by the European Research Council (MagBURST grant 715368), and the PNPS and PNHE programs of CNRS/INSU, co-funded by CEA and CNES. Numerical simulations have been carried out at the CINES on the Jean-Zay supercomputer and at the TGCC on the supercomputer IRENE-ROME (DARI project A130410317).

References

Akgün, T., Reisenegger, A., Mastrano, A., & Marchant, P. 2013, MNRAS, 433, 2445
Barcilon, V. & Pedlosky, J. 1967a, Journal of Fluid Mechanics, 29, 1–16
Barcilon, V. & Pedlosky, J. 1967b, Journal of Fluid Mechanics, 29, 673–690
Barcilon, V. & Pedlosky, J. 1967c, Journal of Fluid Mechanics, 29, 609–621
Barrère, P., Guilet, J., Raynaud, R., & Reboul-Salze, A. 2023, MNRAS, 526, L88
Barrère, P., Guilet, J., Reboul-Salze, A., Raynaud, R., & Janka, H. T. 2022, A&A, 668, A79
Becerra, L., Reisenegger, A., Valdivia, J. A., & Gusakov, M. 2022a, MNRAS, 517, 560
Becerra, L., Reisenegger, A., Valdivia, J. A., & Gusakov, M. E. 2022b, MNRAS, 511, 732
Beniamini, P., Hotokezaka, K., van der Horst, A., & Kouveliotou, C. 2019, MNRAS, 487, 1426
Bochenek, C. D., Ravi, V., Belov, K. V., et al. 2020, Nature, 587, 59
Boscarino, S., Pareschi, L., & Russo, G. 2013, SIAM Journal on Scientific Computing, 35, A22
Braithwaite, J. 2006, A&A, 449, 451
Bugli, M., Guilet, J., Foglizzo, T., & Obergaulinger, M. 2023, MNRAS, 520, 5622
Bugli, M., Guilet, J., & Obergaulinger, M. 2021, MNRAS, 507, 443
Bugli, M., Guilet, J., Obergaulinger, M., Cerdá-Durán, P., & Aloy, M. A. 2020, MNRAS, 492, 58
Burrows, A., Dessart, L., Livne, E., Ott, C. D., & Murphy, J. 2007, ApJ, 664, 416
Cantiello, M., Mankovich, C., Bildsten, L., Christensen-Dalsgaard, J., & Paxton, B. 2014, ApJ, 788, 93
Chan, C., Müller, B., & Heger, A. 2020, MNRAS, 495, 3751
CHIME/FRB Collaboration, Andersen, B. C., Bandura, K. M., et al. 2020, Nature, 587, 54
Coti Zelati, F., Borghese, A., Rea, N., et al. 2021, The Astronomer's Telegram, 14674, 1
Coti Zelati, F., Rea, N., Pons, J. A., Campana, S., & Esposito, P. 2018, MNRAS, 474, 961
Daniel, F., Petitdemange, L., & Gissinger, C. 2023, Physical Review Fluids, 8, 123701
Deheuvels, S., Ballot, J., Beck, P. G., et al. 2015, A&A, 580, A96
Deheuvels, S., Doğan, G., Goupil, M. J., et al. 2014, A&A, 564, A27
Deheuvels, S., Li, G., Ballot, J., & Lignières, F. 2023, A&A, 670, L16
den Hartogh, J. W., Eggenberger, P., & Deheuvels, S. 2020, A&A, 634, L16
Dessart, L., Burrows, A., Livne, E., & Ott, C. D. 2008, ApJ, 673, L43
Dessart, L., Hillier, D. J., Waldman, R., Livne, E., & Blondin, S. 2012, MNRAS, 426, L76
Drout, M. R., Soderberg, A. M., Gal-Yam, A., et al. 2011, ApJ, 741, 97
Duez, V., Braithwaite, J., & Mathis, S. 2010, ApJ, 724, L34
Duez, V. & Mathis, S. 2010, A&A, 517, A58
Duncan, R. C. & Thompson, C. 1992, ApJ, 392, L9
Eggenberger, P., Deheuvels, S., Miglio, A., et al. 2019a, A&A, 621, A66
Eggenberger, P., den Hartogh, J. W., Buldgen, G., et al. 2019b, A&A, 631, L6
Eggenberger, P., Maeder, A., & Meynet, G. 2005, A&A, 440, L9
Evans, W. D., Klebesadel, R. W., Laros, J. G., et al. 1980, ApJ, 237, L7
Ferrario, L. & Wickramasinghe, D. 2006, MNRAS, 367, 1323
Fuller, J. & Lu, W. 2022, MNRAS, 511, 3951
Fuller, J., Piro, A. L., & Jermyn, A. S. 2019, MNRAS, 485, 3661
Gastine, T. & Wicht, J. 2012, Icarus, 219, 428
Gaurat, M., Jouve, L., Lignières, F., & Gastine, T. 2015, A&A, 580, A103
Gehan, C., Mosser, B., Michel, E., Samadi, R., & Kallinger, T. 2018, A&A, 616, A24
Gompertz, B. & Fruchter, A. 2017, ApJ, 839, 49
Gompertz, B. P., O'Brien, P. T., & Wynn, G. A. 2014, MNRAS, 438, 240
Goossens, M., Biront, D., & Tayler, R. J. 1981, Astrophys. Space Sci., 75, 521
Goossens, M. & Tayler, R. J. 1980, MNRAS, 193, 833
Gotz, D., Israel, G. L., Mereghetti, S., et al. 2006, The Astronomer's Telegram, 953, 1
Griffiths, A., Eggenberger, P., Meynet, G., Moyano, F., & Aloy, M.-Á. 2022, A&A, 665, A147
Gubbins, D. & Zhang, K. 1993, Physics of the Earth and Planetary Interiors, 75, 225
Guilet, J., Müller, E., & Janka, H.-T. 2015, MNRAS, 447, 3992
Guilet, J., Reboul-Salze, A., Raynaud, R., Bugli, M., & Gallet, B. 2022, MNRAS, 516, 4346
Hu, R.-Y. & Lou, Y.-Q. 2009, MNRAS, 396, 878
Hüdepohl, L. 2014, PhD thesis, Technical University of Munich, Germany
Hurley, K., Boggs, S. E., Smith, D. M., et al. 2005, Nature, 434, 1098
Hurley, K., Cline, T., Mazets, E., et al. 1999, Nature, 397, 41
Igoshev, A. P., Hollerbach, R., Wood, T., & Gourgouliatos, K. N. 2021, Nature Astronomy, 5, 145
Inserra, C., Smartt, S. J., Jerkstrand, A., et al. 2013, ApJ, 770, 128
Janka, H.-T., Wongwathanarat, A., & Kramer, M. 2022, ApJ, 926, 9
Ji, S., Fuller, J., & Lecoanet, D. 2023, MNRAS, 521, 5372
Kasen, D. & Bildsten, L. 2010, ApJ, 717, 245
Kiuchi, K., Reboul-Salze, A., Shibata, M., & Sekiguchi, Y. 2024, Nature Astronomy, 8, 298
Kouveliotou, C., Fishman, G. J., Meegan, C. A., et al. 1994, Nature, 368, 125
Kuroda, T., Arcones, A., Takiwaki, T., & Kotake, K. 2020, ApJ, 896, 102
Lander, S. K., Andersson, N., Antonopoulou, D., & Watts, A. L. 2015, MNRAS, 449, 2047
Lander, S. K. & Gourgouliatos, K. N. 2019, MNRAS, 486, 4130
Li, G., Deheuvels, S., Ballot, J., & Lignières, F. 2022, Nature, 610, 43
Li, G., Deheuvels, S., Li, T., Ballot, J., & Lignières, F. 2023, A&A, 680, A26
Lin, W., Wang, X., Wang, L., & Dai, Z. 2021, ApJ, 914, L2
Lü, H.-J. & Zhang, B. 2014, ApJ, 785, 74
Ma, L. & Fuller, J. 2019, MNRAS, 488, 4338
Makarenko, E. I., Igoshev, A. P., & Kholtygin, A. F. 2021, MNRAS, 504, 5813
Martin, J., Rea, N., Torres, D. F., & Papitto, A. 2014, MNRAS, 444, 2910
Masada, Y., Takiwaki, T., & Kotake, K. 2022, ApJ, 924, 75
Meduri, D. G., Jouve, L., & Lignières, F. 2024, A&A, 683, A12
Mereghetti, S., Savchenko, V., Ferrigno, C., et al. 2020, ApJ, 898, L29
Metzger, B. D., Beniamini, P., & Giannios, D. 2018, ApJ, 857, 95
Metzger, B. D., Giannios, D., Thompson, T. A., Bucciantini, N., & Quataert, E. 2011, MNRAS, 413, 2031
Mosser, B., Goupil, M. J., Belkacem, K., et al. 2012, A&A, 548, A10
Mösta, P., Richers, S., Ott, C. D., et al. 2014, ApJ, 785, L29
Nicholl, M., Smartt, S. J., Jerkstrand, A., et al. 2013, Nature, 502, 346
Nomoto, K., Maeda, K., Tanaka, M., & Suzuki, T. 2011, Astrophys. Science Sci., 336, 129
Obergaulinger, M. & Aloy, M. Á. 2020, MNRAS, 492, 4613
Obergaulinger, M. & Aloy, M. Á. 2021, MNRAS, 503, 4942
Obergaulinger, M. & Aloy, M. Á. 2022, MNRAS, 512, 2489
Obergaulinger, M., Cerdá-Durán, P., Müller, E., & Aloy, M. A. 2009, A&A, 498, 241
Olausen, S. A. & Kaspi, V. M. 2014, ApJS, 212, 6
Pascal, A. 2021, Theses, Université Paris sciences et lettres
Perna, R. & Pons, J. A. 2011, ApJ, 727, L51
Petitdemange, L., Marcotte, F., & Gissinger, C. 2023, Science, 379, 300
Petitdemange, L., Marcotte, F., Gissinger, C., & Daniel, F. 2024, A&A, 681, A75
Philidet, J., Gissinger, C., Lignières, F., & Petitdemange, L. 2020, Geophysical and Astrophysical Fluid Dynamics, 114, 336
Raynaud, R., Cerdá-Durán, P., & Guilet, J. 2022, MNRAS, 509, 3410
Raynaud, R., Guilet, J., Janka, H.-T., & Gastine, T. 2020, Sci. Adv., 6, eaay2732
Rea, N., Esposito, P., Turolla, R., et al. 2010, Science, 330, 944
Rea, N., Israel, G. L., Esposito, P., et al. 2012, ApJ, 754, 27
Rea, N., Israel, G. L., Pons, J. A., et al. 2013, ApJ, 770, 65
Rea, N., Viganò, D., Israel, G. L., Pons, J. A., & Torres, D. F. 2014, ApJ, 781, L17
Reboul-Salze, A., Guilet, J., Raynaud, R., & Bugli, M. 2021, A&A, 645, A109
Reboul-Salze, A., Guilet, J., Raynaud, R., & Bugli, M. 2022, A&A, 667, A94
Rembiasz, T., Obergaulinger, M., Cerdá-Durán, P., Aloy, M.-Á., & Müller, E. 2017, ApJS, 230, 18
Rheinhardt, M. & Geppert, U. 2002, Phys. Rev. Lett., 88, 101103
Rodríguez Castillo, G. A., Israel, G. L., Tiengo, A., et al. 2016, MNRAS, 456, 4145
Ronchi, M., Rea, N., Graber, V., & Hurley-Walker, N. 2022, ApJ, 934, 184
Schaeffer, N. 2013, Geochemistry, Geophysics, Geosystems, 14, 751
Schneider, F. R. N., Ohlmann, S. T., Podsiadlowski, P., et al. 2019, Nature, 574, 211
Shenar, T., Wade, G. A., Marchant, P., et al. 2023, Science, 381, 761
Spruit, H. C. 1999, A&A, 349, 189
Spruit, H. C. 2002, A&A, 381, 923
Stockinger, G., Janka, H. T., Kresse, D., et al. 2020, MNRAS, 496, 2039
Sukhbold, T., Ertl, T., Woosley, S. E., Brown, J. M., & Janka, H. T. 2016, ApJ, 821, 38
Sukhbold, T., Woosley, S. E., & Heger, A. 2018, ApJ, 860, 93
Svinkin, D., Frederiks, D., Hurley, K., et al. 2021, Nature, 589, 211
Takiwaki, T., Kotake, K., & Sato, K. 2009, ApJ, 691, 1360
Tayler, R. J. 1973, MNRAS, 161, 365
Thompson, C. & Duncan, R. C. 1993, ApJ, 408, 194
Thompson, C. & Duncan, R. C. 1995, MNRAS, 275, 255
Tiengo, A., Esposito, P., Mereghetti, S., et al. 2013, Nature, 500, 312
Tsuzuki, Y., Totani, T., Hu, C.-P., & Enoto, T. 2024, MNRAS, 530, 1885
Vink, J. & Kuiper, L. 2006, MNRAS, 370, L14
White, C. J., Burrows, A., Coleman, M. S. B., & Vartanyan, D. 2022, ApJ, 926, 111
Wicht, J. 2002, Physics of the Earth and Planetary Interiors, 132, 281
Woosley, S. E. 2010, ApJ, 719, L204
Woosley, S. E. & Bloom, J. S. 2006, ARAA, 44, 507
Younes, G., Kouveliotou, C., Jaodand, A., et al. 2017, ApJ, 847, 85
Zahn, J. P., Brun, A. S., & Mathis, S. 2007, A&A, 474, 145
Zhang, B. & Mészáros, P. 2001, ApJ, 552, L35
Zhou, P., Vink, J., Safi-Harb, S., & Miceli, M. 2019, A&A, 629, A51
Zhu, W., Xu, H., Zhou, D., et al. 2023, Science Advances, 9, eadf6198

Appendix A: Measure of the shear rate

The differential rotation is characterized by a dimensionless shear rate $q = r\partial_r \ln\Omega$. We define an effective shear rate based on the time average of the radial rotation profile in the saturated state at the colatitude of $\theta = \pi/8$ rad. We measure an average slope in the range of radii where half of the Tayler mode energy (approximated by the latitudinal magnetic energy E_{B_θ}) is concentrated around its maximum. We chose this particular method because this range of radii is the region where the dynamo occurs. The measures are displayed in Fig. A.1 (red plot) along with other measures made with different methods. Whatever the method used, we see that all the measures follow the same trend with an increase of $q \propto N$ until $N/\Omega_o = 4$ after which the values of q stay almost constant.

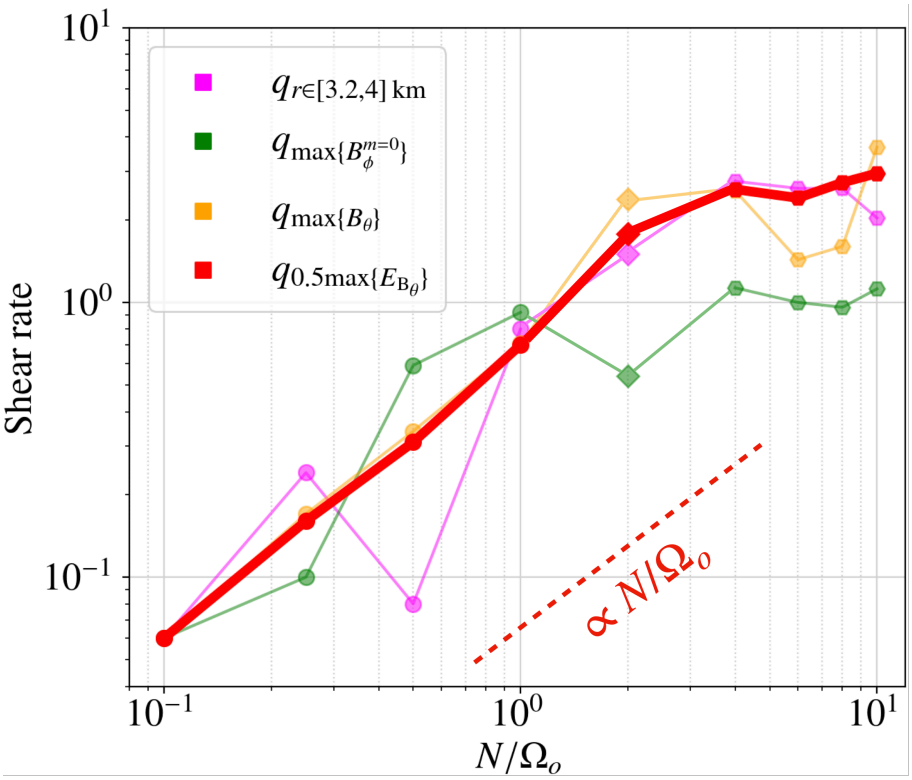

Fig. A.1. Shear rates q measured locally in the simulations as a function of N/Ω_o. The different colours represent distinct methods to measure q: slope in the rotation profile between 3.2 and 4 km (pink), q at the maximum of $B_\phi^{m=0}$ and B_θ (green and orange, respectively), and slope in the range of radii where half of the Tayler mode energy (approximated by the latitudinal magnetic energy E_{B_θ}) is concentrated around its maximum (red).

Appendix B: List of models

Tables B.1–B.3 summarize the key parameters and output quantities of the simulations carried out in this study.

Table B.1. Overview of the stable (or failed) dynamo solutions. All the simulations have the same aspect ratio $\chi = 0.25$, Ekman number $E = 10^{-5}$, Rossby number $Ro = 0.75$, thermal and magnetic Prandtl numbers $Pr = 0.1$ and $Pm = 1$, and the same resolution $(n_r, n_\theta, n_\phi) = (256, 256, 512)$. Note that the run named Ro0.75s is the same as in Barrère et al. (2023). This table displays the input parameter of the runs.

Name	Pm	N/Ω_o	$N_{\mathrm{eff}}/\Omega_o$	Λ_i
Ro0.75s	1	0.1	0.03	10
Pm1Pr0.1NO0.25	1	0.25	0.08	Λ(Ro0.75s)
Pm1Pr0.1NO0.5	1	0.5	0.16	Λ(Ro0.75s)
Pm1Pr0.1NO1	1	1	0.32	Λ(Pm1Pr0.1NO0.5)
Pm2Pr0.1NO2	2	2	0.45	Λ(Pm1Pr0.1NO1)
Pm2Pr0.1NO4	2	4	0.89	Λ(Pm2Pr0.1NO2)
Pm2Pr0.1NO8	2	8	1.79	Λ(Pm2Pr0.1NO4)
Pm4Pr0.1NO4	4	4	0.63	Λ(Pm2Pr0.1NO4)
Pm4Pr0.1NO6	4	6	0.95	Λ(Pm4Pr0.1NO4)
Pm4Pr0.1NO8	4	8	1.26	Λ(Pm2Pr0.1NO8)
Pm4Pr0.1NO10	4	10	1.58	Λ(Pm2Pr0.1NO10)

Table B.2. Same as Table B.1 but this table displays measured values in the simulations used to produce the plots of the paper.

Name	q	Λ	$B_{\rm tor}^{m=0}$ $\left[10^{-3}\sqrt{4\pi\rho d^2\Omega_o}\right]$	$B_{\rm pol}^{m=0}$ $\left[10^{-3}\sqrt{4\pi\rho d^2\Omega_o}\right]$	$B_{\rm dip}$ $\left[10^{-3}\sqrt{4\pi\rho d^2\Omega_o}\right]$	$B_{\rm tot}^{m\neq0}$ $\left[10^{-3}\sqrt{4\pi\rho d^2\Omega_o}\right]$	$v_{\rm tot}^{m\neq0}$ $[10^{-4}d\Omega_o]$
Ro0.75s	0.06	51.85	21	1.7	1.2	9.3	35
Pm1Pr0.1NO0.25	0.17	69.03	24	1.8	1.4	9.7	34
Pm1Pr0.1NO0.5	0.35	74.71	26	2.0	0.87	6.6	36
Pm1Pr0.1NO1	0.69	99.44	31	0.64	0.36	2.6	19
Pm2Pr0.1NO2	2.37	251.25	36	0.82	0.31	1.1	6.0
Pm2Pr0.1NO4	2.57	332.08	41	0.49	0.18	0.61	3.5
Pm2Pr0.1NO8	2.54	531.21	52	0.18	0.10	0.59	3.4
Pm4Pr0.1NO4	2.57	478.89	35	0.46	0.077	0.36	1.6
Pm4Pr0.1NO6	2.59	495.22	35	0.31	0.077	0.31	1.8
Pm4Pr0.1NO8	2.54	714.16	42	0.31	0.077	0.28	1.6
Pm4Pr0.1NO10	3.74	862.86	47	0.15	0.051	0.2	1.1

Table B.3. Following of Table B.2.

Name	$B_sB_\phi/4\pi$ $[10^{-6}\times4\pi\rho d^2\Omega_o^2]$	$B_s^{m=0}B_\phi^{m=0}/4\pi$ $[10^{-6}\times4\pi\rho d^2\Omega_o^2]$	$v_r^{m\neq0}v_\phi^{m\neq0}/4\pi$ $[10^{-8}\times\rho d^2\Omega_o^2]$	$v_s^{m\neq0}v_\phi^{m\neq0}/4\pi$ $[10^{-8}\times\rho d^2\Omega_o^2]$	$l_{\rm TI}$ [km]	$P_{\rm cyc}$ [s^{-1}]	$\alpha_{\rm cyc}$
Ro0.75s	15	2.9	52	76	2.8	–	–
Pm1Pr0.1NO0.25	9.1	2.4	56	89	2.5	–	–
Pm1Pr0.1NO0.5	5.7	1.8	58	110	1.5	–	–
Pm1Pr0.1NO1	3.0	0.84	18	35	0.8	–	–
Pm2Pr0.1NO2	2.2	1.7	2.8	10	0.6	27	0.66
Pm2Pr0.1NO4	1.5	1.4	7	4.4	0.4	12	0.59
Pm2Pr0.1NO8	1.7	1.0	0.52	5.3	0.2	13	0.38
Pm4Pr0.1NO4	0.45	0.63	0.16	0.61	0.4	3	0.62
Pm4Pr0.1NO6	0.53	0.67	0.17	0.94	0.3	16	0.5
Pm4Pr0.1NO8	0.65	0.75	0.12	0.77	0.2	10	0.47
Pm4Pr0.1NO10	0.50	0.52	0.066	0.46	0.15	6	0.57

C.3.4 . Article *From proto-neutron star dynamo to low-field magnetars (submitted)*

From proto-neutron star dynamo to low-field magnetars

Andrei Igoshev[1*], Paul Barrère[2], Raphaël Raynaud[3], Jérome Guilet[2], Toby Wood[4], Rainer Hollerbach[1]

[1*]Department of Applied Mathematics, University of Leeds, Leeds LS2 9JT UK.
[2]Université Paris-Saclay, Université Paris Cité, CEA, CNRS, AIM, 91191 Gif-sur-Yvette, France.
[3]Université Paris Cité, Université Paris-Saclay, CEA, CNRS, AIM, F-91191, Gif-sur-Yvette, France.
[4]School of Mathematics, Statistics and Physics, Newcastle University, Newcastle upon Tyne NE1 7RU UK.

*Corresponding author(s). E-mail(s): a.igoshev@leeds.ac.uk;

Abstract

Low-field magnetars have dipolar magnetic fields that are 10-100 times weaker than the threshold, $\boldsymbol{B \gtrsim 10^{14}}$ G, used to define classical magnetars, yet they produce similar X-ray bursts and outbursts. Using the first direct numerical simulations of magneto-thermal evolution starting from a dynamo-generated magnetic field, we show that the low-field magnetars can be produced as a result of a Tayler–Spruit dynamo inside the proto-neutron star. We find that these simulations naturally explain key characteristics of low-field magnetars: (1) weak ($\lesssim \mathbf{10^{13}}$ G) dipolar magnetic fields, (2) strong small-scale fields, and (3) magnetically induced crustal failures producing X-ray bursts. These findings suggest two distinct formation channels for classical and low-field magnetars, potentially linked to different dynamo mechanisms.

Keywords: neutron stars, dynamo, magnetars, X-ray

Magnetars play a special role in modern high-energy astrophysics. They were suggested as central engines for superluminous supernovae [1, 2] and ultra-long γ–ray bursts [3].

They produce at least a fraction of mysterious Fast Radio Bursts [4, 5]. While Galactic magnetars are scarce due to their short life — with 30 known magnetars, compared with 3500 radio pulsars based on ATNF catalogue v.2.1.1[1] [6] — it is estimated that around 10% of all neutron stars (NSs) undergo a magnetar stage at some point in their evolution [7].

The standard magnetar model explains quiescent X-ray emission, spin period, bursts, outbursts and giant flares observed from Anomalous X-ray Pulsars (AXP) and Soft Gamma Repeaters (SGR) by assuming that these NSs have strong dipolar magnetic fields $\gtrsim 10^{14}$ G [8, 9]. However, a significant fraction of magnetars (5 out of 30 known objects) in fact have dipolar magnetic fields well below 10^{14} G and were therefore named low-field magnetars [10–14]. It has been suggested that low-field magnetars are old neutron stars primarily powered by crust-confined toroidal magnetic fields with strength $\approx 10^{14}$ G [11, 15]. Rea et al. [12] suggested that low-field magnetars were born with both poloidal and toroidal magnetic fields $> 10^{14}$ G, but the poloidal component decayed by a factor of six in ≈ 500 kyr. Phase-resolved X-ray observations show that in two cases low-field magnetars host small-scale magnetic fields which are 10-100 times stronger than their dipolar fields [16, 17].

The origin of magnetar magnetic fields is a subject of debate [18]. Different dynamo mechanisms have been proposed to explain the formation of the strongest magnetic fields, including proto-neutron star convection [8, 19–22], magnetorotational instability [23, 24], and more recently the Tayler–Spruit dynamo [25–27]. The Tayler–Spruit dynamo is a particularly promising mechanism for generating magnetars' magnetic fields in cases when the progenitor core is slowly rotating and the proto-NS is spun up by fallback accretion [26]. In cases of rotation periods slower than ten milliseconds, a normal core-collapse supernova is expected to occur, in agreement with observational constraints for the majority of magnetars [28, 29]. After the first minute, the proto-NS cools down, its crust solidifies and the remnant becomes a NS. After this time, the initially complicated crustal magnetic field slowly relaxes due to Ohmic decay and Hall evolution on a timescale of 10^5–10^6 years [30, 31].

Previous simulations of magneto-thermal evolution have assumed idealised initial conditions rather than magnetic configurations generated by a specific dynamo mechanism. However, the study of more realistic initial conditions is of key importance in order to obtain realistic predictions of magnetar properties. Indeed, Hall evolution has been shown to preserve certain aspects of the initial conditions [32, 33]. Hence, the observational properties of magnetars, and low-field magnetars in particular, should contain information about the proto-NS magnetic field.

Evolution of neutron star magnetic field

The proto-NS dynamo and NS crust stages are modelled separately because of their very different timescales and physical conditions. While the dynamo is formulated as a magnetohydrodynamics (MHD) problem for a stably stratified fluid with shear caused by fallback accretion over a timescale of a few tens of seconds, the magneto-thermal

[1] http://www.atnf.csiro.au/research/pulsar/psrcat

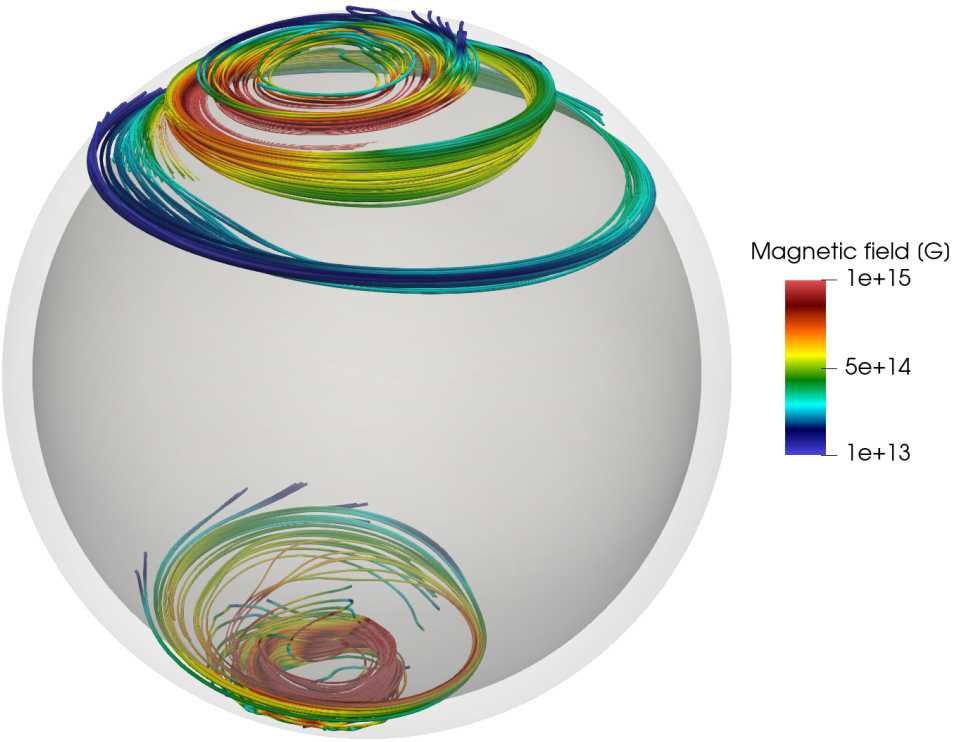

Fig. 1 Magnetic field lines at the beginning of our NS magneto-thermal simulation.

evolution of the NS crust occurs on a much longer timescale of 1 Myr and is formulated as electron-MHD.

The initial condition for our NS simulation is a magnetic field configuration corresponding to a Tayler-Spruit dynamo branch recently discovered in direct numerical simulations and characterised by a dipolar symmetry (i.e. equatorially symmetric) [27]. The initial core temperature is assumed to be 10^8 K. This magnetic field is obtained using the 3D spherical MHD code `MagIC` [34–36] for rotation frequencies of the respective outer and inner spheres $\Omega_o = 4\Omega_i = 628\,\mathrm{rad\,s^{-1}}$ (see Methods Section 1 for a more detailed description). The magnetic field is predominantly toroidal and reaches values up to 3×10^{15} G inside the volume, but the field at the outer boundary is much weaker. Assuming a scenario in which the core magnetic field is expelled to a crust-confined configuration, we extract the magnetic field in the top 10% of the simulation volume and adapt it to our code to model crust-confined NS magneto-thermal evolution (see Methods Section 2, 3). Figure 1 shows the initial configuration of the magnetic field inside the NS crust. We then use the `PARODY` code [37–39] to integrate the coupled magnetic induction and thermal diffusion equations for 1 Myr before analyzing the NS magnetic characteristics (see Methods Section 4).

Figure 2 shows the dipolar and quadrupolar poloidal magnetic field intensities, which are the only components that could contribute significantly to electromagnetic

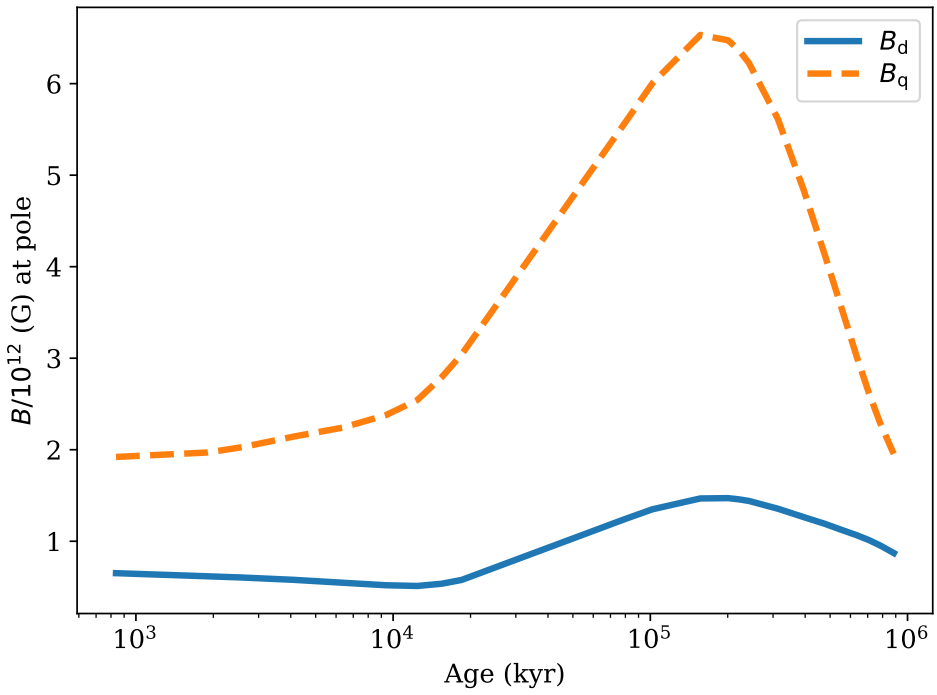

Fig. 2 Evolution of surface dipole (blue solid line) and quadrupole (orange dashed line) magnetic fields.

spin-down. The surface dipolar magnetic field increases by a factor of only three during the first Myr, reaching a maximum a value of 1.5×10^{12} G, and the quadrupole component remains similarly small, with a maximum of around 6×10^{12} G. These values are 2 to 3 orders of magnitude smaller than the internal magnetic field strength in the crust. Figure 3 shows a complex surface magnetic field topology featuring individual arches elongated in the north-south direction. The local field strength at the footpoints of these arches reaches 10^{14} G, 100 times stronger than the dipolar magnetic field. Small-scale magnetic fields remain dominant at all times from the beginning of the evolution until 1 Myr (see Methods Section Figure 6). Our numerical simulation therefore successfully reproduces two crucial properties of low-field magnetars: (1) weak dipolar magnetic field, and (2) presence of very strong (50-100 times stronger) small-scale magnetic fields, similar to those found in SGR 0418+5729 [16] and Swift J1882.3-1606 [17].

Surface temperatures and hot spots

The X-ray observations of low-field magnetars are consistent with thermal emission from isolated hot spots with sizes ≤ 1 km [40] and black body temperatures reaching

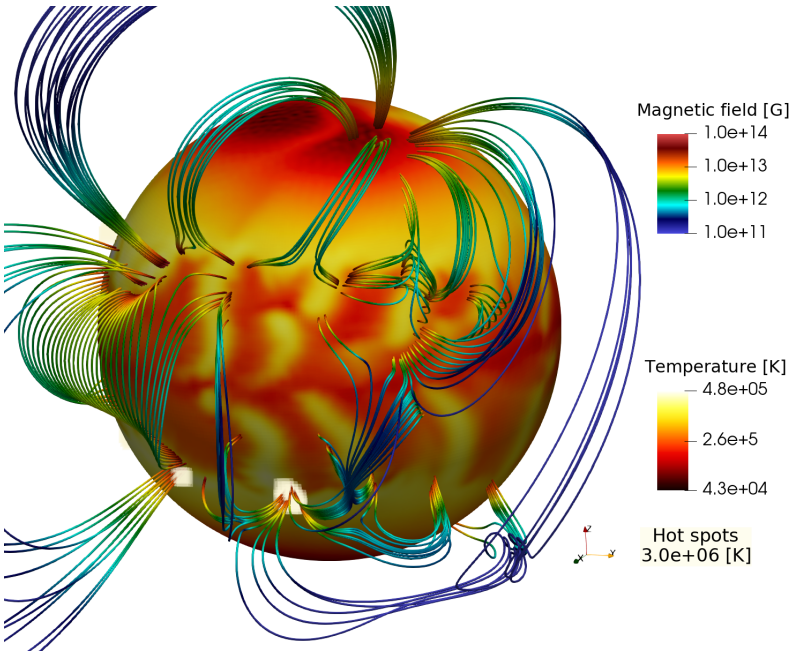

Fig. 3 Surface temperature distribution and external magnetic field structure at age 200 kyr.

$T_{\rm bb} = 0.12 - 0.6$ keV. The bulk NS emission is not detected with typical upper limits $< 10^{31}$ erg/s. SGR 0418+5729 has a pulsed fraction of 62 ± 10 % in the [0.3-1.2] keV range [40]. CXOU J164710.2-455216 and Swift J1822.3-1606 have quiescent pulsed fractions 80 ± 3 % and 38 ± 3 % in the [0.5,10] keV range respectively [41]. The upper limit on the bulk thermal emission indicates that low-field magnetars are at least ≈ 200 kyr old because the bulk X-ray emission drops below 10^{31} erg/s after 200 kyr [42] for strongly magnetised NSs (with internal field strengths $\sim 10^{15}$ G).

Strong magnetic fields could create large surface temperature variations, as can be seen in Figure 3 (and Methods Section Figure 8). We see variations of an order of magnitude between the hottest ($T \approx 4.8 \times 10^5$ K) and coldest ($T \approx 4.3 \times 10^4$ K) regions. These variations could cause up to 20 % pulsed fraction but would stay undetectable because of the low bulk X-ray luminosity 10^{31} erg/s and small effective black body temperature $T_{\rm bb} = 0.028$ keV.

We suggest that the observational properties of low-field magnetars can be explained by magnetospheric heating on the small-scale magnetic arches visible in Figure 3. The twisted magnetic field lines penetrate the NS surface through some of these individual footpoints heating surface and forming hot spots. The size of individual footpoints is a fraction of a kilometre, thus emission generated from these footpoints would have properties of emission seen from low-field magnetars, i.e. very high temperature and small emission area.

Spots are heated by the strongest radial electric currents, which coincide with the strongest radial magnetic fields because $\vec{J} \propto \vec{\nabla} \times \vec{B} = \mu \vec{B}$ according to the force-free condition in the magnetosphere [43]. Here we assume that only footpoints with radial

magnetic field $|B_r| > 7 \times 10^{13}$ G are heated. Under this assumption, it is possible to form up to 10 independent hot spots (see Figure 3) which, if heated to 3×10^6 K, produce luminosity 2×10^{32} erg/s and emission area with radius ≈ 0.9 km. The lightcurve is sine-like with a pulsed fraction reaching 92% for a favourable orientation even without beaming, in agreement with X-ray observations of low-field magnetars (see Methods Section Figures 9 and 10). If we increase the critical $|B_r|$ to larger values then we obtain fewer hot spots with smaller areas, and if we decrease the critical $|B_r|$ then the heated area is increased. If the X-ray thermal emission is indeed generated close to the footpoints of these arches, the arches themselves provide natural sites where Compton scattering occurs and absorption features are formed.

Magnetar bursts

In order to assess whether this magnetic field configuration can power the X-ray activity characteristic of magnetars, we examine the magnetic stresses inside the crust. Bursts and outbursts of magnetars are indeed thought to be caused by crust failure or plastic deformation due to the magnetic stresses [9, 44, 45]. We apply the Lander & Gourgouliatos model [45] and compare the crustal magnetic stresses with the von Mises criterion for crust-yielding (see Methods Section 6). In order to obtain a conservative estimate, the crust is assumed to have completely relaxed only after 2 kyr. Figure 4 shows the average depth of crust failure regions developed at the age of 200 kyr. All the failing regions are located close to the original north and south magnetic poles, coinciding with the regions of strongest magnetic field generated by the proto-NS dynamo. The crust failure regions are much larger in the northern than in the southern hemisphere, due to the properties of the initial magnetic field. This is very different from earlier simulations with simple dipolar initial conditions [46], in which the crust failure occurred around the original magnetic equator.

In order to check further if the magnetar behaviour could continue at timescales comparable to 100 kyr, we made an additional analysis. We assumed that all the stresses were relaxed in the crust after 100 kyr (which is then used as the reference field $\vec{B}_0$ in Methods Section equation 42), and we compute the magnetic stresses after 200 kyr. Even in this case, the stresses in some crust locations are above the yielding value.

The electromagnetic energy that can potentially be released in such a crustal failure is [9]

$$E_{\rm out} = 4 \times 10^{40}\ {\rm erg} \left(\frac{l}{1\ {\rm km}}\right)^2 \left(\frac{|B|}{10^{15}\ {\rm G}}\right)^2 \approx 2 \times 10^{39}\ {\rm erg}\,, \qquad (1)$$

where $l \sim 1$ km is the typical size of the failing region and $|B| \sim 2 \times 10^{14}$ G (see Figure 4). This value is actually well above the typical burst energy $\sim 10^{37}$ erg of two low-field magnetars: SGR J0418+5729 [10] and CXOU J164710.2-455216 [47]. Our modelling provides an upper limit on the extent of crust failure because it maps all the regions which could fail by a certain age. The real size of individual crust failures could be significantly smaller, thus explaining the energy difference between our model and individual bursts observed from magnetars.

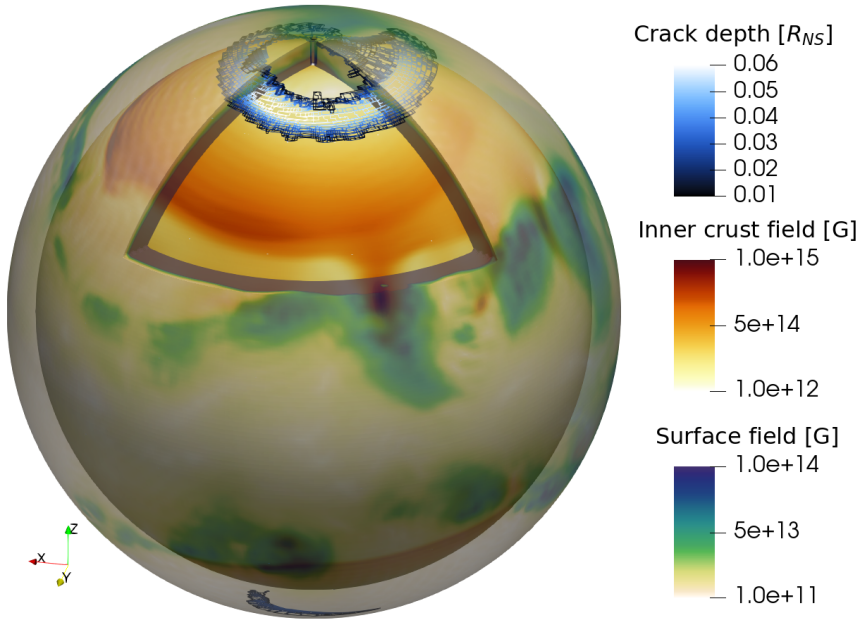

Fig. 4 Surface and inner crust magnetic field developed by 200 kyr. Crust yielding regions are shown in white and blue colours.

Spin periods

By electromagnetic braking alone, neutron stars with dipolar fields of a few times 10^{12} G cannot reach the spin periods of 8-11 s typical for low-field magnetars on a timescale of 1 Myr. However, it is essential to also take accretion into account, since the Tayler–Spruit dynamo can only develop if the proto-NS accretes fallback material, and this accretion will continue even after the NS is formed. Using the formalism by Ronchi et al. [48] to model torques from the fallback disk, we naturally obtained periods of 8-11 s after 170 kyr for NSs with dipolar magnetic field similar to our simulations (see Figure 5). More details about these calculations are summarised in Methods Section 7.

Most of the spin-down occurs during the propeller stage when the NS decelerates due to the interaction of its magnetosphere with the fallback disk (see Methods Section Figure 11). After 200 kyr, this propeller phase has spun the NS down to a rotation period of $P = 8.5$ s and a period derivative $\dot{P} = 8.5 \times 10^{-13}\,\mathrm{s\,s^{-1}}$. According to the standard magnetic dipole spin-down formula, the inferred surface magnetic dipole should then be $B_{\rm dip} \approx 3.8 \times 10^{13}$ G, which overestimates the true surface magnetic dipole in our simulation by a factor of ~ 40. This inferred value of $B_{\rm dip}$ is comparable to Swift J1822.3-1606 (1.4×10^{13} G) and below the upper limit measured for CXOU J164710.2-455216 ($< 6.6 \times 10^{13}$ G) as well as 3XMM J185246.6+003317 ($< 4 \times 10^{13}$ G).

The apparent magnetic field estimated using instantaneous period and period derivative might be smaller if the disk is partially depleted and provides less torque.

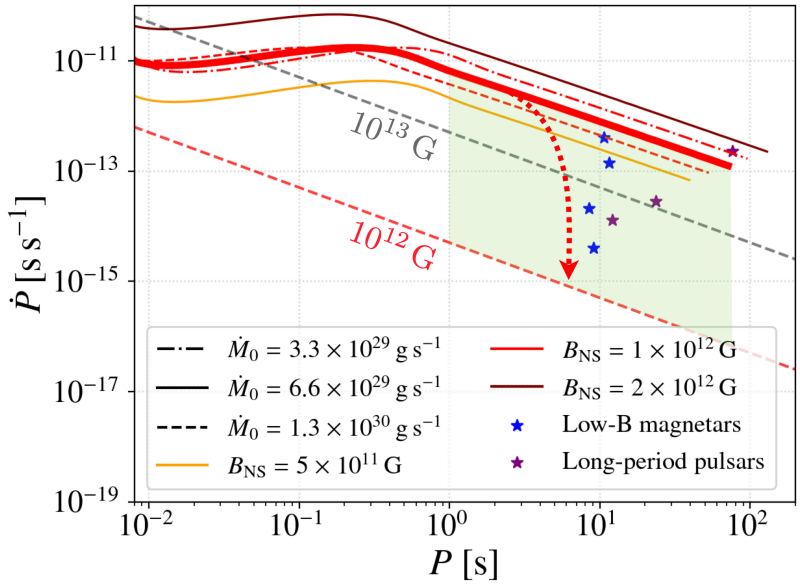

Fig. 5 Time evolution of the spin period P and its time derivative $\dot{P}$ until 10 Myr with small variations of the initial mass accretion rate $\dot{M}$ and dipolar magnetic field $B_{\rm NS}$. The red and grey dashed lines represent the constant dipolar magnetic field lines calculated from the magnetic dipole spin-down formula for 10^{12} G and 10^{13} G, respectively. The green area covers the zone in which the magnetar could end up if the accretion disk is (partially) depleted (for the fiducial parameters $B_{\rm NS} = 10^{12}$ G, $M_{\rm d,0} = 0.01$ M$_\odot$). The red dotted arrow indicates how the $P\dot{P}$ evolution would behave if the disk is completely depleted.

Depending on the exact amount of material left in the disk, the period derivative $\dot{P}$ could range from $\approx 10^{-15}$ (electromagnetic spin-down only) to $\approx 10^{-12}$ (non-depleted disk; green area in Figure 5). All low-field magnetars with a measured period derivative fall within this area.

Impact and future work

Previous magneto-thermal simulations have considered idealised, large-scale magnetic fields [15, 49]. Some of these simulations can be made more similar to low-field magnetars by assuming a magnetar-strength dipolar magnetic field which is then dissipated by an increased crust resistivity [12] [2]. Moreover, these simulations stay highly axially symmetric because of the symmetries of the initial conditions. Although some previous studies have considered more complicated field structures, as expected from proto-NS evolution [50, 51], our study is the first to directly implement the field from a self-consistent dynamo simulation. The crucial properties of our new magnetic field configuration are that this field is predominantly toroidal and is initially localised near the polar regions of the crust. As a consequence, we find that crustal fractures are most likely to occur in these regions.

[2] See e.g. model C0-0-tor with 50% of toroidal magnetic field and initial dipolar magnetic fields of 10^{14} G in [15].

One important advance of this work is understanding that the evolution towards large-scale fields is very limited, with the dipole only growing by a factor of two, contrary to earlier suggestions [18]. In our simulation, the magnetic energy contained in the deep crustal fields, including the toroidal component, is significantly larger than the field which can be estimated from surface dipolar values. We find only a moderate increase of the dipolar component, on a timescale of $\sim 10^5$ years.

In comparison to the model suggested by Rea et al. [12] with an initial dipolar field as strong as 1.5×10^{14} G, the dipolar magnetic field stays very low, $\sim 10^{12}$ G, and does not decay significantly in our simulations.

Our results also suggest an important connection between low-field magnetars and recently discovered long-period radio pulsars, such as PSR J0901-4046 [52]. If the neutron star continues to operate in the propeller phase, it will ultimately reach periods comparable to 75 s by 10 Myr (Figure 5). The external magnetic field configuration remains complex, with large open field-line curvature near the NS surface facilitating radio pulsar operation. Thus, pulsar radio emission could occur if the disk is depleted.

Mahlmann et al. [53] performed numerical simulations for X-ray outbursts with energies up to 10^{43} erg produced by a twisted magnetar magnetosphere. In our simulations, we see the development of individual magnetic arcs and the evolution of their footpoints. Thus, our results can be used as the initial magnetic field for future relativistic magnetosphere simulations.

Our work opens new perspectives for testing extreme dynamos operating in proto-neutron stars. We suggest that different dynamos leave their unique imprint on magnetic field configurations, thus allowing to identify different magnetic amplification processes using the magneto-thermal properties of young isolated neutron stars. While we suggest that the formation of low-field magnetars is linked to the Tayler–Spruit dynamo, the formation of classical magnetars as well as the internal structure of their magnetic fields remains an open question.

References

[1] Wheeler, J. C., Yi, I., Höflich, P. & Wang, L. Asymmetric Supernovae, Pulsars, Magnetars, and Gamma-Ray Bursts. ApJ **537**, 810–823 (2000).

[2] Dessart, L., Hillier, D. J., Waldman, R., Livne, E. & Blondin, S. Superluminous supernovae: ^{56}Ni power versus magnetar radiation. MNRAS **426**, L76–L80 (2012).

[3] Greiner, J. *et al.* A very luminous magnetar-powered supernova associated with an ultra-long γ-ray burst. Nature **523**, 189–192 (2015).

[4] Popov, S. B. & Postnov, K. A. Harutyunian, H. A., Mickaelian, A. M. & Terzian, Y. (eds) *Hyperflares of SGRs as an engine for millisecond extragalactic radio bursts.* (eds Harutyunian, H. A., Mickaelian, A. M. & Terzian, Y.) *Evolution of Cosmic Objects through their Physical Activity*, 129–132 (2010). 0710.2006.

[5] Bochenek, C. D. *et al.* A fast radio burst associated with a Galactic magnetar. Nature **587**, 59–62 (2020).

[6] Manchester, R. N., Hobbs, G. B., Teoh, A. & Hobbs, M. The Australia Telescope National Facility Pulsar Catalogue. AJ **129**, 1993–2006 (2005).

[7] Keane, E. F. & Kramer, M. On the birthrates of Galactic neutron stars. MNRAS **391**, 2009–2016 (2008).

[8] Thompson, C. & Duncan, R. C. Neutron Star Dynamos and the Origins of Pulsar Magnetism. ApJ **408**, 194 (1993).

[9] Thompson, C. & Duncan, R. C. The soft gamma repeaters as very strongly magnetized neutron stars - I. Radiative mechanism for outbursts. MNRAS **275**, 255–300 (1995).

[10] van der Horst, A. J. *et al.* Discovery of a New Soft Gamma Repeater: SGR J0418 + 5729. ApJ **711**, L1–L6 (2010).

[11] Rea, N. *et al.* A Low-Magnetic-Field Soft Gamma Repeater. *Science* **330**, 944 (2010).

[12] Rea, N. *et al.* A New Low Magnetic Field Magnetar: The 2011 Outburst of Swift J1822.3-1606. ApJ **754**, 27 (2012).

[13] Scholz, P. *et al.* Post-outburst X-Ray Flux and Timing Evolution of Swift J1822.3-1606. ApJ **761**, 66 (2012).

[14] Rea, N., Viganò, D., Israel, G. L., Pons, J. A. & Torres, D. F. 3XMM J185246.6+003317: Another Low Magnetic Field Magnetar. ApJ **781**, L17 (2014).

[15] Igoshev, A. P., Hollerbach, R., Wood, T. & Gourgouliatos, K. N. Strong toroidal magnetic fields required by quiescent X-ray emission of magnetars. *Nature Astronomy* **5**, 145–149 (2021).

[16] Tiengo, A. *et al.* A variable absorption feature in the X-ray spectrum of a magnetar. Nature **500**, 312–314 (2013).

[17] Rodríguez Castillo, G. A. *et al.* The outburst decay of the low magnetic field magnetar SWIFT J1822.3-1606: phase-resolved analysis and evidence for a variable cyclotron feature. MNRAS **456**, 4145–4155 (2016).

[18] Sarin, N., Brandenburg, A. & Haskell, B. Confronting the Neutron Star Population with Inverse Cascades. ApJ **952**, L21 (2023).

[19] Raynaud, R., Guilet, J., Janka, H.-T. & Gastine, T. Magnetar formation through a convective dynamo in protoneutron stars. *Science Advances* **6**, eaay2732 (2020).

[20] Raynaud, R., Cerdá-Durán, P. & Guilet, J. Gravitational wave signature of proto-neutron star convection: I. MHD numerical simulations. MNRAS **509**, 3410–3426 (2022).

[21] Masada, Y., Takiwaki, T. & Kotake, K. Convection and Dynamo in Newly Born Neutron Stars. ApJ **924**, 75 (2022).

[22] White, C. J., Burrows, A., Coleman, M. S. B. & Vartanyan, D. On the Origin of Pulsar and Magnetar Magnetic Fields. ApJ **926**, 111 (2022).

[23] Reboul-Salze, A., Guilet, J., Raynaud, R. & Bugli, M. A global model of the magnetorotational instability in protoneutron stars. A&A **645**, A109 (2021).

[24] Reboul-Salze, A., Guilet, J., Raynaud, R. & Bugli, M. MRI-driven $\alpha\Omega$ dynamos in protoneutron stars. A&A **667**, A94 (2022).

[25] Spruit, H. C. Dynamo action by differential rotation in a stably stratified stellar interior. A&A **381**, 923–932 (2002).

[26] Barrère, P., Guilet, J., Reboul-Salze, A., Raynaud, R. & Janka, H. T. A new scenario for magnetar formation: Tayler-Spruit dynamo in a proto-neutron star spun up by fallback. A&A **668**, A79 (2022).

[27] Barrère, P., Guilet, J., Raynaud, R. & Reboul-Salze, A. Numerical simulations of the Tayler-Spruit dynamo in proto-magnetars. MNRAS **526**, L88–L93 (2023).

[28] Vink, J. & Kuiper, L. Supernova remnant energetics and magnetars: no evidence in favour of millisecond proto-neutron stars. MNRAS **370**, L14–L18 (2006).

[29] Martin, J., Rea, N., Torres, D. F. & Papitto, A. Comparing supernova remnants around strongly magnetized and canonical pulsars. MNRAS **444**, 2910–2924 (2014).

[30] Goldreich, P. & Reisenegger, A. Magnetic Field Decay in Isolated Neutron Stars. ApJ **395**, 250 (1992).

[31] Igoshev, A. P., Popov, S. B. & Hollerbach, R. Evolution of Neutron Star Magnetic Fields. *Universe* **7**, 351 (2021).

[32] Hollerbach, R. & Rüdiger, G. Hall drift in the stratified crusts of neutron stars. MNRAS **347**, 1273–1278 (2004).

[33] Wareing, C. J. & Hollerbach, R. Cascades in decaying three-dimensional electron magnetohydrodynamic turbulence. *Journal of Plasma Physics* **76**, 117–128 (2010).

[34] Wicht, J. Inner-core conductivity in numerical dynamo simulations. *Physics of the Earth and Planetary Interiors* **132**, 281–302 (2002).

[35] Gastine, T. & Wicht, J. Effects of compressibility on driving zonal flow in gas giants. Icarus **219**, 428–442 (2012).

[36] Schaeffer, N. Efficient spherical harmonic transforms aimed at pseudospectral numerical simulations. *Geochemistry, Geophysics, Geosystems* **14**, 751–758 (2013).

[37] Dormy, E. *Modélisation Numérique de la Dynamo Terrestre*. Ph.D. thesis, Institut de Physique du Globe de Paris (1997).

[38] Dormy, E., Cardin, P. & Jault, D. MHD flow in a slightly differentially rotating spherical shell, with conducting inner core, in a dipolar magnetic field. *Earth and Planetary Science Letters* **160**, 15–30 (1998).

[39] Aubert, J., Aurnou, J. & Wicht, J. The magnetic structure of convection-driven numerical dynamos. *Geophysical Journal International* **172**, 945–956 (2008).

[40] Guillot, S., Perna, R., Rea, N., Viganò, D. & Pons, J. A. Modelling of the surface emission of the low magnetic field magnetar SGR 0418+5729. MNRAS **452**, 3357–3368 (2015).

[41] Seo, J., Lee, J. & An, H. Correlation Study of Temporal and Emission Properties of Quiescent Magnetars. *Journal of Korean Astronomical Society* **56**, 41–57 (2023).

[42] Potekhin, A. Y. & Chabrier, G. Magnetic neutron star cooling and microphysics. A&A **609**, A74 (2018).

[43] Thompson, C., Lyutikov, M. & Kulkarni, S. R. Electrodynamics of Magnetars: Implications for the Persistent X-Ray Emission and Spin-down of the Soft Gamma Repeaters and Anomalous X-Ray Pulsars. ApJ **574**, 332–355 (2002).

[44] Lander, S. K., Andersson, N., Antonopoulou, D. & Watts, A. L. Magnetically driven crustquakes in neutron stars. MNRAS **449**, 2047–2058 (2015).

[45] Lander, S. K. & Gourgouliatos, K. N. Magnetic-field evolution in a plastically failing neutron-star crust. MNRAS **486**, 4130–4143 (2019).

[46] Wood, T. S. & Hollerbach, R. Three Dimensional Simulation of the Magnetic Stress in a Neutron Star Crust. Phys. Rev. Lett. **114**, 191101 (2015).

[47] Muno, M. P. *et al.* Exciting the magnetosphere of the magnetar CXOU J164710.2-455216 in Westerlund 1. MNRAS **378**, L44–L48 (2007).

[48] Ronchi, M., Rea, N., Graber, V. & Hurley-Walker, N. Long-period Pulsars as Possible Outcomes of Supernova Fallback Accretion. ApJ **934**, 184 (2022).

[49] Igoshev, A. P., Hollerbach, R. & Wood, T. Three-dimensional magnetothermal evolution of off-centred dipole magnetic field configurations in neutron stars. MNRAS **525**, 3354–3375 (2023).

[50] De Grandis, D. *et al.* Three-dimensional Magnetothermal Simulations of Magnetar Outbursts. ApJ **936**, 99 (2022).

[51] Dehman, C., Viganò, D., Ascenzi, S., Pons, J. A. & Rea, N. 3D evolution of neutron star magnetic fields from a realistic core-collapse turbulent topology. MNRAS **523**, 5198–5206 (2023).

[52] Caleb, M. *et al.* Discovery of a radio-emitting neutron star with an ultra-long spin period of 76 s. *Nature Astronomy* **6**, 828–836 (2022).

[53] Mahlmann, J. F. *et al.* Three-dimensional Dynamics of Strongly Twisted Magnetar Magnetospheres: Kinking Flux Tubes and Global Eruptions. ApJ **947**, L34 (2023).

[54] De Grandis, D. *et al.* Three-dimensional Modeling of the Magnetothermal Evolution of Neutron Stars: Method and Test Cases. ApJ **903**, 40 (2020).

[55] Urpin, V. A. & Yakovlev, D. G. Thermogalvanomagnetic Effects in White Dwarfs and Neutron Stars. Soviet Ast. **24**, 425 (1980).

[56] Gudmundsson, E. H., Pethick, C. J. & Epstein, R. I. Structure of neutron star envelopes. ApJ **272**, 286–300 (1983).

[57] Gompertz, B. P., O'Brien, P. T. & Wynn, G. A. Magnetar powered GRBs: explaining the extended emission and X-ray plateau of short GRB light curves. MNRAS **438**, 240–250 (2014).

Acknowledgements

API and RH are supported by STFC grant no. ST/W000873/1, and TSW is supported by STFC grant no. ST/W001020/1. This work was performed using the DiRAC Data Intensive service at Leicester, operated by the University of Leicester IT Services, which forms part of the STFC DiRAC HPC Facility (www.dirac.ac.uk). The equipment was funded by BEIS capital funding via STFC capital grants ST/K000373/1 and ST/R002363/1 and STFC DiRAC Operations grant ST/R001014/1. DiRAC is part of the National e-Infrastructure. This work was also supported by the "Programme National de Physique Stellaire" (PNPS) and the "Programme National des Hautes Énergies" (PNHE) of CNRS/INSU co-funded by CEA and CNES. The authors would like to thank the Isaac Newton Institute for Mathematical Sciences, Cambridge, for support and hospitality during the programme DYT2 where work on this paper was undertaken. JG, RR and PB acknowledge support from European Research Council (ERC starting grant no. 715368 – MagBURST) and from the Très Grand Centre de calcul du CEA (TGCC) and IDRIS for providing computational time on Irene and Jean-Zay (allocations A0110410317, A0130410317, A0150410317).

Data and materials availability

For the proto-NS simulation, we used the MagIC code (commit 2266201a5), which is open source at https://github.com/magic-sph/magic. The magnetar spin-down was calculated with the GRB code (commit 84788793), also publicly available at https://github.com/rraynaud/GRBs. The results of magneto-thermal simulations can be shared under reasonable request.

Methods section

1 Simulation of the proto-neutron star dynamo

We simulate a proto-NS with a mass of 1.4 $M_\odot$ and a radius $R_{\rm NS} = 12\,{\rm km}$. Its interior is modelled as a stably stratified fluid enclosed between two spherical shells. To control the differential rotation, we impose constant rotation frequencies on both shells (spherical Taylor-Couette configuration), with the outer shell rotating faster than the inner shell to be consistent with the fallback formation scenario. We solve the Boussinesq MHD equations by using the pseudo-spectral code `MagIC`. In this code, the different lengths r, the time t, the temperature T, and the magnetic field B are scaled as follows:

$$r \to rd, \qquad t \to (d^2/\nu)t, \qquad T \to (T_o - T_i)T, \qquad B \to \sqrt{4\pi\rho\eta\Omega_o}B\,, \tag{2}$$

with the gap between the two spheres $d = r_o - r_i = 9\,{\rm km}$, the kinematic viscosity $\nu = 3.5 \times 10^9\,{\rm cm^2\,s^{-1}}$, the temperatures of the outer T_o and inner T_i spheres, the constant density $\rho = 4.1 \times 10^{14}\,{\rm g\,cm^{-3}}$, the resistivity $\eta = 3.5 \times 10^9\,{\rm cm^2\,s^{-1}}$, and the rotation rate of the outer sphere $\Omega_o = 628\,{\rm rad\,s^{-1}}$. So, the dimensionless equations solved by `MagIC` read

$$\vec{\nabla}\cdot\vec{v} = 0\,, \tag{3}$$

$$\vec{\nabla}\cdot\vec{B} = 0\,, \tag{4}$$

$$\frac{D\vec{v}}{Dt} + \frac{2}{E}\,\vec{e}_z \times \vec{v} = -\vec{\nabla}p' + \frac{Ra}{Pr}\,T\vec{e}_r + \frac{1}{E\,Pm}\,(\vec{\nabla}\times\vec{B})\times\vec{B} + \Delta\vec{v}\,, \tag{5}$$

$$\frac{DT}{Dt} = \frac{1}{Pr}\,\Delta T\,, \tag{6}$$

$$\frac{\partial\vec{B}}{\partial t} = \vec{\nabla}\times(\vec{u}\times\vec{B}) + \frac{1}{Pm}\,\Delta\vec{B}\,, \tag{7}$$

where $\vec{v}$ and $\vec{B}$ are the velocity and magnetic fields, and p' is the non-hydrostatic pressure. $D/Dt \equiv \partial/\partial t + \vec{v}\cdot\vec{\nabla}$ is the Lagrangian derivative. E, Ra, Pr, and Pm are dimensionless numbers, which depend on the fluid properties. The Ekman number E is defined as the ratio of the rotation period to the viscous timescale

$$E = \frac{\nu}{d^2\Omega_o} = 10^{-5}\,. \tag{8}$$

The thermal and magnetic Prandtl numbers are defined by

$$Pr = \frac{\nu}{\kappa} = 0.1 \qquad \text{and} \qquad Pm = \frac{\nu}{\eta} = 1\,, \tag{9}$$

where $\kappa = 3.5 \times 10^{10}\,\mathrm{cm^2\,s^{-1}}$ is the thermal diffusivity. Finally, the Rayleigh number Ra measures the ratio between the timescales of thermal transport by diffusion to the thermal transport by convection,

$$Ra = \left(\frac{N}{\Omega_o}\right)^2 \frac{Pr}{E^2}\,, \tag{10}$$

where

$$N \equiv \sqrt{-\frac{g_0}{\rho}\left(\left.\frac{\partial\rho}{\partial S}\right|_{P,Y_e}\frac{dS}{dr} + \left.\frac{\partial\rho}{\partial Y_e}\right|_{P,S}\frac{dY_e}{dr}\right)} = 68.2\,\mathrm{s^{-1}} \tag{11}$$

is the Brunt-Väisälä frequency. The gravitational acceleration is assumed purely radial $\vec{g} = g_0 r/r_0 \vec{e}_r$. Y_e, and S are the electron fraction, and the entropy, respectively.

The resolution used is $(n_r, n_\theta, n_\phi) = (257, 256, 512)$. For more information on the numerical methods, see the supplementary materials of [27].

2 Conversion between `MagIC` and `PARODY` codes

The poloidal-toroidal decompositions and thus the magnetic potentials are defined differently in the `MagIC` and `PARODY` codes. Specifically,

$$\vec{B} = \vec{\nabla}\times\vec{\nabla}\times(b^{\mathrm{M}}_{\mathrm{pol}}\vec{e}_r) + \vec{\nabla}\times(b^{\mathrm{M}}_{\mathrm{tor}}\vec{e}_r)\,, \tag{12}$$

$$\vec{B} = \vec{\nabla}\times\vec{\nabla}\times(b^{\mathrm{P}}_{\mathrm{pol}} r\vec{e}_r) + \vec{\nabla}\times(b^{\mathrm{P}}_{\mathrm{tor}} r\vec{e}_r)\,, \tag{13}$$

where the superscript M / P refers to `MagIC` / `PARODY`, respectively.

Moreover, the codes use different normalisation factors C_{lm} for the spherical harmonics $Y_l^m(\theta,\phi)$. The spherical harmonics are normalised as the following in the `PARODY` code

$$C^{\mathrm{P}}_{lm} = \sqrt{(2-\delta_{m,0})(2l+1)\frac{(l-m)!}{(l+m)!}}\,, \tag{14}$$

while the normalisation in the `MagIC` code reads

$$C^{\mathrm{M}}_{lm} = \frac{1}{1+\delta_{m,0}}\sqrt{\frac{(2l+1)}{4\pi}\frac{(l-m)!}{(l+m)!}}\,, \tag{15}$$

where $\delta_{m,0}$ is the Kronecker delta, so $\delta_{m,0} = 1$ if $m = 0$ and it is 0 otherwise.

Thus, for the radial magnetic field, we have

$$B_r = \frac{l(l+1)}{r^2_{\mathrm{m}}}\, b^{lm,\mathrm{M}}_{\mathrm{pol}}(r_{\mathrm{m}})\, C^{\mathrm{M}}_{lm}\, Y_l^m(\theta,\phi) = \frac{l(l+1)}{r_{\mathrm{p}}}\, b^{lm,\mathrm{P}}_{\mathrm{pol}}(r_{\mathrm{p}})\, C^{\mathrm{P}}_{lm}\, Y_l^m(\theta,\phi)\,. \tag{16}$$

Doing this comparison for each (l, m) separately we thus obtain

$$b_{\rm pol}^{lm,{\rm P}}(r_{\rm pol}) = b_{\rm pol}^{lm,{\rm M}}(r_{\rm m})\,\frac{r_{\rm p}}{r_{\rm m}^2}\,\frac{C_{lm}^{\rm M}}{C_{lm}^{\rm P}}\,. \tag{17}$$

Expanding and simplifying this expression we obtain two different equations for axisymmetric and non-axisymmetric poloidal potentials

$$b_{\rm pol}^{l0,{\rm P}}(r_{\rm p}) = \frac{b_{\rm pol}^{l0,{\rm M}}(r_{\rm m})}{\sqrt{4\pi}}\,\frac{r_{\rm p}}{r_{\rm m}^2} \quad \text{for} \quad m = 0\,, \tag{18}$$

$$b_{\rm pol}^{lm,{\rm P}}(r_{\rm p}) = \frac{b_{\rm pol}^{lm,{\rm M}}(r_{\rm m})}{\sqrt{2\pi}} \quad \text{for} \quad m \neq 0\,. \tag{19}$$

Similarly, we can proceed with the θ-component of the magnetic field computed using only the toroidal potential

$$B_\theta = \frac{C_{lm}^{\rm M}}{r_{\rm m}\sin\theta}\,b_{\rm tor}^{lm,{\rm M}}(r_{\rm m})\,\frac{\partial Y_l^m(\theta,\phi)}{\partial\phi} = \frac{C_{lm}^{\rm P}}{\sin\theta}\,b_{\rm tor}^{lm,{\rm P}}(r_{\rm p})\,\frac{\partial Y_l^m(\theta,\phi)}{\partial\phi}\,. \tag{20}$$

Thus, the normalisation is

$$b_{\rm tor}^{lm,{\rm P}}(r_{\rm p}) = b_{\rm tor}^{lm,{\rm M}}(r_{\rm m})\,\frac{C_{lm}^{\rm M}}{C_{lm}^{\rm P}}\,\frac{1}{r_{\rm m}}\,, \tag{21}$$

which simplifies to

$$b_{\rm tor}^{l0,{\rm P}}(r_{\rm p}) = \frac{b_{\rm tor}^{l0,{\rm M}}(r_{\rm m})}{\sqrt{4\pi}}\,\frac{1}{r_{\rm m}} \quad \text{for} \quad m = 0\,, \tag{22}$$

$$b_{\rm tor}^{lm,{\rm P}}(r_{\rm p}) = \frac{b_{\rm tor}^{lm,{\rm M}}(r_{\rm m})}{\sqrt{2\pi}}\,\frac{1}{r_{\rm m}} \quad \text{for} \quad m \neq 0\,. \tag{23}$$

In this work, we preserve the angular structure obtained in dynamo simulations at the surface and in the middle of the crust up to $L_{\rm max} = 30$, which corresponds to surface structures of ≈ 1 km. Analysis of the dynamo simulations reveal that larger-scale structures do indeed dominate the magnetic field. Smaller scale structures are generated during the first kyr via the Hall cascade, see Figure 6.

3 Crust-confined magnetic field configurations

In addition to the technical details in the previous section, the proto-NS dynamo setup and the magneto-thermal crust evolution setup differ in their geometry, having aspect ratios $\chi_{\rm pNS} = 0.25$ and $\chi_{\rm NS} = 0.9$, respectively. Thus, in order to create a magnetic field configuration which is similar to proto-NS results but is also crust-confined, we should extract only the top 10% of the proto-NS simulation.

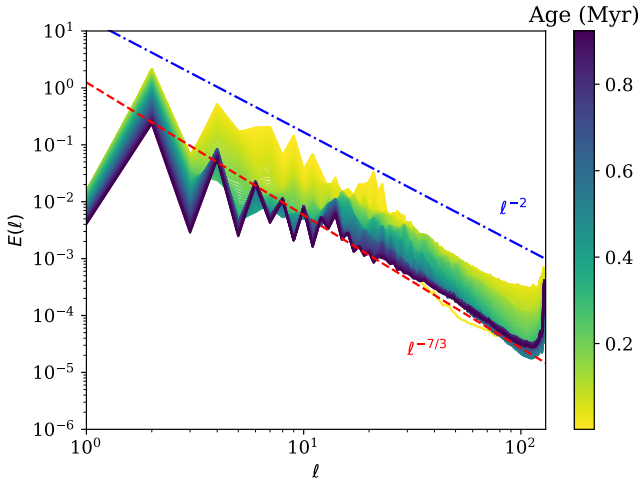

Fig. 6 Evolution of the magnetic energy spectra over 1 Myr.

Our approach for importing the results of the dynamo simulations is to require all components of the magnetic field to be exactly the same at certain points within the crust. We consider the poloidal and toroidal potentials for each individual spherical harmonic, and require both these potentials to exactly coincide with our numerical fits at the following points: $r_1 = 0.93$ and $r_2 = 0.96$. We require our fit for the poloidal potential to coincide at the surface. We also require our poloidal and toroidal potentials to satisfy the potential boundary condition at the surface and the 'no-currents' boundary condition at the core-crust interface.

Similarly to recent work [49] we represent the radial part of the poloidal and toroidal potentials as a polynomial expansion

$$b_{lm}(r) = \frac{a_0 + a_1 r + a_2 r^2 + a_3 r^2 + a_4 r^4}{r} \,. \tag{24}$$

Overall, all conditions for the radial part of the poloidal potential can be written as

$$\begin{aligned} b_p(1) &= \beta_p(1.0)\,, \\ b_p(0.96) &= \beta_p(0.96)\,, \\ b_p(0.93) &= \beta_p(0.93)\,, \\ b_p(r_c) &= 0\,, \\ \tfrac{\partial b_p}{\partial r}(1) + \tfrac{(l+1)}{r} b_p(1) &= 0\,. \end{aligned} \tag{25}$$

Here $\beta_p(r)$ are coefficients of the spectral expansion for poloidal magnetic field extracted from the proto-NS `MagIC` simulations. These conditions are individually

satisfied for each l and m, and translate into the following system of linear equations

$$\begin{aligned}
&a_0 + a_1 + a_2 + a_3 + a_4 &&= \beta_p(1.0)\,,\\
&(a_0 + a_1 r_1 + a_2 r_1^2 + a_3 r_1^3 + a_4 r_1^4)/r_1 &&= \beta_p(r_1)\,,\\
&(a_0 + a_1 r_2 + a_2 r_2^2 + a_3 r_2^3 + a_4 r_2^4)/r_2 &&= \beta_p(r_2)\,,\\
&a_0 + a_1 r_c + a_2 r_c^2 + a_3 r_c^3 + a_4 r_c^4 &&= 0\,,\\
&a_0 l + (l+1)a_1 + (l+2)a_2 + (l+3)a_3 + (l+4)a_4 &&= 0\,.
\end{aligned} \tag{26}$$

For the toroidal potential we use the following conditions

$$\begin{aligned}
b_t(1) &= 0\,,\\
b_t(0.96) &= \beta_t(0.96)\,,\\
b_t(0.93) &= \beta_t(0.93)\,,\\
\partial\left[r b_t(r_c)\right]/\partial r &= 0\,.
\end{aligned} \tag{27}$$

Similarly, $\beta_t(r)$ here are the coefficients of the spectral expansion for the toroidal magnetic field extracted from the proto-NS simulations. These conditions then translate into the linear system

$$\begin{aligned}
&a_0 + a_1 + a_2 + a_3 &&= 0\,,\\
&(a_0 + a_1 r_1 + a_2 r_1^2 + a_3 r_1^3)/r_1 &&= \beta_t(r_1)\,,\\
&(a_0 + a_1 r_2 + a_2 r_2^2 + a_3 r_2^3)/r_2 &&= \beta_t(r_2)\,,\\
&a_1 + 2a_2 r_c + 3a_3 r_c^2 = 0\,.
\end{aligned} \tag{28}$$

4 Simulation of neutron star magneto-thermal evolution

The pseudo-spectral code `PARODY` [37] was modified to solve the following system of dimensionless partial differential equations for magnetic field $\vec{B}$ and temperature T:

$$\frac{\partial \vec{B}}{\partial t} = \mathrm{Ha}\,\vec{\nabla}\times\left[\frac{1}{\mu^3}\vec{B}\times(\vec{\nabla}\times\vec{B})\right] - \vec{\nabla}\times\left[\frac{1}{\mu^2}\vec{\nabla}\times\vec{B}\right] + \mathrm{Se}\,\nabla\left[\frac{1}{\mu}\right]\times\vec{\nabla}T^2\,, \tag{29}$$

$$\frac{\mu^2}{\mathrm{Ro}}\frac{\partial T^2}{\partial t} = \vec{\nabla}\cdot\left[\mu^2\hat{\chi}\cdot\vec{\nabla}T^2\right] + \frac{\mathrm{Pe}}{\mathrm{Se}}\frac{|\vec{\nabla}\times\vec{B}|^2}{\mu^2} + \mathrm{Pe}\,\mu\left[\vec{\nabla}\times\vec{B}\right]\cdot\vec{\nabla}\left[\frac{T^2}{\mu^2}\right]\,, \tag{30}$$

where the first equation is the magnetic induction equation and the second is the thermal diffusion equation. The terms on the right-hand side of the first equation correspond to the Hall effect, Ohmic decay and the Biermann battery effect. The terms on the right-hand side of the second equation correspond to anisotropic thermal diffusion, Ohmic heating and entropy carried by electrons. The derivation of the above equations is summarised in [54]. The same code was also used to compute the evolution of off-centred dipole configurations [49].

The electron chemical potential varies within the crust as

$$\mu(r) = \mu_0 \left[1 + \frac{(1 - r/R_{\rm NS})}{0.0463}\right]^{4/3} . \tag{31}$$

The tensor $\hat{\chi}$ describing the anisotropy of the heat transport is written as:

$$\hat{\chi} = \frac{\delta_{ij} + {\rm Ha}\, B_i B_j/\mu^2 - {\rm Ha}\, \epsilon_{ijk} B_k/\mu}{1 + {\rm Ha}^2\, |\vec{B}|^2/\mu^2} , \tag{32}$$

where δ_{ij} is the Kronecker symbol and ϵ_{ijk} is the Levi-Civita symbol.

The dimensionless Hall (Ha), Seebeck (Se), Péclet (Pe) and Roberts (Ro) parameters depend on the chosen scales for the magnetic field and temperature, which we take to be $B_0 = 10^{14}$ G and $T_0 = 1.0 \times 10^8$ K. The Hall number is defined by

$${\rm Ha} = c\tau_0 \frac{eB_0}{\mu_0} \approx 49.1 , \tag{33}$$

where e is the electron charge, c is the speed of light, $\tau_0 = 9.9 \times 10^{19}$ s is the electron scattering relaxation time [55] and $\mu_0 = 2.9 \times 10^{-5}$ erg is the electron chemical potential at the top of the crust. The Seebeck number is defined by

$${\rm Se} = 2\pi^3 k_{\rm B}^2 T_0^2 n_0 e \frac{c\tau_0}{\mu_0 B_0} \approx 0.052 , \tag{34}$$

where $k_{\rm B}$ is the Boltzmann constant and $n_0 = 2.603 \times 10^{34}$ cm^{-3} is the electron number density at the top of the crust. Finally, the Péclet and Roberts numbers are

$${\rm Pe} = \frac{3}{4\pi} \frac{B_0}{e n_0 c \tau_0} \approx 6.44 \times 10^{-5} , \tag{35}$$

and

$${\rm Ro} = \frac{3}{4\pi^3} \frac{\mu_0^2}{k_{\rm B} T_0} \frac{1}{c^2 \tau_0^2} \frac{1}{e^2 n_0} \approx 3580 . \tag{36}$$

In order to ensure the solenoidality of the magnetic field $\vec{B}$, we write the magnetic field as a sum of poloidal and toroidal parts

$$\vec{B} = \vec{\nabla} \times \vec{\nabla} \times (b_{\rm pol} \vec{r}) + \vec{\nabla} \times (b_{\rm tor} \vec{r}) . \tag{37}$$

The scalar potentials $b_{\rm pol}$ and $b_{\rm tor}$ are expanded in spherical harmonics. We model the core as a perfect conductor, which implies the following inner boundary conditions at $r = 0.9$

$$b_{\rm pol} = 0 \qquad \text{and} \qquad \frac{d(r b_{\rm tor})}{dr} = 0 . \tag{38}$$

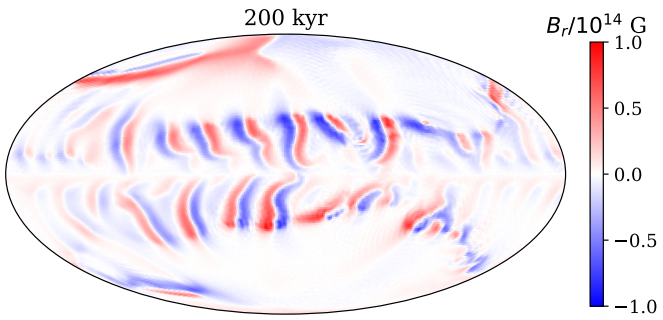

Fig. 7 The surface radial magnetic field after 200 kyr of evolution.

We model the region outside the NS as a vacuum, which implies the following outer boundary conditions at $r = 1$

$$\frac{db_{\rm pol}^{lm}}{dr} + \frac{l+1}{r} b_{\rm pol}^{lm} = 0 \qquad \text{and} \qquad b_{\rm tor} = 0\,, \tag{39}$$

where $b_{\rm pol}^{lm}$ is the coefficient of degree l and order m in the spherical harmonic expansion of the poloidal potential $b_{\rm pol}$.

The temperature is fixed to its initial value at the core–crust boundary (see more details about modelling cooling at the end of the section). The outer boundary condition for the temperature is

$$-\mu^2 \vec{r} \cdot \hat{\chi} \cdot \vec{\nabla}(T^2) = \frac{1}{5} \frac{R_{\rm NS}}{c\tau_0}\, {\rm Se}\, {\rm Pe}\, (T_s/T_0)^4\,, \tag{40}$$

where the (dimensional) surface temperature T_s is related to the crustal temperature T_b as:

$$\left[\frac{T_s}{10^6\ {\rm K}}\right]^2 = \left[\frac{T_b}{10^8\ {\rm K}}\right]\,, \tag{41}$$

using simplified relation [56].

The numerical resolution is $n_r = 96$ grid points in the radial direction and spherical harmonic degrees up to $l_{\rm max} = 128$. We show the surface radial magnetic field as well as the surface temperature at age 200 kyr in Figures 7 and 8. We show the evolution of magnetic energy spectra in Figure 6.

To take into account the NS cooling, we restart calculations at 200 kyr changing the core temperature to 10^6 K. We run calculations for 1 kyr to allow the simulation

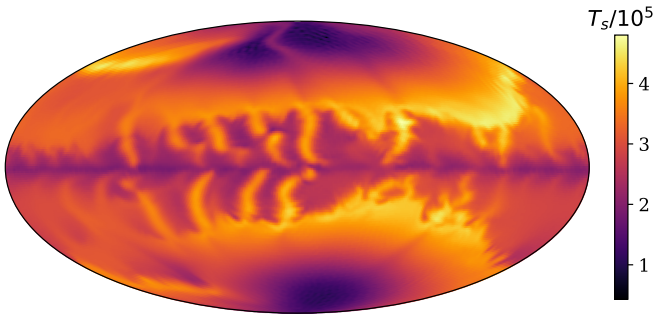

Fig. 8 The surface temperature after 200 kyr of evolution assuming a NS core temperature 10^6 K. No magnetospheric hot spots are shown.

low-field magnetar	χ (rad)	i (rad)	$\Delta\Phi$ (rad)	C-stat
SGR 0418+5729	0.6984	1.264	5.616	6.8
CXOU J164710.2-455216	0.7518	1.085	5.555	29.9
Swift J1822.3-1606	0.0519	0.636	5.625	16.5
3XMM J185246.6+003317	1.093	1.637	5.330	34.7

Table 1 Possible rotational orientation for low-field magnetars assuming that their X-ray lightcurves are produced by hot spots.

to relax, i.e. crust temperatures stop evolving on short timescales, creating a stable surface thermal pattern.

5 Properties of thermal emission

We use the open source code `Magpies`[3] to model X-ray thermal lightcurves. We show these results in Figure 9. The maximum pulsed fraction reaches 93 % for the most favourable orientation of the rotational axis with respect to the original dipole axis.

Similarly to [15] we try to fit the soft X-ray lightcurve in the range 0.3-2 keV. We show the results in Figure 10. We summarise the obliquity angle as well as inclination angles in Table 1. While SGR 0418+5729 and Swift J1822.3-1606 are fitted relatively well, the two remaining magnetars have more features in the lightcurves.

[3] https://github.com/ignotur/magpies

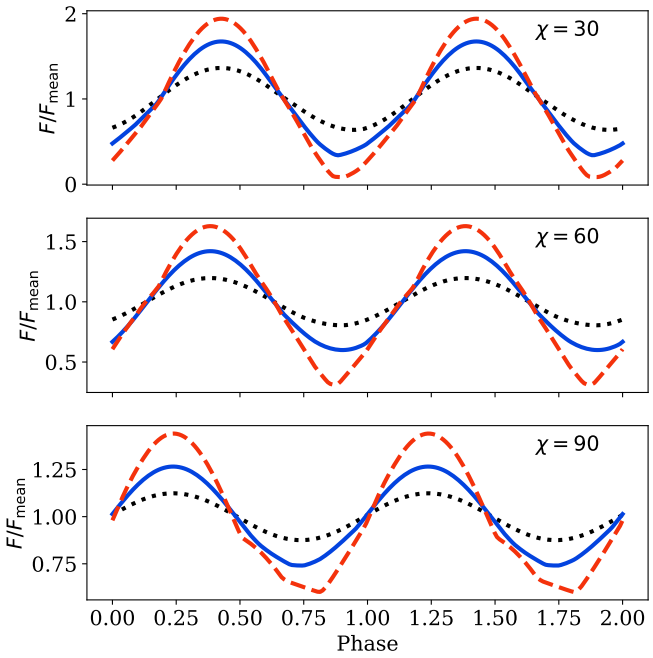

Fig. 9 Soft X-ray lightcurves for the surface thermal map combined with the magnetospheric hot spots. Each panel corresponds to a different obliquity angle χ. The three curves correspond to different inclination angles: black dotted lines are for $i = 30°$, blue solid lines are for $i = 60°$, and red dashed lines are for $i = 90°$.

6 Crust failure

We use here a model developed by [45] based on earlier work by [44]. Essentially, we use the von Mises criterion for crust-yielding following Eq. (14) of [45]:

$$\tau_{\rm el} \leq \frac{1}{4\pi}\sqrt{\frac{1}{3}\vec{B}_0^4 + \frac{1}{3}\vec{B}^4 + \frac{1}{3}\vec{B}_0^2\vec{B}^2 - (\vec{B}\cdot\vec{B}_0)^2}\,. \tag{42}$$

Here $\vec{B}_0$ is the relaxed (initial) state of the magnetic field, which we assume to coincide with our first simulation snapshot at 2 kyr. $\tau_{\rm el}$ is the scalar yield stress. The field $\vec{B}$ is computed at 200 kyr. We compute the critical strain following the procedure by [45] with a correction (private communication by Sam Lander)

$$\tilde{\rho} = 99.6\left(1 - \frac{R_{\rm cc}}{R_{\rm nd}}\right)^2 (1-\mathcal{R})^2 + 0.004\,, \tag{43}$$

where $\mathcal{R}$ is computed as:

$$\mathcal{R} = \frac{r - R_{\rm cc}}{R_{\rm nd} - R_{\rm cc}}\,, \tag{44}$$

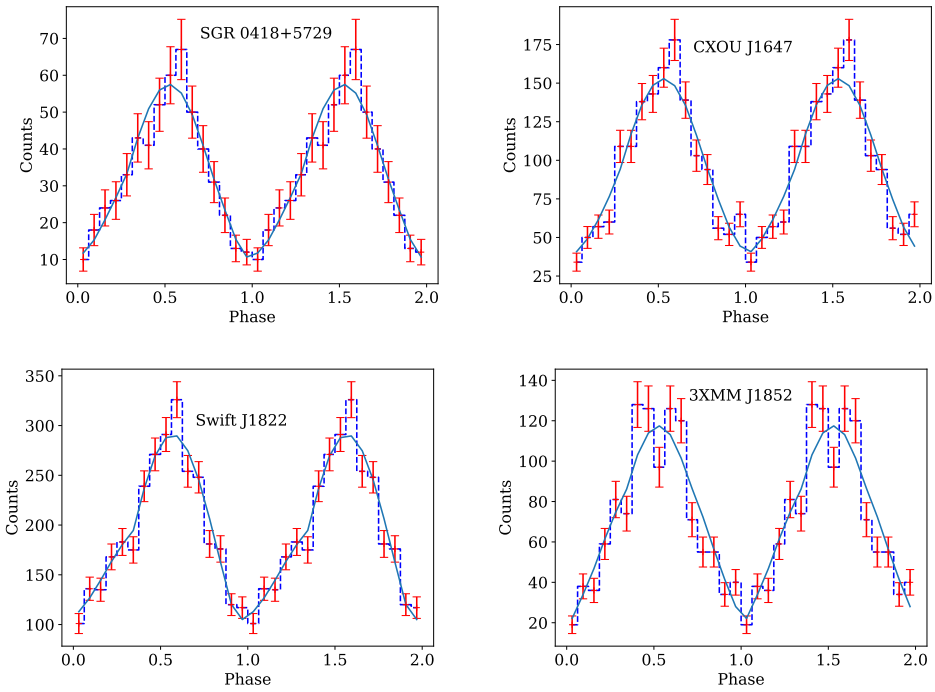

Fig. 10 Observed soft X-ray lightcurves in the range of 0.3-2 keV for low-field magnetars in the quiescent state and the best fits (solid blue line). It is assumed that emission is produced by hot spots formed at the places with radial magnetic field exceeding 7×10^{13} G.

where $R_{\rm cc} = 0.9$ is the location of the crust-core interface and $R_{\rm nd} = 1$ is the location of the neutron-drip point. Thus, our critical strain varies from $\approx 8 \times 10^{26}$ g cm^{-1} s^{-2} close to the neutron-drip boundary to 4.6×10^{29} g cm^{-1} s^{-2} at the core-crust boundary. Following our normalisation, the stress caused by Lorentz forces (right-hand side of equation 42) is multiplied by a numerical factor $(10^{14}$ G$)^2$. This von Mises criterion is written assuming that failure occurs in the form of shearing motion [45].

7 Accretion driven spin-down

To explain the NS spin-down to the regime of low-field magnetars, we invoke the propeller mechanism due to the interaction between the NS magnetic field and the remaining fallback disk. The evolution of the NS-fallback depends on the three different radii: (i) the light cylinder radius, (ii) the magnetospheric radius, and (iii) the corotation radius, which are defined by the respective expressions

$$r_{\rm lc} = \frac{c}{\Omega_{\rm NS}}\,, \tag{45}$$

$$r_{\rm mag} = \mu^{4/7} (G M_{\rm NS})^{-1/7} \dot{M}^{-2/7}\,, \tag{46}$$

$$r_{\rm cor} = \left(\frac{GM_{\rm NS}}{\Omega_{\rm NS}^2}\right)^{1/3} . \tag{47}$$

Here c is the speed of light, and G is the gravitational constant. $M_{\rm NS}$ and $\Omega_{\rm NS}$ are the NS mass and rotation rate; $\mu = B_{\rm NS}R_{\rm NS}^3$ is its magnetic dipole moment. $\dot{M}$ is the accretion rate[4].

If the disk penetrates the magnetosphere ($r_{\rm lc} > r_{\rm mag}$), it can either spin up the NS by accreting matter if $r_{\rm cor} > r_{\rm mag}$, or spin down the NS in a propeller phase if $r_{\rm cor} < r_{\rm mag}$. In this propeller phase, the magnetic field accelerates the inner disk to super-Keplerian speeds, which produces a centrifugal outflow. Angular momentum is therefore transported from the NS toward the disk, which can efficiently spin down the NS.

The modelling of the NS-fallback evolution we use is strongly inspired by [57] except for the mass accretion rate, which reads [48]

$$\dot{M}(t) = \dot{M}_0 \left(1 + \frac{t}{t_\nu}\right)^{-1.2} , \tag{48}$$

where $t_\nu \sim 30$ s is the viscous timescale and $\dot{M}_0 = M_{\rm d,0}/t_\nu \sim 6.5 \times 10^{29}$ g s^{-1} is the initial accretion rate, and $M_{\rm d,0} = 0.01\,{\rm M}_\odot$ is the initial fallback disk mass. The torques exerted on the NS by the accretion disk are given by

$$N_{\rm acc} = \begin{cases} \left(1 - \left(\frac{r_{\rm mag}}{r_{\rm cor}}\right)^{3/2}\right) \sqrt{GM_{\rm NS}R_{\rm NS}\dot{M}^2} & \text{if } r_{\rm mag} > R_{\rm NS} , \\ \left(1 - \left(\frac{\Omega_{\rm NS}}{\Omega_{\rm K}}\right)^{3/2}\right) \sqrt{GM_{\rm NS}R_{\rm NS}\dot{M}^2} & \text{if } r_{\rm mag} < R_{\rm NS} , \end{cases} \tag{49}$$

where $\Omega_{\rm K} = \sqrt{GM_{\rm NS}/R_{\rm NS}^3}$ is the Keplerian angular velocity. The dipole spins the NS down as follows

$$N_{\rm dip} = -\frac{2}{3}\frac{\mu^2\Omega_{\rm NS}^3}{c^3}\left(\frac{r_{\rm lc}}{r_{\rm mag}}\right)^3 . \tag{50}$$

Therefore the NS angular velocity evolves as

$$I_{\rm NS}\dot{\Omega}_{\rm NS} = N_{\rm acc} + N_{\rm dip} , \tag{51}$$

where $I_{\rm NS} = 1.45 \times 10^{45}$ g cm^2 is the NS moment of inertia. Figure 11 shows the time series of the characteristic radii and NS rotation period that result from the solution of equation (51) for $B_{\rm NS} = 10^{12}$ G, $M_{\rm d,0} = 0.01$ M$_\odot$, and an initial rotation period of 10 ms. We clearly find that the NS is strongly spun down during the propeller phase and reaches the period range of the observed low-field magnetars at ~ 170 kyr. This timescale varies up to ~ 550 kyr for $B_{\rm NS} = 5 \times 10^{11}$ G. Figure 11 shows the period and period derivative evolution.

[4]Strictly speaking, $\dot{M}$ is the material loss rate from the accretion disk. In the propeller regime this quantity remains positive even though the material is not accreted onto the neutron star.

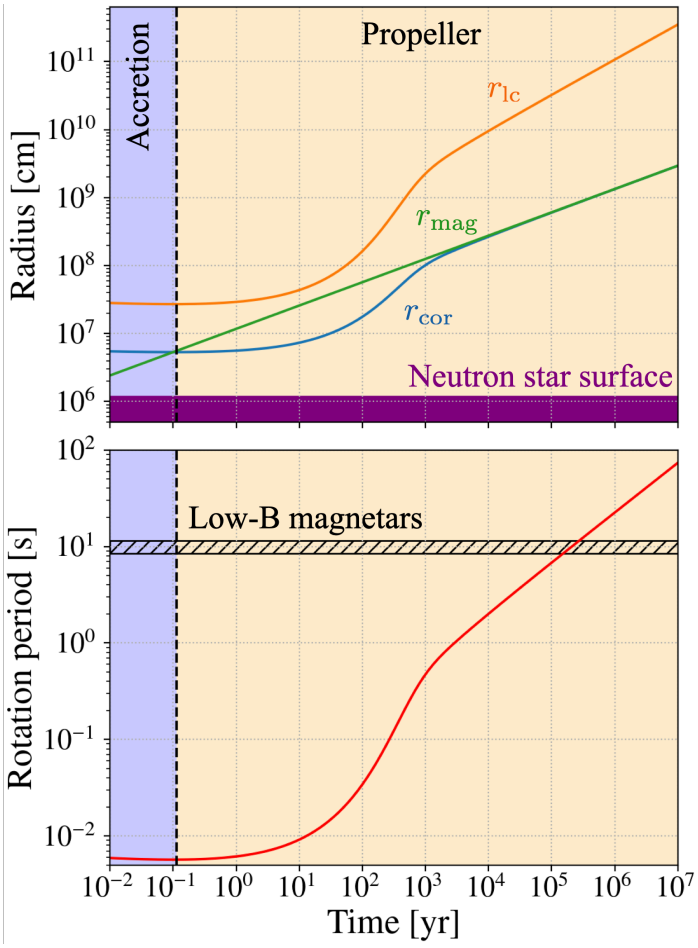

Fig. 11 Time evolution of the characteristic radii (top) and the NS rotation period (bottom) for $B_{\rm NS} = 10^{12}$ G, $M_{\rm d,0} = 0.01$ M$_\odot$, and an initial rotation period of 10 ms. The NS is spun up during the accretion regime (blue region) and strongly spun down in the propeller phase (orange region). The hatched region in the bottom figure represents the range of rotation periods observed in low-field magnetars.

C.3.5 . Article *Tayler-Spruit dynamo in binary neutron star merger remnant (to be submitted)*

Astronomy & Astrophysics manuscript no. output
June 6, 2024

Tayler-Spruit dynamo in binary neutron star merger remnant

Alexis Reboul-Salze[1], Paul Barrère[2], Kenta Kiuchi[1], Raphaël Raynaud[3], Jérôme Guilet[2], Sho Fujiyabashi[1] and Masaru Shibata[1]

[1] Max Planck Institute for Gravitational Physics (Albert Einstein Institute), D-14476 Potsdam, Germany
e-mail: alexis.reboul-salze@aei.mpg.de
[2]Université Paris-Saclay, Université Paris Cité, CEA, CNRS, AIM, 91191, Gif-sur-Yvette, France
[3]Université Paris Cité, Université Paris-Saclay, CNRS, CEA, AIM, F-91191 Gif-sur-Yvette, France

Received ??; ??

ABSTRACT

Context. In binary neutron star mergers, the remnant can be stabilized by differential rotation before it collapses into a black hole. Therefore, the angular momentum transport mechanisms are important to predict the lifetime of the hypermassive neutron star. One such mechanism is the Tayler-Spruit dynamo, and recent simulations have shown that it could grow in the context of the proto-neutron star.
Aims. We aim to examine whether hypermassive neutron stars with high neutrino viscosity could be unstable to the Tayler-Spruit dynamo and how magnetic fields would evolve.
Methods. With a one-zone model based on a 3D GRMHD simulation, we investigate the time evolution of the magnetic fields generated by the dynamo. We also analyze the dynamics of the 3D GRMHD simulation to see whether the dynamo is present.
Results. We find that the Tayler-Spruit dynamo can increase the toroidal magnetic field to $\geq 10^{17}$ G and the dipole to amplitudes $\geq 10^{16}$ G. The dynamo's growth timescale depends on the initial large-scale magnetic field right after the merger. In the case of a long-lived hypermassive neutron star, an initial magnetic field of $\geq 10^{12}$ G would be enough to grow in its lifetime. However, we show that the resolution of current GRMHD simulations is not enough to resolve the Tayler-Spruit dynamo due to the high dissipation at small scales.
Conclusions. Overall, we find that the Tayler-Spruit dynamo could occur in hypermassive neutron stars and shorten its lifetime, which would have consequences on multi-messenger observations.

Key words.

1. Introduction

The association of GW170817 and GRB 170817A confirmed that binary neutron star mergers are the progenitors of some short gamma-ray bursts (Abbott et al. 2017). The nature of the remnant of GW170817 is quite uncertain, and many different parameters can impact the time before its collapse into a black hole. Depending on the hot and dense matter equation of state and the masses of the neutron star, different fates await the remnant after the merger: it can promptly collapse into a black hole, it can also form a hypermassive neutron star, i.e. a neutron star that is stabilized by differential rotation while having a mass higher than the limit mass of a cold non-rotating neutron star M_{TOV}. This remnant can either collapse into a black hole when the angular momentum is transported or be stabilized by the solid body rotation, increasing the limit mass by around $\sim 20\%$. In this stage, the remnant is called a supramassive neutron star and can collapse after losing its rotation by magnetic dipole spin-down on the timescale of minutes, hours or longer and even remain as a stable neutron star if the mass of the remnant is lower than M_{TOV}.

After the merger of two neutron stars, the remaining object can significantly affect the electromagnetic counterparts due to various factors. These factors include powerful neutrino luminosity, strong magnetic fields ($\geq 10^{15}$ G), and rotational energy reservoirs of around 10^{53} erg. Several studies have examined the impact of these factors on post-merger events (Metzger et al. 2008; Bucciantini et al. 2012; Giacomazzo & Perna 2013; Gao et al. 2013; Metzger & Piro 2014; Gompertz et al. 2014; Sarin et al. 2022). Magnetic fields, along with fast rotation, play a critical role in the merger of neutron stars as they can extract rotational energy and serve as a source of energy for relativistic outflows from the merger remnant (Combi & Siegel 2023; Kiuchi et al. 2024). Therefore, understanding the evolution of the magnetic field and the rotation profile of the hypermassive neutron star is crucial in predicting future multi-messenger observations.

During the first few milliseconds after the merger, the magnetic field of the hypermassive neutron star is amplified by the Kelvin-Helmholtz instability due to the shear layer at the surface where the two neutron stars enter into contact. This leads to a strong and small-scale magnetic field. Another mechanism is necessary to get a large-scale magnetic field that could drive an outflow. Two different mechanisms could play this role in different regions of the hypermassive neutron star. Indeed, the remnant from the binary neutron star (BNS) merger has a rotation profile with an angular velocity that increases with radius until 10 km and then decreases afterwards (Kastaun et al. 2016, 2017; Ciolfi et al. 2017, 2019). This rotation profile is, therefore, unstable to the magnetorotational instability after 10 km, and it has been studied in the long-lived remnant case. Notably, it was shown that it could drive a luminous relativistic outflow (Ciolfi 2020; Combi & Siegel 2023; Kiuchi et al. 2024). However, the differential rotation in the core before 10 km, which makes it stable to

the MRI, has never been studied, and this region could be unstable to the Tayler-Spruit dynamo, driven by the Tayler instability.

The Tayler Instability is a type of magnetic instability in flows of electrically conductive and stably stratified fluids where a strong azimuthal magnetic field can become unstable, causing disruptions due to the Lorentz forces that arise from the interaction of currents along the axis of symmetry and magnetic fields (Tayler 1973; Pitts & Tayler 1985). The first model of a dynamo driven by the Tayler instability was proposed by Spruit (2002) to happen in stably stratified and differentially rotating regions. Fuller et al. (2019) have proposed an alternative description to address a few criticisms received by this model (see Denissenkov & Pinsonneault 2007; Zahn et al. 2007). Numerical simulations have been unable to capture the Tayler-Spruit dynamo for a long time. However, recent numerical simulations have finally provided numerical evidence that this dynamo exists (Petitdemange et al. 2023; Barrère et al. 2023; Petitdemange et al. 2024). In the study of the interior physics of stars, the dynamo is often used to explain magnetic field amplification, which could impact angular momentum transport and lead to the magnetic desert in Ap/Bp stars (Rüdiger & Kitchatinov 2010; Szklarski & Arlt 2013; Bonanno & Guarnieri 2017; Ma & Fuller 2019; Bonanno et al. 2020; Jouve et al. 2020). This dynamo process has been recently studied in the context of magnetar formation, providing a new scenario with no initial fast rotation needed (Barrère et al. 2022, 2023).

The Tayler-Spruit has been proposed to transport the angular momentum of the hypermassive neutron star, which would lead it to collapse into a black hole (Margalit et al. 2022). This study estimated the angular momentum transport timescale due to the transport by the theoretical saturated magnetic fields from scalings. However, the neutrino viscosity could make the TS dynamo stable, or it could require a longer time to grow towards the saturated magnetic field strength than the lifetime of the hypermassive neutron star.

Therefore, this paper aims to study whether the conditions in binary neutron star mergers could allow the Tayler-Spruit dynamo to grow and impact the explosion. In particular, this study applies a similar one-zone model to (Barrère et al. 2022) in the framework of binary neutron star merger. The paper is organized as follows: In section 2, we describe how we model the hypermassive neutron star and the equations for a one-zone model of the Tayler-Spruit dynamo. The results of the one-zone models are presented section 3, while we compare the results of the model to the recent super-high resolution GRMHD simulation in section 4. Lastly, the validity of our assumptions is discussed in section 5, and we conclude in section 6.

2. A one-zone model of the Tayler-Spruit dynamo in the HMNS

2.1. Modelling of the hypermassive neutron star

For our hypermassive neutron model, we use the data from a 3D GRMHD simulation with a stiff equation of state, DD2, where the remnant lasts for longer than 150 ms (Paper I). To check whether the Tayler-Spruit (TS) dynamo is relevant for this hypermassive neutron star (HMNS), we look at the rotation profile of the HMNS (Figure 1) at different times. The remnant has a cylindrical rotation profile that shows a large region in positive differential rotation from $R = 5$ km and $R = 10$ km, where the Tayler-Spruit (TS) dynamo could grow. Note that this rotation profile is found to be typical of hypermassive neutron stars in many different simulations (Kastaun et al. 2016, 2017; Ciolfi et al. 2017, 2019). In the following, we use the radius $r = 7$ km as a typical radius for our thermodynamical quantities. At this radius, we have $\Omega = 5468$ s^{-1} and a shear rate of $q = 1.12$.

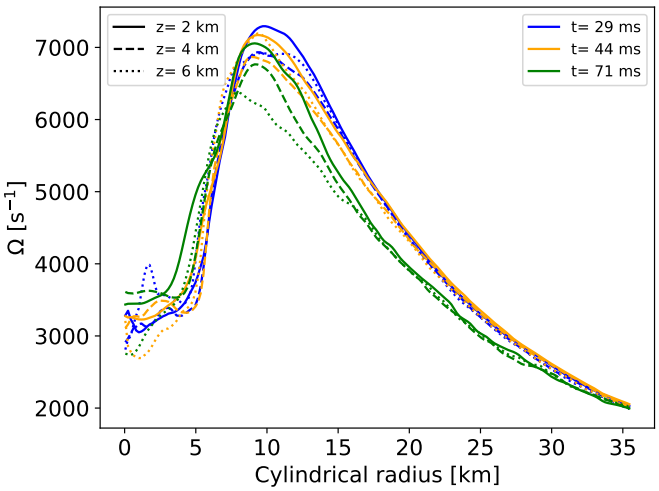

Fig. 1. Azimuthal averaged rotation profile of the remnant as a function of the cylindrical radius, at different times t and vertical position z.

The TS dynamo requires to be convectively stable for its growth. Therefore, we test whether the core of the binary neutron star remnant is convectively stable. For that, we use the relativistic Ledoux criterion, given by

$$C_{\rm L} = \frac{\partial \rho(1+\epsilon)}{\partial r} - \frac{1}{c_s^2}\frac{\partial P}{\partial r}, \tag{1}$$

where ρ, ϵ, c_s, P are the density, internal energy, sound speed and pressure in the remnant. We find that the HMNS is indeed stably stratified, and we use the General Relativistic formula for the Brunt-Väisälä (BV) frequency N derived in Müller et al. (2013):

$$N^2 \equiv -c^2 \frac{\alpha C_{\rm L}}{\rho h \phi^4}\frac{\partial \alpha}{\partial r}, \tag{2}$$

where α, h, ϕ are the lapse function, the specific enthalpy and the conformal factor. This formula comes from the hydrostatic equilibrium written as $\mathcal{G} = c^2 \nabla \ln \alpha$. Since our hypermassive neutron star is rapidly rotating, we prefer to use this definition of hydrostatic equilibrium instead of the one with the pressure gradient for our background. With this formula, we find typical values of $N = 3690$ s^{-1} at a radius of $R_{TI} = 7$ km for the Brunt-Väisälä frequency. The density is equal to $\rho = 3.7 \times 10^{14}$ g cm^3.

We note that in this context, we cannot assume that the rotation rate Ω is much lower than the Brunt-Väisälä frequency, and we assume only that $\omega_{\rm A} \ll \Omega, N$ for section 3. Note that this hypothesis may no longer be valid when we analyze the core dynamics in the GRMHD simulation, as the toroidal magnetic field can be winded to higher values.

2.2. Standard Tayler-Spruit picture

As in Fuller et al. (2019); Barrère et al. (2022), we decompose the velocity and magnetic field components into axisymmetric components noted as B_i or u_i and non-axisymmetric components noted as δB_i and δu_i. For the evolution of the angular velocity,

we consider that the initial value decreases due to the magnetic torque. It gives

$$\dot{\Omega} = -\frac{R_{TI}^2 B_r B_\phi}{I} \tag{3}$$

where I is the moment of inertia of the inner zone below 10 km. The angular momentum is transported by the Maxwell stress tensor and is evolved by

$$\dot{q} = -\gamma_{\rm AM} q = -\frac{B_r B_\phi}{4\pi\rho\Omega R_{TI}^2}\,. \tag{4}$$

The difference between the HMNS model and the PNS model of Barrère et al. (2022) is the geometry: the rotation profile in an HMNS is cylindrical while spherical for a late PNS with fallback accretion. We, therefore use B_r to designate the cylindrical radial field in our study. The derivation of the equations is almost the same except for the equation of B_r. Indeed, in cylindrical coordinates, the growth of the B_r due to the toroidal component of the electromotive force $\mathcal{E}_\phi$ is given by

$$\frac{\partial B_r}{\partial t} = -\frac{\partial \mathcal{E}_\phi}{\partial z} \sim \frac{\mathcal{E}_\phi}{L_z}, \tag{5}$$

where L_z is the vertical wavelength of the Tayler instability. We retrieve the same formula as previous studies in spherical geometry if we assume $L_z \sim R_{TI}$, which we will do for the sake of simplicity.
The magnetic field evolution is therefore governed by the following equations (Barrère et al. 2022)

$$\partial_t B_\phi = (\sigma_{\rm shear} - \gamma_{\rm diss})\, B_\phi = q\Omega B_r - \frac{\omega_{\rm A}^2}{\Omega}\frac{\delta B_\perp^2}{B_\phi}\,, \tag{6}$$

$$\partial_t \delta B_\perp = (\sigma_{\rm TI} - \gamma_{\rm cas})\, \delta B_\perp = \frac{\omega_{\rm A}^2}{\Omega}\delta B_\perp - \frac{\delta v_{\rm A}}{R_{TI}\delta B_\perp}\,, \tag{7}$$

$$\partial_t B_r = (\sigma_{\rm NL} - \gamma_{\rm diss})\, B_r = \frac{\omega_{\rm A}^2}{N\Omega}\frac{\delta B_\perp^2}{\sqrt{4\pi\rho R_{TI}^2}} - \frac{\omega_{\rm A}^2}{\Omega}\left(\frac{\delta B_\perp}{B_\phi}\right)^2 B_r\,, \tag{8}$$

where $\omega_{\rm A}$, $\delta v_{\rm A}$ are respectively the Alfvén frequency of the toroidal magnetic field B_ϕ and the Alfvén speed of the non-axisymmetric component $\delta B_\perp$.

2.3. Diffusive impact on the Tayler-Spruit dynamo

In a hypermassive neutron star, the impact of the neutrinos on the momentum equation can be modelled as a strong viscosity for scales larger than the neutrino mean free path. By taking into account the degeneracy of neutrinos in the core of the HMNS, the viscosity can be estimated by the formula (Margalit et al. 2022)

$$\nu_{\rm deg} = 1.2\times10^{10}\left(\frac{\rho}{10^{14}{\rm g\ cm^{-3}}}\right)\left(\frac{Y_\nu}{0.1}\right) \tag{9}$$

In the case of our model, this gives a viscosity of $\nu = 2.3\times10^9\,{\rm cm^2\,s^{-1}}$ at $r = 7$ km for our model. This would lead to magnetic Prandtl number of

$$Pm \equiv \frac{\nu}{\eta} = 1.8\times10^{14},$$

where η is assumed to be the resistivity due to electron-proton scattering (Thompson & Duncan 1993). The thermal diffusion due to neutrinos is higher than viscosity and the thermal Prandtl number Pr is found to be

$$Pr \equiv \frac{\nu}{\kappa} = 10^{-3} - 10^{-2}$$

(Raynaud et al. 2020; Reboul-Salze et al. 2022).

We check the assumptions that could change in the formalism of Fuller et al. (2019): a magnetostrophic balance (Coriolis-Lorentz force balance) is assumed to derive the equations. Still, a dense balance could also be possible due to neutrinos. To compare the Coriolis force and the viscous force, a local Ekman number can be defined as

$$E = \frac{\nu k_{\rm TI}^2}{\Omega}, \tag{10}$$

where $k_{\rm TI}$ is the wavenumber of the displacements due to the Tayler instability. The minimum of this wavenumber has been estimated by Spruit (2002) as

$$k_{\rm TI} > \frac{N}{R_{TI}\omega_{\rm A}} \tag{11}$$

We also want to have a growth rate of the Tayler Instability that is faster than the viscous timescale, which limits the maximum wavenumber to be smaller than

$$k_{\rm TI}^2 < \frac{\omega_{\rm A}^2}{\Omega\nu} \tag{12}$$

To satisfy both limits, the magnetic field must be stronger than the critical magnetic field

$$B_{\rm crit} = (4\pi\rho R_{TI} N)^{\frac{1}{2}}\,(\nu\Omega)^{\frac{1}{4}} \sim 7.9\times10^{15}{\rm G}, \tag{13}$$

This high critical strength for our model means that the shear must amplify the magnetic field before the Tayler instability can increase the small-scale magnetic field.
We note that this critical magnetic field is a conservative estimate as the recent study of Skoutnev & Beloborodov (2024) show that , in the case of a large cylindrical gradient of the toroidal field, (corresponding to the geometric criterion of Goossens & Tayler (1980)) the criterion depending on diffusivities is

$$\frac{w_A}{2\Omega} \gg \left(\frac{N}{2\Omega}\right)^{1/2}\left(\frac{\eta k_\theta^2}{2\Omega}\right)^{1/4} min(1, \left(\frac{\eta}{\kappa}\right)^{1/4}) \approx 2.15\times10^{-9}. \tag{14}$$

This gives a lower limit for the magnetic field of $B_{\phi,\rm crit} > 1.1\times10^9$ G, which is easily verified with winding of the magnetic field and therefore we keep the viscous criterion to be sure.

The Ekman number for this magnetic field value is $E \sim 1.6\times10^{-6}$, and we can safely assume the magnetostrophic balance. For both wavenumber limits, we can estimate the range of magnetic fields where viscosity will dominate over Coriolis force, i.e. $E > 1$, by

$$B < B_{\rm min,\,visc} = \sqrt{4\pi\rho}N\sqrt{\frac{\nu}{\Omega}} \approx 1.7\times10^{14}{\rm G}, \tag{15}$$

$$B > B_{\rm max,\,visc} = \sqrt{4\pi\rho R_{TI}^2\Omega} \approx 3.5\times10^{17}\ {\rm G}. \tag{16}$$

Therefore, the magnetostrophic balance can be assumed for both the Tayler instability and dynamo phases but not necessarily for the beginning of time evolution. However, the magnetic field strength is amplified to superior values than $B_{\rm min,\,visc}$ by the winding, for which the magnetostrophic balance can

also be assumed. We assume a viscous-Lorentz force balance when the magnetic field is stronger than the maximum value. When $E > 1$, the viscous-Lorentz balance can be written as $\delta v_\perp \sim \delta v_A \omega_A/(\nu k_{TI}^2)$. To obtain this balance from the magnetostrophic balance, $\delta v_\perp \sim \delta v_A \omega_A/\Omega$. The magnetostrophic balance is used to derive the non-linear growth rate of the TS dynamo, and the balance needs to be divided by the Ekman number E with the viscous-Lorentz. The TI wavelength k_{TI} is assumed to be equal to k_{crit} for all the evolution.

In order to take into account the impact of the viscosity in the evolution equations, we modify equation 7 to include the cases where the hypermassive neutron star is stable to the Tayler Instability and modify equation 8 when $E > 1$. First, the equation 7 becomes then

$$\partial_t \delta B_\perp = (\sigma_{TI} - \gamma_{cas})\,\delta B_\perp = \mathcal{B}_{TI}\frac{\omega_A^2}{\Omega}\delta B_\perp - \frac{\delta v_A}{R_{TI}}\delta B_\perp\,, \tag{17}$$

where

$$\mathcal{B}_{TI} = \begin{cases} 0 & \text{if } B < B_{crit} \text{ or } B_r/B_\phi > \omega_A/N \\ 1 & \text{otherwise.} \end{cases} \tag{18}$$

The second condition is to keep the divergence-free property of the axisymmetric field B_ϕ due to the solenoidal condition of the perturbed magnetic field δB. For equation 8, the growth rate of B_r is divided by E if $E > 1$, which gives

$$\partial_t B_r = (\sigma_{NL} - \gamma_{diss})\,B_r = \frac{\omega_A^2}{N\Omega}\frac{\delta B_\perp^2}{\max(1,E)\sqrt{4\pi\rho R_{TI}^2}} - \frac{\omega_A^2}{\Omega}\left(\frac{\delta B_\perp}{B_\phi}\right)^2 B_r\,, \tag{19}$$

3. Results of the one-zone model

3.1. A fiducial case

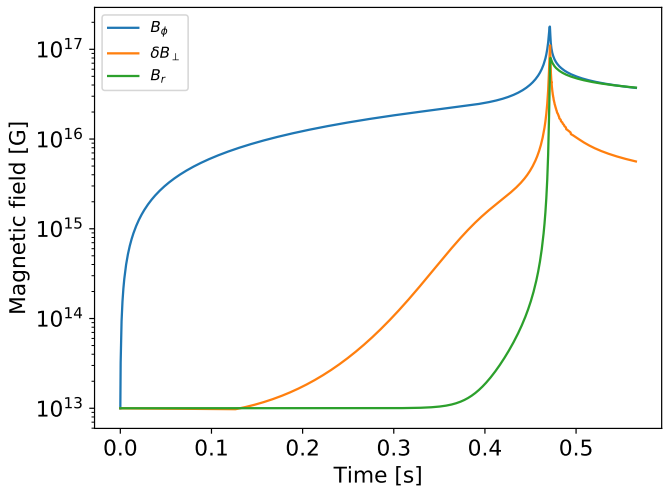

Fig. 2. Time evolution of the magnetic field for a typical hypermassive neutron star with thermodynamic quantities taken $t - t_{merger} = 30$ ms at a radius of $R_{TI} = 7$ km and an initial magnetic field of $B_0 = 10^{13}$ G.

For the first case, we assume the initial large-scale magnetic field to be $B_{r,0} = 10^{13}$ G. Figure 2 shows the time evolution of the magnetic field, the shear rate and the angular velocity. As in Barrère et al. (2022), the evolution can be divided into three phases: the winding phase, the Tayler instability phase and the dynamo phase. In the first phase, the shear amplifies the toroidal magnetic field. The winding phase lasts for around 150 milliseconds. When the toroidal magnetic field is stronger than the critical magnetic field B_{crit}, the non-axisymmetric magnetic field $\delta B_\perp$ grows due to the Tayler instability. The duration of this phase is around 250 milliseconds. When $\delta B_\perp$ becomes strong enough for the non-linear induction to be relevant, the dynamo is entirely in action and increases all the magnetic field components for 80 milliseconds. The dynamo stops when the angular momentum is transported, and the HMNS core is in solid body rotation. At saturation, the toroidal, radial and perturbed magnetic fields are equal to $B_\phi^{sat} = 1.79 \times 10^{17}$ G, $B_r^{sat} = 8.0 \times 10^{16}$ G, $\delta B_\perp^{sat} = 1.11 \times 10^{17}$ G.

We compare the saturation values of the axisymmetric field B_r, B_ϕ obtained by the model to the estimated saturated magnetic field from the following formulas (Spruit 2002; Fuller et al. 2019)

$$B_{F,\phi}^{sat} = \sqrt{4\pi\rho R_{TI}^2}\,\Omega\left(\frac{q\Omega}{N}\right)^{1/3} \approx 2.8 \times 10^{17}\text{ G}, \tag{20}$$

$$B_r^{F,sat} = \sqrt{4\pi\rho R_{TI}^2}\,\Omega\left(\frac{q^2\Omega^5}{N^5}\right)^{1/3} \approx \times 3.3 \times 10^{17}\text{ G}, \tag{21}$$

$$\delta B_\perp^{F,sat} = \sqrt{4\pi\rho R_{TI}^2}\,\Omega\left(\frac{q\Omega}{N}\right)^{2/3} \approx 3.0 \times 10^{17}\text{ G}, \tag{22}$$

$$B_\phi^{S,sat} = \sqrt{4\pi\rho R_{TI}^2}\,q\left(\frac{\Omega^2}{N}\right) \approx, 1.76 \times 10^{17}\text{ G} \tag{23}$$

$$B_r^{S,sat} = \sqrt{4\pi\rho R_{TI}^2}\,q^2\left(\frac{\Omega^4}{N^3}\right) \approx 2.1 \times 10^{17}\text{ G}. \tag{24}$$

These values differ from the results of our models because some of the model's hypotheses are not valid before reaching the predicted saturated values. Indeed, both Fuller's and Spruit's predictions give $w_A > \Omega, N$ with our values. These values are not reached anyway as the differential rotation is quenched before.

With this initial magnetic field, the TS-dynamo could generate an intense dipole and an even stronger toroidal magnetic field when the long-lived remnant of the neutron star mergers survives for longer than 0.5 s.

3.2. The impact of the initial magnetic dipole

For binary neutron star mergers, the duration of the dynamo is quite essential as the remnant may collapse into a black hole (BH). We vary the initial magnetic field strength to study its impact on the dynamo. Figure 3 shows the time evolution for different initial magnetic fields $B_{r,0}$. While the maximum magnetic field is similar in all the cases, the time to reach the saturated decreases with the increase of the initial magnetic field. For $B_{r,0} = 10^{14}$ G, the dynamo saturates in 110 ms. At the same time, it takes 2.4 s for $B_{r,0} = 10^{12}$ G and 125 s for $B_{r,0} = 10^{10}$ G.

To estimate realistically the initial dipole, the magnetic field in the core of the hypermassive neutron star results from the amplification by the Kelvin-Helmholtz (KH) happening at the early times of the merger. Due to this instability, the large-scale initial magnetic field could be amplified from the initial dipole of the neutron star and potentially be stronger than $B_{r,0} = 10^{13}$ G. Therefore, the TS dynamo could saturate in less than 500 milliseconds.

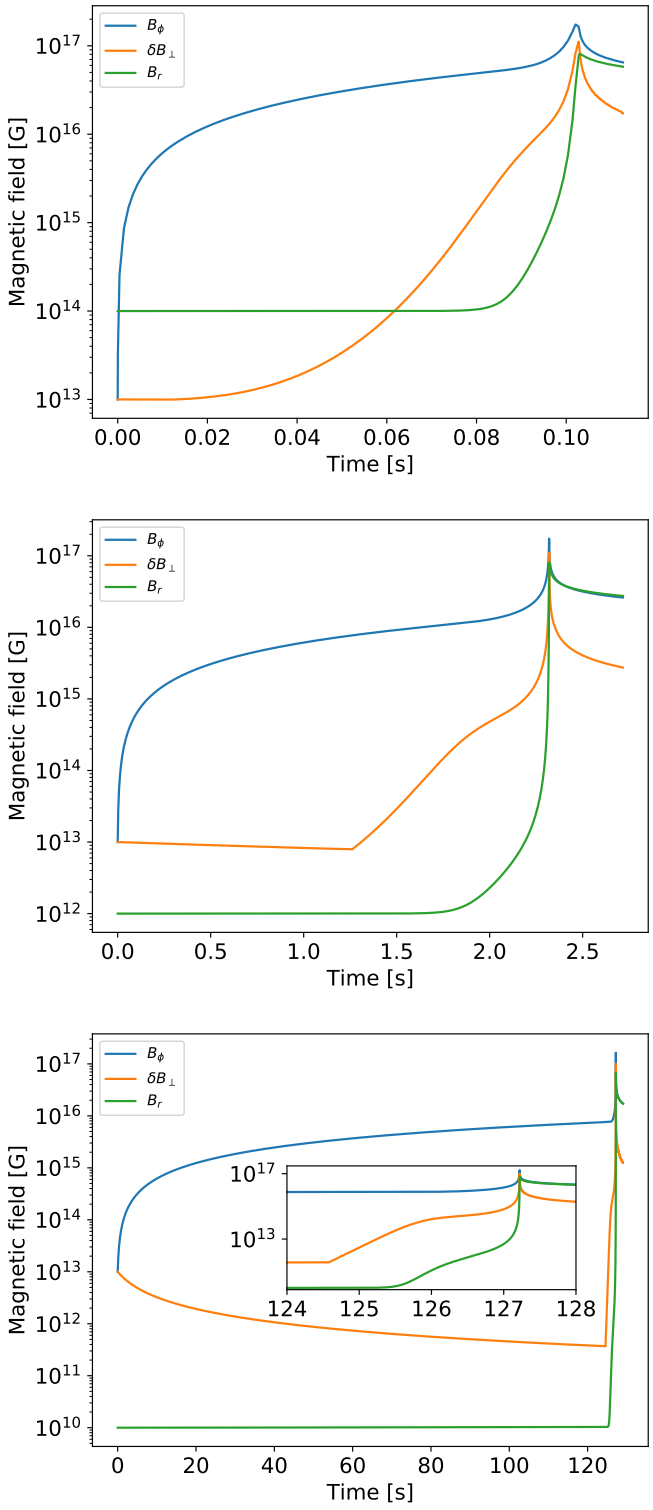

Fig. 3. Time evolution of the magnetic field (Same as figure 2 for different initial magnetic dipole $B_{r,0}$ with $B_{r,0} = 10^{14}$ G (top), $B_{r,0} = 10^{12}$ G (middle) and $B_{r,0} = 10^{10}$ G (bottom).

To complete this picture, we can estimate the timescale for each phase of the dynamo process as in Barrère et al. (2022). The first phase is the winding phase, where the toroidal field is amplified until either it becomes strong enough for the Tayler instability to grow as fast as B_ϕ (Barrère et al. 2022) or that it becomes strong enough to reach the critical magnetic field for

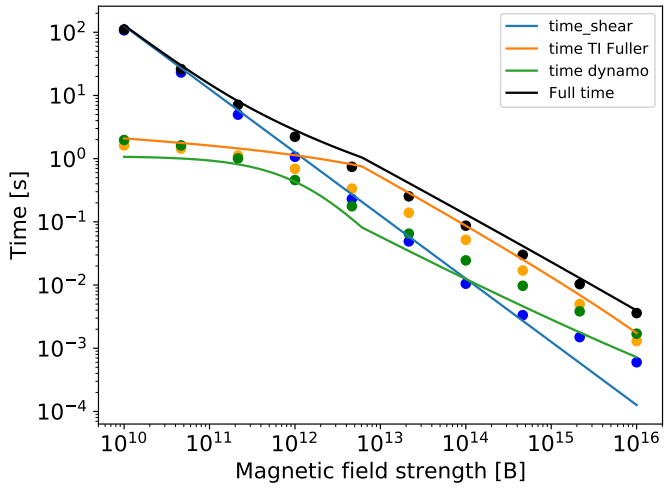

Fig. 4. Timescale of the different phases of the TS dynamo depending on the initial magnetic fields. The points are measured from the one-zone model, while the lines are from the analytical estimates.

the instability to start with the high viscosity. The formula for the winding time is therefore

$$t_{\rm winding} = \frac{\max(\omega_{\rm A,TI}, \omega_{\rm A,crit})}{q\Omega\omega_{r,0}} = \max\left(q^2\omega_{r,0}^2\Omega)^{-1/3}, \frac{\omega_{\rm A,crit}}{q\Omega\omega_{r,0}}\right). \tag{25}$$

At the end of this phase, the toroidal magnetic field is equal to

$$B_\phi(t_{\rm winding}) = q\Omega\, t_{\rm winding} B_{r,0} \tag{26}$$

For the Tayler Instability phase, we use the same scaling (equation 51 in (Barrère et al. 2022)), but we consider that $B_\phi(t_{\rm winding})$ is from the formula above and write the corresponding Alfven frequency $w_{A,winding}$, which gives

$$\tau_{TI} \sim \frac{\Omega}{(w_{A,winding})^2} \ln\left(\frac{w_{A,winding}^2}{\Omega\, \delta v_{A,0}}\right), \tag{27}$$

where $\delta_{A,0} = \delta v_A(t = 0)$.

For the dynamo phase, we use the same formula as Barrère et al. (2022)

$$\tau_{dyn} = \left(\frac{B_\phi}{\partial_t^2 B_\phi}\right)^{1/2} = \frac{\Omega}{w_{A,dyn}^2}\left(\frac{N}{q w_{A,dyn}}\right)^{1/2} \tag{28}$$

We compare these timescale estimates to the one measured in the one-zone model in Figure 4 and find a good agreement. The estimated total dynamo time is a bit higher than the model results, but it shows that the TS dynamo is able to grow in a few seconds as long as the initial magnetic field is higher than 10^{12} G. This Figure shows that the shear time dominates the total time for initial magnetic fields lower than 10^{12} G. In this case, a higher rotation or shear rate would linearly decrease the total dynamo time. For higher initial magnetic fields, the Tayler Instability phase dominates the total time and depends strongly on its growth rate.

4. Comparison with a 3D GRMHD simulation

In the previous section, we showed that the TS dynamo is able to grow and should be seen in simulations as almost all GRMHD simulations start with a dipole higher than 10^{15} G. In this section, we analyze the data of a long-lived scenario in 3D ideal GRMHD simulations to find the Tayler-Spruit dynamo. Therefore, we focus on analyzing the core of the binary neutron star remnant for radii lower than 10 km. The numerical techniques and the study of the other regions of these simulations are detailed in Kiuchi et al. (2024).

4.1. Dynamics of the GRMHD simulation

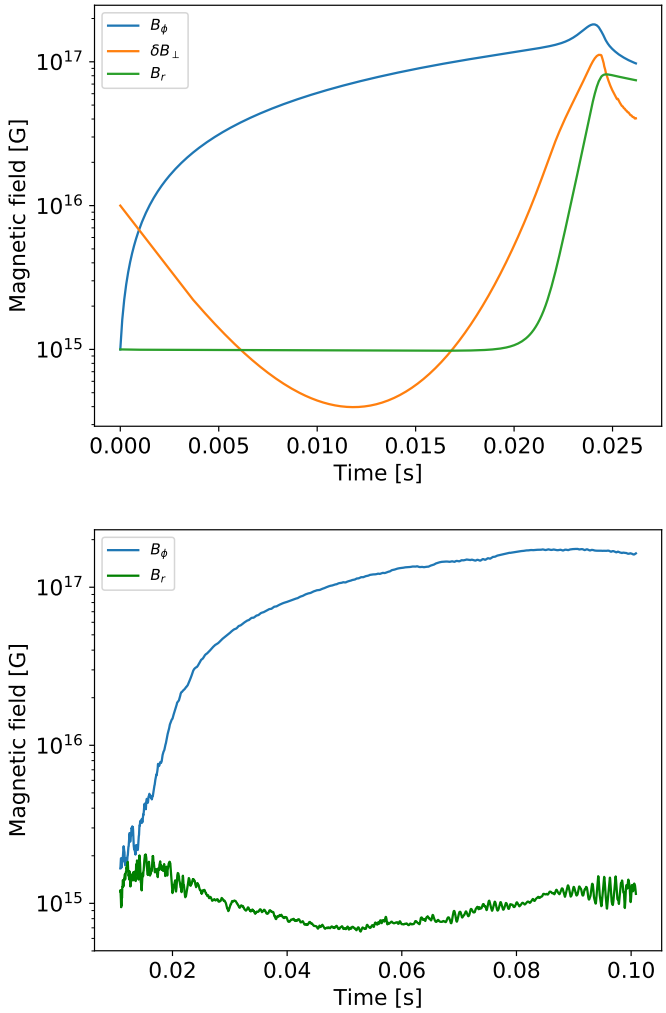

Fig. 5. Time evolution of the magnetic field for the one-zone model (top) with a resistivity of $\eta = 10^{12}\mathrm{cm}^2\mathrm{s}^{-1}$ and for the GRMHD simulation (bottom).

The 3D neutrino radiation GRMHD simulation of a symmetric binary case, with masses of 1.35-1.35 $M_\odot$ and a "hard" equation of state DD2 results in a hypermassive neutron star that survives for timescales >O(1) s. The rotation profile at the equatorial plane in the hypermassive neutron star shows a positive differential rotation until 10 km (Figure 1). This leads to the winding of the poloidal magnetic field in the core of the remnant. Figure 5 compares the time evolution of the simulation and the one-zone model. The one-zone model amplifies the magnetic field to its saturation values in 20 ms, while for the GRMHD simulation, the magnetic field decreases for more than 60 ms and overall stays constant from its initial value. This shows that no dynamo processes occur in the simulation's HMNS core.

To understand why there is no dynamo, we look at a snapshot of simulation in a plane at $z = 2$ km at $t - t_{merger} = 30$ ms (Figure 6). The toroidal magnetic field is indeed amplified to a maximum value of 4×10^{17} G (Left panel of Figure 6). This magnetic field is larger than the critical magnetic field for a strong viscosity, so according to this criterion, the simulation should be unstable to the Tayler Instability.

Another criterion is the solenoidal criterion that assumes that the ratio of the poloidal magnetic field over the toroidal field is larger than the Alfvén frequency divided by the Brunt-Väisälä frequency, which means $B_r N / B_\phi \omega_\mathrm{A} < 1$. This criterion is verified as the radial magnetic B_r, dominated by the non-axisymmetric component (middle panel of Figure 6), is much lower than the toroidal one B_ϕ, while the frequencies are of the same order of magnitude. The non-axisymmetric component of the radial magnetic field is not due to the Tayler Instability as its main mode is an $m = 2$ mode, and the geometry corresponds well to the velocity field in the plane (right panel of Figure 6). The origin of this m=2 mode is well known and comes from the initial geometry and mass ratio of the binary. It is very commonly seen in the post-merger phase of many GR simulations (Topolski et al. 2024). Figure 6 shows that the velocity field is not a purely $m = 2$ mode as the initial $m = 2$ mode can also degrade as a $m = 1$ mode, but it is different from the $m = 1$ mode from Tayler Instability. Indeed, the $m = 2$ and degraded $m = 1$ modes gives the radial magnetic field exactly the same geometry as the toroidal field, which shows its origin as the displacement due to the $m = 1$ and $m = 2$ modes of the velocity field. In any case, these modes amplify the magnetic field to a lower strength than the ones in the one-zone model and are expected to dissipate after a hundred milliseconds after the merger as the gravitational wave luminosity decreases (Radice & Bernuzzi 2023). It might therefore cause a delay in the appearance of the Tayler-Spruit dynamo, but it does not explain why it should not appear later in the simulation.

To be unstable to the Tayler instability, the geometry of the magnetic field is also important, as the size of the magnetic field can limit the wavelength. To estimate what is the maximal wavelength available, we used the geometrical criterion for a wave from Goossens & Tayler (1980)

$$\frac{B_\phi^2}{4\pi R_{TI}^2 \sin\theta}\left(m^2 - 2\cos^2\theta - 2\sin\theta\cos\theta\,\partial_\theta \log B_\phi\right) < 0 \qquad (29)$$

Figure 7 shows the normalized value of this criterion, and we can see that the magnetic field should indeed be unstable to the Tayler instability, but the size of the unstable domain is actually around ≈ 1 km.

Positive differential rotation can stabilize the Tayler Instability, as shown by Kiuchi et al. (2011), but the toroidal magnetic field is decreasing vertically in the north hemisphere in the unstable region (Figure 7), which makes it unstable (see equation 27 of Kiuchi et al. (2011)). From a geometric criterion, the core of the remnant at $t - t_\mathrm{merger} = 30$ ms should be unstable to the Tayler Instability with a fast-growing rate of $\sigma_\mathrm{TI}\, w_A$.

4.2. Numerical dissipation analysis

The absence of the Tayler instability in this 3D simulation could be due to the wavelength of the Tayler instability being lower

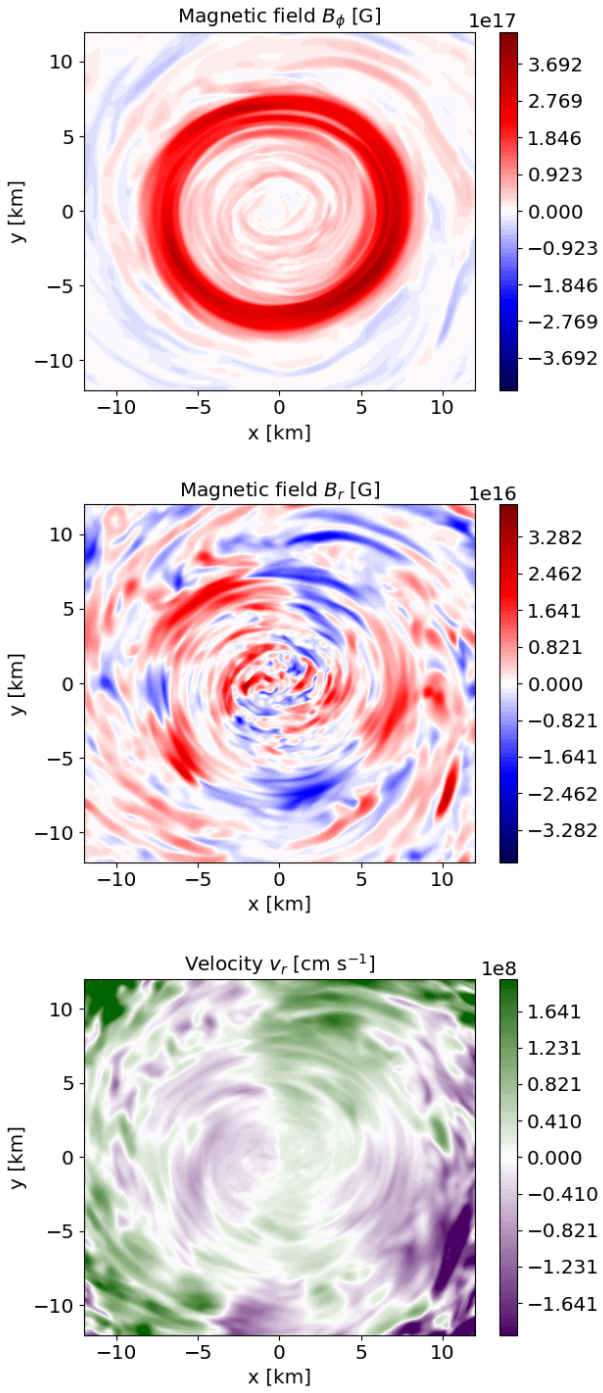

Fig. 6. Snapshot of the toroidal magnetic field (top), radial magnetic field (bottom) and radial velocity in the core of the hypermassive neutron star at $t - t_{\rm merger} = 30$ ms at $z = 2km$

.

than the grid resolution or that the numerical resistivity/viscosity reduces the growth rate of the instability. We, therefore, try to estimate the wavelength of the Tayler instability for the simulation. From the instability criterion, the wavelength $\lambda_{\rm crit}$ at which the Tayler Instability should occur is

$$\lambda_{\rm crit} = \frac{2\pi R_{TI}\omega_{\rm A,crit}}{N} = 2\pi R_{TI}\left(\frac{\Omega}{N}\right)^{1/2}\left(\frac{\nu}{R^2\Omega}\right)^{1/4}. \quad (30)$$

Therefore, this depends on the numerical resistivity/viscosity inside the simulation. We try to estimate the numerical resistivity/viscosity to solve this issue. We use the fitting formula derived for Eulerian MHD codes in Rembiasz et al. (2017):

$$\nu_\star = \mathcal{R}_\nu^{\Delta x}\mathcal{V}\mathcal{L}\left(\frac{\Delta x}{\mathcal{L}}\right)^r, \quad . \quad (31)$$

where $\mathcal{V}, \mathcal{L}$ are the characteristic speed and length of the system and $\mathcal{R}_\nu^{\Delta x}$, r are fitting parameters. We use the fitting parameters for the HLLD solver with the fourth-order Runge Kutta method, as it is the same Riemann Solver used in our GRMHD simulations. We use the fast magnetosonic speed for the characteristic velocity as found in the study $\mathcal{V} = max(v_A, c_s) \approx c_s \approx 1.2\times10^10$ cm s^{-1} for the characteristic speed. Since the numerical resistivity depends on the resolution and on the scale we are considering, i.e. $\lambda_{\rm crit}$, by combining equations 30 and 31, we have to solve the equation

$$\lambda_{\rm crit}^{\frac{r+3}{r-1}} = 2\pi R^{TI}\left(\frac{\Omega}{N}\right)^{1/2}\left(\frac{\mathcal{R}_\nu^{\Delta x}\mathcal{V}\delta x^r}{R_{TI}^2\Omega}\right)^{1/4}, \quad (32)$$

which with $\delta x = 100$ m, $r = 4.95$ and $\mathcal{R}_{\mathcal{T}I_\nu}^{\Delta x} = 42$ gives $\lambda_{\rm crit} = 2$ km at a $R_{TI} = 7$ km. In the case where the geometry does not constrain the wavelength, the Tayler Instability would be resolved well by a hundred-meter resolution.

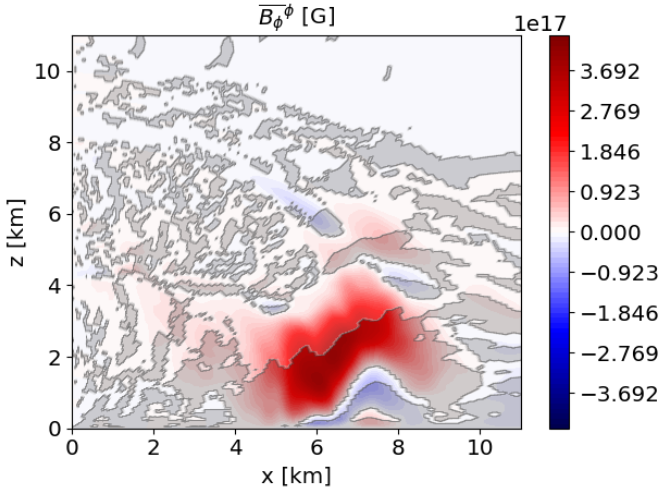

Fig. 7. Snapshot of the axisymmetric toroidal magnetic field in the core of the hypermassive neutron star at $t - t_{\rm merger} = 30$ ms at $z = 2$ km. The grey contours correspond to the regions stable to the Tayler Instability according to the geometric criterion (Equation 29).

$$B_{\phi,crit} = \sqrt{4\pi\rho R_{TI}^2 k_{TI}^2 \eta} \quad (33)$$

However, the unstable region of the magnetic field is limited to ≈ 1 km, and we have, therefore, to limit the wavelength of the Tayler instability. To check the impact of the dissipation of this 1 km wavelength, we solve the local dispersion relation of Acheson & Gibbons (1978) with all three dissipation mechanisms equal to each other, $\nu = \eta = \kappa$. We also assume the magnetic field to be increasing with radii and decreasing vertically and take the other quantities the same as the simulation (see Appendix 7 for more details). We find a good agreement for the growth rate with $\sigma_{TI} \approx \omega_A$ in the case of low dissipation and for the theoretical

dissipation limit given by $\omega_A = k_{TI}^2 \eta$ (Figure 8). We note that for a realistic neutrino viscosity $\nu_{HMNS} = 2.3 \times 10^9$ cm^2 s^{-1}, the growth rate is unchanged for the ideal MHD case. We can then safely use the dissipation limit to compute the critical magnetic field for numerical viscosity/resistivity.

Figure 9 shows the critical magnetic field for the numerical viscosity/resistivity in the code depending on the length scale below 1 km for different resolutions. The magnetic field is close to the critical magnetic field with a 100-meter resolution, which may explain why the simulation is stable to Tayler instability at this resolution.

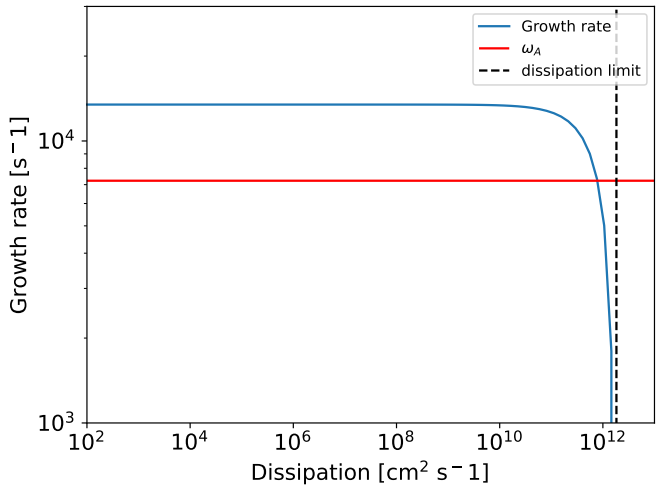

Fig. 8. Growth rate of the Tayler instability depending on the dissipation strength with $\nu = \eta = \kappa$. The red line shows the theoretical growth rate in the regime of $\Omega \ll \omega_A$, and the dashed line is the stabilizing limit given by $k_{TI}^2 \eta = \omega_A$.

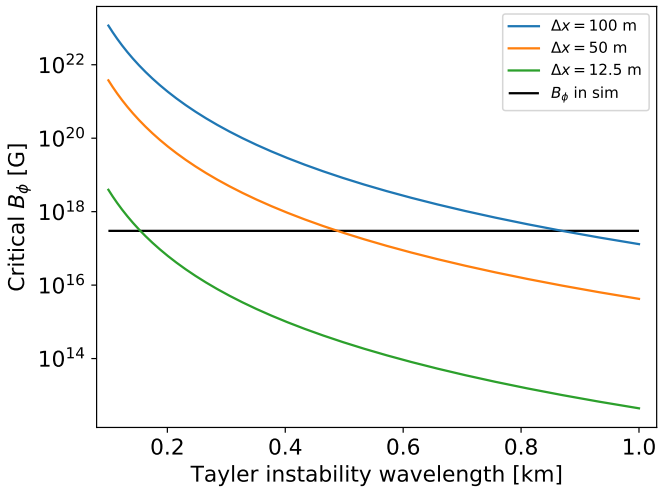

Fig. 9. Critical magnetic field $B_{\phi,\mathrm{crit}}$ (equation 33) in the numerical simulation depending on the wavelength of the Tayler instability for several resolutions. The black line corresponds to the magnetic field in the GRMHD simulation.

5. Discussion

5.1. Comparison with Boussinesq simulations

Using 3D numerical Boussinesq simulations (i.e. with a constant density profile), Barrère et al. (2023) demonstrated the existence of two subcritical Tayler-Spruit dynamos (i.e. driven by the Tayler instability) with a positive shear. Both display magnetic fields differing by their intensity and geometry: hemispherical and dipolar (i.e. equatorially symmetric). The dipolar solution shows the strongest magnetic fields and follows the scalings predicted by Fuller et al. (2019) for the shear rate q: $B_{\mathrm{tor}}^{m=0} \propto q^{1/3}$ and $B_{\mathrm{pol}}^{m=0} \sim B_{\mathrm{dip}} \propto q^{2/3}$. Also, their models are less stratified than the core remnant in the GRMHD simulation with a ratio of the Brunt-Väisälä frequency to the rotation rate of $N/\Omega = 0.1$.

Although the Tayler-Spruit dynamo does not have a signature in the GRMHD simulation, we can provide a proxy for the magnetic field intensity that would be expected if it were operating. Indeed, we first performed a Boussinesq simulation with $N/\Omega_o = 0.5$, which is close to the stratification measured in the core remnant from the GRMHD simulation. Second, we use the dimensionless parameters to scale the magnetic field to a case corresponding to a hypermassive neutron star, even though the parameters chosen in the study correspond to the scenario for supernova fallback. We take the parameters at $t - t_{\mathrm{merger}} = 30$ ms: (i) a radius of our domain of $D = 10$ km, (ii) with an inner rotation of $\Omega_i = 3000\,\mathrm{rad\,s^{-1}}$ and outer rotation of $\Omega_o = 8000\,\mathrm{rad\,s^{-1}}$. Since $E = \frac{\nu}{D^2\Omega_o} = 10^{-5}$ in the Boussinesq simulation, the viscosity is therefore $\nu = 3.9 \times 10^{10}$ cm^2 s^{-1}, which shows that the dynamo can operate even at high viscosity. Finally, by assuming that the scaling found at $N/\Omega_o = 0.1$ is still valid at $N/\Omega_o = 0.5$, we extrapolate the resulting magnetic intensities to $q = 1$, which is the minimum shear rate measured in the 10 km-radius core of the GRMHD simulation. We eventually find magnetic fields that reach $B_{\mathrm{tor}}^{m=0} = 2{\times}10^{16}$ G, $B_{\mathrm{pol}}^{m=0} = 5{\times}10^{15}$ G and $B_{\mathrm{dip}} = 3{\times}10^{15}$ G. Although they are ~ 5 times lower than the one-zone model as already found by (Barrère et al. 2023), the Tayler-Spruit dynamo can, therefore, produce very strong magnetic fields, which are expected for a magnetar remaining from a BNS merger.

5.2. MRI-driven dynamo vs TS dynamo

As it is argued in (Margalit et al. 2022), the TS dynamo could be relevant for the transport of angular momentum when the differential rotation is decreasing with radius. However, depending on the Brunt-Väisälä frequency, this region would be unstable to the MRI, which has a much faster growth rate than the TS dynamo in the fast-rotating case. So, the MRI is expected to saturate first, and the Tayler instability would not impact this region. To confirm this picture, we compute the growth rate of both dynamos in the equatorial plane at $r = 20km$ with a magnetic field of $B_0 = 10^{14}$ G as it is found after the Kelvin-Helmholtz instability. It gives

$$\sigma_{\mathrm{MRI}} = \frac{q\Omega}{2} \approx 2600 s^{-1} \qquad \sigma_{\mathrm{TS}} = \frac{w_{\mathrm{A}}^2}{\Omega} \ll \sigma_{\mathrm{MRI}}, \tag{34}$$

due to $w_{\mathrm{A}} \ll \Omega$. Interactions from the turbulence developed by the MRI and the TS dynamo would occur at the radius where the differential rotation changes sign, making this transition region difficult to study.

5.3. Angular momentum transport and spin-down time

The angular momentum transport timescale due to the Tayler-Spruit corresponds to the time it takes to saturate in this study. Indeed, the dynamo stops when there is no differential rotation. This could be pretty fast or slow depending on the initial magnetic field. One interesting feature is that due to the positive differential rotation, the angular momentum would be transported inwards rather than outwards.

The spin-down time depends on how we consider the generated magnetic field inside the remnant. We first consider that the magnetic field stays buried in the core of the hypermassive neutron star, then it would act as a torque and slows the core down with equation 3. By taking the saturated values, the core would slow down with a rate of

$$\gamma_{sd,core} \equiv \frac{\dot{\Omega}}{\Omega} = -\frac{R_{TI}^2 B_r B_\phi}{I\Omega} \approx 1.94 \times 10^{-3} \mathrm{s}^{-1} \tag{35}$$

We can also assume that the obtained dipole becomes the dipole at the surface of the supramassive neutron star without matter outside. Then, the dipole formula gives the following spin-down rate of

$$\gamma_{sd,dipole} \equiv \frac{\dot{\Omega}}{\Omega} = -\frac{B_r^2 R_{TI}^6 \Omega^2}{6c^3 I} \approx 0.21 \mathrm{s}^{-1} \tag{36}$$

Therefore, this spin-down would be faster and slow the remnant down to the scale of seconds. The remnant's rotational energy would also be emitted in electromagnetic waves. These results depend on the reconfiguration of the magnetic field once the TS dynamo is saturated; this must be further studied for hypermassive neutron stars.

6. Conclusions

We have investigated the Taler-Spruit dynamo in the context of neutron star mergers. Following (Barrère et al. 2022), we developed a one-zone model of the TS dynamo for hypermassive neutron stars with realistic estimates from 3D GRMHD simulations.

We found that the TS dynamo could develop in the core of hypermassive neutron stars due to its positive differential rotation. Due to the impact of neutrino viscosity, the toroidal magnetic field must be amplified to higher values than 7.6×10^{15} G by the winding in order to be Tayler-unstable.

The magnetic field's evolution can be divided into three phases: the winding phase, the Tayler instability phase and the non-linear growth until saturation is reached when the differential rotation has been transported outward by the Maxwell stress. The magnetic field generated by the dynamo saturates at a very high intensity of 1.8×10^{17} G and 8×10^{16} G for the magnetic dipole.

The saturated magnetic field strength does not depend on the initial magnetic field, but the time it takes to reach saturation does. Indeed, the initial magnetic dipole determines the time needed for the saturation of the dynamo, which can range from 100 milliseconds for a magnetic dipole of 10^{14} G or 2.4 seconds for a magnetic dipole of 10^{12} G, which is the order of the HMNS lifetime in the long-lived case, O(1s). In the first case, the transport of angular momentum by the TS dynamo would lead to a faster collapse to a black hole or a faster spin down of the remnant. This shows that the Tayler-Spruit dynamo would be important in the case of a long-lived neutron star remnant as long as the initial magnetic field dipole is higher than 10^{12} G.

However, these results depend on whether the TS dynamo grows fast enough and, therefore, on the resulting magnetic dipole after the Kelvin-Helmholtz instability. Therefore, a study using realistic initial magnetic fields in neutron stars and with a converged growth of the Kelvin-Helmholtz is needed. The value of the magnetic dipole needs to be confirmed by 3D numerical simulation with a background stratification corresponding to a hypermassive neutron star. This is left to a further study with also the question of the interaction of the MRI instability that operates after 10 km and the Tayler-Spruit dynamo.

The TS dynamo operating in a neutron star remnant could have significant consequences for astrophysical observations. First, the angular momentum transport would happen when the dynamo saturates and would collapse if the remnant is more massive than the limit of neutron stars in solid body rotation. Otherwise, it would lead to a supramassive neutron star with a high magnetic field, a proto-magnetar. In the case of the saturated dipole we obtain becomes the surface dipole, the remnant would emit its rotational energy and slow down by magnetic braking. With the dipole we found, the luminosity would be very bright and last a short time. For example, we consider a supramassive neutron star of 2.4 solar masses with a millisecond period. We assume flux conservation from the saturated radial field at $R_{TI} = 7$ km to the surface magnetic dipole at $R_{surface} = 14$ km. This gives a magnetic dipole of 2×10^{16} G and a dipole luminosity of

$$L_{\mathrm{dip}} = \frac{B^2 R_{surface}^6 \Omega^4}{6c^3} \approx 1.16 \times 10^{52} \text{ erg s}^{-1}$$

This luminosity would decrease fast, on the order of several seconds, and when the rotational energy of the remnant is emitted, the remnant would most likely collapse to a black hole or form a stable magnetar. The huge amount of energy emitted would also impact the kilonova.

In addition, having motions due to the Tayler-Spruit dynamo in the neutron star remnant may lead to some emission in gravitational waves for a close event. Using Fuller's formalism, we try estimate the amplitude of the velocity perturbations due to TS dynamo with the formula

$$\delta v_{r,sat} = \delta v_{A,sat} \frac{\omega_{A,sat}^2}{N\Omega} \approx 4.5 \times 10^9 \text{ cm s}^{-1}. \tag{37}$$

For the sake of simplicity, we estimate the strain by using the order of magnitude derived from the quadrupole formula (Kokkotas 2002)

$$h \approx \frac{G}{c^4} \frac{\varepsilon E_{turb}}{D_{GW}},$$

where ε is the efficiency to convert the turbulent energy to gravitational waves that we assume to be low $\varepsilon \approx 5\%$. The kinetic energy is computed, assuming that this velocity is constant in the region from 5 to 10 km and oscillates at the Brunt-Väisälä frequency N. A distance of 1 Mpc would then give a strain of $h \approx 2 \times 10^{-24}$ cm, which would potentially be detectable by the future generation of gravitational detectors.

Investigating the Tayler-Spruit dynamo in binary neutron star merger is therefore important to better understand future multi-messenger observations.

Acknowledgements. This work was supported by the European Research Council (MagBURST grant 715368), and the PNPS and PNHE programs of CNRS/INSU, co-funded by CEA and CNES.

References

Abbott, B. P., Abbott, R., Abbott, T. D., et al. 2017, ApJ, 848, L13
Acheson, D. J. & Gibbons, M. P. 1978, Philosophical Transactions of the Royal Society of London Series A, 289, 459
Barrère, P., Guilet, J., Raynaud, R., & Reboul-Salze, A. 2023, MNRAS, 526, L88
Barrère, P., Guilet, J., Reboul-Salze, A., Raynaud, R., & Janka, H. T. 2022, Astron. Astrophys., 668, A79
Bonanno, A. & Guarnieri, F. 2017, Astronomische Nachrichten, 338, 516
Bonanno, A., Guerrero, G., & Del Sordo, F. 2020, Mem. Soc. Astron. Italiana, 91, 249
Bucciantini, N., Metzger, B. D., Thompson, T. A., & Quataert, E. 2012, MNRAS, 419, 1537
Ciolfi, R. 2020, MNRAS, 495, L66
Ciolfi, R., Kastaun, W., Giacomazzo, B., et al. 2017, Phys. Rev. D, 95, 063016
Ciolfi, R., Kastaun, W., Kalinani, J. V., & Giacomazzo, B. 2019, Phys. Rev. D, 100, 023005
Combi, L. & Siegel, D. M. 2023, Phys. Rev. Lett., 131, 231402
Denissenkov, P. A. & Pinsonneault, M. 2007, ApJ, 655, 1157
Fuller, J., Piro, A. L., & Jermyn, A. S. 2019, MNRAS, 485, 3661
Gao, H., Ding, X., Wu, X.-F., Zhang, B., & Dai, Z.-G. 2013, ApJ, 771, 86
Giacomazzo, B. & Perna, R. 2013, ApJ, 771, L26
Gompertz, B. P., O'Brien, P. T., & Wynn, G. A. 2014, MNRAS, 438, 240
Goossens, M. & Tayler, R. J. 1980, MNRAS, 193, 833
Jouve, L., Lignières, F., & Gaurat, M. 2020, A&A, 641, A13
Kastaun, W., Ciolfi, R., Endrizzi, A., & Giacomazzo, B. 2017, Phys. Rev. D, 96, 043019
Kastaun, W., Ciolfi, R., & Giacomazzo, B. 2016, Phys. Rev. D, 94, 044060
Kiuchi, K., Reboul-Salze, A., Shibata, M., & Sekiguchi, Y. 2024, Nature Astronomy, 8, 298
Kiuchi, K., Yoshida, S., & Shibata, M. 2011, A&A, 532, A30
Kokkotas, K. 2002, Gravitational wave Physics, https://phas.ubc.ca/~halpern/403/references/GW_Physics.pdf
Ma, L. & Fuller, J. 2019, MNRAS, 488, 4338
Margalit, B., Jermyn, A. S., Metzger, B. D., Roberts, L. F., & Quataert, E. 2022, arXiv e-prints, arXiv:2206.10645
Metzger, B. D. & Piro, A. L. 2014, MNRAS, 439, 3916
Metzger, B. D., Quataert, E., & Thompson, T. A. 2008, MNRAS, 385, 1455
Müller, B., Janka, H.-T., & Marek, A. 2013, ApJ, 766, 43
Petitdemange, L., Marcotte, F., & Gissinger, C. 2023, Science, 379, 300
Petitdemange, L., Marcotte, F., Gissinger, C., & Daniel, F. 2024, A&A, 681, A75
Pitts, E. & Tayler, R. J. 1985, MNRAS, 216, 139
Radice, D. & Bernuzzi, S. 2023, ApJ, 959, 46
Raynaud, R., Guilet, J., Janka, H.-T., & Gastine, T. 2020, Science Advances, 6
Reboul-Salze, A., Guilet, J., Raynaud, R., & Bugli, M. 2022, A&A, 667, A94
Rembiasz, T., Obergaulinger, M., Cerdá-Durán, P., Aloy, M.-Á., & Müller, E. 2017, ApJS, 230, 18
Rüdiger, G. & Kitchatinov, L. L. 2010, Geophysical and Astrophysical Fluid Dynamics, 104, 273
Sarin, N., Omand, C. M. B., Margalit, B., & Jones, D. I. 2022, MNRAS, 516, 4949
Skoutnev, V. A. & Beloborodov, A. M. 2024, arXiv e-prints, arXiv:2404.19103
Spruit, H. C. 2002, A&A, 381, 923
Szklarski, J. & Arlt, R. 2013, A&A, 550, A94
Tayler, R. J. 1973, MNRAS, 161, 365
Thompson, C. & Duncan, R. C. 1993, ApJ, 408, 194
Topolski, K., Tootle, S. D., & Rezzolla, L. 2024, ApJ, 960, 86
Zahn, J. P., Brun, A. S., & Mathis, S. 2007, A&A, 474, 145

Appendix

7. Linear study of Tayler instability

We solve Acheson's dispersion relation by using Python (Acheson & Gibbons 1978). We first use symPy to calculate the polynomial coefficients from the relation and then solve the roots of the polynomial numerically. We tested that we recover the dispersion relation in the non-rotating ideal case and the rotating one also as in Kiuchi et al. (2011). We are able to recover the theoretical growth rate in the two opposite limits $\omega_A \ll \Omega$ and $\Omega \ll \omega_A$. The code used to solve the linear dispersion relation is publicly available at the following address https://github.com/alexisreboulsalze/AchesonLinSolve/tree/main.

C.3.6 . Article *Observational characterisation of large-scale transport and horizontal turbulent diffusivity in the quiet Sun (submitted)*

Astronomy & Astrophysics manuscript no. article
April 23, 2024

Observational characterisation of large-scale transport and horizontal turbulent diffusivity in the quiet Sun

F. Rincon[1,2], P. Barrère[1,2,3], and T. Roudier[1,2]

[1] CNRS; IRAP; 14 avenue Edouard Belin, F-31400 Toulouse, France,
[2] Université de Toulouse; UPS-OMP; IRAP: Toulouse, France,
[3] Université Paris-Saclay, Université Paris Cité, CNRS, AIM, 91191, Gif-sur-Yvette, France
e-mail: frincon@irap.omp.eu

April 23, 2024

ABSTRACT

The Sun is a magnetic star, and the only spatio-temporally resolved astrophysical system displaying turbulent magnetohydrodynamic thermal convection. This makes it a privileged object of study to understand fluid turbulence in extreme regimes and its interactions with magnetic fields. Global analyses of high-resolution solar observations provided by the NASA Solar Dynamics Observatory (SDO) can shed light on the physical processes underlying large-scale emergent phenomena such as the solar dynamo cycle. Combining a Coherent Structure Tracking reconstruction of photospheric flows, based on photometric data, and a statistical analysis of virtual passive tracers trajectories advected by these flows, we characterise one of the most important such processes, turbulent diffusion, over an unprecedentedly long monitoring period of six consecutive days of a significant fraction of the solar disc. We first confirm, and provide a new global view of the emergence of a remarkable dynamical pattern of Lagrangian Coherent Structures tiling the entire surface. These structures act as transport barriers on the time and spatial scale of supergranulation and, by transiently accumulating particles and magnetic fields, appear to regulate large-scale turbulent surface diffusion. We then further statistically characterise the turbulent transport regime using two different methods, and obtain an effective horizontal turbulent diffusivity $D = 2 - 3 \times 10^8$ m^2 s^{-1} on the longest timescales considered. This estimate is consistent with the transport coefficients required in large-scale mean-field solar dynamo models, and is in broad agreement with the results of global simulations. Beyond the solar dynamo, our analysis may have implications for understanding the structural connections between solar-surface, coronal and solar-wind dynamics, and it also provides valuable lessons to characterise turbulent transport in other, unresolved turbulent astrophysical systems.

Key words. Sun: photosphere – Convection – Turbulence – Magnetic fields – Dynamo

1. Introduction

1.1. Context and motivation

Thermal convection is one of the most common fluid transport processes encountered in astrophysics, and the Sun and its photosphere provide us with a unique observationally well-resolved example of such (magnetohydrodynamic, MHD) turbulence in highly nonlinear regimes. Indeed, dynamical MHD phenomena on the Sun are now continuously monitored with temporal and spatial resolutions of the order of seconds and hundred kilometers respectively, which are truly astonishing small numbers by astronomical standards. As such, the Sun is a special place to study nonlinear thermal and MHD transport processes, and to understand how they can affect the structure and evolution of many astrophysical systems that can not be resolved by observations, or emulated in laboratory experiments.

While some aspects of solar (MHD) convection, such as solar granulation, are well understood (Nordlund et al. 2009), we still lack definitive answers to many important questions such as how thermal turbulence in the Sun organises on large scales, how it interacts with and amplifies magnetic fields at both large and small-scales, how it transports quantities such as angular momentum or magnetic flux (Miesch 2005; Hathaway & Rightmire-Upton 2012; Charbonneau 2014; Brun & Browning 2017; Rincon & Rieutord 2018). One limitation is that despite much progress in helioseismology, we do not (yet) have time and space-resolved determinations of internal multiscale convective dynamics in the solar convection zone (Gizon et al. 2010; Hanasoge et al. 2012; Švanda 2012; Duvall & Hanasoge 2013; Duvall et al. 2014; DeGrave & Jackiewicz 2015; Hanasoge et al. 2016; Greer et al. 2015; Toomre & Thompson 2015). Photospheric observations still allow for the most direct characterisation of solar convection and are therefore most helpful to put observational constraints on dynamical transport processes, such as turbulent diffusion, which are key to understand emergent dynamical phenomena such as the large-scale dynamo cycle. Given the interfacial nature of the photosphere, understanding magnetic transport there is also critical to understand the energetics and magnetic dynamics of the corona (e.g. Amari et al. 2015), and the near-Sun structure of the solar wind recently uncovered by the Parker Solar Probe (Bale et al. 2019; Kasper et al. 2019). Finally, characterising large-scale solar dynamical processes in detail could provide useful insights into many unresolved similar astrophysical (MHD) turbulent processes (e.g. accretion, star formation, cosmic ray diffusion, galactic and extragalactic magnetogenesis) that can not be modelled in full detail due to their extreme nonlinearity and multiscale essence.

1.2. Solar-surface velocity measurements and their use

The most direct observational inference of multiscale photospheric flows is via measurements of Doppler-projected veloc-

ities (Leighton et al. 1962; Rincon & Rieutord 2018). Even a simple visual inspection of Doppler images clearly reveals the pattern of supergranulation flow "cells" (Hart 1954). The trademark signature of the supergranulation flow is a power excess around $\ell \sim 120 - 130$ (35 Megameters (Mm)) in the spherical harmonics power spectrum of global maps of Doppler-projected velocities obtained either with the MDI instrument aboard SOHO (Hathaway et al. 2000) or with the HMI instrument aboard SDO (Williams et al. 2014; Hathaway et al. 2015). Dopplergrams can be complemented by other observational inference techniques, such as Local Correlation Tracking (LCT, November & Simon 1988) or Coherent Structure Tracking (CST, Rieutord et al. 2007), to reconstruct the horizontal components of the velocity field. Both techniques require photometric data with high spatio-temporal resolution to resolve small-scale structures and motions and are a bit demanding computationally. In particular, the CST, which we use in this paper, requires tracking the motions of a large statistical ensemble of small-scale intensity structures (granules) advected by larger-scale flows (Rieutord et al. 2001). For this reason, they have for a long time mostly been applied to limited field-of-views, obtained from either ground-based (November & Simon 1988; November 1989; Roudier et al. 1999; Rieutord et al. 2001, 2008), or space-based observatories such as TRACE and Hinode (Simon & Shine 2004; Roudier et al. 2009; Rieutord et al. 2010), although local correlation tracking has also been applied to larger patches of MDI data (Shine et al. (2000); Švanda et al. (2007), see Fig. 22 of Nordlund et al. (2009)). However, the availability of highly-resolved full-disc photometric and Doppler data, as now routinely delivered by SDO/HMI, and improved numerical data processing capacities, have opened the 24 h/24 h possibility to infer multiscale flows at the photospheric level from local to fully global scales.

A combined CST/Doppler analysis of full-disc photometric SDO/HMI data allowing reconstruction of the three components of the velocity field was first attempted by Roudier et al. (2012, 2013). LCT was also applied by Langfellner et al. (2015) to 180×180 Mm^2 patches of SDO/HMI images in order to characterise averaged properties of supergranules. A marked improvement on these techniques was introduced by Rincon et al. (2017), hereafter R17, which made it possible to produce accurate full-disc maps (up to 60° from the disc centre) of the Eulerian horizontal and radial flow components at spatial scales larger than 2.5 Mm, with a time cadence of 0.5 h. With this data, R17 could notably calculate the full spherical harmonics kinetic energy spectrum of the radial, poloidal, and toroidal components of the photospheric velocity field over a wide range of horizontal scales. These global measurements separating different flow components notably inspired a new theoretical anisotropic turbulence phenomenology of large-scale photospheric convection. They can also serve as a consistency check for numerical simulations, and were shown by Rincon & Rieutord (2018) to compare well with global simulations of solar convection (Hotta et al. 2014). An alternative technique for the determination of the full surface velocity field over the solar disc based on Doppler data only was recently introduced by Kashyap & Hanasoge (2021).

1.3. Objectives and approach taken in this study

The aim of this work is to further exploit the possibilities offered by the application of the CST to the full-disc, continuous SDO/HMI data stream, to characterise the large-scale transport and turbulent diffusion properties of photospheric flows. Because the technique does not give us access to the vertical dependence of flows, the analysis is necessarily limited to horizontal transport, which is nevertheless dominant at the scales considered as a result of the strong flow anisotropy (R17). In R17, a 24 h sequence of full-disc SDO/HMI data was used, which was sufficient to calculate simple statistical quantities such as kinetic energy spectra. In this paper though, we aim at probing large-scale transport on timescales longer than the 24-48 h correlation time of supergranules, the most energetic dynamical surface structures, and therefore use a significantly longer, uninterrupted six-day sequence. Characterising the dynamics on such a long timescale creates new challenges, such as following regions of interest over a substantial fraction of the solar rotation period, and it is also limited by the lack of precision of the velocity-field deprojection near the solar limb. For this reason, a week is about the maximum continuous integration time achievable with our procedure, but it nevertheless provides us with an unprecedented, statistically-rich turbulent Eulerian velocity-field dataset.

To characterise turbulent transport, we simulate and statistically analyse the Lagrangian dynamics of passive particles virtually distributed over the surface and advected by the inferred, time-evolving Eulerian horizontal velocity field. This, first of all, enables us to derive global maps of Finite Time Lyapunov Exponents (FTLEs), introduced in a solar-surface physics context a few years ago by Yeates et al. (2012), see also Chian et al. (2014). Besides some quantitative insights into the intrinsic chaoticity of solar surface flows, such an analysis enables us to globally map for the first time a network of so-called Lagrangian Coherent Structures (LCS), which are the loci of transient accumulation or rarefaction of tracers. Using passive tracer statistics, we then further probe the transport regime of the flow up to timescales of a week, and derive an associated large-scale turbulent diffusion coefficient at the photospheric level.

This study bears similarities, and shares some diagnostics with a more common approach to transport in solar physics, based on the direct tracking of magnetic elements in magnetograms. However, due to the ephemeral nature, and occasional cancellation of magnetic elements, the latter approach has traditionally been limited to short-time (a few tens of hours at best) intra-supergranule transport, i.e. network formation (Schrijver et al. 1996; Berger et al. 1998; Hagenaar et al. 1999; Utz et al. 2010; Manso Sainz et al. 2011; Abramenko et al. 2011; Orozco Suárez et al. 2012; Giannattasio et al. 2013, 2014; Jafarzadeh et al. 2014; Yang et al. 2015, see Bellot Rubio & Orozco Suárez (2019) for a recent review). A notable exception is Iida (2016), who extended this type of analysis to five consecutive days, albeit with very noisy statistics on the longest times probed. While more indirect, our approach offers a way to bypass such limitations, as virtual passive tracers can be introduced numerically with arbitrary resolution, and followed with more precision, ease, better statistics and for significantly longer times than magnetic elements. Based on a comparison of tracer concentrations and trajectories with HMI magnetograms, we will argue that the transport properties thus obtained are representative of those of the weak (< 100 G), essentially passive, magnetic fields at the surface of the quiet Sun.

Section 2 introduces the observation and velocity datasets, and Sect. 3 the tools of fluid flow analysis applied to the data. Section 4 presents a Lagrangian flow analysis using FTLEs and LCS, and a comparison between the latter and the magnetic network. Sect. 5 provides a phenomenological and quantitative statistical characterisation of turbulent transport and estimates horizontal turbulent coefficient using two different methods. The implications of our work for the broader understanding of large-scale dynamics and turbulent transport are discussed in Sect. 6.

2. Data processing

The data used for this study has already been presented in Roudier et al. (2023) (hereafter R23), and the reduction procedures have been described in R17 and R23. We restate the main information here for the sake of completeness, outlining the differences with R23 where necessary.

2.1. The data

Our analysis is based on six days of uninterrupted high-resolution white-light intensity and Doppler observations of the entire solar disc by the HMI instrument aboard the SDO satellite (Scherrer et al. 2012; Schou et al. 2012). The data was obtained from 26 November (00:00:00 UTC) to 1 December 2018 (23:59:15 UTC),

2.2. Image corrections and derotation

Different procedures, detailed in App. A of R17, were first applied to the images to correct for misalignment, change in size of the solar disc, and the limbshift effect. In a second step, we adjusted the differential rotation profile from the raw Doppler data averaged over one day of observation, and used the resulting rotational velocity signal to derotate all images so as to work in a reference frame corotating with the Sun. This way, any given image pixel after derotation corresponds to a fixed physical location on the solar surface. For the derotation procedure, we used the rotation profile derived by R23,

$$\Omega(\lambda) = A + B\sin^2\lambda + C\sin^4\lambda, \quad (1)$$

where λ = here denotes the latitude, $A = 2.864 \times 10^{-6}$ rad s^{-1}, $B = -5.214 \times 10^{-7}$ rad s^{-1}, and $C = -2.891 \times 10^{-7}$ rad s^{-1}. This corresponds to a velocity of 1.9934 km s^{-1} (14.1781°per day) at the equator.

Derotation was applied to the white light intensity data, correcting the mean differential rotation of the Sun to bring back longitudes related to the solar surface at the same locations for each time deviation from the origin of the first HMI image. The reference time for the CST code was taken at 00:00 UTC, 29 November 2018, the middle of our sequence (see code manual[1]). Accordingly, derotation was applied on 26 to 28 November from the left to the right (east to west) and on 29 November to 1 december from the right to the left (west to east).

2.3. Derivation of the Eulerian photospheric velocity field projected in the CCD plane

We subsequently used the Coherent Structure Tracking (CST) algorithm to derive the projection (u_x, u_y) in the CCD plane of the corotating photospheric Eulerian velocity field on scales larger than 2.5 Mm, tracking ensembles of granules advected by horizontal flows. These are the only components of the flow needed for the Lagrangian tracer analyses performed in this paper (for a reconstruction of the full $(u_r, u_\theta, u_\varphi)$ velocity field in spherical coordinates, see R17).

By means of the derotation procedure, the corotating solar disc areas under consideration effectively remain centered, throughout the analysis, on an effective corotating reference disc centre (chosen as the actual disc centre in the middle time of the full sequence). This enables us to compute Lagrangian tracer trajectories over the chosen area using the in-CCD-plane (u_x, u_y) velocity field. We explain how this is done in Appendix.

[1] https://idoc.ias.u-psud.fr/system/files/user_guide_annex_version1.2_26mars2021.pdf

2.4. Masking and apodising

The determination of velocity fields close to the limb with the CST is more noisy and of lesser quality due to projection and resolution effects. Therefore, we finally apodised the velocity maps obtained with the procedures described above to focus on a limited corotating zone of the surface sufficiently far away from the limb, so that reliable velocity field data could be exploited continuously for several days.

In the following, we present results using circular apodising windows of different angular openings with respect to the disc centre. The rule of thumb here is that the larger the window, the shorter the time over which our Lagrangian tracer analyses can be conducted, as larger regions spend less time in full visibility on the side of the Sun visible to SDO, and sufficiently far away from the limb. We conducted some test analyses to determine which apodising window worked best to track flows reliably over the largest timescale possible, and converged to a circular apodising window of 23.5° opening with respect to the disc centre for the longest six-day Lagrangian tracer analysis presented in Sects. 4-5.

Considering the limitations of the CST to infer flows close to the limb, this masking strategy is the only reasonable course of action to ensure that all successive corotating velocity field data snapshots used to calculate Lagrangian trajectories are equally reliable. Of course, this limits the available corotating fraction of the solar disc used, compared to the full-disc raw intensity observations of SDO, and also explains why our analyses are limited to six days at most, rather than twelve-thirteen days if we were able to infer flows in a given corotating region reliably from the time that region becomes visible on one side of the limb to the time it disappears on the other side.

2.5. The final data product

The final data product, used in the following, is a sequence of 288 velocity-field maps of a single corotating physical area of the solar surface, tracked over six days, with a temporal resolution of 30 min and spatial resolution of 2.5 Mm. The angular opening of the *minimum* 23.5° apodising window used in the paper corresponds to an arc of 574 Mm at the surface, but larger fields of views were also exploited over shorter periods (see Sect. 4). This minimal 23.5° apodised field of view still contains the equivalent of ∼ 350 supergranules of 30 Mm diameter, that is 50 times more than the Hinode field of view. Besides, the continuous monitoring by SDO from space enables continuous tracking and transport of structures and tracers on much longer timescales (up to six days) than possible with ground-based instruments with comparably wide field of views, such as the CALAS camera used at Pic du Midi for a similar purpose a few years ago, which at best only provided continuous monitoring over 7.5 h of a 290×216 Mm^2 field of view containing ∼ 70 supergranules (Rieutord et al. 2008).

Overall, the extents of our field of views and continous monitoring periods ensure that a robust, and unprecedented statistical analysis of turbulent transport on temporal and spatial scales much larger than those of individual supergranules can be carried out with the data.

3. Flow analysis techniques

3.1. Lagrangian analysis of solar surface flows

3.1.1. Finite-time Lyapunov exponents (FTLEs)

The calculation of FTLEs provides a convenient mathematical way of characterising the chaoticity of dynamical systems, and in fluid dynamics to investigate the dynamical Lagrangian properties and organization of a flow. In particular, a flow exhibiting Lagrangian chaos (i.e. exponential divergence of the trajectories of initially close fluid particles) is characterised by the fact that at least one of its Lyapunov exponents is positive. To be more precise, for complex flows, the value of Lyapunov exponents usually depends on the spatial location and time, so instead of a single number, we compute a scalar field of Lyapunov exponents, which itself evolves dynamically in time. Computing a field of FTLEs for a given fluid flow requires to integrate the trajectories of passive Lagrangian tracers in the flow for a target time T. The principles of this kind of calculation are extensively documented in the literature (see e.g. Haller 2001; Shadden et al. 2005; Green et al. 2007; Lekien & Coulliette 2007; Lekien & Ross 2010) and are summarised in Appendix A. Our own implementation is very much based on that described by Lekien & Ross (2010).

The main specificities of the problem at hand are that it has a global spherical, non-Euclidean geometry, and that we only have access to the flow on a single spherical surface. The latter implies that we can not compute the three FTLE scalar fields of the full 3D photospheric flow. However it is still possible to compute two FTLE scalar fields associated with the horizontal flow on the surface[1]. Indeed, as shown by Lekien & Ross (2010), FTLEs for a 2D flow on a smooth non-Euclidean surface such as a sphere can be indirectly inferred from the projection in a 2D plane (in our case, the plane of the sky/CCD) of the Lagrangian tracers trajectories using a mapping (described in App. A.3). This is fortunate, because the projected trajectories are easier to compute than the actual trajectories on a spherical surface, provided that the projection of the velocity field in the projection plane is known. This is the case in our problem: the projection of the photospheric velocity field in the (x, y) plane of the satellite CCD is precisely what the CST algorithm computes.

Our implementation of the FTLE computation algorithm in a 2D plane, including the integration of Lagrangian tracers trajectories described in App. A.1, and subsequent FTLE calculation described in App. A.2, was validated using the chaotic double-gyre analytical flow benchmark (Shadden et al. 2005; Brunton & Rowley 2010). Coming back to the solar problem, we also found that the differences between the 2D plane results and the full spherical analysis always remained relatively small. This is mostly because the limb regions, where projection effects become very important and the surface velocity field itself can not be determined accurately, were mostly ignored throughout the analysis. The spherical and cartesian algorithms give almost identical results close to disc centre.

3.1.2. Imaging Lagrangian coherent structures

Lagrangian coherent structures (LCS) are simply defined as the ridges of a FTLE field $\sigma^T(\boldsymbol{x})$, and as such follow directly from the computation of FTLEs (Shadden et al. 2005). In 2D, they are most easily understood as one-dimensional invariant manifolds acting as transport barriers (although this is not strictly true, see the above paper for a more accurate description), from which particles either diverge (repulsive LCS), or to which they accumulate (attractive LCS). For a given flow, attractive LCS can be imaged using a (positive) FTLE field calculated from the backward-in-time integration of tracers trajectories in that flow (since maximal divergence for negative times implies maximal convergence for positive times), while repulsive LCS are imaged based on the (positive) FTLE field calculated from forward-in-time trajectories. We use both in what follows.

[1] The two FTLEs of the flow on the surface are probably close to two of the three FTLEs of the full 3D flow, because the photospheric velocity field at the large scales considered in this paper is strongly anisotropic with respect to the radial direction (R17).

4. FTLEs and Lagrangian Coherent Structures

In this Section, we describe global full-disc maps of Finite Time Lyapunov Exponents associated with large-scale solar surface convection flows, and further document their main properties.

4.1. Global and local FTLEs and LCS maps

As an introduction, we first present in Fig. 1 the global distribution of 24 h-negative time FTLEs of solar surface flows (in inverse hour units) derived from photospheric velocity field maps obtained on 29 November, 2018, using the technique described in Sect. 3 and in Appendix. This visualization reveals an (horizontally) isotropic tiling of the entire surface by structures/cells delimited by FTLE maxima, of size comparable to that of supergranules. As explained earlier, the use of negative-time FTLEs outlines a network of convergent/attractive (for positive times) spatial loci of passive tracers advected by the flow which, on this timescale, correspond to supergranule boundaries.

This network can be further highlighted by looking at the ridges of the FTLE field, or by emphasizing the maxima of the field using an appropriate colormap. This results in maps of Lagrangian Coherent Structures (LCS) acting as a complex network of transport barriers on the timescale of consideration. In Fig. 2, we show such global maps for FTLE fields computed backward-in-time over different integration times, up to six days. This is, to the best of our knowledge, the first calculation of this type over such long integration times and large areas. The structures are remarkably long-lived, and simple visual inspection reveals their tendency to moderately expand in size as a function of time. We characterise this effect quantitatively in Sect. 4.3.

4.2. LCS and the distribution of magnetic fields

Figures 3-4 show zooms of such maps on a region of 122×122 Mm^2 ($10^\circ \times 10^\circ$) at the (derotated) disc centre, overimposed with SDO/HMI magnetograms. These zoomed maps do not only enable us to better appreciate the mesmerizing structure of these patterns, they also show how much their fine-scale structure correlates with the magnetic network at the surface. As discussed by Yeates et al. (2012), on timescales of the order of the supergranulation timescale, LCS should be associated with regions of magnetic field accumulations. This is exactly what we observe here too: small-scale photospheric magnetic field concentrations appear to correlate extremely well with LCS derived from passive tracers. The results above (Figs. 1-2) therefore offer a striking new global-scale perspective on this phenomenon. Finally, Figs. 3-4 show the trajectories of a few selected tracers with remarkable excursions on the timescales of consideration. We will discuss these in more detail in Sect. 5 in connection with magnetic dynamics and transport.

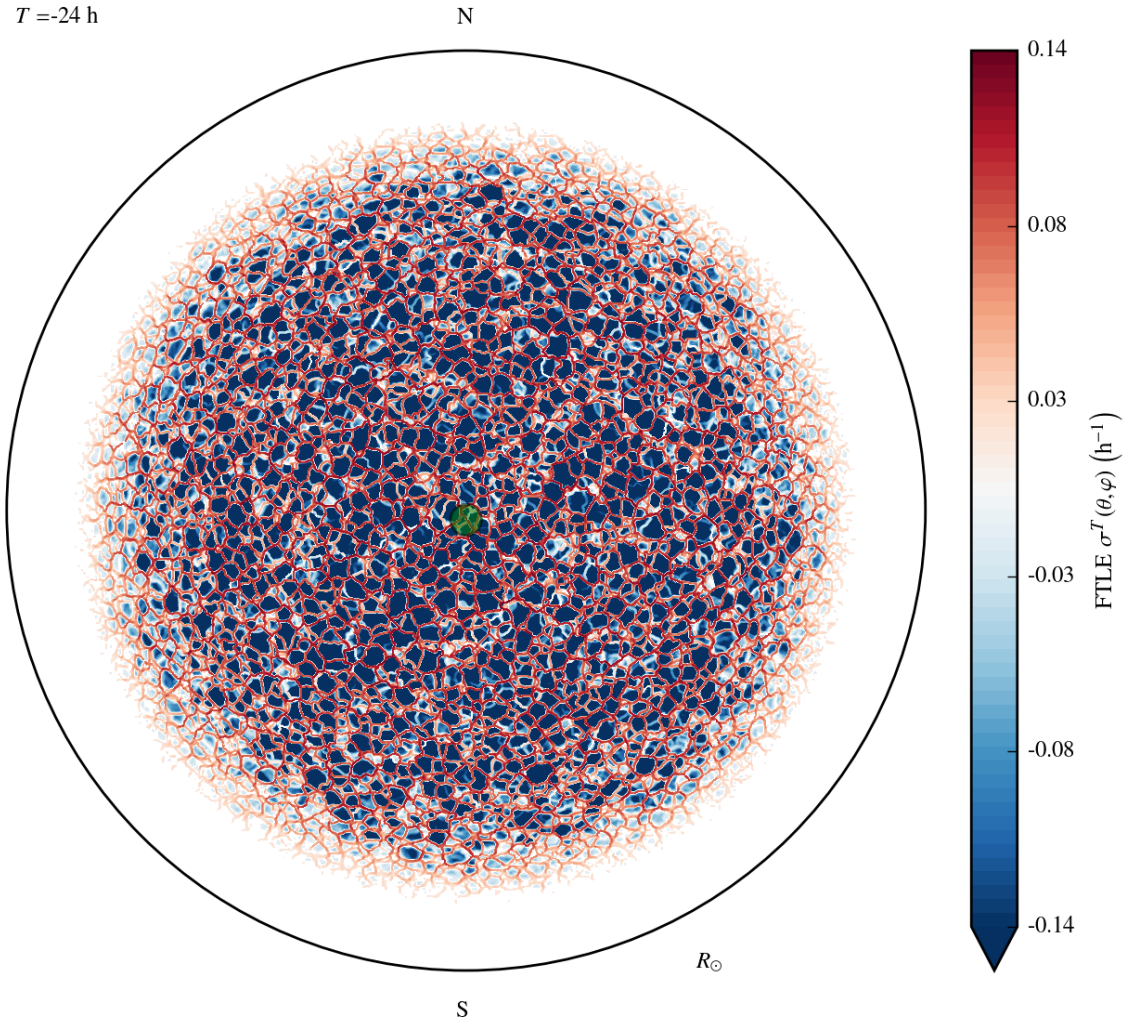

Fig. 1. Global distribution of 24 h, backwards-in-time FTLE of solar surface flows (in inverse hour units) computed using photospheric velocity field maps of 29 November, 2018, up to 60° from the disc centre. The green circle corresponds to a typical 30 Mm supergranule diameter.

4.3. Spectrum, scales and strength of the FTLE field

To be more quantitative, for any FTLE map such as shown in Fig. 1, we compute a typical peak scale of the distribution of FTLEs, corresponding to the wavelength of the LCS/transport barriers, as the integral scale of the FTLE field. To do this, we simply treat each FTLE field as a scalar field $\sigma^T(\theta,\varphi)$ over the sphere apodised by the visibility window, take its harmonic transform, compute the associated spherical harmonics spectrum $E_\sigma(\ell,T)$, and calculate the integral scale of the field, defined as

$$L_\sigma(T) = \frac{\sum_{\ell>50} \frac{2\pi R_\odot}{\ell} E_\sigma(\ell,T)}{\sum_{\ell>50} E_\sigma(\ell,T)} \,. \tag{2}$$

This formula simply weighs each scale by its corresponding energetic spectral content, providing a weighted mean giving more weight to the scales at which the distribution of σ^T contains the most energy. The lower bound in the sum avoids contamination by the large-scale energetic content of the apodising window, with which the true field is convoluted in spectral space. The numerical technique used for the spectral harmonic decomposition of our data fields over apodised fields of views is described in detail in R17, where ample use of it was made to characterise the structure and scale of the turbulent flow itself. Here, we simply apply the same tool to FTLE fields.

Fig. 5 shows the spherical harmonics spectra $E_\sigma(\ell,T)$ of FTLE fields for different target integration times, shown earlier in Fig. 2. As LCS form and evolve, their energy content and peak scale shifts towards larger scales, and the spectrum becomes steeper. By $T = 24$ h, the slope of the spectrum becomes stationary at intermediate scales, but the peak scale continues to increase monotonically on larger times.

The corresponding evolution of L_σ is shown in Fig. 6 as a function of the target time of integration of passive tracers. As this time increases, L_σ increases from 16 Mm at $T = 6$ h to 21 Mm at $T = 72$ h, and subsequently saturates. Thus, LCS, while acting as transport barriers, are "not set in stone" in this kind of time-dependent flow unconstrained by horizontal bound-

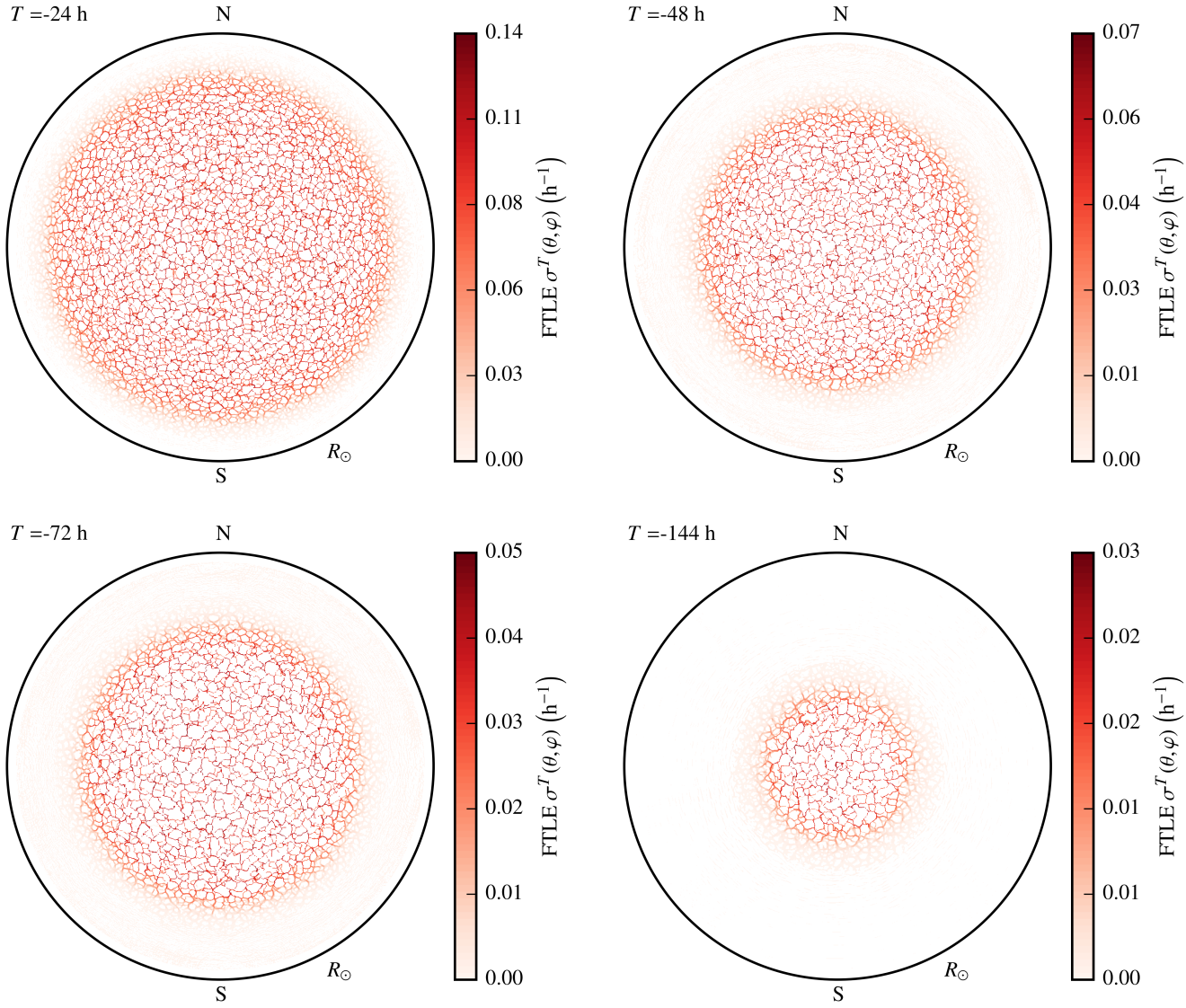

Fig. 2. From left to right and top to bottom: global solar-disc maps of attractive Lagrangian coherent structures imaged as ridges of maxima of the backwards-in-time FTLE field, for different integration times of 1, 2, 3 and 6 days respectively. Increasingly small apodising windows are used for longer time integrations (from 60° opening for T = 24 h to 23.5° opening for T = 144 h) to avoid contamination by imprecise velocity measurements at the limb (see discussion in Sect. 2).

aries[2]. Instead, they themselves appear to be highly dynamical structures that change in time as the flow evolves.

Figure 6 also shows how the r.m.s. value of the FTLE field σ^T evolves with the integration time. This quantity indicates how particles diverge as a function of time. A fast initial divergence over a timescale of a few hours is initially observed ($\sigma_{\rm rms} \sim 0.025$ h^{-1}, with peak values $\sigma_{\rm max} \sim 0.14$ h^{-1} for T = 24 h corresponding to a shortest divergence timescale of just 8 h, see Fig. 1). This shorter timescale roughly corresponds to the time it takes for tracers to be swept by supergranulation-scale flows from a supergranulation cell centre to its periphery. On longer timescales, however, particles tend to get trapped/blocked in the LCS transport barriers associated with supergranule boundaries. As a result, the rate of relative divergence of their trajectories significantly decreases, as visible in Fig. 6, and appears to saturate at $\sigma_{\rm rms} \sim 0.015$ h^{-1}.

Using the long-time asymptoting values reached by L_σ and $\sigma_{\rm rms}$ in Fig. 6, we can infer a first rough dimensional turbulent diffusion coefficient estimate, namely

$$D_\sigma = \frac{\sigma_{\rm rms} L_\sigma^2}{4} \simeq 400 \text{ km}^2 \text{ s}^{-1} = 4 \times 10^8 \text{ m}^2 \text{ s}^{-1} \,. \quad (3)$$

While this simple result should be treated with caution and should only be seen as an order of magnitude estimate, we point out that it provides an interesting connection between LCS, FTLEs and large-scale transport, which we study more quantitatively in the next section.

5. Statistical characterisation of turbulent transport

The previous section aimed at providing a phenomenological perspective on large-scale transport in the quiet photosphere, and

[2] In marine dynamics for instance, LCS can be laminar patterns whose geometry is shaped by coastal/bay topography, and they can be extremely stable over time, leading for example to accumulation of pollutants in particular areas, see e.g. Lekien et al. (2005).

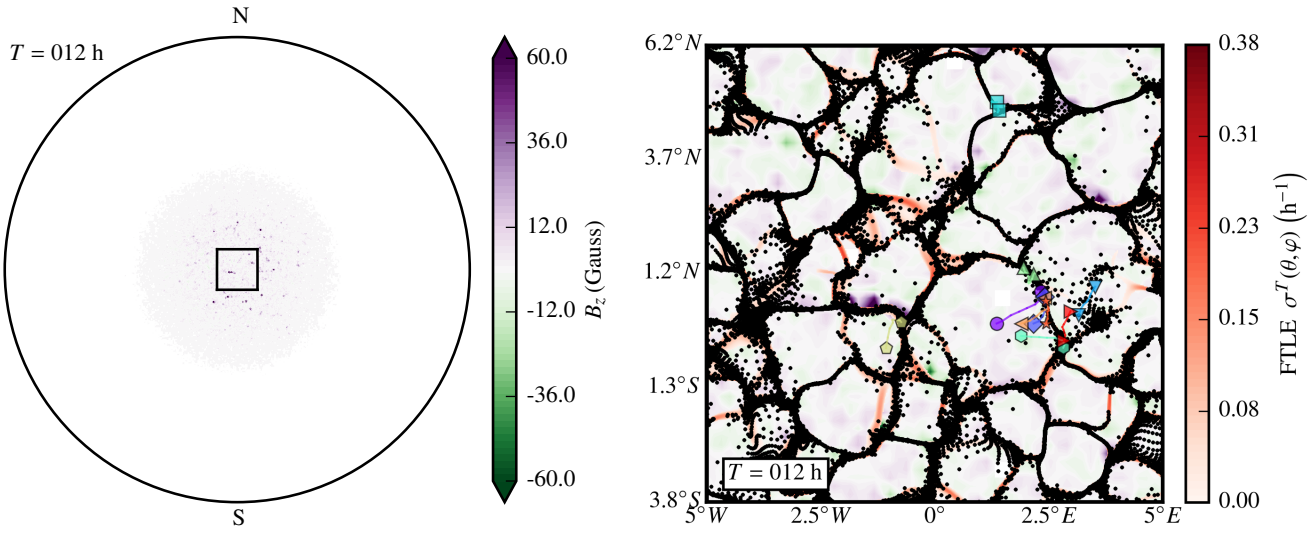

Fig. 3. Left: line-of-sight magnetic field B_z over the central 23.5° region, imaged with SDO/HMI 12 h after the beginning of the observation. Right: zoomed-in centre-disc region of 10° × 10° (frame in left plot) showing attractive LCS calculated for 12 h negative integration time (ridges of the negative-time FTLE field, red colormap), superimposed with passive tracer locations after 12 h positive integration time (black dots), and corresponding local B_z magnetograms (green/purple colormap). The coloured markers and lines tag 12 h (positive time) trajectories of a few selected tracers, see discussion in Sect. 5 and Fig. 7 below (visualization continued for longer times in Fig. 4).

it notably enabled us to pinpoint a global network of Lagrangian coherent structures associated with supergranulation-scale convection as a key physical pattern regulating horizontal turbulent diffusion in this convective fluid system. We now proceed to analyse the horizontal transport process on timescales of up to six days from a more classical statistical perspective, and subsequently attempt to interpret the results through the phenomenology outlined previously.

5.1. Statistics of tracer trajectories

To quantify turbulent transport, we focus on the central 23.5° region, whose velocity field can be reliably inferred throughout our 144 h sequence. We calculate the trajectories of 1024×1024 tracers initially placed on a cartesian grid at the centre of this region, with a resolution of 135 km. We first calculate the ensemble average (denoted by brackets) of the squared distance $d^2_{i,j}(T) = |\boldsymbol{x}_{i,j}(T) - \boldsymbol{x}_{i,j}(0)|^2$ travelled by each (i, j) tracer initially placed on this cartesian grid, as a function of the integration time. On general grounds, we expect

$$\langle d^2 \rangle(T) = cT^\gamma \,, \tag{4}$$

with $\gamma = 1$ corresponding to a random walk diffusion regime, $\gamma > 1$ to an anomalous superdiffusion regime, and $\gamma < 1$ to an anomalous subdiffusion regime. Using power-law fits to Eq. (4), we can then calculate a horizontal 2D-turbulence diffusion coefficient using a formula frequently used in the solar physics context (Monin & Yaglom 1971, see e.g. Hagenaar et al. (1999); Abramenko et al. (2011)),

$$D = \frac{1}{4}\frac{\mathrm{d}\langle d^2 \rangle}{\mathrm{d}T} = \frac{\gamma c}{4} T^{\gamma-1} \,. \tag{5}$$

Note that this transport coefficient usually bears a residual dependence on T if $\gamma \neq 1$, and that this expression also motivates *a posteriori* the specific expression used in Eq. (3) to estimate turbulent diffusion on the basis of the characteristic rate of tracers divergence and spatial scales obtained from our FTLE analysis.

We plot $\langle d^2 \rangle(T)$ and D for our collection of advected tracers in Fig. 7. We obtain a reasonable power-law fit with $\gamma = 1.09$ for intermediate times comparable to $\tau_{SG} = 48$ h, the typical correlation time of supergranulation. This corresponds to an almost-diffusive behaviour with a turbulent diffusion coefficient in the range $D = 200 - 300$ km^2 s^{-1} (inset). A histogram of the distribution of distances travelled by tracers (Fig. 8) further illustrates the spread in distances travelled as a function of time, consistent with a diffusive process.

On the longest times probed though, we find in Fig. 7 a slight increase in transport ($\gamma = 1.57$), corresponding to an enhanced diffusion coefficient $D \simeq 400$ km^2 s^{-1}. To understand the origins of this trend, we isolated a collection of tracers with larger-than-average excursions d from their initial positions. We overplot $d(T)$ for ten of these tracers in the figure using thin color lines and symbols, and further trace their trajectories at the solar surface in Figs. 3-4. A careful examination of these figures reveals that most of these tracers experience secondary transport kicks at a time between 24 h and 72 h comparable to τ_{SG}. These kicks appear to be associated with the regeneration of the supergranulation flow and the emergence of new "explosive granules" (Roudier et al. 2016) that structure supergranules, leading to a transient, more ballistic-like energetic superdiffusive behaviour. Since the average statistical trend at the largest times probed here is dominated by the small collection of tracers in this "non-thermal" tail of the distribution shown in Fig. 8, we argue, consistent with the standard picture of a random walk, that such individual kicks are simply random-walk events associated with the regeneration of the supergranulation flow, and that the accumulation of such events on timescales much larger than τ_{SG} would likely result on long times in an average diffusive-like behaviour. Accordingly, we conjecture that the statistics of $\langle d^2 \rangle$ should eventually settle in such a large-scale turbulent diffusion regime if we could track tracers trajectories for even longer times than we did here to reach a better timescale separation with the typical correlation time of the flow. Despite our best efforts to maximize the consecutive time of observation, reaching this regime unfortunately currently remains impossible, due

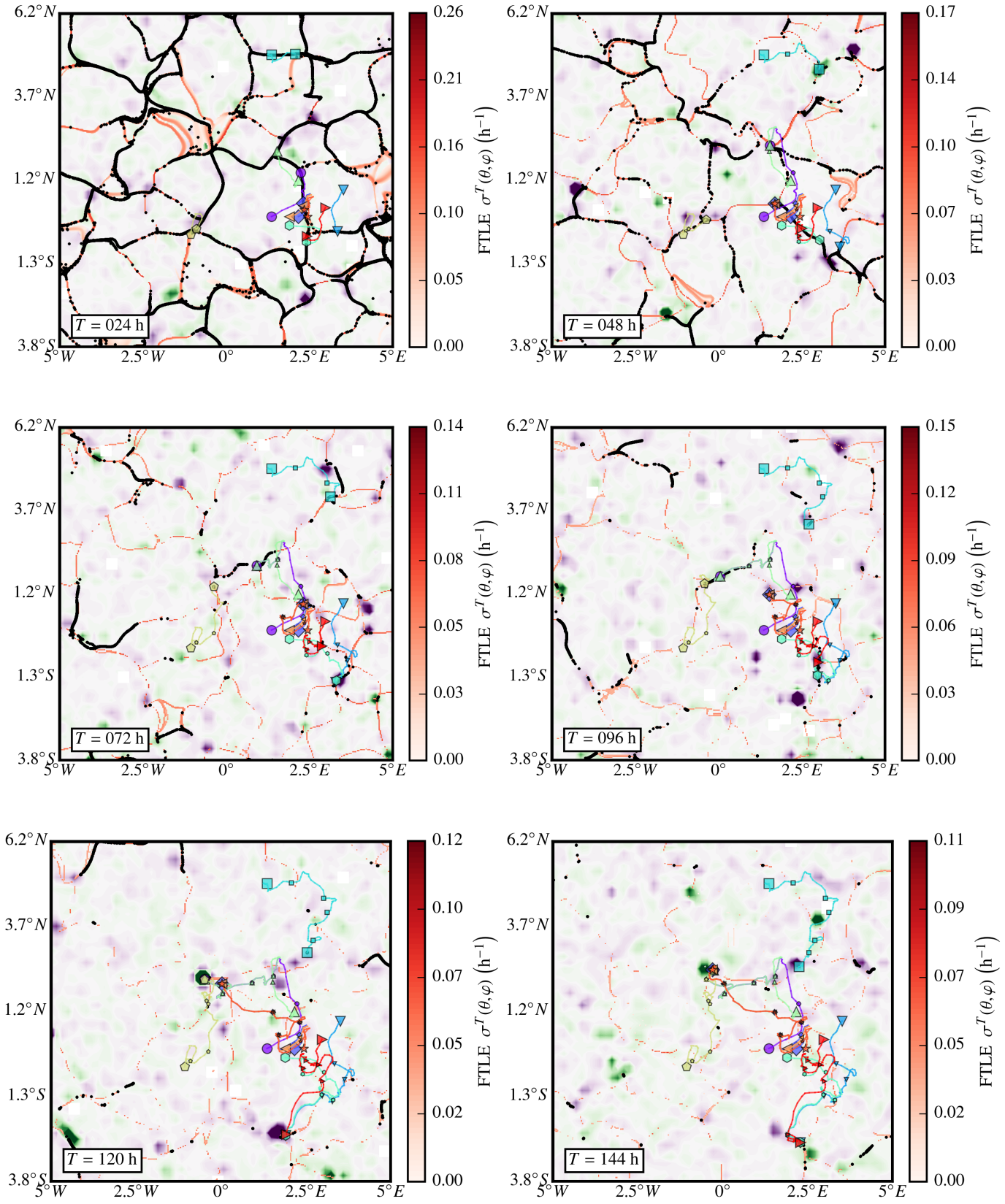

Fig. 4. Continuation of Fig. 3. From top left to bottom right: zoomed-in region (frame in Fig. 3, left) showing attractive LCS calculated for successive negative tracer integration times (red colormap), superimposed with passive tracer locations (black dots) and corresponding local B_z magnetograms (same green/purple colormap as in Fig. 3) at corresponding positive integration times. As mentioned in Sect. 3, tracers accumulate in attractive LCS. Throughout the sequence, LCS and tracer concentrations correlate well with the magnetic network and bright points, respectively. The coloured markers and lines tag (positive-time) trajectories of a few selected tracers: large symbols mark the initial position and current position for the time of integration of each plot, and small symbols the position for every intermediate 24 h (see discussion in Sect. 5 and Fig. 7).

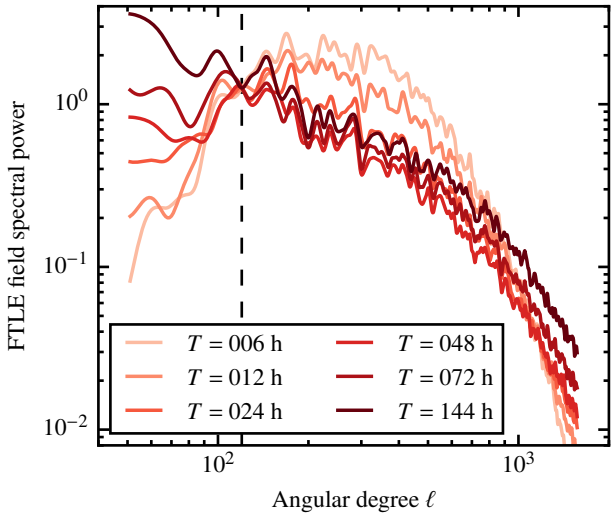

Fig. 5. Spherical harmonics spectra of the FTLE field for different target times. The spectra are normalized to one at the standard supergranulation angular degree scale $\ell = 120$ (dashed vertical line) to highlight the pivot of the spectrum towards larger physical angular scales on longer times.

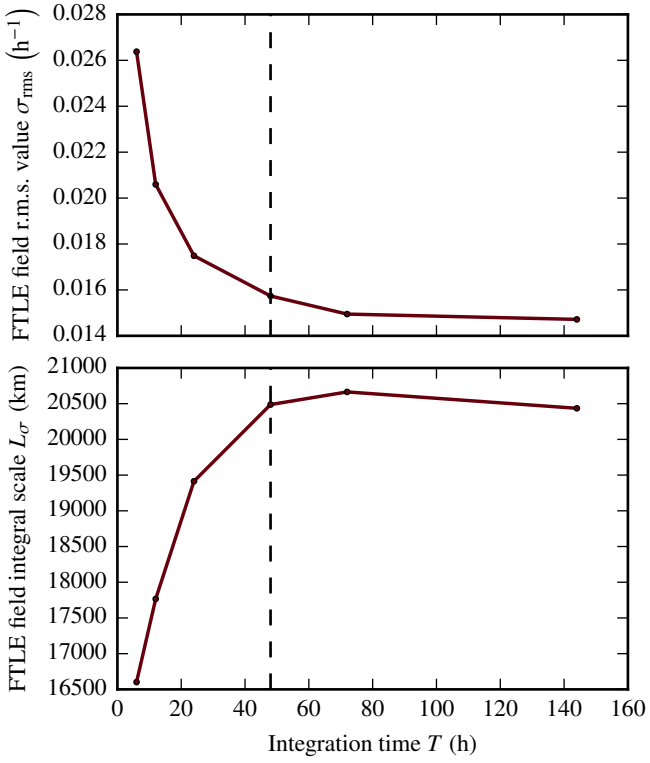

Fig. 6. Change as a function of the FTLE target integration time of the r.m.s. value and integral scale of FTLE distributions, derived from spherical harmonics spectra using Eq. (2). The dashed vertical line shows $\tau_{SG} = 48$ h, the typical correlation time of supergranulation.

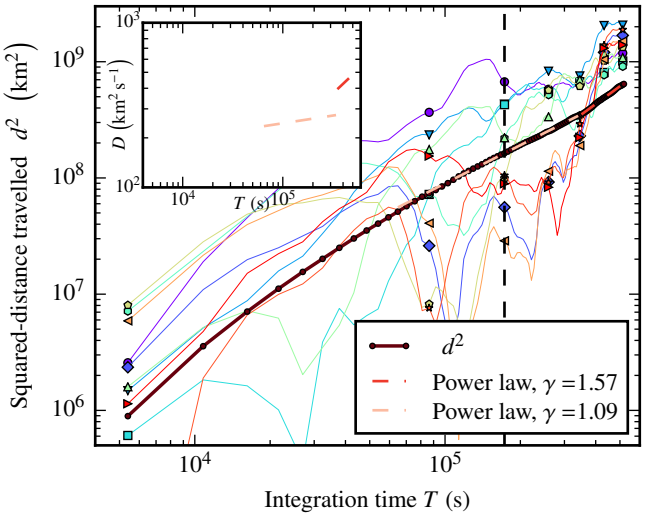

Fig. 7. Ensemble-averaged $\langle d^2 \rangle$ of the quadratic distance travelled by tracers as a function of time (full dark red line), power law fits (lighter red and cream lines), and (inset) corresponding diffusion coefficients as determined by Eq. (5). The thin coloured lines with markers every 24 h show the history of d^2 for individual tracers with larger-than-average excursions on long times. The surface trajectories of these tracers are shown with the same markers and colours in Figs. 3-4.

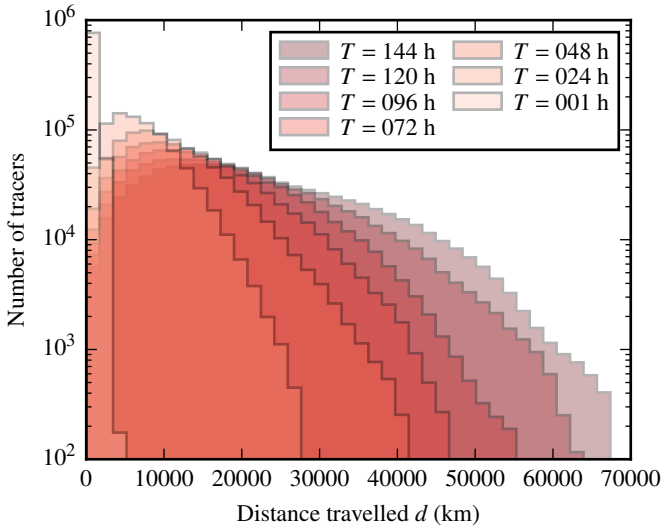

Fig. 8. Time evolution of the histogram distribution of distances travelled by tracers. The tracers showcased by markers in Figs. 3-4 and Fig. 7 all belong to the tail of the distribution at $T = 144$ h.

to the observing limitations stressed in the Introduction and in Sect. 2.4.

With respect to this point, close examination of Figs. 3-4 also reveals that some magnetic concentrations at the surface are subject to the exact same dynamics as these outlier tracers. For instance, an intense violet magnetic concentration located at $(2°E, 2.3°S)$ at $T = 96$ h gets pushed further south in exactly the same way as the tracers tagged with red and cyan triangles between $T = 96$ h and $T = 120$ h, at which time the position of the two tracers almost coincides with that of the magnetic element. The same remark applies at $T = 120$ h to the green magnetic concentration located at $(0.5°W, 2.2°N)$, and to the tracer tagged by a yellow pentagon. This provides further confirmation that the dynamics of tracers and magnetic fields are strongly correlated, and that both are subject to the same kind of average transport and individual transport events/kicks.

5.2. Ink spot experiment

To complement the previous results, and in the spirit of approaching the problem from a large-scale statistical point of view, we finally present a slightly different characterisation of transport by photospheric flows. The idea is to mimic a classical ink spot molecular diffusion experiment in the lab, whereby a circular ink spot is carefully released in water, and its radius subsequently expands diffusively. To do this, we delimit a circular patch of tracers in the initially cartesian grid of tracers (as in Sect. 4, we use a large tracers grid covering the entire solar surface here). We then measure the evolution of their average squared distance from the centre of the spot, i.e.

$$R^2_{\rm spot}(T) = \frac{1}{N} \sum_{i,j \in \,\rm spot} \Big(x_{i,j}(T) - x_{{\rm spot},c}\Big)^2 + \Big(y_{i,j}(T) - y_{{\rm spot},c}\Big)^2 \ , \quad (6)$$

where (x_c, y_c) are the central coordinates of the spot on the CCD grid and N is the number of tracers initially within a radius R_0 of the spot centre. For a diffusive process, a spot of initial radius R_0 will diffuse on a timescale $\tau_D = R_0^2/D$, where D is the diffusion coefficient. For the experiment to be meaningful, we should pick R_0 small enough that τ_D is smaller than, or at most of the order of the observation period, but also large enough that the circular spot itself encompasses at least one typical flow structure, i.e. a supergranule. Indeed, a very large spot would barely start to diffuse on the available time of observation, while a very small one would not feel the statistical effect of turbulent kicks and would also not contain enough tracers to construct a meaningful statistics. In what follows, we chose $R_0 = 28.7$ Mm, which corresponds to an angle with respect to the Sun centre of 2.35°, one-tenth of the opening of the apodising window used for the continuous six-day observation. Based on our earlier estimate for D, such a spot should diffuse on a typical timescale of a month, so we expect to be able to measure the beginning of the diffusion process using our six-day sequence.

A spot of initially this size contains $\sim$ 1380 tracers for our grid of tracers and it samples the flow of only a handful of independent supergranules giving relatively noisy results. To improve the statistics, we therefore replicate the measurement in Eq. (6) for as many spots as possible, packing the 23.5° observation window with non-overlapping circular spots whose centres are contained initially within an opening 21.15° = 23.5° − 2.35° angle from the solar disc centre. For the chosen R_0, this gives us a statistics of 60 spots from which we can calculate $\overline{R^2_{\rm spot}}$, a spot-ensemble average of $R^2_{\rm spot}$. Because the diffusion process takes a few hours to develop, we parameterise the evolution as

$$\overline{R^2_{\rm spot}}(T) = R^2_{\rm spot}(0)\,(1 + cT^\gamma) \ . \quad (7)$$

In Fig. 9, we plot $\overline{R^2_{\rm spot}}/R^2_{\rm spot}(0) - 1$ as a function of the integration time of tracers, and a corresponding power law fit of the evolution for times longer than 24 h. While the observed statistics is neither an exact power law, nor exactly diffusive, diffusion still appears to be a very reasonable first approximation overall, and the scaling exponent $\gamma = 1.15$ is very similar to $\gamma = 1.09$ obtained with the first method used in Sect. 5.1. As in Fig. 7, we also observe that transport is slightly enhanced on late times, for the same reasons. Figure 10 further shows the histogram distribution, as a function of time, of the distance of all the tracers considered in the analysis from their relative spot centre. The results illustrate the diffusion-like spread of the averaged spot.

Using this analysis, we can now estimate a large-scale diffusion coefficient from the power law fit in Fig. 9. For consistency and comparison with the method used in Sect. 5.1, we use again Eq. (5) for this purpose, applied here to $\overline{R^2_{\rm spot}}/R_0^2 - 1$ instead of $\langle d^2 \rangle$. The results, shown in the inset of Fig. 9, give $D_{\rm spot} \simeq 200\,{\rm km^2\,s^{-1}}$ for $T = 48$ h, consistent with the value obtained by the first method in Sect. 5.1.

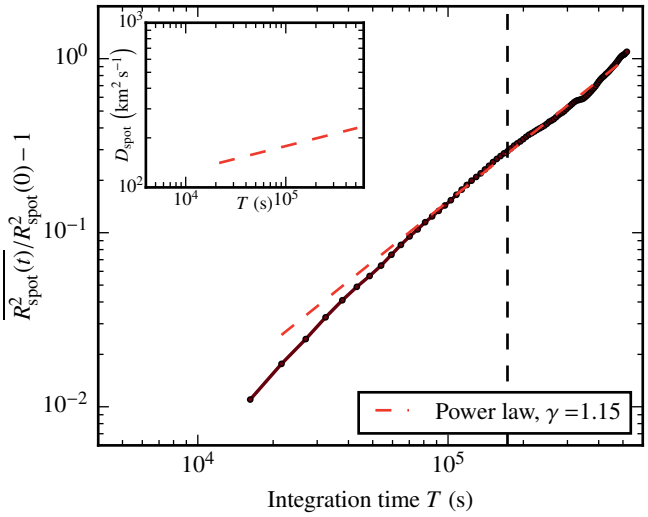

Fig. 9. Time evolution of the ensemble-average normalised radius of circular spots of tracers (full dark red line, see Eq. (7)), and correspondonding power-law fit.

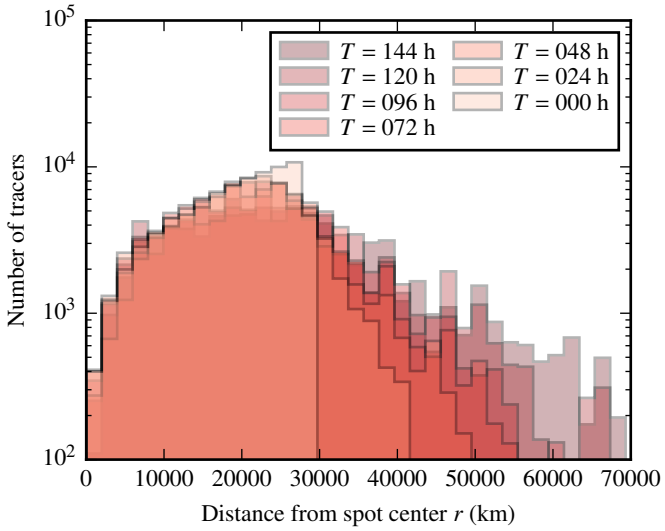

Fig. 10. Time evolution of the histogram distribution of distances travelled by tracers initially enclosed within circular spots of tracers of radius 30 000 km, with respect to their relative spot centres. Together with Fig. 9, the plot highlights the turbulent diffusive spread of tracers.

6. Conclusions and discussion

6.1. Main conclusions

In this paper, we have studied large-scale transport by convection flows in the solar photosphere from an observational perspective, using a Lagrangian passive tracer modelling approach to characterise turbulent diffusion and the formation of dynamical structures and patterns affecting this transport process.

In Sect. 4, we applied Finite Time Lyapunov Exponents (FTLEs) and Lagrangian Coherence Structure (LCS) analysis

techniques to large field of views covering a significant fraction of the solar disc, for unprecedented continuous periods of tracer tracking of up to six days. The large-scale maps we obtained reveal a clear and robust emergent dynamical LCS pattern tiling the solar surface isotropically at supergranulation scales. These results provide a new global perspective, rooted in observational data, of the dynamical interplay between order and chaos at the solar surface. In particular, by transiently accumulating particles and magnetic fields, Lagrangian coherent structures appear to regulate large-scale turbulent surface diffusion in the quiet Sun on long timescales. We also found that characterising their associated basic statistical properties (space and time scales) is sufficient to provide a correct preliminary dimensional order of magnitude estimate of the large-scale turbulent diffusivity.

A more quantitative statistical analysis of large-scale diffusion was presented in Sect. 5 using two different methods: a direct statistical analysis of tracers trajectories, which notably allowed us to pinpoint the role of "large-scale" flow kicks in driving the transport on long timescales, and an analog to an ink spot molecular diffusion laboratory experiment. Both analyses point to an effective horizontal turbulent diffusivity coefficient $D = 2 - 3 \times 10^8$ m^2 s^{-1} on the longest timescales of six days probed. We argued that an analysis on even longer times (much larger than the correlation timescale of supergranulation) would be desirable to make the convergence to an asymptotic, long-time statistical diffusion regime more apparent, but that such an analysis can not be easily conducted currently considering observational constraints.

6.2. Comparison with previous work

The passive tracers advection analysis presented in this paper bears some similarities with a previous analysis of this kind conducted by Roudier et al. (2009) on Hinode data on a 48 h timescale. The authors derived a diffusion coefficient $D \simeq 430\,\mathrm{km^2\,s^{-1}}$, broadly consistent with, but on the higher end of our own estimates. It is possible that the timescale they probed was not long enough to obtain a converged long-time diffusion coefficient, with the statistics being dominated by shorter-time, superdiffusive ballistic advection within supergranules. The present analysis, conducted on times larger than the typical supergranulation lifetime τ_{SG} and on significantly larger fields of views, offers a significant statistical improvement in this respect.

Our results can also be compared with solar studies involving the tracking of magnetic elements. We argued that magnetic transport is overall well captured by the dynamics of virtual passive tracers/corks. The main benefits of the latter, we recall, is that they can be integrated for longer times, provide better statistics and do not suffer from the issue of cancellation/merging effects (see e.g. Iida 2016, for a discussion). As mentioned in the introduction, all studies of this kind so far have focused on smaller fields of views and smaller timescales than the present study. Where the timescales of these studies overlap with ours, we find good agreement with our results. For instance, Hagenaar et al. (1999) derived $D = 200 - 250\,\mathrm{km^2\,s^{-1}}$ for magnetic tracking times in the $19 - 45$ h range; Giannattasio et al. (2013, 2014) report a slightly hyperdiffusive regime with $D = 100 - 400\,\mathrm{km^2\,s^{-1}}$ on supergranulation scales for a few hours. Most other observational solar magnetic turbulent diffusion studies in the literature (e.g. Berger et al. 1998; Utz et al. 2010; Abramenko et al. 2011; Manso Sainz et al. 2011; Jafarzadeh et al. 2014; Yang et al. 2015; Agrawal et al. 2018) have been focused on intra-supergranular /internetwork transport on significantly smaller times ($10^3 - 10^5$ s) and spatial scales of a few megameters at most (see Schrijver et al. (1996); Bellot Rubio & Orozco Suárez (2019) for reviews). They typically obtain diffusion coefficients smaller than $100\,\mathrm{km^2\,s^{-1}}$ that likely correspond to transport by shorter-lived, smaller-scale structures like granules or explosive granules, with only a minor effect of weaker, but much longer-lived supergranulation-scale flows on such short timescales. These studies therefore differ in both scales, scope, goal and spirit from our study, which preferentially targets effective large-scale transport on times comparable to, or larger than the typical supergranulation lifetime $\tau_{\mathrm{SG}} = 48$ h, which we believe is the appropriate limit to gauge the turbulent diffusion relevant to the large-scale solar dynamo problem.

6.3. Implications for solar dynamo modelling

Our long-time observational estimates of turbulent diffusivity, $D \simeq 2 - 3 \times 10^8$ m^2 s^{-1} obtained in Sect. 5, may be used to pin, at the solar photosphere, the profiles of horizontal turbulent magnetic diffusivity used for instance in mean-field models of the solar dynamo (Hazra et al. 2023). If our results hold, some existing models might slightly underestimate this mode of transport (e.g. Rempel 2006, who used 10^8 m^2 s^{-1} at the surface), while others use a turbulent diffusivity value entirely consistent with our observational estimate (e.g. $D \simeq 2.5 \times 10^8$ m^2 s^{-1} in Cameron et al. (2010)). On the other hand, some older flux-transport kinematic dynamo models (Sheeley 1992, 2005, see Schrijver et al. (1996) for a discussion) seemed to require a significantly larger turbulent diffusion coefficient, up to $D \simeq 6 \times 10^8$ m^2 s^{-1}, to produce sensible solar dynamo results. Such a large value is not consistent with even our upper-limit, enhanced transport estimates, $D \simeq 4 \times 10^8$ m^2 s^{-1}, obtained on the longest times probed, and associated with transiently re-accelerated "tail particles" (see inset of Fig. 7 and related discussion in Sect. 5). To be sustained on asymptotically long-times, such a large coefficient would require a significant transport regime change on longer timescales than the six days probed here. Such a dynamical effect is hard to envision at the surface at least, considering that our study already encompasses the main effects of supergranulation-scale convection, the most energetic large-scale flow structure contributing to turbulent transport at the surface.

Further mean-field solar dynamo modelling work by Lemerle et al. (2015) (see their Fig. 8), highlighted in a recent review on surface flux transport by Yeates et al. (2023), found a degeneracy between turbulent diffusivity and meridional flow amplitude parameters on the results of flux-transport dynamo models, which may somehow help to solve this problem. We believe that the multi-pronged statistical characterisation of the horizontal turbulent diffusivity at the photosphere developed in the present paper is sufficiently robust to help lift this degeneracy: our result, $D \simeq 2 - 3 \times 10^8$ m^2 s^{-1}, is very close to the turbulent diffusivity value associated with the maximum fitness contours obtained by Lemerle et al. (2015) in the turbulent diffusivity-meridional flow amplitude plane.

Finally, we note that transport coefficients derived from global numerical simulations of solar MHD convection also seem consistent with our observational estimates (e.g. Fig. 11 of Simard et al. (2016) for the $\beta_{\varphi\varphi}$ transport coefficient corresponding to our observational measurement of the horizontal diffusivity), although they might still slightly underestimate the vigour of the convection at supergranulation scales, and the associated diffusivity.

6.4. Connection with the solar magnetic network, atmosphere and solar wind

It is tempting to conjecture that the prominent global emergent dynamical pattern tiling the surface of the Sun, singled out in this work and best illustrated by Fig. 1, plays a major role in structuring the magnetic interactions between the interior, or at least the subsurface layers of the Sun driving the small-scale surface dynamo, its atmosphere, and possibly also the solar wind. The possible connection of the LCS loci of photospheric magnetic field accumulation with coronal heating has already been pointed out by Yeates et al. (2012). Our new global characterisation reveals the conspicuity, robustness and full extent of this dynamical LCS pattern over the whole solar disc, reinforcing this hypothesis. In this respect, our analysis may also provide new insights into the origin and mechanisms underlying a possible connection, suggested by Fargette et al. (2021), between supergranulation and solar wind magnetic switchbacks encountered by the Parker Solar Probe (Kasper et al. 2019; Bale et al. 2019).

6.5. A new "experimental" measurement of turbulent transport

Moving on to a more fundamental complex physics and fluid-dynamical perspective, we note that turbulent diffusion effects have been observed in various experimental MHD flows, such as the Perm, Wisconsin and VKS dynamo experiments (Frick et al. 2010; Rahbarnia et al. 2012; Miralles et al. 2013), all at relatively large kinetic Reynolds numbers $Re = O(10^6)$ but rather small magnetic Reynolds numbers ($Rm < 100$) not representative of astrophysical regimes such as encountered in planets, stars and galaxies. By using "the Sun as a fluid dynamics lab", our results offer a new, and possibly unique "experimental", *in situ* characterisation of the emergence on times comparable to, or longer than a typical flow correlation time, of turbulent diffusion in stochastic flows with both large kinetic and magnetic Reynolds numbers ($Re = O(10^{10})$, $Rm = O(10^4)$ at the solar surface).

6.6. The pitfalls of mixing-length arguments

Looking at the results from a broader perspective than just the solar context to benefit from the insights of the study of an astrophysical system resolved in both space and time, it is also an interesting exercise to ask why the value of the turbulent diffusivity we obtained is what it is in this system. If the transport is indeed dominated by supergranulation-scale flows, naïvely (by a mixing length argument) one could have expected a transport coefficient of the order of a fraction (typically 1/4 in 2D) of $R_{\rm SG}V_{\rm SG}$, i.e.

$$D = \frac{1}{4}R_{\rm SG}V_{\rm SG} = \frac{1}{4}\frac{R_{\rm SG}^2}{\tau_{\rm NL,SG}} = 1.5\times10^9\,{\rm m^2\,s^{-1}}\,, \tag{8}$$

where we have used $R_{\rm SG} \simeq 1.5\times10^4$ km, and $V_{\rm SG} \simeq 0.4\,{\rm km\,s^{-1}}$ (Rincon & Rieutord 2018), and we have introduced the nonlinear turnover time at the supergranulation scale $\tau_{\rm NL,SG} = R_{\rm SG}/V_{\rm SG} \simeq$ 8 h, which is the sweeping time for a passive tracer to be advected from the centre to the boundary of a supergranule cell. This mixing-length estimate is an order of magnitude higher than our experimental-observational determination. Why is it so ? The reason lies in that we have naïvely used, in the expression above, the turnover time of the flow $\tau_{\rm NL,SG}$, instead of its correlation time, $\tau_{\rm SG}$, which is closer to 48 h. If we repeat the calculation in Eq. (8) with this time instead, we find $D = 2.6\times10^8\,{\rm m^2\,s^{-1}}$, which is now remarkably consistent with our detailed statistical analysis.

The reason why the correlation time of the flow is the relevant quantity to use in a mixing length estimate here is because tracers remain stuck at the boundary of supergranules for a time of the order of $\tau_{\rm SG}$ after they have been advected there on the much shorter $\tau_{\rm NL,SG}$ time. Hence, their effective "random walk" velocity is not $V_{\rm SG} = 0.4\,{\rm km\,s^{-1}}$, but the much smaller $V_{\rm SG}\times(\tau_{\rm NL,SG}/\tau_{\rm SG}) \simeq 70\,{\rm m\,s^{-1}}$. This simple, yet subtle difference finds its roots in the very structure of the flow.

The conclusion of this phenomenological argument is therefore that the structure of a turbulent flow matters a lot when it comes to correctly estimating the magnitude of large-scale turbulent transport. In the example at hand, we showed that the global surface network of transport barriers and LCS at supergranulation scales, vividly illustrated in Fig. 1, plays a key role in the regulation of the effective large-scale transport. We believe that this conclusion pertains to many if not all astrophysical flows, and therefore call for caution with back-of-the-envelope estimates of turbulent transport coefficients based on dimensional arguments, for instance because the correlation time of the flow can significantly differ from its turnover time. In the case of solar surface convection, large-scale structures at the injection scale persist for quite a long time, so that the Strouhal number of the flow, ${\rm St} = \tau_{\rm corr}/\tau_{\rm NL}$, is of the order of 5-6, with significant consequences for the effective turbulent diffusivity.

6.7. Perspectives

The focus of this paper has deliberately been restricted to a subset of all physical solar dynamical transport and large-scale organisation phenomena to which the techniques developed in this work may be applied at global scales. Further investigations of this kind, of possible rotational effects, latitudinal dependences of turbulent diffusivity, global-scale convection (Hathaway et al. 2013; Ballot & Roudier 2024), meridional circulation (Roudier et al. 2018), and of the statistical implications of magnetic flux emergence and further transport at the photosphere (Hathaway & Rightmire-Upton 2012) for the energetics of the upper solar layers (Yeates et al. 2012), would undoubtedly prove very instructive too, and are left for future work.

More broadly, as exemplified by the discussion above, the study of the extreme fluid dynamical system that is the Sun, with the unique benefits in astrophysics of a large spatial and temporal resolution, can still teach us valuable lessons for the future modelling of unresolved astrophysical systems, such as stars or accretion discs, where turbulent flows driven by different hydrodynamic or MHD instabilities also likely play a key role in the overall dynamical and energetic regulation of the system.

Acknowledgements. We thank Peter Haynes and Yves Morel for several interesting conversations and for their invitation to discuss and present a preliminary version of the results at the 2019 TEASAO workshop in the beautiful surroundings of the Saint-Férréol lake, and Michael Nastac for a useful discussion on the theory of anomalous transport scalings in turbulence during an astrophysical plasma workshop organized at the Wolfgang Pauli Institute in Vienna, whose hospitality is gratefully acknowledged. We also thank Nathanaël Schæffer for his assistance with the `SHTns` library (Schaeffer 2013), the SDO/HMI data provider JSOC and the HMI/SDO team members for their hard work. In particular, we are grateful to P. Scherrer, S. Couvidat and J. Schou for sharing information regarding the calibration and removal of systematics of HMI Doppler data. This work was granted access to the HPC resources of CALMIP under the allocation 2011-[P1115]. We thank Nicolas Renon for his assistance with the parallelization of the CST code. This work was supported by COFFIES, NASA Grant 80NSSC20K0602.

References

Abramenko, V. I., Carbone, V., Yurchyshyn, V., et al. 2011, ApJ, 743, 133

Agrawal, P., Rast, M. P., Gošić, M., Bellot Rubio, L. R., & Rempel, M. 2018, ApJ, 854
Amari, T., Luciani, J.-F., & Aly, J.-J. 2015, Nature, 522, 188
Bale, S. D., Badman, S. T., Bonnell, J. W., et al. 2019, Nature, 576, 237
Ballot, J. & Roudier, T. 2024, in preparation
Bellot Rubio, L. & Orozco Suárez, D. 2019, Living Rev. Solar Phys., 16, 1
Berger, T. E., Löfdahl, M. G., Shine, R. A., & Title, A. M. 1998, ApJ, 506, 439
Brun, A. S. & Browning, M. K. 2017, Living Rev. Solar Phys., 14, 4
Brunton, S. L. & Rowley, C. W. 2010, Chaos, 20, 017503
Cameron, R. H., Jiang, J., Schmitt, D., & Schüssler, M. 2010, ApJ, 719, 264
Charbonneau, P. 2014, Annu. Rev. Astron. Astrophys., 52, 251
Chian, A. C.-L., Rempel, E. L., Aulanier, G., et al. 2014, ApJ, 786, 51
DeGrave, K. & Jackiewicz, J. 2015, Solar Phys., 290, 1547
Duvall, T. L. & Hanasoge, S. M. 2013, Solar Phys., 287, 71
Duvall, T. L., Hanasoge, S. M., & Chakraborty, S. 2014, Solar Phys., 289, 3421
Fargette, N., Lavraud, B., Rouillard, A. P., et al. 2021, ApJ, 919, 96
Frick, P. A., Noskov, V. I., Denisov, S. A., & Stepanov, V. A. 2010, Phys. Rev. Lett., 105, 184502
Giannattasio, F., Del Moro, D., Berrilli, F., et al. 2013, ApJ Lett., 770, L36
Giannattasio, F., Stangalini, M., Berrilli, F., Del Moro, D., & Bellot Rubio, L. 2014, ApJ, 788, 137
Gizon, L., Birch, A. C., & Spruit, H. C. 2010, Annu. Rev. Astron. Astrophys., 48, 289
Green, M. A., Rowley, C. W., & Haller, G. 2007, J. Fluid Mech., 572, 111
Greer, B. J., Hindman, B. W., Featherstone, N. A., & Toomre, J. 2015, ApJ, 803, L17
Hagenaar, H. J., Schrijver, C. J., Title, A. M., & Shine, R. A. 1999, ApJ, 511, 932
Haller, G. 2001, Phys. Fluids, 13, 3365
Hanasoge, S., Gizon, L., & Sreenivasan, K. R. 2016, Annu. Rev. Fluid Mech., 48, 191
Hanasoge, S. M., Duvall, T. L., & Sreenivasan, K. R. 2012, Proc. Natl. Acad. Sci., 109, 11928
Hart, A. B. 1954, MNRAS, 114, 17
Hathaway, D. H., Beck, J. G., Bogart, R. S., et al. 2000, Solar Phys., 193, 299
Hathaway, D. H. & Rightmire-Upton, L. 2012, in American Astronomical Society Meeting Abstracts, Vol. 220, American Astronomical Society Meeting Abstracts #220, 110.06
Hathaway, D. H., Teil, T., Norton, A. A., & Kitiashvili, I. 2015, ApJ, 811, 105
Hathaway, D. H., Upton, L., & Colegrove, O. 2013, Science, 342, 1217
Hazra, G., Nandy, D., Kitchatinov, L., & Choudhuri, A. R. 2023, Space Science Rev., 219, 39
Hotta, H., Rempel, M., & Yokoyama, T. 2014, ApJ, 786, 24
Iida, Y. 2016, J. Space Weather Space Clim., 6, A27
Jafarzadeh, S., Cameron, R. H., Solanki, S. K., et al. 2014, A&A, 563, A101
Kashyap, S. G. & Hanasoge, S. M. 2021, ApJ, 916, 87
Kasper, J. C., Bale, S. D., Belcher, J. W., et al. 2019, Nature, 576, 228
Langfellner, J., Gizon, L., & Birch, A. C. 2015, A&A, 581, A67
Leighton, R. B., Noyes, R. W., & Simon, G. W. 1962, ApJ, 135, 474
Lekien, F. & Coulliette, C. 2007, Phil. Trans. R. Soc. Lond., Ser. A, 365, 3061
Lekien, F., Coulliette, C., Mariano, A. J., et al. 2005, Physica D, 210, 1
Lekien, F. & Ross, S. D. 2010, Chaos, 20, 017505
Lemerle, A., Charbonneau, P., & Carignan-Dugas, A. 2015, ApJ, 810, 78
Manso Sainz, R., Martínez González, M. J., & Asensio Ramos, A. 2011, A&A, 531, L9
Miesch, M. S. 2005, Living Rev. Solar Phys., 2, 1
Miralles, S., Bonnefoy, N., Bourgoin, M., et al. 2013, Phys. Rev. E, 88, 013002
Monin, A. S. & Yaglom, A. M. 1971, Statistical Fluid Mechanics: Mechanics of Turbulence (MIT Press)
Nordlund, Å., Stein, R. F., & Asplund, M. 2009, Living Rev. Solar Phys., 6, 2
November, L. J. 1989, ApJ, 344, 494
November, L. J. & Simon, G. W. 1988, ApJ, 333, 427
Orozco Suárez, D., Katsukawa, Y., & Bellot Rubio, L. R. 2012, ApJ, 758, L38
Rahbarnia, K., Brown, B. P., Clark, M. M., et al. 2012, ApJ, 759, 80
Rempel, M. 2006, ApJ, 647, 662
Rieutord, M., Meunier, N., Roudier, T., et al. 2008, A&A, 479, L17
Rieutord, M., Roudier, T., Ludwig, H., Nordlund, Å., & Stein, R. 2001, A&A, 377, L14
Rieutord, M., Roudier, T., Rincon, F., et al. 2010, A&A, 512, A4
Rieutord, M., Roudier, T., Roques, S., & Ducottet, C. 2007, A&A, 471, 687
Rincon, F. & Rieutord, M. 2018, Living Rev. Solar Phys., 15
Rincon, F., Roudier, T., Schekochihin, A. A., & Rieutord, M. 2017, A&A, 599, A69
Roudier, T., Ballot, J., Malherbe, J. M., & Chane-Yook, M. 2023, A&A, 671, A98
Roudier, T., Malherbe, J. M., Rieutord, M., & Frank, Z. 2016, A&A, 590, A121
Roudier, T., Rieutord, M., Brito, D., et al. 2009, A&A, 495, 945
Roudier, T., Rieutord, M., Malherbe, J. M., et al. 2012, A&A, 540, A88
Roudier, T., Rieutord, M., Malherbe, J. M., & Vigneau, J. 1999, A&A, 349, 301
Roudier, T., Rieutord, M., Prat, V., et al. 2013, A&A, 552, A113
Roudier, T., Švanda, M., Ballot, J., Malherbe, J. M., & Rieutord, M. 2018, A&A, 611, A92
Schaeffer, N. 2013, Geochemistry, Geophysics, Geosystems, 14, 751
Scherrer, P. H., Schou, J., Bush, R. I., et al. 2012, Solar Phys., 275, 207
Schou, J., Scherrer, P. H., Bush, R. I., et al. 2012, Solar Phys., 275, 229
Schrijver, C. J., Shine, R. A., Hagenaar, H. J., et al. 1996, ApJ, 468, 921
Shadden, S. C., Lekien, F., & Marsden, J. E. 2005, Physica D, 212, 271
Sheeley, N. R., J. 1992, in Astron. Soc. Pacific Conf. Series, Vol. 27, The Solar Cycle, ed. K. L. Harvey, 1
Sheeley, N. R. 2005, Living Rev. Solar Phys., 2, 5
Shine, R. A., Simon, G. W., & Hurlburt, N. E. 2000, Solar Phys., 193, 313
Simard, C., Charbonneau, P., & Dubé, C. 2016, Adv.Space Res., 58, 1522
Simon, G. W. & Shine, R. A. 2004, in Bulletin of the American Astronomical Society, Vol. 36, American Astronomical Society Meeting Abstracts #204, 712
Toomre, J. & Thompson, M. J. 2015, Space Science Rev., 196, 1
Utz, D., Hanslmeier, A., Muller, R., et al. 2010, A&A, 511, A39
Švanda, M. 2012, ApJ, 759, L29
Švanda, M., Zhao, J., & Kosovichev, A. G. 2007, Solar Phys., 241, 27
Williams, P. E., Pesnell, W. D., Beck, J. G., & Lee, S. 2014, Solar Phys., 289, 11
Yang, Y., Ji, K., Feng, S., et al. 2015, ApJ, 810, 88
Yeates, A. R., Cheung, M. C. M., Jiang, J., Petrovay, K., & Wang, Y.-M. 2023, Space Science Rev., 219, 31
Yeates, A. R., Hornig, G., & Welsch, B. T. 2012, A&A, 539, A1

Appendix A: Computation of Finite-Time Lyapunov exponents

A.1. Computation of Lagrangian tracers trajectories

The trajectories of Lagrangian tracers ("corks") in the (x, y) plane are determined as follows: a cartesian grid of tracers is initially generated in the plane. The time history of the (x, y) projection of the photospheric velocity field $\boldsymbol{u}(x_i, y_j) = (u_x(x_i, y_j), u_y(x_i, y_j))$, determined via the CST algorithm every 30 min, is then used to integrate their position in that plane for a target time T ranging from several hours to several days, by means of numerical integration of an advection equation implemented through the python function `odeint`. The integrator internally sets an adaptative timestep shorter than the time between successive velocity snapshots. At each such timestep, the velocity field at the exact current location of each tracer is interpolated using the running snapshot of the velocity field on the cartesian grid, thanks to the python function `RectBivariateSpline`. Note that using the same velocity field snapshot during 30 min intervals is a reasonable assumption, given that the smallest spatial scales of the photospheric flow inferred via the CST are of the order of 2.5 Mm, and their timescale is of the order of 30 min to 1 hour. Note also that the resolution of the tracers grid on which a FTLE field is to be computed can be finer than the flow itself. Using a high-resolution grid of tracers is in fact essential to identify Lagrangian coherent structures and accurately compute invariant manifolds and transport barriers even when the flow is large-scale (Lekien et al. 2005). For global maps, we used a cartesian grid of up to 1024×1024 tracers encapsulating the full solar disc. This maximal resolution corresponds to an initial spacing between tracers of the order of 1.5 Mm close to the disc centre. The precision of the integration of the tracers trajectories, specified to the numerical integrator, is of the order of 0.3 Mm (in Sect. 5 we also used a much finer local grid of 1024×1024 tracers encompassing $10° \times 10°$ only). The collection of trajectories integrated in the CCD plane then serves as a basis for the computation of FTLE on the sphere, as explained below.

A.2. FTLE in a 2D plane

The Lagrangian trajectory $\boldsymbol{x}(t) = (x(t), y(t))$ of a passive tracer in a 2D plane fluid flow $\boldsymbol{u}(\boldsymbol{x}, t)$ is determined by its initial position $\boldsymbol{x}(t = 0) = \boldsymbol{x}_0$ and the differential equation of motion

$$\dot{\boldsymbol{x}}(t) = \boldsymbol{u}(\boldsymbol{x}(t), t). \tag{A.1}$$

Introducing the flow map for a target integration time T

$$\begin{aligned} \phi^T : \quad & \mathbb{R}^2 \to \mathbb{R}^2 \\ & \boldsymbol{x}_0 \mapsto \boldsymbol{x}(T, \boldsymbol{x}_0)\,, \end{aligned} \tag{A.2}$$

and its Jacobian $d\phi^T/d\boldsymbol{x}_0$, we form the Cauchy-Green deformation tensor

$$\Delta(\boldsymbol{x}_0) = \left(\frac{d\phi^T}{d\boldsymbol{x}_0}\right)^{\mathsf{T}} \left(\frac{d\phi^T}{d\boldsymbol{x}_0}\right). \tag{A.3}$$

The FTLE $\sigma^T(\boldsymbol{x}_0)$ of the flow at $\boldsymbol{x}_0$ is given by

$$\sigma^T(\boldsymbol{x}_0) = \frac{\ln \sqrt{\lambda_{\max}(\Delta(\boldsymbol{x}_0))}}{T}, \tag{A.4}$$

where $\lambda_{\max}$ is the largest eigenvalue of $\Delta(\boldsymbol{x}_0)$.

In practice, the matrix representation J of $d\phi^T/d\boldsymbol{x}_0$ is estimated at each interior point (x_i, y_j) of the cartesian grid on which the tracers are placed at $t = 0$, using a centered finite difference formula. Using the short-hand notation $\boldsymbol{x}_{i,j}(t) \equiv \boldsymbol{x}(t, \boldsymbol{x}_0 = (x_i, y_j))$, we have

$$\mathsf{J}(x_i, y_j) = \begin{pmatrix} \dfrac{x_{i+1,j}(T) - x_{i-1,j}(T)}{x_{i+1,j}(0) - x_{i-1,j}(0)} & \dfrac{x_{i,j+1}(T) - x_{i,j-1}(T)}{x_{i,j+1}(0) - x_{i,j-1}(0)} \\ \dfrac{y_{i+1,j}(T) - y_{i-1,j}(T)}{x_{i+1,j}(0) - x_{i-1,j}(0)} & \dfrac{y_{i,j+1}(T) - y_{i,j-1}(T)}{x_{i,j+1}(0) - x_{i,j-1}(0)} \end{pmatrix}, \tag{A.5}$$

from which $\Delta = \mathsf{J}^{\mathsf{T}}\mathsf{J}$ follows. The FTLE field $\sigma^T(x_i, y_j)$ is finally obtained via Eq. (A.4) by diagonalizing Δ at each grid point.

A.3. Mapping to the sphere

The FTLE of the flow on the sphere is inferred using basically the same algorithm presented above, except that a mapping between the real separations between the tracers and the projected ones in the plane of the sky/satellite CCD must be introduced. The theoretical formalism is described in Lekien & Ross (2010), as well as an example of application on the sphere. The formulae needed to compute FTLEs on the sphere for our particular problem are given below.

To perform the mapping, we introduce the out-of-plane distance z between a point on the solar surface and the plane parallel to the CCD plane and passing through the centre of the Sun,

$$z = \sqrt{R_\odot^2 - (x^2 + y^2)}\,, \tag{A.6}$$

where $R_\odot$ is a fiducial photospheric solar radius. The transformation between the solar disc $D_\odot$ and spherical solar surface manifold $\mathcal{M}$ is then given by the diffeomorphism

$$\begin{aligned} \beta^{-1} : \quad & D_\odot \to \mathcal{M} \\ & (x, y) \mapsto \begin{pmatrix} x \\ y \\ z = \sqrt{R_\odot^2 - (x^2 + y^2)} \end{pmatrix}. \end{aligned} \tag{A.7}$$

Using these definitions, the FTLE field on the sphere is obtained along the exact same lines as in Appendix A.2, except that a more general form of the deformation tensor accounting for the projection effects must be used, namely

$$\Delta(\boldsymbol{x}_0) = \widetilde{\mathsf{J}}(\boldsymbol{x}_0)^{\mathsf{T}}\, \widetilde{\mathsf{J}}(\boldsymbol{x}_0)\,, \tag{A.8}$$

with

$$\widetilde{\mathsf{J}}(\boldsymbol{x}_0) = \mathsf{R}\left(\boldsymbol{x}(T, \boldsymbol{x}_0)\right)\, \mathsf{J}(\boldsymbol{x}_0)\, \mathsf{R}\left(\boldsymbol{x}_0\right)^{-1}\,. \tag{A.9}$$

J is the Jacobian matrix in the projection plane, computed at each grid point via Eq. (A.5) using the projected tracers trajectories. $\mathsf{R}(\boldsymbol{x})$ is a coordinate-dependent upper-triangular matrix obtained by QR decomposition of the derivative of β^{-1}. Its explicit expression for our particular problem is

$$\mathsf{R}(\boldsymbol{x}) = \begin{pmatrix} \sqrt{1 + \dfrac{x^2}{z^2}} & \dfrac{xy}{\left(z\sqrt{R_\odot^2 - y^2}\right)} \\ 0 & \dfrac{R_\odot}{\sqrt{R_\odot^2 - y^2}} \end{pmatrix}. \tag{A.10}$$

Note that since the particles move on the sphere between $t = 0$ and the target time $t = T$, the projection effects at T are different from those at the initial time. This explains why R is evaluated at the final position $\boldsymbol{x}(T)$ on the left of J in Eq. (A.9) and at the initial position $\boldsymbol{x}(0)$ on its right.

Synthèse en français

Les magnétars regroupent deux classes de jeunes étoiles à neutrons isolées dont l'émission en rayon X et γ est alimentée par la diffusion de leurs champs magnétiques extrêmes. Leur large panel d'émissions va des sursauts courts (e.g. Gotz et al., 2006, Coti Zelati et al., 2018) aux éruptions géantes (Evans et al., 1980, Hurley et al., 1999, 2005, Svinkin et al., 2021, Mereghetti et al., 2024) — communément appelées *giant flares* — en passant par des phases caractérisées par une augmentation brutale du flux lumineux, appelées *outbursts*. Cela les différencie des pulsars dont l'émission tire son énergie de la rotation de l'étoile à neutron par le dipôle magnétique. De plus, les magnétars sont aussi à l'origine de certains sursauts radio rapides (CHIME/FRB Collaboration et al., 2020, Bochenek et al., 2020, Mereghetti et al., 2020). Leur activité permet de mesurer leur période de rotation et le ralentissement de celle-ci, qui se sont respectivement de 2–$12\,\mathrm{s}$ et 10^{-12}–$10^{-9}\,\mathrm{s\,s^{-1}}$. En supposant que ce ralentissement soit dû à l'extraction d'énergie rotationnelle par un dipôle magnétique, il est possible de déduire que ce dernier est de 10^{14}–$10^{15}\,\mathrm{G}$ pour les magnétars, ce qui est environ 100 fois plus intense que celui d'un pulsar typique. Certains magnétars — dits *low-field* magnétars — possèdent néanmoins des dipôles entre 6×10^{12} et $3 \times 10^{13}\,\mathrm{G}$, démontrant qu'un fort dipôle n'est pas nécessaire pour reproduire l'émission à haute énergie des magnétars classiques (Rea et al., 2010, 2012a, 2014). L'observation de raies d'absorptions proton cyclotron venant des deux magnétars à faible dipôle suggère cependant la présence d'un champ magnétique non-dipolaire d'environ $30 - 170$ fois plus fort que le dipôle (Tiengo et al., 2013, Rodríguez Castillo et al., 2016). La prédominance d'une composante non-dipolaire est confortée par l'interprétation de modulations observées dans les courbes de lumière de certains magnétars comme des mouvements de précessions dues à une composante toroïdal d'environ $10^{16}\,\mathrm{G}$ (Makishima et al., 2014, 2016, 2019, 2021).

Les magnétars et les étoiles à neutrons en général, sont le produit de l'effondrement du cœur d'une étoile massive — ayant au moins huit fois la masse du Soleil — lors de son explosion en supernova gravitationnelle. En effet, à la fin de leur vie, ces étoiles forment un cœur composé principalement de fer qui finit par s'effondrer à cause de la force de gravité, une fois qu'il atteint la masse de Chandrasekhar. Le cœur stellaire passe d'un rayon d'un millier de kilomètres à un peu moins d'une centaine de kilomètres en environ un centième de seconde, formant une proto-étoile à neutrons avec une densité extrême de l'ordre de $10^{14}\,\mathrm{g\,cm^{-3}}$. Dans ces conditions, les atomes de fer se dissocient et les protons deviennent des neutrons par capture électronique. Cette dernière réaction produit une très large quantité de neutrinos dont une fraction est absorbée par la matière formant un choc d'accrétion autour de l'objet compact. Dans le cas des supernovæ standards, le chauffage de la matière dû à l'absorption des neutrinos — et renforcé par des instabilités hydrodynamiques comme la convection et la *Standing Accretion Schock Instability* (e.g. Blondin et al., 2003, Foglizzo et al., 2007, Yamasaki & Foglizzo, 2008, Kazeroni et al., 2017, 2018, Walk et al., 2023, Buellet et al., 2023) — permet d'augmenter le rayon choc. Une fois sorti du cœur de l'étoile, le choc souffle les couches externes de l'étoile, constituant l'explosion en supernova. La proto-étoile à neutron continue de refroidir et de se contracter jusqu'à atteindre un rayon d'environ $12\,\mathrm{km}$

et former une étoile à neutrons.

En présence d'une rotation rapide avec une période de quelques millisecondes, les magnétars pourraient aussi être le moteur central d'explosions plus énergétiques et lumineuses que les explosions classiques par émission de neutrinos comme les hypernovæ — qui sont parfois associées à des sursauts γ longs — et les supernovæ superlumineuses. Le dipôle magnétique extrême d'un jeune magnétar pourrait efficacement extraire l'énergie rotationnelle pour l'injecter dans l'éjecta de l'explosion. Si cette injection d'énergie est tardive, elle permet d'expliquer la courbe de lumière des supernovæ superlumineuses (e.g. Woosley, 2010, Kasen & Bildsten, 2010, Nicholl et al., 2013, Inserra et al., 2013, Margalit et al., 2018, Lin et al., 2021). Pour les hypernovæ, les modèles de *magnétars milliseconde* reproduit fidèlement la courbe de lumière rémanente de certains sursauts γ longs (e.g. Nomoto et al., 2011, Metzger et al., 2015, Cano et al., 2016, Gompertz & Fruchter, 2017, Margalit et al., 2018, Lin et al., 2020). En outre, le cisaillement de dipôle magnétique en champs magnétique toroïdal peut expliquer la formation de jets qui se propagerait à travers les couches externes de l'étoile, provoquant une explosion dite magnétorotationnelle (e.g. Burrows et al., 2007, Dessart et al., 2008, Takiwaki et al., 2009, Kuroda et al., 2020, Bugli et al., 2020, 2021, 2023, Obergaulinger & Aloy, 2020, 2021, 2022). Ce type d'explosion est un bon candidat pour expliquer les sursauts γ long associé aux hypernovæ (e.g. Duncan & Thompson, 1992, Woosley & Bloom, 2006, Drout et al., 2011, Nomoto et al., 2011, Gompertz & Fruchter, 2017, Metzger et al., 2018). Enfin, ces magnétars milliseconde peuvent être le résultat d'une fusion de deux étoiles à neutrons, ce qui expliquerait la phase de plateau observée dans la courbe de lumière de certains sursauts γ courts (Metzger et al., 2008, Lü & Zhang, 2014, Gompertz et al., 2014).

Les magnétars sont alors des objets astrophysiques fondamentaux du ciel transitoire. L'origine de leur champ magnétique extrême est alors cruciale pour expliquer les phénomènes mentionnés plus tôt. Cette question reste ouverte, mais plusieurs pistes sont envisagées. Tout d'abord, un scénario suggère que ces champs magnétiques proviennent de celui du cœur de l'étoile progénitrice qui a été amplifié par conservation du flux magnétique lors de l'effondrement du cœur (Ferrario & Wickramasinghe, 2006). Le champ magnétique initial peut avoir été généré par effet dynamo dans les zones internes de l'étoile — soit durant son évolution (Augustson et al., 2016, Varma & Müller, 2023, Leidi et al., 2023), soit lors la fusion de deux étoiles massives (Schneider et al., 2019, 2020) — ou peut provenir d'un champ fossile (Braithwaite & Spruit, 2004, 2017). Néanmoins, aucune contrainte observationnelle n'existe sur le champ magnétique du cœur de fer, ce qui rend ce scénario incertain.

Une autre classe de scénarios arguent que le champ magnétique est amplifié par effet dynamo dans la proto-étoile à neutrons nouvellement formée. Avant le travail de cette thèse, deux dynamos ont été étudiées à travers des simulations numériques tridimensionnelles : les dynamos entretenues par les instabilités convective (Thompson & Duncan, 1993, Raynaud et al., 2020, 2022, White et al., 2022, Masada et al., 2022) et magnétorotationnelle (e.g. Mösta et al., 2015, Guilet & Müller, 2015, Guilet et al., 2022, Reboul-Salze et al., 2021, 2022). Ces simulations numériques montrent que ces effets peuvent générer des champs magnétiques de l'ordre de ceux des magnétars dans le cas de rotations rapides de la proto-étoile à neutrons. Ces scénarios permettent donc d'expliquer la formation des magnétars dans les explosions extrêmes. Cependant, la rotation de la proto-étoile à neutrons est supposée venir de celle de l'étoile progénitrice. Or, il est incertain s'il y a assez de l'étoile en rotation rapide pour former l'entière population des magnétars via ces dynamos. En outre, les explosions standards exigent des rotations plus lentes (au moins $5\,\mathrm{ms}$, Vink & Kuiper, 2006) comme dé-

montré par la mesure de l'énergie cinétique de rémanents de supernovæ associées à des magnétars (Vink & Kuiper, 2006, Martin et al., 2014, Zhou et al., 2019). Cela indique aussi que les magnétars se forment avec une période de rotation initiale d'au moins $5\,\mathrm{ms}$ et sont issus d'explosions standards. Enfin, la fraction de supernovæ extrêmes est d'environ $1\,\%$, ce qui est plus petit que la fraction $10\,\%$ estimée pour les magnétars parmi les jeunes étoiles à neutrons (Kouveliotou et al., 1994, Gill & Heyl, 2007, Beniamini et al., 2019).

Pour surmonter ces incertitudes, il est donc nécessaire d'établir un scénario de formation des magnétars incluant des proto-étoiles à neutrons avec un champ magnétique faible et les étoiles progénitrices avec une rotation lente. Dans cette thèse, nous investiguons un nouveau scénario de formation pour les magnétars. Dans celui-ci, la rotation est déterminée par l'accrétion asymétrie de matière initialement éjectée, mais restée gravitationnellement liée à la proto-étoile à neutrons finissant par retomber vers l'objet compacte environ $10\,\mathrm{s}$ après l'explosion (comme observé dans les simulations tridimensionnelles de Chan et al., 2020, Stockinger et al., 2020, Janka et al., 2022). L'accélération de la surface de la proto-étoile à neutrons génère une rotation différentielle favorisant le développement de la dynamo de Tayler-Spruit, ce qui amplifie le champ magnétique. Cette dernière se développe dans les régions stablement stratifiées et est entretenue par une instabilité de la composante toroïdale du champ magnétique appelée instabilité de Tayler (Tayler, 1973, Goossens et al., 1981). Les modélisations analytiques de cet effet dynamo (Spruit, 2002, Fuller et al., 2019) fournissent des prédictions sur l'intensité du champ magnétique et du transport de moment cinétique dans l'état saturé de la dynamo. Celles-ci sont largement utilisées dans les codes unidimensionnels d'évolution stellaire (e.g. Eggenberger et al., 2019a,c, 2022, den Hartogh et al., 2020, Moyano et al., 2024). L'existence de cette dynamo est, néanmoins, restée longtemps controversée, car jamais clairement identifiée dans des simulations numériques directes. Il faut attendre les récentes simulations produites par Petitdemange et al. (2023) pour démontrer l'existence de la dynamo de Tayler-Spruit.

Dans un premier temps, nous avons établi un modèle semi-analytique capturant l'évolution temporelle de la rotation de la surface et du cisaillement dans la proto-étoile à neutrons dus au fallback. En étendant le formalisme de (Fuller et al., 2019) pour la dynamo de Tayler-Spruit, nous modélisons aussi l'évolution du champ magnétique. Cela permet d'établir si la dynamo peut produire des champs magnétiques de l'ordre de celui des magnétars. La résolution des équations composant le modèle montre qu'un magnétar classique (dipôle magnétique plus fort que $4.4 \times 10^{13}\,\mathrm{G}$) peut être formé pour des masses de fallback accrétées supérieures à $1.1 \times 10^{-2}\,\mathrm{M}_\odot$, ce qui correspond à **une période de rotation inférieure à $28\,\mathrm{ms}$**. Cette période maximale est en accord avec la période minimale de $5\,\mathrm{ms}$ mesurée par Vink & Kuiper (2006) pour des magnétars formés dans des supernovæ standards. En outre, le champ magnétique est dominé par la composante azimutale, ce qui est en accord avec les indications de la présence d'un fort champ non-dipolaire prédominant dans les magnétars.

Les résultats de ce modèle, détaillés dans Barrère et al. (2022), sont très prometteurs, mais reposent néanmoins sur des fortes approximations pour outrepasser la forte non-linéarité du mécanisme dynamo. De plus, le modèle est une zone et ne donne pas d'information sur la géométrie du champ magnétique généré. Une seconde partie de ce travail de thèse consiste alors à investiguer la dynamo de Tayler-Spruit en utilisant des simulations numériques directes tridimensionnelles. Pour cela, nous avons recours au code pseudo-spectral `MagIC` (Wicht, 2002, Gastine & Wicht, 2012), qui résout les équations de la magnétohydrodynamique (MHD) en géométrie sphérique dans l'approximation Boussinesq — et anélastique, mais nous ne

l'utilisons pas dans cette thèse. Le fluide est confiné dans une configuration de Couette sphérique pour produire de la rotation différentielle, c'est-à-dire que des rotations solides de différentes fréquences sont imposées sur les sphères internes et externes. Nous précisons que la sphère externe tourne plus rapidement que l'interne pour rester cohérent avec notre nouveau scénario. Dans cette thèse, nous avons principalement mesuré l'impact du cisaillement et de la stratification stable sur la dynamo de Tayler-Spruit. Cette grande étude numérique est constituée de trois articles — dont un publié (Barrère et al., 2023), un soumis (Barrère et al., 2024b), et un en cours d'écriture (Barrère et al., 2024a) — a permis de mettre en évidence plusieurs résultats de premier plan :

- Nous démontrons l'existence de cette dynamo dans cette configuration et confirmons **son caractère sous-critique**.

- Nous reportons pour la première fois **trois comportements dynamiques** différents de la dynamo : stationnaire avec un champ magnétique symétrique/dipolaire par rapport à l'équateur, hémisphérique, et avec un champ magnétique montrant des renversements. Cette riche dynamique est semblable à celle observée dans l'expérience *Von Karman Sodium*. Elle peut être interprétée comme l'interaction de deux modes grandes échelles avec des symétries équatoriales opposées dictée par la brisure de la symétrie équatoriale de l'écoulement.

- La branche stationnaire/dipolaire de la dynamo de Tayler-Spruit est **en accord global avec les lois d'échelles établies par (Fuller et al., 2019) mais avec un facteur de normalisation d'environ** 0.01, c'est-à-dire que le champ magnétique toroidal axisymmétrique — qui prédomine — est 100 fois plus faible que prédit analytiquement.

- Cette même branche produit les champs magnétiques les plus forts et est donc la plus pertinente pour expliquer la formation des magnétars. Le résultat précédent implique, cependant, qu'il faut **une période de rotation maximale de $6\,$ms** pour former les champs magnétiques d'un magnétar classique. Cette limite est proche de la période minimale de $5\,\mathrm{ms}$ évoquée plus tôt. Néanmoins, la dynamo génère des champs magnétiques supérieurs à $10^{14}\,\mathrm{G}$ pour des périodes plus petites que $60\,\mathrm{ms}$, ce qui pourrait être suffisant pour produire l'activité à haute énergie des magnétars comme le démontre l'existence des magnétars à faible dipôle magnétique.

Enfin, les magnétars observés sont des étoiles à neutrons froides. Pour compléter notre étude, nous investiguons l'évolution à long terme d'un champ magnétique généré par la dynamo de Tayler-Spruit. Ce travail a été fait en collaboration avec le chercheur Andrei Igoshev qui a produit les simulations tridimensionnelles de l'évolution magnéto-thermique sur $1\,\mathrm{Ma}$ dans une croûte d'étoile à neutrons froide avec une version modifiée du code `PARODY`. Notre étude démontre que le champ magnétique généré par la dynamo de Tayler-Spruit peut **reproduire les caractéristiques principales d'un magnétar à faible dipôle magnétique**:

- Un dipôle à la surface de l'ordre de $10^{12}\,\mathrm{G}$ et un champ magnétique toroïdal de grande échelle de $10^{15}\,\mathrm{G}$.

- Fractures de la croûte provoquée par un champ magnétique local intense qui pourrait être à l'origine des sursauts courts en rayons X.

- Raies d'absorption proton cyclotron dans le spectre en rayons X dues à la présence d'arcs magnétiques de $10^{14}\,\mathrm{G}$ à la surface.
- Points chauds locaux à la surface aux pieds de ces arcs magnétiques pouvant reproduire les courbes de lumières d'un magnétar.
- Période de rotation ralentie jusqu'au valeurs typiques de $8\text{–}11\,\mathrm{s}$ grâce à l'interaction entre le magnétar et le disque composé du fallback dans le régime dit *propeller*.

Ce travail fait, ainsi, pour la première fois le lien entre l'effet dynamo dans les proto-étoiles à neutrons et les magnétars et ouvre la voie vers l'étude des signatures de chaque scénario de formation sur les observables associées aux magnétars.

Pour conclure, ce travail de thèse montre que notre nouveau scénario est prometteur pour expliquer la formation d'au moins une fraction des magnétars et est une avancée importante dans l'étude de ces objets astrophysiques. La mise en évidence de la riche physique derrière la dynamo de Tayler-Spruit a aussi des implications importantes dans le cadre de la physique stellaire et de l'étude des dynamos astrophysiques en général.

Pour clôturer ce manuscrit, je tiens à mentionner que ce travail de thèse s'est fait en parallèle d'un engagement dans les luttes politiques qui m'a permis d'affiner ma compréhension du monde qui m'entoure, et aussi de murir politiquement et en tant que personne.

Ainsi, je voudrais remercier toutes les personnes qui militent pour construire une société anti-sexiste, anti-fasciste, anti-coloniale, anti-impérialiste, anti-validiste, anti-capitaliste, anti-raciste, écologique et libertaire.

Que crèvent les fascismes, les autoritarismes, les impérialismes, et toutes les structures de pouvoir, leurs dispositifs de maintien de l'ordre et leurs frontières.
Que vivent la lutte et la société libertaire.

Bibliography

Abdo, A. A., Ackermann, M., Ajello, M., et al. 2010, ApJ, 708, 1254

Acheson, D. J. & Gibbons, M. P. 1978, Philosophical Transactions of the Royal Society of London Series A, 289, 459

Acuna, M. H., Connerney, J. E. P., Ness, N. F., et al. 1999, Science, 284, 790

Afsariardchi, N., Drout, M. R., Khatami, D. K., et al. 2021, ApJ, 918, 89

Aguilera, D. N., Pons, J. A., & Miralles, J. A. 2008, A&A, 486, 255

Ahmad, A., González, M., Hennebelle, P., & Commerçon, B. 2023, A&A, 680, A23

Akaho, R., Nagakura, H., & Foglizzo, T. 2024, ApJ, 960, 116

Akgün, T., Reisenegger, A., Mastrano, A., & Marchant, P. 2013, MNRAS, 433, 2445

Akiyama, S., Wheeler, J. C., Meier, D. L., & Lichtenstadt, I. 2003, ApJ, 584, 954

Amit, H., Christensen, U. R., & Langlais, B. 2011, Physics of the Earth and Planetary Interiors, 189, 63

An, H., Kaspi, V. M., Archibald, R., & Cumming, A. 2013, ApJ, 763, 82

Anderson, P. W. & Itoh, N. 1975, Nature, 256, 25

Andresen, H., Glas, R., & Janka, H. T. 2021, MNRAS, 503, 3552

Andresen, H., Müller, E., Janka, H. T., et al. 2019, MNRAS, 486, 2238

Archibald, R. F., Kaspi, V. M., Ng, C. Y., et al. 2013, Nature, 497, 591

Ascher, U. M., Ruuth, S. J., & Spiteri, R. J. 1997, Applied Numerical Mathematics, 25, 151, special Issue on Time Integration

Ascher, U. M., Ruuth, S. J., & Wetton, B. T. R. 1995, SIAM Journal on Numerical Analysis, 32, 797

Aubert, J., Aurnou, J., & Wicht, J. 2008, Geophysical Journal International, 172, 945

Aubert, J., Gastine, T., & Fournier, A. 2017, Journal of Fluid Mechanics, 813, 558

Augustson, K. C., Brun, A. S., & Toomre, J. 2016, ApJ, 829, 92

Augustson, K. C., Brun, A. S., & Toomre, J. 2019, ApJ, 876, 83

Baade, W. & Zwicky, F. 1934, Proceedings of the National Academy of Science, 20, 254

Bagchi, P., Layek, B., Saini, D., et al. 2024, arXiv e-prints, arXiv:2403.11539

Balbus, S. A. & Hawley, J. F. 1991, ApJ, 376, 214

Ballot, J. 2004, PhD thesis, Universite Paris Sud (Paris XI), France

Bamba, A. & Williams, B. J. 2022, Supernova Remnants: Types and Evolution (Springer Nature Singapore), 1–12

Barcilon, V. & Pedlosky, J. 1967a, Journal of Fluid Mechanics, 29, 1–16

Barcilon, V. & Pedlosky, J. 1967b, Journal of Fluid Mechanics, 29, 673–690

Barcilon, V. & Pedlosky, J. 1967c, Journal of Fluid Mechanics, 29, 609–621

Barkat, Z., Rakavy, G., & Sack, N. 1967, Phys. Rev. Lett., 18, 379

Barnes, J., Duffell, P. C., Liu, Y., et al. 2018, ApJ, 860, 38

Barrère, P., Guilet, J., Rayanud, R., & Reboul-Salze, A. 2024a, To be submitted in Physical Review of Fluids

Barrère, P., Guilet, J., Raynaud, R., & Reboul-Salze, A. 2023, MNRAS, 526, L88

Barrère, P., Guilet, J., Raynaud, R., & Reboul-Salze, A. 2024b, arXiv e-prints, arXiv:2407.01775

Barrère, P., Guilet, J., Reboul-Salze, A., Raynaud, R., & Janka, H. T. 2022, A&A, 668, A79

Batchelor, G. K. 1950, Proceedings of the Royal Society of London Series A, 201, 405

Becerra, L., Reisenegger, A., Valdivia, J. A., & Gusakov, M. 2022a, MNRAS, 517, 560

Becerra, L., Reisenegger, A., Valdivia, J. A., & Gusakov, M. E. 2022b, MNRAS, 511, 732

Belkacem, K., Marques, J. P., Goupil, M. J., et al. 2015a, A&A, 579, A31

Belkacem, K., Marques, J. P., Goupil, M. J., et al. 2015b, A&A, 579, A30

Bendre, A. B., Schober, J., Dhang, P., & Subramanian, K. 2023, arXiv e-prints, arXiv:2308.00059

Beniamini, P., Hotokezaka, K., van der Horst, A., & Kouveliotou, C. 2019, MNRAS, 487, 1426

Beniamini, P., Wadiasingh, Z., & Metzger, B. D. 2020, MNRAS, 496, 3390

Berger, E., Kulkarni, S. R., & Chevalier, R. A. 2002, ApJ, 577, L5

Berhanu, M., Monchaux, R., Fauve, S., et al. 2007, EPL (Europhysics Letters), 77, 59001

Bernstein, I. B., Frieman, E. A., Kruskal, M. D., & Kulsrud, R. M. 1958, Proceedings of the Royal Society of London Series A, 244, 17

Bersten, M. C., Benvenuto, O. G., Orellana, M., & Nomoto, K. 2016, ApJ, 817, L8

Bethe, H. A. & Wilson, J. R. 1985, ApJ, 295, 14

Bhandare, A., Kuiper, R., Henning, T., et al. 2020, A&A, 638, A86

Bhat, P., Ebrahimi, F., & Blackman, E. G. 2016, MNRAS, 462, 818

Bibby, J. L., Crowther, P. A., Furness, J. P., & Clark, J. S. 2008, MNRAS, 386, L23

Bignami, G. F., Caraveo, P. A., De Luca, A., & Mereghetti, S. 2003, Nature, 423, 725

Bionta, R. M., Blewitt, G., Bratton, C. B., et al. 1987, Phys. Rev. Lett., 58, 1494

Blondin, J. M., Gipson, E., Harris, S., & Mezzacappa, A. 2017, ApJ, 835, 170

Blondin, J. M. & Mezzacappa, A. 2007, Nature, 445, 58

Blondin, J. M., Mezzacappa, A., & DeMarino, C. 2003, ApJ, 584, 971

Bloom, J. S., Frail, D. A., & Kulkarni, S. R. 2003, ApJ, 594, 674

Bochenek, C. D., Ravi, V., Belov, K. V., et al. 2020, Nature, 587, 59

Bollig, R., Yadav, N., Kresse, D., et al. 2021, ApJ, 915, 28

Bonafede, A., Feretti, L., Murgia, M., et al. 2010, A&A, 513, A30

Bonanno, A. & Guarnieri, F. 2017, Astronomische Nachrichten, 338, 516

Bonanno, A., Guerrero, G., & Del Sordo, F. 2020, MEMSAI, 91, 249

Boscarino, S. 2007, SIAM Journal on Numerical Analysis, 45, 1600

Boscarino, S. 2009, Applied Numerical Mathematics, 59, 1515

Boscarino, S., Pareschi, L., & Russo, G. 2013, SIAM Journal on Scientific Computing, 35, A22

Boussinesq, J. 1903, Théorie analytique de la chaleur mise en harmonic avec la thermo- dynamique et avec la théorie mécanique de la lumière T. 2. (Gauthier-Villars)

Braginsky, S. I. & Roberts, P. H. 1995, Geophysical and Astrophysical Fluid Dynamics, 79, 1

Braithwaite, J. 2006, A&A, 449, 451

Braithwaite, J. 2008, MNRAS, 386, 1947

Braithwaite, J. 2009, MNRAS, 397, 763

Braithwaite, J. & Spruit, H. C. 2004, Nature, 431, 819

Braithwaite, J. & Spruit, H. C. 2017, Royal Society Open Science, 4, 160271

Brandenberger, R., Cyr, B., & Varna Iyer, A. 2017, arXiv e-prints, arXiv:1707.02397

Brandenburg, A. 2001, ApJ, 550, 824

Brandenburg, A. 2005, Astronomische Nachrichten, 326, 787

Brandenburg, A. 2015, in Astrophysics and Space Science Library, Vol. 407, Magnetic Fields in Diffuse Media, ed. A. Lazarian, E. M. de Gouveia Dal Pino, & C. Melioli, 529

Brandenburg, A. 2018, Journal of Plasma Physics, 84, 735840404

Brandenburg, A. & Rempel, M. 2019, ApJ, 879, 57

Brandenburg, A. & Subramanian, K. 2005, Phys. Rep., 417, 1

Bretz, J., van Eysden, C. A., & Link, B. 2021, MNRAS, 504, 5880

Brown, B. P., Vasil, G. M., & Zweibel, E. G. 2012, ApJ, 756, 109

Buellet, A. C., Foglizzo, T., Guilet, J., & Abdikamalov, E. 2023, A&A, 674, A205

Bugli, M., Guilet, J., Foglizzo, T., & Obergaulinger, M. 2023, MNRAS, 520, 5622

Bugli, M., Guilet, J., & Obergaulinger, M. 2021, MNRAS, 507, 443

Bugli, M., Guilet, J., Obergaulinger, M., Cerdá-Durán, P., & Aloy, M. A. 2020, MNRAS, 492, 58

Bugnet, L. 2020, PhD thesis, Univers Université Paris Cité

Bullard, E. & Gellman, H. 1954, Philosophical Transactions of the Royal Society of London Series A, 247, 213

Burrows, A., Dessart, L., Livne, E., Ott, C. D., & Murphy, J. 2007, ApJ, 664, 416

Burrows, A. & Goshy, J. 1993, ApJ, 416, L75

Camilo, F., Ransom, S. M., Halpern, J. P., & Reynolds, J. 2007, ApJ, 666, L93

Camilo, F., Ransom, S. M., Halpern, J. P., et al. 2006, Nature, 442, 892

Cano, Z., Johansson Andreas, K. G., & Maeda, K. 2016, MNRAS, 457, 2761

Cantiello, M., Mankovich, C., Bildsten, L., Christensen-Dalsgaard, J., & Paxton, B. 2014, ApJ, 788, 93

Carilli, C. L. & Taylor, G. B. 2002, ARA&A, 40, 319

Carpenter, M. H., Kennedy, C., Bijl, H., Viken, S., & Vatsa, V. N. 2005, Journal of Scientific Computing, 25, 157

Castillo, F., Reisenegger, A., & Valdivia, J. A. 2020, MNRAS, 498, 3000

Cattaneo, F. & Hughes, D. W. 1996, Phys. Rev. E, 54, R4532

Cavaglieri, D. & Bewley, T. 2015, Journal of Computational Physics, 286, 172

Chabanat, E., Bonche, P., Haensel, P., Meyer, J., & Schaeffer, R. 1998, Nucl. Phys. A, 635, 231

Chan, C., Müller, B., & Heger, A. 2020, MNRAS, 495, 3751

Charbonneau, P. & Sokoloff, D. 2023, Space Sci. Rev., 219, 35

Chevalier, R. A. 1989, ApJ, 346, 847

CHIME/FRB Collaboration, Amiri, M., Andersen, B. C., et al. 2021, ApJS, 257, 59

Chime/Frb Collaboration, Andersen, B. C., Bandura, K., et al. 2023, ApJ, 947, 83

CHIME/FRB Collaboration, Andersen, B. C., Bandura, K. M., et al. 2020, Nature, 587, 54

Chime/Frb Collaboration, Andersen, B. C., Bandura, K., Bhardwaj, M., et al. 2022, Nature, 607, 256

Ching, T. C., Li, D., Heiles, C., et al. 2022, Nature, 601, 49

Ciolfi, R. & Rezzolla, L. 2013, MNRAS, 435, L43

Clark, J. S., Muno, M. P., Negueruela, I., et al. 2008, A&A, 477, 147

Cline, K. S., Brummell, N. H., & Cattaneo, F. 2003, ApJ, 599, 1449

Cline, T. L., Desai, U. D., Teegarden, B. J., et al. 1982, ApJ, 255, L45

Cockburn, B., Lin, S.-Y., & Shu, C.-W. 1989, Journal of Computational Physics, 84, 90

Coleman, M. S. B. & Burrows, A. 2022, MNRAS, 517, 3938

Corbel, S. & Eikenberry, S. S. 2004, A&A, 419, 191

Corbet, R. H. D., Smale, A. P., Ozaki, M., Koyama, K., & Iwasawa, K. 1995, ApJ, 443, 786

Cordes, J. M. & Chatterjee, S. 2019, ARA&A, 57, 417

Cordes, J. M. & Lazio, T. J. W. 2002, arXiv e-prints, astro

Coti Zelati, F., Borghese, A., Rea, N., et al. 2021, The Astronomer's Telegram, 14674, 1

Coti Zelati, F., Rea, N., Pons, J. A., Campana, S., & Esposito, P. 2018, MNRAS, 474, 961

Courant, R., Friedrichs, K., & Lewy, H. 1928, Mathematische Annalen, 100, 32

Cowling, T. G. 1933, MNRAS, 94, 39

Şaşmaz Muş, S., Aydın, B., & Göğüş, E. 2014, MNRAS, 440, 2916

Cutler, C. & Lindblom, L. 1987, ApJ, 314, 234

Daniel, F., Petitdemange, L., & Gissinger, C. 2023, Physical Review Fluids, 8, 123701

Davies, B., Figer, D. F., Kudritzki, R.-P., et al. 2009, ApJ, 707, 844

Davies, C. R. & Hughes, D. W. 2011, ApJ, 727, 112

De Grandis, D., Taverna, R., Turolla, R., et al. 2021, ApJ, 914, 118

De Grandis, D., Turolla, R., Taverna, R., et al. 2022, ApJ, 936, 99

De Luca, A., Caraveo, P. A., Mereghetti, S., Tiengo, A., & Bignami, G. F. 2006, Science, 313, 814

Debye, P. & Hückel, E. 1923, Zur Theorie der Elektrolyte. I. Gefrierpunktserniedrigung und verwandte Erscheinungen

Deheuvels, S., Ballot, J., Beck, P. G., et al. 2015, A&A, 580, A96

Deheuvels, S., Li, G., Ballot, J., & Lignières, F. 2023, A&A, 670, L16

Dehman, C., Viganò, D., Ascenzi, S., Pons, J. A., & Rea, N. 2023, MNRAS, 523, 5198

Deller, A. T., Camilo, F., Reynolds, J. E., & Halpern, J. P. 2012, ApJ, 748, L1

den Hartogh, J. W., Eggenberger, P., & Deheuvels, S. 2020, A&A, 634, L16

Denissenkov, P. A. & Pinsonneault, M. 2007, ApJ, 655, 1157

Dessart, L., Burrows, A., Livne, E., & Ott, C. D. 2008, ApJ, 673, L43

Dessart, L., Hillier, D. J., Waldman, R., Livne, E., & Blondin, S. 2012, MNRAS, 426, L76

Dexter, J. & Kasen, D. 2013, ApJ, 772, 30

Dhillon, V. S., Marsh, T. R., Hulleman, F., et al. 2005, MNRAS, 363, 609

Dhillon, V. S., Marsh, T. R., Littlefair, S. P., et al. 2011, MNRAS, 416, L16

Dhillon, V. S., Marsh, T. R., Littlefair, S. P., et al. 2009, MNRAS, 394, L112

Dib, R. & Kaspi, V. M. 2014, ApJ, 784, 37

Dietrich, W. & Wicht, J. 2013, Physics of the Earth and Planetary Interiors, 217, 10

Donati, J. F. & Landstreet, J. D. 2009, ARA&A, 47, 333

Dormy, E. 1997, PhD thesis, Institut de Physique du Globe de Paris

Dormy, E. 2011, Journal of Fluid Mechanics, 688, 1

Dormy, E. 2016, J. Fluid Mech., 789, 500

Dormy, E., Oruba, L., & Petitdemange, L. 2018, Fluid Dyn. Res., 50, 011415

Drout, M. R., Soderberg, A. M., Gal-Yam, A., et al. 2011, ApJ, 741, 97

Duez, V., Braithwaite, J., & Mathis, S. 2010, ApJ, 724, L34

Duez, V. & Mathis, S. 2010, A&A, 517, A58

Duncan, R. C. & Thompson, C. 1992, ApJ, 392, L9

Durant, M. & van Kerkwijk, M. H. 2006, ApJ, 652, 576

Eatough, R. P., Falcke, H., Karuppusamy, R., et al. 2013, Nature, 501, 391

Edwards, R. T., Hobbs, G. B., & Manchester, R. N. 2006, MNRAS, 372, 1549

Eggenberger, P., Buldgen, G., & Salmon, S. J. A. J. 2019a, A&A, 626, L1

Eggenberger, P., Buldgen, G., Salmon, S. J. A. J., et al. 2022, Nature Astronomy, 6, 788

Eggenberger, P., Deheuvels, S., Miglio, A., et al. 2019b, A&A, 621, A66

Eggenberger, P., den Hartogh, J. W., Buldgen, G., et al. 2019c, A&A, 631, L6

Eggenberger, P., Maeder, A., & Meynet, G. 2005, A&A, 440, L9

Eggenberger, P., Meynet, G., Maeder, A., et al. 2008, Ap&SS, 316, 43

Elfritz, J. G., Pons, J. A., Rea, N., Glampedakis, K., & Viganò, D. 2016, MNRAS, 456, 4461

Ertl, T., Woosley, S. E., Sukhbold, T., & Janka, H. T. 2020, ApJ, 890, 51

Evans, W. D., Klebesadel, R. W., Laros, J. G., et al. 1980, ApJ, 237, L7

Federrath, C. 2016, Journal of Plasma Physics, 82, 535820601

Ferrario, L. & Wickramasinghe, D. 2006, MNRAS, 367, 1323

Field, G. B. & Blackman, E. G. 2002, ApJ, 572, 685

Finn, J. M. & Ott, E. 1988, Physics of Fluids, 31, 2992

Flowers, E. & Ruderman, M. A. 1977, ApJ, 215, 302

Foglizzo, T., Galletti, P., Scheck, L., & Janka, H. T. 2007, ApJ, 654, 1006

Fowler, W. A. & Hoyle, F. 1964, ApJS, 9, 201

Fromang, S., Papaloizou, J., Lesur, G., & Heinemann, T. 2007, A&A, 476, 1123

Frost, A. J., Sana, H., Mahy, L., et al. 2024, Science, 384, 214

Fryer, C. L. 2009, ApJ, 699, 409

Fuller, J., Cantiello, M., Stello, D., Garcia, R. A., & Bildsten, L. 2015, Science, 350, 423

Fuller, J. & Lu, W. 2022, MNRAS, 511, 3951

Fuller, J. & Ott, C. D. 2015, MNRAS, 450, L71

Fuller, J., Piro, A. L., & Jermyn, A. S. 2019, MNRAS, 485, 3661

Gabler, M., Cerdá-Durán, P., Stergioulas, N., Font, J. A., & Müller, E. 2016, MNRAS, 460, 4242

Gabler, M., Cerdá-Durán, P., Stergioulas, N., Font, J. A., & Müller, E. 2018, MNRAS, 476, 4199

Gaensler, B. M., McClure-Griffiths, N. M., Oey, M. S., et al. 2005, ApJ, 620, L95

Gal-Yam, A. 2012, Science, 337, 927

Gal-Yam, A. 2019, ARA&A, 57, 305

Galama, T. J., Vreeswijk, P. M., van Paradijs, J., et al. 1998, Nature, 395, 670

Gallet, B. & Pétrélis, F. 2009, Phys. Rev. E, 80, 035302

Gastine, T. & Wicht, J. 2012, Icarus, 219, 428

Gaurat, M., Jouve, L., Lignières, F., & Gastine, T. 2015, A&A, 580, A103

Gavriil, F. P., Dib, R., & Kaspi, V. M. 2011, ApJ, 736, 138

Gavriil, F. P., Kaspi, V. M., & Woods, P. M. 2002, Nature, 419, 142

Gehan, C., Mosser, B., Michel, E., Samadi, R., & Kallinger, T. 2018, A&A, 616, A24

Gill, R. & Heyl, J. 2007, MNRAS, 381, 52

Gissinger, C. 2010, Phys. Rev. E, 82, 056302

Gissinger, C., Petitdemange, L., Schrinner, M., & Dormy, E. 2012, Phys. Rev. Lett., 108, 234501

Glampedakis, K., Andersson, N., & Samuelsson, L. 2011, MNRAS, 410, 805

Glampedakis, K. & Jones, D. I. 2014, MNRAS, 439, 1522

Glas, R., Just, O., Janka, H. T., & Obergaulinger, M. 2019, ApJ, 873, 45

Gogus, E., Kouveliotou, C., & Younes, G. 2020, The Astronomer's Telegram, 14085, 1

Gompertz, B. & Fruchter, A. 2017, ApJ, 839, 49

Gompertz, B. P., O'Brien, P. T., & Wynn, G. A. 2014, MNRAS, 438, 240

Goossens, M. 1980, Geophysical and Astrophysical Fluid Dynamics, 15, 123

Goossens, M., Bironi, D., & Tayler, R. J. 1981, Astrophys. Space Sci., 75, 521

Goossens, M. & Tayler, R. J. 1980, MNRAS, 193, 833

Gotthelf, E. V. & Halpern, J. P. 2009, ApJ, 695, L35

Gotthelf, E. V., Halpern, J. P., & Seward, F. D. 2005, ApJ, 627, 390

Gotz, D., Israel, G. L., Mereghetti, S., et al. 2006, The Astronomer's Telegram, 953, 1

Gough, D. O. 2007, Astronomische Nachrichten, 328, 273–285

Gough, D. O. 2015, Space Sci. Rev., 196, 15

Gourgouliatos, K. N., Wood, T. S., & Hollerbach, R. 2016, Proceedings of the National Academy of Science, 113, 3944

Göğüş, E., Woods, P. M., Kouveliotou, C., et al. 2011, ApJ, 740, 55

Gregory, P. C. & Fahlman, G. G. 1980, Nature, 287, 805

Griffiths, A., Eggenberger, P., Meynet, G., Moyano, F., & Aloy, M.-Á. 2022, A&A, 665, A147

Grunhut, J. H., Wade, G. A., Neiner, C., et al. 2017, MNRAS, 465, 2432

Gruzinov, A. V. & Diamond, P. H. 1994, Phys. Rev. Lett., 72, 1651

Gubbins, D. & Zhang, K. 1993, Physics of the Earth and Planetary Interiors, 75, 225

Guerrero, G., Del Sordo, F., Bonanno, A., & Smolarkiewicz, P. K. 2019, MNRAS, 490, 4281

Guilet, J., Bauswein, A., Just, O., & Janka, H.-T. 2017, MNRAS, 471, 1879

Guilet, J. & Fernández, R. 2014, MNRAS, 441, 2782

Guilet, J. & Müller, E. 2015, MNRAS, 450, 2153

Guilet, J., Müller, E., & Janka, H.-T. 2015, MNRAS, 447, 3992

Guilet, J., Reboul-Salze, A., Raynaud, R., Bugli, M., & Gallet, B. 2022, MNRAS, 516, 4346

Gulminelli, F. & Raduta, A. R. 2015, Phys. Rev. C, 92, 055803

Gusakov, M. E. & Kantor, E. M. 2013, MNRAS, 428, L26

Haensel, P. & Zdunik, J. L. 2007, Ap&SS, 308, 363

Haskell, B. & Melatos, A. 2015, International Journal of Modern Physics D, 24, 1530008

Hathaway, D. H. 2010, Living Reviews in Solar Physics, 7, 1

Hawley, J. F., Gammie, C. F., & Balbus, S. A. 1996, ApJ, 464, 690

Heger, A., Woosley, S. E., & Spruit, H. C. 2005, ApJ, 626, 350

Held, L. E. & Mamatsashvili, G. 2022, MNRAS, 517, 2309

Held, L. E., Mamatsashvili, G., & Pessah, M. E. 2024, MNRAS, 530, 2232

Helfand, D. J., Chatterjee, S., Brisken, W. F., et al. 2007, ApJ, 662, 1198

Hellier, C. 1994, MNRAS, 271, L21

Henriksson, K. T. & Wasserman, I. 2013, MNRAS, 431, 2986

Herault, J., Rincon, F., Cossu, C., et al. 2011, Phys. Rev. E, 84, 036321

Hewish, A., Bell, S. J., Pilkington, J. D. H., Scott, P. F., & Collins, R. A. 1968, Nature, 217, 709

Heyl, J., Taverna, R., Turolla, R., et al. 2024, MNRAS, 527, 12219

Hillebrandt, W., Nomoto, K., & Wolff, R. G. 1984, A&A, 133, 175

Hiramatsu, D., Howell, D. A., Van Dyk, S. D., et al. 2021, Nature Astronomy, 5, 903

Hirata, K., Kajita, T., Koshiba, M., et al. 1987, Phys. Rev. Lett., 58, 1490

Hobbs, G. B., Edwards, R. T., & Manchester, R. N. 2006, MNRAS, 369, 655

Hollerbach, R. 2003, J. Fluid Mech., 492, 289

Hosseinzadeh, G., Valenti, S., McCully, C., et al. 2018, ApJ, 861, 63

Howe, R. 2009, Living Reviews in Solar Physics, 6, 1

Hüdepohl, L. 2014, PhD thesis, Technical University of Munich, Germany

Hughes, D. W. 2018, Journal of Plasma Physics, 84, 735840407

Hughes, D. W. & Cattaneo, F. 2008, Journal of Fluid Mechanics, 594, 445

Huppenkothen, D., D'Angelo, C., Watts, A. L., et al. 2014, ApJ, 787, 128

Hurley, K., Boggs, S. E., Smith, D. M., et al. 2005, Nature, 434, 1098

Hurley, K., Cline, T., Mazets, E., et al. 1999, Nature, 397, 41

Hurley, K., Rowlinson, A., Bellm, E., et al. 2010, MNRAS, 403, 342

Hurley-Walker, N., Zhang, X., Bahramian, A., et al. 2022, Nature, 601, 526

Igoshev, A. P., Frantsuzova, A., Gourgouliatos, K. N., et al. 2022, MNRAS, 514, 4606

Igoshev, A. P., Hollerbach, R., Wood, T., & Gourgouliatos, K. N. 2021, Nature Astronomy, 5, 145

Inserra, C., Smartt, S. J., Jerkstrand, A., et al. 2013, ApJ, 770, 128

Isern, J., García-Berro, E., Külebi, B., & Lorén-Aguilar, P. 2017, ApJ, 836, L28

Israel, G., Covino, S., Mignani, R., et al. 2005a, A&A, 438, L1

Israel, G. L., Belloni, T., Stella, L., et al. 2005b, ApJ, 628, L53

Israel, G. L., Coti Zelati, F., Borghese, A., et al. 2021, The Astronomer's Telegram, 14679, 1

Israel, G. L., Esposito, P., Rea, N., et al. 2016, MNRAS, 457, 3448

Israel, G. L., Mereghetti, S., & Stella, L. 1994, ApJ, 433, L25

Iwamoto, K., Mazzali, P. A., Nomoto, K., et al. 1998, Nature, 395, 672

Jafari, A., Vishniac, E. T., Kowal, G., & Lazarian, A. 2018, ApJ, 860, 52

Jameson, A., Schmidt, W., & E., T. 1981, 14th Fluid and Plasma Dynamics Conference

Janka, H. T. 2001, A&A, 368, 527

Janka, H. T. 2004, in Young Neutron Stars and Their Environments, ed. F. Camilo & B. M. Gaensler, Vol. 218, 3

Janka, H.-T., Wongwathanarat, A., & Kramer, M. 2022, ApJ, 926, 9

Jennings, R. L. & Weiss, N. O. 1991, MNRAS, 252, 249

Jermyn, A. S., Bauer, E. B., Schwab, J., et al. 2023, ApJS, 265, 15

Ji, S., Fuller, J., & Lecoanet, D. 2023, MNRAS, 521, 5372

Johansson, O. & Kreiss, H.-O. 1963, BIT Numerical Mathematics, 3, 97

Jouve, L., Gastine, T., & Lignières, F. 2015, A&A, 575, A106

Jouve, L., Lignières, F., & Gaurat, M. 2020, A&A, 641, A13

Kaplan, D. L., Chakrabarty, D., Wang, Z., & Wachter, S. 2009, ApJ, 700, 149

Käpylä, P. J., Browning, M. K., Brun, A. S., Guerrero, G., & Warnecke, J. 2023, Space Sci. Rev., 219, 58

Käpylä, P. J., Korpi, M. J., & Brandenburg, A. 2009, A&A, 500, 633

Kargaltsev, O., Durant, M., Misanovic, Z., & Pavlov, G. G. 2012, Science, 337, 946

Kasen, D. & Bildsten, L. 2010, ApJ, 717, 245

Kashiyama, K., Ioka, K., & Mészáros, P. 2013, ApJ, 776, L39

Kaspi, V. M. & Beloborodov, A. M. 2017, ARA&A, 55, 261

Kaspi, V. M., Gavriil, F. P., Woods, P. M., et al. 2003, ApJ, 588, L93

Kazantsev, A. P. 1968, Soviet Journal of Experimental and Theoretical Physics, 26, 1031

Kazeroni, R., Guilet, J., & Foglizzo, T. 2016, MNRAS, 456, 126

Kazeroni, R., Guilet, J., & Foglizzo, T. 2017, MNRAS, 471, 914

Kazeroni, R., Krueger, B. K., Guilet, J., Foglizzo, T., & Pomarède, D. 2018, MNRAS, 480, 261

Keil, W., Janka, H. T., & Mueller, E. 1996, ApJ, 473, L111

Kelly, D. C. 1973, ApJ, 179, 599

Kennedy, C. A. & Carpenter, M. H. 2003, Applied Numerical Mathematics, 44, 139

Kern, B. & Martin, C. 2002, Nature, 417, 527

Keszthelyi, Z., Meynet, G., Martins, F., de Koter, A., & David-Uraz, A. 2021, MNRAS, 504, 2474

Keszthelyi, Z., Meynet, G., Shultz, M. E., et al. 2020, MNRAS, 493, 518

Kirillov, O. N., Stefani, F., & Fukumoto, Y. 2014, Journal of Fluid Mechanics, 760, 591

Kiuchi, K., Reboul-Salze, A., Shibata, M., & Sekiguchi, Y. 2024, Nature Astronomy, 8, 298

Kjær, K., Leibundgut, B., Fransson, C., Jerkstrand, A., & Spyromilio, J. 2010, A&A, 517, A51

Knobloch, E. & Landsberg, A. S. 1996, MNRAS, 278, 294

Knobloch, E., Tobias, S. M., & Weiss, N. O. 1998, MNRAS, 297, 1123

Kochukhov, O., Shultz, M., & Neiner, C. 2019, A&A, 621, A47

Koliogiannis, P. S. & Moustakidis, C. C. 2019, Ap&SS, 364, 52

Korte, M. & Mandea, M. 2019, Geochemistry, Geophysics, Geosystems, 20, 3801

Kouveliotou, C. 1999, Proceedings of the National Academy of Science, 96, 5351

Kouveliotou, C., Dieters, S., Strohmayer, T., et al. 1998, Nature, 393, 235

Kouveliotou, C., Fishman, G. J., Meegan, C. A., et al. 1994, Nature, 368, 125

Kouveliotou, C., Strohmayer, T., Hurley, K., et al. 1999, ApJ, 510, L115

Kozyreva, A., Blinnikov, S., Langer, N., & Yoon, S. C. 2014, A&A, 565, A70

Krause, F. & Raedler, K. H. 1980, Mean-field magnetohydrodynamics and dynamo theory

Kriss, G. A., Becker, R. H., Helfand, D. J., & Canizares, C. R. 1985, ApJ, 288, 703

Kulkarni, S. R., Frail, D. A., Kassim, N. E., Murakami, T., & Vasisht, G. 1994, Nature, 368, 129

Kulkarni, S. R., Kaplan, D. L., Marshall, H. L., et al. 2003, ApJ, 585, 948

Kulsrud, R. M. & Zweibel, E. G. 2008, Reports on Progress in Physics, 71, 046901

Kumar, P. & Bošnjak, Ž. 2020, MNRAS, 494, 2385

Kuroda, T., Arcones, A., Takiwaki, T., & Kotake, K. 2020, ApJ, 896, 102

Lamb, R. C. & Markert, T. H. 1981, ApJ, 244, 94

Landau, L. D. 1932, Phys. Zs. Sowjet, 1, 285

Landeau, M., Aubert, J., & Olson, P. 2017, Earth and Planetary Science Letters, 465, 193

Landeau, M., Fournier, A., Nataf, H.-C., Cébron, D., & Schaeffer, N. 2022, Nature Reviews Earth and Environment, 3, 255

Lander, S. K. 2013, Phys. Rev. Lett., 110, 071101

Lander, S. K. 2021, MNRAS, 507, L36

Lander, S. K. 2023, ApJ, 947, L16

Lander, S. K., Andersson, N., Antonopoulou, D., & Watts, A. L. 2015, MNRAS, 449, 2047

Lander, S. K. & Gourgouliatos, K. N. 2019, MNRAS, 486, 4130

Langlais, B., Purucker, M. E., & Mandea, M. 2004, Journal of Geophysical Research (Planets), 109, E02008

Lantz, S. R. 1992, PhD thesis, Cornell University, New York

Larmor, J. 1919, Report of the British Association

Laros, J. G., Fenimore, E. E., Fikani, M. M., Klebesadel, R. W., & Barat, C. 1986, Nature, 322, 152

Laros, J. G., Fenimore, E. E., Klebesadel, R. W., et al. 1987, ApJ, 320, L111

Larson, R. B. 1969, MNRAS, 145, 271

Lattimer, J. M. & Schutz, B. F. 2005, ApJ, 629, 979

Lattimer, J. M. & Swesty, D. F. 1991, Nuc. Phys. A, 535, 331

Layek, B., Godaba Venkata, D., & Yadav, P. 2023, Phys. Rev. D, 107, 023004

Layek, B. & Yadav, P. R. 2020, MNRAS, 499, 455

Lee, T. D. 1950, The Astrophysical Journal, 111, 625

Leidi, G., Andrassy, R., Higl, J., Edelmann, P. V. F., & Röpke, F. K. 2023, A&A, 679, A132

Lenters, G. T., Woods, P. M., Goupell, J. E., et al. 2003, ApJ, 587, 761

Lesur, G. & Ogilvie, G. I. 2008, A&A, 488, 451

Levin, L., Bailes, M., Bates, S., et al. 2010, ApJ, 721, L33

Li, G., Deheuvels, S., Ballot, J., & Lignières, F. 2022, Nature, 610, 43

Li, G., Deheuvels, S., Li, T., Ballot, J., & Lignières, F. 2023, A&A, 680, A26

Li, X.-D. 2007, ApJ, 666, L81

Lin, W., Wang, X., Wang, L., & Dai, Z. 2021, ApJ, 914, L2

Lin, W. L., Wang, X. F., Wang, L. J., & Dai, Z. G. 2020, ApJ, 903, L24

Lingam, M. & Loeb, A. 2017, ApJ, 837, L23

Liu, H. & Zou, J. 2006, Journal of Computational and Applied Mathematics, 190, 74, special Issue: International Conference on Mathematics and its Application

Livingstone, M. A., Kaspi, V. M., & Gavriil, F. P. 2010, ApJ, 710, 1710

Lorimer, D. R., Bailes, M., McLaughlin, M. A., Narkevic, D. J., & Crawford, F. 2007, Science, 318, 777

Lü, H.-J. & Zhang, B. 2014, ApJ, 785, 74

Lu, W., Kumar, P., & Zhang, B. 2020, MNRAS, 498, 1397

Lynch, R. S., Archibald, R. F., Kaspi, V. M., & Scholz, P. 2015, ApJ, 806, 266

Lyubarsky, Y. 2020, ApJ, 897, 1

Lyutikov, M. 2006, MNRAS, 367, 1594

Ma, L. & Fuller, J. 2019, MNRAS, 488, 4338

Makarenko, E. I., Igoshev, A. P., & Kholtygin, A. F. 2021, MNRAS, 504, 5813

Makishima, K., Enoto, T., Hiraga, J. S., et al. 2014, Phys. Rev. Lett., 112, 171102

Makishima, K., Enoto, T., Murakami, H., et al. 2016, Publi. of the Astrophys. Soc. of Japan, 68, S12

Makishima, K., Enoto, T., Yoneda, H., & Odaka, H. 2021, MNRAS, 502, 2266

Makishima, K., Murakami, H., Enoto, T., & Nakazawa, K. 2019, Publi. of the Astrophys. Soc. of Japan, 71, 15

Marchant, P. & Moriya, T. J. 2020, A&A, 640, L18

Margalit, B., Metzger, B. D., & Sironi, L. 2020, MNRAS, 494, 4627

Margalit, B., Metzger, B. D., Thompson, T. A., Nicholl, M., & Sukhbold, T. 2018, MNRAS, 475, 2659

Markey, P. & Tayler, R. J. 1973, MNRAS, 163, 77

Martin, J., Rea, N., Torres, D. F., & Papitto, A. 2014, MNRAS, 444, 2910

Masada, Y., Takiwaki, T., & Kotake, K. 2022, ApJ, 924, 75

Masada, Y., Takiwaki, T., Kotake, K., & Sano, T. 2012, ApJ, 759, 110

Mazets, E. P., Golenetskii, S. V., Ilinskii, V. N., et al. 1981, Ap&SS, 80, 3

Mazets, E. P., Golenetskii, S. V., Il'Inskii, V. N., et al. 1979a, Soviet Astronomy Letters, 5, 163

Mazets, E. P., Golenetskij, S. V., & Guryan, Y. A. 1979b, Soviet Astronomy Letters, 5, 343

Mazets, E. P., Golentskii, S. V., Ilinskii, V. N., Aptekar, R. L., & Guryan, I. A. 1979c, Nature, 282, 587

Mazzali, P. A., McFadyen, A. I., Woosley, S. E., Pian, E., & Tanaka, M. 2014, MNRAS, 443, 67

Meduri, D. G., Jouve, L., & Lignières, F. 2024, A&A, 683, A12

Mereghetti, S., Esposito, P., Tiengo, A., et al. 2006, ApJ, 653, 1423

Mereghetti, S., Pons, J. A., & Melatos, A. 2015, Space Sci. Rev., 191, 315

Mereghetti, S., Rigoselli, M., Salvaterra, R., et al. 2024, Nature

Mereghetti, S., Savchenko, V., Ferrigno, C., et al. 2020, ApJ, 898, L29

Mereghetti, S., Tiengo, A., Esposito, P., et al. 2005, ApJ, 628, 938

Mestel, L. 2001, in Astronomical Society of the Pacific Conference Series, Vol. 248, Magnetic Fields Across the Hertzsprung-Russell Diagram, ed. G. Mathys, S. K. Solanki, & D. T. Wickramasinghe, 3

Metzger, B. D., Beniamini, P., & Giannios, D. 2018, ApJ, 857, 95

Metzger, B. D., Margalit, B., Kasen, D., & Quataert, E. 2015, MNRAS, 454, 3311

Metzger, B. D., Margalit, B., & Sironi, L. 2019, MNRAS, 485, 4091

Metzger, B. D., Quataert, E., & Thompson, T. A. 2008, MNRAS, 385, 1455

Meynet, G., Eggenberger, P., & Maeder, A. 2011, A&A, 525, L11

Mezzacappa, A., Marronetti, P., Landfield, R. E., et al. 2020, Phys. Rev. D, 102, 023027

Milisavljevic, D., Margutti, R., Parrent, J. T., et al. 2015, ApJ, 799, 51

Mingarelli, C. M. F., Levin, J., & Lazio, T. J. W. 2015, ApJ, 814, L20

Mininni, P. D., Gómez, D. O., & Mahajan, S. M. 2005, ApJ, 619, 1019

Mitchell, J. P., Braithwaite, J., Reisenegger, A., et al. 2015, MNRAS, 447, 1213

Moffatt, H. K. 1970, Journal of Fluid Mechanics, 41, 435

Moffatt, H. K. 1978, Magnetic field generation in electrically conducting fluids

Moffatt, H. K. & Proctor, M. R. E. 1982, Geophysical and Astrophysical Fluid Dynamics, 21, 265

Moffatt, H. K. & Saffman, P. G. 1964, Physics of Fluids, 7, 155

Moffatt, K. & Dormy, E. 2019, Self-exciting fluid dynamos, Vol. 59 (Cambridge University Press)

Monchaux, R., Berhanu, M., Aumaître, S., et al. 2009, Physics of Fluids, 21, 035108

Monchaux, R., Berhanu, M., Bourgoin, M., et al. 2007, Phys. Rev. Lett., 98, 044502

Mosser, B., Goupil, M. J., Belkacem, K., et al. 2012, A&A, 548, A10

Most, E. R., Nathanail, A., & Rezzolla, L. 2018, ApJ, 864, 117

Mösta, P., Ott, C. D., Radice, D., et al. 2015, Nature, 528, 376

Mösta, P., Richers, S., Ott, C. D., et al. 2014, ApJ, 785, L29

Moyano, F. D., Eggenberger, P., & Salmon, S. J. A. J. 2024, A&A, 681, L16

Muş, S. Ş., , S., Göğüş, E., et al. 2015, ApJ, 807, 42

Müller, B. 2023, MNRAS, 526, 2880

Muno, M. P., Clark, J. S., Crowther, P. A., et al. 2006, ApJ, 636, L41

Muno, M. P., Gaensler, B. M., Clark, J. S., et al. 2007, MNRAS, 378, L44

Ng, C. Y., Romani, R. W., Brisken, W. F., Chatterjee, S., & Kramer, M. 2007, ApJ, 654, 487

Nicholl, M., Smartt, S. J., Jerkstrand, A., et al. 2013, Nature, 502, 346

Nimmo, K., Hessels, J. W. T., Kirsten, F., et al. 2022, Nature Astronomy, 6, 393

Nomoto, K., Maeda, K., Tanaka, M., & Suzuki, T. 2011, Astrophys. Science Sci., 336, 129

Nousek, J. A., Kouveliotou, C., Grupe, D., et al. 2006, ApJ, 642, 389

Oberbeck, A. 1879, Annalen der Physik, 243, 271

Obergaulinger, M. & Aloy, M. Á. 2017, MNRAS, 469, L43

Obergaulinger, M. & Aloy, M. Á. 2020, MNRAS, 492, 4613

Obergaulinger, M. & Aloy, M. Á. 2021, MNRAS, 503, 4942

Obergaulinger, M. & Aloy, M. Á. 2022, MNRAS, 512, 2489

Obergaulinger, M., Cerdá-Durán, P., Müller, E., & Aloy, M. A. 2009, A&A, 498, 241

O'Brien, P. T., Willingale, R., Osborne, J., et al. 2006, ApJ, 647, 1213

Ofek, E. O., Muno, M., Quimby, R., et al. 2008, ApJ, 681, 1464

Olausen, S. A. & Kaspi, V. M. 2014, ApJS, 212, 6

Orszag, S. A. 1970, Journal of the Atmospheric Sciences, 27, 890

Ott, C. D., Burrows, A., Thompson, T. A., Livne, E., & Walder, R. 2006, ApJS, 164, 130

Otto, K., Oertel, M., & Schaefer, B.-J. 2020, European Physical Journal Special Topics, 229, 3629

Ouazzani, R. M., Marques, J. P., Goupil, M. J., et al. 2019, A&A, 626, A121

Paczynski, B. 1992, Acta Astron., 42, 145

Page, K. L., Barthelmy, S. D., Klingler, N. J., Kuin, N. P. M., & Lien, A. Y. 2020, The Astronomer's Telegram, 14083, 1

Parker, E. N. 1955, ApJ, 121, 491

Pascal, A. 2021, Theses, Université Paris sciences et lettres

Pascal, A., Novak, J., & Oertel, M. 2022, MNRAS, 511, 356

Pavlov, G. G., Zavlin, V. E., Aschenbach, B., Trümper, J., & Sanwal, D. 2000, ApJ, 531, L53

Paxton, B., Bildsten, L., Dotter, A., et al. 2011, ApJS, 192, 3

Paxton, B., Cantiello, M., Arras, P., et al. 2013, ApJS, 208, 4

Paxton, B., Marchant, P., Schwab, J., et al. 2015, ApJS, 220, 15

Paxton, B., Schwab, J., Bauer, E. B., et al. 2018, ApJS, 234, 34

Paxton, B., Smolec, R., Schwab, J., et al. 2019, ApJS, 243, 10

Perna, R. & Pons, J. A. 2011, ApJ, 727, L51

Petitdemange, L., Marcotte, F., & Gissinger, C. 2023, Science, 379, 300

Petitdemange, L., Marcotte, F., Gissinger, C., & Daniel, F. 2024, A&A, 681, A75

Pétrélis, F., Fauve, S., Dormy, E., & Valet, J.-P. 2009, Phys. Rev. Lett., 102, 144503

Petroff, E., Hessels, J. W. T., & Lorimer, D. R. 2019, A&A Rev., 27, 4

Petroff, E., Hessels, J. W. T., & Lorimer, D. R. 2022, A&A Rev., 30, 2

Philidet, J., Gissinger, C., Lignières, F., & Petitdemange, L. 2020, Geophysical and Astrophysical Fluid Dynamics, 114, 336

Pignata, G., Stritzinger, M., Soderberg, A., et al. 2011, ApJ, 728, 14

Pinçon, C., Petitdemange, L., Raynaud, R., et al. 2024, arXiv e-prints, arXiv:2403.08405

Pons, J. A., Reddy, S., Prakash, M., Lattimer, J. M., & Miralles, J. A. 1999, ApJ, 513, 780

Pons, J. A. & Viganò, D. 2019, Living Reviews in Computational Astrophysics, 5, 3

Popov, S. B. & Turolla, R. 2012, Ap&SS, 341, 457

Potter, A. T., Chitre, S. M., & Tout, C. A. 2012, MNRAS, 424, 2358

Pouquet, A., Frisch, U., & Leorat, J. 1976, Journal of Fluid Mechanics, 77, 321

Powell, J. & Müller, B. 2020, MNRAS, 494, 4665

Prat, V., Mathis, S., Neiner, C., et al. 2020, A&A, 636, A100

Racine, É., Charbonneau, P., Ghizaru, M., Bouchat, A., & Smolarkiewicz, P. K. 2011, ApJ, 735, 46

Radice, D., Morozova, V., Burrows, A., Vartanyan, D., & Nagakura, H. 2019, ApJ, 876, L9

Rädler, K. H. 1969a, Veroeffentlichungen der Geod. Geophys, 13, 131

Rädler, K. H. 1969b, Monatsber. Deutsch. Akad Wissenschaftliche Berlin, 11, 194

Raduta, A. & Gulminelli, F. 2019a, Nuclear Physics A, 983, 252

Raduta, A. & Gulminelli, F. 2019b, Nuclear Physics A, 983, 252

Rahman, N., Janka, H. T., Stockinger, G., & Woosley, S. E. 2022, MNRAS, 512, 4503

Rakavy, G. & Shaviv, G. 1967, ApJ, 148, 803

Ravelet, F., Berhanu, M., Monchaux, R., et al. 2008, Phys. Rev. Lett., 101, 074502

Rayleigh, L. 1916, The London, Edinburgh, and Dublin Philosophical Magazine and Journal of Science, 32, 529

Raynaud, R., Cerdá-Durán, P., & Guilet, J. 2022, MNRAS, 509, 3410

Raynaud, R., Guilet, J., Janka, H.-T., & Gastine, T. 2020, Sci. Adv., 6, eaay2732

Raynaud, R., Petitdemange, L., & Dormy, E. 2015, MNRAS, 448, 2055

Raynaud, R. & Tobias, S. M. 2016, J. Fluid Mech., 799, R6

Rea, N., Borghese, A., Esposito, P., et al. 2016, ApJ, 828, L13

Rea, N., Esposito, P., Turolla, R., et al. 2010, Science, 330, 944

Rea, N., Israel, G. L., Esposito, P., et al. 2012a, ApJ, 754, 27

Rea, N., Israel, G. L., Pons, J. A., et al. 2013, ApJ, 770, 65

Rea, N., Pons, J. A., Torres, D. F., & Turolla, R. 2012b, ApJ, 748, L12

Rea, N., Testa, V., Israel, G. L., et al. 2004, A&A, 425, L5

Rea, N., Viganò, D., Israel, G. L., Pons, J. A., & Torres, D. F. 2014, ApJ, 781, L17

Reboul-Salze, A., Guilet, J., Raynaud, R., & Bugli, M. 2021, A&A, 645, A109

Reboul-Salze, A., Guilet, J., Raynaud, R., & Bugli, M. 2022, A&A, 667, A94

Reichley, P. E. & Downs, G. S. 1969, Nature, 222, 229

Reiners, A. 2012, Living Reviews in Solar Physics, 9, 1

Renzo, M., Farmer, R., Justham, S., et al. 2020, A&A, 640, A56

Rheinhardt, M. & Geppert, U. 2002, Phys. Rev. Lett., 88, 101103

Richardson, D., Branch, D., Casebeer, D., et al. 2002, AJ, 123, 745

Rincon, F. 2019, Journal of Plasma Physics, 85, 205850401

Rincon, F., Ogilvie, G. I., & Proctor, M. R. E. 2007, Phys. Rev. Lett., 98, 254502

Rincon, F., Ogilvie, G. I., Proctor, M. R. E., & Cossu, C. 2008, Astronomische Nachrichten, 329, 750

Riols, A. 2014, Theses, Université Toulouse 3Paul Sabatier

Riols, A., Rincon, F., Cossu, C., et al. 2013, Journal of Fluid Mechanics, 731, 1

Riols, A., Rincon, F., Cossu, C., et al. 2017, A&A, 598, A87

Roberts, L. F. 2012, PhD thesis, University of California, Santa Cruz

Roberts, L. F. & Reddy, S. 2017, 1605

Roberts, P. H. & Soward, A. M. 1972, Annual Review of Fluid Mechanics, 4, 117

Rodríguez Castillo, G. A., Israel, G. L., Tiengo, A., et al. 2016, MNRAS, 456, 4145

Rogachevskii, I. & Kleeorin, N. 2003, Phys. Rev. E, 68, 036301

Romani, R. W. & Ng, C. Y. 2003, ApJ, 585, L41

Ronchi, M., Rea, N., Graber, V., & Hurley-Walker, N. 2022, ApJ, 934, 184

Rothschild, R. E., Kulkarni, S. R., & Lingenfelter, R. E. 1994, Nature, 368, 432

Routray, T. R., Sahoo, S., Viñas, X., Basu, D. N., & Centelles, M. 2024, arXiv e-prints, arXiv:2404.05910

Ruderman, M. 1976, ApJ, 203, 213

Rüdiger, G., Gellert, M., Hollerbach, R., Schultz, M., & Stefani, F. 2018, Phys. Rep., 741, 1

Rüdiger, G. & Kitchatinov, L. L. 2010, Geophysical and Astrophysical Fluid Dynamics, 104, 273

Rüdiger, G. & Schultz, M. 2010, Astronomische Nachrichten, 331, 121

Sana, H., de Mink, S. E., de Koter, A., et al. 2012, Science, 337, 444

Schaeffer, N. 2013, Geochemistry, Geophysics, Geosystems, 14, 751

Schlüter, A. & Biermann, L. 1950, Zeitschrift Naturforschung Teil A, 5, 237

Schneider, F. R. N., Ohlmann, S. T., Podsiadlowski, P., et al. 2020, MNRAS, 495, 2796

Schneider, F. R. N., Ohlmann, S. T., Podsiadlowski, P., et al. 2019, Nature, 574, 211

Schöller, M., Hubrig, S., Fossati, L., et al. 2017, A&A, 599, A66

Scholz, P., Ng, C. Y., Livingstone, M. A., et al. 2012, ApJ, 761, 66

Schönberg, M. & Chandrasekhar, S. 1942, ApJ, 96, 161

Schrinner, M., Petitdemange, L., Raynaud, R., & Dormy, E. 2014, A&A, 564, A78

Schrinner, M., Rädler, K. H., Schmitt, D., Rheinhardt, M., & Christensen, U. 2005, Astronomische Nachrichten, 326, 245

Schrinner, M., Rädler, K.-H., Schmitt, D., Rheinhardt, M., & Christensen, U. R. 2007, Geophysical and Astrophysical Fluid Dynamics, 101, 81

Schwaiger, T., Gastine, T., & Aubert, J. 2019, Geophysical Journal International, 219, S101

Seilmayer, M., Stefani, F., Gundrum, T., et al. 2012, Phys. Rev. Lett., 108, 244501

Seshasayanan, K. & Gallet, B. 2019, J. Fluid Mech., 864, 971

Seward, F. D., Charles, P. A., & Smale, A. P. 1986, ApJ, 305, 814

Shannon, R. M. & Johnston, S. 2013, MNRAS, 435, L29

Shen, H., Toki, H., Oyamatsu, K., & Sumiyoshi, K. 1998a, Nuc. Phys. A, 637, 435

Shen, H., Toki, H., Oyamatsu, K., & Sumiyoshi, K. 1998b, Progress of Theoretical Physics, 100, 1013

Shen, H., Toki, H., Oyamatsu, K., & Sumiyoshi, K. 2011, ApJS, 197, 20

Shenar, T., Wade, G. A., Marchant, P., et al. 2023, Science, 381, 761

Shull, P., J. 1983, ApJ, 275, 611

Shultz, M. E., Wade, G. A., Rivinius, T., et al. 2019a, MNRAS, 490, 274

Shultz, M. E., Wade, G. A., Rivinius, T., et al. 2019b, MNRAS, 485, 1508

Shultz, M. E., Wade, G. A., Rivinius, T., et al. 2018, MNRAS, 475, 5144

Sikora, J., Wade, G. A., Power, J., & Neiner, C. 2019, MNRAS, 483, 3127

Simard, C., Charbonneau, P., & Dubé, C. 2016, Advances in Space Research, 58, 1522

Sinha, M. & Sedrakian, A. 2015, Phys. Rev. C, 91, 035805

Snelders, M. P., Nimmo, K., Hessels, J. W. T., et al. 2023, Nature Astronomy, 7, 1486

Spada, F., Gellert, M., Arlt, R., & Deheuvels, S. 2016, A&A, 589, A23

Spruit, H. C. 1999, A&A, 349, 189

Spruit, H. C. 2002, A&A, 381, 923

Spruit, H. C. 2008, 983, 391

Stanley, S., Elkins-Tanton, L., Zuber, M. T., & Parmentier, E. M. 2008, Science, 321, 1822

Steenbeck, M., Krause, F., & Rädler, K. H. 1966, Zeitschrift Naturforschung Teil A, 21, 369

Stockinger, G., Janka, H. T., Kresse, D., et al. 2020, MNRAS, 496, 2039

Strohmayer, T. E. & Watts, A. L. 2005, ApJ, 632, L111

Strugarek, A., Beaudoin, P., Charbonneau, P., & Brun, A. S. 2018, ApJ, 863, 35

Strugarek, A., Beaudoin, P., Charbonneau, P., Brun, A. S., & do Nascimento, J. D. 2017, Science, 357, 185

Subramanian, K. 2019, Galaxies, 7, 47

Subramanian, K. & Brandenburg, A. 2014, MNRAS, 445, 2930

Sukhbold, T., Ertl, T., Woosley, S. E., Brown, J. M., & Janka, H. T. 2016, ApJ, 821, 38

Sukhbold, T. & Woosley, S. E. 2014, ApJ, 783, 10

Sukhbold, T., Woosley, S. E., & Heger, A. 2018, ApJ, 860, 93

Summa, A., Janka, H.-T., Melson, T., & Marek, A. 2018, ApJ, 852, 28

Suwa, Y. & Tominaga, N. 2015, MNRAS, 451, 282

Svinkin, D., Frederiks, D., Hurley, K., et al. 2021, Nature, 589, 211

Szklarski, J. & Arlt, R. 2013, A&A, 550, A94

Taddia, F., Sollerman, J., Fremling, C., et al. 2019, A&A, 621, A71

Takiwaki, T., Kotake, K., & Foglizzo, T. 2021, MNRAS, 508, 966

Takiwaki, T., Kotake, K., & Sato, K. 2009, ApJ, 691, 1360

Tam, C. R., Gavriil, F. P., Dib, R., et al. 2008, ApJ, 677, 503

Tam, C. R., Kaspi, V. M., van Kerkwijk, M. H., & Durant, M. 2004, ApJ, 617, L53

Taverna, R. & Turolla, R. 2024, Galaxies, 12, 6

Tayler, R. J. 1973, MNRAS, 161, 365

Tendulkar, S. P., Cameron, P. B., & Kulkarni, S. R. 2012, ApJ, 761, 76

Tendulkar, S. P., Cameron, P. B., & Kulkarni, S. R. 2013, ApJ, 772, 31

Testa, V., Rea, N., Mignani, R. P., et al. 2008, A&A, 482, 607

Thompson, C. & Duncan, R. C. 1993, ApJ, 408, 194

Thompson, C. & Duncan, R. C. 1995, MNRAS, 275, 255

Thompson, C. & Duncan, R. C. 1996, ApJ, 473, 322

Thornton, D., Stappers, B., Bailes, M., et al. 2013, Science, 341, 53

Tiengo, A., Esposito, P., Mereghetti, S., et al. 2013, Nature, 500, 312

Tobias, S. M. 1996, ApJ, 467, 870

Tobias, S. M. 2021, Journal of Fluid Mechanics, 912, P1

Tobias, S. M., Cattaneo, F., & Brummell, N. H. 2011, ApJ, 728, 153

Tolstov, A., Nomoto, K., Blinnikov, S., et al. 2017, ApJ, 835, 266

Totani, T. 2013, PASJ, 65, L12

Truemper, J., Pietsch, W., Reppin, C., et al. 1978, ApJ, 219, L105

Turolla, R., Zane, S., Pons, J. A., Esposito, P., & Rea, N. 2011, ApJ, 740, 105

Vainshtein, S. I. & Kichatinov, L. L. 1983, Geophysical and Astrophysical Fluid Dynamics, 24, 273

Valerin, G., Pumo, M. L., Pastorello, A., et al. 2022, MNRAS, 513, 4983

van der Horst, A. J., Connaughton, V., Kouveliotou, C., et al. 2010, ApJ, 711, L1

van der Horst, A. J., Kouveliotou, C., Gorgone, N. M., et al. 2012, ApJ, 749, 122

van Paradijs, J., Taam, R. E., & van den Heuvel, E. P. J. 1995, A&A, 299, L41

Varma, V. & Müller, B. 2023, MNRAS, 526, 5249

Vasil, G. M., Lecoanet, D., Augustson, K., et al. 2024, Nature, 628, 769

Vaĭnshteĭn, S. I. & Zel'dovich, Y. B. 1972, Soviet Physics Uspekhi, 15, 159

Vaĭnshteĭn, S. I. 1970, Soviet Journal of Experimental and Theoretical Physics, 31, 87

Viganò, D., Garcia-Garcia, A., Pons, J. A., Dehman, C., & Graber, V. 2021, Computer Physics Communications, 265, 108001

Viganò, D., Rea, N., Pons, J. A., et al. 2013, MNRAS, 434, 123

Vink, J. & Kuiper, L. 2006, MNRAS, 370, L14

Vogl, C. J., Steyer, A., Reynolds, D. R., Ullrich, P. A., & Woodward, C. S. 2019, Journal of Advances in Modeling Earth Systems, 11, 4228

Walk, L., Foglizzo, T., & Tamborra, I. 2023, Phys. Rev. D, 107, 063014

Wang, L. & Wheeler, J. C. 1998, ApJ, 504, L87

Wang, Z., Bassa, C., Kaspi, V. M., Bryant, J. J., & Morrell, N. 2008, ApJ, 679, 1443

Weiss, N. O. 2005, Astronomische Nachrichten, 326, 157

Wheeler, J. C., Kagan, D., & Chatzopoulos, E. 2015, ApJ, 799, 85

Wheeler, J. C., Yi, I., Höflich, P., & Wang, L. 2000, ApJ, 537, 810

White, C. J., Burrows, A., Coleman, M. S. B., & Vartanyan, D. 2022, ApJ, 926, 111

Wicht, J. 2002, Physics of the Earth and Planetary Interiors, 132, 281

Woods, P. M., Kouveliotou, C., van Paradijs, J., et al. 1999, ApJ, 524, L55

Woosley, S. E. 1993, ApJ, 405, 273

Woosley, S. E. 2010, ApJ, 719, L204

Woosley, S. E. & Bloom, J. S. 2006, ARAA, 44, 507

Woosley, S. E. & Heger, A. 2021, ApJ, 912, L31

Wright, G. A. E. 1973, MNRAS, 162, 339

Yamasaki, T. & Foglizzo, T. 2008, ApJ, 679, 607

Yao, J., Zhu, W., Manchester, R. N., et al. 2021, Nature Astronomy, 5, 788

Yao, J. M., Manchester, R. N., & Wang, N. 2017, ApJ, 835, 29

Younes, G., Guver, T., Wadiasingh, Z., et al. 2020, The Astronomer's Telegram, 14086, 1

Younes, G., Kouveliotou, C., Jaodand, A., et al. 2017, ApJ, 847, 85

Zahn, J. P., Brun, A. S., & Mathis, S. 2007, A&A, 474, 145

Zaire, B., Jouve, L., Gastine, T., et al. 2022, MNRAS, 517, 3392

Zane, S., Taverna, R., González-Caniulef, D., et al. 2023, ApJ, 944, L27

Zavlin, V. E., Pavlov, G. G., Sanwal, D., & Trümper, J. 2000, ApJ, 540, L25

Zeldovich, I. B. & Ruzmaikin, A. A. 1956, Zh. Eksp. Teor. Fiz., 31, 154

Zel'dovich, Y. B., Ruzmaikin, A. A., Molchanov, S. A., & Sokolov, D. D. 1984, Journal of Fluid Mechanics, 144, 1

Zhang, B. 2014, ApJ, 780, L21

Zhang, B., Fan, Y. Z., Dyks, J., et al. 2006, ApJ, 642, 354

Zhou, P., Vink, J., Safi-Harb, S., & Miceli, M. 2019, A&A, 629, A51